
1227

TRANSPORTATION RESEARCH RECORD

Rigid and Flexible Pavement Design and Analysis

*Unbound Granular Materials, Tire
Pressures, Backcalculation, and
Design Methods*

TRANSPORTATION RESEARCH BOARD
NATIONAL RESEARCH COUNCIL
WASHINGTON, D.C. 1989

Transportation Research Record 1227
Price: \$32.00

mode
1 highway transportation

subject areas
21 facilities design
24 pavement design and performance
54 operations and traffic control

TRB Publications Staff

Director of Publications: Nancy A. Ackerman
Senior Editor: Edythe T. Crump
Associate Editors: Naomi C. Kassabian
Ruth S. Pitt
Alison G. Tobias
Production Editor: Kieran P. O'Leary
Graphics Coordinator: Karen L. White
Office Manager: Phyllis D. Barber
Production Assistant: Betty L. Hawkins

Printed in the United States of America

Library of Congress Cataloging-in-Publication Data
National Research Council. Transportation Research Board.

Rigid and flexible pavement design and analysis : unbound granular materials, tire pressures, backcalculation, and design methods.
p. cm.—(Transportation research record, ISSN 0361-1981 ; 1227)

Papers presented at the 68th annual meeting of the Transportation Research Board.

ISBN 0-309-04822-2

1. Pavements, Concrete—Design and construction. 2. Pavements, Asphalt concrete—Design and construction. 3. Pavements, Concrete—Testing. 4. Pavements, Asphalt concrete—Testing. I. National Research Council (U.S.). Transportation Research Board. Meeting (68th : 1989 : Washington, D.C.) II. Series.

TE7.H5 no. 1227

[TE278]

388 s dc20

[625.8'4]

90-5785
CIP

Sponsorship of Transportation Research Record 1227

GROUP 2—DESIGN AND CONSTRUCTION OF TRANSPORTATION FACILITIES

Chairman: Raymond A. Forsyth, California Department of Transportation

Pavement Management Section

Chairman: R. G. Hicks, Oregon State University

Committee on Rigid Pavement Design

Chairman: Walter P. Kilaeski, The Pennsylvania State University
Ernest J. Barenberg, Albert J. Bush III, Robert R. Costigan, Ray H. Fowler, Kathleen Theresa Hall, David J. Halpenny, Amir N. Hanna, Michael P. Jones, T. J. Larsen, Jo A. Lary, Robert R. Long, Jr., Richard A. McComb, B. Frank McCullough, John Minor, Theodore L. Neff, Thomas J. Pasko, Jr., Mauricio Poblete, Michel Ray, Surendra K. Saxena, Gary Wayne Sharpe, Shiraz D. Tayabji, Mang Tia, James H. Woodstrom, William A. Yrjanson, John P. Zaniewski

Committee on Flexible Pavement Design

Chairman: Joe P. Mahoney, University of Washington
Secretary: James A. Sherwood, Federal Highway Administration
Douglas I. Anderson, Chris A. Bell, Jacques Bonnot, Elton R. Brown, James L. Brown, Stephen F. Brown, George R. Cochran, N. F. Coetzee, David C. Esch, C. R. Freeme, Newton Jackson, W. N. Lofroos, Kenneth H. McGhee, Carl L. Monismith, William A. Nokes, Adrian Pelzner, William A. Phang, John L. Rice, James A. Scherocman, James F. Shook, Herbert F. Southgate, T. Paul Teng, Marshall R. Thompson, Harry H. Ulery, Jr.

Committee on Strength and Deformation Characteristics of Pavements

Chairman: J. Brent Rauhut, Brent Rauhut Engineering, Inc.
Mark Anderson, Gilbert Y. Baladi, Richard D. Barksdale, Stephen F. Brown, Albert J. Bush III, Yu T. Chou, George R. Cochran, Billy G. Connor, Mark P. Gardner, Amir N. Hanna, R. G. Hicks, Lynne H. Irwin, William J. Kenis, Thomas W. Kennedy, Robert L. Lytton, Michael S. Mamlouk, Frank Meyer, Lutfi Raad, Richard B. Rogers, Byron E. Ruth, Stephen B. Seeds, Roger E. Smith, R. N. Stubstad, Marshall R. Thompson, Per Ullidtz, Jacob Uzan, Thomas D. White

George W. Ring III, Transportation Research Board staff

Sponsorship is indicated by a footnote at the end of each paper. The organizational units, officers, and members are as of December 31, 1988.

NOTICE: The Transportation Research Board does not endorse products or manufacturers. Trade and manufacturers' names appear in this Record because they are considered essential to its object.

Transportation Research Board publications are available by ordering directly from TRB. They may also be obtained on a regular basis through organizational or individual affiliation with TRB; affiliates or library subscribers are eligible for substantial discounts. For further information, write to the Transportation Research Board, National Research Council, 2101 Constitution Avenue, N.W., Washington, D.C. 20418.

Transportation Research Record 1227

Contents

Foreword	vii
<hr/>	
Temperature Curling in Rigid Pavements: An Application of Dimensional Analysis	1
<i>Anastasios M. Ioannides and Ricardo A. Salsilli-Murua</i>	
<hr/>	
Field Performance Review of Unbonded Jointed Concrete Overlays	12
<i>G. F. Voigt, Michael I. Darter, and Sam Carpenter</i>	
<hr/>	
Performance Evaluation of Experimental Pavement Designs at Clare, Michigan	24
<i>David G. Peshkin, Kurt D. Smith, Michael I. Darter, and Charles J. Arnold</i>	
<hr/>	
Probabilistic Design of Flexible and Rigid Pavements Using AASHTO Equations	34
<i>Adnan A. Basma and Adli H. Al-Balbissi</i>	
<hr/>	
Evaluating Structural Damage of Flexible Pavements Using Cracking and Falling Weight Deflectometer Data	44
<i>Peter Sebaaly, Nader Tabatabaee, Ramon Bonaquist, and David Anderson</i>	
<hr/>	
Analysis of Full-Depth Asphalt Concrete Pavements Using Shakedown Theory	53
<i>Lutfi Raad, Dieter Weichert, and Ali Haidar</i>	
<hr/>	
Effects of Transverse Distribution of Heavy Vehicles on Thickness Design of Full-Depth Asphalt Pavements	66
<i>R. Buiter, W. M. H. Cortenraad, A. C. van Eck, and H. van Rij</i>	
<hr/>	

Fatigue Life and Permanent Deformation Characteristics of Asphalt Concrete Mixes <i>Gilbert Baladi</i>	75
Fatigue Model to Assess Pavement Damage <i>Shekhar Govind and C. Michael Walton</i>	88
Effect of Tire Pressure on Flexible Pavement Response and Performance <i>Ramon Bonaquist, Roger Surdahl, and Walla Mogawer</i>	97
Effects of Tires and Tire Pressures on Road Pavements <i>Matti Huhtala, Jari Pihlajamäki, and Markku Pienimäki</i>	107
Effect of Tire Pressure and Type on Response of Flexible Pavement <i>Peter Sebaaly and Nader Tabatabaee</i>	115
Improved Characterization Model for Granular Bases <i>Robert P. Elliott and Lourdesnathan David</i>	128
Rapid Shear Strength Evaluation of In Situ Granular Materials <i>Michael E. Ayers, Marshall R. Thompson, and Donald R. Uzarski</i>	134
Determination of Deflection of Pavement Systems Using Velocity Transducers <i>Soheil Nazarian and Albert J. Bush III</i>	147
Shakedown and Fatigue of Pavements with Granular Bases <i>Lutfi Raad, Dieter Weichert, and Ali Haidar</i>	159
Influence of Aggregate Shape on Base Behavior <i>Richard D. Barksdale and Samir Y. Itani</i>	173

Effects of Unknown Rigid Subgrade Layers on Back-Calculation of Pavement Moduli and Projections of Pavement Performance	183
<i>Robert C. Briggs and Soheil Nazarian</i>	
<hr/>	
Heavy Vehicle Evaluation for Overload Permits	194
<i>Walter P. Kilareski</i>	
<hr/>	
Development of a Rational Thickness Design Method for Rigid Pavements	205
<i>Chung-Lung Wu and Mang Tia</i>	
<hr/>	
Maximum Entropy Spectral Analysis of Transverse Crack Spacing in Continuously Reinforced Concrete Pavements	219
<i>Jian Lu, B. Frank McCullough, and C. L. Saraf</i>	

Foreword

The 21 papers in this Record are concerned with the design and performance of flexible and rigid pavements, including both laboratory and field performance evaluations, field and laboratory test methods, and new analytical tools. The papers should be of interest to pavement designers, pavement management engineers, and materials specialists.

On the subject of concrete pavements, Ioannides and Salsilli-Murua use dimensional analysis to mechanistically determine tensile bending stresses in concrete pavements due to the combined effects of thermal stresses, slab weight, and applied loads. When temperature differentials range from 15° to 40°F and the load-size ratio is 0.1, they find that tensile bending stresses are much higher than those predicted by the Westergaard solution. Voight et al. evaluate a nationwide survey of the performance of 14 unbonded concrete overlays. Their findings provide the basis for important design and construction recommendations. Peshkin et al. report on the performance of experimental concrete pavement sections having three types of base courses, skewed and perpendicular joints, edge drains, and dowelled and undowelled joints. Epoxy-coated dowels, edge drains, permeable base course, and sealed joints appear to be beneficial to concrete pavement performance. Wu and Tia describe a computer program to design and evaluate jointed concrete pavements to resist fatigue cracking. Using spectral analysis of crack spacing in continuously reinforced concrete pavements, Lu et al. suggest that the rate of change in uniformity of crack spacing can be related to the performance of these types of pavements and, further, that it is highly correlated with the type of aggregate in the concrete.

In the group of papers dealing with test methods and models, Basma and Al-Balbissi apply statistics and probability theory to AASHO Road Test data to illustrate how the pavement design process can be made more sensitive to many variables. Raad et al. use a numerical algorithm incorporating stress-dependent resilient modulus behavior of the subgrade to develop limiting criteria for vertical stresses and strains in an asphalt concrete pavement on top of the subgrade layer. Comparisons between shakedown (accumulation of plastic strain) and fatigue and rutting predictions are presented. Baladi describes a much improved indirect tensile strength test apparatus. Test results can be used to predict fatigue and plastic deformation of asphalt concrete pavements when several mixture parameters, the applied load, and mixture temperature are known. Govind and Walton develop an asphalt concrete pavement fatigue model by using the theory of wave propagation in an elastic medium. The model is calibrated using AASHO Road Test data. Nazarian and Bush present the limitations and advantages of theoretical alternatives available to determine the deflection-time history of pavements using geophones (velocity transducers). They present a case study of measurements and data analysis using a preferred method. In another paper by Raad et al., cyclic triaxial loadings are shown to condition test specimens so that no further consolidation takes place and fatigue resistance is increased. Briggs and Nazarian present a theoretical study in which it was determined that a rigid layer having a modulus no more than 4 times that of the subgrade will adversely affect the backcalculated pavement modulus when the rigid layer is less than 60 in. from the surface.

Tire pressures and loads are the subject of three papers. Bonaquist et al. present another paper in their series of reports on the FHWA accelerated loading facility (ALF). Surface deflections, surface strains, and strains at the bottom of the asphalt layer were measured under combinations of loads and tire pressures. Sebaaly and Tabatabaee, using the BISAR program, analyze asphalt concrete pavements to predict tensile strain at the bottom of the asphalt layer, compressive stress at the asphalt-layer interface, and surface deflection for laboratory-measured contact pressure distributions of underloaded, loaded, and overloaded radial, bias ply, and wide-base single tires. Buiter et al. describe the measurement of lateral distribution of trucks in the Netherlands and relate this distribution to the thickness design of asphalt pavements.

Sebaaly et al. and Kilaeski discuss pavement distress measurements and analyses. The former report that accelerated pavement loadings with the ALF indicate that structural capacity can decrease before it is manifested by surface cracking. Backcalculated moduli are reduced 50 percent before AASHO class 2 and 3 cracking appears at the surface. The latter describes a computer study of damage to flexible and rigid pavements subjected to overloads on four- and five-axle units. Stresses due to edge loading on concrete pavements and tensile strain at the bottom of asphalt concrete pavements were used as damage criteria.

Characterization of aggregates is the topic of another group of papers. Elliot and David develop a stress-ratio characterization model based on laboratory resilience tests. The stress-ratio model appears to be realistic for granular materials whose modulus decreases with an increasing level of stress. Ayers et al. compare results obtained by using a drop-weight cone penetrometer with triaxial test results. The penetrometer is less repeatable but is very rapid and permits the evaluation of larger volumes of material economically. Barksdale and Itani determined that a single triaxial test of aggregates confined by 6 psi pressure can be used to develop a rut index.

Temperature Curling in Rigid Pavements: An Application of Dimensional Analysis

ANASTASIOS M. IOANNIDES AND RICARDO A. SALSILLI-MURUA

This paper presents a closed-form solution to the problem of a slab-on-grade under combined temperature and wheel loading, derived on the basis of finite element results. This solution is in the form of a multiplication factor (function of the temperature differential) to be applied to the Westergaard equation to determine the maximum combined tensile stress in the slab under edge loading. In addition, a sound, engineering approach to numerical, experimental, and field data interpretation is proposed, founded on the principles of dimensional analysis. In view of the wide variety of available data, including those from the Strategic Highway Research Program and from finite element studies, the major problem confronting the profession today is no longer one of data availability, but one of data interpretation. In addressing this problem, the general trend in the last three decades has been to show an overwhelming preference for, and an unlimited confidence in, the results of sophisticated statistical analyses, without much consideration of the underlying engineering interactions among the host of input parameters involved. Although in a highly empirical field such as the study of pavement behavior regression techniques will always be an invaluable tool, the profession can benefit immensely by using dimensional analysis to determine the engineering dependent and independent variables to be examined. Without such exercise of engineering judgment, regression is lamentably bound to remain just that.

An analytical solution to the problem of a rigid pavement slab-on-grade under the combined action of a temperature gradient and externally applied wheel loads has not been forthcoming in recent years, despite considerable progress achieved in related areas. The major reason for this shortfall is the complexity introduced by the loss of support experienced by a curled slab, thereby rendering the principle of superposition inapplicable. Thus, it has long been recognized that merely summing up the stresses due to the applied wheel loads and those induced by curling (1,2) is an inadequate and often erroneous approach (3,4).

An obvious recourse to the lack of a closed-form solution would be to use data obtained from finite element (FE) or other numerical procedures and to verify such predictions by comparing them to actual field observations. Sophisticated FE codes are currently available for routine execution and can provide an enormous amount of pertinent information in a reasonable amount of time. In parallel, the Strategic Highway Research Program (SHRP) promises to supply a large variety of carefully collected in situ data that could also be used in this respect. Thus, the problem confronting the profession today is no longer one of data availability, but one of

data interpretation. This paper addresses the issue of data interpretation using the principles of dimensional analysis for the case of the problem at hand, although the concepts presented are applicable to many other areas of scientific endeavor.

DIMENSIONAL ANALYSIS AND DATA INTERPRETATION

The need for dimensional analysis in those areas where available analytical tools are not capable of yielding exact solutions and which, therefore, are heavily involved with numerical and empirical work, is well recognized in several branches of engineering—most notably in fluid mechanics. Consider, for instance, the comments of Roberson and Crowe (5). They stress that in such fields, "it is essential that researchers employ dimensionless parameters [for] analyzing model studies and for correlating the results of experimental research." For example, "by considering a nondimensional form of Bernoulli's equation we will have made a tremendous reduction in experimental work from that required before considering the nondimensional form. The process of nondimensionalizing the equation reduces the correlating parameters from five to two."

As a result, considerable time savings are realized with respect to data collection, because the nondimensional factorial is much smaller than its dimensional counterpart. Note that as with the Bernoulli equation, it is often possible to have "a clue about the governing equation" from previous theoretical investigations, which may themselves be incomplete. Nonetheless, "by considering the dimensionless form of that equation, we [are] able to obtain a set of dimensionless parameters with which to correlate our data" (5).

Dimensional analysis is not unknown in transportation facilities studies. It is encountered in the works of such notable pioneers as Westergaard, Bradbury, Burmister, Odemark, Pickett, and Losberg, to name a few, although this is often done in passing and in a nonsystematic fashion. Burmister's work is a case in point.

In his classic paper (6), Burmister presented his two-layer system solution in terms of two dimensionless independent variables (E_1/E_2 and h/a) and one nondimensional dependent variable (F_w)—the latter being a correction factor for the existing one-layer, Boussinesq solution. Here, E_1 and E_2 are the moduli of the top and bottom layers, respectively, h is the thickness of the top layer, and a is the radius of the applied load.

Significantly less attention was drawn to Burmister's comments at the First International Conference on the Structural Design of Asphalt Pavements in 1962 (7). At that conference, he advocated that the "principles of dimensional analysis should be rigorously followed, involving fundamental dimensionless ratios which have physical significance." This approach not only provides a useful way to present theoretical and analytical data, but it is also "a more basic approach in a comprehensive evaluation of field data, leading to dimensionally correct empirical relations" (7).

The first step in applying the principles of dimensional analysis to pavement systems is to distinguish between input parameters and independent variables entering the analysis, as well as distinguishing between output values and dependent variables. It is often assumed that these pairs of terms have identical meanings, thus resulting in extremely long factorials and incomplete (often misleading) data interpretation. Rauhut et al. (8), for example, conclude (in good humor) that "measuring all of the possible main effects and interactions between the 30 factors [involved in a typical execution of computer program VESYS] at two levels each would have required 2^{30} (slightly more than 10^9) separate observations." Regression algorithms obtained in this way cannot be applied to data other than the data for which the algorithms were developed.

In contrast, establishing independent and dependent variables, by combining a number of input parameters and output values into nondimensional forms, merely recognizes the fundamental engineering interactions between the factors involved. This is preferable to delegating this cardinal engineering task to the statistician or, more commonly, to the "black box" of sophisticated and complex statistical computer packages.

Previous investigations (9,10,11), showed how the Westergaard problem of a slab-on-grade can be reduced to a nondimensional equation of the form:

$$R^* = f(\log [a/l]) \quad (1)$$

where

- R^* = dimensionless response,
- f = logarithmic function of a/l sought,
- a = radius of the applied load, and
- l = radius of relative stiffness of slab-subgrade system, given by

$$l = [Eh^3/12(1 - \mu^2)k]^{1/4} \quad (2)$$

where

- E = slab Young's modulus,
- h = slab thickness,
- μ = slab Poisson ratio, and
- k = modulus of subgrade reaction.

The well-known Westergaard equations essentially present the functional forms of f for the particular cases of the three primary maximum responses; namely, deflection, δ , bending stress, σ , and subgrade stress, q , for each of the three fundamental loading conditions (i.e., interior, edge, and corner). The nondimensional responses, R^* , can be extracted from these equations, as follows (12):

$$R^* = [\delta D/Pl^2] \text{ or } R^* = [\delta kl^2/P] \text{ for deflection,}$$

$$R^* = [q l^2/P] \text{ for subgrade stress, and}$$

$$R^* = [\sigma h^2/P] \text{ for bending stress.} \quad (3)$$

In these responses, D is the flexural stiffness of the slab, which is equal to $Eh^3/12(1 - \mu^2)$, and P is the total applied load.

Thus, five of Westergaard's six input parameters $\{E, \mu, h, k, \text{ and } a\}$ are lumped into a single nondimensional ratio, a/l , which defines uniquely each of the nondimensional responses, independent of the values of the individual parameters. Therefore, even though each particular input parameter may change, the nondimensional response of the system (which involves the sixth input parameter, P) is unaltered, if a/l remains constant. As in Bernoulli's problem, Westergaard's is thus reduced to one of a single independent variable, a/l , and three dependent variables (the three nondimensional responses).

Several extensions based on Westergaard's work are now possible. To account for the finite extent of concrete pavement slabs, Ioannides et al. (13) introduced the normalized length term, L/l , assuming that the width, W , of the slab was equal to its length, L . Thus, Westergaard's solutions may be corrected for the effect of slab size, using data from FE studies. Similarly, the effect of dual-wheel loads, may be quantified by S/a or S/l , where S is the spacing of the two loads (14).

Note that all independent variables, as well as all calculated responses are expressed in the form of nondimensional ratios. This allows results obtained from one given set of input parameters to be used to predict the response under a number of other combinations of parameters, giving the same independent variables. As a corollary, only a limited amount of data (obtained from FE studies, laboratory tests, or field observations) is sufficient to describe most pavements of practical interest.

IDENTIFYING THE INDEPENDENT VARIABLES FOR CURLING ANALYSIS

When considering the effects of a temperature gradient through the thickness of the slab, it is necessary to seek the nondimensional independent variables involved, in addition to a/l and L/l . Input parameters to this problem usually include the following:

- α = coefficient of thermal expansion of concrete, $LL^{-1} \cdot T^{-1}$,
- g = temperature gradient, TL^{-1} ,
- ΔT = temperature differential between top and bottom, T , and
- γ = unit weight of concrete, FL^{-3} .

Here the three primary or basic dimensions are abbreviated as length, L , force, F , and temperature, T .

Examining available analytical solutions for this problem (1,2,15-17), it soon becomes apparent that the pertinent independent variable driving the system is the nondimensional product of $\alpha \Delta T$. In contrast, the temperature gradient, g , is a dimensional parameter and is inadequate to describe the system, unless the slab thickness, h , and the system of units used are also specified. For example, if a linear temperature distribution is assumed, g is constant through the thickness,

and

$$\alpha\Delta T = \alpha gh \quad (4)$$

Note that the form of the independent variable, $\alpha\Delta T$, already indicates that an accurate determination of α is just as significant as establishing the value of ΔT . In other words, the sensitivity of the system response to changes in α is just as pronounced as the corresponding sensitivity to variations in ΔT . Therefore, focusing attention and resources on determining ΔT may not be justifiable, unless an equal effort is expended in determining α . Nonetheless, in an analytical study as that presented herein, a constant value of α may be used. Results obtained may easily be adjusted for a different value of α , as necessary.

The self-weight of the slab, determined by γ , must also be accounted for in curling analysis. This is because of (a) the lack of full contact between the subgrade and the slab and (b) the restraint provided by the dead weight to the stress-free curling of the slab into a spherical surface, as predicted by the physics of the problem. The self-weight, however, is of a similar nature as the externally applied wheel loads. Thus, it may be accounted for by adjusting the form of the nondimensional responses and need not be considered as an independent variable.

Reference to analytical studies (2), as well as FE investigations (18), indicates that the sensitivity of the system to the slab size factor, L/l , is significantly more pronounced under a temperature gradient than under flat-slab conditions. A value of L/l between 5 and 8 is usually adequate to give an infinite slab response under no-temperature gradient (13), whereas under curling conditions this ratio is closer to 15.

FINITE ELEMENT FACTORIAL USED

The value of the preliminary considerations presented above is appreciated when examining the factorial that was used to study the response of the system under curling conditions. It was decided to eliminate slab length effects, so an L/l value of about 16 was adopted. The width, W , of the slab was initially set to 144 in. (or $W/l = 3.61$ to 7.66); but to conclude the study, the sensitivity of the calculated responses to this factor was also examined.

The following levels were considered for the other two independent variables:

$$a/l = 0.05, 0.1, 0.2, 0.3, \text{ and}$$

$$\alpha\Delta T = \pm 5.5 \times 10^{-5}, \pm 1.375 \times 10^{-4}, \pm 2.2 \times 10^{-4}$$

For a constant α value of $5.5 \times 10^{-6} \text{ } ^\circ\text{F}^{-1}$, the latter correspond to a temperature differential of ± 10 , ± 25 , and $\pm 40^\circ\text{F}$.

In a preliminary study (4), it was determined that the edge loading condition is critical under curling conditions, as well as under no-temperature differential. Analyses were therefore conducted only for a single square (size $c \times c$) or rectangular (size $2c \times c$) edge load. Thus, using a mere 24 FE runs, it is possible to bracket the vast majority of all conceivable slab, subgrade, and temperature conditions. The only restriction here is the infinite-slab assumption. The input parameters for the 24 cases studied are listed in Table 1.

Finite element program ILLI-SLAB (19,20) was used in this investigation. An iterative procedure is used to account for the effect of temperature curling and to accommodate regaining of subgrade support under load (4). In this respect, the FE formulation used follows closely that proposed by Huang and Wang (21). In designing the FE mesh, guidelines established in earlier studies were followed (20, 22).

ILLI-SLAB RESULTS

Figure 1 summarizes the data obtained for maximum combined normalized tensile stress at top or bottom of the slab for the three daytime and nighttime temperature differentials investigated. A short discussion of these follows.

Positive ΔT : Slab Curled Down (Daytime Conditions)

The maximum combined tensile-bending stress, $\sigma_{t \text{ max}}$, under an edge load on a slab that is curled down occurs at the bottom fiber of the slab at the location of the load. This will be the controlling stress for fatigue calculations because of its magnitude and location, as well as the higher number of traffic loads applied during the day. A much smaller tensile stress also arises at the top fiber of the slab, along the loaded edge at a distance of less than l from the slab corner.

Negative ΔT : Slab Curled Up (Nighttime Conditions)

The maximum combined tensile-bending stress under such conditions generally occurs at the top fiber of the slab, at some distance from the center of the load. This distance is usually between 2 and $4l$, the larger values correspond to low a/l and low $\alpha\Delta T$ values. Exceptions to this general pattern arise for high a/l and low $\alpha\Delta T$ values, when the maximum tensile occurs at the underside of the slab, at the location of the load. In such cases, however, this tensile stress is relatively small, being of the same order of magnitude as Westergaard's prediction ($\Delta T = 0$), and is generally only slightly greater than the corresponding maximum tensile stress arising at the top of the curled slab.

General Discussion of Results

As expected, the absolute value of the nondimensional bending stress ($\sigma h^2/P$) increases dramatically as $\alpha\Delta T$ increases, especially at low a/l values. In all these analyses, the unit weight of concrete, γ , was set at 0.087 pci (or 150 pcf), and its Poisson ratio, μ , was assumed to be 0.15; the maximum stress is normalized in terms of the external load, P , only. Although these choices are fairly inconsequential for the relatively long slabs considered here, a more general and rigorous examination of the nondimensional response would involve, in addition, both γ and μ . Unfortunately this is not feasible at this time.

In comparison, Westergaard's solution ($\Delta T = 0$) is of almost

TABLE 1 FINITE ELEMENT ANALYSES CONDUCTED

RUN	ΔT °F	h in.	E Mpsi	k pci	ℓ in.	L in.	W/ ℓ	P kips	c in.	a in.	a/ ℓ	σ_t max. psi
1.1	40	10.59	5	200	39.89	630	3.61	1.25	2.5*	1.995	0.05	620
1.2	40	8.23	4	300	28.21	450	5.10	2.5	5	2.821	0.1	595
1.3	40	9.97	3	400	28.21	450	5.10	10	10	5.642	0.2	599
1.4	40	7.16	2	500	18.81	300	7.66	10	10	5.642	0.3	612
2.1	25	10.59	5	200	39.89	630	3.61	1.25	2.5*	1.995	0.05	400
2.2	25	8.23	4	300	28.21	450	5.10	2.5	5	2.821	0.1	413
2.3	25	9.97	3	400	28.21	450	5.10	10	10	5.642	0.2	458
2.4	25	7.16	2	500	18.81	300	7.66	10	10	5.642	0.3	511
3.1	10	10.59	5	200	39.89	630	3.61	1.25	2.5*	1.995	0.05	186
3.2	10	8.23	4	300	28.21	450	5.10	2.5	5	2.821	0.1	234
3.3	10	9.97	3	400	28.21	450	5.10	10	10	5.642	0.2	323
3.4	10	7.16	2	500	18.81	300	7.66	10	10	5.642	0.3	421
4.1	-10	10.59	5	200	39.89	630	3.61	1.25	2.5*	1.995	0.05	-152
4.2	-10	8.23	4	300	28.21	450	5.10	2.5	5	2.821	0.1	-130
4.3	-10	9.97	3	400	28.21	450	5.10	10	10	5.642	0.2	-126
4.4	-10	7.16	2	500	18.81	300	7.66	10	10	5.642	0.3	-140
5.1	-25	10.59	5	200	39.89	630	3.61	1.25	2.5*	1.995	0.05	-370
5.2	-25	8.23	4	300	28.21	450	5.10	2.5	5	2.821	0.1	-308
5.3	-25	9.97	3	400	28.21	450	5.10	10	10	5.642	0.2	-251
5.4	-25	7.16	2	500	18.81	300	7.66	10	10	5.642	0.3	-207
6.1	-40	10.59	5	200	39.89	630	3.61	1.25	2.5*	1.995	0.05	-587
6.2	-40	8.23	4	300	28.21	450	5.10	2.5	5	2.821	0.1	-485
6.3	-40	9.97	3	400	28.21	450	5.10	10	10	5.642	0.2	-372
6.4	-40	7.16	2	500	18.81	300	7.66	10	10	5.642	0.3	-281

Note: For all runs, $\alpha = 5.5 \times 10^{-6} \text{ } \epsilon/\text{ } ^\circ\text{F}$; $\mu = 0.15$; $p = 100 \text{ psi}$; $W = 144 \text{ in.}$; $\gamma = 0.087 \text{ pci} = 150 \text{ pcf}$; $L/\ell \approx 16$.

* : Load dimensions are $c \times c$, except starred cases for which load dimensions are $2c \times c$.

σ_t max. is a tensile stress occurring at the bottom of the slab for +ve ΔT and at the top of the slab for -ve ΔT .

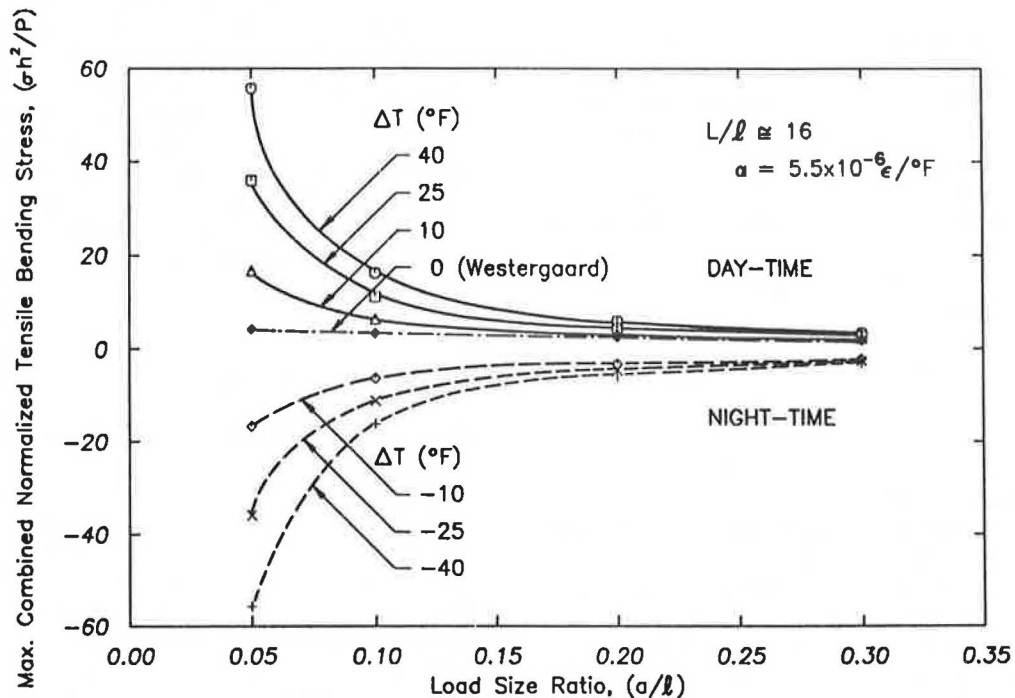


FIGURE 1 Maximum combined normalized tensile stress under edge loading as a function of (a/ℓ) and $(\alpha\Delta T)$.

insignificant magnitude. The ratio, ρ , is defined as

$$\rho = \left(\frac{\sigma_{t \max}}{\sigma_{t \text{ Wes}}} \right) \quad (5)$$

where $\sigma_{t \max}$ is the maximum combined tensile stress under curling and load, and $\sigma_{t \text{ Wes}}$ is the maximum tensile stress predicted by Westergaard ($\Delta T = 0$).

It is possible to use FE data to derive a closed-form equation to estimate $(\sigma_{t \max})$ under any combination of load and temperature conditions. Figure 2 shows the variation of the absolute value of ρ with a/l , for various temperature differentials. It was observed that downward curling (daytime) is slightly more detrimental than upward curling (nighttime). When fatigue consumption is considered, daytime curling will probably be more critical, because of the location of the maximum tension (at the bottom of the slab under the load) and the higher number of applied traffic loads. For these reasons—as a first attempt—the following formula was derived for ρ , based only on the daytime FE results presented in Figure 2:

$$\rho = A + B \{a/l\} + C \{\log_{10}(a/l)\} \quad (6)$$

where A , B , and C are functions of ΔT only, as follows:

$$A = 1.0 - 0.9152 \Delta T \quad (7)$$

$$B = 1.6215 \Delta T \quad (8)$$

$$C = -0.8713 \Delta T \quad (9)$$

Note that Equations 7–9 are presented in terms of ΔT (in °F) for clarity, assuming α equals $5.5 \times 10^{-6} \text{ } \epsilon/\text{°F}$. The fundamental relation, of course, involves $\alpha \Delta T$. It would be easy, however, to redefine A , B , and C for any other α value. Furthermore, in certain areas where nighttime truck traffic is significant, its effect on fatigue consumption may also be

accounted for in a fashion similar to that adopted here for the daytime stresses. The form of Equations 6–9 will remain unaltered, and only the nondimensional coefficients will need to be modified for this purpose.

Equation 6 applies to an infinite-slab condition, since an L/l value of about 16 was retained in all the FE runs used in its derivation. A significant decrease in the maximum combined tensile stress may be expected to occur as the slab size decreases below about $L/l = 8$. This is evident if one considers the steep slope of the C-coefficient curve presented by Bradbury (2). In addition, for slabs of infinite length, the maximum combined tensile stress is independent of the chosen value of γ . This, however, is not true for shorter slabs. For the latter, the combined stress is also drastically reduced as γ decreases. This assertion is confirmed by additional FE data, not presented herein.

Thus, the effect of decreasing γ is to make the slab behave as if it were shorter. Stated another way, this implies that the lighter the slab is, the longer it must be before the slab acts as an infinite slab. A theoretical explanation for this is that self-weight in heavy slabs imposes a restraint that is sufficient to ensure full contact under the interior portion of the slab, away from any edges and corners. This support condition was considered by Westergaard (1) as a necessary consequence of the infinite-slab assumption.

The effect of increasing the magnitude of the externally applied load is similar—the higher the applied load, the shorter the L/l value required for infinite-slab conditions. In this sense, the nature of the self-weight of the slab is similar to that of the externally applied load, as stated earlier. Thus, an equation similar to Equation 6 derived for shorter slabs (which would be of greater practical interest) must incorporate the effect of γ . It is expected, however, that this will be achieved by modifying the form of the dependent variable (nondimensional combined bending stress), rather than any of the governing independent variables.

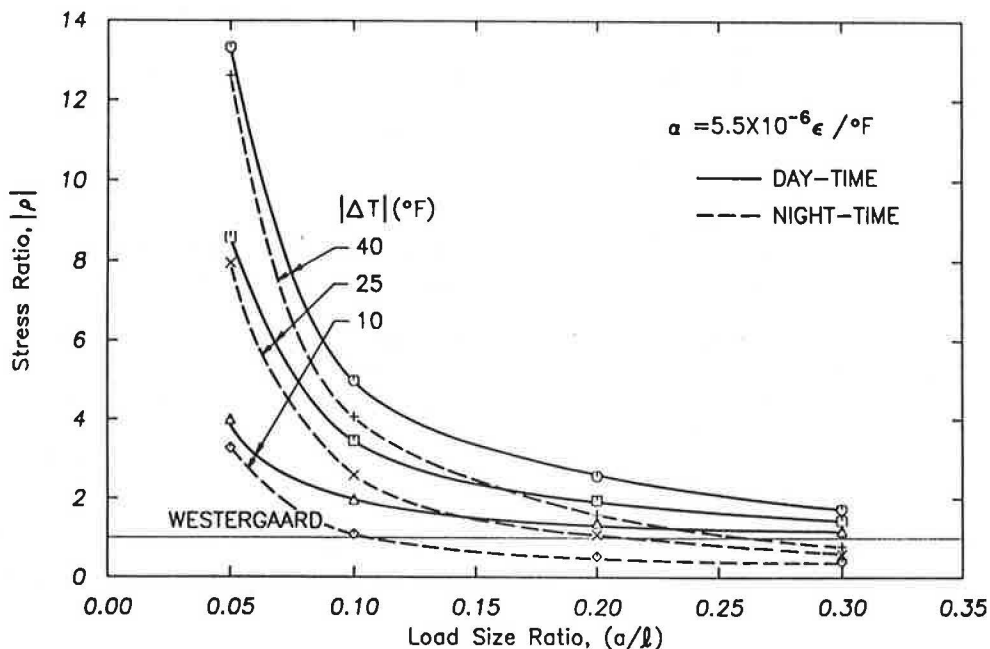


FIGURE 2 Multiplication factor, ρ , for estimating maximum combined tensile stress.

Equation 6 shows that ρ decreases as $\alpha\Delta T$ decreases or as a/l increases. It should be noted that for a/l values larger than about 0.2, Equation 6 suggests that ρ increases as a/l increases, albeit slightly. Any increase, however, is highly questionable and is probably related to the slab size effect mentioned above. Thus, Equation 6 is more reliable for $a/l \leq 0.2$.

Finally, a point needs to be made with respect to the regression technique used to derive Equation 6 from the FE data on which it is based. Twelve observations are considered and the coefficient of determination, R^2 , is 0.985. This is gratifyingly high, but one also must consider the ratio of (predicted/observed) values. These give a mean of 1.005 (cf. 1.00 for a perfect fit) and a coefficient of variation 16 percent (cf. 0.000 for a perfect fit). The latter is, therefore, fairly high. It is only when considering these three statistics together that the goodness of the fit may be evaluated. An R^2 value in the upper nineties is a necessary, but not a sufficient, condition for adequate predictions. This calls for considerable caution (to say the least) when using regression algorithms with significantly lower R^2 values.

Depending on the values of $\alpha\Delta T$ and a/l , stresses as high as 15 times Westergaard's may be obtained. As $\alpha\Delta T$ increases, the turning point in the curves—indicating more pronounced sensitivity to changes in a/l —occurs at increasingly higher values of a/l , as compared to the Westergaard solution. These values are often of considerable practical interest. At a lower $\alpha\Delta T$ and higher a/l , nighttime (upward) curling may result in a lower stress than predicted by Westergaard. The importance of such stress relief in fatigue calculation should not be overestimated, however, because of the location of the maximum stress (at the top fiber at some distance from the load) and the relatively low number of traffic loads applied during the night.

It should be stressed that the form of the independent variable, a/l , implies that the sensitivity of the pavement system response to changes in load radius, a , is just as pronounced as the effect of variations in its radius of relative stiffness, l . Furthermore, altering the value of the load radius causes a more pronounced response change than is effected by varying any one of the individual parameters entering l , (e.g., E , h , and k). This is obvious, since l is the fourth root of the combination of these parameters, while the load radius enters the driving ratio of a/l in its first power.

Compared with Westergaard's solution ($\Delta T = 0$), the sensitivity of the normalized response to changes in a/l , resulting from variations in a or l , is tremendously more pronounced, particularly for a/l values between 0.05 and 0.1. This is the range in which a large number of actual pavements and loads fall.

The preceding considerations suggest that the equivalent single-axle load (ESAL) concept, which states that all traffic loads are reduced to an equivalent single-axle load of a standard weight, is flawed; because it most often implicitly assumes a constant value of load radius. This criticism is not a novel idea. Thirty years ago, in enumerating the limitations of equivalent wheel-load analysis, Yoder (23) listed a number of factors that cause the pavement system to deviate from the assumptions of linear elasticity and full contact, including loss of subgrade strength and plastic subgrade deformation. He also stated that "warping of rigid pavements and subsequent loss of pavement contact must be taken into consideration."

Huang attempted to account for the contact radius in developing equivalency factors (24,25). Although application of the principles of dimensional analysis is evident in Huang's studies, his assumption was that "the change in load factor due to the change in contact radius is not very large so that a straight line interpolation should give a fairly accurate load factor for any other contact radii" (24). This may hold reasonably true for a full-contact analysis, such as Burmister's or Westergaard's, but as the data presented here show, such an expectation is unrealistic when the assumption of full contact is no longer satisfied.

Under linear elastic conditions, a much more fundamental reduction would have been to express mixed, multiple-wheel traffic in terms of an equivalent radius of the applied load. Recent research efforts at the University of Illinois have suggested that it would be possible to derive with reasonable accuracy an equivalent single-axle radius (ESAR) for any arbitrary gear configuration, simply as a function of its geometry (size and spacing of tire prints). This leads to the ESAR concept that offers a unique opportunity for replacing the empirical ESAL approach with a mechanistic procedure.

Even under stress-dependent (nonlinear) conditions, the need to reduce general traffic to an equivalent radius of applied load is still more urgent than the need for an equivalent magnitude of load. The major reason, of course, for the preference given to the ESAL concept is that axle loads are much easier to determine and control than are tire contact radii. Regrettably, the system response is naturally oblivious to matters of practical expediency.

EFFECT OF SLAB WIDTH

In the preceding FE analyses, the slab width, W , was maintained at 144 inches; i.e., the value of W/l (which can be expected to be the more fundamental slab width variable) ranged between 3.61 and 7.66. To examine the effect of slab width, nine additional FE runs were conducted. The results indicated that although the maximum combined normalized bending stress generally increases as W/l increases, this effect becomes negligible for W/l values in excess of about 3.5. The 24 cases considered above are, therefore, judged to be fairly insensitive to this effect.

RECONSIDERATION OF ZERO-MAINTENANCE RESULTS

The dimensional analysis approach to data interpretation presented above may be applied in a re-examination of existing data bases. As an illustration, the data base generated by the zero-maintenance (ZM) study (18) was selected, because it was one of the largest available. The data consisted of analytical results, obtained by performing a series of runs, using an FE program developed at the University of Kentucky by Huang and Wang (21). This is a precursor to ILLI-SLAB and is sometimes referred to as KENWINK. For the case of an 18-kip single-axle load perpendicular to the longitudinal slab edge, the data base included a complete factorial of 432 runs for the following factors and levels:

Slab thickness, $h = 8, 10, \text{ and } 14 \text{ in.}$,
 Subgrade modulus, $k = 50, 200, \text{ and } 500 \text{ pci}$,
 Thermal gradient, $g = -1.5, 0, \text{ and } +3.0^\circ\text{F/in.}$,
 Slab length, $L = 15, 20, 25, \text{ and } 30 \text{ ft}$, and
 Erodability, $e_s: 0, 12, 36, \text{ and } 60 \text{ in.}$

The slab considered consisted of one layer with a modulus, E , of $5.0 \times 10^6 \text{ psi}$ and a Poisson ratio, μ , of 0.15. The concrete coefficient of thermal expansion, α , was set at $5.0 \times 10^{-6} \text{ }^\circ\text{F}^{-1}$. The unit weight of concrete used was not explicitly stated but this was probably 150 pcf. The width of the slab, W , was held constant at 144 in. ($W/l = 2.071$ to 5.602). The load was applied by two wheels, each 15 by 12 in. at a center-to-center spacing, S , of 78 in. ($S/a = 10.3$) under 50 psi of pressure. The FE mesh used was relatively coarse, and some detrimental effects of this factor on the results obtained are discussed below.

Note that the ZM factorial is considerably longer than the ILLI-SLAB factorial presented earlier, but this is primarily a consequence of the implicit assumption that h , k , and g are fundamental independent variables. It is clear now that this is not the case, because the independent variables have been shown to be the nondimensional ratios, a/l and $\alpha\Delta T$, while h , k , and g are merely input parameters. Furthermore, the effect of the slab size is purportedly accounted for by the input parameter, L , whereas the fundamental independent variable is the nondimensional ratio L/l . Similarly, the effect of the loss of subgrade support in a longitudinal strip along the loaded slab edge was investigated during the ZM study in terms of the erodability, e_s . This gives the width of a zero-subgrade modulus strip along the loaded edge (in inches). It

may be postulated that the independent variable governing this aspect of the response is the nondimensional ratio, e_s/l .

For the case of no-temperature differential, Figure 3 compares the Westergaard solution and the ZM FE results for different values of the erodability ratio, e_s/l . On the basis of an earlier investigation (14), and for the sake of simplicity, the effect of the second tire may be considered negligible in calculating the Westergaard response. Thus, the solution shown in Figure 3 assumes a total load, P , of 9,000 pounds, applied over a circle, radius $a = 7.57 \text{ in.}$, under a uniform pressure, p , of 50 psi. Also note that the original data in the ZM report were extrapolated to yield the values corresponding to the rounded e_s/l values shown in Figure 3.

As expected, as e_s/l increases, the nondimensional maximum combined tensile stress arising in the slab increases substantially. The ZM report gave no indication as to the location of this stress (i.e., whether it occurs at the edge under the load or elsewhere) at the top or bottom fiber of the slab. Such information is essential in calculating fatigue consumption.

Comparing the curve for $e_s/l = 0$ to the Westergaard curve in Figure 3, provides an estimate of the effects of the FE mesh used. Good agreement is obtained at high values of a/l , due to the corresponding high L/l values (Westergaard assumes an infinite slab). For intermediate a/l values, the FE results are about 10 percent higher than Westergaard's. This discrepancy is due to the coarseness of the mesh in the vicinity of the load (26).

Finally, the curve for $e_s/l = 0$ bends over toward the Westergaard curve at low a/l , but this is not an indication of better agreement between the two solutions. Rather, it is due to the low L/l values, corresponding to these a/l values. The ZM results suggest that, for $\Delta T = 0$, results are not affected by

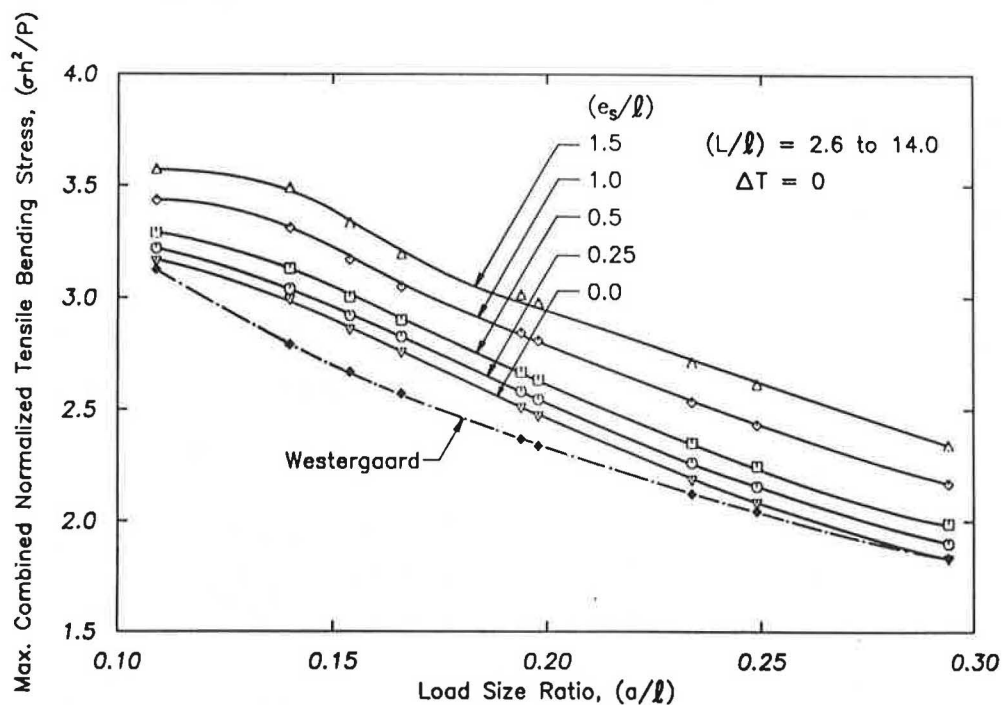


FIGURE 3 Zero maintenance results for $\Delta T = 0$: effect of erodability.

changes in slab size. This, of course, is only true for L/l in excess of about 5, and is certainly inapplicable in the case of L/l values as low as 2.588, associated with some low a/l results in Figure 3.

Notwithstanding these limitations, Figure 3 provides a concise graphic depiction of the effect of erodability on the maximum bending stress. When the data are presented in this fashion, responses may be predicted for cases involving values of the individual parameters (e.g., a , P , E , μ , h , k , and e_s) other than those on which Figure 3 is based. Four separate figures are used in the ZM report (18) to present the data obtained; each is applicable to a specific combination of the input parameters.

Using the dimensional analysis approach, the same data are replotted in a single graph (Figure 3). In this graph, the data line up to form smooth continuous curves, even though points on the same curve assume different input parameters, such as k and h . This confirms the validity of the proposed interpretation method. Figure 3 also allows a direct comparison with Westergaard, and an estimation of the error introduced by the characteristics of the FE mesh.

For the case of full subgrade support ($e_s/l = 0$), Figures 4 through 6 show the effect of slab size on the nondimensional combined maximum tensile stress under edge loading and a temperature differential. This stress is plotted versus a/l , for various values of L/l and $\alpha\Delta T$. Once again, the raw ZM data were extrapolated to give the responses at the rounded L/l values shown in these figures.

In examining these results, it was observed that for the dead and wheel loads considered there is a limiting value of L/l beyond which the slab behaves as an infinite slab. This value is also a function of a/l and $\alpha\Delta T$, but the effect of a/l is quite negligible. It is noted that the limiting L/l value is slightly more sensitive to changes in $\alpha\Delta T$ when considering upward curling (nighttime). Under both night and day temperature

differentials, a slab size of $15l$ or more may be necessary for infinite-slab response. This validates the choice made earlier in performing the runs for the ILLI-SLAB factorial.

The ZM results suggest that limiting the L/l ratio to about 4 will ensure that the combined stresses under $\Delta T = +30^\circ\text{F}$ (or less) will not exceed a value equal to about twice that predicted by Westergaard. This seems to hold reasonably true for any load size ratio a/l . Allowing the L/l ratio to reach 8 will cause a stress that is three times as large as Westergaard's. Thus, it appears necessary to reconsider conventional practice with respect to the selection of maximum slab size. The prevalent recommendation in the United States is that L (in feet) should not exceed 1.75 times the thickness, h , of the slab (in inches), or $L/h \leq 21$. On the other hand, recent European experience (27,28) suggests a somewhat longer maximum slab length, or $L/h \leq 25$.

The fact that the pertinent fundamental engineering independent variables are not L and W , but the nondimensional ratios, L/l and W/l , clearly means that any criteria developed cannot be expressed in terms of dimensional quantities (e.g., W equals 14 ft). The slab dimensions in feet cannot be determined until the properties of pavement, including its support, are known. Furthermore, it is evident that a criterion in terms of L/h , say, is much more relevant, because it accounts for the most important property of the slab, namely its thickness. Nonetheless, it is interesting to observe that such properties as E and k are not reflected in such a criterion either. It is therefore not surprising that the U.S. and European experience differs somewhat. This is presumably in response to the different soil conditions and concrete mixing practices in these two parts of the world.

Figure 7 compares the L/h criteria most commonly used in the United States and in Europe to the proposed L/l criterion (29). Contrary to the implication of an L/h design criterion, size-related problems may arise in a pavement as k increases.

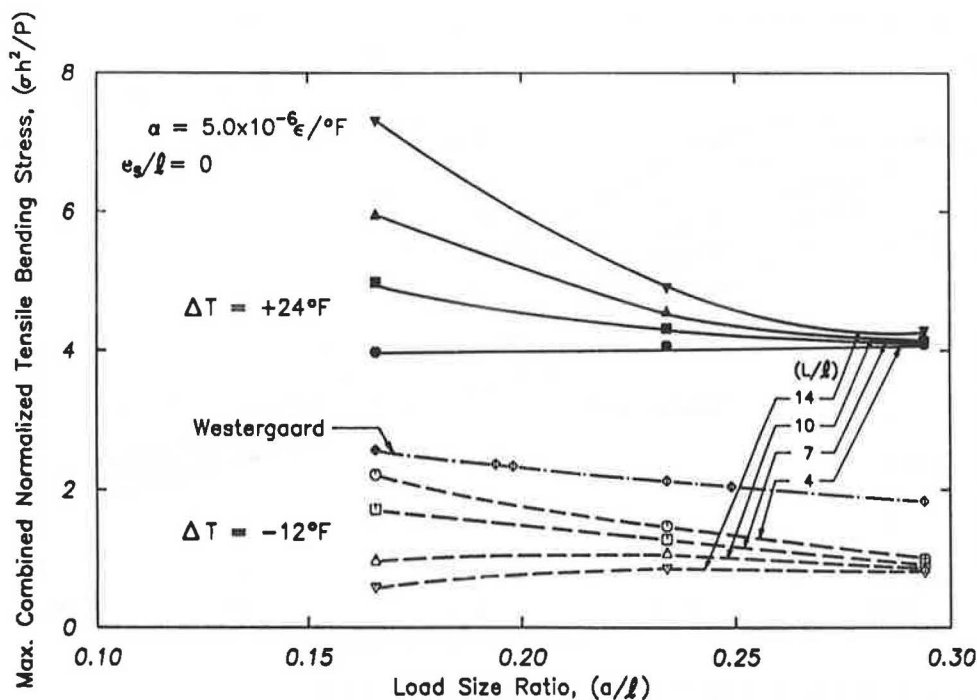


FIGURE 4 Effect of slab size: $\Delta T = -12$ and $+24^\circ\text{F}$.

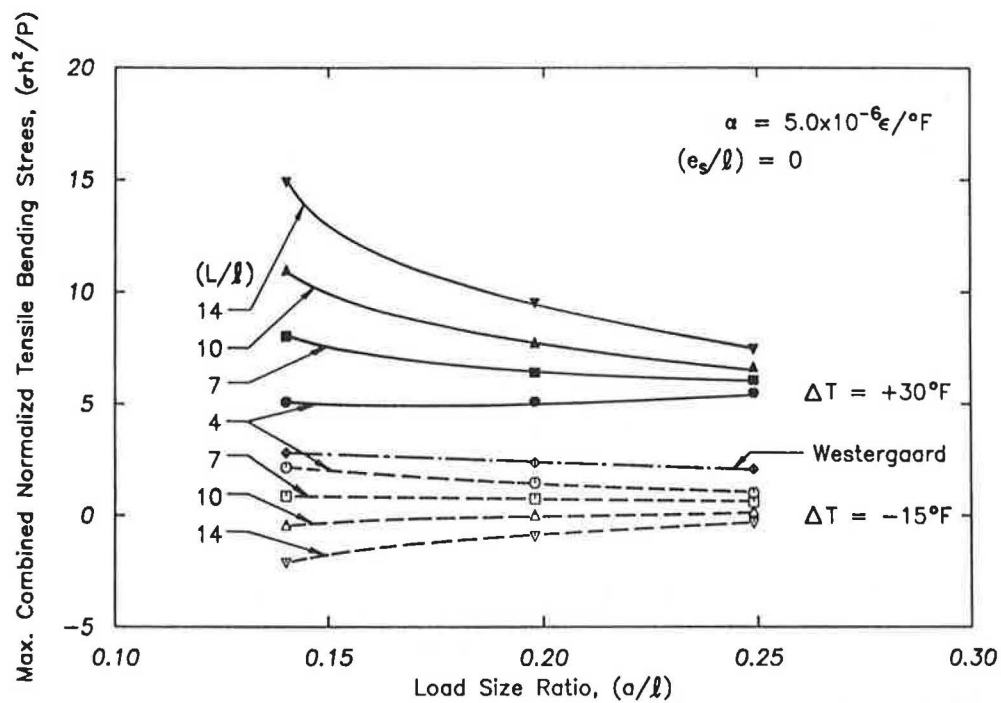


FIGURE 5 Effect of slab size: $\Delta T = -15$ and $+30^\circ\text{F}$.

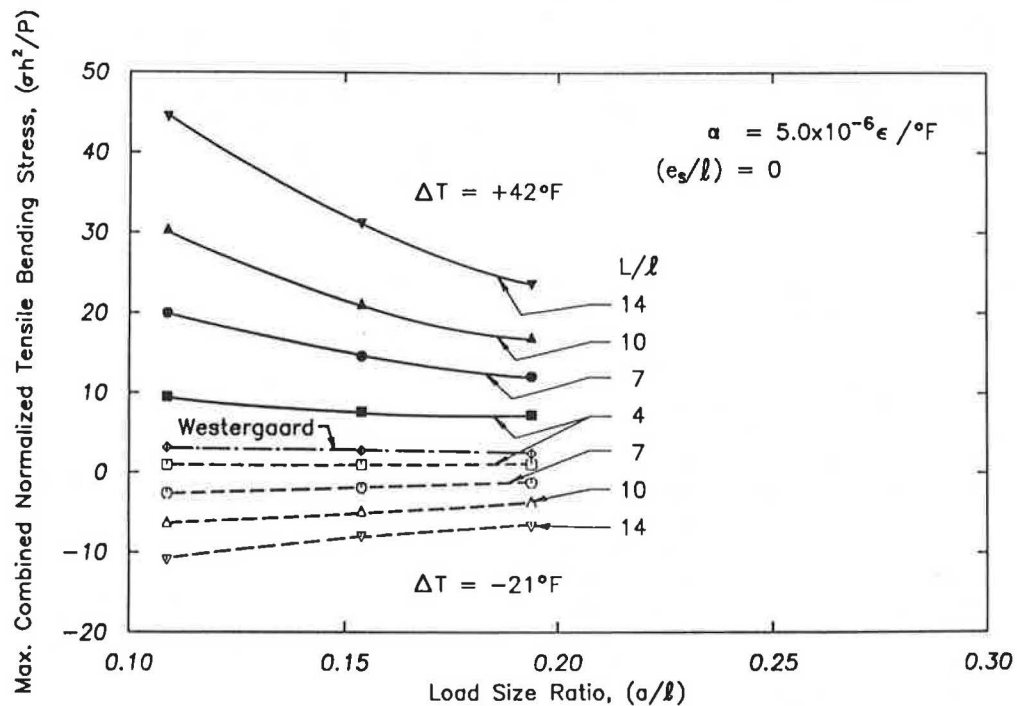


FIGURE 6 Effect of slab size: $\Delta T = -21$ and $+42^\circ\text{F}$.

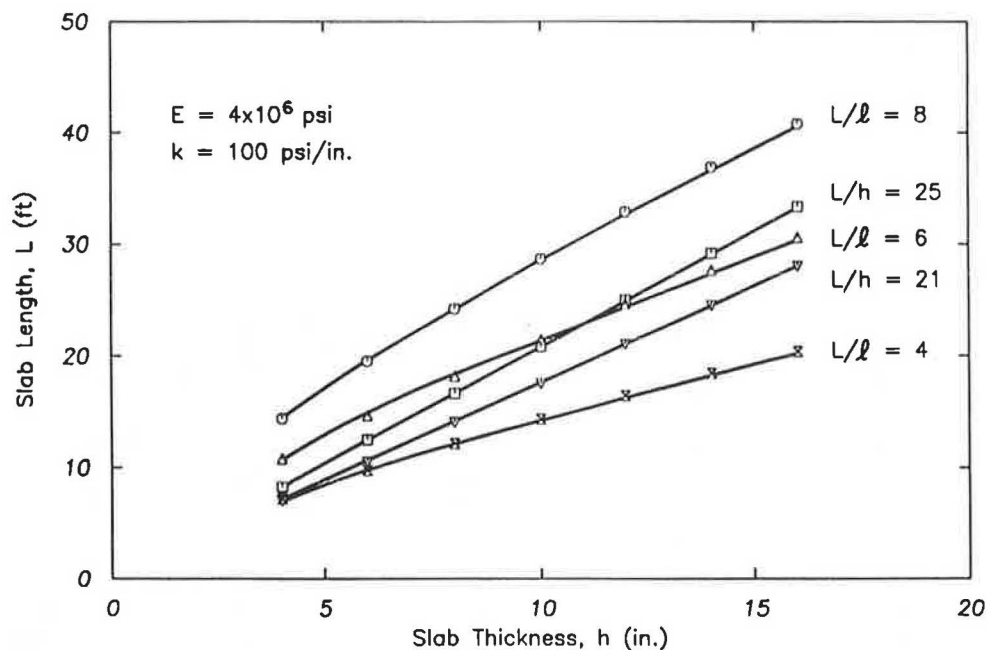


FIGURE 7 Comparison of slab length criteria (29).

It is also evident that decreasing E will have a similar effect. In contrast, an L/l criterion will result in shorter slabs under both of these conditions. Another interesting observation is that slab lengths determined according to the two L/h criteria lie for the most part within the range defined by $L/l = 4$ and $L/l = 6$. Thus, the former is shown to be a fairly conservative choice, while $L/l = 5$ appears to be a promising alternative. The ultimate choice, of course, should be tested against local experience. As noted earlier, the maximum combined tensile stress increases at a decreasing rate as W increases, tending to a constant value at about $W/l = 4$. This gives support to setting $L = W$.

CONCLUSION

The purpose of this paper has been twofold: (a) to present a solution to the problem of a slab-on-grade under combined temperature and wheel loading, and, just as importantly, (b) to propose a sound engineering approach to numerical, experimental, and field data interpretation. The principles of dimensional analysis, so fruitfully used in other branches of engineering, have largely been ignored in transportation facilities studies, particularly since the introduction of computers in the early 1960s. Despite occasional and admirable exceptions, the general trend in the last three decades has been to show an overwhelming preference for and an unlimited confidence in the results of sophisticated statistical analyses—without much consideration of the underlying engineering interactions among the host of input parameters involved.

Although in a highly empirical field, such as the study of pavement behavior, regression techniques will always be an invaluable tool, the profession can benefit immensely by using dimensional analysis to determine the engineering dependent and independent variables to be examined. Without such

exercise of engineering judgment, regression is lamentably bound to remain just that.

ACKNOWLEDGMENTS

The investigations for this paper were conducted under a research project sponsored by FHWA, U.S. Department of Transportation. Carol A. Nolan was the project administrator, and Stephen W. Forster was the contracting officer's technical representative. The useful comments of M. I. Darter and Roger M. Larson, and the assistance of Lynn Kastel in drafting the figures, are greatly appreciated.

REFERENCES

1. H. M. Westergaard. Analysis of the Stresses in Concrete Roads Caused by Variations in Temperature. *Public Roads*, Vol. 8, No. 3, May 1927, pp. 54–60.
2. R. D. Bradbury. *Reinforced Concrete Pavements*. Wire Reinforcement Institute, Washington, D.C., 1938.
3. L. W. Teller and E. C. Sutherland. The Structural Design of Concrete Pavements. *Public Roads*, Vol. 16, No. 8, Oct. 1935, pp. 145–158; Vol. 16, No. 9, Nov. 1935, pp. 169–197; Vol. 16, No. 10, Dec. 1935, pp. 201–221; Vol. 17, No. 7, Sept. 1936, pp. 175–192; Vol. 23, No. 8, April, May, June 1943, pp. 167–212.
4. G. T. Korovesis and A. M. Ioannides. Discussion of "Effect of Concrete Overlay Debonding on Pavement Performance," by T. Van Dam, E. Blackmon, and M. Y. Shahin. In *Transportation Research Record 1136*, TRB, National Research Council, Washington, D.C., 1987, pp. 129–132.
5. J. A. Roberson and C. T. Crowe. *Engineering Fluid Mechanics*, 2nd ed., Houghton Mifflin Company, Boston, Mass., 1980.
6. D. M. Burmister. The Theory of Stresses and Displacements in Layered Systems and Applications to the Design of Airport Runways. *HRB Proc.*, Vol. 23, 1943, pp. 126–148.

7. D. M. Burmister. Open Floor Discussion, Session 1, *Proc., 1st International Conference on the Structural Design of Asphalt Pavements*. University of Michigan, Ann Arbor, 1962, p. 15.
8. J. B. Rauhut, J. C. O'Quin, and W. R. Hudson. Sensitivity Analysis of FHWA Structural Model VESYS IIM. In *Proc., 4th International Conference on the Structural Design of Asphalt Pavements*, University of Michigan, Ann Arbor, Vol. I, 1977, pp. 139–147.
9. A. M. Ioannides. Dimensional Analysis in NDT Rigid Pavement Evaluation. *Journal of Transportation Engineering*, ASCE (In press).
10. A. M. Ioannides. Discussion of "Response and Performance of Alternate Launch and Recovery Surfaces that Contain Layers of Stabilized Material," by R.R. Costigan and M.R. Thompson, In *Transportation Research Record 1095*, TRB, National Research Council, Washington, D.C., 1986, pp. 70–71.
11. A. M. Ioannides. *Analysis of Slabs-on-Grade for a Variety of Loading and Support Conditions*. Ph.D. thesis. University of Illinois, Urbana, Ill., 1984.
12. A. M. Ioannides. Finite Difference Solution for Plate on Elastic Solid. *Journal of Transportation Engineering*, ASCE, Vol. 114, No. 1, Jan. 1988, pp. 57–75.
13. A. M. Ioannides, M. R. Thompson, and E. J. Barenberg. Westergaard Solutions Reconsidered. In *Transportation Research Record 1043*, TRB, National Research Council, Washington, D.C., 1985, pp. 13–23.
14. A. M. Ioannides. Discussion of "Thickness Design of Roller-Compacted Concrete Pavements," by S.D. Tayabji and D. Halpenny. In *Transportation Research Record 1136*, TRB, National Research Council, Washington, D.C., 1987, pp. 31–32.
15. J. Thomlinson. Temperature Variations and Consequent Stresses Produced by Daily and Seasonal Temperature Cycles in Concrete Slabs. *Concrete and Constructional Engineering*, Vol. 35, No. 6, June 1940, pp. 298–307 and Vol. 35, No. 7, July 1940, pp. 352–360.
16. S. G. Bergström. Temperature Stresses in Concrete Pavements. *Proceedings No. 14 (Handlingar)*, Swedish Cement and Concrete Research Institute at the Royal Institute of Technology, Stockholm, Sweden, 1950.
17. K. H. Lewis and M. E. Harr. Analysis of Concrete Slabs on Ground Subjected to Warping and Moving Loads. In *Highway Research Record 291*, HRB, National Research Council, Washington, D.C., 1969, pp. 194–211.
18. M. I. Darter. *Design of Zero-Maintenance Plain Jointed Concrete Pavement: Vol. I—Development of Design Procedures*. Report FHWA-RD-77-111. Federal Highway Administration, Washington, D.C., June 1977.
19. A. M. Tabatabaie and E. J. Barenberg. Structural Analysis of Concrete Pavement Systems. *Transportation Engineering Journal*, ASCE, Vol. 106, No. TE5, Sept. 1980, pp. 493–506.
20. A. M. Ioannides, M. R. Thompson, and E. J. Barenberg. Finite Element Analysis of Slabs-On-Grade Using a Variety of Support Models. In *Proc., Third International Conference on Concrete Pavement Design and Rehabilitation*, Purdue University, April 23–25, 1985, pp. 309–324.
21. Y. H. Huang and S. T. Wang. Finite-Element Analysis of Rigid Pavements with Partial Subgrade Contact. In *Transportation Research Record 485*, TRB, National Research Council, Washington, D.C., 1974, pp. 39–54.
22. A. M. Ioannides. The Problem of a Slab on an Elastic Solid Foundation in the Light of the Finite Element Method. In *Proc., 6th International Conference on Numerical Methods in Geomechanics*, Paper No. 408, Innsbruck, Austria, April 11–15, 1988, pp. 1059–1064.
23. E. J. Yoder. *Principles of Pavement Design*. John Wiley and Sons, Inc., New York, 1959.
24. Y. H. Huang. Chart for Determining Equivalent Single-Wheel Loads. *Journal of the Highway Division*, ASCE, Vol. 94, No. HW2, November 1968, pp. 115–127.
25. Y. H. Huang. Computation of Equivalent Single-Wheel Loads Using Layered Theory. In *Highway Research Record 291*, HRB, National Research Council, Washington, D.C., 1969, pp. 144–155.
26. A. M. Ioannides. Insights from the Use of Supercomputers in Analyzing Rigid and Flexible Pavements. Presentation to Committee on Rigid Pavements (A2B02), 66th Annual Meeting of the Transportation Research Board, Washington, D.C., January 1987.
27. J. Eisenmann. Discussion, Session 1B: Westergaard Theories. Workshop on Theoretical Design of Concrete Pavements. Epen, The Netherlands, June 5–6, 1986.
28. A. Lampinen. Design of Concrete Pavements in Finland. Workshop on Theoretical Design of Concrete Pavements. Epen, The Netherlands, June 5–6, 1986.
29. A. M. Ioannides and R. A. Salsilli-Murua. *Slab Length, Slab Width and Widened Lanes Effects in Rigid Pavements*. University of Illinois, Urbana, Ill., 1988.

Publication of this paper sponsored by Committee on Rigid Pavement Design.

Field Performance Review of Unbonded Jointed Concrete Overlays

G. F. VOIGT, MICHAEL I. DARTER, AND SAM CARPENTER

This paper describes a nationwide pavement survey and evaluation of 14 unbonded concrete overlays. A comprehensive distress survey was performed, past traffic equivalent single-axle loads were estimated, and design, subgrade, and climatic data were obtained. The data were evaluated, and the results are summarized. Overall, unbonded overlays have performed quite well with little deterioration to date. Specific conclusions are presented to aid in the future design of unbonded overlays.

Portland cement concrete unbonded overlays are designed with an interlayer between the new overlay and the existing slab to isolate the overlay from distress in the underlying pavement and, thereby, eliminate reflective cracking (1,2). This type of overlay has been used effectively over both concrete and bituminous pavements (2-5). Particular economic and performance advantage is gained when used on existing pavements that have become significantly deteriorated. Until recently, no effort has been made to document the performance of this technique nationwide. However, increased attention focused on rutting and reflective cracking of bituminous overlays (and the steady increase in the cost of bituminous materials) has led to further review of this and other alternative concrete resurfacing methods.

CONCRETE OVERLAY PLACEMENT—STATE OF THE ART

Several advancements in the concrete pavement field should work as a catalyst to increase the use of unbonded, and other types, of concrete overlays. Advances in construction time required and the ability to construct adjacent to traffic lanes are two of the advantages of asphalt concrete overlays. However, fast track paving and zero-clearance pavers have allowed concrete overlays to be constructed competitively in terms of these variables.

Since 1985, several states have constructed overlays, both bonded and unbonded, using high early strength (fast track) concrete mixes. Mix designs have consisted of Type I cement with admixtures, Type II with admixtures, and also proprietary cementitious materials (6,7). Strengths have been developed that will allow the pavement to be opened to traffic in as few as 24 hours, and success has been obtained in rural, semi-rural, and urban conditions (7). No fast-track concrete overlays are contained in the data base, however.

Recent developments by several paving equipment manufacturers will have a profound effect on overlay selection. Zero-clearance paving machines will allow the placement of overlay concrete adjacent to lanes carrying traffic. Because of this, lane closure and traffic control measures under conventional concrete placement standards will no longer be required. When used in combination with fast track concrete mix designs, the placement of unbonded and other concrete overlay types using zero-clearance pavers will be even more competitive.

UNBONDED OVERLAY DESIGN AND PERFORMANCE—REPRESENTATIVE PROJECTS

Fourteen unbonded overlay sections were identified by state highway agencies and included in the data base. The following describes the location, original pavement design, overlay construction techniques, traffic, environmental conditions, and performance for four representative projects. Several of these projects contain more than one uniform section, which is defined as an original pavement and overlay containing uniform design factors (such as surface preparation, thickness, reinforcement, and traffic). Table 1 summarizes the design and construction factors for each unbonded concrete overlay contained in the data base.

Illinois: East-West Tollway (I-5)

Location

The project begins on the East-West Tollway near Naperville at approximately Milepost 142 and extends 5 miles to Milepost 147.

Original Pavement Design

The original pavement, built in 1958, was a four-lane, jointed, reinforced concrete pavement (8). The slabs were 10 inches thick and placed on 4 inches of gravel-sand subbase and 10 inches of select subgrade. The transverse contraction joints were spaced 50 feet apart and were dowelled with 1.0-inch diameter dowels spaced 12 inches on centers (8). The original design made no provisions for subsurface drainage.

G. F. Voigt, American Concrete Pavement Association, 3800 N. Wilke Road, Arlington Heights, Ill. 60004. M. I. Darter and S. Carpenter, Department of Civil Engineering, University of Illinois, 208 N. Romine Street, Urbana, Ill. 61801.

TABLE 1 DESIGN AND CONSTRUCTION DATA FOR UNBONDED CONCRETE OVERLAYS

PROJECT CODE	PROJECT DESCRIPTION	DEBONDING MATERIAL	DEBONDING LAYER THICKNESS (inches)	OVERLAY THICKNESS (inches)	OVERLAY PAVEMENT TYPE	JOINT SPACING (feet)	JOINTING ARRANGEMENT	YEAR OF OVERLAY CONSTR.
A	IL East-West Tollway	Sand-Asphalt	0.50	8.00	PLAIN	14.50-R*	MIS**	1981
B(1)	GA I-85 Braselton	Curing Comp.	0.20	6.00	PLAIN	30.00	MATCH	1975
B(2)	GA I-85 Braselton	Curing Comp.	0.20	6.00	PLAIN	15.00	MATCH	1975
C	MI US 23 Dundee	Hot-Mix	0.75	7.00	REINF	41.00	MIS	1984
D	PN I-376 Pittsburg	Hot-Mix	1.00	8.00	REINF	30.75	MIS	1983
E	OH I-70 Springfield	Hot-Mix	1.00	10.00	REINF	60.00	MIS	1984
F	OH US-33 Russels Pnt.	Hot-Mix	0.75	7.00	PLAIN	13.50-R	MIS	1982
G(1)	CO I-25 Mead	Thin AC w/ Sand Cover	0.25	6.25	PLAIN	14.50-R	MIS	1985
G(2)	CO I-25 Mead	Thin AC w/ Sand Cover	0.25	7.75	PLAIN	14.50-R	MIS	1985
G(3)***	CO I-25 Mead	Thin AC w/ Sand Cover	0.25	7.75	PLAIN	14.50-R	MIS	1985

* Indicates Random Joint Spacing (Average Shown).

** MIS = Mismatched Jointing.

*** Overlay Included Tied Concrete Shoulders.

Unbonded Overlay Rehabilitation Design

Considerable effort was spent on pre-overlay repair and concurrent improvements. The pavement was overlaid in 1969 with a 3-inch course of asphalt concrete (8). Prior to the placement of the unbonded overlay in 1981, the asphalt overlay material was removed with a cold milling machine. Once exposed, the concrete pavement was patched full depth at various locations where prior failures, such as blow-ups and joint deterioration had been previously patched by maintenance crews, or at unpatched joints showing severe deterioration (8). The design of the unbonded overlay section consisted of an 8-inch plain-jointed overlay constructed on an approximately 0.5-inch bond-breaking layer, which was placed directly on the existing concrete pavement (8). In general, the following design and construction procedures were used for the typical section (8):

1. After removing the existing overlay and placing full-depth patches, the exposed concrete pavement was surfaced with a bituminous prime coat and then a sand-asphalt bond-breaking layer, which was intended to provide a slip plane for the overlay pavement.

2. A nominal 8-inch lift of portland cement concrete followed the application of the bond-breaking layer. Early obser-

vation during the construction of pressure relief joints showed evidence that the overlay concrete was bonding to the sand-asphalt layer. To counteract this bonding action, the bond-breaking layer was sprayed with water just ahead of the paving operation. When, after a few days, no signs of reflection cracking were found on the areas in which the bonding was initially discovered, the application of water was discontinued for subsequent paving.

3. Perpendicular contraction joints were sawed into the overlay pavement at random intervals from 12 to 18 feet. Placement of these joints was made to ensure that no overlay contraction joint would occur within 2 feet of cracks and joints in the underlying pavement. This effectively created sleeper slabs beneath each overlay contraction joint. The designers relied on this for load transfer and did not use dowels in these joints.

Traffic

The average daily traffic (ADT) and percent trucks in the survey year was given as: ADT = 30,500, percent trucks = 24 (8). Accumulated 18-kip equivalent single-axle loads (ESALs) on the outer lane of the overlay at the time of survey were estimated to be 4.516 million.

Observed Distress

The pavement was surveyed in July 1985 and, after 4 years of service, the overlay was performing well. Surveys were performed in both the eastbound and westbound lanes and the pavement appeared to be in slightly worse condition in the westbound direction. No transverse fatigue cracking occurred in the lanes of either direction; however, some longitudinal cracking was found in the outer lane in the westbound direction. This cracking, located in the outer wheel-path, was tight and showed no signs of deterioration. No corner breaks were observed, indicating no loss of support beneath the overlay slabs. The joints, which did not contain dowels, showed no signs of significant distresses (such as corner or transverse spalling). The mean faulting of the overlay joints in the eastbound drive lane was 0.05 inches while the westbound drive lane exhibited a mean faulting of 0.08 inches. The differing conditions between the eastbound and westbound lanes may be most likely attributed to the joint sealant conditions. A 75 percent failure occurred in the sealant on the first 500-foot sample unit and a 25 percent failure rate occurred on the second 500-foot sample unit. The failure mode of the sealant was adhesion failure with the joint reservoir walls. Although the sealant performed poorly, no evidence of pumping was found in either sample unit. This is a significant finding that exhibits the beneficial effects of mismatching joints in the overlay with those in the underlying slab. Through mismatching the joint locations, no direct access is available for the subbase and/or subgrade fines to come up to the overlay.

Georgia: I-85

Location

The project is located on I-85 in Gwinnet County near the town of Braselton about 30 mi north of Atlanta. The project extends from Milepost 123 to approximately Milepost 123.25.

Original Pavement Design

The original pavement was built in 1960. The design consisted of 9-in. thick, jointed plain concrete slabs placed over a 3-in. premixed bituminous stabilized crushed aggregate base course and a soil-aggregate subbase (9). Transverse contraction joints were spaced at 30-ft centers and relied on aggregate interlock for load transfer (9). Slotted 6-in. diameter drainage pipes were placed beneath the shoulder in all cut areas (9).

Unbonded Overlay Rehabilitation Design

Subsealing of the existing pavement slabs was performed (9). Shattered slabs were removed and replaced with undowelled full-depth patches. The overlay consisted of a 6-in. plain jointed pavement. One section included 30-ft joint spacings, where joints were constructed directly over existing joints. Another section included 15-ft joint spacings, where joints were matched with the existing joints and also constructed at the midpoint between existing joints. The overlay joints that matched the existing joints were dowelled with 1½-in. dowels. Dowels

were not placed in joints constructed at the mid-slab location (9). Ten-foot plain tied concrete shoulders on the outer lane and 4-ft plain tied concrete shoulders on the inner lane were also included in the design. The following design and construction procedures were used in constructing this overlay in 1975 (9):

1. Just before paving operations began, the exposed concrete pavement was given a coat of curing compound. The application of this compound was to be used as the bond-breaking layer between the new overlay concrete and the existing surface.
2. A 6-in. lift of portland cement concrete followed the application of the bond-breaking layer.
3. Shoulder paving followed mainline paving. The shoulder was not keyed, but was tied with tiebars spaced on 30-in. centers.
4. Contraction joints were sawed into the mainline overlay pavement in the locations described above. Transverse joints in the shoulders were sawed at 30-ft intervals.
5. Transverse joints were sealed with an open-cell neoprene joint sealant and the longitudinal shoulder joint was sealed with hot-pour asphalt sealant.

Traffic

The ADT and percent trucks in the survey year was given as ADT = 10,922, percent trucks = 25 (10). Accumulated 18-kip ESALs on the outer lane of the overlay at the time of survey were estimated to be 6.736 million.

Observed Distress

The pavement was surveyed in January 1986 in both of the southbound lanes on both the 30-ft joint spacing and 15 ft joint spacing sections. A 645-ft sample unit was taken on the 15-ft joint spacing section, and a 630-ft sample unit on the 30-ft section. After 10 years of service, both sections contained significant cracking—the 30-ft section contained 180 ft per 1,000 ft of low severity cracking and the 15-ft section contained 285 ft per 1,000 ft of cracking. On the 30-ft section, 53 percent of the slabs were cracked near the midslab region. Typically only one crack formed at this location, but two cracks in the midslab region were also noted. This cracking is attributed to differential curling of the overlay over the stiff underlying pavement. None of the cracks, however, had deteriorated into working cracks. The cracks noted on the 15-ft section were also only low severity, tight hairline cracks. The cracking was mostly located near the joints where problems were encountered during the paving of the overlay. Although little longitudinal cracking was noted on the outer lane of the 30-ft section, just 16 ft per 1,000 ft, the inner lane contained just over 100 ft per 1,000 ft of pavement. Not nearly as marked a difference was noted on the 15-ft section where the inner lane exhibited 145 ft per 1,000 ft and the outer lane only 96 ft per 1,000 ft of pavement. The longitudinal cracking may be attributed to the curling phenomena and an inadequately formed centerline joint. The average faulting was not significant, as it involved just 0.01 in. on the 30-ft section and 0.03 in. on the 15-ft section. No other structural-related problems

were evident. The surface on both sections showed some wear in isolated areas but, in general, was showing good performance.

Colorado: I-25

Location

The project is located north of Denver near the town of Mead. The overlay extends from approximately Milepost 246 to Milepost 253.

Original Pavement Design

The original pavement was built in 1964. The pavement was plain jointed with an average contraction joint spacing of 20 ft. These joints were not dowelled and, thus, relied on aggregate interlock for load transfer (personal communication with Hutter, Werner, Kiljin, John of Colorado Department of Transportation, DOT 1986). Slabs were constructed 8-in. thick and were placed over a 6-in. crushed granular base course. This pavement system was placed on a coarse-grained subgrade soil, with no provision of subsurface drainage (personal communication, Hutter et al., 1986).

Unbonded Overlay Design

Within the locations described previously, three overlay sections were constructed with differing designs in the summer of 1985. Two overlay thicknesses were used, 6.25 in. and 7.75 in. (personal communication, Hutter et al., 1986). Tied concrete shoulders were also used. The sections will herein be referred to as sections A, B, and C. Section A consisted of a 6.25-in. overlay with tied shoulders. On section B, a 7.75-in. overlay was constructed without tying the shoulders, and Section C consisted of a 7.75-in. overlay with tied shoulders. Joint spacing on the overlay was a random 14, 13, 15, 12 ft, skewed, and did not contain dowels. The following procedures were used to construct the overlay (personal communication, Hutter et al., 1986):

1. The surface of the existing pavement was swept of debris prior to placing an asphalt concrete bond-breaking layer. This layer was constructed 0.5 in. thick.
2. The overlay was paved to the thicknesses described above. The lanes were tied with 30-in. No. 4 tiebars spaced 30-in. on centers.
3. Where tied shoulders were used, the shoulders were also tied to the mainline pavement with 30-in. No. 4 tiebars spaced 30 in. on centers. Shoulders were constructed 10 ft wide on the outer lane and 4 ft wide on the inner lane. The shoulders were paved at a steeper cross slope than the mainline pavement.
4. Joints were sawed in the overlay and shoulders at a skew of 2 ft per lane (12 ft). The overlay joints were constructed as weakened plane joints and were sawed to match those on the lanes.

Traffic

The ADT and percent trucks in the survey year was ADT = 25,100, percent trucks = 16 (personal communication, Hutter

et al., 1986). Accumulated 18-kip ESALs on the outer lane of the overlay at the time of survey were estimated to be 0.920 million.

Observed Distress

The surveys on this pavement were performed in late June 1986. In each section, one 500-ft sample unit was taken. The overlay had been in service for only one year at that time; therefore, the development of significant fatigue and environment-related distress was limited.

Section	Overlay Thickness (in.)	Shoulder
A	6.25	Tied
B	7.75	Untied
C	7.75	Tied

No evidence of cracking was found in any of the three sections. The faulting in the outer lane ranged from 0.00 in. on Section B to just 0.01 in. on Sections A and C. On the inner lane, the faulting was 0.01 on both Sections B and C, and 0.00 in. on Section A. The joints were not spalled, and the concrete showed no sign of surface or mix-related defects. The shoulders on Sections A and C had performed well, although on Section C three transverse cracks had developed at the location of joints in the mainline pavement. It was apparent that these cracks had developed prior to the joint sawing operation and were left to perform as contraction joints, because no reservoir had been sawed in these locations.

Pennsylvania: I-376

Location

The project is located in eastern Pittsburgh. The overlay extends from Milepost 4.5 to Milepost 12.0.

Original Project Design

The original pavement constructed in 1946, was a four-lane jointed reinforced concrete pavement (personal communication, Grambling and Wade, Pennsylvania DOT, 1985). The slabs were 10 in. thick placed on 8 in. of crushed aggregate subbase. Load transfer was provided in the transverse contraction joints by 1.25-in. diameter dowels spaced 12 in. on centers. The slabs were 90 ft long and reinforced with welded wire fabric. Longitudinal drainage pipes were provided at the shoulders continuously along the project.

Unbonded Overlay Design

The overlay was constructed in 1983. Full-depth retrofit concrete shoulders were designed as part of the overlay. The overlay slabs were 8 inches thick with a joint spacing of 30.75 ft. The overlay joints contained 1.25-in. diameter dowels on 12-in. centers. The following procedures were used to construct the overlay (personal communication, Grambling, 1985).

- Onto the surface of the existing pavement, an asphalt concrete bond-breaking layer was applied to a thickness of approximately 1.0 in. As a further means by which to break the bond between the existing pavement and the new overlay, polyethylene sheeting was placed on top of that layer.

- The overlay was paved to a thickness of 8 in. The lanes were tied with 30-in. No. 5 tiebars spaced 30 in. on centers.

- The shoulders were also tied to the mainline pavement with 30-in. No. 4 tiebars spaced 30 in. on centers. Shoulders were constructed 10 ft wide on the outer lane and 4 ft wide on the inner lane. The shoulders were paved at a steeper cross slope than the mainline pavement.

- Joints were sawed in the overlay and shoulders at a skew of 2 ft per lane (12 ft). Sealant was placed in the joints prior to opening to traffic.

Traffic

The ADT and percent trucks in the survey year was given as ADT = 67,500, percent trucks = 8 (personal communication, Grambling, 1985). Accumulated 18-kip ESALs on the outer lane of the overlay at the time of survey were estimated to be 1.822 million.

Observed Distress

The overlay on this route was surveyed in late August 1985. Surveys were conducted in both directions. At that time, the overlay contained a significant amount of cracking. In the eastbound lanes, two 1,000-ft sample units were taken, both located in sections of cut of between 16 and 40 ft. There was an average of 162 ft of low severity transverse cracking per 1,000 ft of pavement in the outer lane, and 60 ft per 1,000 ft in the inner lane. In the westbound direction, two sample units were taken, one in a similar cut section to those in the eastbound direction, and one in a section at grade. The amount of transverse cracking in the cut section was 110 ft per 1,000 ft of low severity in the outer lane and 90 ft in the inner. This is similar to that found in the eastbound lanes. In the section built at the in situ gradeline, there was slightly more low severity transverse cracking—384 ft per 1,000 ft in the outer lane and 30 ft per 1,000 ft in the inner lane. The cracks were almost exclusively located at midslab and were not found on the outer lane, which indicates that they had developed due to curling stresses. In either direction, the transverse joint faulting of the outer lane joints was only 0.04 in. The shoulders experienced tremendous movement, heaving between 0.07 and 0.63 in. and settling 0.18 and 0.52 in.

Although no direct correlation could be made to any of the measurements and observations of other distresses or conditions, the nonuniform movement of the shoulder slabs indicated a frost heave problem. The tiebars along the lane/shoulder joint are most likely failed due to the movement as well. Low severity longitudinal cracking on the average of 20 ft per 1,000 ft of pavement was found on the sample units in the eastbound direction, while an average of 62 ft per 1,000 ft of pavement of low severity transverse cracking was found in the westbound direction.

OVERALL UNBONDED OVERLAY PERFORMANCE

The performance of any rigid pavement rehabilitation technique can be measured by three basic factors (1):

1. The ability of that technique to correct the problems for which it was designed,
2. The ability of the materials used in constructing the technique to withstand the environment and maintain durability and structural integrity, and
3. The ability of the technique to serve future traffic loadings.

Table 2 gives a summary of unbonded concrete overlay distress observed on each uniform section.

Transverse Cracking

Field Observation

Only 2 of the 14 unbonded overlay uniform sections contained deteriorated (medium to high severity) transverse cracking. These sections are located on the two Georgia I-85 joint plain concrete pavement (JPCP) overlays. Less than 24 ft per 1,000 ft of traffic lane was measured on each section. These overlays were placed over a debonding layer of curing compound. Figure 1 shows the distribution of transverse cracking for each unbonded overlay surveyed. In each case, most of the cracking was located in the center region of the slab.

Development

Transverse cracking on unbonded overlays can develop from at least three major causes (or a combination of these): reflection cracking, thermal curling, and traffic load fatigue damage (1).

Reflection cracking on unbonded overlays may result when the overlay is built over a thin and/or stiff debonding medium (1). However, the typical interlayer of AC or other type of asphaltic materials, such as slurry seal, usually prevents the development of reflection cracking. The Georgia I-85 6-inch thick overlay contained, on average, nearly 330 ft of outer lane transverse cracking per 1,000 ft of roadway. Almost all of this was low severity, tight-hairline cracking. Georgia Department of Transportation (DOT) officials reported that the curing compound, used as a debonding medium, was not effective (9). Thus, the probable cause of some of this cracking was reflection from the underlying slabs.

Thermal curling may be an even more severe problem in unbonded overlays. Figure 2 illustrates the temperature differential through a standard unbonded overlay section (11,12). The unbonded overlay and debonding medium will dampen virtually all of the temperature variation in the underlying slab. Thus, the overlay slabs, which will experience a significant temperature differential from surface to base, will tend to curl over the existing pavement slabs.

The curling action of the unbonded overlay slab is not significantly restrained at the interface, as it is on a bonded concrete overlay; therefore, the slab may actually lift off the underlying slab. Lifting will cause a void between the overlay

TABLE 2 SUMMARY OF UNBONDED CONCRETE OVERLAY FAULTING AND CRACKING OBSERVED ON EACH UNIFORM SECTION SURVEYED

PROJECT CODE	AGE (yr)	ADT	% TRUCKS	ACCUM. 18 kip ESAL (millions)	MEAN FAULTING (inches)	LOW SEV. TRAN. CRACK (ft/1000 ft)	MED SEV. TRAN. CRACK (ft/1000 ft)	LOW SEV. LONG. CRACK (ft/1000 ft)	MED SEV. LONG. CRACK (ft/1000 ft)
A*	4	30500	24	4.516	0.05 0.08	0 0	0 0	0 77	0 0
B(1)	10	10922	25	6.736	0.03	429	24	261	0
B(2)	10	10922	25	6.737	0.03	189	12	101	0
C*	1	19400	17	0.380	0.02 0.01	0 0	0 0	0 0	0 0
D*	2	67092	8	1.822	0.04 0.04	162 247	0 0	0 4	0 0
E	1	26900	26	1.321	0.005	119	0	0	0
F*	3	5470	19	0.732	0.02 0.03	0 0	0 0	0 0	0 0
G(1)	1	25100	16	0.920	0.00	0	0	0	0
G(2)	1	25100	16	0.920	0.01	0	0	0	0
G(3)**	1	25100	16	0.920	0.01	0	0	0	0

* For two lane roads, data for both drive lanes (directions) are shown.

** Overlay Included Tied Concrete Shoulders.

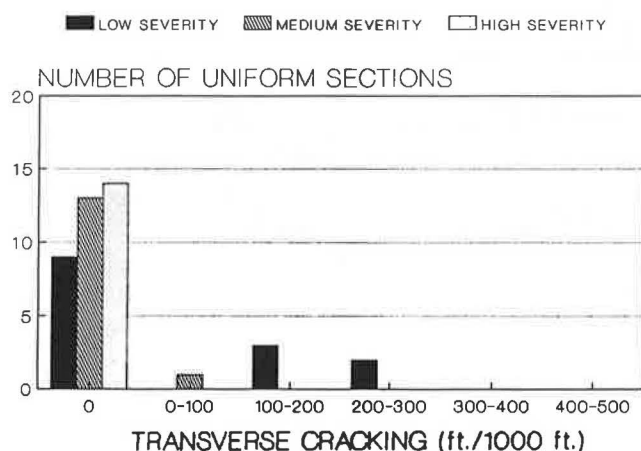


FIGURE 1 Distribution of severity of transverse cracking in outer lane on unbonded concrete overlays.

slab and existing pavement surface (Figure 3). When this void develops from curling during the daytime, the void will be at the center region of the slab. Tensile stresses at the bottom of the overlay will occur as a result of the curl (due to the weight of the slab pulling down). The tensile stresses from curling in addition to load-induced tensile stresses (which will

be greater than normal because of the loss of support beneath the slab) will create a critical stress. The typical location of the initiation and propagation of transverse cracking is from the longitudinal outer slab edge where resultant stresses will be the highest.

Other factors that contribute greatly to this problem are the increased effective (composite) foundation k -value of the portland cement concrete (PCC) and interlayer, and the transverse joint spacing used in the overlay. It is well documented that cracking is more likely to occur on slabs that have a longer joint spacing.

This is well illustrated on Georgia I-85 in which the original pavement joint spacing was 30 ft. Joints were matched at 30 feet on one overlay section and intermediate joints were sawed at mid-slab for an effective spacing of 15 ft on the other overlay section. Many of the 30-foot overlay panels had developed mid-panel cracks; significantly fewer cracks were observed in the 15-ft panels (9).

Two strategies can be used against cracking due to thermal curling in the overlay: preventive design and expected maintenance. Expected maintenance does not attempt to inhibit cracking, but instead uses steel reinforcement to hold cracking together once it has developed. Preventive design, on the other hand, attempts to limit crack development through design considerations.

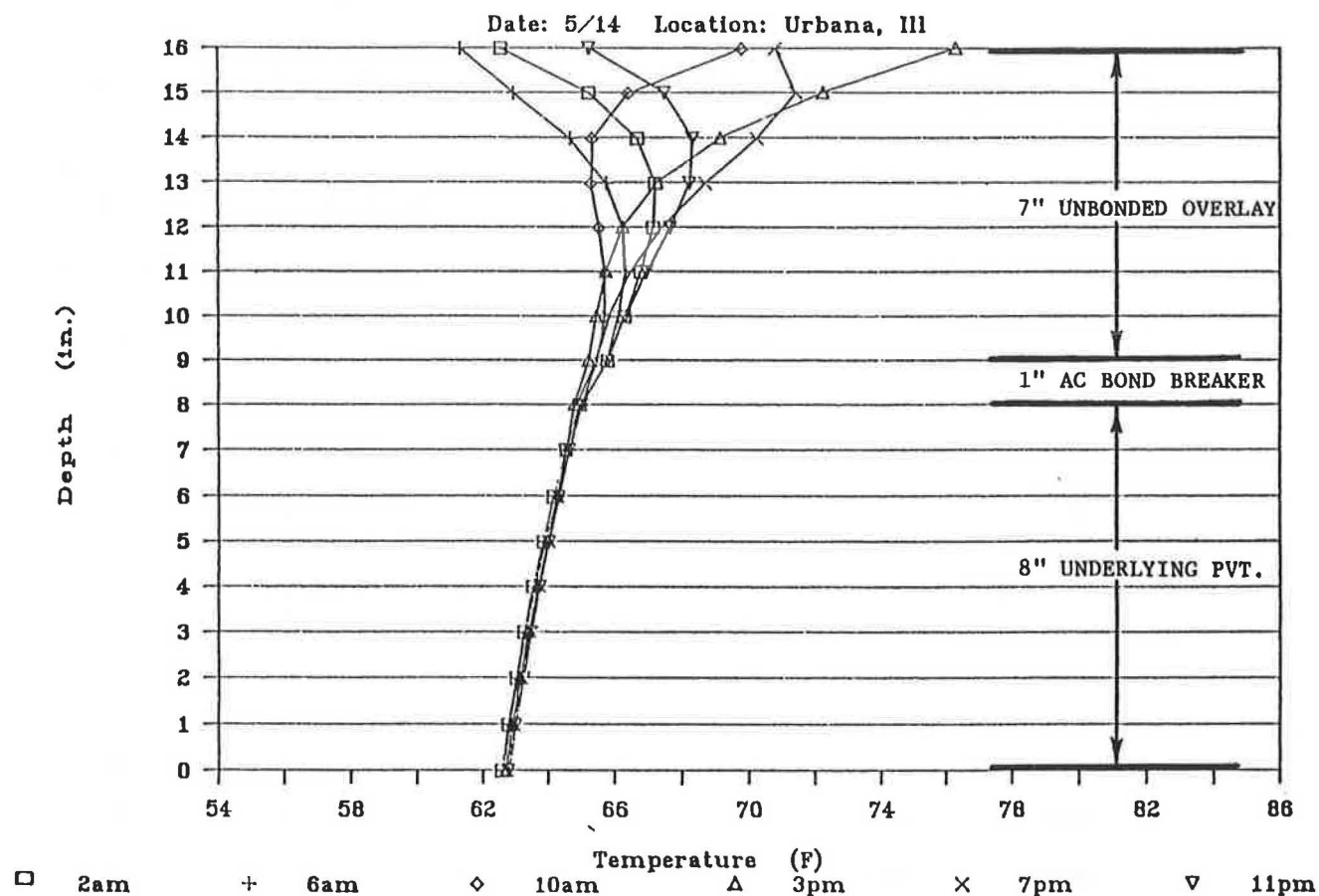


FIGURE 2 Temperature profile (for mid-May) through an unbonded overlay cross section for 16-in. pavement.

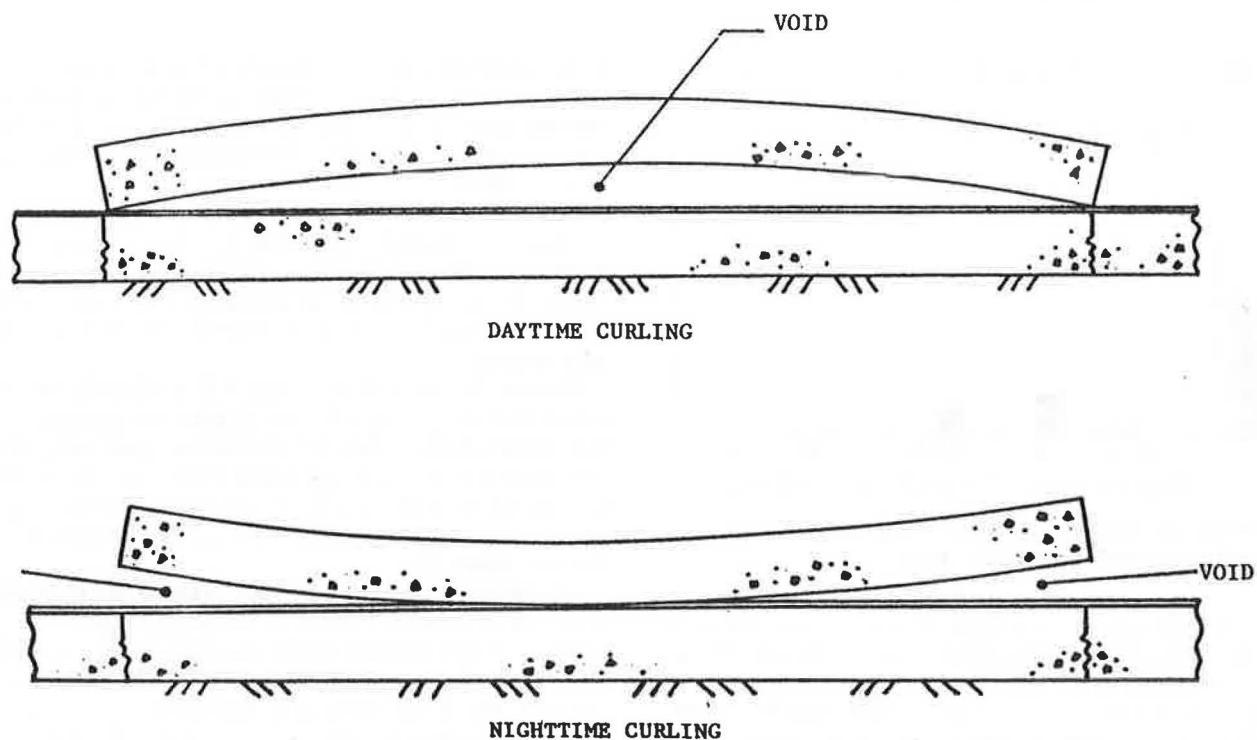


FIGURE 3 Development of void under unbonded concrete pavements from the differential curling phenomenon.

The typical procedure that has been used to design against the development of cracking due to curling stresses has been to limit the joint spacing (in feet) to less than twice the pavement depth (in inches). However, this rule of thumb was based on limiting curling stresses in slabs placed on foundation k -values below about 300 pounds per cubic inch (pci). Experience has shown that slabs constructed using the $2 \times h$ rule of thumb on stiff foundations, such as treated base courses or existing pavement structures, may indeed still crack. This has led to consideration of an alternate procedure, the L/l ratio, for determining joint spacing on stiff foundations (13).

Unlike the $2 \times h$ rule, this ratio does consider the effective slab support directly through the radius of relative stiffness. The L/l ratio is the length of slab (in inches) divided by the radius of relative stiffness (13).

$$L/l = \frac{L}{(E * h^3 / 12 * (1 - \mu^2) * k)^{1/4}}$$

where

- l = radius of relative stiffness (in.),
- L = length of slab (in.),
- E = modulus of elasticity of the pavement,
- h = thickness of the pavement,
- μ = Poisson's ratio, and
- k = modulus of subgrade reaction (pci).

Analysis of the overlay sections, and additional projects revealed a critical L/l ratio of about 7 (7). These have been plotted on a graph of L/l envelopes and are shown in Figure 4. The critical L/l ratio ($L/l = 7$) results in joint spacing determinations of approximately 1.9 to 1.6 times the overlay thickness, as overlay thickness varies from 6 inches to 12 in.

The L/l ratio will vary dependent on the effective foundation support (k -value) used in determining the radius of relative stiffness. For this analysis, the effective k -value used was 500 pci. Although it is likely that the effective support from an underlying rigid pavement system is probably much higher, many design procedures limit foundation k -values at 500 pci; therefore, this was the value adopted.

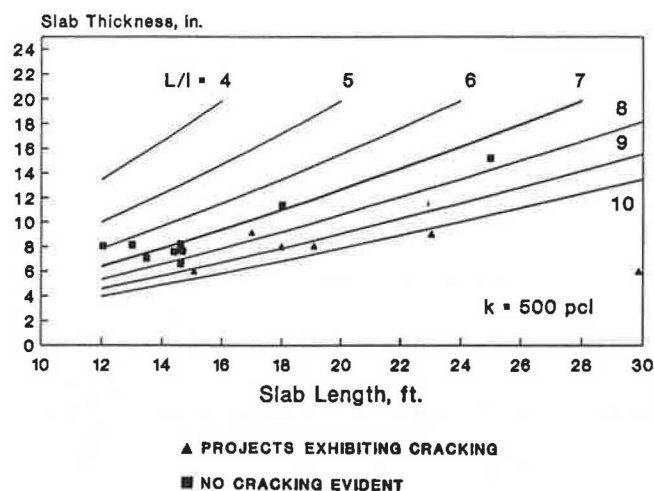


FIGURE 4 L/l ratio envelopes (unbonded overlays) for slabs on a stiff foundation ($k = 500$ pci, $E = 4 \times 10^6$ psi, Poisson's ratio = 0.15).

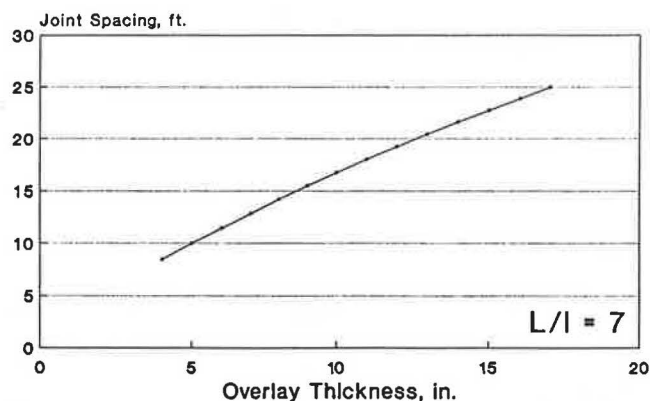


FIGURE 5 Sensitivity of joint spacing to overlay thickness maintaining an L/l ratio of 7 (unbonded overlays).

Figure 5 shows the sensitivity of joint spacing to overlay thickness maintaining the critical L/l . It is interesting to note that as slab thickness increases, the L/l ratio induces a larger constraint on maximum allowable joint spacing.

Where using a preventive design approach, it is recommended that a maximum L/l of 7 be maintained. Where longer joint spacing is used, cracking will likely develop and slabs should be reinforced heavily to hold the discontinuities together.

Longitudinal Cracking

Field Observation

Only two projects contained a significant amount of longitudinal cracking. Figure 6 shows the longitudinal cracking distribution for the unbonded overlay sections contained in the data base.

The Georgia I-85 6-in.-thick overlay contained, on average, approximately 180 ft of outer lane longitudinal cracking per 1,000 ft of roadway. All of this was low severity, tight-hairline cracking. The probable cause of the longitudinal cracking was reflection from cracking in the underlying slabs that was not arrested by the curing compound debonding medium (9).

The Illinois East-West Tollway also contained longitudinal cracking in the westbound direction. That cracking was attributed to late sawing of the longitudinal joint as reported by the resident engineer (8).

Development

The development of longitudinal cracking on unbonded overlays can be attributed to curling stresses, reflection cracking, and late sawing of the longitudinal lane joints (1).

The thermal gradient problem described earlier could possibly contribute to the development of longitudinal cracks. However, the development is less likely because the effective slab width is only 12 ft (one lane width), which may not be enough to develop large curling stresses.

Longitudinal cracks in the existing pavement will reflect through the overlay if the debonding medium is not adequate. The movements of the overlay and existing pavements must

be separated by the debonding medium for proper performance of the overlay.

Proper sawing depth (at least $\frac{1}{3}$ the slab thickness) and timely sawing of the longitudinal joint are probably most critical.

Faulting and Pumping

Field Observation

Excellent load transfer efficiency and protection against pumping, loss of support, and faulting stems from the ability to mismatch the joints in an unbonded overlay from those in the underlying pavement. Mismatching provides a sleeper slab type arrangement (see Figure 7). The deflection profile under load is altered as the sleeper slab arrangement dampens deflections at the base of the underlying slab. Figure 8 illustrates the dampening effect. Most importantly, good assur-

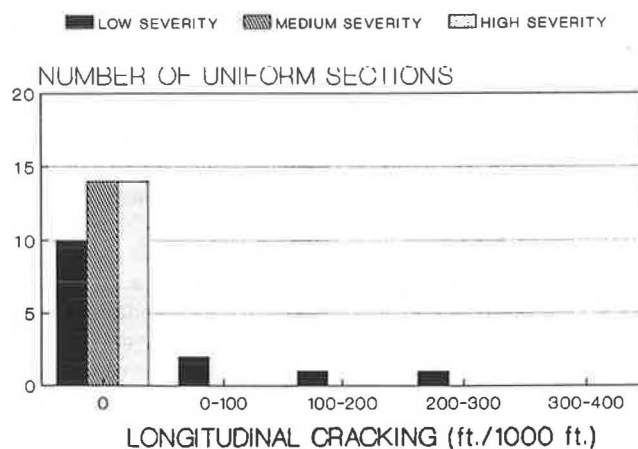
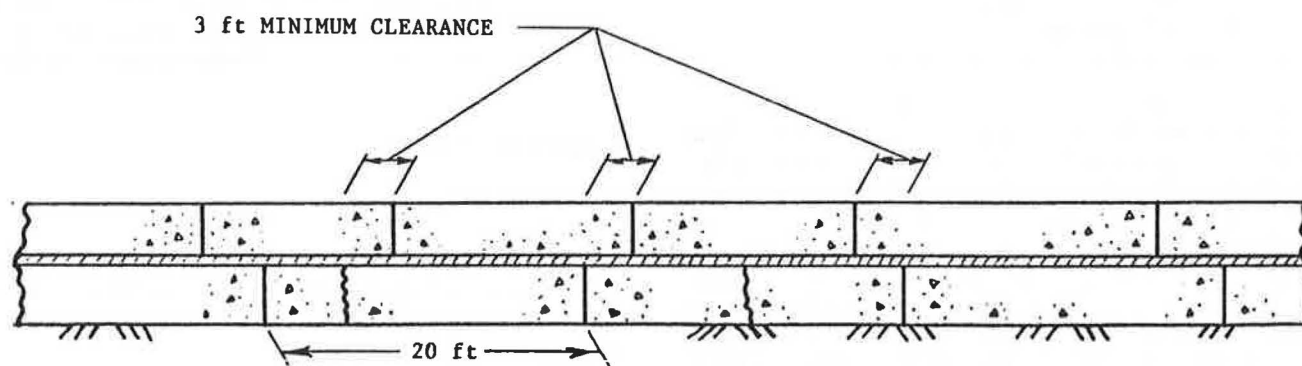
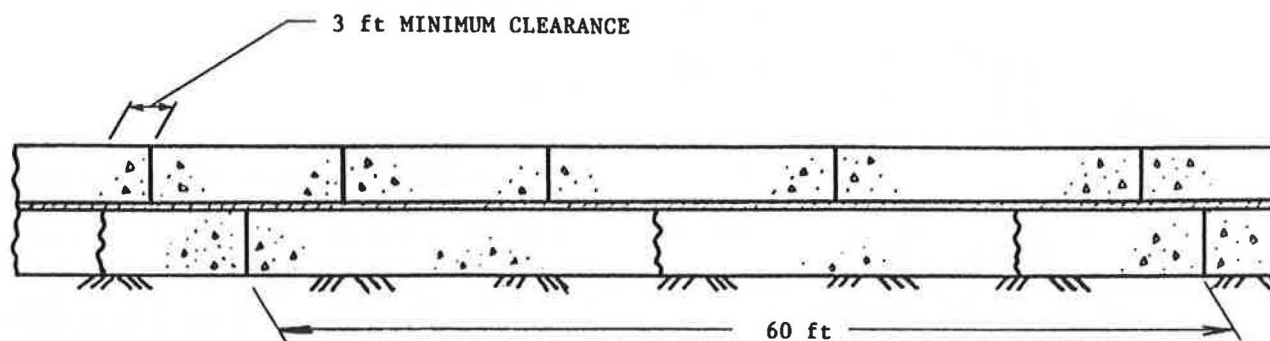


FIGURE 6 Distribution of severity of longitudinal cracking in the outer lane on unbonded concrete overlays.



A. Placement of Overlay Joints over Existing 20 ft JPCP Pavement.



B. Placement of Overlay Joints over Existing 60 ft JPCP Pavement.

FIGURE 7 Details for mismatching overlay joints with joint in the existing pavement.

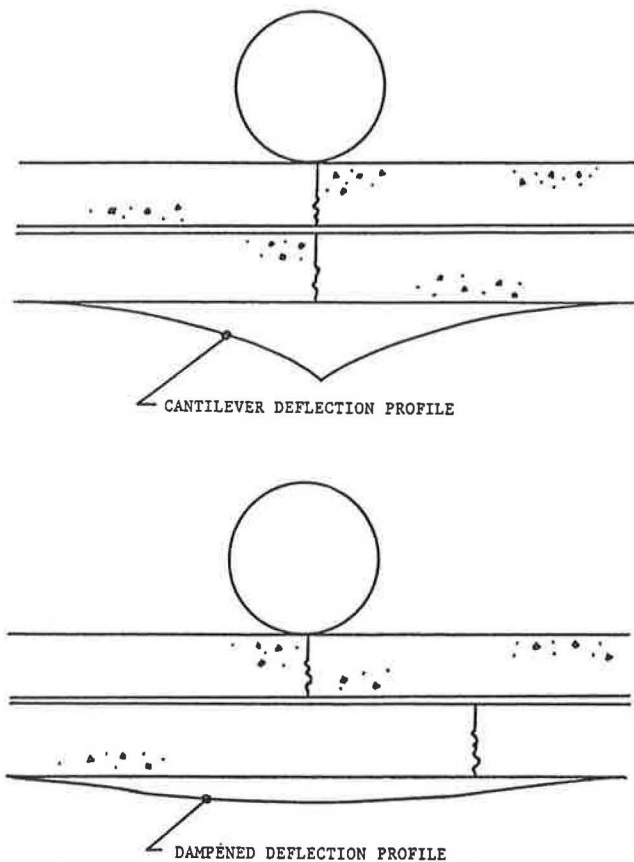


FIGURE 8 Effectiveness of mismatched joints in inhibiting development of faulting and pumping.

ance that load transfer efficiency will be maintained over the life of the overlay is gained when the ability to mismatch joints is used in design.

No significant faulting was measured on any of the uniform sections. The high was 0.08 in. and the low was 0.0 in., while the average faulting for all projects was only 0.03 in. All sections were constructed with mismatched joints except those on Georgia I-85. However, even on Georgia I-85 (with the cracking problems it developed), faulting averaged just 0.03 in. No visual pumping problem was found on any uniform section surveyed; this correlates well with the low faulting observed.

Development

Faulting and pumping in unbonded overlays are reduced by several factors (1):

1. Nonrodible layers (existing PCC slabs and bond-breaker material) beneath the overlay slabs,
2. Dowels providing some load transfer in the overlay, and
3. The mismatching of the overlay joints.

The deflection at the bottom of the existing slab or where the erodible base materials are found is reduced significantly after the overlay is in place. This limits the potential for pumping erosion to create voids and loss of support, which cause faulting development (1).

Distress Potpourri

Other distresses and deterioration may develop in unbonded overlays such as D-cracking, reactive aggregate deterioration, or scaling. These distresses, however, are material or construction related. If an overlay should develop distresses of this nature, it is not a design problem. Proper specifications and inspection should prevent the occurrence of these problems. However, where the use of aggregates susceptible to D-cracking is unavoidable, recent studies in Ohio have shown that reducing the maximum coarse aggregate size used in the concrete mix to 1/2 in. should eliminate the development of aggregate durability problems (14).

Joint deterioration in unbonded overlays, while a possibility, is not likely to occur because of the short joint spacings specified (1). Very little joint deterioration existed in the pavements surveyed.

UNBONDED CONCRETE OVERLAY FAULTING MODEL

Although considerable analysis on the data base for unbonded concrete overlays was conducted, only one model (joint faulting) could be developed from the data. The analysis on other performance indicators was limited by the small number of occurrences of these problems and the limited number of uniform sections of this overlay type.

The model, developed using SHAZAM statistical analysis software, for joint faulting in unbonded concrete overlays is as follows (15):

$$\text{FAULT} = 0.28615 \text{ ESAL}^{0.39654} \times [0.0987 (1 + \text{DOWEL})^{-0.51083}]$$

where

FAULT = the mean faulting at the overlay joints (in inches),

ESAL = equivalent single-axle loads accumulated on the overlay (in millions), and

DOWEL = diameter of dowel bars placed in the overlay (in inches) (0 if no dowel bars were used in the overlay). Note that all dowel bar spacing was 12 inches on centers.

Statistics:

$$R^2 = 0.51$$

$$\text{SEE} = 0.02 \text{ inches (standard error of estimate)}$$

$$n = 23 \text{ sample units}$$

Equation Range of Applicability:

ESAL—equivalent single-axle load data ranged from 0.73 million to 7.0 million accumulated on the overlay.

DOWEL—the diameter of the dowel bars in the existing pavement ranged between 0 (no dowels) and 1.625 in.

A sensitivity plot for the faulting equation is given in Figure 9. It is evident that faulting in unbonded overlays is not

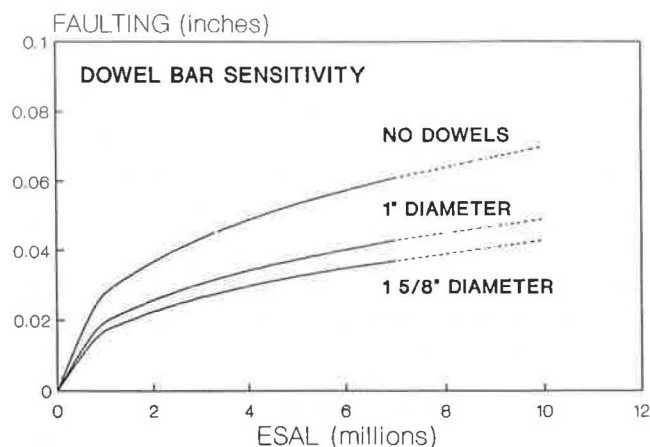


FIGURE 9 Sensitivity of unbonded overlay faulting model to dowel bar diameter.

a significant problem. Faulting typically becomes detrimental when it is more than 0.13 in. for JPCP and 0.25 in. for joint reinforced concrete pavement (JRCP) (16).

An interesting point arises when considering the differences among dowel diameters. As was also discovered with bonded overlays (17), the effects of dowel diameter are not as great on unbonded overlays as on new pavement sections. This may be attributable to the increased slab support from the underlying pavement, mismatched joint arrangement, and the more erosion-resistant asphalt concrete (AC) and PCC beneath the overlay. Figure 10 compares new pavement faulting predicted with the COPES model (19) to faulting modeled by the unbonded overlay model. Without dowels, new pavements fault far more than unbonded overlays. However, with dowels, the predicted faulting is quite similar for both.

OTHER PERFORMANCE INDICATORS

The one major concern for cracking, is that the stiff base would increase thermal curling stresses to a detrimental point. This effect was seen on the Georgia I-85 sections where the original pavement had a 30-ft joint spacing. The unbonded overlay cracked in the middle region of the 30-ft slabs. Where a 15-ft joint spacing was used, no cracks occurred in the overlay (9). Thus, shorter joints *must* be provided in the overlay to control cracking.

CONCLUSIONS

Unbonded concrete overlays have been used successfully to resurface existing concrete pavements with extensive deterioration. The performance of practically all of the 14 uniform sections of unbonded concrete overlays was very good, with no significant deterioration. No special construction techniques are needed in the construction of unbonded overlays. The following are overall conclusions and recommendations.

1. Thermal curling stresses are critical in unbonded concrete overlays because the temperature gradient through the overlay becomes large during many days and nights of the year, and because of the very stiff support from the existing

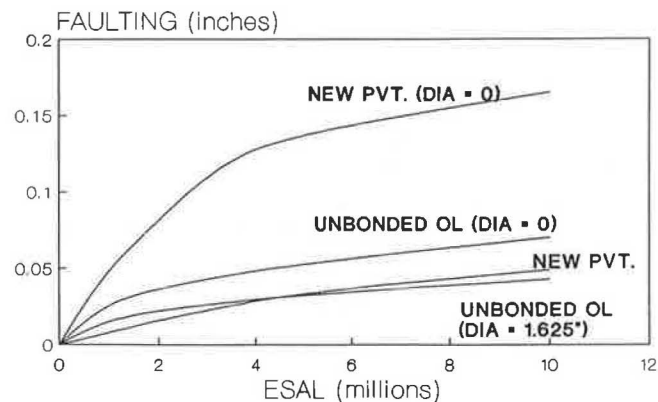


FIGURE 10 Comparison of predicted faulting on unbonded overlays to predicted new pavement faulting.

slab. At these times, curling may cause the overlay slab to lift from the underlying slab and create voids between the slabs, which (when combined with traffic load stresses and the stiff foundation of the underlying slab) can cause transverse cracking. It is highly recommended that the overlay joint spacing be kept short. Maintaining an L/l of between 6 and 7 should ensure that cracking will not develop in the overlay. Short joint spacing will also reduce the need for dowel bars, because the lineal movement from thermal contraction and expansion will be small and aggregate interlock should be maintained. If, however, longer slabs are used, reinforcement *must* be included to keep the cracks tight.

2. When a debonding medium that is not efficient in separating the overlay from the existing slab is used, reflective cracking may result. This has been due mainly to inadequate materials and insufficient debonding layer thickness. It is recommended that where joint and crack faulting is significant, and slabs are highly deteriorated, a minimum one inch of hot-mix asphalt concrete should be used as the debonding medium. Slurry seal has also been effective as a debonding medium; however, only where faulting in the existing slab is not significant and can be covered by this material.

3. Unbonded overlays without dowels fault very little (maximum measured was 0.04 in.), which is far less than new pavements without dowels for the same number of ESALs. The development of faulting in unbonded overlays is not reduced much by the use of dowels in the transverse joints. This has been attributed to fairly nonerodible and stiff foundation support from the underlying slab and mismatched joint locations. It is suggested that under normal traffic conditions (less than 0.8 million 18-kip ESAL per year) dowels are probably not needed in the transverse overlay joints for short-jointed JPCP. It is still recommended that they be placed in log-jointed JRCP overlays, however. The predictive model for faulting can be used to predict faulting for a recommended overlay design to determine whether substantial faulting will occur.

4. Visual pumping was not observed in the field distress surveys. This is attributed to lack of erodible materials beneath the overlay slab, greatly reduced deflections of the slabs, and mismatched joints that alter the deflection basin developed under load. With these effects, there is very little potential for pumping in unbonded overlays.

5. Longitudinal cracking can be attributed mainly to the late sawing or improper depth of the longitudinal centerline

joint. To help control the cracking and provide a significant weakened plane, it is recommended that the centerline joint be sawed at least one-third the thickness of the slab. Timing is very critical in formation of this joint; sawing should be started as soon as possible after overlay placement.

6. Although matching the overlay joints to the existing pavement joints is not recommended, joint placement is not a critical concern in unbonded overlays. It is recommended that the joints be placed at least 3 ft from existing transverse joints or working cracks. This will ensure the load transfer benefits mentioned.

ACKNOWLEDGMENTS

The information contained in this paper was developed under contract with the U.S. Department of Transportation, Federal Highway Administration. The authors express their appreciation to Stephen Forster of FHWA and to the DOTs that were visited. Thanks are also given to the Illinois State Toll Highway Authority.

REFERENCES

1. M. I. Darter, S. H. Carpenter, M. Herrin, E. J. Barenberg, B. J. Dempsey, M. R. Thompson, R. E. Smith, and M. B. Snyder. Techniques for Pavement Rehabilitation. *Participant's Notebook*, revised, National Highway Institute/FHWA, 1984.
2. Transportation Research Board. *Resurfacing with Portland Cement Concrete*. National Cooperative Highway Research Program Synthesis of Highway Practice 99, 1982.
3. V. A. Gould. Summarized Committee Report 1948-1960: Salvaging Old Pavements by Resurfacing. *Highway Research Bulletin* 290, HRB, National Research Council, Washington, D.C., 1961.
4. Iowa Department of Transportation. PCC Inlay—Thin-Bonded PCC Overlay—Unbonded PCC Overlay. Iowa Highway Project Open House, 1983.
5. American Concrete Paving Association and Portland Cement Association. *Concrete Resurfacing 1977 Condition Survey*, 1977.
6. G. Calvert and J. Lane. *Thin Bonded Concrete Overlay with Fast Track Concrete*. Iowa Department of Transportation, Ames, 1985.
7. Iowa Concrete Paving Association. *Iowa Fast Track 1987*. Bulletin, 1987.
8. F. Biancalana and B. Ratterree. Unbonded Nonreinforced PCC Overlay Construction on Illinois State Toll Highway Authority East-West Tollway. Presented at 62nd Annual Meeting, Transportation Research Board, 1983.
9. H. L. Tyner, W. Gulden, and D. Brown. Resurfacing of Plain Jointed Concrete Pavements. In *Transportation Research Record* 814, TRB, National Research Council, Washington, D.C., 1981, pp. 41-44.
10. Georgia Department of Transportation. *Traffic Data*, 1985.
11. B. J. Dempsey and M. R. Thompson. *A Heat-Transfer Model for Evaluating Frost Action and Temperature Related Effects in Multilayered Pavement Systems*. Illinois Cooperative Highway Research Program Project IHR-401, Highway Research Program, University of Illinois, 1969.
12. D. P. Dewitt and F. P. Incropera. *Fundamentals of Heat Transfer*. John Wiley & Sons, 1981.
13. A. M. Ioannides and R. A. Salsilli-Murua. *Slab Length, Slab Width and Widened Lane Effects*. FHWA Report, University of Illinois at Urbana, Dec. 1988.
14. American Concrete Pavement Association. Ohio D-Cracking Test Pavement. *Concrete Pavement Progress*, Vol. 24, No. 4, 1988.
15. K. J. White and N. G. Horsman. *SHAZAM, the Econometrics Computer Program*. Version 5, Users' Reference Manual, 1985.
16. R. E. Smith, M. I. Darter, and S. M. Herrin. *Highway Pavement Distress Identification Manual*. U.S. Department of Transportation/FHWA, Washington, D.C., 1979.
17. M. I. Darter, J. M. Becker, M. B. Snyder, and R. E. Smith. *Concrete Pavement Evaluation System (COPES)*. NCHRP Report No. 277, 1984.

Publication of this paper sponsored by Committee on Rigid Pavement Design.

Performance Evaluation of Experimental Pavement Designs at Clare, Michigan

DAVID G. PESHKIN, KURT D. SMITH, MICHAEL I. DARTER, AND
CHARLES J. ARNOLD

As part of a major research project to evaluate the performance and rehabilitation of rigid pavements in the U.S., an experimental pavement project in Clare, Michigan, was the subject of an in-depth field survey and evaluation. Different pavement designs were evaluated, including jointed reinforced concrete pavement with aggregate bases, and jointed plain concrete pavement (JPCP) with aggregate, permeable asphalt-treated, and dense-graded asphalt-treated bases (ATB). Other variables included in this experiment were skewed joints and perpendicular joints, doweled and non-doweled sections, and sections with and without edge drains. Extensive field testing, including condition surveys, deflection testing, and coring/boring, was performed on the project. The results of this study reveal a notable difference in performance of the different sections. The worst-performing sections were the non-doweled JPCP constructed on a dense-graded ATB, which retained moisture and accelerated the deterioration of the underside of the concrete slab. The best performing section had a permeable ATB. This pavement section was designed so that no excess moisture was available to accelerate moisture-related distresses. Epoxy-coated dowels, edge drainage, and joint sealant appeared to have had a beneficial effect on pavement performance.

As part of the first phase of an FHWA study entitled *Performance/Rehabilitation of Rigid Pavements*, innovative jointed concrete pavement designs were subjected to extensive in-service testing, evaluation, and analysis. The overall goal of the study is to identify successful means of improving Portland Cement Concrete (PCC) pavement performance. Of special interest are the evaluation of methods to reduce pavement slab deflections and improve pavement subdrainage.

A review of the available literature, contacts with state and FHWA researchers, and communication with other members of the research community resulted in the identification of 16 viable experimental pavement projects for inclusion in this study (representing 80 sections). These projects were located in ten states and provinces, covering a wide range of environments, traffic, and functional classifications. Key design features of interest used to identify these sections were: variations in slab thickness, jointed plain concrete pavement (JPCP) versus jointed reinforced concrete pavement (JRCP), different base types, variation in joint spacing, skewed versus perpendicular joints, different load transfer devices and types of corrosion protection, the effect of tied PCC shoulders/wid-

ened lanes, and the effect of different subdrainage design. Some projects incorporated several of these features; while others studied the effect of changes in only one variable.

One interesting experimental project is located on U.S. 10 near Clare, Michigan. Constructed in 1975, this experiment was conducted primarily to evaluate the performance of JPCP placed on different base types (including untreated aggregate), permeable asphalt-treated aggregate, and a dense-graded asphalt-treated aggregate base. Conventional JRCP sections were also included. The experimental design variables evaluated in this project include the different base types noted above, JPCP versus JRCP, and doweled and non-doweled joints. One section that had a concrete on-ramp adjacent and tied to the outer lane was also included. All sections had full-depth asphalt concrete (AC) shoulders. Some experimental designs were located in areas of poorer drainage or where the water table approached within 5 feet of the subbase. These areas had retrofitted longitudinal edge drains consisting of an aggregate (French) drain added in the subbase, directly beneath the lane-shoulder interface. The inclusion of these drains effectively introduced subdrainage as a design variable.

The setup of the experiment included three replicates of each of four pavement designs, with drained and non-drained sections located in each design group, for a total of 24 possible sections. With the addition of the section having a tied concrete acceleration ramp, there were actually 25 candidate sections for this study. From these sections (designated as MI 1-1 through MI 1-25), eight sections were surveyed and tested in 1987. Two sections (MI 1-1a and 1-1b) were included as control sections. They represented Michigan Department of Transportation's (DOT's) then-current design of 9 in. of JRCP constructed on a 4-in. aggregate base, with perpendicular joints spaced at 71.2-ft intervals. Michigan 1-1a was the control section with retrofitted subdrainage. All dowels used were 1.25-in. round, epoxy, and liquid-coated bars. The remaining sections were 9-in. JPCP slabs with skewed random joint spacing patterns of 13, 19, 18, and 12 ft (if not doweled) and 13, 17, 16, and 12 ft (if doweled). A 10-in. sand subbase was present under all of the sections. The factorial design of this experiment is given in Table 1. In addition to trying to obtain as complete a factorial design as possible, section selection was made by observing the following general criteria. Where possible, the segment should be located on a tangent with a minimal vertical grade, it should not have an adjacent acceleration or deceleration ramp, it should not include or be near

D. G. Peshkin, K. D. Smith, and M. I. Darter, ERES Consultants, Inc. 1401 Regency Drive East, Savoy, Ill. 61874. C. J. Arnold, Michigan Department of Transportation, P.O. Box 30049, Lansing, Mich. 48909.

any permanent pavement structures (e.g., bridges), and it should be as close to at-grade as possible. General design information for the selected sections is found in Table 2.

CLIMATE

The U.S. can be divided into climatic zones, according to criteria proposed by Thornthwaite, and refinements made in the moisture-accelerated distress (MAD) system (1,2). The four zones are a simplified division, proposed for use by the Strategic Highway Research Program (SHRP) (3). Projects for the FHWA study were selected by climatic zone so that experimental sections in different states would have a common environment. These pavement sections are located in

the central part of Michigan in a wet-freeze environmental zone. The project site has a Thornthwaite moisture index of 30, an Army Corps of Engineers freezing index of 875, and receives 32 in. of precipitation annually. The highest average daily maximum temperature is 82°F and the lowest average daily minimum temperature is 11°F. This describes a location with a fairly severe climate, including a large amount of excess moisture, numerous freeze-thaw cycles, and large temperature variations throughout the year.

TRAFFIC

U.S. 10 is a four-lane divided highway (two lanes in each direction). The roadway's functional classification is Rural

TABLE 1 EXPERIMENTAL DESIGN MATRIX FOR U.S. 10 (CLARE, MICHIGAN)

PAVEMENT TYPE	JOINT SPACING	BASE TYPE	EDGE DRAIN		NO EDGE DRAIN	
			Skewed Joints	Perpendicular Joints	Skewed Joints	Perpendicular Joints
			No Dowels	Dowels	No Dowels	Dowels
JPCP	12-13-17-16	AGG		1 - 7a		1 - 7b
	12-13-19-18	PATB	1 - 4a			
		ATB	1 - 10a		1 - 10b 1 - 25	
JRCP		AGG		1 - 1a		1 - 1b

All sections were constructed on a 10-in. sand subbase and had a full-depth asphaltic concrete shoulder.

TABLE 2 U.S. 10 DESIGN DATA

	1 - 1a	1 - 1b	1 - 4a	1 - 7a	1 - 7b	1 - 10a	1 - 10b	1 - 25
Joint Spacing, feet	71.2	71.2	13-19-18-12	13-17-16-12	13-17-16-12	13-17-18-12	13-19-18-12	13-19-18-12
% Steel	0.15	0.15	N/A	N/A	N/A	N/A	N/A	N/A
Skewed Joints	N	N	Y	N	N	Y	Y	Y
Base Type	AGG	AGG	PATB	AGG	AGG	ATB	ATB	ATB
Dowel Diameter, inches	1.25	1.25	None	1.25	1.25	None	None	None
Dowel Coating	Liquid Asphalt/Epoxy	Liquid Asphalt/Epoxy	---	Liquid Asphalt/Epoxy	Liquid Asphalt/Epoxy	---	---	---
Shoulder Type	AC	AC	AC	AC	AC	AC	AC	PCC [•]

[•] Partially Tied Acceleration Lane

Principal Arterial. From its opening to traffic in 1975 through 1987, the pavement had sustained the following cumulative 18-kip equivalent single-axle load (ESAL) applications: 885,000 ESALs in the outer lane and 78,000 ESALs in the inner lane. This represents relatively light truck traffic for a 12-year period. Historical W-4 tables were used to calculate the truck factor needed for these ESAL calculations. Weigh-in-motion (WIM) data were also collected on U.S. 10 using portable equipment over a 48-hour period during 1987. In addition to providing estimates of average daily traffic (ADT), percent trucks, lane distribution, and directional distribution, which are very rough indications of the actual values over time, WIM data provided a very good approximation of the actual truck factors for the section. Table 3 summarizes the traffic data.

The 1987 two-way ADT provided by Michigan DOT was approximately 5,100 vehicles per day, including 8 percent heavy trucks. The WIM data collected at the project site provided a two-way traffic count of 5,900 vehicles per day, including 14 percent heavy trucks.

MAINTENANCE AND REHABILITATION

Longitudinal underdrains were installed as a rehabilitation measure under the shoulders of some of the pavement sections with the dense-graded asphalt-treated and aggregate base

courses (MI 1-1a, 1-7a, and 1-10a). The sections with a dense-graded asphalt-treated base (ATB) had shown moisture-related distresses early on, and by 1980, it had become clear that excess moisture must be removed from the pavement. Additionally, some of the sections have received longitudinal joint sealing.

PHYSICAL TESTING RESULTS

Cores from slab centers and from typical transverse joints were retrieved from the pavement sections in 1987. The center cores were tested using the split tensile test to indicate the concrete strength. The split tensile strength values were used to estimate the modulus of rupture. The mean modulus of rupture was 748 psi—indicative of sound concrete.

The joint cores were visually inspected for signs of deterioration beneath the joint or for any signs of material durability distress, such as microcracking in the aggregate. The joint cores taken from the pavement sections indicated that a small amount of concrete deterioration was present directly beneath the joint. Comparatively more deterioration was noted on the sections with dense-graded ATB courses. These particular joint cores also displayed some cracking in the coarse aggregate, typical of the initial stages of D cracking.

Deflection testing with a falling weight deflectometer (FWD)

TABLE 3 TRAFFIC SUMMARY

• Original 20-Year Design Traffic		
2-Way ADT – 5,150		
% Trucks – 5%		
• 1987 Estimated		
2-Way ADT – 5,100		
% Trucks – 8.0%		
1987 WIM Data		
2-Way Traffic Count – 5900		
% Trucks – 14%		
• 1987 ESAL's from W-4		
Outer	Inner	
Lane -- <u>71,175</u>	Lane -- <u>6,189</u>	
• 1987 Estimated Cumulative ESAL's		
Outer	Inner	
Lane -- <u>887,000</u>	Lane -- <u>78,000</u>	

was performed on the sections in 1987 to characterize layer moduli, determine load transfer efficiencies at the transverse joint, and detect voids under the slab corners. The elastic modulus of the concrete (E), the composite k -value (on top of the base), and the load transfer values are summarized for each section in Tables 4 and 5. These were all calculated using the deflection data.

The slab E -values averaged 5,865,000 psi for all of the sections, which is indicative of strong concrete. The foundation support dynamic k -values for the sections varied as follows:

Base Type	Composite k -value (pci)	Avg Mid-Slab Deflection (mils)
Aggregate	303	3.25
Dense-graded ATB	469	2.40
Permeable ATB	468	2.87

It should be noted that a 10-in. sand subbase was located beneath each of the various base types and that the subgrade soil is classified as an AASHTO A-2-4 material.

The two asphalt-treated bases showed greater slab support than the aggregate base. Surprisingly, the permeable asphalt-treated base (PATB) showed the same support as the dense-

graded asphalt-treated base. The PATB was constructed with 2 to 3 percent 85 to 100 pen AC, 2 to 6 percent fly ash, and a uniform-graded, large top-size aggregate. The dense-graded layer was constructed with 6 to 8 percent of 250 to 300 pen AC. The center slab deflections were highest for the aggregate base course sections, and much lower for the dense-graded ATBs and PATBs. The trend shown in the center slab deflections mirror the k -value results.

Load transfer efficiencies at the transverse joints were calculated for each section. The average load transfer efficiencies were much higher for the doweled sections (92 percent) with 1.25-in. diameter, epoxy-coated dowels, than for the non-doweled pavement sections (34 percent). These results correspond with the transverse joint faulting measured on the nondoweled sections over dense-graded ATBs, where erosion occurred.

Using void-detection procedures described in NCHRP 1-21, voids (or loss of support) were detected at slab corners in several of the sections (4). This was also the case in the permeable base section. The void-detection results and other joint data are shown in Table 6. The edge drains appeared to reduce somewhat the amount of loss of support. A com-

TABLE 4 MATERIAL TESTING RESULTS

		1 - 1a	1 - 1b	1 - 4a	1 - 7a	1 - 7b	1 - 10a	1 - 10b	1 - 25
PCC	E, ksi*	5450	5790	5880	6340	6090	6230	5280	N/A
	M_r , psi (cores)	744	---	756	744	---	---	---	N/A
Base	Type	AGG	AGG	PATB	AGG	AGG	ATB	ATB	ATB
	Perm, ft/hr	0.04	0.01	397	1.22	0.02	0.00	0.00	0.00
	k_{eff} , pci*	353	300	468	292	269	436	502	N/A
Subbase	Perm, ft/hr	0.25	2.98	1.10	0.01	2.01	4.48	2.02	0.32
Subgrade	AASHTO Class	A-2-4	A-2-4	A-2-4	A-2-4	A-2-4	A-2-4	A-2-4	A-2-4
	Perm, ft/hr	0.50	0.46	0.50	0.07	0.11	0.14	0.47	0.62

* Backcalculation from FWD.

TABLE 5 FWD TEST DATA

		JRCP 71 ft Doweled		12-19 ft JPCP	JRCP 12-17 ft Doweled		12-19 ft JPCP		
		1 - 1a	1 - 1b	1 - 4a	1 - 7a	1 - 7b	1 - 10a	1 - 10b	1 - 25
Mid-Slab Defl., Mils	High	3.2	4.7	2.6	3.7	3.8	2.7	3.6	N/A
	Low	2.8	2.8	2.1	2.8	3.3	2.2	2.3	N/A
	Avg.	3.0	3.4	2.4	3.1	3.5	2.5	2.6	N/A
Corner Defl., Mils	Loaded Corner	6.7	10.3	21.8	26.3	31.8	13.7	20.4	N/A
	Unloaded Corner	6.0	6.4	3.7	23.0	27.2	5.1	7.2	N/A
	Adjusted LTE	98	72	19	100	100	41	42	N/A
Percent Corners with Voids		0	15	75	94	100	70	100	N/A

parison of the percent voids at corners in sections with similar base types, with and without edge drains, shows 0 versus 15, 85 versus 100, and 70 versus 100.

DRAINABILITY OF PAVEMENT SECTIONS

A drainage analysis was performed on each section to evaluate the section's ability to remove water from the pavement structure. Among the factors considered in determining the pavement drainage coefficient (C_d) for each section were: environment, layer drainage, time of saturation, longitudinal and transverse slopes, and material characteristics. The procedure followed to determine drainage coefficients is that described by Carpenter (5). It is a rational approach that evaluates the permeabilities of the subsurface pavement layers, the pavement cross section, and the amount of available moisture, and provides an assessment of the overall drainability. The resulting drainage coefficients are presented in Table 7. The actual range of drainage coefficients is from 1.25, which signifies excellent drainage, to 0.70, which is representative of very poor drainage.

DETERIORATION OF PAVEMENT SECTIONS

Distress surveys were conducted on these pavements following procedures described in the *Distress Identification Manual*

for *Long-Term Pavement Performance Studies* (6). The data collected follow as closely as possible the long-term pavement performance (LTPP) procedures described in this manual and in the *LTPP Data Collection Guide*, so that this study's data base is compatible with the LTPP data base (3). The results of the extensive distress survey conducted on each pavement section are summarized in Tables 8 and 9. The relative performance of each pavement section with respect to the primary performance indicators is discussed below for the outer lane only.

Joint Spalling

Any evaluation of joint spalling must consider the fact that the large aggregate in the concrete slab was susceptible to freeze-thaw damage, or D cracking. Therefore, the more water available to saturate the slab over long periods of time, the greater the extent of D cracking. This was observed during the field survey and in the joint cores retrieved from transverse joints. Deterioration due to D cracking along the longitudinal joint had already led to maintenance patching of this joint in many areas of this project at the time of the survey.

The 71-ft JRCF showed no medium- or high-severity joint spalling. However, the joint spalling on the JPCF section varied greatly with base type. The dense-graded ATBs had much greater transverse joint spalling than either the aggre-

TABLE 6 RESULTS FROM DEFLECTION TESTING AND ANALYSIS

Section	Base Type	Dowels	Sub-drainage	Corners with Voids (%)	LTE (%)	Max Corner Deflection (mils)
1-1a	Granular	Yes	Yes	0	98	8.5
1-1b	Granular	Yes	No	15	72	17.9
1-4a	Permeable	No	Yes	85	19	34.3
1-7a	Granular	Yes	Yes	85	100	29.5
1-7b	Granular	Yes	No	100	100	37.2
1-10a	Asphalt	No	Yes	70	41	19.4
1-10b	Asphalt	No	No	100	42	27.9

TABLE 7 DRAINAGE COEFFICIENTS FOR CLARE, MICHIGAN

SECTION	JOINT SPACING, ft	PAVEMENT TYPE	BASE TYPE	SUBDRAINAGE TYPE	DRAINAGE COEFFICIENT, C_d
1-1a	71.2	JRCF	AGG	Edge Drains	1.00
1-1b	71.2	JRCF	AGG	No Edge Drains	0.90
1-4a	12-19	JPCF	PATB	Edge Drains	1.10
1-7a	12-17	JPCF	AGG	Edge Drains	0.90
1-7b	12-17	JPCF	AGG	No Edge Drains	0.85
1-10a	12-19	JPCF	ATB	Edge Drains	0.80
1-10b	12-19	JPCF	ATB	No Edge Drains	0.70
1-25	12-19	JPCF	ATB	No Edge Drains	0.70

TABLE 8 PERFORMANCE DATA SUMMARY—OUTER LANE

	1 - 1a	1 - 1b	1 - 4a	1 - 7a	1 - 7b	1 - 10a	1 - 10b	1 - 25
Average PSR	3.6	3.3	3.9	3.6	3.7	2.9	2.8	2.9
Mays RI, IN/MI	96	91	48	58	36	98	104	159
Avg. Transverse Faulting, IN	0.05	0.08	0.03	0.04	0.04	0.14	0.19	0.20
Transverse Cracks/Mile	0	5	0	0	0	0	18	29
Longitudinal Cracking, LIN FT/MI	0	0	0	0	0	0	0	0
Pumping	N	N	N	N	N	L	L	L
Percent Spalled Joints	0	0	9	12	11	41	63	75

TABLE 9 PERFORMANCE DATA SUMMARY—INNER LANE

	1 - 1a	1 - 1b	1 - 4a	1 - 7a	1 - 7b	1 - 10a	1 - 10b	1 - 25
Average PSR	3.9	3.2	4.0	3.8	4.0	3.0	3.6	3.4
Mays RI, IN/MI	76	74	40	51	44	78	80	103
Avg. Transverse Faulting, IN	0.04	0.04	0.00	0.02	0.03	0.03	0.03	0.01
Transverse Cracks/Mile	0	10	0	0	0	0	0	0
Longitudinal Cracking, LIN FT/MI	0	0	0	0	0	0	0	0
Pumping	N	N	N	N	N	L	L	L
Percent Spalled Joints	0	0	2	0	0	32	43	25

gate or permeable base, which had about the same amount of joint spalling.

Base Type	Joint Spacing (ft)	Dowels	Joint Spalling (%)
Aggregate	71	Yes	0, 0 (two sections)
PATB	12-19	No	9
Aggregate	12-17	Yes	11, 12
Dense Asphalt	12-19	No	47, 65, 87

Those sections with dense-graded ATBs and full-depth AC shoulders result in bathtub-type designs, from which water does not readily drain. This results in continual saturation of the PCC slab when excess moisture is available which, in turn, causes acceleration of the deterioration of both the transverse and longitudinal joints. The aggregate bases had greater permeability and, thus, drained free water more rapidly. The permeable asphalt section was designed with a higher permeability, over 1,000 ft/day, than either of the other two base designs. This design can be considered free-draining, essentially reducing the time the concrete slab is sitting in water to zero.

Best Performance

The pavement sections displaying the best performance, in terms of joint spalling, had a 9-in. JRC or JPCP slab on the

aggregate base or the nondoweled JPCP slab on the PATB course.

Worst Performance

The worst performance, in terms of joint spalling, was demonstrated by the pavement sections with 9-in. JPCP nondoweled slabs on dense-graded ATB course.

Joint Faulting

Joint faulting varied greatly between test sections. The permeable base JPCP section with no dowels had practically no faulting. The JPCP and JRC sections with 1.25-in., epoxy-coated dowel bars and an aggregate base also had very little faulting. The dense-graded asphalt base JPCP sections showed a large amount of faulting and are candidates for rehabilitation due to the excessive roughness. Faulting on isolated joints of these sections is approaching one inch. The faulting results are summarized below:

Base Type	Joint Spacing (ft)	Dowels	Faulting (in.)
Permeable	12-19	No	0.03
Aggregate	12-17	Yes	0.04, 0.04
Aggregate	71	Yes	0.05, 0.08
Dense asphalt	12-19	No	0.14, 0.19, 0.20

While it might not be expected that a concrete slab would fault on a stabilized base, evidently the dense ATB held free moisture that accelerated the deterioration of the bottom of the slab (7). Thus, the source of erodible material was not the base, as is typically the case.

Some of the sections contained longitudinal edge drains. The following comparisons of faulting can be made:

Drains	Base Type	Joint Spacing (ft)	Dowels	Faulting (in.)
No	Aggregate	12-17	Yes	0.04
Yes	Aggregate	12-17	Yes	0.04
No	Aggregate	71	Yes	0.08
Yes	Aggregate	71	Yes	0.05
No	Dense asphalt	12-19	No	0.19, 0.20
Yes	Dense asphalt	12-19	No	0.14

The short-jointed sections on aggregate bases showed no difference in faulting, with or without edge drains. However, among the long-jointed sections and the sections on dense-graded asphalt bases, the sections having no edge drains had about 33 percent more faulting than sections with edge drains. Any conclusions regarding the occurrence of faulting must be considered in light of the low number of cumulative ESALs on these sections.

Best Performance

Pavement sections with the best performance, in terms of joint faulting, had the following design features:

- Nine-inch JPCP slab on PATB course without load-transfer devices,
- Nine-inch JPCP slab on aggregate base course with load-transfer devices, and
- Nine-inch JRCF slab on aggregate base course with load-transfer devices and edge drains.

Worst Performance

The pavement section displaying the worst performance, in terms of joint faulting, had a 9-in. slab on dense-graded ATB course without load-transfer devices.

Transverse Cracking

Very little transverse cracking, measured by the number of deteriorated 12-ft cracks per mile, occurred on the experimental sections. The JRCF had practically no deteriorated transverse cracks, even though cracking is expected on these designs. A possible explanation lies in the use of dowels that were coated with epoxy and then dipped in asphalt to prevent initial bonding to the concrete, and subsequent corrosion and corresponding joint lockup. Elsewhere in Michigan, on older sections with uncoated and corroded dowels, pull-out tests have shown that the dowels have a high pull-out resistance and that the reinforcing steel will yield before a locked-up joint opens (8).

The JPCP sections with either a permeable base or aggregate base had no transverse cracking. The three JPCP sections with dense-graded ATBs had 18, 29, and 159 cracks/mile. These can be compared to a critical level of about 70 cracks/

mile, at which rehabilitation is needed. The absence of cracking in most sections is also probably a result of the relatively low level of truck traffic over the 12 years of service life.

Best Performance

In terms of deteriorated transverse cracks, the best performance was exhibited by pavement sections having 9-in. JRCF slab on aggregate base course, and 9-in. JPCP doweled slab on aggregate base or the 9-in. nondoweled slab on the permeable base course.

Worst Performance

The worst performance, in terms of deteriorated transverse cracks, was displayed by pavement sections with 9-in. JPCP slab over dense-graded ATB course.

Longitudinal Cracking

No longitudinal cracking occurred on any of the pavement sections. According to plans, the longitudinal joint was sawcut to a depth of 2.75 inches.

Present Serviceability Rating and Roughness

The rideability of the sections was measured using a Mays meter to obtain a roughness index (RI), and by assigning a present serviceability rating (PSR) to each section. These results varied considerably and are shown below.

Base Type	Joint Spacing	Dowels	Mays RI (in./mi)	PSR
Permeable	12-19	No	48	3.9
Aggregate	12-17	Yes	58, 36	3.6, 3.7
Aggregate	71	Yes	91, 96	3.3, 3.6
Dense asphalt	12-19	No	98, 104, 159	2.8, 2.9, 2.9

The smoothest riding (and highest panel PSR) section after 12 years is the JPCP having a permeable base. This section had the least faulting and joint spalling, and no cracking. The roughest sections were those with dense-graded ATB. These sections had the most faulting, cracking, and joint spalling.

EFFECT OF DESIGN FEATURES ON PAVEMENT PERFORMANCE

Several of the design features had a significant influence on the performance of the pavement sections. The relative effects of these design features are summarized below.

Base Type

The dense-graded ATB course sections were the poorest performers of all base types. This is based on the amount of transverse cracking, spalled joints, and joint faulting—all of which caused significant roughness in the pavements. The PATB sections performed the best, showing little faulting or

joint spalling, and no cracking. The aggregate base course sections performed well, as they had only slightly more deterioration than the permeable base sections. These sections all contained dowels, which have a major effect on the reduction of faulting.

Extensive coring performed by the Michigan DOT on the dense-graded ATB sections indicated that the bottom of the slab joints were severely deteriorated (9). However, the asphalt base course was in good condition. This illustrates the deleterious effects of free water on concrete slabs when no positive drainage system is present, even in the presence of relatively low levels of traffic (9).

Joint Load Transfer

Sections with dowels had much higher measured deflection load transfer. However, no direct comparison can be made between sections with and without dowels. The only comparisons that can be made for faulting are the following:

Section	Dowels	Faulting (in.)	Drainage Coefficient	Load Transfer (%)
JPCP/PATB	No	0.03	1.1	19
JPCP/Aggregate	Yes	0.04	0.87	100
JPCP/ATB	No	0.19	0.76	42

Faulting is clearly affected by the drainability of the base course and by the presence of dowels. For the specific traffic, subgrade, and climate of this project, the JPCP with permeable base did not appear to need dowels to prevent faulting. Dowels used with the much less permeable aggregate base, however, did prevent faulting. It should be noted that this is only after 12 years of relatively light traffic. The low load transfer efficiency and high corner deflections indicate that epoxy-coated dowels may be necessary for satisfactory long-term performance. The Michigan DOT would include dowels on all pavements with higher traffic volumes.

Edge Drains

The replicate sections with and without edge drains showed the significant benefit of the inclusion of those drains. The use of edge drains resulted in approximately 33 percent less faulting, compared to the identical sections without edge drains. The sections with edge drains also showed about 15 percent fewer corners with voids, or loss of support. The effect of edge drains on any other distress is not apparent, except that for the dense-graded ATBs. Less joint spalling occurred with drains (47 percent joints) than without drains (65 to 87 percent).

Joint Spacing

A direct comparison of joint spacing can be made between the 71-ft JRCP and the 12-17 ft JPCP with aggregate bases:

Joint Spacing (ft)	Faulting (in.)	Cracking (crks/mi)	Joint Spalling (%)	Roughness (in./mi)	PSR
71	0.07	3	0	94	3.4
12-17	0.04	0	12	47	3.7

The overall performance of these sections is roughly comparable; the only significant difference being the greater roughness and lower PSR for the JRCP section. However, according to the Michigan DOT, the long-jointed sections were slightly rougher, even at construction. It is interesting to note that the drainage coefficient for the long-jointed sections is higher than for the short slabs. The excellent drainage characteristics of these sections may have mitigated some of the distresses often associated with long-jointed pavements.

Concrete Acceleration Ramp

One short section included a tied concrete acceleration ramp adjacent to the outer traffic lane. This section also contained the dense-graded ATB course, no subdrainage, and no dowel bars. There was no joint sealant between the lane and acceleration ramp, thus freely allowing moisture to enter the pavement structure. Also, poorly installed, expansion-anchored lane ties across the lane-ramp longitudinal joint failed shortly after construction. The performance of this section was as poor as the two other sections with asphalt shoulders and asphalt base. The presence of the tied acceleration ramp had no effect on its performance.

COMPARISON OF OUTER AND INNER LANE PERFORMANCE

Although being subjected to far fewer traffic loadings than the outer lane, the performance of the inner lane sections provided an interesting comparison. Table 10 compares the inner and outer lane performance for sections with three different base types

Faulting in the inner lane is far less than in the outer lane for the dense-graded asphalt-treated section, but only slightly less for the aggregate base sections. The effect of heavy truck loads on movement of the material generated by the deterioration of the slab is apparent. Higher joint spalling occurred in the outer lane than the inner lane for the JPCP sections, indicating that truck traffic can break down concrete that has been weakened from microcracks caused by freeze-thaw damage. Also, the main contact point between slabs in these sections was just below the joint seal, as the bottom of the joint face had been eaten away by freeze-thaw damage. However, the main cause of joint spalling is not related to truck loadings, but to the disintegration of the concrete near the joints. Roughness and PSR indicated worse performance in the outer lane than in the inner lane, probably due to increased faulting and joint spalling.

For the sections constructed with the PATB material, no difference in performance could be discerned between the two traffic lanes.

SUMMARY AND CONCLUSIONS

The most significant conclusion that can be drawn from these experimental pavements is that the section with PATB course performed slightly better than any other section. This section had short joint spacing (12 to 19 ft) and no dowels. The design of this section provided rapid subdrainage of water entering

the pavement section. The rapid removal of water meant that moisture was not present long enough to accelerate erosion of the base or concrete slab, as occurred in other sections. The effect on the pavement's performance was that both joint faulting and spalling were greatly reduced. This is only after 12 years of relatively light traffic, however.

The low load transfer efficiency and high corner deflections for this section raise concerns about the ability of this design to provide satisfactory, long-term performance. Since dowels cannot be economically retrofitted on short slab, jointed-concrete pavements, it is believed that the inclusion of 1.25-in. diameter, epoxy-coated dowel bars in the originally constructed pavement would provide an economical guarantee of long-term performance.

The worst performing sections included those having a dense-

graded ATB course with the standard full-depth asphaltic concrete shoulder. These sections trapped free water for long periods of time. This led to serious erosion of the underside of the slab, which resulted in faulting, saturation of the concrete, and freeze-thaw damage and spalling at the transverse and longitudinal joints. These sections also had a significant amount of transverse slab cracking.

The aggregate base sections with dowels performed very well; much better, in fact, than the dense-graded ATB pavements. The granular base of these sections provided some vertical drainage. The drainage afforded by this layer was evidently sufficient to reduce the amount of time that free water remained beneath the slab. The 1.25-in. epoxy-coated dowels in these pavements also helped to prevent faulting of the joints.

TABLE 10 OUTER AND INNER LANE PERFORMANCE COMPARISONS

JRCP WITH AGGREGATE BASE, 71-ft Joints

<u>Variable</u>	<u>Inner Lane</u>	<u>Outer Lane</u>
ESAL's (millions)	0.08	0.90
Jt. Spall, percent	0	0
Jt. Fault, in	0.04	0.07
T. Cracks, no./mi	5	3
L. Cracks, lin ft/mi	0	0
Roughness, in/mi	75	94
PSR	3.5	3.4

JPCP WITH AGGREGATE BASE, 12-17 ft Joints

<u>Variable</u>	<u>Inner Lane</u>	<u>Outer Lane</u>
ESAL's (millions)	0.08	0.90
Jt. Spall, percent	2	12
Jt. Fault, in	0.03	0.04
T. Cracks, no./mi	0	0
L. Cracks, lin ft/mi	0	0
Roughness, in/mi	47	47
PSR	3.9	3.7

JPCP WITH DENSE ASPHALT-TREATED BASE, 12-19 ft Joints

<u>Variable</u>	<u>Inner Lane</u>	<u>Outer Lane</u>
ESAL's (millions)	0.08	0.90
Jt. Spall, percent	49	66
Jt. Fault, in	0.02	0.18
T. Cracks, no./mi	0	0
L. Cracks, lin ft/mi	0	0
Roughness, in/mi	87	120
PSR	3.3	2.9

JPCP WITH PERMEABLE ASPHALT-TREATED BASE, 12-19 ft Joints (for comparison)

<u>Variable</u>	<u>Inner Lane</u>	<u>Outer Lane</u>
ESAL's (millions)	0.08	0.90
Jt. Spall, percent	2	9
Jt. Fault, in	0	0.03
T. Cracks, no./mi	0	0
L. Cracks, lin ft/mi	0	0
Roughness, in/mi	41	47
PSR	4.0	3.9

Edge drains placed along some of the sections reduced joint faulting by about 33 percent. Some evidence is available to show that joint spalling was also reduced.

The joint performance of the 71-ft JRCP was excellent in terms of spalling. This may be attributable to the good performance of the preformed compression seals, that apparently kept out incompressibles, and the granular base, that provided some subdrainage so that significant D cracking had not yet developed at the time of the survey. The dowels have not contributed to joint distress and have not resulted in deteriorated transverse cracking.

The drainage coefficients calculated for these sections reveal a trend that is followed in the performance of the sections. That is, the sections with the best drainage characteristics had the best performance and the sections with the worst drainage characteristics had the worst performance.

Finally, the doweled pavement sections of this project represent one of the earliest applications of epoxy-coated dowel bars. Their excellent performance, in both the long-jointed and short-jointed sections, suggests possible benefits to be derived from application of a rust inhibitor to such devices.

REFERENCES

1. C. W. Thornthwaite. An Approach Toward a Rational Classification of Climate. *Geographical Review*, Vol. 38, No. 1, 1948.
2. S. H. Carpenter, M. I. Darter, B. J. Dempsey, and S. Herrin. *A Pavement Moisture Accelerated Distress (MAD) Identification System*—Volume 1. Final Report, FHWA/RD-81/079, September 1981.
3. J. B. Rauhut, M. I. Darter, et al. Data Collection Guide for Long-Term Pavement Performance Studies. Draft, June 1987.
4. J. A. Croveti and M. I. Darter. Void Detection Procedures. NCHRP 1-21, Appendix C, March 1985.
5. S. H. Carpenter. Selecting AASHTO Drainage Coefficients. Presented at the 68th Annual Meeting of the Transportation Research Board, 1989.
6. K. D. Smith, M. I. Darter, et al. *Distress Identification Manual for Long-Term Pavement Performance Studies*. Report No. FHWA/RD-87, December 1987.
7. T. M. Green, and E. C. Novak, Jr. *Drainage and Foundation Studies for an Experimental Short Slab Pavement*. Research Report No. R-1041, Michigan Department of State Highways and Transportation, 1977.
8. C. J. Arnold. *Performance of Several Types of Corrosion Resistant Load Transfer Bars, for as Much as 21 Years of Service in Concrete Pavements*. Research Report No. R-1151, Michigan Department of State Highways and Transportation, Aug. 1980.
9. C. J. Arnold. *The Relationship of Aggregate Durability to Concrete Pavement Performance, and the Associated Effects of Base Drainability*. Research Report No. R-1158, Michigan Department of State Highways and Transportation, 1981.

Publication of this paper sponsored by Committee on Rigid Pavement Design.

Probabilistic Design of Flexible and Rigid Pavements Using AASHTO Equations

ADNAN A. BASMA AND ADLI H. AL-BALBISSI

This paper applies statistical and probabilistic methods to the design of pavements, using the existing AASHTO equations. The major purpose for applying such methods was to assess the variation of the pavement geometry as a function of the variabilities of design factors. A linear first-order approximation was applied on the AASHTO pavement design equation to determine the effect of the variation of traffic and soil support value on the variation of structural number for flexible pavement and the effect of the variation of traffic and concrete flexural strength on the variation of slab thickness for rigid pavements. The mean and variance equations for the pavement geometry were derived by using Taylor's series expansion about the mean. Nomographic solutions of these equations are provided, which would prove helpful in practical applications. The final design thickness of the pavement for a specific service life and design parameters variability is obtained by combining the nomographic solutions with the least cost concept, thereby satisfying economy, performance and statistical design requirements. Examples to illustrate the use of this technique in the design of both flexible and rigid pavements are presented.

The design of pavement systems, from a practical point of view, involves the selection and assignment of specific values for several design factors. However, the design input parameters are rarely, if ever, unique or constant values. Strictly speaking, every design factor studied and analyzed possesses some degree of variability and randomness in its measurement. It is not surprising, for instance, in a given design situation, to find subgrade support value for a single soil varying rather considerably over a wide range. The recent recognition of these probabilistic random properties of design and material factors has brought great attention to the use of statistical concepts within the field of pavement technology. Application of statistical and probabilistic methods to the design of pavement systems would seem to be, therefore, an essential step toward improving existing design procedures. Probabilistic techniques have been used extensively for several years in various areas of engineering. The consideration of material variations, traffic load uncertainties, and soil properties variabilities in the design of pavements has been strongly advocated by several researchers. Probabilistic methods have been applied to flexible pavement design and analysis by Darter et al. (1–4) and McManus and Barenberg (5). Applications to rigid pavements were made by Kher and Darter (6, 7).

Even though all pavement-design methods, in particular the AASHTO design, consider the effect of factors such as subgrade, pavement layer strength, traffic characteristics, and

environmental conditions on the pavement geometry (thickness), these methods do not take into account the variabilities of these design parameters. On the basis of an extensive survey, Von Quintus et al. (8) indicated that pavements designed using the conventional AASHTO method did not last the entire intended 20-year period. They observed that in most cases, the in-service life of these pavements was between 8 and 12 years. Furthermore, Von Quintus et al. stated that highways in many of the urban and suburban areas throughout the United States are subjected to unusually heavy traffic volumes and traffic loading uncertainties, which often cause pavements to deteriorate early. Hence, designing pavements using the conventional AASHTO method, which is considered to be a deterministic solution, would prove to be insufficient. However, the inclusion of probabilistic concepts in the AASHTO equations may provide a better and more realistic pavement-design method. The introduction of such a concept, thus, represents an attempt to amplify the AASHTO design methodology.

The objective of this study was to extend on the AASHTO design equations and to show how the uncertainties in design factors affect the variation of thickness requirement in pavements. The AASHTO Interim Guide equations for flexible and rigid pavements provide the basic structural design models. Through a first-order linear approximation of the AASHTO equations, the impact of the most significant design parameter variabilities (such as traffic and soil support value for flexible, and traffic and concrete strength for rigid) on the variation of pavement geometry was evaluated and quantified for three types of pavements—secondary ($P_t = 2.0$), primary ($P_t = 2.5$), and premium ($P_t = 3.0$). In order to satisfy both structural design requirements and economy, the above solution (presented in a nomographic form) was combined with the least-cost analysis concept; thereby, producing a design thickness corresponding to a predetermined structural reliability.

GENERAL FRAMEWORK

A combination of existing design procedure (9), statistical techniques (10–12), and the least-cost concept (3,13) was used in developing the statistical design thickness requirements for both flexible and rigid pavements. The AASHTO equations form the basis for structural design. For flexible pavements, this equation relates traffic repetitions to structural number, soil support value, and regional factor and is written sym-

bolically as follows:

$$\log W = 9.36 \log(SN + 1) - 0.20 + \log[0.37(4.2 - P_t)] \\ \div \{0.40 + [1,094/(SN + 1)^{5.19}]\} \\ + 0.38(SSV - 3.0) - 0.97 \log(R_f) \quad (1)$$

where

W = total number of 18-kip equivalent axle loads (EAL),
 SN = weighted structural number,
 P_t = terminal serviceability index,
 SSV = soil support value, and
 R_f = regional factor.

On the other hand, for rigid pavements, the AASHTO model expresses traffic repetitions in terms of concrete slab thickness and working strength as well as modulus of subgrade reaction. This equation is presented mathematically as follows:

$$\log W = 7.35 \log(D + 1) - 0.06 + \log[0.333(4.5 - P_t)] \\ \div \{1 + [1.624 \times 10^7 / (D + 1)^{8.46}]\} \\ + (4.22 - 0.32P_t) \left(\log \frac{S_c}{690} \lambda \right) \quad (2)$$

where

D = concrete slab thickness in inches,
 S_c = concrete working strength (psi),
 E = concrete modulus of elasticity (psi),
 k = modulus of subgrade reaction (pci), and
 $\lambda = (D^{0.75} - 1.132) / \{D^{0.75} - [18.42 / (E/k)^{0.25}]\}$.

One tacit drawback, however, in the AASHTO design procedure is that it does not account for the variations in the design factors. To overcome this deficiency, a first-order linear approximation was applied to Equations 1 and 2 to estimate the variation of pavement design thickness as a function of the variabilities of other design factors. The final design process entails the combination of the aforementioned method with the least-cost concept; thereby, satisfying both statistical safety and economy.

VARIABILITIES IN PAVEMENT DESIGN INPUTS

It has been said that nearly every measurable component used in pavement design possesses some degree of variability. Indeed, to those who are closely affiliated with pavement design and performance, the word variability has much meaning. In designing pavement systems, one must inevitably estimate many inputs from information that is, by and large, limited. In many cases, such design inputs vary and are rarely unique or constant. Thus, available deterministic design procedures are, in a sense, inadequate.

However, if input parameters' variabilities are identified and magnitudes quantified, they can be incorporated into the design process to produce a more realistic design procedure. Many of the variabilities have been reported in the literature, namely by Darter et al. (1) and by AASHTO (9). In the current research context, the variabilities (expressed in terms of a mean value and a coefficient of variation) of such design

inputs as traffic and subgrade strength (for flexible) and traffic and concrete flexural strength (for rigid) pavements will be considered, and their impact on thickness design will be evaluated. A brief discussion of the variation of these factors follows.

Variations in Traffic

Perhaps the most variable and uncertain design input is the traffic loadings and traffic repetitions expected over the life of the pavement. Many factors give rise to uncertainty in traffic prediction, which include social and economic factors as well as others. Such variabilities and uncertainties become most evident on high-volume freeways. On the New Jersey Turnpike, pavement design was based on 20 million applications, but estimates indicated that the 20-year count was over 90 million vehicle applications. In Kentucky, using a new method, Deacon and Lynch (14) observed that the equivalent wheel loads over a 20-year period for 20 locations varied dramatically from actual counts. They stated that, in general, actual traffic will usually fall between one-half and two times the best estimate.

Variations in Subgrade Strength

Regardless of the type of pavement and the method of design being used, usually one starts by assessing the soil areas that are expected to be the subgrade. Inescapably, several laboratory and field tests must be conducted. In many cases, one would be surprised to find that even within presumably homogenous soil areas, soil properties exhibit considerable variation. Several researchers have emphasized this fact (10,9,13) and have further observed that variations and dispersions in different soil properties vary widely, as indicated by the coefficient of variation (standard deviation divided by the mean). They also noted that the highest coefficient of variation occurred in the strength properties of soils.

In the AASHTO design procedure for flexible pavements, the strength of the subgrade is expressed by the soil support value, SSV. However, the arbitrary manner in which soil support value was introduced into the AASHTO procedure makes it an input value that cannot be directly obtained by testing and, therefore, must be correlated (in one way or another) to measurable soil strength properties (California bearing ratio, CBR; triaxial strength; resilient modulus, M_R ; etc.) Such correlations were established by Utah (15,16) and Van Til et al. (17). The latter was based on a theoretical layered analysis. With the suggested values in these references of SSV for different CBR and M_R , a regression analysis was performed, which resulted in the following equations:

$$SSV = 1.57 + 1.46 \ln CBR \\ r^2 = 0.989, SE = 0.069 \quad (3)$$

and

$$SSV = -0.032 + 2.73 \ln M_R \\ r^2 = 0.996, SE = 0.103 \quad (4)$$

where CBR is in percent and M_R in units of 10^3 psi.

In order to express mathematically the variation of SSV in terms of the variations of CBR and M_R , a first-order linear approximation for the variance (discussed in detail in the next section) was applied to Equations 3 and 4, and the result is the following:

$$\text{Var}[\text{SSV}] = 1.46\overline{\text{CBR}} \cdot \text{CV}^2[\text{CBR}] \quad (5)$$

and

$$\text{Var}[\text{SSV}] = 2.73\overline{M_R} \cdot \text{CV}^2[M_R] \quad (6)$$

where

$\text{Var}[\text{SSV}]$ = the variance of SSV,
 $\overline{\text{CBR}}$ and $\overline{M_R}$ = the mean of CBR and M_R ,
 respectively, and
 $\text{CV}[\text{CBR}]$ and $\text{CV}[M_R]$ = the coefficient of variation of
 CBR and M_R , respectively.

Figure 1 is a graphical presentation of Equations 3, 4, 5, and 6. It should be pointed out that Equations 3 and 4 are

considered to be the mean value equations for SSV, as defined by the first-order linear approximation.

On the other hand, the strength of soil in the AASHTO design method for rigid pavements is designated by the modulus of subgrade reaction, k , which is determined by means of the plate-bearing test. Usually, this test is time consuming and, except for special cases, is rarely performed for design of rigid pavements. Typical values can be easily obtained for different soils from tables such as the Unified Soil Classification system. These values are not expected to vary greatly and are justified for design of rigid highway pavements (12). Furthermore, it can be seen (from Equation 2) that the modulus k is relatively insensitive in the analysis of rigid pavements. Therefore, the effect of the variation of subgrade modulus on the variation of concrete slab thickness will be excluded from this analysis.

Variation in Pavement Layer Strength

Generally speaking, the variability of layer strength is a function of the type of material, layer location, and (probably

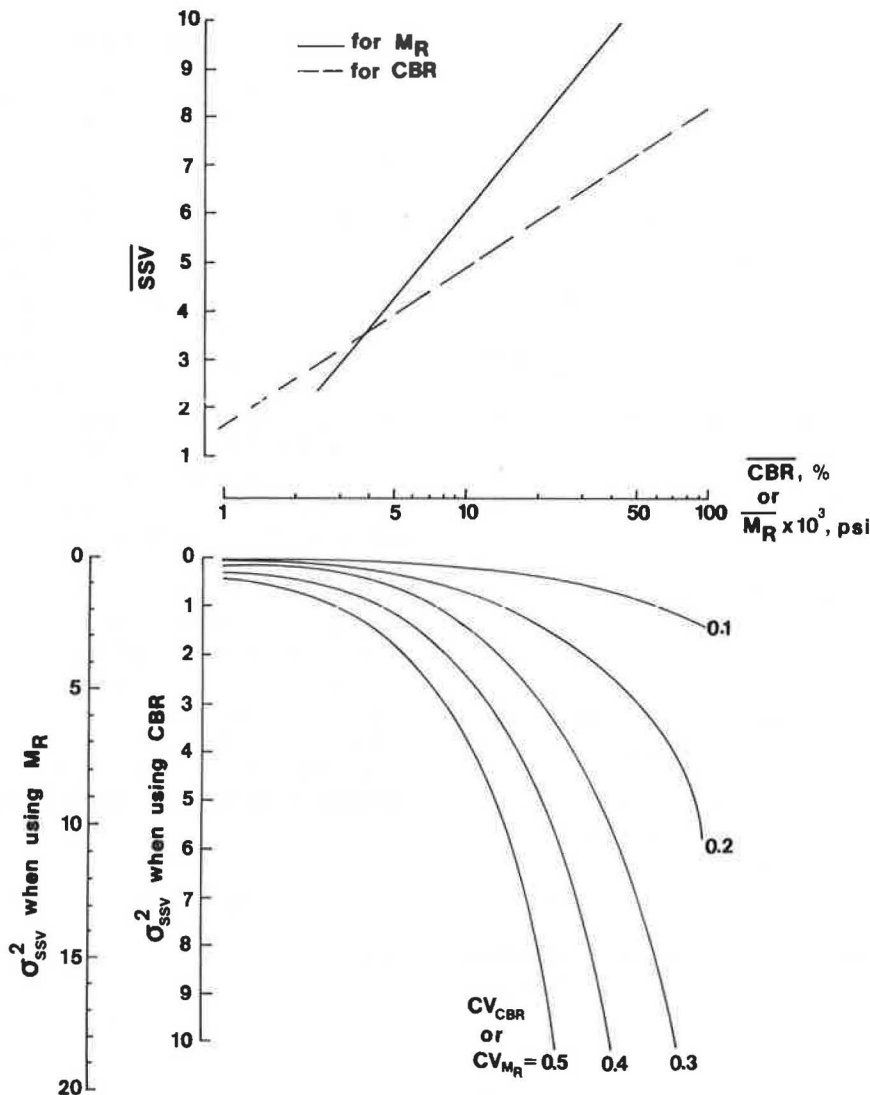


FIGURE 1 Variation of soil support value related to variation of CBR or M_R .

most important) the construction control exercised to obtain uniformity in the material. Strength variability in pavement layer, in general, is expected to decrease as one proceeds toward the natural foundation soil. This may be explained by the fact that, during the life of the pavement, layers (especially those on the surface) are exposed to many performance variations that are directly related to traffic loadings, environmental conditions, maintenance procedures, and occurrence of distresses along the pavement.

In addition, it has been observed (12) that the variability in layer strength data tends to increase as the mean strength increases, especially in flexible pavements. Furthermore, the relationship between the standard deviation and the mean suggests that the use of the coefficient of variation, CV, is a more practical way of describing strength variability.

From the data presented in the literature (12,18), it can be seen that typical values for the CV of the subbase and base range from 15 to 40 percent, whereas the asphalt concrete surface layer has a slightly higher CV. The modulus of rupture variability data of Portland cement concrete, on the other hand, has been found to be a function of the mean compressive strength value (18) with common CV values ranging from 10 to 15 percent.

PROBABILISTIC DESIGN OF PAVEMENTS

Selecting the most effective and economical design for a given project is imperative to the pavement engineer and at the core of all engineering practice. The overwhelming demand for better design processes in pavement technology arises from the limited pavement funds, materials, public need for better performance, and less traffic delay due to maintenance. Therefore, choosing an optimal design is a matter of vital importance. Application of probabilistic techniques to pavement design and analysis may help attain greater optimization in many ways. Probabilistic techniques allow direct consideration of variations and uncertainties in design inputs and, thus, the thickness of the pavement may be increased, depending on these variations, to reduce occurrence of random distresses based on a given reliability. The reliability of the design, R , can be defined as the probability that the actual thickness will not exceed the design thickness obtained,

$$R = P(t_a \leq t) \quad (7)$$

where

- P = probability of occurrence,
- t_a = actual thickness for which the pavement should have been designed given certain conditions, and
- t = thickness for which pavement was designed given the same certain conditions as t_a .

Alternatively, the probability of failure, P_f , can be defined as

$$P_f = 1 - R \quad (7a)$$

To evaluate the reliability of a design, one must first assess the variation of pavement thickness based on the variations of the design inputs; i.e., estimate the mean and variance (or standard deviation). The AASHTO design equations (Equa-

tions 1 and 2) are used for this purpose. The two basic assumptions made in this analysis are (a) the design input parameters are independent random variables, and (b) the pavement thickness is normally distributed.

The earlier assumption could be easily verified, whereas the latter may have one drawback in that the tails of a normal distribution tend toward infinity and can take on negative values, where, in reality, pavement thickness is positive and bounded. However, since the reliability, R , is comparatively larger for pavements, the effect of the exact shape of the tails is relatively insignificant, and, thus, the assumption of normality seems viable. Furthermore, because, in practice, the choice of the probability distribution may also be dictated by mathematical convenience, and because the normal distribution is mathematically simple with a wide availability of information (probability tables) associated with it, the normal model is frequently used in pavement engineering—even when, at times, there is no basis for such a model.

Since t_a is normal, it should be transformed to standard normal (i.e., normal variate with mean zero and standard deviation of one) so that R can be estimated from normal tables.

$$z_t = \frac{t - \bar{t}}{\sigma_t} \quad (8)$$

where

- z_t = standard normal variate of t ,
- \bar{t} = mean thickness of pavement, and
- σ_t = standard deviation of pavement thickness.

The reliability may be found from normal tables as

$$R = P(z_{t_a} \leq z_t) \quad (9)$$

In other words, the reliability is the area under the standard normal, bounded between $-\infty$ and z_t . Determination of \bar{t} and σ_t is the next task.

Mean and Standard Deviation of Pavement Thickness

To assign reasonable values for the pavement thickness, whether flexible or rigid, it would be necessary to relate it to some input design parameters. Such relationships, as mentioned earlier, are readily available in the literature—one of which is the AASHTO design equations. However, these best-fit formulas between the pavement thickness, t (dependent variable), and several design inputs, X_i (independent variable), might qualify as the mean-value function of the dependent variable, in the light of the data, with no consideration given to the variation of the dependent or independent variables. Hence, the design equations provided will not suffice, but will aid in determining the variation of t from the variations of X_i . In other words, if any of the basic (independent) variables is random, the dependent variable will likewise be random; its probability distribution, as well as its moments (mean and variance), will be functionally related and may be derived from those of the basic random variables using the best models (AASHTO equations).

In general, if t is a function of several variables,

$$t = g(X_1, X_2, \dots, X_n) \quad (10)$$

the exact moments of t may be obtained as the mathematical expectation of $g(X_1, X_2, \dots, X_n)$; hence, the mean or expected value of t , $E(t)$, and the variance, $\text{Var}(t)$, could be evaluated as follows:

$$\begin{aligned} E(t) &= \int_{-\infty}^{+\infty} \dots \int_{-\infty}^{+\infty} g(X_1, X_2, \dots, X_n) \\ &\quad \times f_{X_1, X_2, \dots, X_n}(X_1, X_2, \dots, X_n) \\ &\quad dX_1 dX_2, \dots, dX_n \end{aligned} \quad (11)$$

and

$$\begin{aligned} \text{Var}(t) &= \int_{-\infty}^{+\infty} \dots \int_{-\infty}^{+\infty} [g(X_1, X_2, \dots, X_n) - E(t)]^2 \\ &\quad \times f_{X_1, X_2, \dots, X_n}(X_1, X_2, \dots, X_n) dX_1 dX_2 \dots dX_n \end{aligned} \quad (12)$$

Here, $f_{X_1, X_2, \dots, X_n}(X_1, X_2, \dots, X_n)$ is the joint probability distribution function of X_1, X_2, \dots, X_n . Because the design inputs are independent

$$\begin{aligned} f_{X_1, X_2, \dots, X_n}(X_1, X_2, \dots, X_n) &= f_{X_1}(X_1) \\ &\quad \times f_{X_2}(X_2), \dots, f_{X_n}(X_n) \end{aligned} \quad (13)$$

where $f_{X_1}(X_1), f_{X_2}(X_2), \dots, f_{X_n}(X_n)$ are the probability distribution of X_1, X_2, \dots, X_n respectively.

Clearly, to evaluate the mean and variance of t with the above equations (Equations 11 through 13), information on $f_{X_1}(X_1), f_{X_2}(X_2), \dots, f_{X_n}(X_n)$ is needed. However, in many cases the density functions of X_1, X_2, \dots, X_n may not be known. Furthermore, even when such density functions are known, the integrations indicated above may be difficult to perform. For these reasons, approximate mean and variance of t would be practically useful and may be obtained as follows.

Expand the function $g(X_1, X_2, \dots, X_n)$ in a Taylor's series expansion about the mean. Assuming independence of X_1, X_2, \dots, X_n , the resulting expressions, if we truncate at the linear terms, are as follows:

$$\bar{t} = g(\bar{X}_1, \bar{X}_2, \dots, \bar{X}_n) \quad (14)$$

$$\sigma_t^2 = \sum_{i=1}^n \left(\frac{\partial t}{\partial X_i} \right)^2 \sigma_{X_i}^2 \quad (15)$$

where bars are used above the terms to indicate their means, and σ^2 represents the variance of the terms.

This method of approximating the mean and variance has been used extensively in design models (1,2,6) and was proven effective (within ± 10 percent of actual values) especially when the variance of X_i is small relative to $g(\bar{X}_1, \bar{X}_2, \dots, \bar{X}_n)$.

Evaluating the mean and variance of the design parameters is the key to applying Equations 14 and 15 to any pavement

design model that needs some consideration. The soil support value, for example, could vary greatly from point to point along the pavement. Estimating its mean and variance during the service life of the pavement is not an easy task. In addition, SSV will vary throughout the year depending on several factors, such as moisture. However, the variabilities in the design parameter could be assessed from past experience or from testing, if required. These variabilities are then combined, using Equations 14 and 15, to obtain \bar{t} and σ_t .

In the AASHTO model for flexible pavements, Equation 1, the pavement thickness is described by SN, which is a function of several variables; thus, by using Equation 14, the mean of SN can be written as follows:

$$\overline{\text{SN}} = f(\overline{W}, \overline{\text{SSV}}, \overline{R_f}, \overline{P_t}) \quad (16)$$

which is Equation 1 with bars over the terms to indicate the mean values.

Determination of the variance of SN is the next task. Using Equation 15, the variance of SN can be written as,

$$\begin{aligned} \sigma_{\text{SN}}^2 &= \left(\frac{\partial \text{SN}}{\partial W} \right)^2 \sigma_W^2 + \left(\frac{\partial \text{SN}}{\partial \text{SSV}} \right)^2 \sigma_{\text{SSV}}^2 \\ &\quad + \left(\frac{\partial \text{SN}}{\partial R_f} \right)^2 \sigma_{R_f}^2 + \left(\frac{\partial \text{SN}}{\partial P_t} \right)^2 \sigma_{P_t}^2 \end{aligned} \quad (17)$$

where the partial derivatives of SN (with respect to the design parameters) are evaluated at \overline{W} , $\overline{\text{SSV}}$, $\overline{R_f}$, and $\overline{P_t}$. If R_f and P_t are kept constant, that is, they do not vary their respective variance, $\sigma_{R_f}^2$ and $\sigma_{P_t}^2$ are zero, Equation 17 becomes

$$\sigma_{\text{SN}}^2 = \left(\frac{\partial \text{SN}}{\partial W} \right)^2 \sigma_W^2 + \left(\frac{\partial \text{SN}}{\partial \text{SSV}} \right)^2 \sigma_{\text{SSV}}^2 \quad (18)$$

Differentiating Equation 1 according to Equation 18 and substituting, the final result for the variance of SN is

$$\sigma_{\text{SN}}^2 = \left(\frac{1}{K_f} \right)^2 [(CV_W)^2 + 0.1452 \sigma_{\text{SSV}}^2] \quad (19)$$

where

$$\begin{aligned} K_f &= \frac{9.36}{\overline{\text{SN}} + 1} + \log 0.38(4.2 - P_t) \\ &\quad \times \left\{ \frac{5677.86(\text{SN} + 1)^{4.19}}{[0.4(\text{SN} + 1)^{5.19} + 1094]^2} \right\} \end{aligned}$$

and CV_W is the coefficient of variation of W .

With a similar approach, the mean and variance of the concrete slab thickness, D , for rigid pavements, are computed and the results are

$$\overline{D} = f(\overline{W}, \overline{S_c}, \overline{P_t}, \overline{k}) \quad (20)$$

and

$$\sigma_D^2 = \left(\frac{1}{K_r} \right)^2 \left[(CV_W)^2 + (CV_{S_c})^2 \left(\frac{4.22 - 0.32P_t}{2.3} \right)^2 \right] \quad (21)$$

where

$$K_r = \frac{7.35}{\bar{D} + 1} + \frac{13.74 \times 10^7 (\bar{D} + 1)^{7.46} \log 0.333(4.5 - P_t)}{[(\bar{D} + 1)^{8.46} + 1.624 \times 10^7]^2}$$

CV_w and CV_{S_c} are the coefficient of variation of W and S_c , respectively. Observe that Equation 20 is identical to Equation 2 with bars used over the expressions to represent the mean values.

Nomographic Solutions

The simplicity afforded by nomographic solutions in practical applications is appealing. For this reason, the expected variation in pavement thickness (flexible and rigid) is presented in a nomographic form. Figures 2 and 3 are solutions for Equations 16 and 19, respectively; whereas Figures 4 and 5 are solutions for Equations 20 and 21, respectively. Figure 6 compares values calculated by using the equations and values obtained from the nomographs. Clearly, the closeness of these points to the equality line easily verifies the accuracy of the nomographs.

Selecting Appropriate Reliability Based on Least-Cost Concept

Assuming that the pavement thickness is a normal variate with a known mean and variance (or standard deviation), the

reliability of a pavement thickness, t_a , can be evaluated by normal distribution tables. Conversely, given the reliability, the pavement thickness can be estimated. For example, consider that for certain conditions the mean slab thickness is 7 in. with a standard deviation of 0.4 in. In statistical terms, a 7-in. concrete slab will have a 50 percent reliability. In other words, if a 7-in. concrete slab is selected as a design thickness for the conditions given, 50 percent of such pavement will deteriorate early and reach its terminal serviceability before the intended design life. On the other hand, if the reliability is to be increased (say to 99 percent), the thickness should be $t = 7 + z_t(0.4)$. Using the normal distribution tables and for $R = 0.99$, $z_t = 2.33$, and thus $t = 8$ in.

The above example indicates that the design can represent an underdesign or overdesign, depending on the reliability value selected. Generally speaking, if the mean thickness is selected, about one-half the road will be underdesigned and one-half overdesigned. On the other hand, if a value corresponding to a high reliability is selected, most of the road will be overdesigned. Therefore, an optimal design will be of interest. Such a design will serve both statistical safety (reliability) and economy. For this purpose, the least-cost concept proposed by Yoder (13) is adopted.

The least-cost analysis just mentioned, suggests that the optimum design value (this term is adjusted to optimum pavement thickness in this paper) depends on the variability of the soil deposit and the traffic conditions in the site. Yoder presented several curves that relate percentile value (labeled as reliability here) for least cost as a function of soil variability (coefficient of variation), traffic, and unit cost of the pavement structure. These curves are modified and represented here in Figure 7. In this figure, cost includes both initial cost and

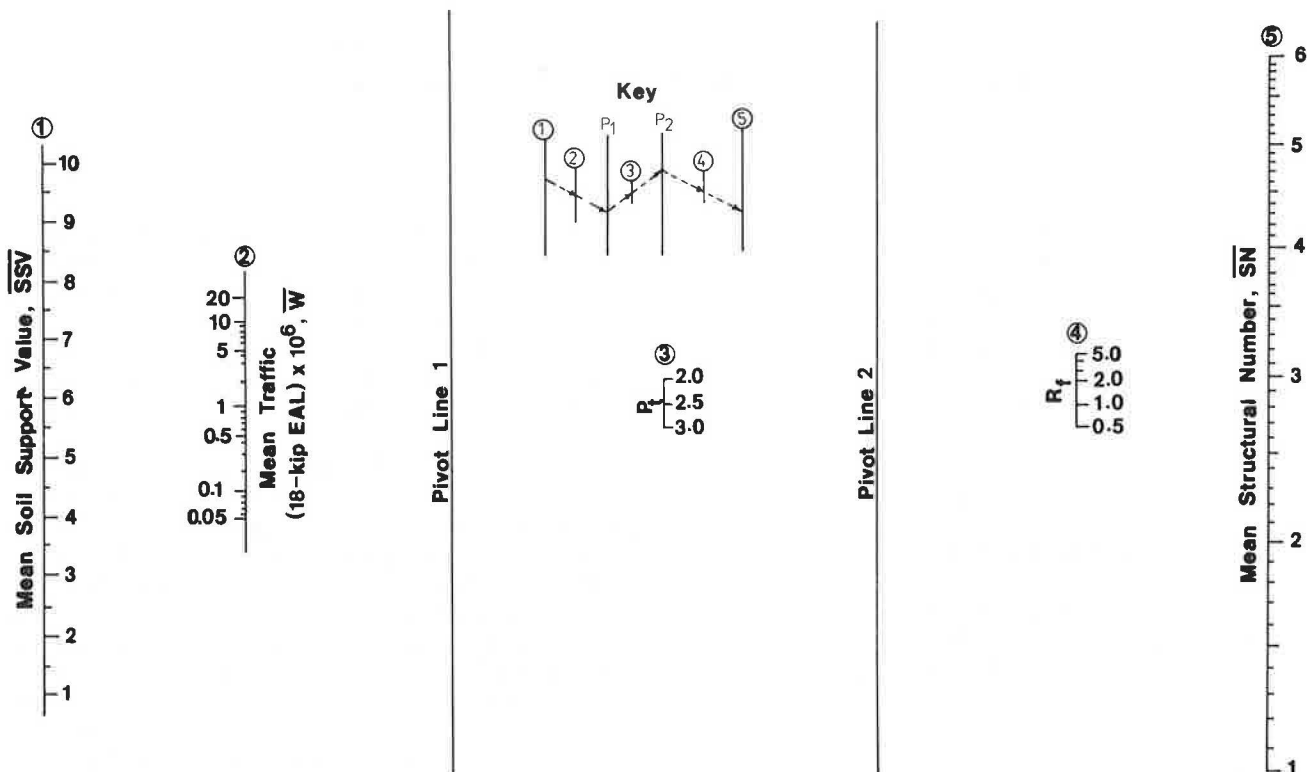


FIGURE 2 Nomograph for mean structural number, \overline{SN} .

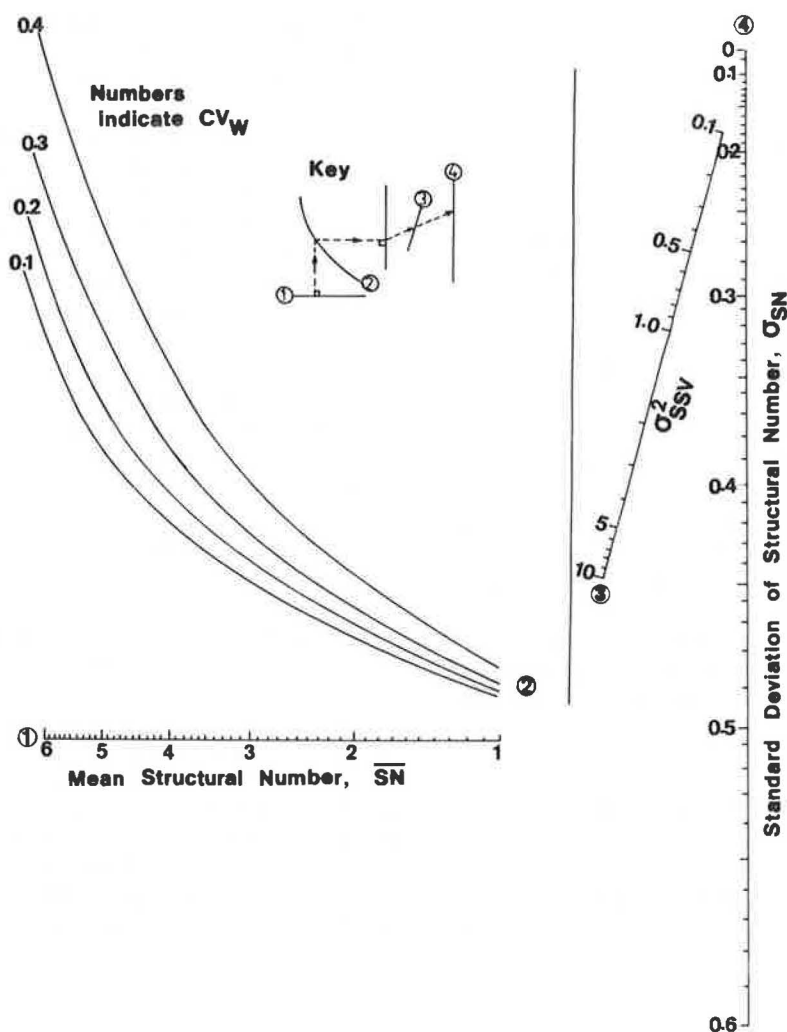


FIGURE 3 Nomograph for standard deviation of structural number, σ_{SN} .

maintenance cost needed to repair parts of the road that have been underdesigned. In addition, the cost ratio, CR, is defined as the ratio of the unit cost of maintenance to the unit initial cost. Estimates of this factor must be made to use this method. However, and based on the data presented, CR has a weighted average of 2, 3, and 4 respectively for roads with low ($< 10^5$ EAL), medium ($10^5 - 10^6$ EAL) and high ($> 10^6$ EAL) traffic. Therefore, by knowing traffic, CR could be approximated; and with the CV of soil deposit, the reliability of producing an optimum design can be evaluated.

Example of Statistical Pavement Design

This example is presented to illustrate the use of the statistical design charts. Consider a two-layered flexible pavement (asphalt concrete and gravel base) with the following input data:

Factor	Mean Value	CV	Variance
W, EAL	5×10^6	0.40	4.0×10^{12}
SSV	7	0.40	7.84
P_t	2.5	—	—
R_f	2.0	—	—

Enter Figure 2 with the mean value of the design factors to obtain the mean structural number, $\overline{SN} = 3.4$. With \overline{SN} and the other inputs, enter Figure 3 and obtain the standard deviation of structural number $\sigma_{SN} = 0.58$. With the traffic of 5×10^6 18-kip EAL, CR = 3, and $CV_{SSV} = 0.40$ (or 40 percent), obtain reliability for optimum design, $R = 84$ percent or the area bounded between $-\infty$ and z under standard normal curve is 0.84, thus, $z = 1.0$. Therefore, $SN = 3.4 + (1.0) \times (0.58) = 3.98$. This implies that, for the conditions given, a pavement with $SN = 3.4$ will have a reliability of 50 percent, whereas the optimum design of $SN = 3.98$ will have $R = 84$ percent. In other words, if we consider a 10-in. gravel base (layer coefficient $a_2 = 0.14$), this pavement will require a 6.1-in. asphalt concrete ($a_1 = 0.42$) for an optimum design with a reliability of 84 percent. If the AASHTO design were to be followed with no consideration given to the variations, a 4.8-in. asphalt concrete layer will suffice. However, this pavement will have only 50 percent reliability and, thus, will have a 50 percent chance of failure before its design life (20 years) ends, whereas the pavement with $R = 84$ percent will have only a 16 percent chance of failure.

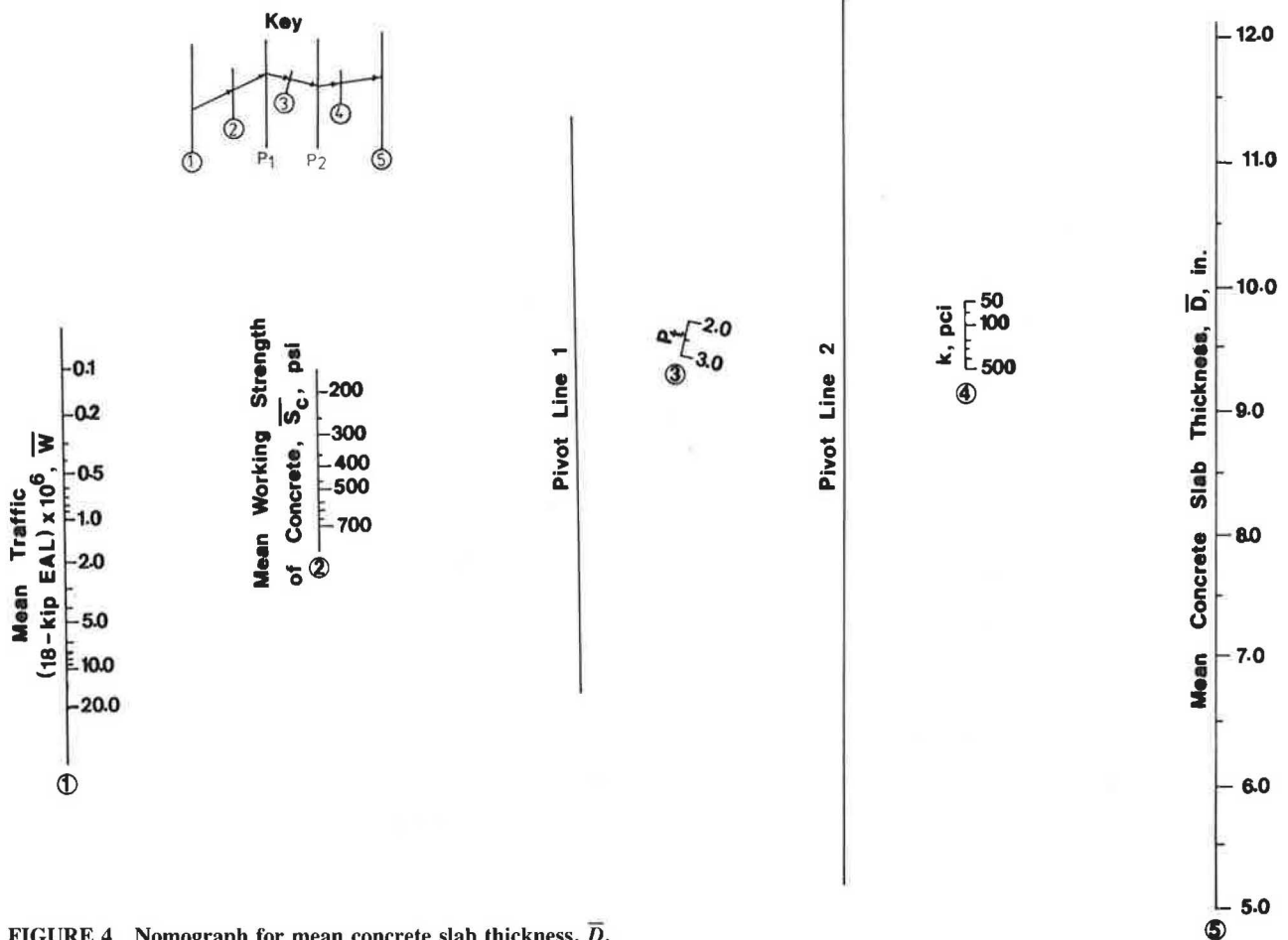


FIGURE 4 Nomograph for mean concrete slab thickness, \bar{D} .

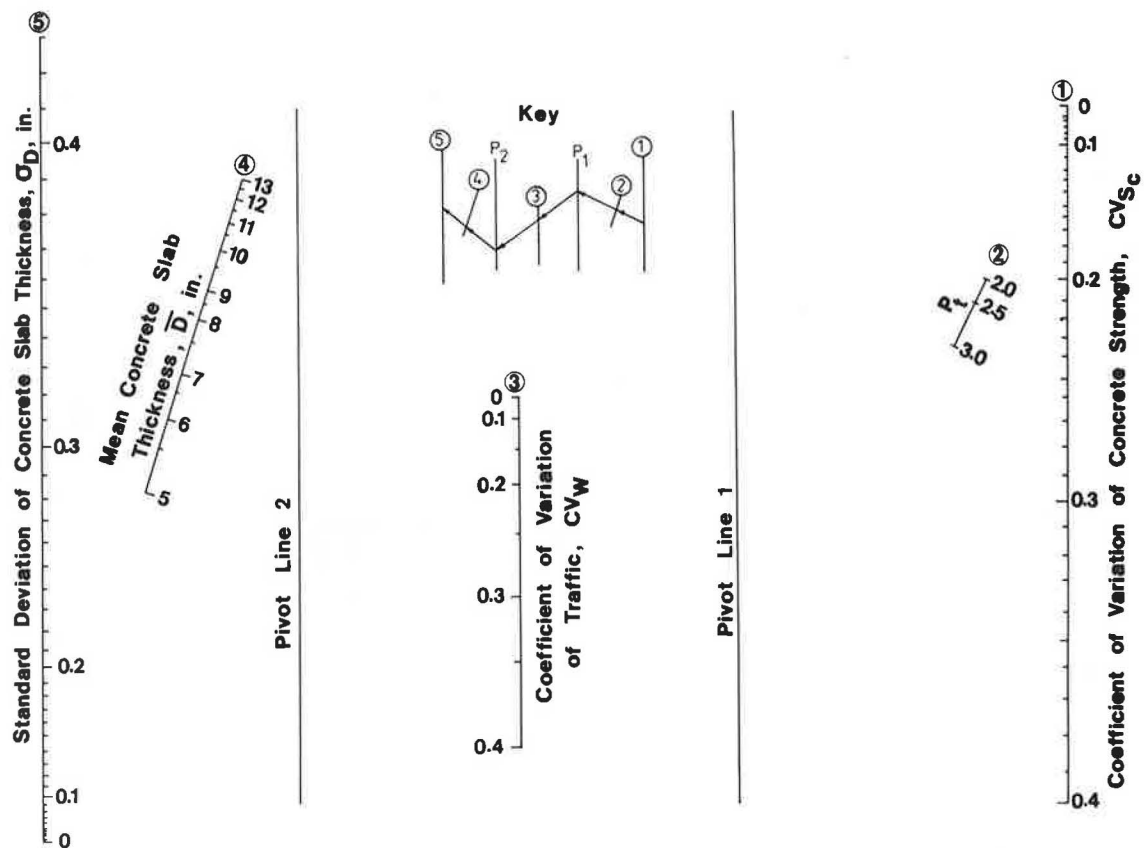


FIGURE 5 Nomograph for standard deviation of concrete slab thickness, σ_D .

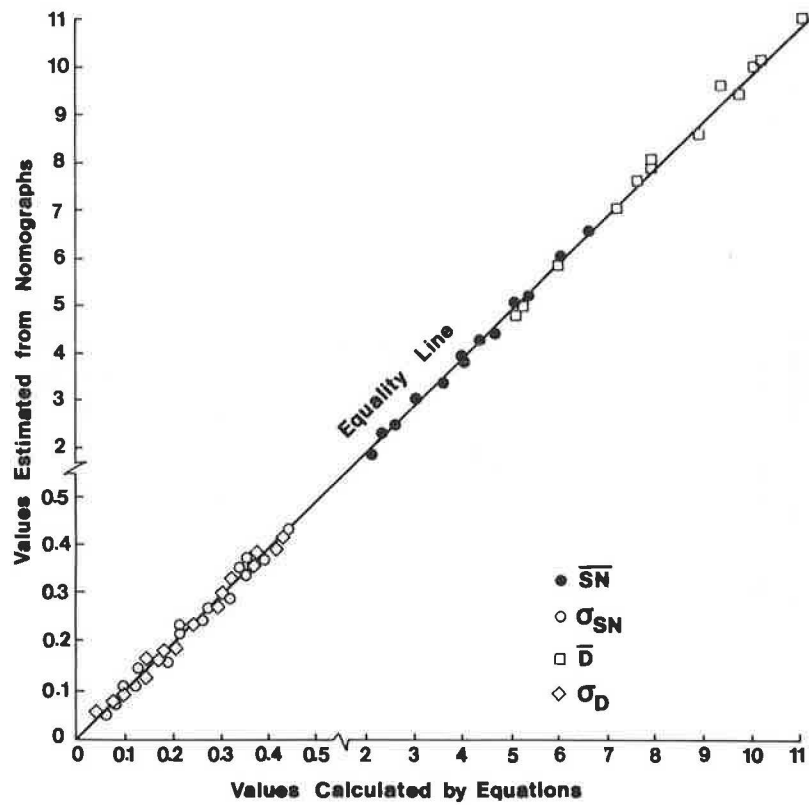


FIGURE 6 Comparisons among values, by equations and nomographs.

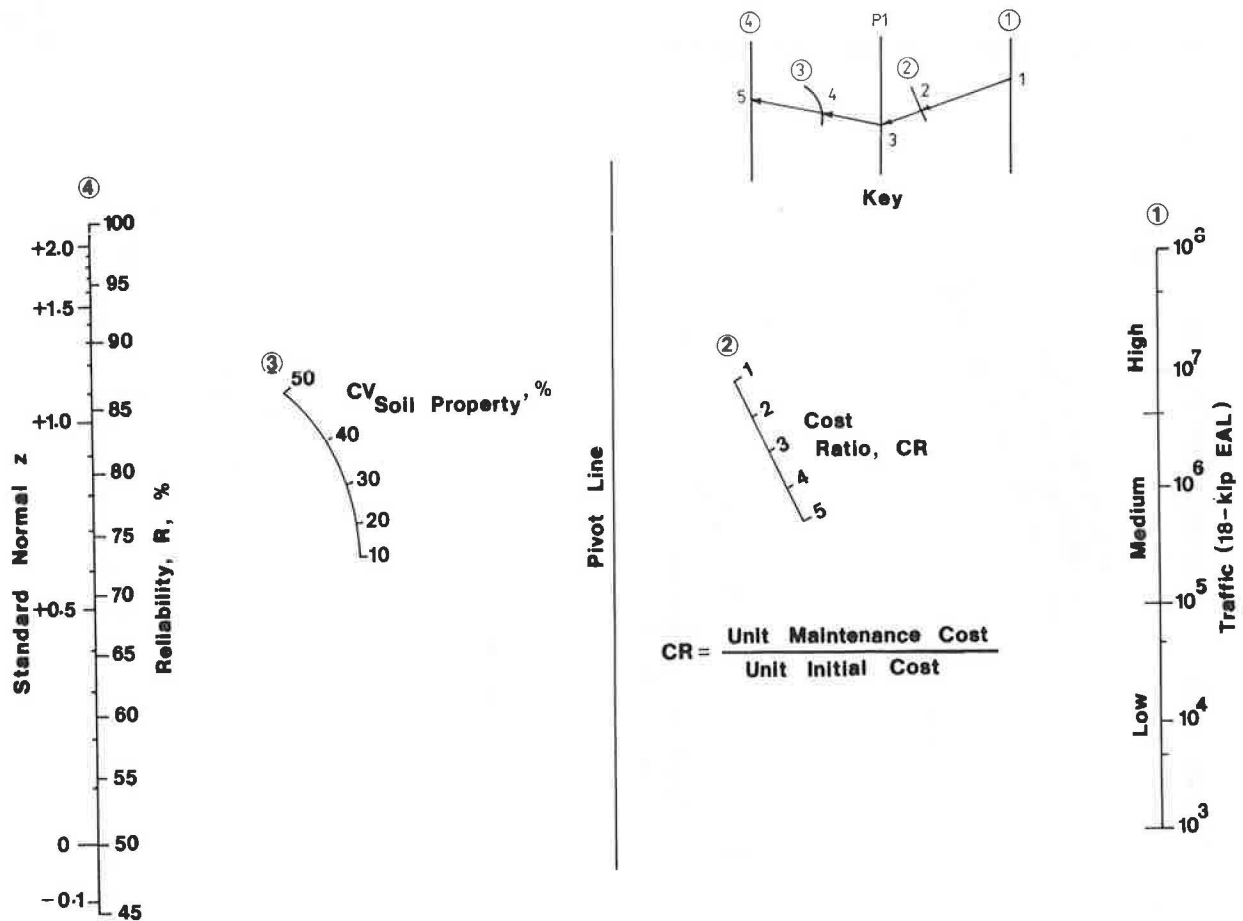


FIGURE 7 Reliability, R , for the least-cost design.

SUMMARY

Pavements, as do many other structures, possess random variabilities associated with almost all design parameters. Conventional pavement design models, in which the design factors are treated as deterministic quantities, would seem inadequate. In these cases, using a probabilistic approach accounts for the variabilities in design parameters, whereas statistical analysis quantifies their effects. However, strict reliance on results obtained by probabilistic and statistical methods should not be exercised but must rather be complemented by sound engineering judgment. Yet, applying probabilistic and statistical techniques to the analysis design of pavements, as has been done in this paper, provides the means for some important applications that were not previously possible. These include the following:

1. The ability to make the design process sensitive and adjustable for many variabilities and uncertainties in design parameters.
2. Providing standards for conducting design optimization; and
3. Affording the means for designing at different levels of reliability and, thus, design adequacy can be easily estimated.

REFERENCES

1. M. I. Darter, W. R. Hudson, and J. L. Brown. Statistical Variation of Flexible Pavement Properties and Their Consideration in Design. In *Proc., Association of Asphalt Paving Technologists*, Vol. 42, 1973, pp. 589-615.
2. M. I. Darter, B. F. McCullough, and J. L. Brown. Reliability Concepts Applied to the Texas Flexible Pavement System. In *Highway Research Record 407*, HRB, National Research Council, Washington, D.C., 1972, pp. 146-161.
3. M. I. Darter, W. R. Hudson, and R. C. G. Hass. Selection of Optimal Pavement Designs Considering Reliability, Performance, and Costs. In *Transportation Research Record 485*, TRB, National Research Council, Washington, D.C., 1974, pp. 67-79.
4. M. I. Darter and W. R. Hudson. *Probabilistic Design Concepts Applied to Flexible Pavement Design System*. Research Report 123-18. Texas Highway Department, Texas Transportation Institute, May 1973.
5. P. F. McManus and E. J. Barenberg. Impact of Subgrade Variability on Pavement Construction-Maintenance Cost Trade-offs. In *Special Report 148*, TRB, National Research Council, Washington, D.C., 1974, pp. 12-23.
6. P. K. Kher and M. I. Darter. Probabilistic Concepts and Their Applications to AASHTO Interim Guide for Design of Rigid Pavements. In *Highway Research Record 466*, HRB, National Research Council, Washington, D.C., 1973.
7. M. I. Darter. Probabilistic Applications to Rigid Pavement Structure. Presented at the ASCE Specialty Conference on Probabilistic Methods in Engineering, Stanford University, Stanford, Calif., June 24-26, 1974.
8. J. L. Von Quintus, F. N. Finn, W. R. Hudson and F. L. Roberts. *Flexible and Composite Structures for Premium Pavements, Vol. 1, Development of Design Procedure*. Draft Report, FHWA-RD-80, Federal Highway Administration, December 1979.
9. *Interim Guide for Design of Pavement Structures*. AASHTO, Washington, D.C., 1981.
10. D. R. Benjamin and C. A. Cornell. *Probability, Statistics, and Decision for Civil Engineers*. McGraw-Hill, N.Y., 1970.
11. H. Findakly, F. Moavenzadeh, and J. Soussou. Stochastic Model of Pavement Systems. *Transportation Engineering Journal*, Vol. 100, No. TE 1, Feb. 1972, pp. 57-70.
12. E. J. Yoder and M. W. Witzczak. *Principles of Pavement Design*, 2nd ed. Wiley, N.Y., 1975.
13. E. J. Yoder. Selection of Soil Strength Values for the Design of Flexible Pavements. In *Highway Research Record 276*, HRB, National Research Council, Washington, D.C., 1969.
14. J. A. Deacon and R. L. Lynch. *Determination of Traffic Parameters for the Prediction, Projection, and Computation of EWLS*. Final Report KYHPR-64-21, Kentucky Highway Department, 1968.
15. *Manual of Instructions, Part 8: Materials*. Utah State Department of Highways, n.d.
16. *The Repeatability of Test Results Using Various California Bearing Ratio Procedures and Resistance R-Value*. Utah Research Report 500-908, Utah State Department of Highways, Materials and Testing Division, Utah Project HPR-1 (5), August 1967.
17. C. J. Van Til, B. F. McCullough, B. A. Vallerger, and R. G. Hicks. *Evaluation of AASHTO Interim Guides for Design of Pavement Structures*. NCHRP Report 128, HRB, National Research Council, Washington, D.C., 1972.
18. G. B. Sherman. In Situ Materials Variability. In *Special Report 126*, HRB, National Research Council, Washington, D.C., 1971, pp. 180-188.

Publication of this paper sponsored by Committee on Flexible Pavement Design.

Evaluating Structural Damage of Flexible Pavements Using Cracking and Falling Weight Deflectometer Data

PETER SEBAALY, NADER TABATABAEE, RAMON BONAQUIST, AND DAVID ANDERSON

The relationship between surface cracking and the structural capacity of both thin and thick pavement structures was investigated using field data from the FHWA Pavement Testing Facility test sections. The test sections were loaded with the Accelerated Loading Facility. Surface cracking was evaluated in terms of lineal cracking and AASHTO Class 2 and 3 cracking; structural capacity was evaluated in terms of peak deflections and back-calculated moduli of the asphalt concrete layer under falling weight deflectometer testing. The field data indicated a definite lag between the loss of structural capacity and the appearance of surface cracking for both thin and thick pavements. Because a structural capacity loss may exist before cracks appeared on the surface, the use of surface cracking to indicate structural condition may be misleading in several cases. Field data on peak deflections indicated that the deflection ratio may reach a value of 2 before any surface cracking appears and a value of 3 before any AASHTO Class 2 and 3 cracking appears on the surface. The back-calculated moduli of the asphalt layer were reduced by 50 percent before any lineal cracking or AASHTO Class 2 and 3 cracking appeared on the surface.

The failures of flexible pavements under traffic loading are classified under two categories: functional and structural. The functional performance is usually evaluated through subjective measurements conducted at the pavement surface. Manual surveys (such as crack mapping and visual observations) and automated photographic techniques (such as the Pasco and ARAN systems and the laser survey system) have been extensively used in various pavement management systems (PMS).

The structural performance of pavement is seldom evaluated at the network level. The majority of the techniques available to evaluate the adequacy of pavement structure are used at the project level. The functional performance surveys at the network level are often used as catalysts for more sophisticated structural adequacy evaluations at the project level. This process of pavement performance monitoring would be acceptable if a direct relationship existed between surface distresses and the structural capacity of pavements. For example, the lack of alligator cracks on the surface of a pavement structure may not be interpreted as a guarantee of the structural adequacy of the pavement. On the other hand, the first appearance of alligator cracking may be the result of the total

loss of the structural capacity of the pavement. Therefore, indicators that have been used as triggering devices in various PMS practices may not be appropriate.

The research presented in this paper examines the relationship between the structural and functional performance parameters. Two pavement structures were tested using the FHWA Accelerated Loading Facility (ALF). Among the various performance parameters studied were the surface cracking and load-deflection response of the pavement structures under falling weight deflectometer (FWD) loading. The correlation between the amount of surface cracking and the actual structural loss of various pavement sections was investigated.

BACKGROUND

Surface distress surveys play a primary role in pavement management systems used throughout most state and local agencies. The findings of the AASHTO Road Test have been used to recommend that riding quality as expressed by the present serviceability index (PSI) would suffice as an indicator of pavement performance (1). However, little weight was given to the presence of surface cracking and the actual fatigue of the asphalt concrete materials. The PSI is still commonly used, and the most recent versions of the equation do not include any contribution from cracking or surface fatigue (2, p. 224).

Many PMS use surface cracking as an indicator of the structural condition of a pavement. Various levels of cracking serve as triggers for determining maintenance and rehabilitation needs. By using surface cracking to indicate structural condition, these systems assume a relationship exists between surface cracking and loss of structural capacity. The remainder of this paper investigates the reliability of this assumption.

DATA COLLECTION

Pavement Testing Facility

The data for this evaluation were obtained during the first phase of research at the FHWA Pavement Testing Facility (PTF). This facility is an outdoor, full-scale pavement testing laboratory that includes (a) the ALF testing machine, (b) two instrumented, asphalt concrete test pavements, and (c) a computer-controlled data-acquisition system.

P. Sebaaly, N. Tabatabaee, and D. Anderson, Pennsylvania Transportation Institute, Research Building B, University Park, Pa. 16802. R. Bonaquist, Office of Research, Development, and Technology, FHWA, 6300 Georgetown Pike, HR-20, McLean, Va. 22101.

The ALF is used to simulate traffic loading. It models one-half of a dual-tire, single axle and can apply loads ranging from 9,400 to 22,500 lb. The test wheels travel at 12 mi/hr over 40 ft of pavement. To simulate highway traffic, the loads are applied in one direction and are normally distributed over a 48-in. wheel path.

Each test lane is divided into four sections for a total of eight test sections. Lane 1 consists of 5 in. of asphalt concrete over 5 in. of crushed aggregate base. Lane 2 consists of 7 in. of asphalt concrete over 12 in. of crushed aggregate base.

Test Conditions and Failure Modes

Data from six of the eight test sections were used in this study. Table 1 presents the load, tire pressure, testing period, and number of applied-load repetitions. The test section was considered to have failed when the average rutting reached a value of 0.5 in. or the lineal cracking reached a value of 50

in./ft². After each test section failed, a postmortem evaluation was conducted to determine the mode of failure. This evaluation consisted of excavating the pavement layers; obtaining transverse profiles, density measurements, and samples for laboratory testing; and documenting the cracking and rutting through a cross section of the pavement.

If the section showed an average rutting of 0.5 in., the failure mode was considered to be rutting; however, if the section showed a lineal cracking value of 50 in./ft², the failure mode was considered to be fatigue. Fatigue of the asphalt concrete was the predominant failure mode for the tests used in this evaluation. Lane 1, Section 3 failed prematurely as a result of cracking that emanated from two core holes in the test section. Portions of the test section, however, showed little distress when trafficking was stopped; had the test continued, these areas would probably have failed as a result of fatigue. Excessive rutting in the subgrade was the primary failure mode only for the thin pavement trafficked with heavy loads.

TABLE 1 TEST CONDITIONS

Test Section	Load, lb	Tire		Start Date	End Date	AASHO	
		Pressure, psi				Load Applications	Equivalence Factors
Lane 1, Section 1	14,100	100		3/24/88	4/04/88	37,033	5.49
Lane 1, Section 2	11,600	100		12/14/87	2/18/88	147,696	2.53
Lane 1, Section 3	11,600	100		9/04/86	2/23/86	66,523	2.53
Lane 1, Section 4	16,400	100		3/01/88	3/08/88	14,240	10.50
Lane 2, Section 2	19,000	140		6/18/87	1/24/87	578,142	11.5
Lane 2, Section 3	19,000	100		1/08/87	6/04/87	502,662	11.5

Pavement Performance Monitoring

Routine performance monitoring at the PTF included periodic measurements of cracking, rutting, slope variance, FWD deflections, and strain at the bottom of the asphalt layer. For this study, only the cracking and FWD deflection data were considered.

A manual procedure was used to measure cracking. On a regular schedule, a clear plastic sheet was placed over the test section and the cracks were traced onto the plastic, using different color markers each time a crack survey was performed. The test section was then divided into eight 4-ft-long by 6-ft-wide subsections. The total length of all cracks in each subsection was measured with a map wheel, and the surface area of AASHO Class 2 and Class 3 cracking was estimated.

Surface deflections were measured periodically with a Phoenix Model ML 1,000 FWD. Loads ranging from 7 to 14 kip were applied through a 5.9-in.-diameter plate. Surface deflections were measured with geophones at six radial offsets ranging from the center of the loading plate to 50 in., and FWD tests were conducted in each of the eight subsections used for the crack survey.

DATA REDUCTION

Cracking

In most distress surveys, load-associated cracking is measured using a procedure similar to that developed during the AASHO Road Test. At the road test, three severity levels were identified for load-associated cracking: *Class 1* cracking was defined as disconnected hairline cracks running parallel to each other;

further development of cracking to form a pattern of blocks was defined as *Class 2* cracking; and *Class 3* cracking was defined as *Class 2* cracking that has progressed to the point that the blocks have become loose and rocked under traffic. The area of pavement surface exhibiting each class of cracking was measured and normalized with regard to 1,000 ft². Only the areas of AASHO Class 2 and 3 cracking are considered in most distress surveys.

Because the test sections at the PTF are only 32 ft long, it was possible to track cracking more closely than described above. Each time a crack survey was conducted, the total length of all cracks within a test section was carefully measured using a map wheel. Because the surface area over which the cracking was measured remained constant, the total crack length represented crack density. The average accumulation of total crack length and AASHO Class 2 and 3 cracking as a function of cumulative 18-kip equivalent single-axle load (ESAL) is presented in Figures 1 and 2 for typical tests on Lanes 1 and 2, respectively. From these figures, it is apparent that any small changes in the cracked surface would appear in the measurement of crack length long before they would appear in the measurement of AASHO Class 2 and 3 cracking. An example of the increased sensitivity is presented in Figure 3, which shows two areas with the same surface area of AASHO Class 2 cracking. It is obvious, however, that these areas have different total crack lengths.

FWD Deflections

FWD deflections were used in two approaches to monitor the structural performance of the test sections. In the first, the variations of the peak deflections were compared at various

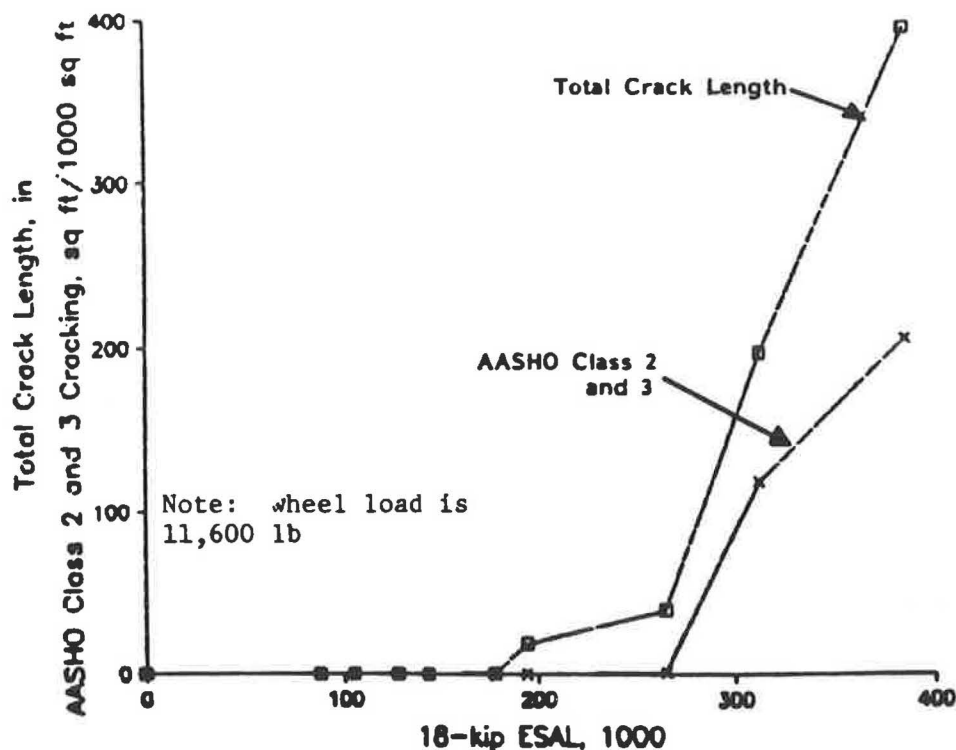


FIGURE 1 Typical accumulation of cracking for Lane 1.

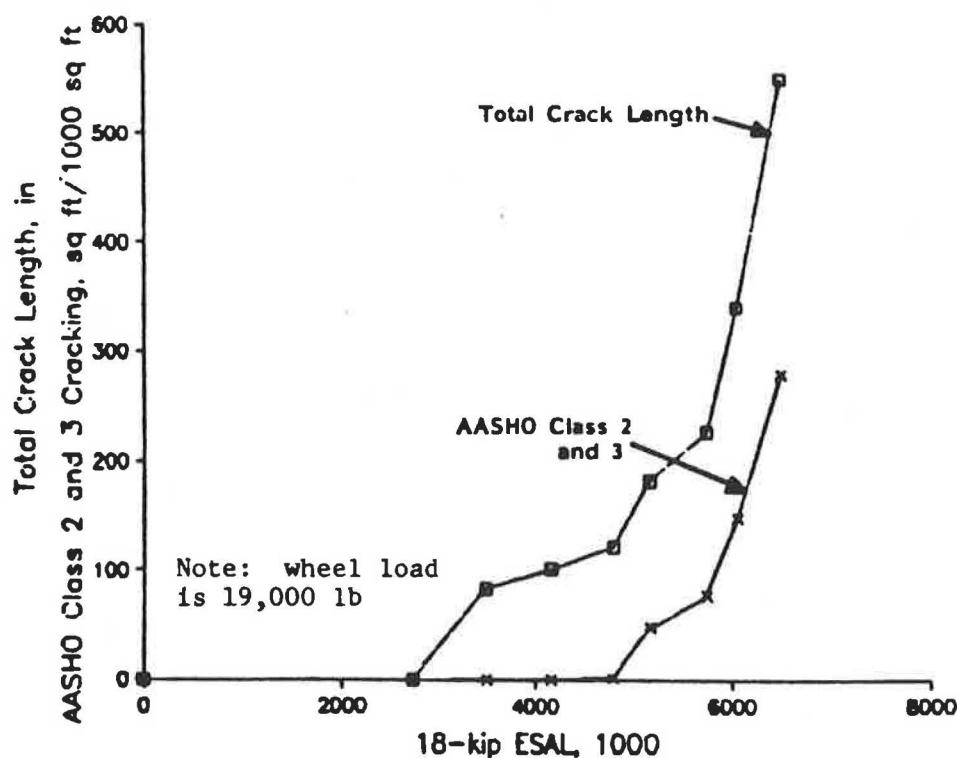


FIGURE 2 Typical accumulation of cracking for Lane 2.

ESAL values. In the second, the FWD deflection basins were used to back-calculate the pavement layers' moduli. The back-calculated moduli were compared at various ESAL intervals throughout each test period.

The significance of both approaches in evaluating pavement actual structural capacity depends on the accuracy and precision of the FWD equipment in collecting the surface-deflection basins. To minimize any potential error from the FWD measurement, a testing scheme was implemented by which three replicates of the FWD deflections were obtained at each point. The average deflection basins were then used in the analysis of both approaches.

The FWD testing periods were spaced throughout the loading life of each test section in order to evaluate the section's capacity at various ESAL levels. The pavement temperature changes from one test period to another, which greatly affects the response of the asphalt concrete layers. Consequently, it was necessary to measure the temperature throughout the asphalt layer and correct the peak deflections and the back-calculated moduli to a base temperature.

There are various methods by which the deflections and moduli values could be temperature corrected. This study used the method recommended by the new *AASHTO Pavement Design Guide* (3). The variations of temperature throughout the asphalt concrete were monitored by thermocouples embedded at various depths. The thermocouple temperatures were read at the beginning and at every hour during each FWD testing period. The average pavement temperature was calculated as the average of the various thermocouple temperatures at the hour nearest the time the FWD test was conducted. Using the average pavement temperatures, the temperature correction factors for the peak deflections and the back-calculated moduli were obtained from the corresponding AASHTO curves (3). The correction factors

were used in the following equations:

$$Fd = \frac{d_1(70^\circ\text{F})}{d_1(T)}$$

$$Fe = \frac{E_{70^\circ\text{F}}}{E_T}$$

where

Fd = AASHTO adjustment factor for peak deflection,

$d_1(70^\circ\text{F})$ = FWD peak deflection at 70°F ,

$d_1(T)$ = FWD peak deflection at test temperature,

Fe = AASHTO adjustment factor for back-calculated moduli,

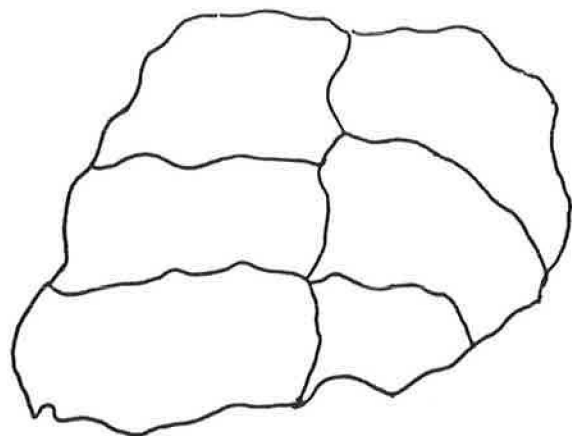
$E_{70^\circ\text{F}}$ = resilient modulus of the asphalt layer at 70°F , and

E_T = resilient modulus of the asphalt layer at test temperature.

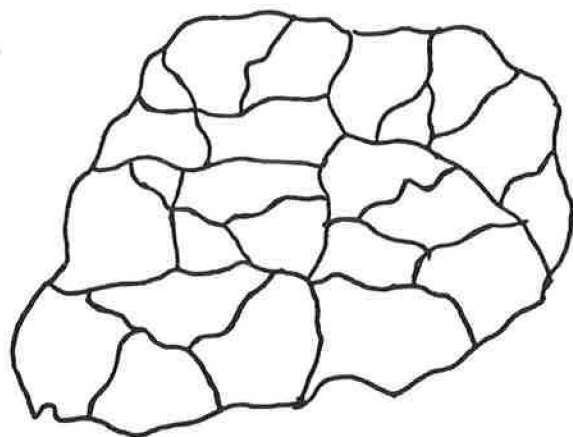
Peak Deflection and Back-Calculated Moduli

Because the peak FWD deflections were measured at slightly different load levels, the deflections must be adjusted to a common load before they can be compared. The linearity of the FWD load-deflection response of the PTF test sections was investigated by Anderson et al. (4, p. 111), who recommended that the assumption of linearity is valid for the given range of FWD loads (from 8,000 to 14,000 lb). In this study, the FWD peak deflections were adjusted to a 12,000-lb. load.

The back-calculated moduli for certain stations were not calculated because the measured deflections were greater than



a. Low total crack length



b. High total crack length

FIGURE 3 Sensitivity of crack length procedure to changes in cracking.

80 mils. With deflections greater than 80 mils, the measuring capacity of the FWD sensors is exceeded. Also, deflections as large as this imply a cracked pavement, which violates the assumption that the asphalt concrete is a continuous medium.

The back-calculated moduli were evaluated using the BACKCHEV program (5). This back-calculation technique uses a constrained search where the moduli of each layer are bonded within reasonable limits. The percentage of allowable total error between the measured and calculated deflections for all six sensors was 10, which is equivalent to an average error of 1.5 percent at each sensor.

The back-calculated moduli for all FWD tests in this research were evaluated under the same initial moduli, deflection tolerance, and upper and lower bounds of each layer's moduli. This back-calculation approach minimized the effect of non-uniqueness of the back-calculated moduli on the final results.

ANALYSIS

Fatigue Cracking

Surface cracking is, perhaps, a good indicator of the structural condition of a pavement section for use in PMS. Most pave-

ment engineers agree that load-associated cracks initiate near the bottom of the asphalt layer, where tensile strains are highest. Repeated traffic loads then propagate the cracks to the surface, eventually forming the block or alligator pattern characteristic of fatigue cracking. The rate of crack propagation through the asphalt depends on combinations of various factors: (a) the thickness of the asphalt layer, (b) the maximum size of aggregate in the asphalt mix, (c) environmental conditions, and (d) the magnitude and frequency of loading. Therefore, no general rate of crack propagation can be identified for any pavement system.

Peak Deflections

When a crack initiates, the structural capacity of the pavement section is reduced. The crack decreases the section of the asphalt layer available to resist tension, resulting in higher pavement deflections. Figures 4, 5, and 6 show this increase in deflection as a function of 18-kip ESAL for FWD tests conducted on Lanes 1 and 2, respectively. The data are presented as a deflection ratio, defined as

$$D_{\text{ratio}} = \frac{d_{l(x)}}{d_{l(0)}}$$

where

D_{ratio} = deflection ratio,

$d_{l(x)}$ = FWD deflection at the middle of the loading plate at x number of 18-kip ESALs adjusted to a 12,000-lb load, at 70°F, and

$d_{l(0)}$ = FWD deflection at the middle of the loading plate before trafficking adjusted to a 12,000-lb load, at 70°F.

Also shown in these figures is the accumulation of total crack length and area of AASHTO Class 2 and 3 cracking as a function of 18-kip ESAL. Figures 4 and 5 represent data from Lane 1, Section 1 and Lane 1, Section 2 tests, respectively. The data from these two tests were not combined because each test showed a different mode of failure.

The failure of Lane 1, Section 1 was a combination of fatigue failure of the asphalt layer and rutting of the subgrade, whereas the failure of Lane 1, Section 2 was a total asphalt fatigue failure. Comparisons of the deflection ratio and cracking show the deflection ratio can increase to 2 before any cracking appears at the pavement surface, and to 3 before significant AASHTO Class 2 cracking occurs. In the case of Lane 1, Section 1 (rutting and fatigue failure), the cracking appeared at a deflection ratio of 1.5.

Because the PTF test sections model one-half of a 12-ft-wide lane and the wheel path is 48-in. wide, AASHTO Class 2 and 3 cracking of 100 ft²/1,000 ft² represents approximately 15-percent wheel path cracking. At this level of cracking, the deflection ratio was approximately 2. Figure 6 represents data from Lane 2 tests, which show that the deflection ratio can increase to between 2.5 and 3.0 before any cracking appears at the pavement surface.

Back-Calculated Moduli

In layer theory analyses, it is assumed that the reduction in structural capacity from fatigue cracking results from a decrease

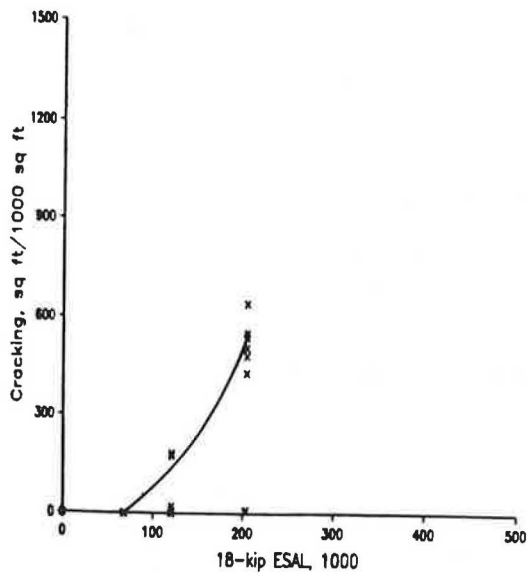
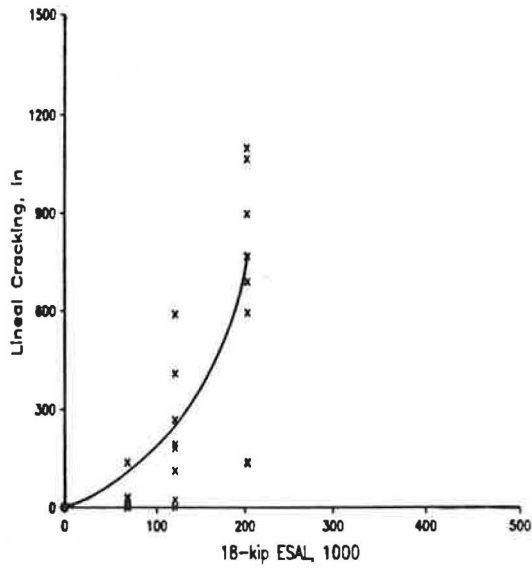
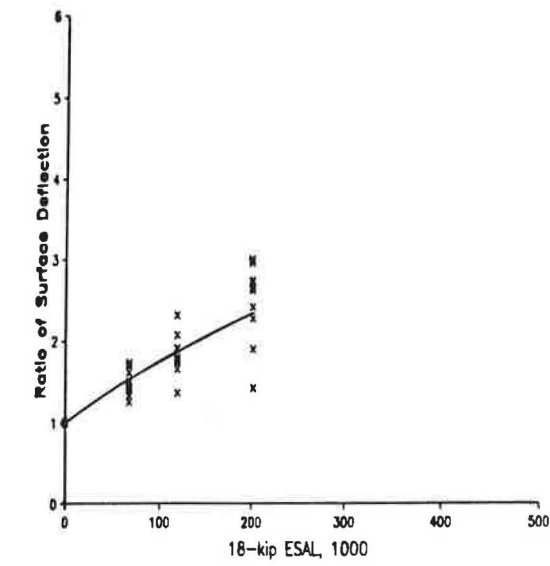


FIGURE 4 Variations of ratio of surface deflection, lineal cracking, and AASHO cracking as a function of 18-kip ESAL repetitions for Lane 1, Section 1.

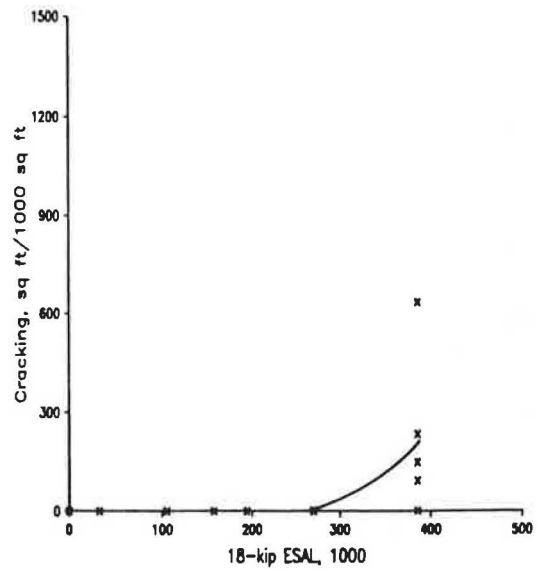
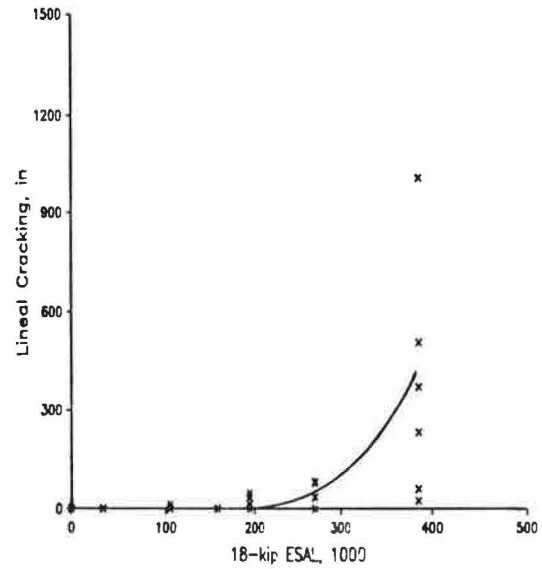
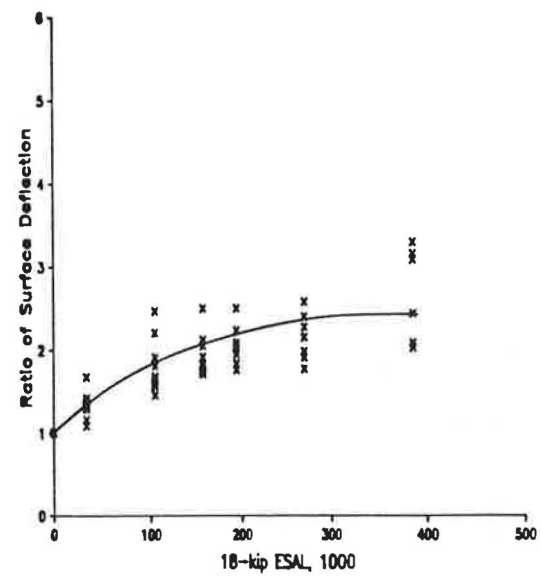


FIGURE 5 Variations of ratio of surface deflection, lineal cracking, and AASHO cracking as a function of 18-kip ESAL repetitions for Lane 1, Section 2.

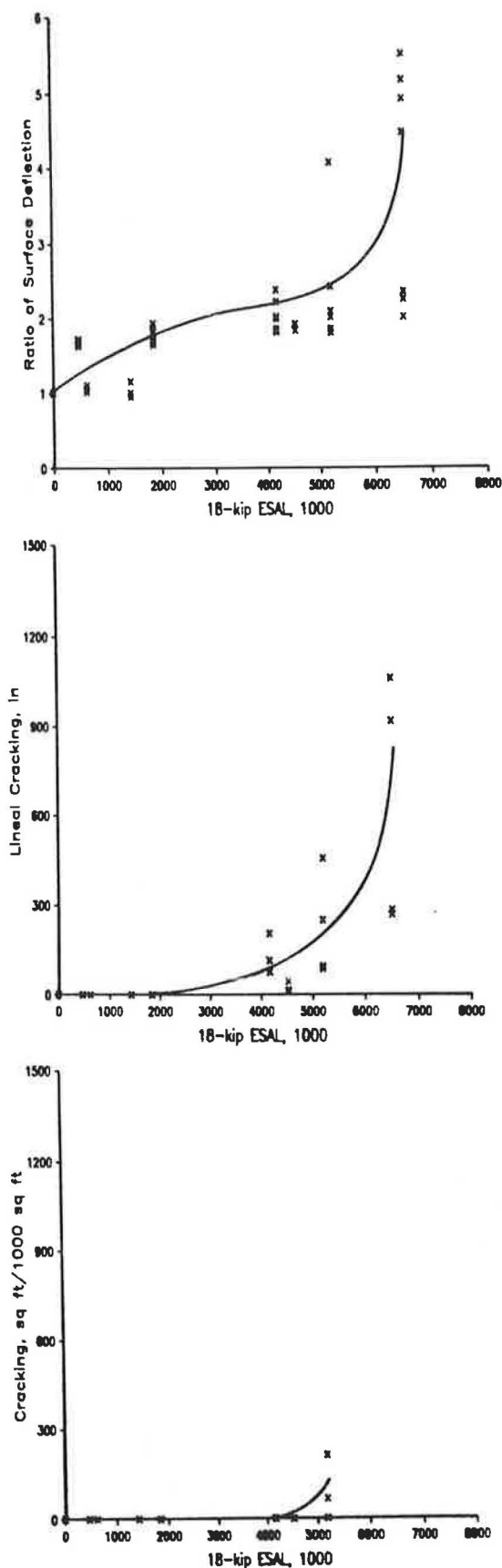


FIGURE 6 Variation of ratio of surface deflection, lineal cracking, and AASHO cracking as a function of 18-kip ESAL repetitions for Lane 2 tests.

in the modulus of the asphalt concrete layer. Figures 7, 8, and 9 show the decrease in the modulus of the asphalt concrete layer as a function of 18-kip ESAL for Lanes 1 and 2, respectively. The data are presented as modulus ratio, defined as

$$M_{\text{ratio}} = \frac{M_{r(x)}}{M_{r(0)}}$$

where

M_{ratio} = modulus ratio,
 $M_{r(x)}$ = back-calculated asphalt concrete modulus at x number of 18-kip ESALs, adjusted to 70°F, and
 $M_{r(0)}$ = back-calculated asphalt concrete modulus before trafficking, adjusted to 70°F.

Also shown in these figures is the accumulation of total crack length and area of AASHO Class 2 and 3 cracking as a function of ESAL. Comparisons of modulus ratio and cracking show the modulus ratio can decrease to 0.50 before any cracking appears at the pavement surface, and to 0.30 before significant AASHO Class 2 cracking occurs. With 15-percent wheel path AASHO Class 2 and 3 cracking, the modulus ratio was 0.5.

Laboratory-Resilient Moduli

To ensure that the increased deflections and decreased back-calculated moduli presented in the previous sections resulted from load-associated damage, rather than moisture damage or other environmental effects, laboratory-resilient modulus data were analyzed. Cores were cut from the PTF test sections shortly after construction in September 1986 and again during each of the postmortem evaluations. Laboratory-resilient modulus data were obtained from indirect tensile tests on these cores. Complete analysis of the data is documented in Anderson et al. (4). The data did not show a definite decrease in modulus with time, as would be expected if the damage were purely environmental.

In addition, the resistance of the wearing and binder mixes to moisture damage was estimated by measuring the tensile strength and resilient modulus of selected cores before and after conditioning. The conditioning consisted of vacuum saturation with tap water at room temperature. (The results of these tests are also documented in Anderson et al.) The saturation caused no significant decrease in the tensile strength or modulus of the cores. The tensile strength and modulus actually increased for some of the cores, which is a common occurrence for moisture-resistant mixes.

SUMMARY AND CONCLUSIONS

Field data from the PTF sections have indicated a time lag exists between the appearance of surface cracking and the reduction in structural capacity of flexible pavement systems. The use of surface cracking as a catalyst for maintenance and rehabilitation needs may not be justified. The study shows that the peak deflections and the back-calculated moduli of the asphalt layer from FWD measurements may reach critical levels before any type of cracking appears on the surface. Even though some of the PTF sections showed different fail-

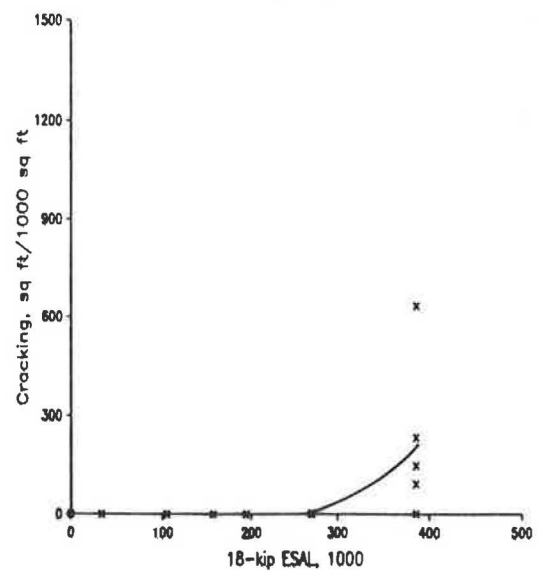
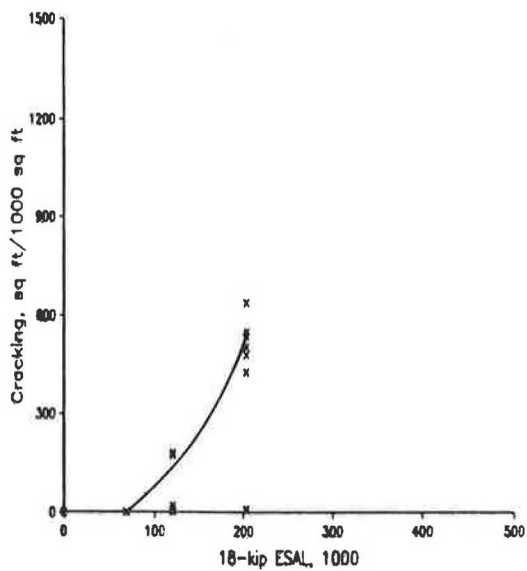
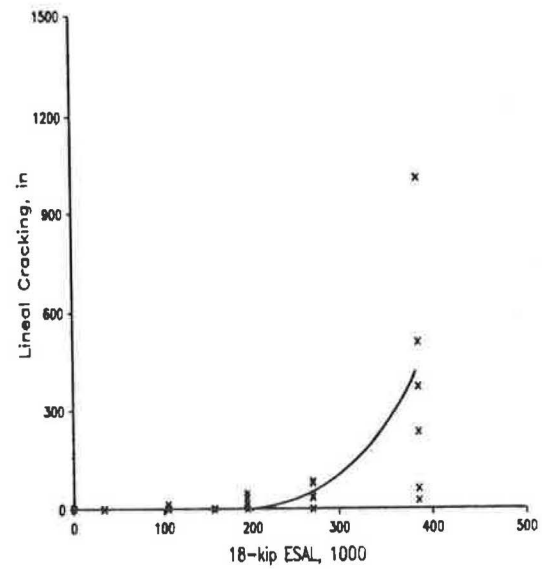
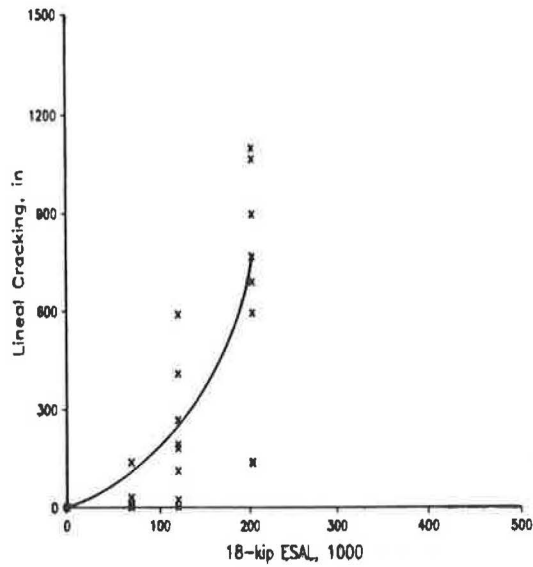
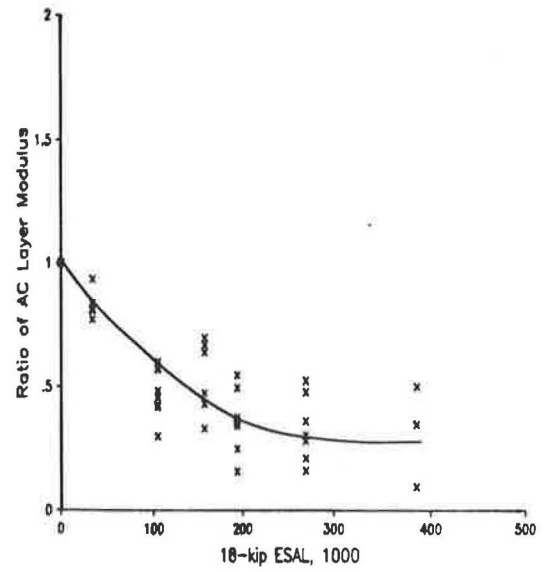
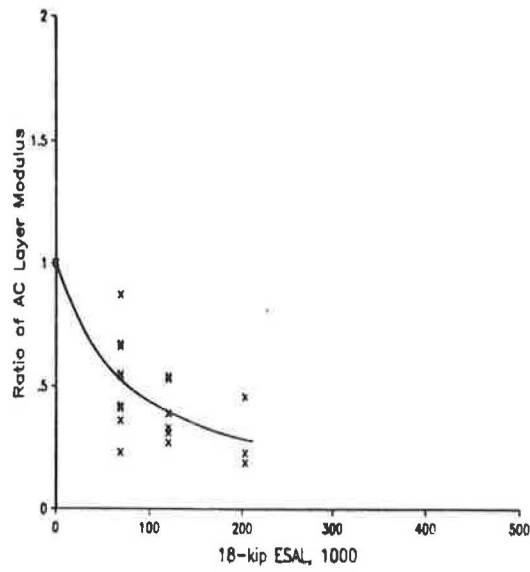


FIGURE 7 Variation of ratio of AC layer modulus, lineal cracking, and AASHO cracking as a function of 18-kip ESAL repetitions for Lane 1, Section 1.

FIGURE 8 Variation of ratio of AC layer modulus, lineal cracking, and AASHO cracking as a function of 18-kip ESAL repetitions for Lane 1, Section 2.

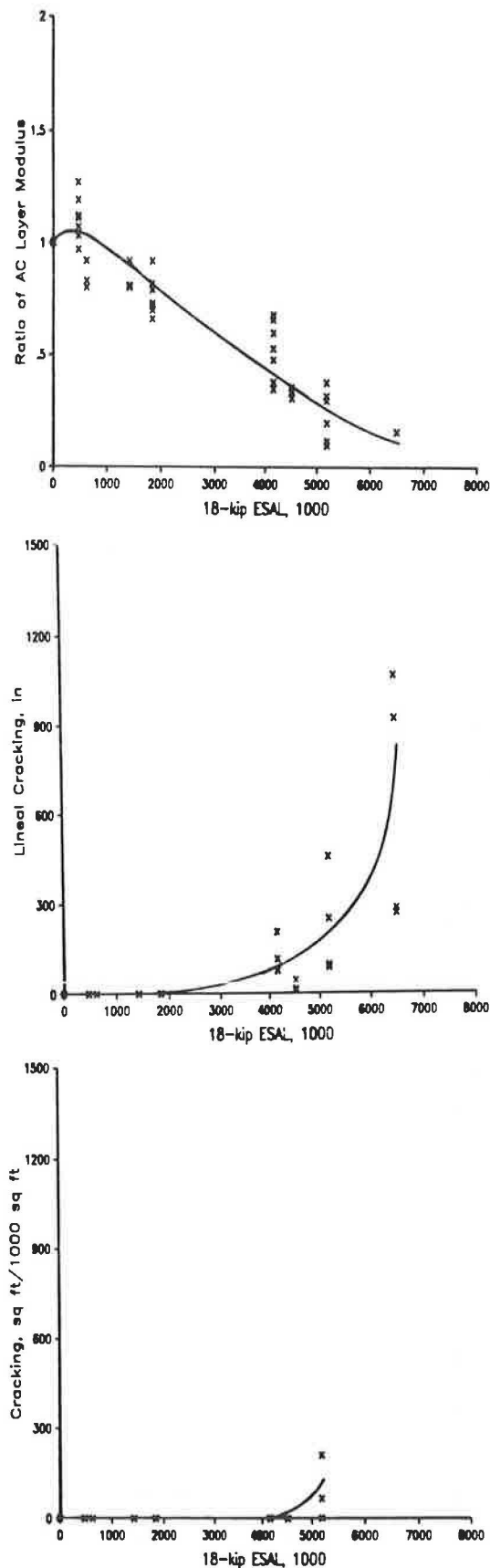


FIGURE 9 Variation of ratio of AC layer modulus, lineal cracking, and AASHTO cracking as a function of 18-kip ESAL repetitions for Lane 2 tests.

ure modes (fatigue or rutting), field data indicated that the lag between structural capacity reduction and surface cracking exists at all test sections. Based on field data from tests on thin (Lane 1) and thick (Lane 2) pavement structures, the following conclusions were drawn:

- Good correlation is shown between the reduction in the back-calculated moduli of the asphalt layer and the increase in peak deflection as a function of 18-kip ESAL repetition, given that both parameters are corrected to a common base temperature.
- Small changes in the cracked surface would appear in the measurement of crack length long before they would appear in the measurement of AASHTO Class 2 and 3 cracking.
- The field data show a definite lag between the reduction in the structural capacity of the pavement and the appearance of surface cracking. The lag is even longer if the AASHTO Class 2 and 3 cracking is used in the measurement procedure.
- The ratio of the existing asphalt layer moduli to the initial moduli may reach a value of 0.5 before any cracking appears on the surface. If the AASHTO Class 2 and 3 cracking is used, the ratio may become as low as 0.3.
- The ratio of the measured peak deflection to the initial peak deflection may reach a value of 2 before any cracking appears on the surface. If the AASHTO Class 2 and 3 cracking is used, the ratio may reach as high as 3.
- In the case of thin pavements, the lag between the structural capacity reduction and surface cracking may be in terms of a couple hundred thousand 18-kip ESAL repetitions. However, in the case of thick pavements, the lag may be in terms of 2 to 3 million 18-kip ESAL repetitions.
- The use of 10 to 15 percent AASHTO Class 2 and 3 wheel path cracking, which represents 100 ft²/1,000 ft² at the PTF sections, is not justified for structural capacity evaluation. A reduction of 50 percent in the modulus of the asphalt concrete layer and an increase of 200 percent in the peak deflection may occur before the 100 ft²/1,000 ft² cracking is reached.
- Field data from the PTF sections show no definite relationship between deflection under load and surface cracking. Consequently, deflection measurement is a better indicator of the structural capacity of the pavement than any other crack measurement technique.

REFERENCES

1. Highway Research Board. *The AASHTO Road Test*. Special Reports 61A-61G, HRB, National Research Council, Washington, D.C., 1962.
2. D. R. Luhr, D. A. Anderson, and E. G. Fernando. *Development of Material Structural Coefficients and Evaluation of Material Behavior*. Final Report, FHWA/PA 84-028, Volume 6, December 1984.
3. *AASHTO Guide for Design of Pavement Structures*. AASHTO, Washington, D.C., 1986.
4. D. A. Anderson, P. Sebaaly, N. Tabatabaee, R. Bonaquist, and C. Churilla. *Pavement Testing Facility—Pavement Performance of the Initial Two Test Sections*. Final Report, FHWA/RD-88/060, February 1988.
5. P. Sebaaly and M. S. Mamlouk. Typical Curves for Evaluation of Pavement Stiffness from Dynaflect Measurements. In *Transportation Research Record 1070*, TRB, National Research Council, Washington, D.C., 1986, pp. 43–53.

Analysis of Full-Depth Asphalt Concrete Pavements Using Shakedown Theory

LUTFI RAAD, DIETER WEICHERT, AND ALI HAIDAR

Full-depth asphalt concrete pavements are generally designed to resist fatigue and rutting when subjected to repeated traffic loads. Of particular importance in this case is whether such pavements will exhibit increased accumulation of plastic strains under long-term, repeated loading conditions that will eventually lead to incremental collapse or whether the accumulation of plastic strains will cease and a shakedown condition is reached. In this paper, the shakedown theory is used in the analysis of full-depth asphalt concrete pavements overlying clay subgrade. The proposed numerical algorithm incorporates the stress-dependent resilient behavior of the subgrade. The influences of stiffness and strength of the subgrade, and thickness and temperature of the asphalt concrete on shakedown behavior are illustrated. Results are used to develop shakedown-limiting criteria in terms of vertical stresses and strains acting on top of the subgrade layer. Moreover, comparisons among shakedown, fatigue, and rutting predictions are presented.

Full-depth asphalt concrete pavements are generally designed to account for fatigue and rutting. Design criteria, in terms of maximum allowable values for both the tensile strain on the underside of the asphalt concrete layer and vertical strain on top of the subgrade, have been established and are used as the basis for selecting the design thickness (1, 2). Of particular importance is whether such pavements will exhibit increased accumulation of plastic strains under long-term, repeated loading conditions that may lead to eventual collapse or whether the accumulation of plastic strains will cease and a shakedown condition will be reached.

The shakedown theory was first presented by Melan (3). According to this theory, a system will shake down under repeated cyclic loads if a self-equilibrated, time-independent, residual-stress field could be found such that equilibrium conditions, boundary conditions, and yield conditions are satisfied within the system. In this case, the material is assumed to be elastic-ideally plastic with convex yield surface, applicable normality condition, and negligible viscous and inertia effects. The theory has been applied to discrete structures (4, 5) and more recently to general continua, including pavements (6–8).

In this paper, an attempt is made to use the shakedown theory to analyze full-depth asphalt concrete pavements overlying clay subgrade. The proposed algorithm incorporates the stress-dependent resilient behavior of the subgrade. The influ-

ences of stiffness and strength of the subgrade, and thickness and temperature of the asphalt concrete layer on shakedown behavior are illustrated, and results are used to develop shakedown-limiting criteria in terms of vertical stresses and strains acting on top of the subgrade layer. Moreover, comparisons of shakedown, fatigue, and rutting predictions are presented.

PROPOSED ANALYTICAL MODEL

In the proposed method of analysis, the two-layer system is discretized into a series of rectangular finite elements (Figure 1). A quasi-static analysis is implemented, whereby inertia and viscous effects are assumed negligible. If stress states σ^o , σ^s , and σ^r correspond respectively to body forces, P^o , statically applied loads, f^s , and repeated loads, f^r , then the system will not collapse under repeated loads—provided a stress increment, $\Delta\sigma$, can be found such that equilibrium conditions, boundary conditions, and yield conditions are satisfied. If the system under consideration is assumed to be elastic-ideally plastic with convex yield surface (i.e., the Mohr-Coulomb yield criterion is adopted in this case) and applicable normality condition, then the determination of the shakedown load for a plane strain or a plane stress reduces to an optimization

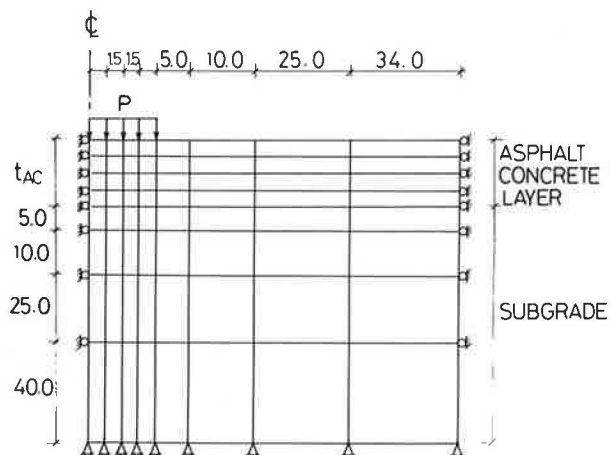


FIGURE 1 Finite element representation of the pavement structure (P = applied surface load (psi); t_{ac} = thickness of asphalt concrete layer; all indicated dimensions are in inches).

problem stated mathematically as follows:

Minimize

$$Q = -\alpha + \sum_{i=1}^{NP} (S_{xi})^2 + \sum_{i=1}^{NP} (S_{yi})^2 \quad (1)$$

Subject to the following constraints:

$$\alpha > 0 \quad (2)$$

$$f(\sigma) \leq 0 \quad (3)$$

$$\sigma_3 \geq -2 C \tan(45 - \phi/2) \quad (4)$$

where

$$\begin{aligned} NP &= \text{number of nodal points,} \\ \alpha &= \text{load multiplier associated with repeated loads, } f^a, \\ &\text{and} \\ \sigma &= (\sigma_{ij})_o + (\sigma_{ij})_s + \alpha (\sigma_{ij})_a + \Delta\sigma_{ij} \end{aligned} \quad (5)$$

where

$$\begin{aligned} (\sigma_{ij})_o, (\sigma_{ij})_s, \text{ and } (\sigma_{ij})_a &= \text{stresses due to body forces, } P^o, \\ &\text{statically applied forces, } f^s, \text{ and} \\ &\text{repeated loads, } f^a, \text{ respectively at} \\ &\text{the center of a given element;} \\ \Delta\sigma_{ij} &= \text{arbitrary stress increment applied} \\ &\text{at the center of each element;} \\ S_{xi}, S_{yi} &= \text{resultant forces in the } x \text{ and } y \\ &\text{directions at a nodal point with} \\ &\text{respect to a global set of coordi-} \\ &\text{nates } x-y; \text{ and} \\ f &= \text{yield function with yield occur-} \\ &\text{ring when } f \geq 0. \end{aligned}$$

In this case, f represents the Mohr-Coulomb failure criterion as given by

$$f = \sigma_1 - \sigma_3 \tan^2(45 + \phi/2) - 2 C \tan(45 + \phi/2) \quad (6)$$

where

$$\begin{aligned} \sigma_1 \text{ and } \sigma_3 &= \text{major and minor principal stresses,} \\ C &= \text{cohesion, and} \\ \phi &= \text{angle of friction.} \end{aligned}$$

The optimization procedure for minimizing Q and obtaining the shakedown solution is described elsewhere (8, 9). More recently, the procedure has been extended to include the nonlinear, stress-dependent resilient properties of granular and subgrade layers in pavements (10, 11). A typical representation of the subgrade resilient modulus with repeated deviator stress is shown in Figure 2. A series of iterative steps using finite element analysis is conducted so that the stresses at the center of each element satisfy the stress-dependent modulus relationships. A new shakedown load is then calculated using the newly determined moduli at the center of elements. The procedure is repeated until convergence is attained whereby the shakedown load in two consecutive steps reaches essentially the same value; hence, shakedown conditions are satisfied simultaneously with the stress-dependent moduli relations.

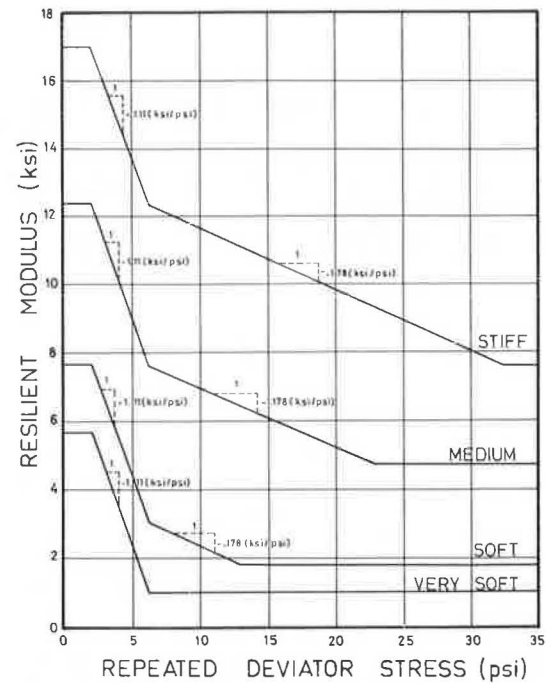


FIGURE 2 Resilient properties of subgrade (15).

APPLICATIONS

Materials Characterization

The asphalt concrete mix properties considered in the analysis correspond to mix M27 as designated by Salam (12). The mix aggregates consisted of 63.5 percent fine aggregate and 36.5 percent coarse aggregate of crushed Watsonville granite. A 7-percent asphalt cement with a 60 to 70 penetration grade was used. The average air void content was 0.82 percent and the average specific gravity was 2.53. The volume concentrations of aggregate and asphalt were 0.84 and 0.16, respectively. Specimens prepared using the designated mix were tested for the purpose of determining strength, stiffness, and fatigue properties. The variations of stiffness and strength parameters (cohesion, C_{ac} , and angle of friction ϕ_{ac}) with mix temperature are shown in Figures 3 and 4, respectively.

The subgrade was assumed to exhibit stress-dependent resilient properties. Typical relations between the deviator stress and resilient modulus (defined as the ratio of repeated stress to recoverable or resilient strain) are shown in Figure 2.

A summary of asphalt concrete and subgrade properties for all the cases used in the study is presented in Tables 1 and 2, respectively.

Shakedown Behavior

Results of analyses to investigate the influence of the asphalt concrete layer thickness and temperature, and subgrade stiffness and strength on shakedown behavior could be summarized as follows:

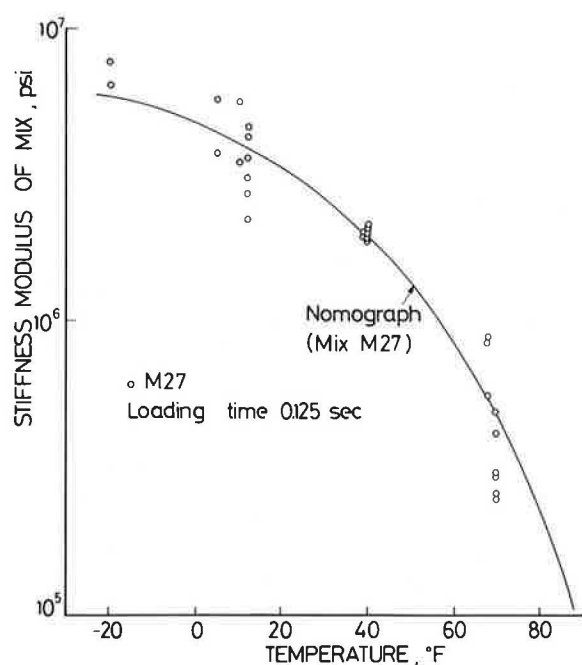


FIGURE 3 Variation of mix stiffness with temperature (12).

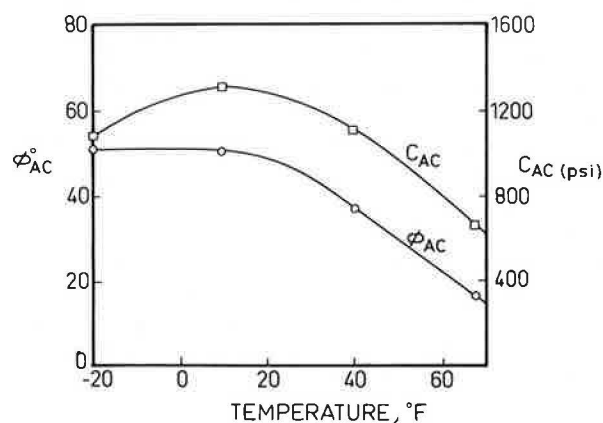


FIGURE 4 Variation of strength parameters with mix temperature (12).

1. The shakedown load seems to decrease with increase in temperature of the asphalt concrete layer above 40°F. Such behavior reflects probably the predominant effect of the subgrade on shakedown. An increase in asphalt concrete temperature would reduce the stiffness of the asphalt concrete layer and would, therefore, result in a larger transfer of applied load to the subgrade (Figures 5–7). On the other hand, for values of asphalt concrete layer temperature under 40°F, shakedown behavior becomes influenced essentially by the asphalt concrete layer. A decrease in layer temperature in this case would be reflected in an increase in its stiffness and strength. The asphalt concrete layer would, therefore, carry a larger proportion of the applied load, which could result in a lower shakedown capacity—particularly for thinner surfaces and stiffer subgrades as illustrated in Figures 6 and 7.

TABLE 1 ASPHALT CONCRETE MIX PROPERTIES USED IN SHAKEDOWN ANALYSIS

Layer Temperature (°F)	Strength Parameter		Modulus of Elasticity (psi)
	C_{ac} (psi)	ϕ_{ac} (°)	
10	1300	50	3.0×10^6
40	1100	35	1.0×10^6
68	650	17	5.0×10^5
90	400	10	1.0×10^5

NOTE: Poisson's ratio was assumed equal to 0.35. Density used was 140 lb/ft³.

TABLE 2 SUBGRADE PROPERTIES USED IN SHAKEDOWN ANALYSIS

Subgrade	Strength Parameters	
	C_s (psi)	ϕ_s (°)
Soft	3	0
Medium	6	0
Stiff	12	0

NOTE: Resilient properties for soft, medium, and stiff subgrade are presented in Figure 2. Poisson's ratio was assumed equal to 0.45. Density was equal to 115 lb/ft³. The at-rest coefficient of earth pressure was assumed equal to 0.5.

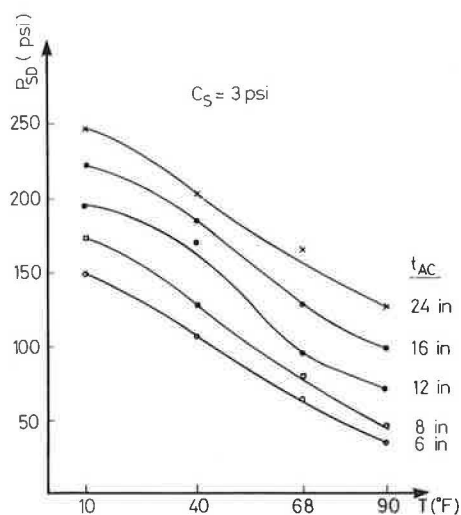


FIGURE 5 Variation of shakedown load for soft subgrade conditions.

2. The shakedown load increases with increasing subgrade strength as illustrated in Figures 8 and 9. However, the beneficial effect of subgrade strength on shakedown behavior is less for thinner asphalt concrete sections and lower asphalt concrete temperature. The shakedown capacity in this case is limited by the strength of the surface layer.

3. The influence of thickness of asphalt concrete layer on shakedown is shown in Figures 10 and 11. An increase in thickness of the asphalt concrete layer results in an increase in the shakedown load. This increase would be greater for a stiff subgrade support than for soft subgrade conditions. It should be noted that, in case of the stiff subgrade (Figure 11) and for thicknesses of the asphalt concrete layer less than about 20 in., the shakedown load increases with increasing layer temperature above 10°F but decreases as the tempera-

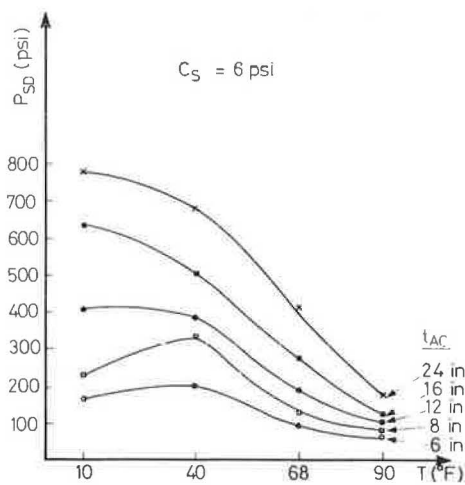


FIGURE 6 Variation of shakedown load for medium subgrade conditions.

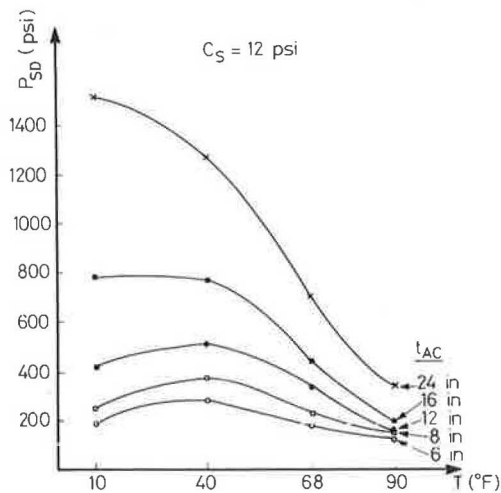


FIGURE 7 Variation of shakedown load for stiff subgrade conditions.

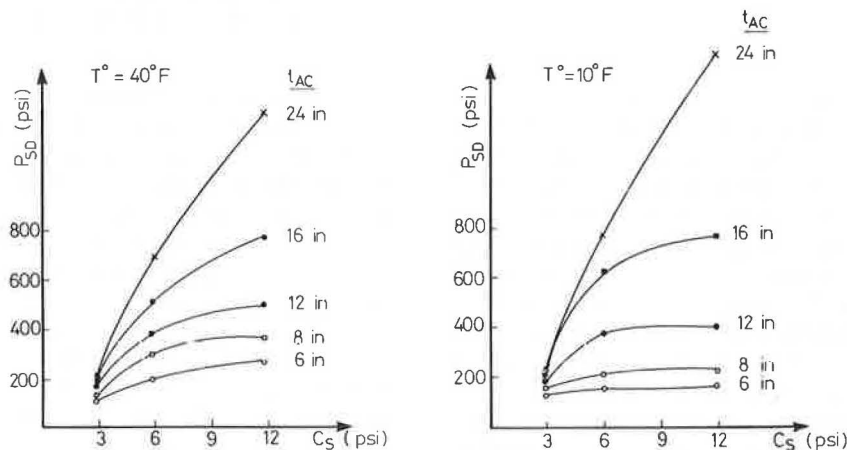


FIGURE 8 Influence of subgrade strength on shakedown for pavement temperatures of 40°F and 10°F.

ture exceeds 40°F. On the other hand, for asphalt concrete layer thicknesses greater than about 20 in., an increase in layer temperature would result in a decrease in shakedown capacity.

Limiting Criteria

In many situations, limiting values in the critical response parameters have been proposed as means of predicting pavement performance. Specifically, in full-depth asphalt concrete pavements, the accumulation of plastic strains (i.e., rutting) has been linked to vertical strains and/or vertical stresses on the top part of the subgrade. An attempt is made in this paper to determine limiting criteria associated with shakedown behavior. Analyses were conducted to determine the shakedown loads for asphalt concrete layer thicknesses of 6, 8, 12, 16, and 24 in. and for the subgrade and temperature conditions summarized in Tables 1 and 2. Plane strain finite element analyses were then performed using the nonlinear stress-dependent resilient properties of the subgrade in order to determine the response of pavement sections under the applied shakedown load. Limiting criteria in terms of subgrade vertical stress, σ_v , and vertical subgrade strain, ϵ_v , were determined. Attempts to develop other limiting criteria using pavement response parameters, such as surface and subgrade deflections, and tensile stresses and strains on the underside of the asphalt concrete layer were not conclusive.

Results presented in Figure 12 indicate that the ratio of subgrade normal stress, σ_v , to subgrade shear strength, C_s , lies essentially between 3 and 4 for all the asphalt concrete layer thicknesses and subgrade stiffnesses considered—provided the asphalt concrete layer temperature is greater than 40°F. However, for cases where the temperature drops to 10°F and for asphalt concrete layer thicknesses less than 12 in., the ratio σ_v/C_s drops to a value between 2 and 3. This reflects the greater mobilization of tensile stresses in the surface layer that would result in lower values of vertical stresses acting on the top of the subgrade at shakedown. The average values of critical normal stress in this case are in the range of 10 to 40 psi.

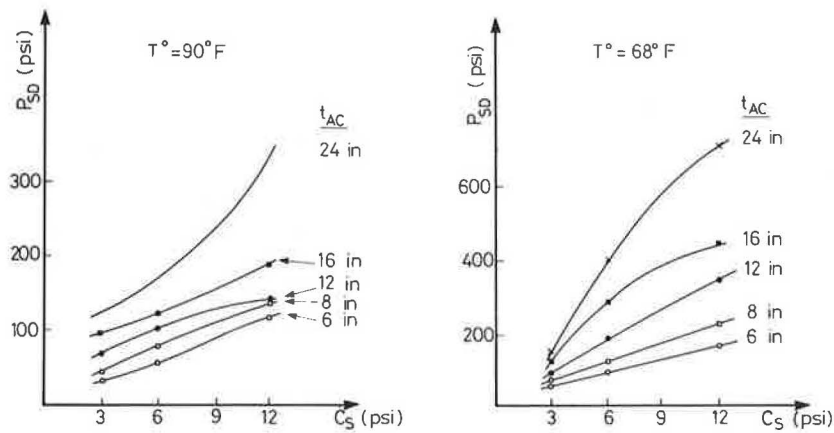


FIGURE 9 Influence of subgrade strength on shakedown for pavement temperatures of 90°F and 68°F.

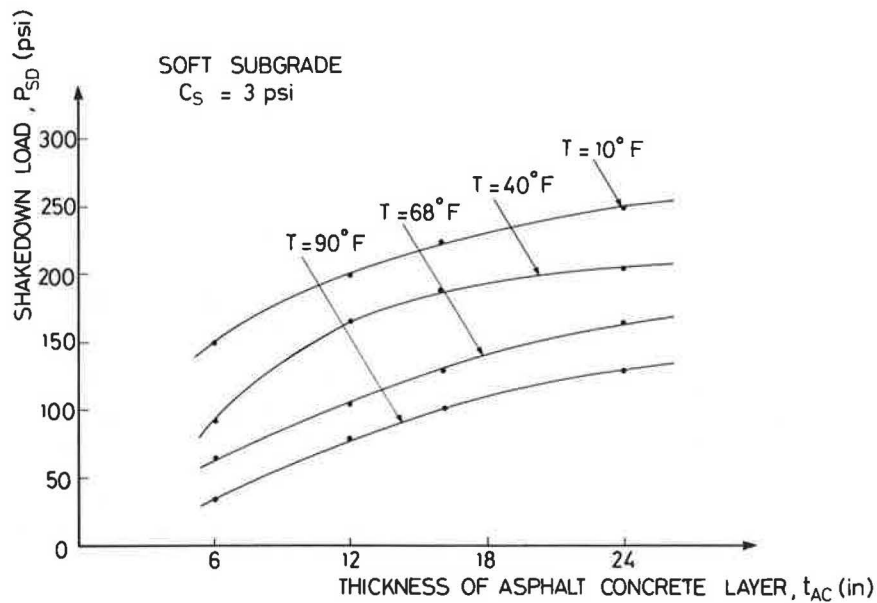


FIGURE 10 Influence of asphalt concrete layer thickness on shakedown for soft subgrade.

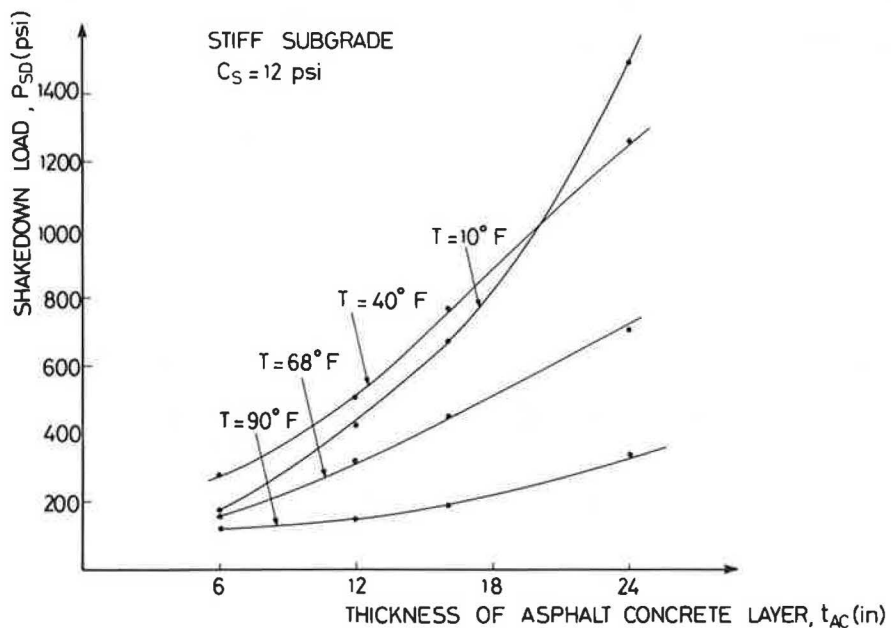


FIGURE 11 Influence of asphalt concrete layer thickness on shakedown for stiff subgrade.

Available subgrade normal stress criteria include work by the British Railway (13) and Peattie (14). The British Railway determined through repetitive triaxial testing that, in general, most subgrade soils exhibit a threshold stress of 20 psi or less. Peattie proposed allowable values for subgrade normal stress for 1 million stress applications in the range of 2 to 22 psi for subgrade California Bearing Ratio (CBR) values between 3 and 20, respectively. These values are generally lower than those obtained from shakedown loading.

Results of shakedown normal strains on top of the subgrade are presented in Figure 13. Values indicate that the limiting vertical strain, ϵ_v , on top of the subgrade is dependent on the stiffness of the subgrade. The limiting vertical strain, ϵ_v , is given in this case as

$$1 \times 10^{-3} < \epsilon_v < 2.5 \times 10^{-3} \text{ for soft subgrade} \quad (7)$$

$$1.5 \times 10^{-3} < \epsilon_v < 3.0 \times 10^{-3} \text{ for medium subgrade} \quad (8)$$

$$2.5 \times 10^{-3} < \epsilon_v < 4.0 \times 10^{-3} \text{ for stiff subgrade} \quad (9)$$

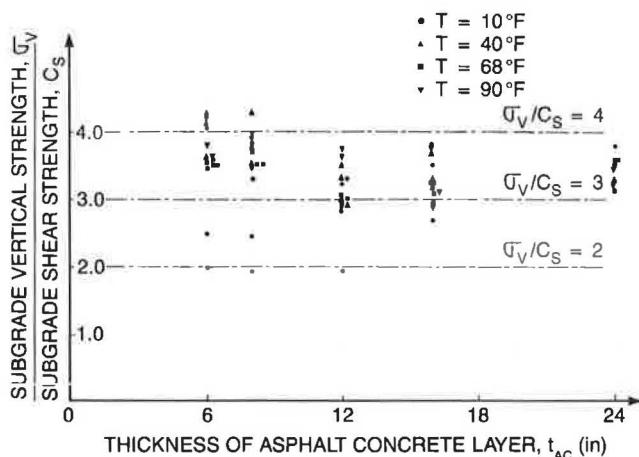


FIGURE 12 Limiting subgrade normal stress criteria.

Data summarizing available limiting subgrade normal strain criteria were presented by Figueroa (15). The data presented indicate that normal strain values associated with 10^6 repetitions lie in the range of 0.10×10^{-3} to 1.5×10^{-3} . These values are generally lower than the shakedown normal subgrade strains. According to the criteria presented by Figueroa, the shakedown normal strain values in constraints 7, 8, and 9 would probably induce failure after 10^3 to 10^4 strain repetitions.

The larger values of subgrade normal stress and strain obtained from shakedown analysis could indicate a more severe loading condition or could be a result of the conservative interpretation of pavement serviceability data when determining the existing criteria. Although shakedown loading could result in low pavement serviceability, it may nevertheless be used as an upper bound which, if exceeded, would lead to incremental collapse. Moreover, if the applied loads are kept below the shakedown limit, pavement maintenance will be more effective, because the rate of accumulation of plastic strains will eventually cease and the pavement system will exhibit a stable response.

Shakedown Versus Fatigue

It is of practical significance to determine whether a given pavement under existing or projected fatigue loading will shakedown. In this respect, if the shakedown limit is not exceeded, the rate of accumulation of permanent strains and the associated pavement distress will be less and pavement maintenance will be more effective in comparison with the case where shakedown conditions are exceeded. To illustrate this, analyses were performed to compare shakedown and fatigue behavior. The asphalt concrete was analyzed assuming layer temperature values of 10°F and 68°F for stiff and soft subgrade conditions. The fatigue criterion used was proposed by Monismith et al. (16) and is illustrated in Figure 14.

Results of analyses presented in Figures 15 through 18 indicate a significant influence of subgrade conditions on pavement performance. For the case of a stiff subgrade, fatigue of the asphalt concrete layer seems to be the predominant

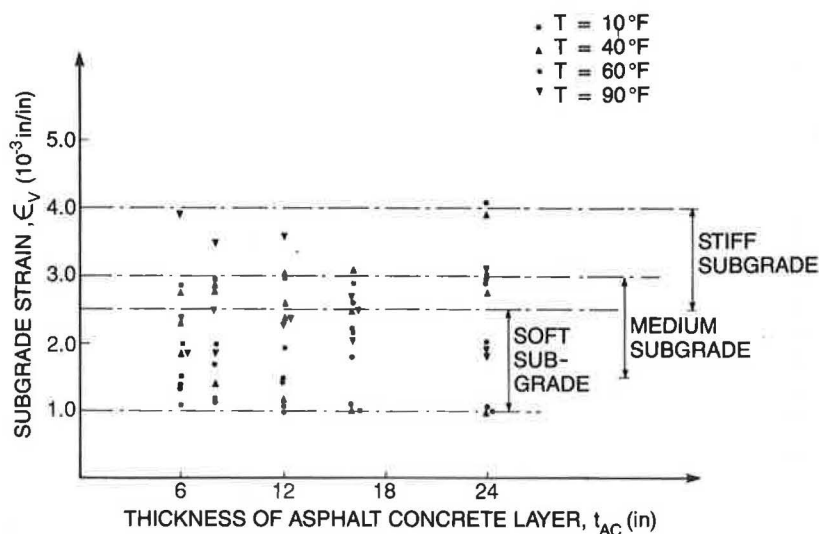


FIGURE 13 Limiting subgrade normal strain criteria.

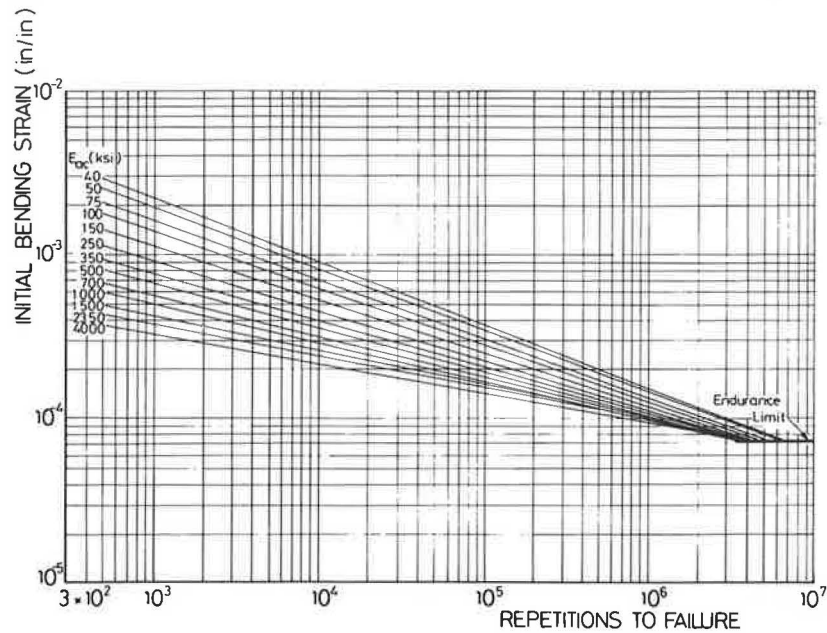


FIGURE 14 Fatigue failure criteria for asphalt concrete mixes (16).

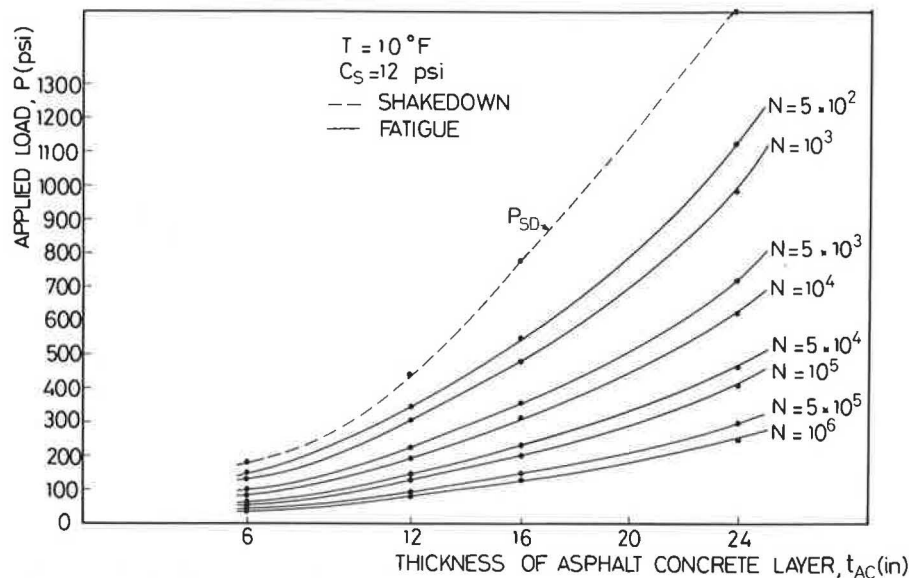


FIGURE 15 Fatigue and shakedown loadings for stiff subgrade conditions and $T = 10^{\circ}\text{F}$.

distress mode, and the loads required to induce fatigue failure are smaller than the shakedown loads for all the pavement temperatures and thicknesses considered (Figures 15 and 16). On the other hand, for the case of a soft subgrade, fatigue and/or rutting could be the governing modes of distress depending on pavement thickness, pavement temperature, and magnitude and repetitions of the applied load (Figures 17 and 18). For a given applied load in this case, an increase in pavement thickness will increase the resistance to fatigue and rutting. Moreover, for a given temperature, pavement sections designed to carry a certain number of load repetitions in fatigue may or may not shakedown depending on pavement thickness. For example, assuming a pavement temperature of

68°F and a design number of load repetitions equal to 10^4 , a 6-in.-thick asphalt concrete (design load equal to 35 psi) will stabilize and attain shakedown, whereas a 24-in.-thick asphalt concrete layer (design load equal to 195 psi) will not shakedown and will exhibit incremental collapse (Figure 18). Moreover, an increase in pavement temperature reduces both its fatigue and shakedown capacity.

It is interesting to note that if pavement overloading occurs and reaches a value equal to or greater than the shakedown limit, then fatigue and rutting for relatively thin pavement sections (thickness less than 8 inches) and temperature greater than 68°F could take place after only a few load repetitions (fewer than 1,000).

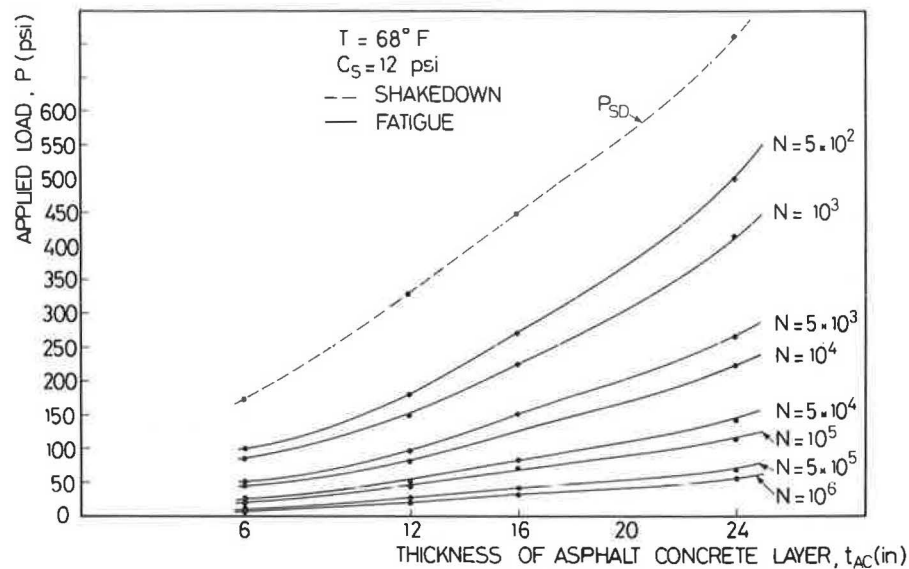


FIGURE 16 Fatigue and shakedown loadings for stiff subgrade conditions and $T = 68^{\circ}\text{F}$.

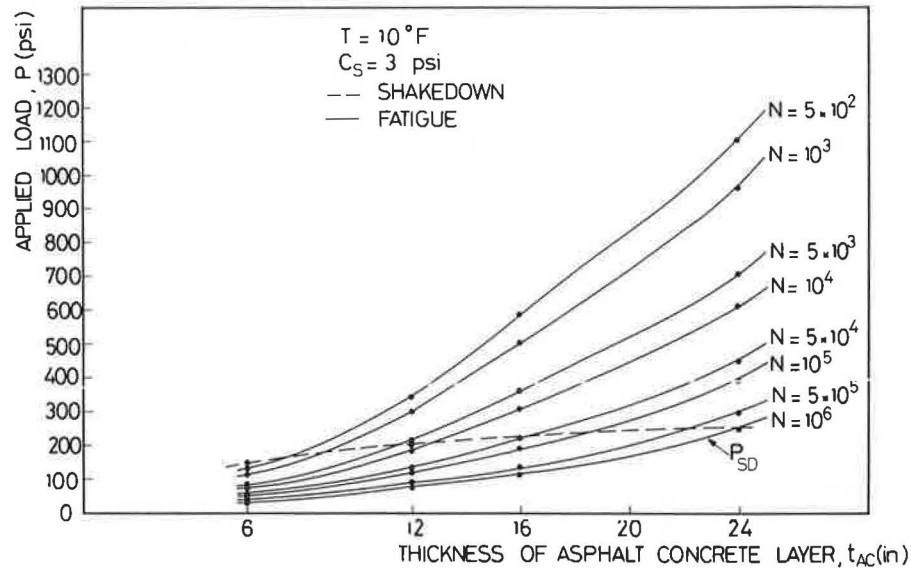


FIGURE 17 Fatigue and shakedown loadings for soft subgrade conditions and $T = 10^{\circ}\text{F}$.

Shakedown Versus Rutting

To assess the magnitude and rate of rutting associated with repeated shakedown load applications, a typical example—consisting of an 8-in. asphalt concrete layer over a stiff subgrade—was considered. The section was subjected to a variable number of load applications of magnitude equal to $0.75 P_{sd}$, P_{sd} , and $1.25 P_{sd}$, where P_{sd} is equal to the shakedown load. The asphalt concrete layer was subdivided into two layers of equal thickness. Weather data used by Monismith et al. (17) were used in this case to compute pavement monthly temperature distribution. The corresponding traffic-weighted mean stiffness induced by load repetitions was determined based on repeated flexural beam test data presented by

Monismith et al. (16). A summary of temperature, stiffness, and strength characteristics of the asphalt concrete layer is presented in Table 3. The influence of temperature variation over a typical year's time was considered in determining an effective shakedown load using Miner's cumulative damage hypothesis. The effective shakedown load, P_{sd} , could be obtained as follows:

$$\frac{1}{n} \sum_{i=1}^n P_{sd}/P_{sdi} = 1 \quad (10)$$

where P_{sdi} equals shakedown load determined for a representative period (i) and n equals total number of representative periods.

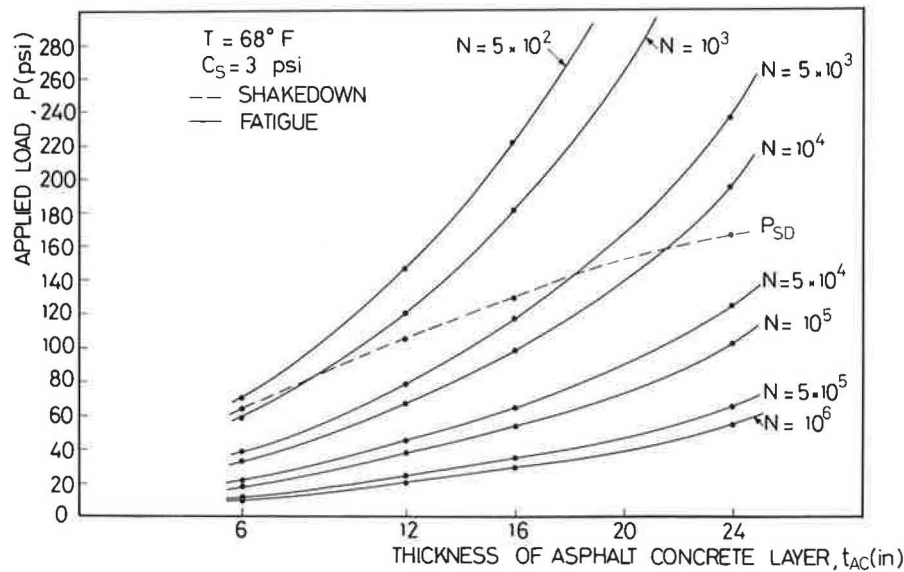


FIGURE 18 Fatigue and shakedown loadings for soft subgrade conditions and $T = 68^\circ\text{F}$.

In this example, each month of the year was considered a representative period, and the total number, n , was equal to 12. The variation of shakedown load, P_{sdi} , over a 1-year period is shown in Figure 19. The stress state was then estimated for loading conditions corresponding to $0.75P_{sd}$, P_{sd} , and $1.25P_{sd}$ for every month of the year. Plane strain finite element analysis that incorporates the stress-dependent resilient properties of the subgrade was used for this purpose.

The magnitude of vertical permanent strains, ϵ_z , under the center of the applied wheel load was determined using the method proposed by Monismith et al. (17). In this case

$$\epsilon_z = R [\sigma_z - \nu(\sigma_x + \sigma_y)] \quad (11)$$

where

$\sigma_z, \sigma_y, \sigma_x$ = stresses in vertical, radial, and tangential directions, respectively,
 ν = Poisson's ratio, and
 R = permanent strain parameter.

The corresponding rut depth, D , is then expressed as

$$D = \sum_{i=1}^s \epsilon_{zi} h_i \quad (12)$$

where

h_i = thickness of sublayer (i),
 ϵ_{zi} = permanent strain at center of sublayer (i), and
 s = number of sublayers considered.

For the asphalt concrete layer,

$$R_b = \Delta(T) N^\alpha \sigma^{\beta-1} t \quad (13)$$

where

$$\Delta(T) = B T e^{-A/T} \quad (14)$$

α, β, B, A = material coefficients determined experimentally,
 t = loading time (sec),
 N = number of load repetitions,
 T = absolute temperature, and
 $\sigma = \sigma_z - \nu(\sigma_x + \sigma_y)$.

For the subgrade,

$$R_s = \frac{1}{l - m\sigma} \left(\frac{N}{N_o} \right)^b \quad (15)$$

where l, m, b equal material coefficients and N_o equals number of repetitions at which coefficients are determined. Material coefficients [determined by Monismith et al. (17)] for the asphalt concrete layer used in the analysis are summarized as follows (maximum $m\sigma$ in Equation 15 used for $0.75P_{sd}$ and P_{sd} was 0.90; maximum $m\sigma$ in Equation 15 used for $1.25P_{sd}$ was 0.95):

Coefficient	Amount
l	0.27×10^{-4}
m	0.027
b	0.24
N_o	10,000

Material coefficients (17) for the subgrade used in the analysis are as follows (time of loading assumed was 0.10 sec):

Coefficient	Amount
A	1.02×10^4
B	9.24×10^6
α	0.44
β	0.82

Results of analyses illustrating the variation of rut depth, D , and rate of rutting with applied load repetitions, dD/dN , are presented in Figures 20 and 21, respectively.

Results indicate that most rutting occurs in the subgrade (Figure 20). Significant increase in rutting occurs when the

TABLE 3 SUMMARY OF DATA USED IN RUTTING EXAMPLE

Month	Lay. No.	Pavt. Temp. °F	S_{mix} (10^2) $\times 10^6$	S_{mix} (10^3) p s i	S_{mix} (10^4)	S_{mix} (10^5)	C_{mix} psi	ϕ_{mix}	$\Delta(T)$ $\times 10^{-7}$
Jan	1	44.5	1.75	1.642	1.40	0.805	1046	34	3.88
	2	43.6	1.80	1.688	1.44	0.828	1054	35	3.63
Feb	1	50.5	1.36	1.276	1.088	0.626	954	30	6.03
	2	49.3	1.43	1.341	1.144	0.658	966	31	5.52
Mar	1	53.1	1.24	1.163	0.992	0.570	908	28	7.27
	2	51.6	1.31	1.229	1.048	0.603	931	29	6.53
Apr	1	58.1	0.98	0.919	0.784	0.451	815	24	10.38
	2	56.0	1.08	1.013	0.864	0.497	846	25	8.95
May	1	65.2	0.65	0.61	0.52	0.299	708	18	17.0
	2	62.7	0.76	0.713	0.608	0.350	754	20	14.3
Jun	1	73.0	0.40	0.375	0.32	0.184	546	12	28.8
	2	70.0	0.485	0.455	0.388	0.223	600	14	23.6
July	1	85.5	0.147	0.138	0.118	0.068	339	3	65.1
	2	80.8	0.225	0.211	0.180	0.103	415	6	48.1
Aug	1	82.3	0.200	0.188	0.16	0.092	395	5	53.0
	2	78.3	0.265	0.248	0.212	0.122	460	9	40.9
Sept	1	73.9	0.37	0.347	0.296	0.170	544	11	30.6
	2	70.9	0.45	0.422	0.360	0.207	590	14	25.1
Oct	1	63.3	0.70	0.657	0.560	0.322	730	18	15.2
	2	61.6	0.77	0.722	0.616	0.354	770	20	13.3
Nov	1	52.8	1.26	1.182	1.008	0.580	924	27	7.12
	2	51.7	1.30	1.219	1.040	0.600	937	28	6.58
Dec	1	44.9	1.71	1.604	1.368	0.787	1040	32	4.0
	2	44.2	1.76	1.651	1.408	0.810	1052	35	3.79

Notes

- C_{mix} , ϕ_{mix} are cohesion and friction of the asphalt concrete mix respectively
- S_{mix} is the stiffness of the asphalt concrete mix. Reduction of S_{mix} is determined for average monthly load repetitions of 10^2 , 10^3 , 10^4 , and 10^5 .

shakedown load, P_{sd} , is increased by 25 percent. The pavement experiences a rut depth of about 2 inches after 1 million repetitions when the applied load is equal to the shakedown load, whereas the predicted rut depth reaches 6 in. for the same number of repetitions if the shakedown load is increased by 25 percent. Moreover, the rate of accumulation of permanent deflections, dD/dN , seems to decrease with the number of load applications as shown in Figure 21. However, when the applied load is equal to $1.25 P_{sd}$, then the rate of accumulation of rutting, dD/dN , will cease to decrease at about

1 million repetitions—indicating an increased accumulation of plastic strains that will eventually lead to incremental collapse.

SUMMARY AND CONCLUSIONS

An attempt has been made to apply the shakedown theory in the analysis of full-depth asphalt concrete pavements overlying clay subgrade using a numerical algorithm that incor-

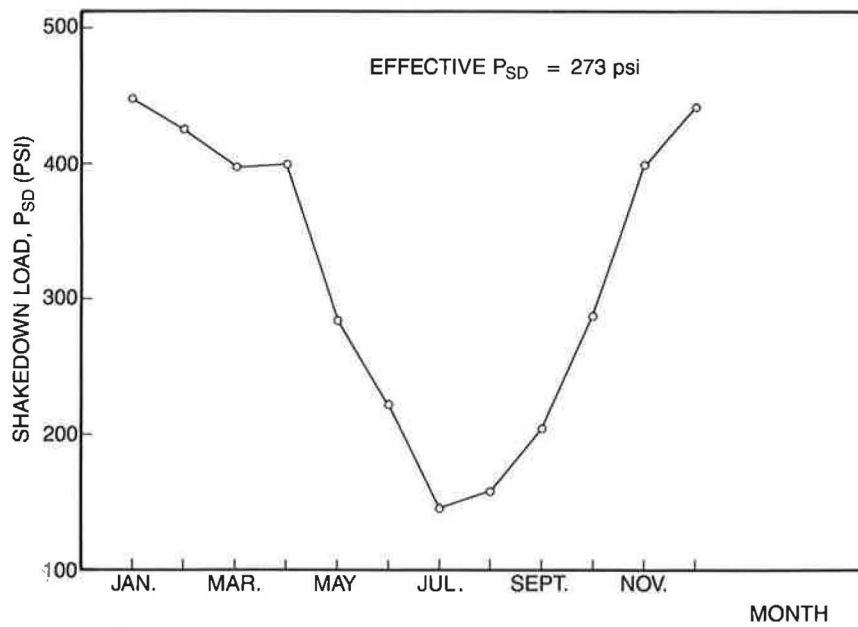


FIGURE 19 Variation of shakedown load over a 1-year period.

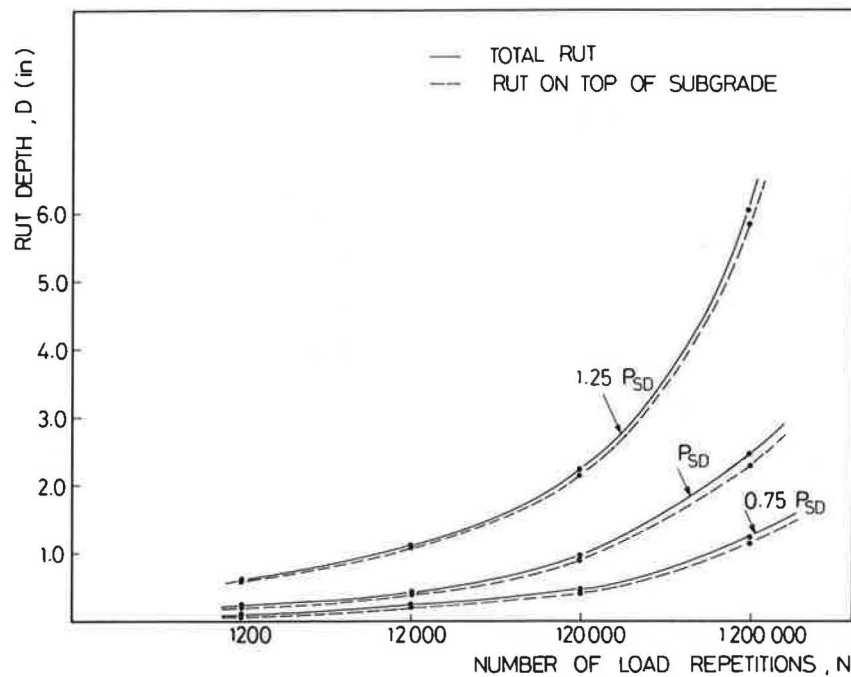


FIGURE 20 Rut depth variation with magnitude and number of load applications.

porated the stress-dependent resilient properties of the subgrade. The influences of stiffness and strength of the subgrade, and thickness and temperature of the asphalt concrete layer on shakedown behavior were investigated and several conclusions were reached:

1. The effect of subgrade conditions in terms of stiffness and strength has a predominant effect on the shakedown behavior of full-depth asphalt concrete pavements. The shakedown load increases with increase in subgrade stiffness, and the increase is more pronounced for thick pavement sections at higher temperatures. The shakedown load also increases with increase in thickness of the asphalt concrete layer. The increase is greater for stiffer subgrades. Moreover, for pavements overlying stiff subgrades, the loads required to induce fatigue failure are smaller than shakedown loads, whereas for soft subgrades, fatigue and/or rutting could be the governing modes of failure.
2. An increase in pavement temperature reduces the shakedown capacity of the pavement. However, for stiff subgrades

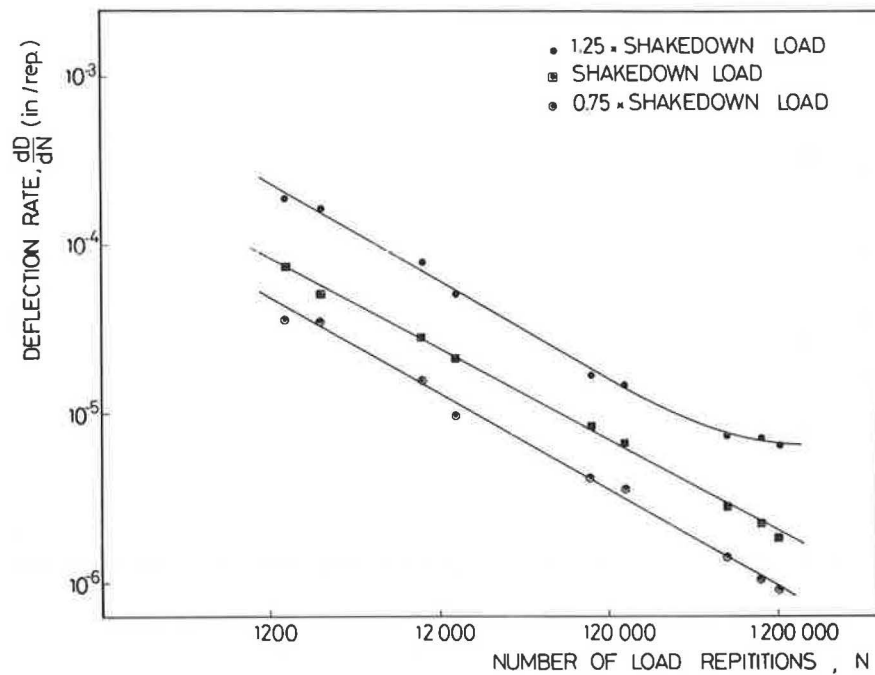


FIGURE 21 Influence of repeated load magnitude on rate of permanent deflections.

and pavement thicknesses less than 20 in. the shakedown load increases as the temperature increases in the range of 10°F to 40°F.

3. Limiting criteria in terms of subgrade normal stress and normal strain have been developed using plane strain finite element analysis of full-depth asphalt concrete pavements subjected to shakedown loads. The limiting ratio, σ_v/C_v , ranges between 2 and 4, whereas the limiting normal strains, ϵ_v , depend on subgrade stiffness and vary between 10^{-3} and 4.0×10^{-3} .

4. Exceeding the shakedown limit would increase significantly the magnitude of rut depth and the rate of accumulation of permanent deflections, thereby leading to incremental collapse of the pavement structure.

The results presented in this study reflect the significance of shakedown capacity on pavement performance. However, additional research is needed to verify analytical predictions and to assess pavement serviceability under shakedown loading conditions for the purpose of developing improved pavement design and maintenance procedures.

ACKNOWLEDGMENTS

The studies described herein were supported by a grant from the University Research Board of the American University of Beirut. The authors are grateful for this support.

REFERENCES

1. A. S. Vesic and L. Domaschuk. *Theoretical Analysis of Structural Behavior of Road Test Flexible Pavements*. NCHRP Report 10, National Research Council, Washington, D.C., 1964.
2. Shell International Petroleum Company Limited. *Shell Pavement Design Manual Asphalt—Asphalt Pavements and Overlays for Road Traffic*. London, England, 1978.
3. E. Melan. Theorie Statisch Unbestimmter Systeme aus idealplastischen Baustoff. *Sitzungsberichte der Akademie der Wissenschaften in Wien*, Vol. 2a, 1936, pp. 145–195.
4. W. A. M. Alwis and P. Grundy. Shakedown of Plates under Moving Loads. In *Proc., 7th Australian Conference on Mechanics of Structures and Materials*, 1980, pp. 191–196.
5. G. Maier and L. Corradi. Upper Bounds on Dynamic Deformations of Elastoplastic Continua. *Meccanica*, Vol. 10, March 1974, pp. 30–35.
6. R. W. Sharp. Pavement Design Based on Shakedown Analysis. In *Transportation Research Record 1022*, TRB, National Research Council, Washington, D.C., 1985, pp. 99–107.
7. R. W. Sharp and J. R. Booker. Shakedown of Pavements Under Moving Surface Loads. *Journal of the Transportation Engineering Division*, ASCE, Vol. 110, No. TE1, 1984, pp. 1–14.
8. L. Raad, D. Weichert, and W. Najm. Stability of Multilayer Systems Under Repeated Loads. In *Transportation Research Record 1207*, TRB, National Research Council, Washington, D.C., 1988, pp. 181–186.
9. L. Raad, W. Najm, D. Weichert and J. Grob-Weege. Application of Shakedown Theory in Soil Mechanics. *Zeitschrift für Angewandte Mathematik und Mechanik*, Vol. 69, Issue 4/5, 1988.
10. D. Weichert, J. Grob-Weege, L. Raad, and W. Najm. Numerical Application of Shakedown Theory to Non-Linear Transportation Support Systems. *Zeitschrift für Angewandte Mathematik und Mechanik*, Vol. 69, Issue 4/5, 1988.
11. W. S. Najm. *Numerical Application of Shakedown Theory to Multilayer Systems*. M. E. thesis. American University of Beirut, Beirut, Lebanon, 1987.
12. Y. M. Salam. *Characterization of Deformation and Fracture of Asphalt Concrete*. Ph.D. dissertation. University of California, Berkeley, 1971.
13. J. M. Waters and J. M. Shenton. Track Foundation Design. *The Railway Gazette*, Oct. 4, 1968.
14. K. R. Peattie. A Fundamental Approach to the Design of Flexible Pavements. In *Proc., International Conference on the Structural Design of Asphalt Pavements*, University of Michigan, Ann Arbor, 1962, pp. 403–411.

15. J. L. Figueroa. *Resilient Based Flexible Pavement Design Procedure for Secondary Roads*. Ph.D. dissertation. University of Illinois at Urbana-Champaign, 1979.
16. C. L. Monismith, J. A. Epps, D. A. Kasianchuk, and D. B. McLean. *Asphalt Mixture Behavior in Repeated Flexure*. Report TE-70-5, University of California, Berkeley, 1970.
17. C. L. Monismith, K. Inkabi, C. R. Freeme, and D. B. McLean. A Subsystem to Predict Rutting in Asphalt Concrete Pavement

Structures. In *Proc., Fourth International Conference on the Structural Design of Asphalt Pavements*, University of Michigan, Ann Arbor, 1977, pp. 529–539.

Publication of this paper sponsored by Committee on Flexible Pavement Design.

Effects of Transverse Distribution of Heavy Vehicles on Thickness Design of Full-Depth Asphalt Pavements

R. BUITER, W. M. H. CORTENRAAD, A. C. VAN ECK AND H. VAN RIJ

One of the most important parameters involved in the design of road pavements is the expected traffic load. This factor has a direct bearing on the thickness requirements of the pavement. For practical purposes, only the loading from heavy-goods vehicles should be considered as, in comparison, the loading from private cars has a negligible effect. When deciding on the layer thicknesses of a road pavement, it is essential to know whether the traffic will be concentrated in one wheel path, or distributed across the width of the traffic lane. When commercial vehicles travelling along a roadway use wheel paths that are transversely distributed across the traffic lane (lateral shifts of the wheel path), the pavement is less severely loaded at representative points in the cross section than when the vehicles all follow the same wheel path (uniform wheel path). The Road and Hydraulic Engineering Division of the Dutch Department of Public Works has carried out further research into the phenomenon of transversely distributed heavy-goods vehicles and the effect of lateral shifts of the wheel path on the design of flexible pavements. The study was particularly concerned with investigating how this phenomenon relates to roads with a full-depth asphalt pavement with specific material properties.

The first part of the research project involved studying the influence of the width of the traffic lane on the wheel-path distribution. Relevant field data were obtained from tests conducted with a specially developed measuring system. It was shown that the lateral wheel-shift pattern of heavy-goods vehicles could be accurately represented by a normal distribution. The standard deviation (also called the lateral spread) associated with the normal distribution was taken to determine the extent to which wheel paths were spread out across the traffic lane. By dividing the traffic lanes into three width classes, characteristic lateral spreads were determined, which could be used as a basis for designing suitable asphalt layer thicknesses.

During the second phase of the research project, a design factor (the wheel-path shift factor) was defined to account for lateral shifts of the wheel path. This enabled the thickness of the asphalt layer to be linked to the lateral spread (or standard deviation) of the normal distribution. Furthermore by applying the wheel-path shift factor (or simply called the shift factor) to various traffic loads, a relationship was established between the thickness requirements of the asphalt and the lateral spread of the normal distribution. The maximum horizontal (tangential) strain occurring at the bottom of the asphalt

layer was assumed to be representative of the likely fatigue effects in the structure.

The third phase of the research work involved comparing the new approach for dealing with lateral shifts in the wheel paths with the method that had been used in the Netherlands until recently. It was concluded that the previous basis for estimating the effects of lateral wheel-path shift phenomena was incorrect. As a result, the new approach outlined in this paper has now been incorporated into the *Pavement Design Manual* used by the Road and Hydraulic Engineering Division, Department of Public Works, in the Netherlands.

EFFECT OF LANE WIDTH ON LATERAL SPREAD

Lane Width

Several factors influence whether a driver follows a fixed wheel path. Some such factors include the following:

- Weather conditions (such as wind and precipitation),
- Time (hour, day, month),
- Heavy-goods vehicle used (type, load, and width),
- Traffic conditions (speed, intensity, proportion of heavy-goods vehicles, oncoming traffic, traffic restrictions, and visibility),
- Road characteristics (type of road, road surface, number of lanes, road roughness, traffic-lane width, width of the hard shoulder, superelevation, alignment, and road markings), and
- Environment (open area, woodlands, built-up area, flyovers, tunnels, traffic barriers, and obstacles).

In the literature (1–7) dealing with the subject of transverse distributions of traffic loads caused by heavy-goods vehicles, it is generally concluded that the width of the traffic lane is the most significant parameter in determining the extent to which the wheel paths are distributed over the road surface.

The other factors mentioned above are primarily concerned with the most heavily loaded point in the pavement structure. The shape of the transverse distribution and, therefore, the extent to which damage is caused to the pavement structure below the most heavily loaded point are less affected by such factors. As a consequence, the current investigations have been restricted to examining the role played by the traffic-lane width in lateral wheel-path shift phenomena.

Measurements of Lateral Wheel-Path Shifts

Measurements of lateral wheel-path shifts were made in the right-hand wheel track of the right-hand traffic lane (the most heavily loaded lane) of three motorways having three lanes in each direction (2×3), fifteen motorways with two lanes in each direction (2×2), and three roads with one lane in each direction (2×1) (see Table 1). Every effort was made to conduct the measurement trials under similar circumstances so that weather and road conditions would not adversely affect the results.

In the majority of the cases, the width of the hard shoulder at the measuring location was greater than 1.20 m. All measurements were carried out on straight horizontal sections of

road. Although most of the roads selected for inclusion in this study were constructed from asphaltic concrete, two sets of measurements were conducted on cement concrete roads. Only heavy-goods vehicles were included in these measurement trials, which were always carried out during the day. No measurements were taken in traffic jams, and vehicles that changed traffic lanes were excluded from the study.

Measuring Equipment

Work has also been carried out in other countries to study the transverse distribution of heavy-goods vehicles on road pavements. However, due to the lack of suitable, commercially avail-

TABLE 1 MEASUREMENT LOCATIONS AND RECORDED RESULTS

Road nr.	Measurement		Width		Spread	Lanes
	Location	Date	B [m]	S [m]		
13	Delft	15-07-82	3.16	0.234	2x3	
12	Bodegraven	21-07-82	3.55	0.265	2x2	
20	Vlaardingen	25-07-82	3.26	0.294	2x2	
16	Willemssdorp	27-07-82	3.50	0.276	2x3	
216	Rotterdam	29-07-82	3.20	0.228	2x2	
15	Rotterdam	20-08-82	3.50	0.313	2x3	
12	Zoetermeer	03-09-82	3.50	0.301	2x2	
27	Maarssen	16-09-82	3.50	0.270	2x2	
12	Harmelen	20-04-83	3.30	0.267	2x2	
225	Amerongen	09-05-83	3.10	0.249	2x1	
4	Hoogmade	09-03-84	3.24	0.224	2x2	
44	Noordwijk	12-03-84	2.98	0.235	2x2	
12	Harmelen	14-03-84	3.28	0.293	2x2	
28	Hulshorst	04-04-84	3.47	0.305	2x2	
--	Bergschenhoek	27-11-84	3.41	0.252	2x1	
59	Vlijmen	04-10-85	3.40	0.304	2x2	
27	Lexmond	30-05-86	3.32	0.309	2x2	
59	Volkerak	14-08-86	3.20	0.268	2x1	
44	Sassenheim	05-11-86	3.30	0.263	2x2	
44	Sassenheim	12-11-86	2.99	0.237	2x2	
44	Wassenaar	02-12-86	3.15	0.257	2x2	

able equipment, most of the research institutes involved have been obliged to develop their own measuring devices for registering the transverse position of wheels (8-10).

The Road Research and Development Branch of the Road and Hydraulic Engineering Division has also developed equipment capable of performing such measurements. The sensing element in this unit consists of a thin mat of synthetic material, which can be readily attached to the road surface using double-sided adhesive tape. The mat contains 120 switch elements, each 0.02 m wide. As a wheel or wheel configuration crosses the sensor, several switches are activated, and the information is registered by means of a microcomputer. This allows conclusions to be drawn from the recorded bit-

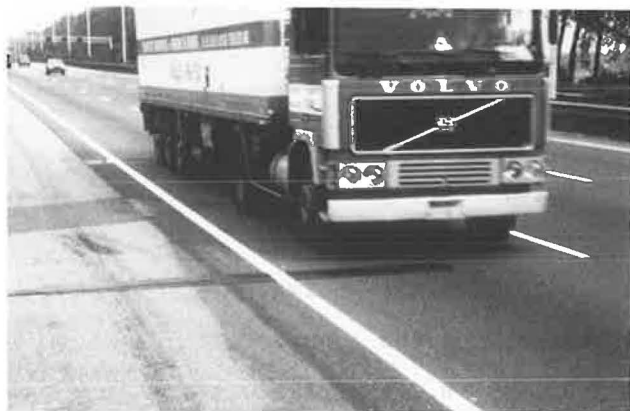


FIGURE 1 Sensing mat for measuring lateral shifts of the wheel path.

pattern about the transverse position and width of the tires that crossed the mat.

The computer software is able to distinguish between three types of tires: single-wheel, wide tire (super single), and twin-wheel. The distinction between single-wheel and wide tires depends on the width of the tire tread. Tires with a tread width of 0.25 m or more are classified as wide.

Measurement Results

An example of the results obtained during a typical measurement (Figure 1) is given in Figure 2. This diagram shows the overall lateral wheel-shift pattern recorded at the Willemsoorp location on the A16 motorway. The number of switch movements at each contact point on the mat is plotted as a function of its transverse position. The position of the mat relative to the right-hand edge marker on the road is also shown.

It can be clearly seen that the overall lateral wheel-shift pattern of all the recorded wheel paths is well described by a bell-shaped normal distribution with lateral spread (S), as shown by the bold line in Figure 2. The lateral spread can be approached by the standard deviation from standard statistics. The calculated lateral spread, the corresponding measured traffic lane width (B), and the number of lanes are given in Table 1 for each of the measurement locations. These results have been plotted in Figure 3.

The lateral spread associated with the different distributions can be seen to increase with the width of the traffic lane. As a result of the relatively low correlation coefficient ($r = 0.63$) between the width of the traffic lane and the lateral spread,

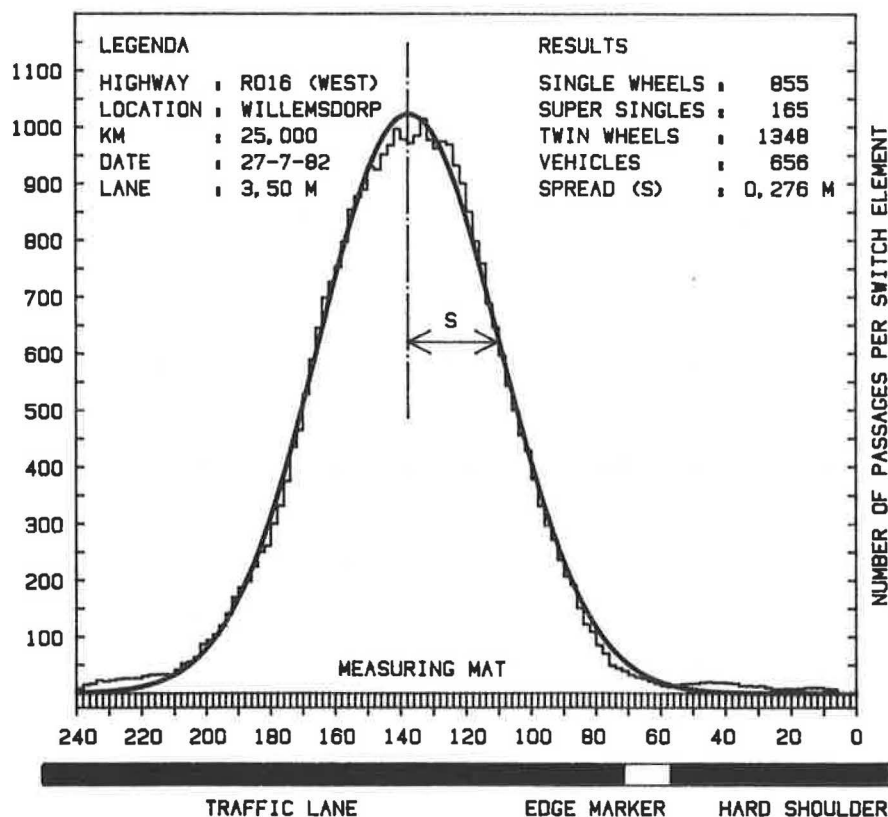


FIGURE 2 Measured lateral wheel-shift pattern.

it was decided that a linear regression analysis would be inappropriate. As a practical solution, the fairly narrow range of traffic lane widths was subdivided into three classes, 0.25 m apart (Figure 3). The average lateral spread of the normal distributions for each width classification has been determined and is shown in Table 2.

Analysis of the results revealed no grounds for deriving different average lateral spreads for each type of road. Moreover, the measurements showed that the center of the normal distribution—which is considered to be the most heavily loaded point—is not at a constant distance from the right-hand edge marker on the road. An explanation of this phenomenon is outside the scope of the present paper. Finally, it should be noted that research has shown (11,12) that the observed lateral spread cannot be simply linearly extrapolated to traffic lane widths outside the measured range.

RELATIONSHIP BETWEEN SPREAD AND ASPHALT THICKNESS

Design of Full-Depth Asphalt Pavements

In discussing the relationship between the lateral spread and the thickness requirements of an asphalt course for given

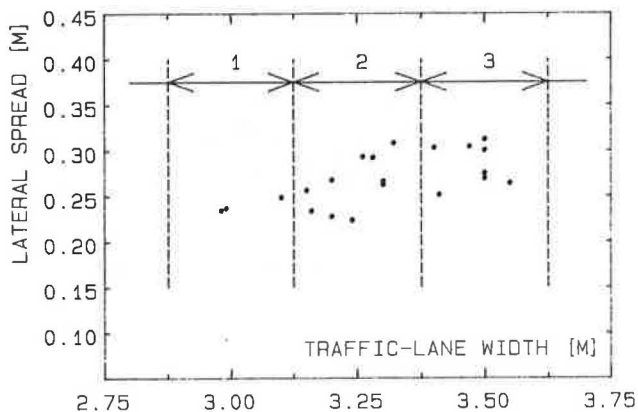


FIGURE 3 Calculated lateral spread plotted as a function of the measured lane width.

traffic loading conditions, attention is specifically focused in this paper on full-depth asphalt pavements. The required thickness of the asphalt layer is dependent on traffic load, climate, and the material properties of both the asphalt and the base course (subbase and subgrade).

It is generally recognized that material properties are extremely difficult to measure accurately in the field. As a result, such properties are usually determined in the laboratory using standard tests. For instance, in the case of asphalt-based materials, dynamic flexural tests are typically used to measure stiffness and fatigue characteristics. The conditions under which bending tests of this type are carried out are strictly limited, with restrictions being placed on the size of the specimens and the test temperatures. Although these tests are conducted at several stress or strain levels, only one frequency is used (13). It is clear that the test conditions in the laboratory are not directly comparable to the actual situation in the field. In general, no consideration is given to the random loading spectrum, the random rest periods, or the seasonal influences that occur in practice.

To be able to translate the traffic loading distribution in practice into a design load, certain correction factors must be applied. The Road and Hydraulic Engineering Division uses an asphalt healing factor, to deal with the effects of intermittent loading and self-healing of asphalt material. Road damage in practice increases gradually. Based on a desired percentage of damage after the design life, a certain discrepancy between the design load and the traffic load should be created by multiplying the traffic load by a safety factor. In the future, a probabilistic approach of road design should give a prediction of damage based on variation in design parameters. A detailed treatment of the healing factor and the safety factor and how they should be applied is outside the scope of this paper (14).

Lateral shifts of the wheel path cause the traffic load to be distributed across the transverse section. This means that, for a given traffic load, the asphalt course need not be as thick as when the traffic is concentrated in a uniform wheel path. The favorable effect of lateral shifts of the wheel path can be expressed by means of the shift factor.

In order to design a pavement for a specific application, the expected practical traffic load must first be expressed as a number of standard axle loads (for instance, 100 kN). To

TABLE 2 AVERAGE LATERAL SPREAD PER TRAFFIC LANE WIDTH CLASSIFICATION

Traffic-lane width [m]			Average spread [m]
Class	From - To	Average	
1	2.88 - 3.12	3.00	0.24
2	3.13 - 3.37	3.25	0.26
3	3.38 - 3.62	3.50	0.29

convert this traffic load ($N1$) to an equivalent number of standard axle loads ($N0$) to be applied under design conditions, the following equation is used:

$$N0 = V \times H \times F \times N1 \quad (1)$$

where

V = shift factor for the traffic load,

H = asphalt healing factor,

F = safety factor,

$N1$ = traffic load (standard axle loads of 100 kN), and

$N0$ = design load (standard axle loads of 100 kN).

The stiffness and fatigue properties of various gravel asphaltic concrete mixes were determined in the laboratory (15) and found to comply with the current requirements of the Dutch Department of Public Works (16).

Calculations were carried out with the BISAR computer program (17) and the stiffness and fatigue properties found in the laboratory to determine the relation between the design loading conditions ($N0$) to be imposed and the required asphalt thickness. This is illustrated in Figure 4. The calculations were performed assuming an air temperature of 14°C, a subgrade modulus of 100 MPa, the wheel configuration as described in the Shell method (18), and a standard axle load of 100 kN. To calculate the asphalt stiffness, the procedure described in the Shell method was used (18).

The following section describes how this information can be used to incorporate the shift factor into the design procedure for selecting the correct layer thickness of an asphalt pavement.

Assumptions Made in Deriving Shift Factor

In deriving a design factor to account for lateral shifts of the wheel path, it was assumed that the transverse position of the wheels was independent of the wheel-load configuration. This assumption was necessary because data from axle-load measurements were not available. The passage of each wheel or wheel configuration was assumed to be equivalent to one standard load (in this case a point load) of a particular magnitude.

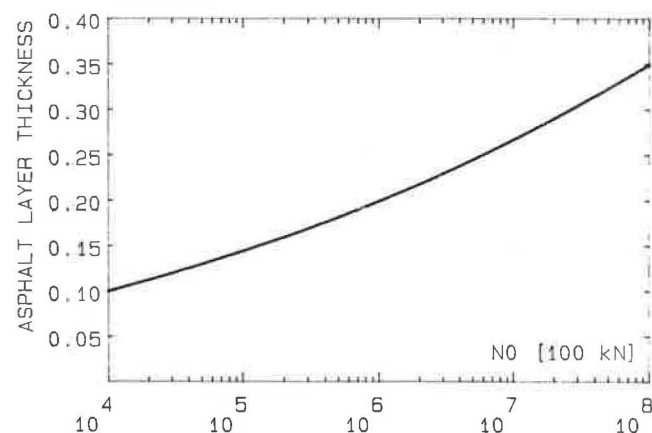


FIGURE 4 Thickness of the asphalt layer as a function of the design load.

Furthermore, the following conditions were also assumed:

1. The transverse distribution of standard loads could be represented by a normal distribution (Figure 5);
2. The number of standard loads imposed at a distance (x) from the center of the transverse distribution could be calculated from the normal distribution;
3. The full-depth asphalt pavement could be reduced to a two-layer linear elastic system (Figure 6);
4. The horizontal tangential strain at the bottom of the asphalt layer could be regarded as the representative strain in pavement design; and
5. For asphalt, a relation exists between the induced horizontal tangential strain and the number of allowable load repetitions (Figure 7).

Derivation of Shift Factor

For the purpose of this paper, the shift factor (V) for fatigue damage has been defined as the quotient of D_v and D_s . D_v equals the fatigue damage induced at a particular point on the underside of the flexible pavement by a number of trans-

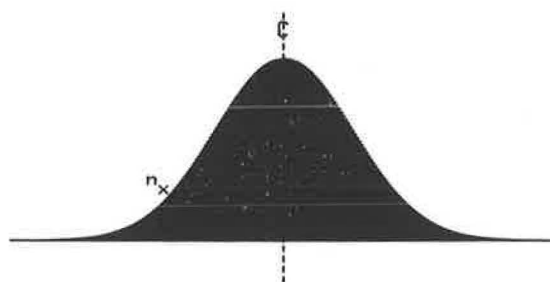


FIGURE 5 Transverse distribution of a given standard load.

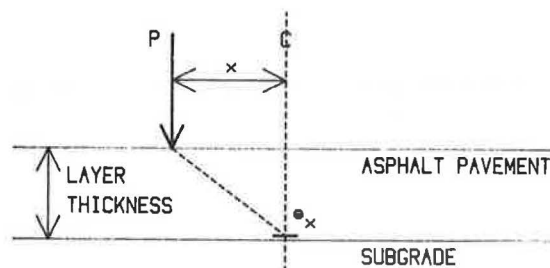


FIGURE 6 Two-layer linear-elastic asphalt pavement

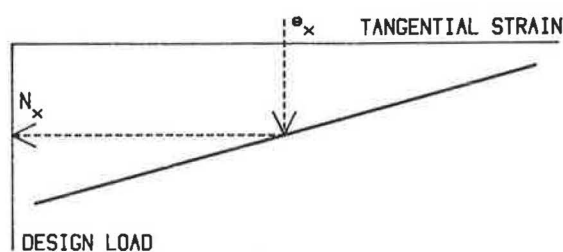


FIGURE 7 Asphaltic concrete fatigue line (15).

versely distributed heavy vehicles passing over the cross section, and D_s is the fatigue damage caused at the same point by the same number of heavy vehicles—now assumed to be traveling in a single path above this point.

In deriving the shift factor, it was assumed that the fatigue-damage mechanism in asphalt can be described by Miner's linear damage law (19). The fatigue damage that is induced by a number of standard loads imposed at a given distance from the center line on the underside of the asphalt layer at the midpoint of the transverse distribution can be determined as follows:

1. Determine the number of standard loads (n_x) imposed at a distance (x) from the center line (Figure 5);
2. Calculate the horizontal tangential strain (e_x) that is induced on the underside of the asphalt layer at the midpoint, by a single standard load (P) imposed at a distance (x) from the center line (Figure 6);
3. Determine the service life (N_x) that is associated with the calculated horizontal tangential strain level (Figure 7);
4. The amount of fatigue damage induced on the underside of the asphalt layer at the center line, by a single standard load (P) imposed at a distance (x) from the center line is $1/N_x$; and
5. For a number of n_x standard loads imposed at the same given point, the amount of fatigue damage induced on the underside of the asphalt layer at the center line will be equivalent to n_x/N_x .

To assess accurately the total amount of fatigue damage induced (D_v), the transverse distribution of standard loads was calculated in 240 positions, each separated by a distance of 0.01 m. Summation of the fatigue damage caused by the number of standard loads at each position resulted in the following expression:

$$D_v = (n_1/N_1) + (n_2/N_2) + \dots + \dots + (n_{240}/N_{240}) \quad (2)$$

To determine the fatigue damage, D_s , the following approach was used. It was assumed that the distributed loading pattern, as referred to above, could be effectively replaced by the same collection of loads now concentrated at the midpoint. One standard load imposed at the center of the transverse distribution, was assumed to induce an amount of fatigue damage given by $1/N_s$. Summing the fatigue damage contribution caused by the loading per position placed in the center resulted in the following expression for the total amount of fatigue damage caused by the concentrated loading:

$$D_s = (n_1/N_s) + (n_2/N_s) + \dots + \dots + (n_{240}/N_s) \quad (3)$$

Including Shift Factor in Design Method

The relation between the traffic load (N_1) and the thickness requirements of an asphalt layer is shown in Figure 8 for a range of shift factors. The data presented in this figure have been calculated on the basis of the information contained in Figure 4 and by using Equation 1. The values of the correction factors applied in Equation 1 were $H = 0.25$ and $F = 6.00$.

In Figure 2, it is shown that each measured distribution has its own lateral spread (S). Once the standard load and trans-

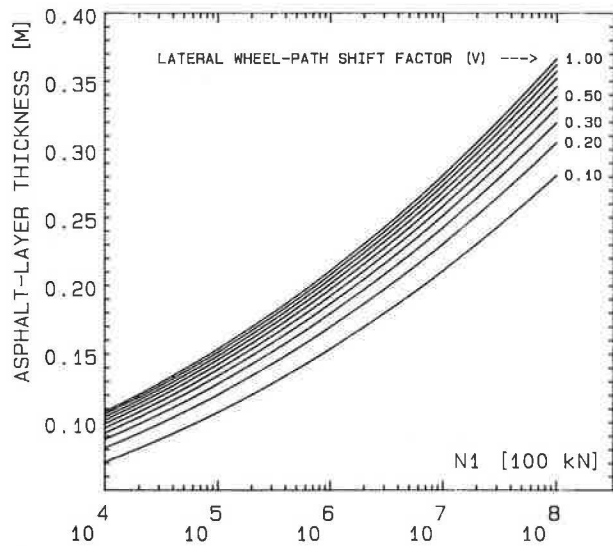


FIGURE 8 Thickness of the asphalt layer as a function of traffic load and shift factor for gravel asphaltic concrete (16) and a subgrade modulus of 100 MPa.

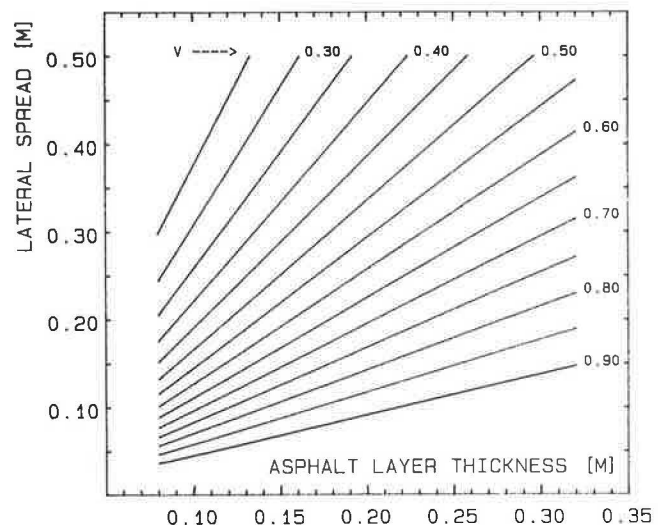


FIGURE 9 Thickness of the asphalt layer as a function of lateral spread and shift factor for gravel asphaltic concrete (16) and a subgrade modulus of 100 MPa.

verse position have been selected and the necessary assumptions have been made regarding the material properties of the asphalt and the subgrade, the induced tangential strain becomes a relatively simple function of the thickness of the asphalt layer (Figure 6). Shift factors (V) can, therefore, be determined for given combinations of lateral spread (S) and asphalt thickness, on the basis of Equations 2 and 3. Buiter and Pronk give more precise details of the background to the calculation procedure (20).

Figure 9 shows typical shift factors (as a function of lateral spread and asphalt thickness) for the gravel asphaltic concrete mixes and subgrade referred to previously. It can be seen that the derived shift factors are variable quantities, even when the lateral spread (and hence traffic-lane width) is constant.

The shift factors increase with the thickness of the asphalt layer, which means that the effect of shifts in the wheel path are correspondingly smaller in thicker asphalt layers.

The method embodied in this approach was applied to the preparation of design charts as outlined below. For a constant traffic load (N_1), the required asphalt thickness was determined for various shift factors (V) using Figure 8. Following this, for each combination of shift factor and asphalt thickness, the associated lateral spread was read off from Figure 9. Finally Figure 10 was constructed, describing the relation between the required asphalt thickness and the associated lateral spread for a given traffic load (N_1). It should be noted that Figures 4, 8, 9, and 10 are strictly valid for the set of material properties associated with the asphalt and subgrade concerned.

COMPARISON OF OLD AND NEW APPROACHES

In the approach described in this paper, the shift factor is dependent on (a) the lateral spread in the transverse distribution of heavy-goods vehicles, (b) the asphalt thickness, and (c) the material properties of the asphalt and the subgrade.

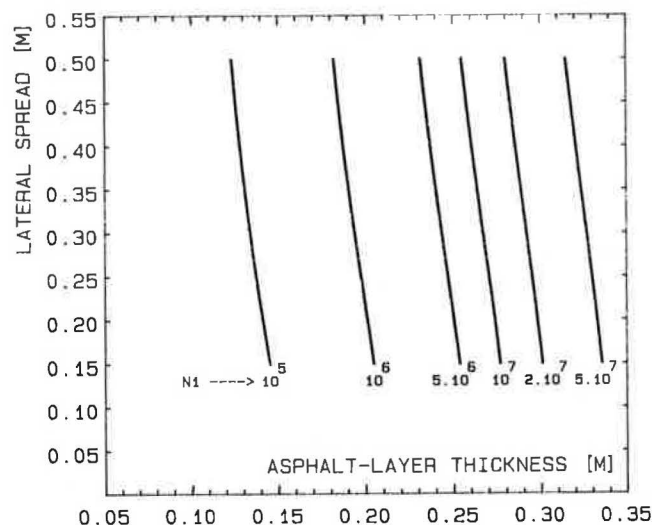


FIGURE 10 Thickness of the asphalt layer as a function of lateral spread and traffic load for gravel asphaltic concrete (16) and a subgrade modulus of 100 MPa.

TABLE 3 SHIFT FACTORS BASED ON NEW APPROACH FOR THREE CLASSES OF LANE WIDTH AND DIFFERENT TRAFFIC LOADS

Lane width [m]			Traffic load (N_1)					
Class	B	S	1.10^5	1.10^6	5.10^6	1.10^7	2.10^7	5.10^7
1	3.00	0.24	0.484	0.621	0.703	0.734	0.763	0.797
2	3.25	0.26	0.451	0.588	0.673	0.705	0.736	0.772
3	3.50	0.29	0.408	0.543	0.630	0.664	0.696	0.736

TABLE 4 THICKNESS REQUIREMENTS BASED ON NEW APPROACH FOR THREE CLASSES OF LANE WIDTH AND DIFFERENT TRAFFIC LOADS

Lane width [m]			Traffic load (N_1)					
Class	B	S	1.10^5	1.10^6	5.10^6	1.10^7	2.10^7	5.10^7
1	3.00	0.24	0.138	0.198	0.247	0.271	0.295	0.330
2	3.25	0.26	0.136	0.196	0.246	0.269	0.294	0.329
3	3.50	0.29	0.134	0.194	0.244	0.267	0.292	0.327

In Table 3, the shift factors based on this approach are given for the three classes of traffic-lane width (Table 2) and for different traffic loads ($N1$). The thickness requirements for asphalt layers of roads with lane widths within the three classes have also been calculated on the basis of the new approach. These thicknesses are presented in Table 4 for different traffic loads ($N1$). It can be seen that, for a given traffic load, only small differences exist in the thickness requirements among the three width categories.

In the Road and Hydraulic Engineering Division design method applied until recently, a constant (and therefore fundamentally incorrect) shift factor was used per traffic-lane width. This approach was based on the Shell method (18) and resulted in a constant shift factor of 0.40 being assumed for a traffic-lane width of 3.50 m. Table 5 gives the shift factors based on the old and new approaches for different traffic loads ($N1$) and for lane-width Class 3 (Table 2). The thickness requirements for asphalt courses determined on the basis of the old approach are shown in Table 6, where they are compared with lane-width Class 3 values taken from Table 4.

As the traffic load ($N1$) and, therefore, the thickness of the asphalt pavement increase, the difference in thickness requirements between the two methods becomes more apparent. It has been shown that, particularly in the case of heavily loaded motorways, the incorrect application of shift factors has led to significant deviations, as compared with the new approach. In the context of a general review, which aimed to bring theory and empirical method closer together, the approach described in this paper is one of the improvements that have been incorporated into the design method used by the Road and Hydraulic Engineering Division (21).

Even though the maximum difference of 22 mm (Table 6) is small when compared to the precision associated with other design parameters (for example, the standard deviation of the asphalt layer thickness is frequently greater than 10 to 15 mm), the research reported in this paper has produced valuable information that also can be used in a more probabilistic approach to road design.

CONCLUSIONS AND RECOMMENDATIONS

The variable shift factor presented in this paper is dependent on the wheel-path shift pattern, the asphalt concrete thickness and the material properties of the asphalt concrete and the subgrade. Assessing the effects of lateral shifts in the wheel path by using a constant shift factor for a given width of traffic lane is, therefore, fundamentally incorrect.

Use of a constant shift factor of 0.40 for lane widths of 3.50 m can lead to considerable differences in the asphalt thickness requirements, when compared with the described method based on variable shift factors. In the case of motorways that are subject to heavy traffic loads, a first-order thickness difference is predicted, which is equivalent to incorrectly estimating the traffic load by a factor of 2.

It is recommended that design methods, based on a constant shift factor per traffic-lane width, should be changed and that consideration should be given to the new techniques that have been developed. These are felt to provide a better insight into the significance of such effects on the different types of construction.

TABLE 5 COMPARISON OF SHIFT FACTOR BASED ON NEW AND OLD APPROACHES FOR DIFFERENT TRAFFIC LOADS AND LANE WIDTH CLASS 3

Traffic load	1.10^5	1.10^6	5.10^6	1.10^7	2.10^7	5.10^7
New approach	0.408	0.543	0.630	0.664	0.696	0.736
Old approach	0.400	0.400	0.400	0.400	0.400	0.400

TABLE 6 COMPARISON OF THICKNESS REQUIREMENTS BASED ON NEW AND OLD APPROACHES FOR DIFFERENT TRAFFIC LOADS AND LANE WIDTH CLASS 3

Traffic load	1.10^5	1.10^6	5.10^6	1.10^7	2.10^7	5.10^7
New approach	0.134	0.194	0.244	0.267	0.292	0.327
Old approach	0.134	0.187	0.230	0.251	0.273	0.305
Difference	0.000	0.007	0.014	0.016	0.019	0.022

ACKNOWLEDGMENTS

This research project was conducted at the Road Engineering Branch, Road and Hydraulic Engineering Division. Appreciation is extended to all those who have in any way contributed to this project. More particularly, the authors want to thank J. H. Geerts, E. Vos, P. Hopman, and A. C. Pronk.

REFERENCES

1. J. T. Pauls. Transverse Distribution of Motor Vehicle Traffic on Paved Highways. *Public Roads*, Vol. 6, No. 1, 1925, pp. 1–13.
2. A. Taragin. Effect of Roadway Width on Vehicle Operation. *Public Roads*, Vol. 24, No. 6, 1945, pp. 143–160.
3. A. Taragin. Driver Behavior Related to Types and Widths of Shoulders on Two-Lane Highways. *Public Roads*, Vol. 29, No. 9, 1957, pp. 197–205.
4. A. Taragin. Lateral Placements of Trucks on Two-Lane Highways and Four-Lane Divided Highways. *Public Roads*, Vol. 30, No. 3, 1958, pp. 71–75.
5. I. Scazziga. Effects of the Transverse Distribution of Heavy Loads on the Design of Flexible Pavements. Question II, Flexible Pavements, Switzerland. Presented at 15th PIARC World Road Congress, Mexico, 1975.
6. W. Leutzbach, W. Maier, and M. Döhler. Untersuchung des Spurverhaltens von Kraftfahrzeugen auf Landstrassen durch Vervollgungsfahrten. *Strasse und Autobahn*, Vol. 8, 1981, pp. 301–304.
7. E. McSweeney. Wheelpath Distribution and Pavement Design. Intern Rapport 908, Vegdirektoratet Veglaboratoriet, Oslo, Norway, 1979.
8. J. H. Mathewson, R. Brenner, and R. J. Reiss. A Segmented Electrical Element for Detecting Vehicular Traffic. *HRB Proc.*, HRB, National Research Council, Washington, D.C., 1949, pp. 374–383.
9. A. De Henau. Verkeersanalyse in het kader van wegverhardingen. *De Wegentechniek*, Vol. 12, No. 4, 1967, pp. 35–54.
10. I. Scazziga. Erhebungen über die Beanspruchung der Strassen durch schwere Motorwagen. Mitteilung No. 32. Institut für Strassen-, Eisenbahn- und Felsbau, Technische Hochschule, Zürich, 1976.
11. A. Kasahare. Wheel Path Distribution of Vehicles on Highways. *Proc., 1st International Symposium on Bearing Capacity of Roads and Airfields*, Trondheim, Norway, 1982, pp. 413–420.
12. K. Himeno, T. Watanabe, and T. Maruyama. Estimation of Fatigue Life of Asphalt Pavement. *Proc., 6th International Conference on the Structural Design of Asphalt Pavements*, Vol. 1, University of Michigan, Ann Arbor, 1987, pp. 272–289.
13. P. C. Hopman. Asphalt Fatigue Research: How and Why. *Wegen*, Vol. 61, No. 7/8, 1987, pp. 265–268 (in Dutch).
14. J. H. Swart and A. E. van Dommelen. Design of Asphaltic Concrete Pavements of Motorways. *Wegen*, Vol. 62, No. 1, 1988, pp. 20–26 (in Dutch).
15. F. Geysendorpher and P. C. Hopman. Fatigue Properties and Dynamic Stiffness Moduli of Gravel Asphaltic Concrete "Eisen 1978." *Wegen*, Vol. 61, No. 10, 1987, pp. 346–351 (in Dutch).
16. Department of Public Works. "Eisen 1978": Requirements for Building Materials in Road Construction. Staatsuitgeverij, The Hague, 1978 (in Dutch).
17. D. L. de Jong, M. G. F. Peutz, and A. R. Korswagen. Computer Program BISAR—Layered Systems Under Normal and Tangential Surface Loads. Koninklijke/Shell-Laboratorium, Amsterdam, External Report AMSR.006.73, 1973.
18. A. I. M. Claessen, J. M. Edwards, P. Sommer, and P. Ugé. Asphalt Pavement Design—The Shell Method. *Proc., 4th International Conference on the Structural Design of Asphalt Pavements*, Vol. 1, University of Michigan, Ann Arbor, 1977, pp. 39–72.
19. M. A. Miner. Cumulative Damage in Fatigue. *Journal of Applied Mechanics*, Vol. 12, No. 3, 1945, pp. 159–164.
20. R. Buiter and A. C. Pronk. Mechanical Aspects of the Transverse Distribution of Heavy-Loads Vehicles. Report WOX-N-87-31. Road and Hydraulic Engineering Division, Ministry of Transport and Public Works, Delft, Netherlands, 1987 (in Dutch).
21. *Road Engineering Manual—Pavement Design*. Road and Hydraulic Engineering Division, Ministry of Transport and Public Works, Delft, Netherlands, Nov. 1987 (in Dutch).

Publication of this paper sponsored by Committee on Flexible Pavement Design.

Fatigue Life and Permanent Deformation Characteristics of Asphalt Concrete Mixes

GILBERT BALADI

New laboratory and field relationships between asphalt mix variables and their fatigue life and permanent deformation characteristics are presented and discussed. It is shown that the laboratory fatigue life and plastic deformation of laboratory specimens can be predicted from a knowledge of several parameters pertaining to the compacted asphalt mix, magnitude of the applied load, and test temperature. Predictions of the fatigue life and rut depth of asphalt pavements require, in addition to the above parameters, the compressive and tensile strains of the asphalt course, as well as the moduli of the different pavement layers. During the course of the laboratory investigation, a new indirect tensile test apparatus was designed, fabricated, and used to conduct cyclic load indirect tensile tests using Marshall-type specimens and various asphalt concrete mixes. The test results indicate that the indirect tensile test can be used to characterize the fatigue life of asphalt concrete mixes.

The design of flexible pavements has rapidly evolved from empirical and semi-empirical procedures to design methods based on elastic and/or viscoelastic theories (1-7). Today, many highway agencies use such methods in one form or another to design new, reconstructed, and/or overlaid asphalt pavements. This use requires a thorough knowledge of the basic structural properties (resilient characteristics, fatigue life, and plastic deformation) of the asphalt layer that are functions of the asphalt mix variables and the properties of the various layers in the pavements (8-13).

Several tests and test equipment have been developed and used in laboratories to evaluate the structural properties of asphalt mixes (14-27). It was found that (regardless of the complexity of the tests, test procedures, and test equipment) different tests yield different results and that the test results are difficult to reproduce (12). Further, existing asphalt concrete mix design procedures are based on parameters that do not necessarily have any relationship to the structural design of asphalt pavements and their fatigue lives (15,12).

EXPERIMENTAL PROGRAM

Recognizing the need to tailor the asphalt mix design procedures to the optimum structural properties of the mix and to be able to obtain these parameters from simple tests, a research project sponsored by FHWA was undertaken at the Department of Civil and Environmental Engineering at Mich-

igan State University (MSU). The objectives of the program included the following:

1. The selection of a simple test and test procedure that would allow the highway engineer to determine the fundamental engineering properties required for the structural design of asphalt pavements.
2. A study of the repeatability of the test results and the number of tests required to reliably obtain the structural properties of the asphalt materials.

Several laboratory tests and test procedures were used, including triaxial (constant and variable cyclic loads), cyclic flexural tests, Marshall tests, indirect tensile tests (constant and variable cyclic loads), and creep tests. The initial test results indicate the following:

1. The repeatability of test results is poor.
2. The material properties obtained from the different tests are substantially different.
3. The results from the indirect tensile test are the most promising, although they are not consistent.

The last observation was made after examining the results of 24 tests (12 tests at a cyclic load of 500 lb and 12 tests at 100 lb) that were conducted, in triplicate, using existing (Schmidt) apparatus. It was found that the inconsistency of the test results was related to equipment problems rather than to the test mode (28-31). In recognition of these problems, a new indirect tensile test apparatus was designed at MSU and fabricated by the Michigan Department of Transportation (MDOT). The new apparatus was capable of measuring the specimen deformation in three directions (30-31). Further, test results obtained using the new apparatus were very consistent and reproducible (27-31). It was found that the maximum difference in the test results for any triplicate was 7 percent. Nevertheless, the new apparatus was used to characterize the structural properties and fatigue lives of various asphalt mixes.

LABORATORY TESTS

Three tests were conducted using the new indirect tensile test apparatus: indirect tensile tests, indirect constant peak cyclic load tests, and indirect variable peak cyclic load tests.

The indirect tensile tests (INTT) used a standard Marshall

loading frame and deformation rate. In this test mode, some of the test specimens were conditioned as standard Marshall specimens. Other specimens were dry-conditioned and tested at 60, 25, and 5°C (140, 77, and 40°F).

The *indirect constant peak cyclic load* (INCCL) tests used an MTS hydraulic system. In this test, the specimens were subjected to a constant, sustained load followed by a constant peak cyclic load of 500 lb (i.e., stress-controlled tests) applied at a frequency of two cycles per second with a loading time of 0.1 sec and a relaxation period of 0.4 sec. Some of the test specimens were subjected to a maximum of 500,000 cycles. Measurements of the elastic, total, and plastic (permanent) deformations were collected along the vertical and horizontal diameters, and along the thickness of the specimen. The data were then analyzed to obtain the resilient and plastic characteristics of the specimens and their fatigue lives.

Indirect variable peak cyclic load (INVCL) tests used an MTS hydraulic system in the stress-controlled mode. Basically, the test procedure was the same as that of the INCCL except that, after the application of the sustained load, the specimen was subjected to 100-, 200-, and 500-lb peak cyclic loads, with each load being applied for only 1,000 cycles. It should be noted that a magnitude of the cyclic load of 500 lb implies that the cyclic stresses at the center of the specimen were 239 psi in compression and 80 psi in tension; for 200 lb, cyclic stresses were 96 and 32 psi; and for 100 lb, stresses were 47.8 and 16 psi. Also, for all three magnitudes (100, 200, and 500 lb), the shear stresses at the center of the specimen were zero.

One hundred and fifty specimens were tested in the INTT, 75 in the INCCL, and 75 in the INVCL methods. A complete tabulation of the test results has been given by Baladi (31).

It should be noted that for the remainder of this paper, the term *sample* is used to describe a cylindrical sample (8.5 in. high and 4 in. in diameter) that was prepared at a certain density and percent air voids. After preparation, each cylindrical sample was sawed into three (triplicate) test specimens (each 2.5 in. high and 4 in. in diameter).

TEST SPECIMENS

One hundred and twenty-five samples (375 specimens) were made and tested using the new indirect tensile test apparatus (75 for each of the INCCL and INVCL tests, and 150 for the INTT). The samples were made using the following materials:

1. Three types of aggregate (crushed and angular limestone, relatively rounded river-deposited natural aggregate, and a mix of 50 percent by weight per sieve of the crushed limestones and natural aggregates),
2. Fly ash mineral filler,
3. Two aggregate gradations (see Figure 1), and
4. Three viscosity-graded asphalt cements (AC-10, AC-5, and AC-2.5).

For each material combination, a constant percent asphalt content was used (the percent asphalt content at 3 percent air voids as determined from the standard Marshall mix design). The test samples were compacted near three values of the percent air void (3, 5, and 7) by varying the foot pressure and the number of tappings of a kneading compactor. For each material combination and percent air void, a cylindrical sample 10.16 cm in diameter and 22 cm high (4 in. by 8.5 in.)

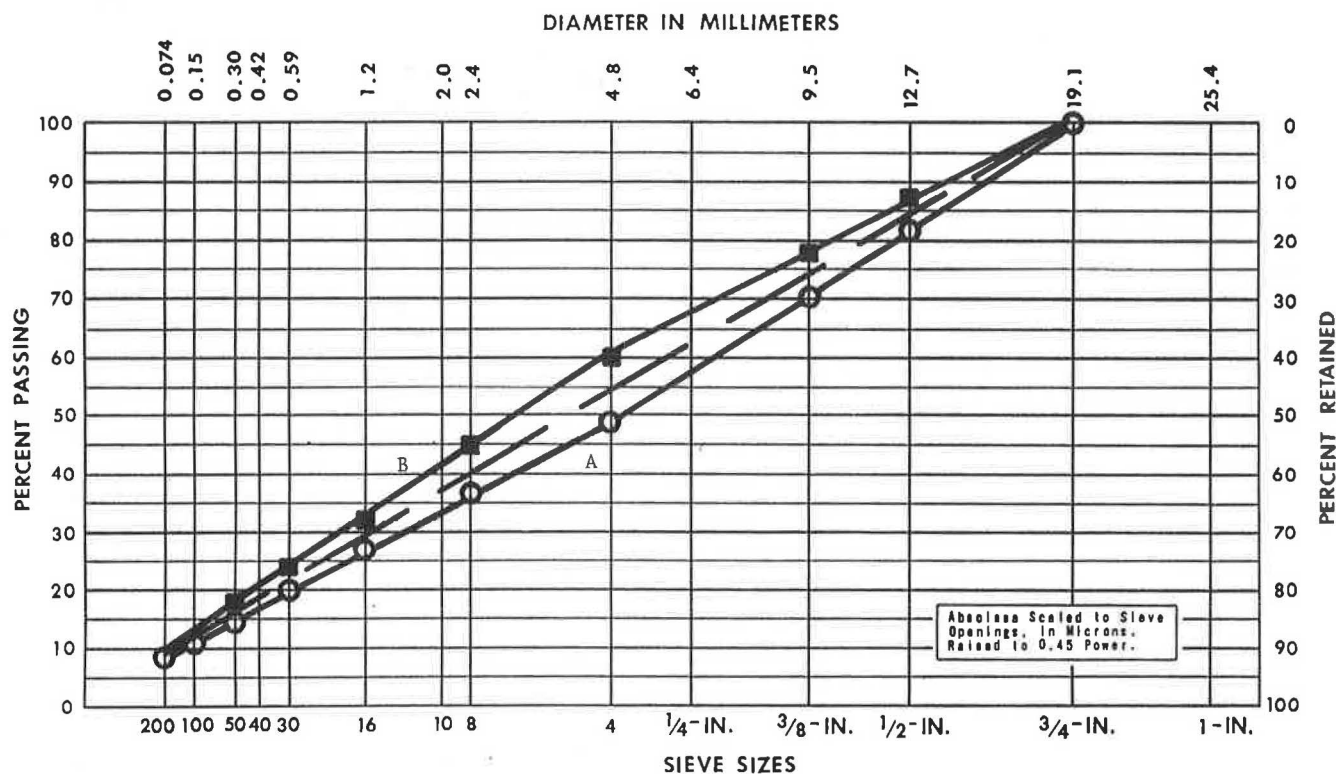


FIGURE 1 Gradations A and B of the aggregates and the straight-line gradation.

was made. Later, the sample was sawed into three 6.3 cm high (2.5 in.) Marshall-size specimens. The three specimens (a triplicate) were then tested under the same conditions (test temperature, cyclic load, and test type) using the new indirect tensile test apparatus.

TEST RESULTS AND ANALYSIS

Indirect Tensile Tests

As noted previously, 150 Marshall-type specimens were tested to failure using the new indirect tensile test apparatus and the standard Marshall loading frame and deformation rate. During the tests, the applied load and the total deformations along the vertical and horizontal diameters, and along the thickness of the specimen, were measured. The maximum values of the applied load at failure (P) were used to obtain the compressive and tensile strengths of the specimens (24–26). The measured values of the deformation at failure (DH) along the horizontal diameter represented the maximum tensile deformation to which the specimen could be subjected to prior to failure. Figure 2 depicts typical plots of the horizontal deformation at failure versus the percent air voids of the INTT specimens tested at 77°F. For all tests at 40, 77, and 140°F, these values were analyzed and statistically correlated to the specimen, mix, and test variables. The following equation was obtained:

$$\ln(DH) = 5.887 + (0.06931)(AV) + (0.0003901)(KV) + (0.03382)(ANG) \\ R^2 = 0.925, SE = 0.003 \quad (1)$$

where

\ln = natural logarithmic operator,
 AV = percent air voids ($AV = 3$ to 7),
 KV = kinematic viscosity at 275°F (AASHTO T-201) (centistokes),
 ANG = aggregate angularity,
 R^2 = coefficient of correlation, and
 SE = standard error.

Figure 3 shows the measured and calculated DH values using Equation 1. The line of equality between measured and calculated values is also shown in the figure. It should be noted that the maximum percent difference between the arithmetic values of the calculated (using Equation 1) and measured data is 37. The majority of the estimated values, however, are within 7 percent. The significance of this equation is discussed later. Two important aspects can be deduced from Equation 1:

1. The total horizontal deformation at failure of a Marshall-type specimen is a function of AV , KV , and ANG . Increasing AV from 3 to 7 percent results in an increase in DH by a factor of 1.49. Increasing KV from 159 to 270 centistokes yields an increase in DH by a factor of 1.04. Finally, using angular aggregate causes an increase in the value of DH by a factor of 1.07 relative to rounded aggregates.

2. The total deformations at failure are independent of the test temperature. However, the magnitude of the applied loads at failure for the higher temperature specimens was much lower than that at the lower temperatures.

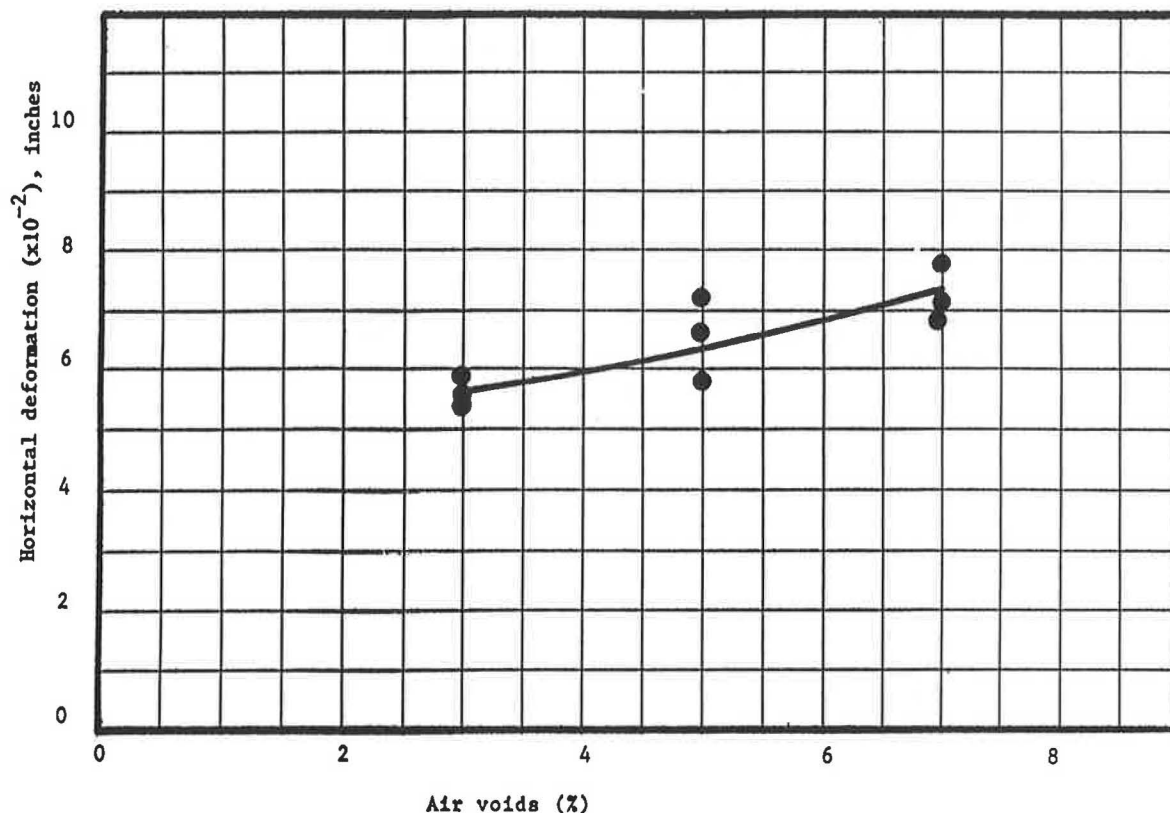


FIGURE 2 Typical plots of the horizontal deformation of INTT specimens versus the percent air voids in the compacted asphalt mix.

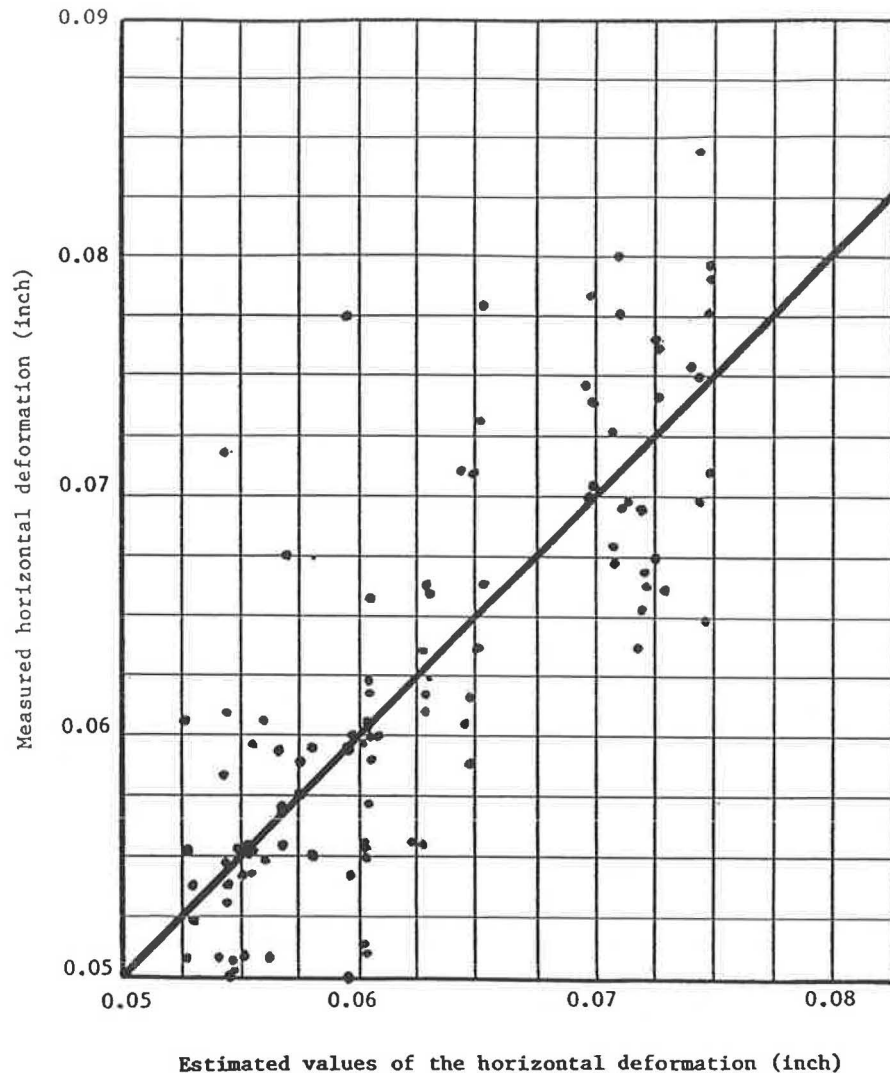


FIGURE 3 Measured and estimated values of the horizontal deformation at failure for the INTT specimens.

Indirect Constant and Variable Cyclic Load Tests

Seventy-five Marshall-type specimens were tested to failure in each of the INCCCL and INVCL tests using the new indirect tensile test apparatus. During the tests, the applied sustained and cyclic loads; the number of load applications; and the elastic, total, and plastic deformations (CD,s) along the horizontal diameter (CD1), the vertical diameter (CD2), and the thickness of the specimens (CD3) were measured. The test results are reported in Baladi (31). Typical plots of CD2 and CD1, versus the number of load applications for three values of the percent air voids of the INCCCL test specimens that were tested at 77°F, are shown in Figures 4 and 5, respectively. It should be noted that each data point in these figures represents a triplicate.

The cumulative plastic deformations (CD2 and CD1) measured (respectively) along the horizontal and vertical diameters of both the INCCCL and INVCL test specimens were

analyzed and statistically correlated to the mix, specimen, and test variables. The objective of the analysis was twofold:

1. Study the tensile plastic deformations (CD2) along the horizontal diameter and determine their relationships to the fatigue lives of the test specimens.
2. Study the compressive plastic deformations (CD1) along the vertical diameter and determine their relationships to the rut depth of actual pavements.

Nevertheless, Equations 2 and 3 are the resulting statistical equations.

$$\begin{aligned} \ln(\text{CD2}) = & -12.789 + (0.07034)(\text{TT}) \\ & + (0.5018)[\ln(N)] + (1.154)[\ln(\text{CL})] \\ & + (0.3215)(\text{AV}) + (0.001026)(\text{KV}) \end{aligned}$$

$$R^2 = 0.967, \text{ SE} = 0.299 \quad (2)$$

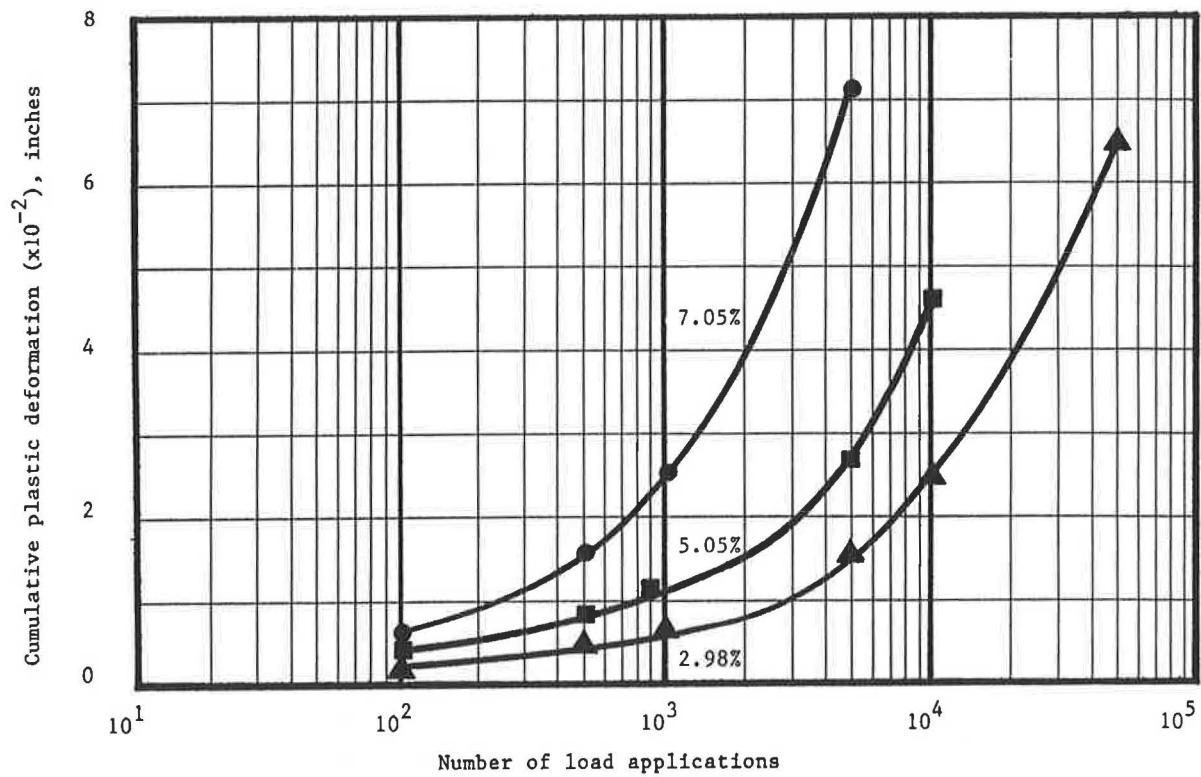


FIGURE 4 Typical plots of the horizontal cumulative plastic deformations of the INCCL test specimens versus the number of load applications for three values of the percent air voids.

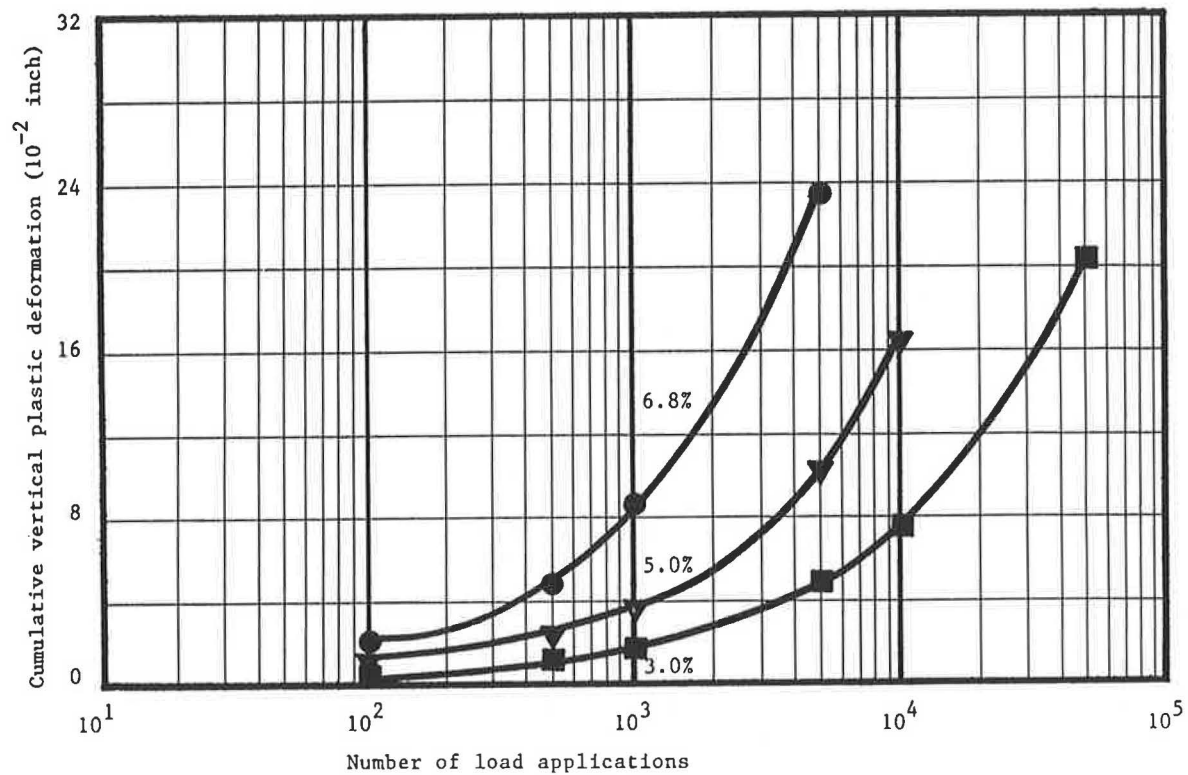


FIGURE 5 Typical plots of the vertical cumulative plastic deformations of the INCCL test specimens versus the number of load applications for three values of the percent air voids.

$$\begin{aligned}\ln(\text{CD1}) = & -11.615 + (0.07028)(\text{TT}) \\ & + (0.5000)[\ln(N)] + (1.148)[\ln(\text{CL})] \\ & + (0.3326)(\text{AV}) - (0.001007)(\text{KV})\end{aligned}$$

$$R^2 = 0.96, \text{SE} = 0.36 \quad (3)$$

where

CD2 = plastic deformation along the horizontal diameter (inch $\times 10^{-4}$),
 CD1 = plastic deformation along the vertical diameter (inch $\times 10^{-4}$),
 TT = test temperature ($^{\circ}\text{F}$),
 N = number of load applications, and
 CL = cyclic load (lb).

It should be noted that the independent variables in Equations 2 and 3 are listed in the order of their significance (e.g., TT is the most significant variable, while KV is the least significant). A sensitivity analysis of the arithmetic (not logarithmic) values of CD2 and CD1 to the range of the independent variables was made, and the results are reported by Baladi (31). For completion, a summary of this analysis is presented below.

Increasing TT from 40 to 77 $^{\circ}\text{F}$ increases the values of CD2 and CD1 by a factor of about 13.5. Higher number of load applications yield higher values of CD2 and CD1. Increasing the magnitude of the cyclic load from 100 to 500 lb increases the values of CD2 and CD1 by a factor of about 6.4 (i.e., nonlinear material). Increasing AV from 3 to 7 percent causes both CD2 and CD1 to increase by a factor of about 3.8. Increasing KV from 159 to 270 centistokes decreases the values of CD2 and CD1 by a factor of about 1.12. Finally, aggregate angularity has an insignificant effect on the values of CD2 and CD1.

FATIGUE LIFE

Fatigue life data for asphalt mixes have been accumulated in large quantities since the early 1950s. Traditionally, these data are plotted as stress or strain amplitude versus the resulting life, commonly known as *S-N curves*. For asphalt mixes, as for most other materials, fatigue life increases steadily with decreasing stress or strain amplitude until the stress or strain level of the fatigue limit is reached; below which, the life apparently becomes infinitely long. In general, stresses at or below the fatigue limit cause only elastic strains. It should be emphasized that cyclic plastic strains are ultimately responsible for fatigue damage and the consequent fatigue failure. A perfectly elastic material will never experience fatigue damage regardless of the number of load applications.

Because asphalt mixes are weaker in tension than in compression, it was thought that measuring the plastic deformation along the horizontal diameter of the Marshall-type specimens subjected to cyclic loads may yield a measure of the fatigue life of the specimens. In doing so, a problem was encountered: a proper definition of the fatigue life of the test specimen. Currently, no standard definition of fatigue life of asphalt mixes is universally adopted although, several definitions are used by different investigators (21–23). Thus, a new definition was introduced prior to the analysis.

For the purpose of this study, the fatigue life of the INCCCL

test specimens is defined as follows: "Fatigue lives of the INCCCL and INVCL test specimens are defined herein by the number of load applications at which the cumulative horizontal plastic deformation (CD2) along the horizontal diameter reaches a value equal to 95 percent of the total horizontal deformation failure (*DH*) of a compatible specimen tested to failure using the INTT mode."

It should be noted that this definition was established after visually examining the conditions of the INCCCL and INVCL test specimens during and after each test. It was noted that a hair crack (along the vertical diameter) was initiated in the specimen (and failure occurred shortly after) when the value of CD2 reached a value equal to about 95 percent of the total horizontal deformation at failure of a compatible specimen tested using the INTT mode.

Using the above definition of fatigue life, the arithmetic version of the right-hand side of Equation 1 was multiplied by 0.95 and the results were substituted for CD2 in Equation 2. After arranging terms and substituting *N* with *N_{FL}* (the number of load applications at fatigue life), the following equation was obtained.

$$\begin{aligned}\ln(N_{\text{FL}}) = & 36.631 - (0.1402)(\text{TT}) \\ & - (2.300)[\ln(\text{CL})] - (0.5095)(\text{AV}) \\ & - (0.001306)(\text{KV}) + (0.06403)(\text{ANG})\end{aligned} \quad (4)$$

Sensitivity analysis of Equation 4 yielded the following points:

1. The fatigue life of indirect tensile test specimens increases as the temperature decreases. Decreasing temperatures from 77 to 40 $^{\circ}\text{F}$ increases the fatigue life by a factor of 179. This does not necessarily mean that higher temperatures cause more cracks. It simply means that, at lower temperatures (stiffer asphalt), the magnitude of the plastic deformation per one load application is lower than that at the higher temperatures. Lower plastic deformations result in a higher number of load applications to fatigue failure. It should be noted that lower temperatures cause shrinkage cracks in flexible pavements that are not load related. Temperature cracks were not investigated in this study.
2. Increasing the magnitude of the cyclic load from 100 to 500 lb causes a decrease in the fatigue life by a factor of about 40.
3. The fatigue life decreases as the percent air voids in the mix increases. Increasing AV from 3 to 4 percent yields a decrease in *N_{FL}* by a factor of 7.7.
4. Decreasing KV from 270 to 159 centistokes increases fatigue life by a factor of about 1.16; that is, harder asphalts cause lower fatigue life.
5. Angular aggregate increases fatigue life by a factor of 1.14, relative to rounded aggregate.
6. For the limited range of the aggregate gradation used in this study, gradation has no significant effect on the fatigue life.

In a qualitative sense, the above observations (except Item 4) are compatible to those found in the literature for the controlled-stress tests. Quantitatively, the magnitude of the effects of the test and specimen variables on the fatigue life is different. In addition, the fatigue lives of the indirect tensile

test specimens were found to be much shorter than those obtained from flexural beam tests (see Figure 6). This difference could be attributed to the stress distribution within the test specimens, specimen configuration, and the boundary conditions of both tests.

Equation 4 was used to calculate the fatigue lives of various INCCL specimens for several combinations of the specimen and test variables. Figure 7 depicts the fatigue curves at 77°F for three values of the percent air voids and three values of the kinematic viscosity. Similar plots at 40°F can be obtained.

The applicability of Equation 4, or any fatigue equation, to field conditions must be examined. Recall that fatigue life is affected by the stress distribution in the materials as well as the environmental conditions. Field conditions cannot be duplicated exactly in the laboratory. Hence, any prediction of pavement fatigue life based on laboratory test results is problematic. Equation 4, on the other hand, can be used to assess the effects of different materials, specimen variables, and temperatures on fatigue life. Equation 4 is not recommended, however, to be used in predicting fatigue life of in-service pavements without a proper calibration using field data. A limited field calibration is presented below.

Field Observations

Limited field observations of in-service flexible pavements in Michigan have indicated that the actual fatigue lives of the pavements were about 20 times higher than those estimated using Equation 4. Incorporating this factor into the equation, arranging terms, and designating the fatigue life of an in-service pavement by (FL) yields:

$$\begin{aligned} \ln(FL) = & 42.63 - (0.1402)(TT) \\ & - (2.3)[\ln(CL)] - (0.5095)(AV) \\ & - (0.001306)(KV) + (0.06403)(ANG) \end{aligned} \quad (5)$$

It should be noted that Equation 5 is based on a limited number of field observations (10 pavement sections). Consequently, the accuracy of the equation should be checked as more field data become available. Further, because fatigue life of an asphalt pavement is a function of not only the properties of the AC surface but also those of the underlying materials, and because Equation 5 does not account for the properties of the various layers, it is difficult, physically, to support the results of Equation 5. This problem, however, was solved using a recent development at MSU and the MDOT.

MICH-PAVE

Recently, a nonlinear finite element computer program, MICH-PAVE, for designing flexible pavements was developed at MSU for the MDOT. The program is capable of calculating stresses and strains and the surface deflection developed in the pavement section due to a wheel load. Using the output of the MICH-PAVE program for existing 10 pavement sections (see Table 1) with known fatigue life and cross sections, Equation 5 was recalibrated. In the calibration process, the following information was used:

1. The actual fatigue lives of 10 pavement sections located in Indiana and Michigan.
2. The strains (calculated using the MICH-PAVE pro-

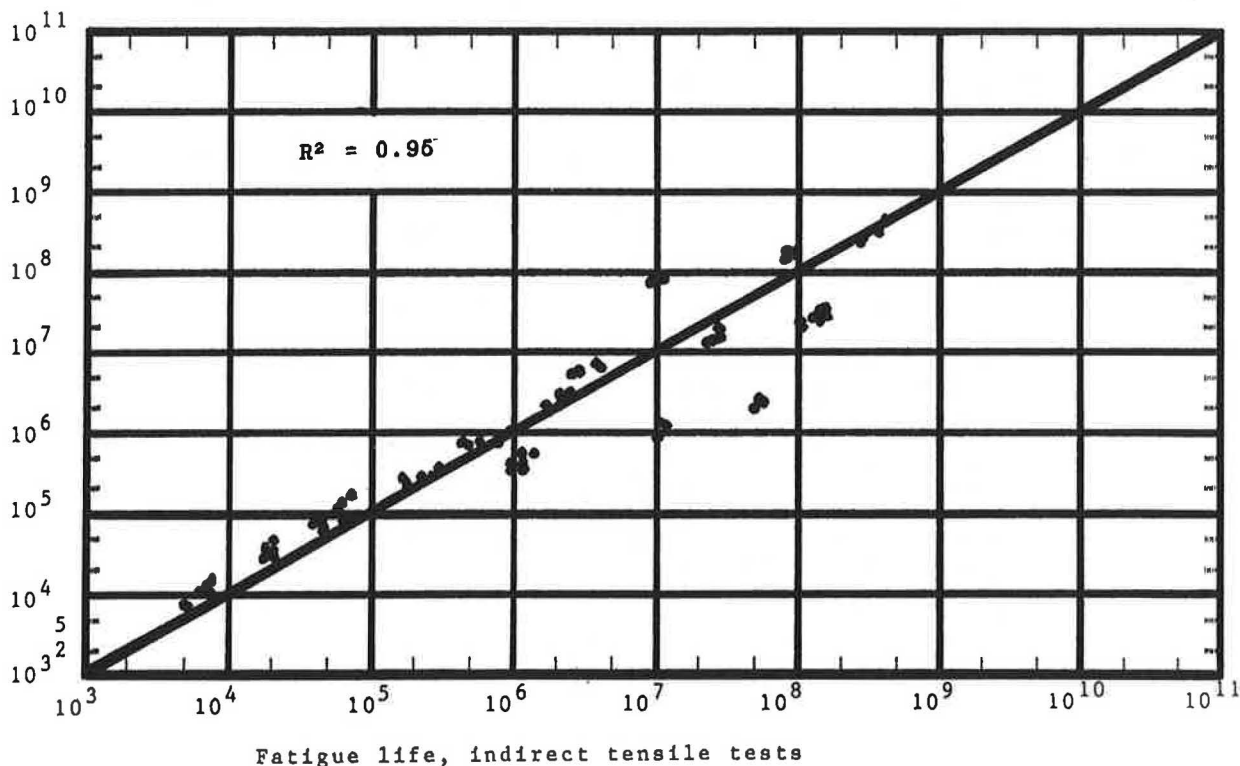


FIGURE 6 Fatigue lives of the INCCL test specimens versus those of flexural beam test specimens.

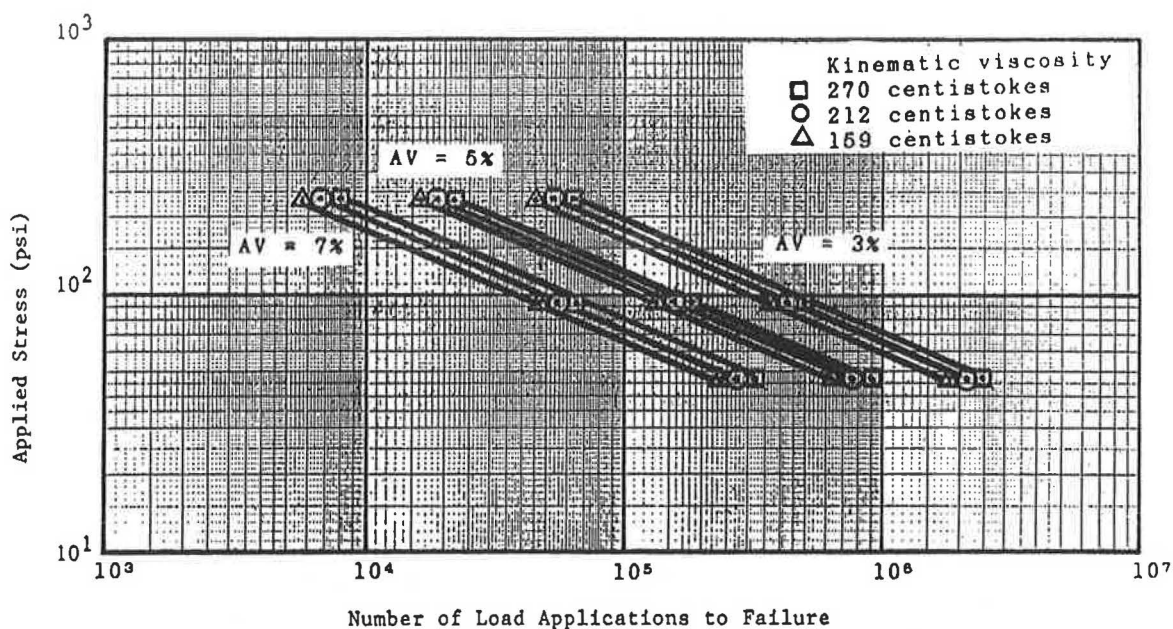


FIGURE 7 Fatigue curves of the INCCL test specimens.

TABLE 1 FATIGUE LIVES AND RUT DEPTHS OF 10 IN-SERVICE PAVEMENT SECTIONS

Site	AC	Base	Subbase	Roadbed	Fatigue life (10 ⁶ ESAL)			Rut depth (in)	
	TAC/MR in/ksi	TB/MR in/ksi	TSB/MR in/ksi	MR ksi	FL(1)	FL(2)	AASHTO	RD(1)	RD(2)
IN1	4.0/500	12/60	6/12	6	1.9000	2.20000	0.7500	0.3	.123
IN1	5.0/500	12/60	6/12	6	5.5000	5.30000	1.7500	0.2	.101
IN1	6.0/500	12/60	6/12	6	9.7000	11.50000	3.7000	-	.087
IN2	3.0/150	12/25	-	4	0.0090	0.00425	0.0135	0.2	.303
IN3	3.0/150	6/30	-	6	0.0122	0.00206	0.0052	-	.347
IN4	3.0/150	10/25	-	4	0.0040	0.00226	0.0070	-	.316
MIU1	4.0/150	10/20	36/9	3	0.0820	0.06659	0.6200	<0.1	.047
MIU2	2.5/150	20/20	10/9	3	0.0410	0.02689	0.2800	<0.1	.086
MIU3	6.0/350	16/20	13/9	3	0.5000	0.53555	1.0000	0.5-1	.029
MIU4	4.5/350	12/20	70/9	3	5.4750	4.96000	45.0000	<0.1	-

IN1 = a pavement which was overlaid twice, each overlay consist of one inch thick AC;

AC = asphalt concrete;

TAC = thickness of the asphalt concrete course (inch);

TB = thickness of the base layer (inch);

TSB = thickness of the subbase (inch)

MR = resilient modulus of the designated layer (ksi); MRb : resilient modulus of the base layer (ksi); MRsb : resilient modulus of the subbase layer (ksi);

FL(1) = actual fatigue life of the pavement section (ESAL);

FL(2) = fatigue life calculated using equation 6 (ESAL);

AASHTO = fatigue life calculated using the 1986 AASHTO guide (ESAL);

RD(1) = measured rut depth (inch); and

RD(2) = rut depth calculated using equation 7 (inch).

Note: for all pavement sections located in Indiana (IN1 through IN4) an average annual air temperature of 75 °F was used, for Michigan sections (MIU1 through MIU4), 66°F was used.

gram) developed at the bottom fiber of the asphalt course due to an 18-kip axle load with 100 psi tire pressure.

3. The peak surface deflection (deflection under the center of the load) of the pavements, which was calculated using the MICH-PAVE program.

4. The thicknesses and properties of the various pavement layers.

5. Equation 5 with an average temperature of 66°F (TT in the equation), the actual (as-designed) air voids of the AC surface, the actual kinematic viscosity of the original AC binder, and 200 pounds (CL term in the equation) that correspond to a tire pressure of 100 psi.

The calibration process yielded the following fatigue life equation.

$$\begin{aligned} \log(\text{ESAL}) = & -2.544 + (0.154)(\text{TAC}) \\ & + (0.0694)(\text{TB}_{\text{EO}}) \\ & - (2.799)[\log(\text{SD})] \\ & - (0.261)(\text{AV}) \\ & + (0.917)[\log(\text{MR}_{\text{B}})] \\ & + (0.0000269)(\text{MR}_{\text{RB}}) \\ & - (1.0964)[\log(\text{TS})] \\ & + (1.173)[\log(\text{CS})] \\ & - (0.001)(\text{KV}) + (0.064)(\text{ANG}) \end{aligned} \quad (6)$$

where

log = base 10 logarithmic operator,

ESAL = number of 18-kip equivalent single-axle loads (ESALs) to fatigue life,

TAC = thickness of AC course (in.),

TB_{EO} = equivalent thickness of base material (in.), which is the actual thickness of the base layer plus the equivalent thickness of the subbase layer; equivalent thickness of the subbase layer is equal to the actual thickness of the subbase layer reduced by the ratio of the modulus of the subbase to that of the base material,

SD = surface deflection (in.),

MR_{B} = resilient modulus of the base material (psi),

MR_{RB} = the resilient modulus of the roadbed soil (psi),

TS = tensile strain at the bottom of the AC fiber,

CS = compressive strain at the bottom of the AC layer, and

ANG = aggregate angularity (4 for 100 percent crushed material, 2 for rounded river-deposited material, and 3 for a 50-percent mix of crushed and rounded aggregate).

Equation 6 seems to be very accurate, and it reasonably predicts the actual fatigue lives of the 10 pavement sections. In comparison, the 1986 AASHTO equation predicted the fatigue lives of the same sections to within a factor of 10. Nevertheless, the actual fatigue lives of the 10 pavement sections and their calculated fatigue lives using Equation 6 and the 1986 AASHTO design guide are listed in Table 1. It should be noted that, relative to Equation 6, the pavement surface

deflection and the tensile and compressive strains at the bottom fiber of the asphalt course are functions of the properties of all layers in the pavement section as well as the applied load, hence, these terms are not independent variables.

In addition, a comparison between Equation 6 and the 1986 AASHTO equation was made using 30 arbitrarily selected pavement sections with various layer thicknesses and material properties (see Table 2). First, all the sections were analyzed using the MICH-PAVE computer program to obtain the various parameters (CS, TS, and SD due to an 18-kip single-axle load with 100 psi tire pressure) needed for inputs to Equation 6. The fatigue lives of all 30 sections were then calculated using Equation 6, as well as the 1986 AASHTO equation. The results are listed in Table 2 and are plotted in Figure 8. It should be noted that (for all sections) the ratio of the fatigue lives calculated using the AASHTO equation to those obtained using Equation 6 varied from 0.45 to 1.46.

RUT DEPTH

Plastic deformations along the vertical diameter (CD1) of the Marshall-size specimen (see Equation 3) were related to the rut depth of flexible pavements using field data obtained from seven pavement sections in Michigan and Indiana (see Table 1). First, each section was analyzed using the MICH-PAVE computer program. The resulting stresses, strains, surface deflection, and layer properties were then used to calibrate Equation 3. This resulted in the following equation:

$$\begin{aligned} \log(\text{RD}) = & -1.6 + (0.067)(\text{AV}) \\ & - (1.4)[\log(\text{TAC})] + (0.07)(\text{AAT}) \\ & - (0.000434)(\text{KV}) \\ & + (0.15)[\log(\text{ESAL})] \\ & - (0.4)[\log(\text{MR}_{\text{RB}})] \\ & - (0.50)[\log(\text{MR}_{\text{B}})] \\ & + (0.1)[\log(\text{SD})] \\ & + (0.01)[\log(\text{CS})] \\ & - (0.7)[\log(\text{TB}_{\text{EO}})] \\ & + (0.09)\{\log[50 - (\text{TAC} + \text{TB}_{\text{EO}})]\} \end{aligned} \quad (7)$$

where

RD = rut depth (in.),

ESAL = the number of 18-kip ESALs at which the rut depth is being calculated,

SD = pavement surface deflection (in.), and

AAT = average annual temperature (°F).

It should be noted that the values of the moduli of the base and roadbed soil of Equations 6 and 7 are the yearly average values (effective values). These effective values are normally influenced by the freezing index and the seasonal variations of the moisture content of the base and roadbed soil. A procedure for calculating the effective moduli values can be found in the 1986 AASHTO guide for the design of pavement structures. Nevertheless, measured and calculated rut depths of

TABLE 2 FATIGUE LIVES AND RUT DEPTHS OF 30 ARBITRARILY SELECTED PAVEMENT SECTIONS

SEC NO.	TAC	TB	AV	MR (ksi)			STRAINS		SD (in)	FATIGUE LIFE		RUT DEPTH (in)
				AC	BASE	RB	TS	CS		AASHTO	EQUATION 6	
1	2	6	7	200	25.9	3	343	143	.1074	212	134	0.58
2	4	6	7	200	19.2	3	602	302	.0836	778	631	0.32
3	8	6	7	200	11.9	3	371	315	.0548	8767	9970	0.22
4	2	6	7	200	73.6	3	82	57	.0826	1261	*	*
5	8	6	7	200	24.8	3	298	317	.0516	23340	30622	0.18
6	8	6	7	200	38.0	3	247	318	.0495	45325	66288	0.16
7	2	6	5	350	24.5	3	457	121	.1012	446	328	0.50
8	2	6	3	500	23.2	3	476	98	.0954	835	933	0.44
9	8	6	5	350	10.0	3	232	163	.0459	47196	32677	0.21
10	8	6	3	500	8.8	3	156	100	.0408	210720	114230	0.19
11	2	9	7	200	24.2	3	298	240	.0953	784	629	0.57
12	2	12	7	200	22.7	3	295	293	.0874	1865	1606	0.54
13	4	9	7	200	56.3	3	184	322	.0594	26190	28509	0.24
14	4	12	7	200	54.4	3	174	353	.0539	87556	69653	0.22
15	4	6	7	200	58.0	3	222	274	.0677	6051	8318	0.26
16	2	6	7	200	24.2	6	340	244	.0685	1351	1190	0.58
17	2	6	7	200	28.7	9	328	292	.0531	3631	3891	0.56
18	8	6	5	350	11.9	9	204	167	.0230	680635	467143	0.17
19	8	12	3	500	10.5	9	141	102	.0193	5310000	4790000	0.11
20	8	12	3	500	12.6	25	130	105	.0120	73000000	66900000	0.10
21	8	12	3	500	35.2	9	108	108	.0170	34400000	29600000	0.08
22	8	12	3	500	38.9	25	98	111	.0097	539000000	512000000	0.07
23	8	18	3	500	10.5	9	140	102	.0196	8410000	11900000	0.10
24	8	18	3	500	11.8	25	133	104	.0127	95000000	132000000	0.08
25	8	18	3	500	33.6	9	104	109	.0165	95400000	84500000	0.07
26	8	18	3	500	49.1	25	87	116	.0097	2092600000	1286000000	0.06
27	8	18	5	350	23.4	9	161	184	.0202	11300000	11800000	0.09
28	8	18	5	350	26.3	25	150	188	.0128	193000000	148000000	0.08
29	8	18	5	350	37.3	9	132	191	.0185	44300000	30100000	0.08
30	8	18	5	350	40.2	25	124	195	.0114	640000000	399000000	0.07

TAC = THICKNESS OF THE AC COURSE (in) TB = THICKNESS OF THE BASE (in)
 AV = PERCENT AIR VOIDS OF THE AC MR = RESILIENT MODULUS (ksi)
 AC = ASPHALT CONCRETE RB = ROADBED SOILS
 TS = TENSILE MICROSTRAIN (BOTTOM OF AC) CS = COMPRESSIVE MICROSTRAIN
 SD = SURFACE DEFLECTION * = SHEAR FAILURE
 NOTE: THE RUT DEPTH IS CALCULATED AT THE FATIGUE LIFE OF THE PAVEMENT SECTION
 AND AN AVERAGE ANNUAL TEMPERATURE OF 75 °F.

the seven in-service pavement sections are listed in Table 1. In addition, the rut depths due to a number of ESALs equal to the fatigue lives of the 30 arbitrarily selected pavement sections were calculated using Equation 7 and are listed in Table 2.

Two important points should be noted.

1. Equation 7 is based on limited field data. Hence, it should be used with extreme caution and the equation should be calibrated as more field data become available.

2. For each arbitrarily selected pavement section of Table 1, the surface deflections and the compressive and tensile strains due to several axle loads (3,000 to 32,000 lb) and for various trucks (single-axle, semi, and tandem) were also calculated. It was noted that the AASHTO equivalent load factors

provided in the 1986 AASHTO design guide for terminal serviceability of 2.5 are related to the pavement surface deflection (SD in Table 1) calculated under the center of the load. The relationship can be expressed as follows:

$$ELF = (SD_i/SD_{18})^{4.25} \quad (8)$$

where

ELF = AASHTO equivalent load factor obtained for a terminal serviceability index of 2.5 using the 1986 AASHTO design guide,

SD₁₈ = surface deflection due to 18-kip single-axle load, and

SD_i = surface deflection for load *i*.

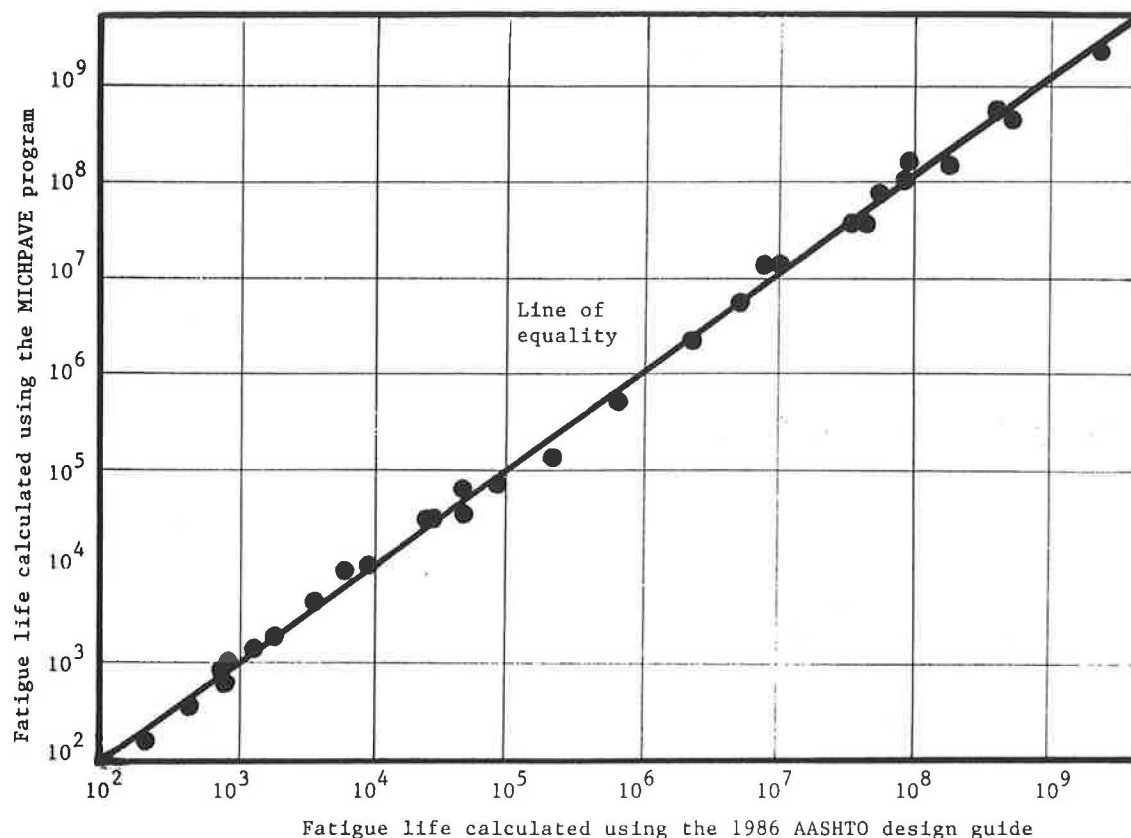


FIGURE 8 Fatigue lives of 30 arbitrarily selected pavement sections calculated using the MICH-PAVE program versus those calculated using the 1986 AASHTO Design Guide.

The significance of Equation 8 is that, because the surface deflection of a pavement section varies with time (seasonal variations) as well as with the pavement conditions, the ELF (a measure of relative load-related damage) of any vehicle including the 18-kip single-axle load is not constant. For example, the load-related damage of an 18-kip single-axle load traveling a pavement section in the spring (thaw condition) is higher than that delivered during summer conditions. Similarly, the load-related damage delivered to a pavement section increases as the pavement develops more cracks. The values of ELF provided in the AASHTO design guide do not account for seasonal variations and/or deteriorating pavement conditions. For example, the ELF value of an 18-kip single-axle load is one, regardless of the value of the structural number (SN) of the pavement. The value of SN for a given pavement section changes and it is a function of time (seasonal variation) and pavement conditions. Hence, the ELF value for an 18-kip single-axle truck is not constant. Equation 8 can be used to assess the ELF for the load-related damage of any vehicle, including the 18-kip single-axle load. This can be accomplished using the following steps:

1. Establish a standard design value of the surface deflection (standard design deflection; SDD) for the pavement section in question due to 18-kip single-axle load. This design value (constant with time and deteriorating pavement conditions) is the denominator of Equation 8.
2. Measure the surface deflection (SD) of any vehicle including an 18-kip single-axle load at any time and for any

pavement condition. This value is the numerator of Equation 8.

3. Calculate the ELF.

The advantages of the above procedure and Equation 8 include the following:

1. The ELF of an 18-kip single-axle load calculated immediately after construction can be used to determine construction quality and/or as a part of the construction specifications.
2. A maximum threshold value of ELF for an 18-kip single-axle load can be established, above which the structural capacity of the pavement is rendered unacceptable. Thus, the critical time for rehabilitation can be established.
3. The values of ELF with time can be used to estimate past and predict future structural performance of the pavements.

IMPLEMENTATION

The advantage of Equations 6 and 7 is that, for most mechanistic pavement design procedures (e.g., CHEV5, ELSYM, MICH-PAVE, ILLI-PAVE, VESYS), the parameters (e.g., CS, TS, SD, and MR) of Equations 6 and 7 are typically calculated. The calculated values can be used as inputs into the equations to predict the fatigue life and rut depth of the pavement that is being designed.

Equations 6 and 7 can be used to design a pavement cross

section such that the limiting acceptable value of the rut depth (established by the state highway agency) and the fatigue life of the pavement section are reached at the same time (the intended design life of the pavement). That is, the equations will allow the engineer to balance the pavement design between fatigue life and rut depth.

It is of utmost importance to note that temperature cracks, stripping, and other distresses should also be considered in the design of flexible pavements. Further, Equations 6 and 7 are based on limited field data, hence, further calibration and/or verification may be required.

SUMMARY AND CONCLUSIONS

The capability of predicting the fatigue life and rut depth of asphalt pavements is essential for the structural design of pavement structures. These predictions become increasingly important as more highway engineers use pavement design systems based on elastic and/or viscoelastic theories that require estimates of the fatigue life. Further, a proper asphalt concrete mix design procedure should be based on the fundamental properties and fatigue life of the mix. A new indirect tensile test apparatus was designed and used in this study to obtain the asphalt mix properties and fatigue life. The indirect tensile test is simple and yields consistent results. Fatigue lives calculated using Equation 6 were compatible to those obtained for 10 pavement sections and to a certain extent were compatible to those obtained using the AASHTO equation for 30 arbitrarily selected pavement sections.

Considering the test results and the analytical and statistical analyses, the following conclusions were drawn:

1. The indirect tensile test can be used to study the effects of the test, specimen, and asphalt mix variables on its fatigue life and plastic deformation.
2. Test results obtained using the new indirect tensile test apparatus are consistent and reproducible.
3. The test temperature and the percent air void in the mix have the greatest influence on the fatigue life and rut depth of the mix.
4. The fatigue life of asphalt concrete increases as the temperature decreases, the percent air void of the AC mix decreases, the stiffness of the AC binder decreases, and/or the aggregate angularity increases.
5. Most existing mechanistic design procedures are capable of calculating the parameters needed for inputs to Equations 6 and 7.
6. Equations 6 and 7 represent two steps in the right direction for the prediction of fatigue life and rut depth of asphalt pavements. The equations can be programmed as a part of almost all existing mechanistic design procedures.
7. Further calibration and verification of Equations 6 and 7 should be accomplished on a continuing basis as more data become available.

RECOMMENDATIONS

Existing asphalt mix design procedures, such as Marshall and Hveem, possess no relationship to the structural properties and fatigue life of asphalt concrete mixes. These properties

are needed, and they are essential to the proper design of flexible pavement structures. A proper asphalt mix design procedure should be tailored to optimize the values of the structural properties of the mix. The results and analyses presented in this paper and those presented elsewhere (28,29) indicate that the structural properties of asphalt concrete mixes can be obtained using cyclic load tests and the new indirect tensile test apparatus. Consequently, it is highly recommended that the new indirect tensile test apparatus be used to establish a new asphalt mix design procedure, whereby the mix design parameters can be obtained based on the structural properties of the mix.

ACKNOWLEDGMENT

The author expresses his deep gratitude to the FHWA for financial support and to the personnel at the MDOT Division of Testing and Technology for their understanding and valuable contributions.

REFERENCES

1. *AASHTO Interim Guide for Design of Pavement Structures*. AASHTO, Washington, D.C., 1981.
2. G. Y. Baladi. *Characterization of Flexible Pavement: A Case Study*. Special Technical Paper 807. American Society for Testing and Materials, 1983, pp. 164–171.
3. W. J. Kenis. *Material Characterizations for Rational Pavement Design*. Special Technical Paper 561. American Society for Testing and Materials, 1973, pp. 132–152.
4. J. S. Miller, J. Uzan, and M. W. Witzak. Modification of the Asphalt Institute Bituminous Mix Modulus Predictive Equation. In *Transportation Research Record 911*, TRB, National Research Council, Washington, D.C., 1983, pp. 27–36.
5. L. W. Nijboer. Mechanical Properties of Asphalt Materials and Structural Design of Asphalt Roads. *Proc., 33rd Annual Meeting*, HRB, National Research Council, Washington, D.C. Vol. 33, 1954, pp. 185–200.
6. J. F. Shook and B. F. Kallas. Factors Influencing Dynamic Modulus of Asphalt Concrete. *Proc. AAPT*, Vol. 38, 1969, pp. 140–178.
7. E. J. Yoder and M. W. Witzak. *Principles of Pavement Design*, 2nd ed., John Wiley and Sons, Inc., New York, 1975.
8. The Asphalt Institute. *Asphalt Overlays for Highway and Street Rehabilitation*. The Asphalt Institute, Manual Series No. 17, College Park, Md., June 1983.
9. S. F. Brown and K. E. Cooper. A Fundamental Study of the Stress-Strain Characteristics of a Bituminous Material. *Proc. AAPT*, Vol. 49, 1980, pp. 476–499.
10. F. N. Finn. *NCHRP Report 39: Factors Involved in the Design of Asphaltic Pavement Surfaces*. HRB, National Research Council, Washington, D.C., 1967, pp. 1–112.
11. B. F. Kallas and J. F. Shook. Factors Influencing Dynamic Modulus of Asphalt Concrete. *Proc. AAPT*, Vol. 38, 1969, p. 140.
12. H. L. Von Quintus, J. B. Rauhut, and T. W. Kennedy. Comparisons of Asphalt Concrete Stiffness as Measured by Various Testing Techniques. *Proc. AAPT*, Vol. 51, 1982, pp. 35–52.
13. M. W. Witzak and R. E. Root. *Summary of Complex Modulus Laboratory Test Procedures and Results*. American Society for Testing and Materials, Special Technical Paper No. 561, 1974, pp. 67–94.
14. *AASHTO Test and Material Specifications*. Parts I and II, 13th edition, AASHTO, Washington, D.C., 1982.
15. *Mix Design Methods for Asphalt Concrete and Other Hot-Mix Types*. Manual Series No. 2, The Asphalt Institute, College Park, Md., 1979.
16. M. H. Farzin, R. J. Krizek, and R. B. Corotis. Evaluation of Modulus and Poisson's Ratio From Triaxial Tests. In *Transportation Research Record 1227*, TRB, National Research Council, Washington, D.C., 1982, pp. 1–12.

- tation Research Record 537, TRB, National Research Council, Washington, D.C., 1975, pp. 69–80.
17. W. H. Goetz. Comparison of Triaxial and Marshall Test Results. *Proc. AAPT*, Vol. 20, 1951, pp. 200–245.
 18. G. Gonzalez, T. W. Kennedy, and J. N. Anagnos. *Evaluation of the Resilient Elastic Characteristics of Asphalt Mixtures Using the Indirect Tensile Test*. Report No. CFHR 3-9-72-183-6, Transportation Planning Division, Texas State Department of Highways and Public Transportation, Austin, Tex., Nov. 1975.
 19. W. O. Hadley and H. Vahida. A Fundamental Comparison of the Flexural and Indirect Tensile Tests. Presented at the Annual Meeting, Transportation Research Board, January 1983.
 20. J. F. Hills and W. Heukelom. The Modulus and Poisson's Ratio of Asphalt Mixes. *Journal of the Institute of Petroleum*, Vol. 55, Jan. 1969, pp. 27–35.
 21. T. W. Kennedy. Characterization of Asphalt Pavement Materials Using the Indirect Tensile Test. *Proc. AAPT*, Vol. 46, 1977, pp. 132–150.
 22. C. L. Monismith. Flexibility Characteristics of Asphalt Paving Mixtures. *Proc. AAPT*, Vol. 27, 1958, pp. 74–106.
 23. P. S. Pell and S. F. Brown. The Characteristics of Materials for the Design of Flexible Pavement Structures. *Proc., 3rd International Conference on the Structural Design of Asphalt Pavements*, University of Michigan, Ann Arbor, Vol. 1, 1972, pp. 326–342.
 24. S. P. Timoshenko and J. N. Goodier. *Theory of Elasticity*, McGraw Hill Book Company, New York, 1970.
 25. M. A. Young and G. Y. Baladi. *Repeated Load Triaxial Testing, State of the Art*. Michigan State University, Division of Engineering Research, 1977.
 26. G. Y. Baladi. *Linear Viscosity*, U.S. Army Corps of Engineers, Waterways Experiment Station, Vicksburg, Miss., Oct. 1985, pp. 1–6.
 27. G. Y. Baladi. *Numerical Implementation of a Transverse-Isotropic, Inelastic, Work-Hardening Constitutive Model*. Soil Dynamics Division, Soils and Pavement Laboratory, U.S. Army Corps of Engineers, Waterways Experiment Station, Vicksburg, Miss., pp. 1–12, 1983.
 28. G. Y. Baladi, R. S. Harichandran, and R. W. Lyles. New Relationships Between Structural Properties and Asphalt Mix Parameters. In *Transportation Research Record 1171*, TRB, National Research Council, Washington, D.C., 1988, pp. 168–177.
 29. G. Y. Baladi, R. W. Lyles, and R. S. Harichandran. Asphalt Mix Design: an Innovative Approach. In *Transportation Research Record 1171*, TRB, National Research Council, Washington, D.C., 1988, pp. 160–167.
 30. G. Y. Baladi and J. H. De Foe. *The Indirect Tensile Test: A New Horizon*. Interim Report FHWA, U.S. Department of Transportation, March 1987.
 31. G. Y. Baladi. *Integrated Material and Structural Design Method For Flexible Pavements*. Final Report No. FHWA/RD-88/109, 110 and 118, Sept. 1987.

Publication of this paper sponsored by Committee on Flexible Pavement Design.

Fatigue Model to Assess Pavement Damage

SHEKHAR GOVIND AND C. MICHAEL WALTON

This paper attempts to derive a general model for fatigue failure. Initially, the problem studied is the relation between the displacement response of a pavement system and the stresses generated by the dynamic application of a load. This is carried out through an analytical model using the theory of wave propagation in an elastic medium. The ultimate objective is forecasting fatigue damage to pavement systems caused by the passage of large trucks. In this regard, a theory is developed to relate fatigue damage to applied stresses. The fatigue model is calibrated by pavement performance data obtained from the AASHO Road Test. Equivalent fatigue damage is computed on a linear damage scale for different axle weights.

In recent years, the number of large combination trucks on the nation's highways has increased dramatically. Many of these trucks have higher axle loads and different axle configurations. This has resulted in increased pavement damage and imprecise forecasts of pavement wear. The end results of the exercise presented in this paper provide a means of forecasting fatigue damage to pavement caused by varied axle configurations and axle weights. Even though the methodology in this case has been applied to predict damage to pavements, the technique developed here is more general and could be applied to any instance where fatigue failure is being studied.

In general, the issue is one of a technique for estimating fatigue damage. In particular, the problem is to determine equivalent axle loads for different axle configurations and axle weights. Starting with the narrower of the two problems, it is known that pavement damage increases nonlinearly with axle weight. Doubling the axle weight would not just double the pavement damage, it would actually raise it by an order of magnitude. The AASHO equivalent single-axle load (ESAL) values were computed on the basis of test data provided by axle loads in the range of 10 to 30 kips. Therefore, extrapolating axle loads beyond 30 kips to forecast pavement wear would be a risky exercise. Further, there is no means of unlinking the damage caused by a steering axle from the damage caused by the load axle of the truck. The methodology developed in this study allows any axle load to be simulated and computes the damage caused by that load with respect to the damage caused by any other axle load.

A similar situation exists in forecasting pavement damage as a function of axle configuration. The AASHO damage equation implicitly recognizes that axles placed in close proximity cause less damage when compared to the same axles placed far apart. For example, the damage caused by a 36-kip tandem axle is approximately 30 percent less than the damage caused by two passes of an 18-kip single axle. How-

ever, according to the AASHO formulation, all tandem-axle configurations are treated similarly. It does not matter whether the axles are 2, 4, or 6 ft apart. According to the AASHO equation, all three configurations (with identical axle loads) are calculated to cause the same amount of damage. The fatigue damage model presented here provides for a technique to make a logical distinction among trucks having different axle configurations.

BACKGROUND

A number of experiments have been conducted relating to the effects of dynamic loads on pavements. The stated objective of most of these studies is to determine the effects of dynamic wheel loads on pavement systems. The eventual objective is, ostensibly, to relate dynamic wheel loads to pavement damage, thus advancing pavement design standards or accurately predicting the life of pavement systems for different magnitudes of axle loads. In other words, the entire problem is being viewed at two levels. The first level concerns the accurate estimation of dynamic loads. The second level deals with mapping the dynamic loads by means of transforms, either to produce design criteria or to predict life. The results from studies falling in the first level may indicate that the dynamic response of the system is governed by several factors (vehicle type, all aspects of the vehicle suspension, the speed of the vehicle, the surface profile and pavement composition, and axle loads).

Sweatman (1) studied different suspension systems and found that torsion-bar suspensions with hydraulic shock absorbers worked best in reducing dynamic loads. Apart from the study cited here, Lee et al. (2) conducted numerous investigations on the different aspects of weigh-in-motion (WIM), for example, the effects of surface profiles on WIM data. In these cases, only the dynamic load at a specific time, $t = t_0$, was obtained, because currently, WIM devices cannot provide the entire spectrum of the load across time. Researchers in other countries have provided a more complete picture of this spectrum (3). A method to obtain specific frequency ranges associated with different suspension systems and vehicles was also established by Gillespie et al. (4). As noted in this study, almost all of the measured vibrations for a truck fell between frequency values of 0 and 20 Hz.

Sousa et al. (5) attempted to determine how the stress field would differ under a moving load, when compared to a static load. Cole and Huth (6) also previously examined special cases of this problem; namely, a line load with a constant velocity, versus a static line load. Recent efforts have been

directed at providing a dynamic interpretation of dynaflect measurements. Shao (7) studied surface waves (Rayleigh waves) generated by the impact of the falling weight to determine material properties. Sebaaly et al. (8) used a multi-degree of freedom elasto-dynamic analysis based on fundamental material properties (e.g., Young's modulus and mass density) to correlate the impact with the measured displacements.

Such techniques are a result of recent advancements in the arena of nondestructive pavement testing by considering wave propagation. Typical examples of this type of research are provided by Shao (7) and Douglas and Eller (9), who use spectral analysis of surface waves for their dynamic interpretations. The problem, however, remains in the accurate determination of the elastic properties of the different layers present in the pavement system.

PAVEMENT DAMAGE AND AASHO DATA

Several methods are available to classify the state of pavements. These range from a visual inspection and scoring system to making precise measurements on the surface of the pavement to determine the slope variance, rut depth, and other variables. In most cases, each methodology has been constructed for its own specialized information-processing purpose.

Currently, the relative damage caused to pavement by different axle weights is determined by data derived from AASHO Road Tests conducted three decades ago. The empirical formulation is such that all damage estimates are scaled relative to the damage caused by one pass of an 18,000-lb single axle. For example, the damage caused by the passage of one 26,000-lb single axle is calculated to be equivalent to the damage caused by 4.3 passes of an 18,000-lb single axle—or one 44,000-lb tandem axle is calculated to be equivalent to 3.0 passes of an 18,000-lb single axle. In this manner, all damages are scaled on the basis of an ESAL number (10).

There could be a number of different ways of looking at the AASHO Road Test data. Both the section on the inner lane and its adjacent section on the outer lane were designed and built together in the same manner. It is, therefore, safe to assume that two sections that are adjacent to each other in the inner and outer lanes, start out with the same value for their present serviceability index (psi). This allows the direct comparison of the number of load applications it took for either lane to get from its original (unknown) psi value to a value of 3.5 psi, for example.

Table 1 is an example of the AASHO Road Test data configured for three sets of ratios of the relative life of identical adjacent flexible pavement sections for Loop Number 6. The only assumed initial difference between adjacent sections in the inner and outer lanes is the applied load. The first and the second columns list the section numbers in Lane 1 and Lane 2, respectively. The third column is the ratio of the number of load applications required in Lane 2 to change the psi value from 3.5 to 3.0 and the number of load applications required in Lane 1 to change the psi value from 3.5 to 3.0. The fourth column is the fraction obtained from the number of load applications on Lane 2 required to change the initial psi value to a psi value of 3.5, divided by the number of load applications on Lane 1 required to change the initial psi value to 3.5. Similarly, the fifth and last column is the fraction

TABLE 1 AASHO ROAD TEST DATA FOR FLEXIBLE PAVEMENT SECTIONS IN LOOP 6

Lane 1 Section	Lane 2 Section	L_2/L_1 3.0 to 3.5	L_2/L_1 3.5	L_2/L_1 3.0
307	308	0.2	0.9	0.4
309	310	0.4	1.6	1.1
253	254	0.5	0.7	0.6
329	330	0.6	2.0	1.6
311	312	0.8	3.2	2.0
327	328	0.8	0.4	0.5
271	272	0.8	0.8	0.8
297	298	0.9	1.5	1.3
331	332	0.9	1.2	1.0
303	304	1.1	2.7	2.0
269	270	1.3	3.2	1.7
261	262	1.4	1.4	1.4
321	322	1.4	3.0	2.1
267	268	1.5	1.1	1.2
315	316	1.7	0.9	1.3
323	324	1.8	1.1	1.2
319	320	2.0	2.2	2.2
259	260	2.0	1.0	1.3
313	314	2.3	1.6	2.0
335	336	2.3	0.5	1.1
255	256	2.7	1.0	2.0
325	326	5.0	0.9	1.1
299	300	5.5	1.4	2.7
305	306	6.1	1.4	2.8
317	318	9.2	2.4	4.2
263	264	9.4	1.3	3.3
257	258	18.4	1.1	5.2
Mean		3.00	1.5	1.79
Std. Dev.		3.97	0.79	1.1

obtained from the number of load applications on Lane 2 divided by the number of load applications on Lane 1 for corresponding changes from the initial psi value to 3.0. Data from all the AASHO Road Test flexible pavement loops were similarly coded for this analysis.

SIMULATION MODEL

A brief discussion of the model used to simulate the stress fields generated within the pavement systems of the AASHO experiment follows. A detailed review of these procedures can be found in Govind (11). Values of all pertinent variables used in the program correspond to the values of these variables recorded during the AASHO experiment.

Consider an isolated elastic homogeneous layer. Displacements at the top of the layer and the bottom of the layer can be represented by a function of time, $d(t)$. For horizontal displacements (in the plane of the layer), this function could be expanded as a double Fourier series (i.e., a Fourier transform) in Cartesian coordinates. In cylindrical coordinates, the variation in the radial direction would be given by a modified Bessel function of integer order and in the circumferential direction by a Fourier series.

Each term of the series for the displacements maps onto a particular wave number. Further, every term in the infinite series for displacements at the top layer corresponds to a similar term in the series for displacements at the bottom layer. Now, it is possible to determine a closed-form analytical solution and develop a transfer function that relates the top displacements to the bottom ones. A similar procedure can be adopted to obtain the transfer function for stresses as well.

Thompson (12) proposed such a model for the propagation of waves in an elastic medium 37 years ago, and it has remained the basis for a majority of the studies conducted since then in this area. Haskell's (13) work is also recognized as one of the earlier efforts in this formulation. An alternative to this method has recently been discussed by Kausel and Roesset (14), when they applied classical structural analysis concepts to Thompson's techniques and constructed a stiffness matrix for each layer. Their study details how a dynamic stiffness matrix can be obtained by mapping the displacements at the top of a layer to the stresses at the top of the layer (instead of comparing them with the displacements at the bottom of the layer).

By compiling the stiffness matrices for each layer and assembling them, one can obtain the stiffness matrix for the entire pavement structure. This essentially provides a transfer function that relates displacements to stresses at each layer. Because displacements and stress involve Bessel's functions and trigonometric terms, the transfer functions comprising the stiffness matrix will be transcendental functions as well. For each term of the series decomposition (for a particular wave number), a result could be obtained. Finally, the results for each term in the series would have to be combined by numerical integration to obtain a solution for a given load distribution. Such procedures have been implemented both for Cartesian coordinates and cylindrical coordinates.

According to the theoretical formulation, the variation of stress and displacement with depth is described by transcendental functions. If the depth of the layer was small, the variations being studied could be approximated between the top and the bottom of the layer by a straight line—this would represent a linear approximation. Higher order polynomial expansions could also be used here to advantage. In any case, if the layers are thin enough, linear approximations have been found to be extremely efficient in terms of both accuracy and time.

For the case of a half-space soil profile with a rigid bedrock, Waas (15) and Kausel (16) suggested a procedure to determine the wave numbers and the mode shapes (corresponding to the eigen values and the eigen vectors, respectively) of the propagating waves for a fixed frequency. By transforming these mode shapes, Kausel was also able to obtain explicit solutions for the displacements caused by dynamic loads. As remarked earlier, his formulation is efficient computationally but requires many layers to model deep soil profiles.

Figures 1 through 4 show a typical stress and displacement field generated in the pavement system by the simulation model as a result of the passage of a 3S2 tractor-semitrailer. The observed stress and displacement are similar in nature to the pore pressure curve actually measured under a pavement during the passage of a truck (17).

DESCRIPTION OF MECHANISTIC MODEL

For this study, a finite-element program was implemented to perform stress analysis. The simulation depends on considering steady-state harmonic forces and displacements at a given frequency. These are transmitted through an elastic isotropic medium as compression and shear waves, as well as surface waves. This can be said to be the primary difference between this model and other multi-layered elastic systems.

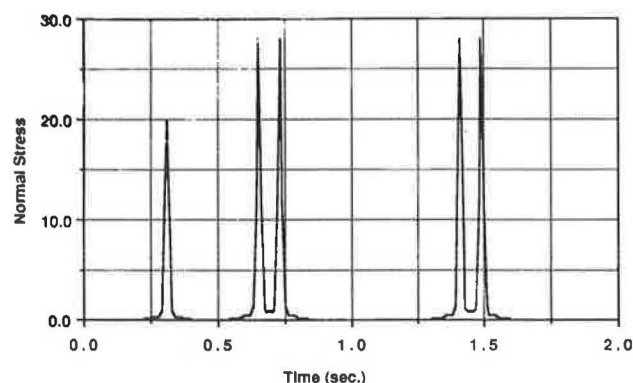


FIGURE 1 Normal stress profile 1 ft below the pavement surface for a 3S2 truck.

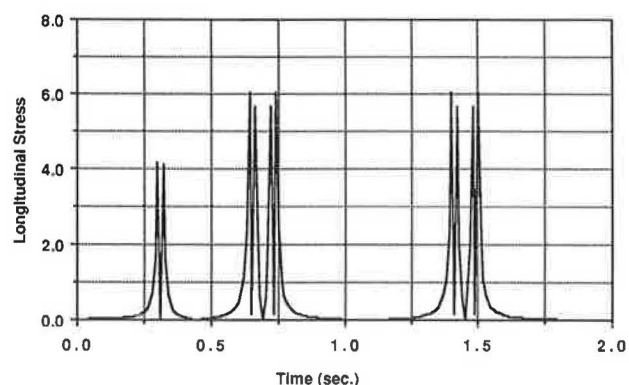


FIGURE 2 Longitudinal stress profile 1 ft below the pavement surface for a 3S2 truck.

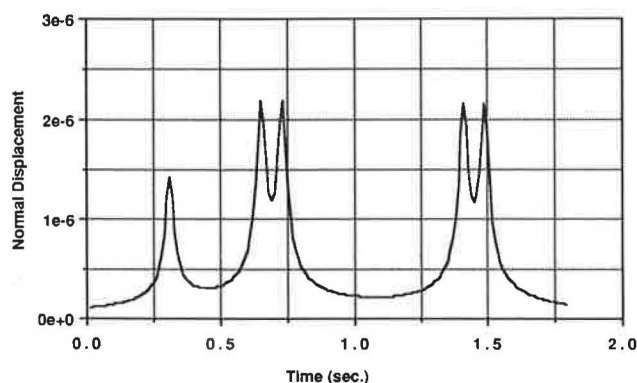


FIGURE 3 Normal displacement 1 ft below the pavement surface for a 3S2 truck.

For a harmonic excitation (caused, say, by a rotating vibrating tire), the solutions at the frequency should correspond directly to the desired displacements. For a transient load, the time history of the force spectrum has to be decomposed into different components using Fourier transforms. Results obtained for each term of the series are then combined and an inverse Fourier transformation is applied to obtain the variation of the displacements over time. Once the displacements and stresses are known at time $t = t_0$, the process is repeated for a new loading position that would correspond to

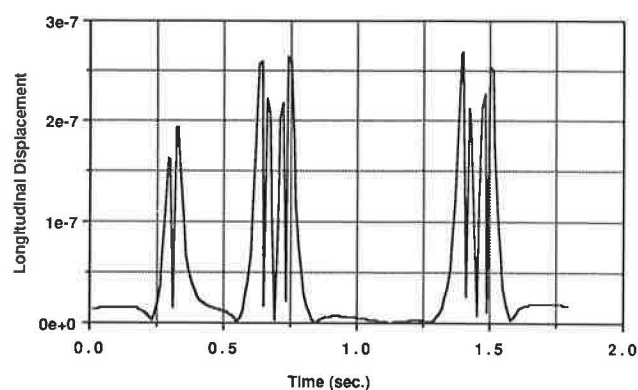


FIGURE 4 Longitudinal displacement 1 ft below the pavement surface for a 3S2 truck.

the driven movement of a vehicle. A time history of stresses can be built in this manner for any location in the pavement system.

Program Review

Six loading schemes are represented in the current program: vertical point load, horizontal point load, vertical disc load, in-plane vertical line load, in-plane horizontal line load, and anti-plane line load. These schemes should be sufficient for our purpose of modeling the vehicle-pavement interaction. The program was tested for different static loads and the result has been found to agree with results obtained through Boussinesque solution and classical elastic theory. Because of the program's large memory requirements, it can be executed on only mainframe computers with one or more gigabytes of memory. The typical execution time on the CRAY-XMP is about 1,000 cpu sec for a 5-axle vehicle driven over 100 ft with 40 discrete frequencies sampled every 0.1 sec.

Input Variables

Input data can be thought of in three groups. The first group deals with the pavement profile. The second group is the frequency ranges to be studied. Finally, the third group of data concerns attributes of the vehicle. A line-by-line discussion of input variables is provided below.

NLAY	Stores the total number of layers in the pavement system. It should include all layers in the pavement, base, subbase, and any geological deposits beneath.
ROCK	This defines the presence of rock or half-space profiles beneath the pavement system. The difference in the behavior of the two profiles would be in their wave-reflection characteristics.
THIK	Defines the thickness of each layer identified in NLAY.
RRO	Contains the value of the mass density of the material in each layer.
VS	Stores the velocity of the shear wave in each layer material.
ANU	Poisson's ratio for the layer material.

DAMP	The damping coefficient that provides the amount of internal damping of each material layer.
NSFR	Number of set of frequencies in the range to be studied.
NFR	Number of frequencies.
OFR	Starting frequency.
DFR	Increment in frequency.
ID	Layer interface where stress and displacement will be computed.
NAXL	Number of axles.
PL	Load on each axle.
X	Spacing between axles.
TRW	Wheel path width.
VEL	Truck velocity.
DX	Incremental movement of load.
LOADT	Load type. Choice of vertical and horizontal point load, disk load, ring load and line load, torsion ring and disk load, and rocking ring and disk load.

Output Variables

There are five output variables. Normal displacements and longitudinal displacements are computed along with normal stresses and longitudinal stresses. These are output along with the time at which these dynamic stresses are recorded. By reducing the input variable, ΔX , it is possible to get as thin a slice of time as is desired. It should be emphasized that apart from the time variable, no units are attached to either the displacement numbers or the stress numbers. The numbers that represent stress and displacement are merely transfer functions that have not been scaled to any particular units and should be used primarily for comparison among themselves.

One limitation of the program is its inability to calculate stresses at the surface of the pavement. This is due to the existence of singularities as point loads are converted to stresses. In computing for different frequencies, a frequency of zero will also produce a singularity.

DAMAGE TRANSFORM

For the purposes of this study, damage transforms are defined as any system of mapping from a load (or stress) domain to a linear damage domain. This concept will be used to transform the simulated stress field of the AASHO experiment to a damage scale, and the results will be compared with the ESAL values established by AASHO to quantify pavement damage as a function of axle loads.

With respect to fatigue, it is not only the magnitude of the force that determines the extent of fatigue damage but also the rate at which it is applied and withdrawn. For cyclic loadings, this is equivalent to assuming that damage would be a function of both the amplitude and the frequency of the load pattern. In other words, it is not just the magnitude of the applied force, stress, or energy that matters in determining the extent of fatigue damage; what also matters is the rate at which it is applied. Therefore, the rate of change of force, stress, or energy might correspond better to our concepts of damage.

A technique of analysis based on similitude study is a prac-

tical approach to addressing this complex engineering problem. In the classical sense, the similitude technique (also referred to as dimensional analysis) consists of a study of three stages. In the first stage, the predominant variables of the problem are recognized for grouping into meaningful dimensionless groups. The second stage in the study consists of setting the criteria for similitude by deciding the relative importance of the dimensionless groups of the variables of the problem. The third stage is the actual execution of the similarity criteria in making a mechanistic model, deciding the kinematic conditions, testing the process, and predicting the behavior of the prototype in view of the dynamic parameters involved.

An attempt is now made to construct a damage model, using dimensional analysis. As discussed earlier, the rate of change of energy (which is power) may be identified as one effective parameter to represent damage. Using the notation L equals the length dimension, T equals the time dimension, and M equals the mass dimension, the following dimensional representations can be stated.

$$\text{Power} = \frac{ML^2}{T^3} \quad (1)$$

A factor not included in our damage discussions so far concerns the size of the specimen being tested for damage. A larger specimen would more likely have a higher capacity to absorb and dissipate the energy it receives as opposed to a smaller specimen with the same material properties. It would seem reasonable that the rate of change of applied energy, or power, should be normalized by the volume of the specimen to account for the size factor. That leads to considering the power expended per unit volume for similitude analysis with damage.

$$\text{Power per unit volume} = \frac{M}{LT^3} \quad (2)$$

Returning briefly to the results obtainable from the dynamic simulation model, it can be stated that the stress and displacement histories of a pavement system can be constructed not only across time at a particular point in space, but also for a particular time at a number of points. In other words, stresses and displacement can be plotted either against time for a constant distance, or they can be plotted against distance at a given value of time. This directly provides us with the following functions.

$$\text{Stress} = f(\text{distance})_{\text{constant time}} = f(\text{time})_{\text{constant distance}}$$

$$\text{Displacement} = f(\text{distance})_{\text{constant time}} = f(\text{time})_{\text{constant distance}}$$

The advantage of representing these variables in their different functional forms is that the exact differential with respect to both time and distance can now be evaluated. For example, consider stress as a function of time. Using the notation ∂ to denote the process of partial differentiation, σ for stress, t for time, and x for distance, the stress function becomes

$$\left[\frac{\partial \sigma(t, x)}{\partial t} \right]_{x=\text{const.}} = \frac{\delta \sigma}{\delta t} \quad (3)$$

The left-hand side of the equation can be evaluated by using

the results of the simulation model provided that ∂t , the time increment used, is of a small magnitude. The function could then be represented as

$$\left[\frac{\partial \sigma(t, x)}{\partial t} \right] = \frac{d\sigma}{dt} \quad (4)$$

Examining Equations 2 and 4, it can be seen that they both have the same dimensional form (i.e., power per unit volume and the time rate of change of stress are dimensionally identical).

$$\frac{d\sigma}{dt} = \frac{M}{LT^3} \quad (5)$$

This provides a basis for considering the rate of change of stress (which is dimensionally equivalent to power per unit volume) as one of the parameters used to derive a damage function. This damage function could also be represented as a stress-ratio dimensionless number by comparing the damage caused by one event with the damage caused by another event.

To relate the function to specific events of stress application over time, some form of average or sum over the time period of the event would have to be evaluated. Absolute values for the exact differential would have to be used in the averaging process because a negative rate of change of stress would tend to cancel out the positive rate of change of stress in a symmetrical stress-time curve with the axis of symmetry parallel to the stress axis. This would be further justified if one kept in mind that it is the cumulative effect of all subevents within an event that should be accounted for, and averaging is the simplest of the many techniques to accomplish it. If the differential is summed over time, some form of normalization with respect to time should also be considered. An event that allowed more than one stress peak to occur could be divided into subsets of smaller events, each containing only one stress peak (i.e., one stress cycle per event subset). The effect of the event in its totality will be represented by a cumulative sum of the effects of the event in each subset.

In accordance with the above discussions, the formulation of the methodology of one damage transform follows. Consider a loading event, R , that generates a stress field, $\sigma(t)$. The function defining $\sigma(t)$ is such that m changes occur in the sign of the slope of the stress curve. The time, t , at each successive change of the slope from negative to positive is denoted by $(t_1 \dots t_m)$. The peak P_1 starts at time $t = t_0$ and ends at time $t = t_1$; the peak P_2 starts at time $t = t_1$ and ends at time $t = t_2$ and so on. For the event R , the cumulative effect of the m different subevents could be represented by an n th power for each peak.

$$\left(\frac{1}{t_1 - t_0} \int_{t_0}^{t_1} \left| \frac{\delta \sigma}{\delta t} \right| dt \right)^n + \left(\frac{1}{t_2 - t_1} \int_{t_1}^{t_2} \left| \frac{\delta \sigma}{\delta t} \right| dt \right)^n + \dots \quad (6)$$

For the final result to be sensitive to all individual subevents, the sum for each peak must be raised to the power n

before being added. That assumes the transform is a power law function.

Once such summations are obtained for separate events, it should now be possible to obtain a dimensionless rate of change of stress (or power per unit volume) ratio that would compare the effects of the different events. Let us denote for the event R comprising m separate subevents D_i , each D comprises a single stress peak.

$$\sum_{i=1}^m D_i^n = \sum_{i=1}^m \left(\frac{1}{t_{i-1} - t_i} \int_{t_{i-1}}^{t_i} \left| \frac{\delta\sigma}{dt} \right| dt \right)^n \quad (7)$$

If now it was decided to compare the effect of the damage caused by a single-peak event, R_a (having a dimensionless number, D_a , denoting damage by the only stress peak) as a fraction of the damage caused by a single-peak event R_b (having a dimensionless number, D_b , denoting damage by the only stress peak), the ratio of the two damages could be computed by Equation 8. In this equation, L denotes the life of the specimen.

$$\left(\frac{D_a}{D_b} \right)^n = \left(\frac{L_b}{L_a} \right) \quad (8)$$

Here, L_a and L_b would correspond to the effective number of loading/unloading cycles to failure of the two specimens undergoing the events a and b (i.e., they are the variables denoting life).

The damage transform seen in Equation 8 is conceptually similar to ideas proposed by Palmgren (18) in his treatise on the phenomenon of fatigue failure in ball and roller bearings. The main difference between the two procedures is that Palmgren used force as his choice of variable from which to derive a dimensionless ratio. His number corresponds to a dimensionless force ratio and depicts the ratio of the life, L_1 , as determined by force, F_1 , with respect to the life, L_2 , as determined by force, F_2 . Palmgren found that, for his data, the best regression fit was obtained for n equals 3.

$$\left(\frac{F_1}{F_2} \right)^n = \left(\frac{L_2}{L_1} \right) \quad (9)$$

The damage numbers, D_i and D_k , can be thought of in terms similar to that proposed by Palmgren. The difference would be that instead of force ratios, power per unit volume ratios are used. The value of n would be quite different in Equations 8 and 9, being dependent on the interactions of a host of variables that are completely different for ball bearings and pavements. One can now establish the relation presented in Equation 8. The damage number derived from this representation may be more accurate in predicting actual damage than the ESAL numbers because of reasons outlined earlier. This methodology may be applied to determine the relative damage caused by any event with respect to the damage caused by another event.

It should be pointed out that other similar dimensionless numbers can also be derived here using not just stress, but a host of other functions as well. Not all these dimensionless damage numbers may eventually be independent of each other as per Buckingham's π theorem, which provides that a set of

n physical quantities with r base dimensions may always be arranged to form an infinite number of dimensionless groups, of which only $(n - r)$ dimensionless parameters are independent. Therefore, if two or more variables from elasticity are finally transformed onto a damage scale, all would not be expected to be independent.

DISCUSSION OF RESULTS

The results presented and discussed here deal with the calibration of the proposed fatigue model. Initially, a regression model was used to determine the bounds of the value of n in the equations

$$D = \int_{t_0}^{t_1} \frac{1}{t_1 - t_0} \left| \frac{\delta\sigma}{dt} \right| dt \quad (10)$$

and

$$\left(\frac{D_a}{D_b} \right)^n = \left(\frac{L_b}{L_a} \right) \quad (11)$$

where D_a and D_b are the damage transforms for the events a and b , and L_a and L_b are the lives of the specimens for the events a and b , respectively.

The data used to calibrate the model were obtained from the AASHO Road Test data set and comprise the data for flexible pavements (Table 1 is an example of the data from Loop Number 6). The traffic on each lane was simulated to obtain the damage transforms, and the value of n was found so as to equate the life ratios as a power of the ratios of the damage transform.

A regression was performed on these data with the intent of finding the range of the value that the variable n could take and not just with the idea of fixing the best fit on the data with a particular value of n . Once a range had been determined for the variable, it would be easy to check how the equation behaved for different values of n within the bounds. In effect, a sensitivity analysis of the equation could now be performed and the results compared to the AASHTO ESAL values. Figure 5 shows the plot of the residual sum of squares

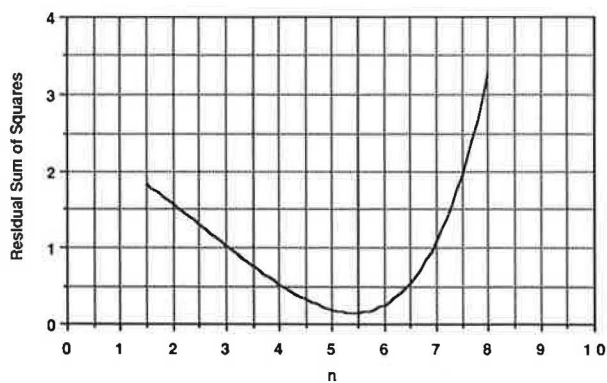


FIGURE 5 Residual sum of squares plotted against n for Equations 10 and 11, using AASHO Road Test data for flexible pavements.

for Equation 11 and life ratios of initial to 3.5 psi plotted with respect to the values of n . From Figure 5, it can be seen that the value of the sum of squares is below 1 for n values between 3.0 and 7.0, with a smaller rate of change of slope observed toward the value of 3.0 than toward 7.0, where a rapid rate of change of slope can be seen. This implies that the actual value of n may be more biased toward 3.0 than toward 7.0 or higher. In any event, the range $3 \leq n \leq 7$ should clearly provide us with a value of n that would serve as a good model for the AASHO data.

Tables 2 through 7 show how the ESAL values for different axle loads are computed according to Equations 10 and 11 with respect to a single 18-kip axle load for different values of n . The denominator, D_b , in the damage ratio of Equation 11 corresponds to the stress peak for a standard 18-kip single axle. Therefore, these tables are identical to computing 18-kip ESAL factors. Table 8 lists the ESAL values used by AASHO for a flexible pavement at a psi of 3.0. On inspection, it can be seen that the ESAL values for n in the range computed here are similar to the range of ESAL values provided by AASHO. For example, when n equals 4.6 (Table 2), the equivalent damage for different axle loads predicted by the model corresponds closely to the ESAL factors established by AASHO for a pavement at a psi of 3.0 and a structural number of 1 (Table 8).

CONCLUSIONS

By comparing the AASHO ESAL values for different psi levels and the ESAL values computed by means of the damage model (Tables 2 through 8), it is apparent that both equivalency factors belong to the same family of damage curves. The techniques used in this study can be easily applied to axle

load ranges that were not covered by the AASHO Road Test data and precise ESAL values obtained for those ranges. This methodology has also been applied to determine damage numbers resulting from the effects of axle spacing in tandem axles (19). This is another area where AASHO equivalents are not precise.

TABLE 3 SENSITIVITY ANALYSIS OF ESAL WITH RESPECT TO n IN EQUATION 11: n -VALUES 4.45–4.25

Load (kips)	n Values				
	4.45	4.40	4.35	4.30	4.25
2	0.00	0.00	0.00	0.00	0.00
4	0.00	0.00	0.00	0.00	0.00
6	0.01	0.01	0.01	0.01	0.01
8	0.03	0.03	0.03	0.03	0.03
10	0.07	0.08	0.08	0.08	0.08
12	0.16	0.17	0.17	0.17	0.18
14	0.33	0.33	0.34	0.34	0.35
16	0.59	0.60	0.60	0.61	0.61
18	1.00	1.00	1.00	1.00	1.00
20	1.60	1.59	1.58	1.58	1.57
22	2.44	2.41	2.39	2.37	2.34
24	3.61	3.56	3.51	3.46	3.41
26	5.14	5.05	4.96	4.87	4.78
28	7.19	7.04	6.88	6.73	6.58
30	9.56	9.32	9.09	8.86	8.64
32	12.91	12.54	12.19	11.84	11.51
34	17.10	16.57	16.05	15.54	15.06
36	22.36	21.59	20.85	20.14	19.45
38	27.83	26.81	25.83	24.88	23.97
40	35.41	34.02	32.68	31.40	30.17
42	43.77	41.95	40.20	38.53	36.93
44	52.72	50.42	48.23	46.12	44.11
46	65.17	62.18	59.33	56.61	54.02
48	79.01	75.23	71.62	68.19	64.92
50	93.48	88.83	84.41	80.22	76.23

TABLE 2 SENSITIVITY ANALYSIS OF ESAL WITH RESPECT TO n IN EQUATION 11: n -VALUES 4.70–4.50

Load (kips)	n Values				
	4.70	4.65	4.60	4.55	4.50
2	0.00	0.00	0.00	0.00	0.00
4	0.00	0.00	0.00	0.00	0.00
6	0.01	0.01	0.01	0.01	0.01
8	0.02	0.02	0.02	0.03	0.03
10	0.06	0.07	0.07	0.07	0.07
12	0.15	0.15	0.15	0.16	0.16
14	0.31	0.31	0.32	0.32	0.33
16	0.58	0.58	0.58	0.59	0.59
18	1.00	1.00	1.00	1.00	1.00
20	1.64	1.64	1.63	1.62	1.61
22	2.56	2.54	2.51	2.49	2.46
24	3.89	3.83	3.78	3.72	3.67
26	5.64	5.54	5.44	5.34	5.24
28	8.04	7.86	7.69	7.52	7.35
30	10.85	10.58	10.31	10.06	9.80
32	14.90	14.48	14.07	13.67	13.29
34	20.06	19.43	18.82	18.23	17.66
36	26.63	25.71	24.83	23.98	23.16
38	33.55	32.32	31.13	29.99	28.89
40	43.27	41.57	39.94	38.37	36.86
42	54.12	51.87	49.71	47.65	45.66
44	65.87	63.00	60.26	57.63	55.12
46	82.41	78.63	75.02	71.58	68.30
48	100.99	96.16	91.55	87.16	82.99
50	120.62	114.62	108.93	103.51	98.37

TABLE 4 SENSITIVITY ANALYSIS OF ESAL WITH RESPECT TO n IN EQUATION 11: n -VALUES 4.20–4.00

Load (kips)	n Values				
	4.20	4.15	4.10	4.05	4.00
2	0.00	0.00	0.00	0.00	0.00
4	0.00	0.00	0.00	0.00	0.00
6	0.01	0.01	0.01	0.01	0.01
8	0.03	0.04	0.04	0.04	0.04
10	0.09	0.09	0.09	0.09	0.10
12	0.18	0.19	0.19	0.19	0.20
14	0.35	0.36	0.36	0.37	0.37
16	0.61	0.62	0.62	0.62	0.63
18	1.00	1.00	1.00	1.00	1.00
20	1.56	1.55	1.54	1.53	1.53
22	2.32	2.30	2.27	2.25	2.23
24	3.36	3.31	3.27	3.22	3.17
26	4.69	4.61	4.52	4.44	4.36
28	6.44	6.30	6.16	6.02	5.89
30	8.42	8.21	8.00	7.80	7.61
32	11.18	10.86	10.56	10.26	9.97
34	14.58	14.13	13.68	13.25	12.84
36	18.78	18.13	17.51	16.91	16.33
38	23.09	22.24	21.42	20.64	19.88
40	28.98	27.84	26.75	25.70	24.69
42	35.40	33.92	32.51	31.16	29.87
44	42.19	40.35	38.60	36.91	35.31
46	51.54	49.18	46.92	44.77	42.72
48	61.81	58.85	56.03	53.35	50.79
50	72.44	68.84	65.42	62.17	59.08

TABLE 5 SENSITIVITY ANALYSIS OF ESAL
WITH RESPECT TO n IN EQUATION 11:
 n -VALUES 3.95–3.75

Load (kips)	n Values				
	3.95	3.90	3.85	3.80	3.75
2	0.00	0.00	0.00	0.00	0.00
4	0.00	0.00	0.00	0.00	0.00
6	0.01	0.01	0.01	0.02	0.02
8	0.04	0.04	0.04	0.05	0.05
10	0.10	0.10	0.10	0.11	0.11
12	0.20	0.21	0.21	0.21	0.22
14	0.37	0.38	0.38	0.39	0.39
16	0.63	0.63	0.64	0.64	0.65
18	1.00	1.00	1.00	1.00	1.00
20	1.52	1.51	1.50	1.49	1.49
22	2.21	2.18	2.16	2.14	2.12
24	3.13	3.08	3.04	3.00	2.95
26	4.28	4.20	4.12	4.05	3.98
28	5.76	5.64	5.51	5.39	5.27
30	7.42	7.23	7.05	6.87	6.70
32	9.68	9.41	9.14	8.88	8.63
34	12.43	12.04	11.66	11.30	10.94
36	15.77	15.23	14.71	14.20	13.72
38	19.15	18.45	17.77	17.12	16.49
40	23.72	22.79	21.89	21.03	20.21
42	28.62	27.43	26.29	25.20	24.15
44	33.77	32.30	30.89	29.54	28.26
46	40.76	38.89	37.11	35.41	33.78
48	48.36	46.04	43.83	41.73	39.74
50	56.14	53.35	50.70	48.18	45.78

TABLE 7 SENSITIVITY ANALYSIS OF
ESAL WITH RESPECT TO n IN
EQUATION 11: n -VALUES 3.45–3.30

Load (kips)	n Values			
	3.45	3.40	3.35	3.30
2	0.00	0.00	0.00	0.00
4	0.01	0.01	0.01	0.01
6	0.02	0.02	0.03	0.03
8	0.06	0.06	0.07	0.07
10	0.13	0.14	0.14	0.14
12	0.25	0.25	0.26	0.26
14	0.42	0.43	0.43	0.44
16	0.67	0.67	0.68	0.68
18	1.00	1.00	1.00	1.00
20	1.44	1.43	1.43	1.42
22	2.00	1.98	1.96	1.94
24	2.71	2.67	2.63	2.59
26	3.56	3.50	3.43	3.37
28	4.62	4.52	4.42	4.32
30	5.76	5.61	5.47	5.33
32	7.27	7.06	6.86	6.67
34	9.04	8.75	8.48	8.21
36	11.12	10.74	10.37	10.02
38	13.18	12.70	12.23	11.78
40	15.89	15.26	14.66	14.09
42	18.72	17.94	17.20	16.48
44	21.63	20.69	19.78	18.92
46	25.49	24.32	23.21	22.14
48	29.60	28.18	26.83	25.54
50	33.72	32.04	30.45	28.93

TABLE 6 SENSITIVITY ANALYSIS OF ESAL
WITH RESPECT TO n IN EQUATION 11:
 n -VALUES 3.70–3.50

Load (kips)	n Values				
	3.70	3.65	3.60	3.55	3.50
2	0.00	0.00	0.00	0.00	0.00
4	0.00	0.00	0.00	0.00	0.01
6	0.02	0.02	0.02	0.02	0.02
8	0.05	0.05	0.05	0.06	0.06
10	0.11	0.12	0.12	0.12	0.13
12	0.22	0.23	0.23	0.24	0.24
14	0.40	0.40	0.41	0.41	0.42
16	0.65	0.65	0.66	0.66	0.66
18	1.00	1.00	1.00	1.00	1.00
20	1.48	1.47	1.46	1.46	1.45
22	2.10	2.08	2.06	2.04	2.02
24	2.91	2.87	2.83	2.79	2.75
26	3.90	3.83	3.76	3.69	3.63
28	5.16	5.05	4.93	4.83	4.72
30	6.53	6.37	6.21	6.06	5.90
32	8.39	8.15	7.92	7.70	7.48
34	10.60	10.27	9.94	9.63	9.33
36	13.24	12.79	12.35	11.93	11.52
38	15.89	15.30	14.74	14.20	13.68
40	19.41	18.65	17.92	17.21	16.54
42	23.15	22.19	21.27	20.38	19.53
44	27.02	25.85	24.72	23.64	22.61
46	32.23	30.76	29.35	28.00	26.72
48	37.83	36.02	34.29	32.65	31.09
50	43.51	41.34	39.29	37.34	35.48

TABLE 8 ESAL FACTORS FOR FLEXIBLE PAVEMENTS
AT A PSI OF 3.0 (I_0)

Load (kips)	Pavement Structural Number (SN)					
	1	2	3	4	5	6
2	0.00	0.00	0.00	0.00	0.00	0.00
4	0.00	0.00	0.01	0.00	0.00	0.00
6	0.01	0.03	0.03	0.02	0.01	0.01
8	0.04	0.07	0.08	0.06	0.04	0.03
10	0.08	0.13	0.17	0.13	0.10	0.09
12	0.17	0.23	0.30	0.26	0.21	0.19
14	0.33	0.39	0.47	0.45	0.39	0.36
16	0.59	0.63	0.69	0.69	0.65	0.62
18	1.00	1.00	1.00	1.00	1.00	1.00
20	1.60	1.53	1.41	1.38	1.44	1.51
22	2.47	2.29	1.96	1.83	1.97	2.16
24	3.67	3.33	2.69	2.39	2.60	2.96
26	5.29	4.72	3.65	3.08	3.33	3.91
28	7.43	6.56	4.88	3.93	4.17	5.00
30	10.20	8.90	6.50	5.00	5.10	6.30
32	13.80	12.00	8.40	6.20	6.30	7.70
34	18.20	15.70	10.90	7.80	7.60	9.30
36	23.80	20.40	14.00	9.70	9.10	11.00
38	30.60	26.20	17.70	11.90	11.00	13.00
40	38.80	33.20	22.20	14.60	13.10	15.30
42	48.80	41.60	27.60	17.80	15.50	17.80
44	60.60	51.60	34.00	21.60	18.40	20.60
46	74.70	63.40	41.50	26.10	21.60	23.80
48	91.20	77.30	50.30	31.30	25.40	27.40
50	110.00	94.00	61.00	37.00	30.00	32.00

With respect to the physical significance of n , it could represent the structural strength of the pavement. A lower value of n might imply a strong and well-designed pavement with respect to the load being carried on it, while a higher value of n would be used for pavements that are underdesigned for the load they experience. In this respect, n behaves as an inverse function of the pavement structural number (SN), the index used by AASHO to quantify the quality of pavements. An interesting side note to Equation 11 is that because the ratio of the damage transforms D_a and D_b is being raised to a power n , when D_a is less than D_b the nature of the family of damage curves changes. For this reason, Equation 11 should be used only if D_a is greater than D_b .

In conclusion, it should be stated that the damage model developed and presented here provides an excellent alternative to the AASHO values for 18-kip ESAL. Further, when compared to the AASHO procedure, it also provides a more accurate means of determining the ESAL for tandem axles with nonuniform spacings. It should also be recognized that the methodology is completely general and may be used for studying any fatigue damage-related phenomenon.

REFERENCES

1. P. F. Sweatman. *A Study of Dynamic Wheel Forces in Axle Group Suspensions of Heavy Vehicles*. Special Report No. 27, Road Research Board, June 1983.
2. C. E. Lee, B. Izadmehri, and R. B. Machemehl. *Demonstration of Weigh-In-Motion Systems for Data Collection and Enforcement*. Research Report 557-1F, Center for Transportation Research, University of Texas at Austin, Austin, Tex., Dec. 1985.
3. D. R. Leonard, J. W. Grainger, and R. Eyre. *Loads and Vibrations Caused by Eight Commercial Vehicles with Gross Weight Exceeding 30 Tons*. TRRL Laboratory Report 582, Transport and Road Research Laboratory, Great Britain, 1974.
4. T. D. Gillespie, et al. *Influence of Size and Weight Variables on the Stability and Control Properties of Heavy Trucks*. Report No. UMTRI-83-10/2, University of Michigan, 1983.
5. J. B. Sousa, J. Lysmer, S. S. Chen, and C. L. Monismith. *Response of Asphalt Concrete Pavements to Dynamic Truck Loads*. Institute of Transportation Studies, University of California, Berkeley, March 1987.
6. J. Cole and J. Huth. Stresses Produced in a Half-Plane by Moving Loads. *Journal of Applied Mechanics*, Dec. 1958, p. 433.
7. K-Y. Shao. *Dynamic Interpretation of Dynaflect, Falling Weight Deflectometer and Spectral Analysis of Surface Waves Tests on Pavement Systems*. Ph.D. dissertation. Department of Civil Engineering, University of Texas at Austin, Austin, Tex., Dec. 1985.
8. B. E. Sebaaly, M. S. Mamlouk, and T. G. Davies. *Dynamic Analysis of Falling Weight Deflectometer Data*. In *Transportation Research Record 1070*, TRB, National Research Council, Washington, D.C., 1986, pp. 63-68.
9. R. A. Douglas and G. L. Eller. *Nondestructive Pavement Testing by Wave Propagation: Advanced Methods of Analysis and Parameter Management*. In *Transportation Research Record 1070*, TRB, National Research Council, Washington, D.C., 1986, pp. 53-64.
10. *AASHTO Interim Guide for Design of Pavement Structures*. AASHTO, Washington, D.C., 1985.
11. S. Govind. *A Dynamic Analysis of Pavement Systems to Determine a Damage Transform from Stress Fields*. Ph.D. dissertation. Department of Civil Engineering, University of Texas at Austin, Austin, Tex., May 1988.
12. W. T. Thompson. Transmission of Elastic Waves through a Stratified Soil Medium. *Journal of Applied Physics*, Vol. 21, Feb. 1950.
13. N. A. Haskell. The Dispersion of Surface Waves on Multilayered Media. *BSSA*, Vol. 43, No. 1, Feb. 1953.
14. E. Kausel and J. M. Roesset. Stiffness Matrix for Layered Soils. *BSSA*, Vol. 71, No. 6, Dec. 1981.
15. G. Waas. *Linear Two-Dimensional Analysis of Soil Dynamics Problem on Semi-Infinite Layered Media*. Ph.D. dissertation. Department of Civil Engineering, University of California, 1972.
16. E. Kausel. *An Explicit Solution for the Green Functions for Dynamic Loads in Layered Media*. Research Report R81-13, Department of Civil Engineering, Massachusetts Institute of Technology, Cambridge, 1981.
17. M. Hyodo, K. Yasahara, and H. Murata. Traffic-Induced Pore Pressure and Deformation of Soft Clay Deposit Beneath Embankment. *Proc., International Symposium on Geotechnical Engineering in Soft Soils*, Mexico City, 1987.
18. A. Palmgren. *Ball and Roller Bearing Engineering*. S. H. Burbank & Co., Inc., Philadelphia, Pa., 1945.
19. S. Govind, D. A. Faria, R. B. Machemehl, and C. M. Walton. *Analysis and Forecast of Truck Traffic Loads and the Relative Damage to Pavement Systems as a Function of Axle Configurations*. Research Report Number 378-1F, Center for Transportation Research, The University of Texas at Austin, Nov. 1987.

Publication of this paper sponsored by Committee on Flexible Pavement Design.

Effect of Tire Pressure on Flexible Pavement Response and Performance

RAMON BONAQUIST, ROGER SURDAHL, AND WALLA MOGAWER

The effects of tire pressure on flexible pavement response and performance were evaluated using data from the first phase of research at the FHWA Pavement Testing Facility. The Accelerated Loading Facility testing machine was used to simulate traffic loading. The response evaluation included measuring surface deflections, surface strains, and strains at the bottom of the asphalt layer for various combinations of load and tire pressure. The data showed little effect due to tire pressure at all load levels. The performance evaluation included an evaluation of differences in rutting and cracking for two test sections trafficked with the same load but different tire pressures. The data showed increased rutting and cracking for the section trafficked with the higher tire pressure; however, this section was thinner and trafficked at a higher temperature than the low tire pressure section. Based on postmortem evaluations of the two sections and an analysis of pavement strains using layer theory, the increased rutting was due mainly to the higher temperature. On the basis of classical fatigue models, the increased cracking was found to result primarily from the combined effects of higher pavement temperature and thinner pavement structure.

In recent years, the effects of increased truck tire pressures on flexible pavement performance have become a subject of great concern. Various researchers have used analytical methods to attribute decreased fatigue life, increased rutting, and accelerated serviceability loss to the effects of increased tire pressure (1-3). This paper presents an analysis of the impact of tire pressure on flexible pavement response and performance on the basis of data collected during the first phase of research at the FHWA Pavement Testing Facility (PTF).

The Pavement Testing Facility is an outdoor, full-scale pavement testing laboratory located at the Turner-Fairbank Highway Research Center in McLean, Virginia. The purpose of the PTF is to quantify the performance of full-scale test pavements under accelerated loading. The facility comprises the Accelerated Loading Facility (ALF) test machine; two 200-ft-long, instrumented asphalt concrete test pavements; and a computer-controlled data-acquisition system.

The ALF, shown in Figure 1, simulates one-half of a dual-tire single axle, and can apply loads ranging from 9,400 to 22,500 lb. The test wheels travel at 12 mi/hr over 40 ft of pavement. To simulate highway traffic, the loads are applied in one direction and are normally distributed about a 48-in. wheelpath.

Each test lane is divided into four sections for a total of eight test sections. Cross sections for the two lanes are shown

in Figure 2. Typical Virginia Department of Transportation (DOT) materials were used in the pavements. The wearing and binder courses consist of crushed aggregate and AC-20 asphalt. The crushed aggregate base is dense graded, and contains a high amount of fines, approximately 50 percent passing the No. 8 sieve. The subgrade is classified as an AASHTO A-4(0) soil.

The pavement instrumentation and data-acquisition system form an integral part of the PTF. The pavement instrumentation consists of thermocouples and moisture cells at various depths in the pavement, strain gauges at the bottom of the asphalt binder, and a linear variable differential transformer (LVDT) for dynamic surface deflection. Signals from the various instruments are directed through signal conditioning equipment to analog to digital converters mounted in a personal microcomputer. Software was developed to collect environmental and pavement response data as part of the routine operation of the PTF.

The effects of tire pressure on flexible pavements were evaluated in two ways. First, deflections and strains for various combinations of load and tire pressure were measured and compared. Second, rutting and cracking for two test sections trafficked with the same load but different tire pressures were analyzed. The remainder of this paper describes these two evaluations.

PAVEMENT RESPONSE EVALUATION

Experimental Design

The objective of the pavement response experiment was to compare pavement responses for various combinations of load and tire pressure for two types of tires. The experiment consisted of measuring surface deflection, surface strain, and strain at the bottom of the asphalt layer for three load levels, three tire pressures, and two tire types. Table 1 summarizes the experimental design. The experiment was conducted on Lane 2 of the PTF in July 1987 and Lane 1 in December 1987.

Instrumentation

The pavement instrumentation included an LVDT to measure surface deflections and strain gauges at the surface and the bottom of the asphalt layer. The LVDT was mounted to a reference beam placed adjacent to the test pavement and

R. Bonaquist and R. Surdahl, Turner-Fairbank Highway Research Center, FHWA, 6300 Georgetown Pike, McLean, Va. 22101. W. Mogawer, Civil Engineering Department, University of Rhode Island, Kingston, R.I. 02881.



FIGURE 1 Accelerated Loading Facility testing machine.

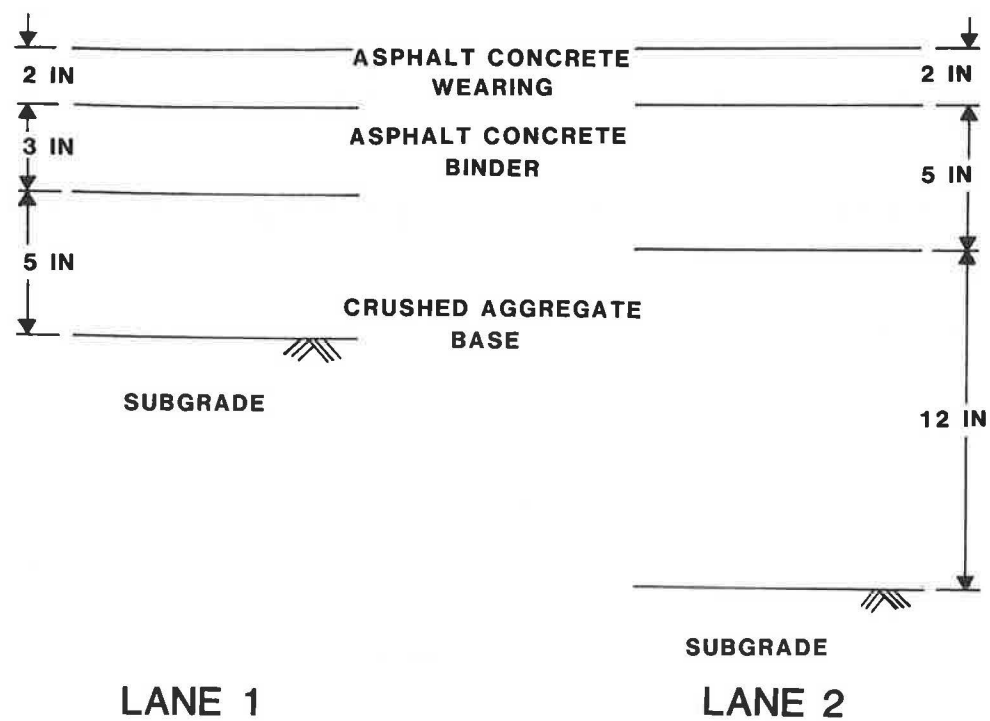


FIGURE 2 Pavement Testing Facility pavement cross sections.

TABLE 1 EXPERIMENTAL DESIGN

Load (lb)	Tire Pressures (psi)					
	Radial			Bias Ply		
	76	108	140	76	108	140
9,400	X	X	X	X	X	X
14,100	X	X	X	X	X	X
19,000	X	X	X	X	X	X

measured the pavement deflection 27 in. from the center of the dual wheels.

Surface strains were measured with 2-in. gauge length bonded foil resistance strain gauges. The gauges were installed in shallow slots cut in the pavement surface. Surface strains were measured in the transverse direction both between the dual wheels and under the center of one tire.

Strains at the bottom of the asphalt layer were measured using strain gauges installed at the interface between the asphalt binder and the crushed aggregate base during construction. These gauges consisted of a strain gauge encapsulated in a plastic strip. The plastic strip was anchored in the asphalt by two transverse beams attached to the ends of the strip. The resulting strain gauge formed an H shape (4). The strains at the bottom of the asphalt layer were measured in the longitudinal direction under the inside edge of one of the dual tires.

Response curves for the various instruments were obtained by using the PTF data-acquisition system to monitor the instruments as the ALF wheels traversed the pavement. For each response measurement, a temperature profile for the asphalt layer was obtained using thermocouples installed adjacent to the response instrumentation.

Results

Typical response curves for deflection and strain are shown in Figure 3. Of particular interest is the response curve for longitudinal strain at the bottom of the asphalt layer. This response curve shows a strain reversal when the load passed over the gauges. As the load approached the gauges, compressive strains were induced at the bottom of the asphalt layer. When the load was over the gauges, tensile strains occurred, and finally, compressive strains were once again induced as the load moved away from the gauges.

In analyzing the data, only the peak responses were considered. These responses and the corresponding pavement temperatures are summarized in Tables 2 and 3 for tests conducted on Lanes 1 and 2, respectively. Figures 4, 5, and 6 compare peak responses for surface deflection, surface strain, and strain at the bottom of the asphalt layer using data from the Lane 2 tests. The Lane 1 data show similar effects. These comparisons showed that the effect of tire pressure on the measured responses was small. Increasing the tire pressure from 76 to 140 psi increased the measured responses only 2 to 10 percent. On the other hand, increasing the load from 9,400 to 19,000 lb increased the measured responses 200 to 400 percent. Additionally, the data do not show any consistent trends with respect to tire type. For Lane 2 at the higher load levels, the bias ply tires resulted in higher strains than the radial tires. This effect was probably due to temperature,

rather than tire type. The average pavement temperatures during the bias ply tests at these loads were from 6° to 10°F higher than those during the corresponding radial tire tests. Laboratory resilient modulus data show that this temperature difference would result in a 100,000-psi decrease in the resilient modulus for the asphalt layer.

PAVEMENT PERFORMANCE EVALUATION

During the first phase of research at the PTF, two test sections, Lane 2, Section 3 (Test 2-3), and Lane 2, Section 2 (Test 2-2), were trafficked with the same load but different tire pressures. The wheel load was 19,000 lb and the tire

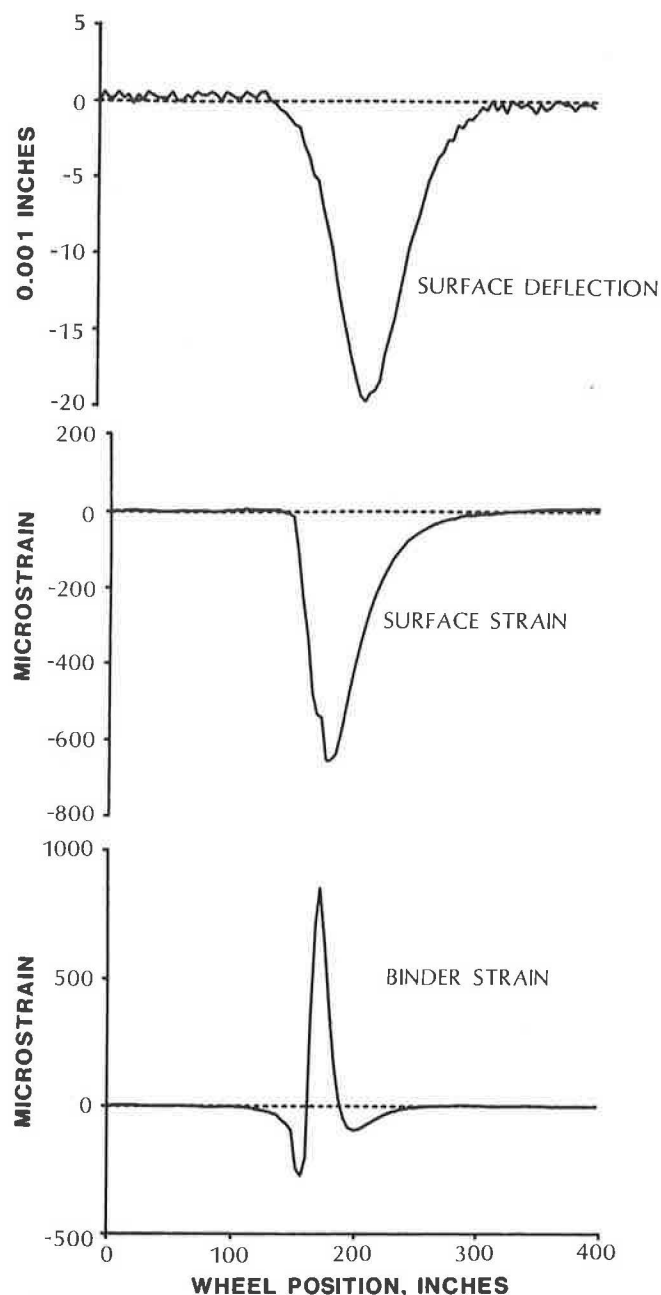


FIGURE 3 Typical response curves.

TABLE 2 SUMMARY OF PAVEMENT RESPONSE DATA FOR LANE 1

Tire	Load	Pressure	Temp.	Surface	Surface	Strain	Binder
Type	(lb)	(psi)	(F)	Deflection	Between	Under	Strain
				(0.001in)	(micro)	(micro)	(micro)
Radial	9,400	76	41.8	8.2	--	-231	212
Radial	9,400	108	42.0	8.1	--	-152	194
Radial	9,400	140	42.1	10.9	--	-201	111
Radial	14,100	76	40.7	14.6	--	-233	292
Radial	14,100	108	40.4	15.1	--	-349	267
Radial	14,100	140	40.8	15.7	--	-294	284
Radial	19,000	76	39.4	26.8	-314	-514	351
Radial	19,000	108	39.4	26.6	-310	-510	377
Radial	19,000	140	39.3	25.3	-306	-514	381
Bias	9,400	76	39.5	10.8	-148	-208	159
Bias	9,400	108	38.9	14.1	-179	-279	123
Bias	9,400	140	38.7	14.1	-168	-276	185
Bias	14,100	76	39.0	18.7	-253	-374	249
Bias	14,100	108	38.8	18.9	-242	-380	277
Bias	14,100	140	38.8	19.0	-248	-372	257
Bias	19,000	76	38.0	26.4	-322	-506	363
Bias	19,000	108	38.6	26.3	-321	-487	374
Bias	19,000	140	38.5	26.3	-330	-519	375

Note "-" denotes compression.

"--" denotes data unavailable.

pressures were 100 psi and 140 psi for Test 2-3 and Test 2-2, respectively. This section describes an evaluation of the effect of tire pressure on rutting and cracking for these two test sections.

Test Conditions

Load and tire pressure were carefully controlled during these tests. Pavement performance, however, may have been significantly affected by other test conditions including environment and construction variability which could not be controlled. These test conditions were quantified as outlined below to aid in the interpretation of the rutting and cracking data.

Temperature and moisture conditions have a significant impact on flexible pavement performance. The stiffness of asphalt concrete is affected by temperature, and the stiffness

of subgrade soils and granular base materials is affected by moisture. Test 2-3 was conducted from January 8 to June 6, 1987, and Test 2-2 was conducted from June 18 to November 24, 1987. To quantify the thermal conditions during testing, daily maximum and minimum air temperatures were obtained from the National Oceanic and Atmospheric Administration weather station at Dulles International Airport, which is located 25 miles west of the PTF. Average air temperatures calculated from this data are shown in Figure 7.

The average air temperature for the first half of Test 2-2 was approximately 80°F, compared to only 40°F for the first half of Test 2-3. Moisture cells, oven-dried samples, and back-calculated moduli from periodic falling weight deflectometer (FWD) tests were used to track moisture content changes. These three methods indicated that moisture equilibrium was reached before trafficking Test 2-3, and moisture conditions remained constant throughout Tests 2-3 and 2-2 (7).

TABLE 3 SUMMARY OF PAVEMENT RESPONSE DATA FOR LANE 2

				Surface	Surface	Strain	Binder
Tire	Load	Pressure	Temp.	Deflection	Between	Under	Strain
	(lb)	(psi)	(F)	(0.001in)	(micro)	(micro)	(micro)
Radial	9,400	76	82.9	5.6	-224	-306	331
Radial	9,400	108	81.7	--	-214	-287	287
Radial	9,400	140	82.2	6.6	-249	-259	307
Radial	14,100	76	79.2	--	-351	-500	508
Radial	14,100	108	78.4	--	-343	-456	504
Radial	14,100	140	78.8	--	-367	-503	553
Radial	19,000	76	78.6	20.3	-527	--	664
Radial	19,000	108	78.3	22.9	-479	--	673
Radial	19,000	140	78.4	22.8	-496	--	699
Bias	9,400	76	85.6	8.0	-224	-287	357
Bias	9,400	108	86.5	7.9	-238	-242	285
Bias	9,400	140	82.9	9.5	-323	--	385
Bias	14,100	76	85.6	14.0	-447	--	617
Bias	14,100	108	84.9	14.3	-474	--	655
Bias	14,100	140	85.1	15.1	-503	--	712
Bias	19,000	76	88.5	19.9	-609	--	857
Bias	19,000	108	88.0	20.1	-662	--	885
Bias	19,000	140	89.4	20.0	-663	--	870

Note "-" denotes compression.

"--" denotes data unavailable.

Thickness and density are two construction variables that have a significant impact on flexible pavement performance. The structural capacity of a pavement is influenced directly by the thickness of the component layers, and density affects the stiffness of paving materials. Pavement layer thicknesses were obtained by differential leveling during construction. Table 4 presents average layer thicknesses for Tests 2-3 and 2-2. Both the asphalt concrete and the crushed aggregate base were approximately 0.5 in. thinner in Test 2-2 than Test 2-3.

In-place densities of the subgrade soil and crushed aggregate base were measured with a nuclear density gauge during construction. The asphalt concrete wearing and binder densities were obtained using cores from untrafficked areas of each section. Table 5 presents average layer densities for Tests 2-2 and 2-3. These data indicate the materials in both test sections were well compacted. The air void content of the asphalt

layers and the density of the crushed aggregate base and subgrade were slightly higher in Test 2-2 than in Test 2-3.

The overall effect of the construction variability was evaluated using nondestructive testing. Deflections for each layer were measured with a falling weight deflectometer. The deflection at the middle of the loading plate was used in conjunction with layer theory to calculate a composite modulus. This composite modulus is a measure of the structural capacity of the pavement. Table 6 presents average composite moduli for FWD tests conducted at the surface of each layer. These data show Test 2-2 initially had a lower structural capacity than Test 2-3.

In summary, Test 2-2 represents a worst-case condition. In addition to the higher tire pressure, the pavement temperature during testing was also higher, and the initial structural capacity was lower than Test 2-3.

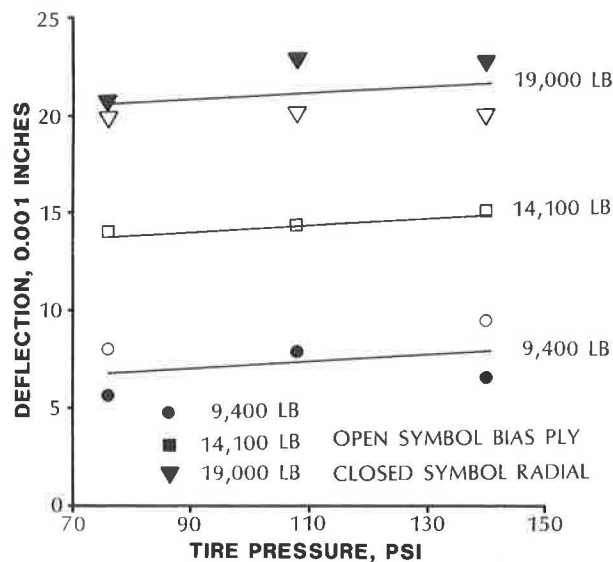


FIGURE 4 Effect of tire pressure on surface deflection for Lane 2.

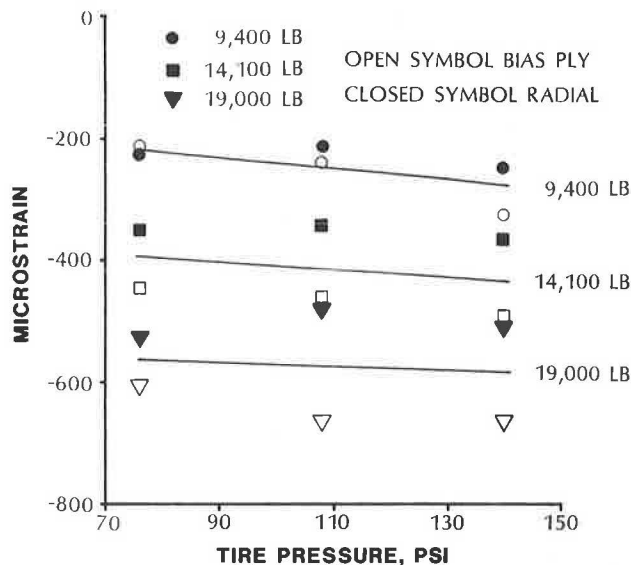


FIGURE 5 Effect of tire pressure on surface strain for Lane 2.

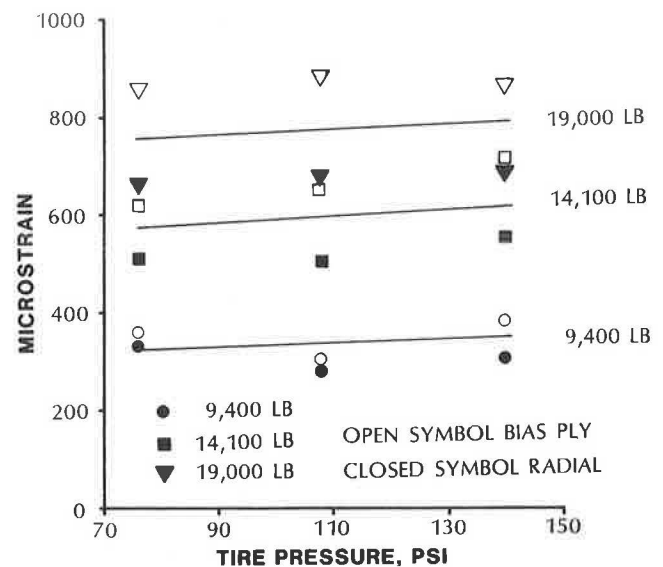


FIGURE 6 Effect of tire pressure on strain at the bottom of the asphalt layer for Lane 2.

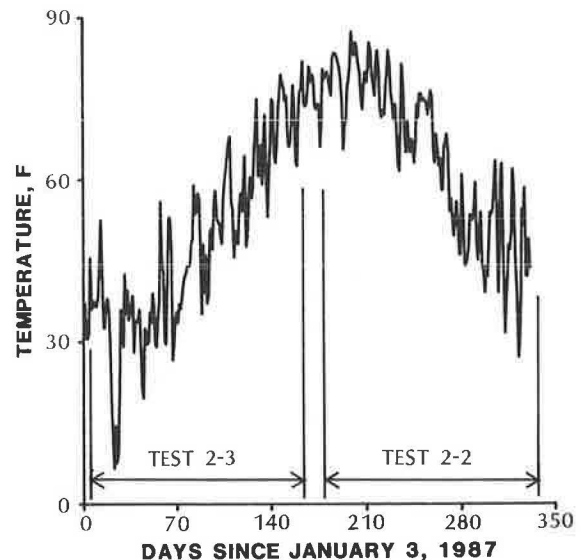


FIGURE 7 Average air temperatures during Tests 2-2 and 2-3.

Results

At the PTF, rutting and cracking data were collected periodically during trafficking. Rutting was obtained by differential leveling at 10 locations along each test section. At each location, the elevation of the pavement surface was measured every 6 inches across the pavement to produce a transverse profile. To eliminate initial surface irregularities from the rut depth data, profiles obtained before trafficking were used as references. Subsequent profiles were subtracted from the appropriate reference to calculate rut depths.

A manual procedure was also used to measure cracking. On a regular schedule, a clear plastic sheet was placed over the test section and the cracks were traced onto the plastic. Different color markers were used each time a crack survey was performed. The test section was then divided into eight

4-ft long by 6-ft wide subsections. The length of cracking in each subsection was measured with a map wheel, and the surface area of AASHTO Class 2 and Class 3 cracking was estimated.

Comparisons of average rutting and cracking for Tests 2-3 and 2-2 are presented in Figures 8 and 9. The comparisons show Test 2-2 had significantly higher rutting than Test 2-3, and cracking began much sooner in Test 2-2. These effects were the result of the higher tire pressure, higher temperature, and thinner pavement structure in Test 2-2.

Analysis

After each test section failed, a postmortem evaluation was conducted in an area of the test section exhibiting average

TABLE 4 AVERAGE PAVEMENT THICKNESSES

Layer	Thickness (in.)	
	Test 2-2	Test 2-3
Asphalt concrete	6.8	7.3
Crushed aggregate base	11.2	11.8
Total	18.0	19.1

rutting and cracking. This evaluation consisted of excavating each layer of the pavement, and obtaining profiles, density measurements, and samples for laboratory testing. The findings of these evaluations were used in conjunction with layer theory to estimate the relative influence of tire pressure, temperature, and thickness on the observed rutting and cracking.

Profiles obtained from the postmortem evaluations indicated that the majority of the rutting in Tests 2-3 and 2-2 occurred in the crushed aggregate base. This rutting is generally governed by the vertical compressive strain at the top of the crushed aggregate base. The ELSYM5 computer program was used to calculate this strain for various temperatures using the load, pavement thicknesses, and tire pressures from the PTF tests.

Moduli for the asphalt concrete at different temperatures were obtained from Figure 10, which shows the modulus-versus-temperature relationship for the PTF asphalt concrete, based on indirect tension tests on cores removed from the

pavement shortly after construction. The moduli of the crushed aggregate base and subgrade were assumed constant at 20,000 psi and 8,000 psi, respectively.

Figure 11 presents the calculated vertical compressive strains at the top of the crushed aggregate base. These data show temperature had the greatest effect on this strain. Assuming an average pavement temperature of 40° and 80°F for the first half of Tests 2-3 and 2-2, respectively, temperature accounted for 66 percent of the increase in the calculated strain at the top of the crushed aggregate base. Tire pressure accounted for 18 percent of the increase, and the 0.5-in. difference in asphalt thickness accounted for the other 12 percent.

Thus, the difference in rutting between Tests 2-3 and 2-2 was due mainly to the higher temperature during Test 2-2. Test 2-2 was trafficked in the summer and fall under relatively high pavement temperatures, while Test 2-3 was trafficked in the winter and spring under much lower pavement temper-

TABLE 6 AVERAGE COMPOSITE MODULI

Layer	Composite Moduli (ksi)	
	Test 2-2	Test 2-3
Subgrade	7.0	8.4
Base	12.0	15.4
Wearing	41.5	49.4

TABLE 5 AVERAGE LAYER DENSITIES

	Test 2-2	Test 2-3
Subgrade		
Average Dry Density, pcf	125.0	119.5
AASHTO T180 Max. Dry Density, pcf	121.7	121.7
Crushed Aggregate Base		
Average Dry Density, pcf	149.3	146.2
AASHTO T180 Max. Dry Density, pcf	152.4	152.4
Lower Lift Binder		
Average Density, pcf	158.3	158.0
Average Air Voids, %	4.3	4.4
Upper Lift Binder		
Average Density, pcf	155.9	161.1
Average Air Voids, %	5.7	2.6
Wearing		
Average Density, pcf	153.8	154.9
Average Air Voids, %	5.4	4.7

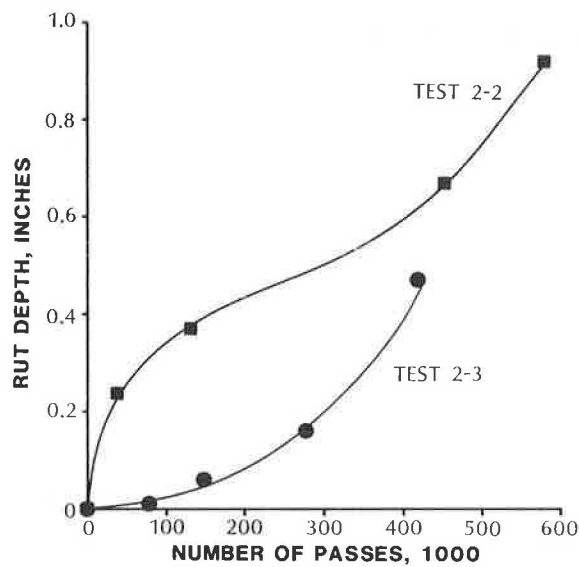


FIGURE 8 Average rutting for Tests 2-2 and 2-3.

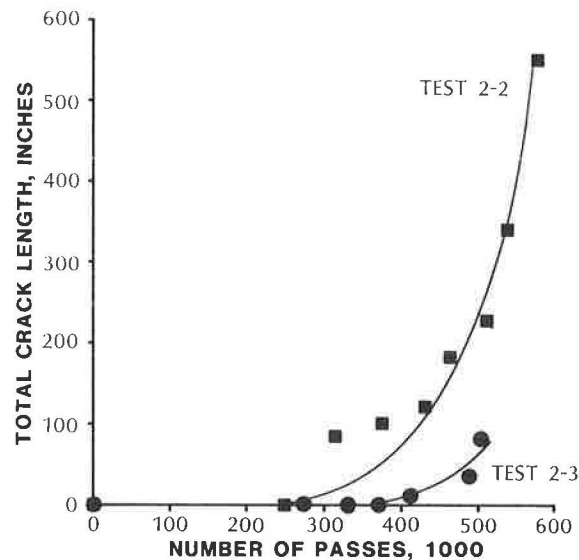


FIGURE 9 Average cracking for Tests 2-2 and 2-3.

atures. The vertical compressive strain at the top of the crushed aggregate base increased with increasing temperatures. At high temperatures, this strain was further increased by higher tire pressure, and decreasing asphalt thickness.

The failure mode for Tests 2-3 and 2-2 was fatigue of the asphalt concrete. This type of failure is generally governed by the tensile strain at the bottom of the asphalt layer. The ELSYM5 computer program was used to calculate this strain for various temperatures using the load, thicknesses, and tire pressures from the PTF tests. The moduli described in the rutting analysis were also used in this analysis. The fatigue damage caused by one repetition of the load for each test condition was calculated using Miner's Law and the following distress prediction model for fatigue cracking (6):

$$N_f = K_1 \left(\frac{1}{e_t} \right)^{3.29} \left(\frac{1}{E^*} \right)^{0.85}$$

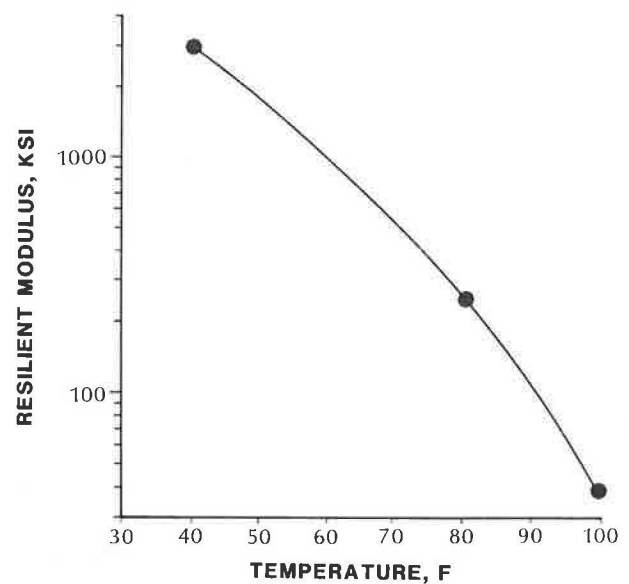


FIGURE 10 Resilient modulus versus temperature curve for PTF asphalt concrete.

where

N_f = fatigue life,
 e_t = tensile strain at the bottom of the asphalt layer,
 E^* = dynamic modulus of the asphalt layer, and
 K_1 = constant.

Figure 12 presents this damage normalized with respect to 70°F, 100-psi tire pressure, and the thickness for Test 2-3. These data show the combined effects of temperature and difference in pavement thickness had the greatest effect on fatigue damage. Assuming average pavement temperatures of 40° and 80°F for Tests 2-3 and 2-2, respectively, temperature only accounted for 14 percent of the difference in expected fatigue damage. At the higher temperature, however, the 0.5-in. difference in asphalt thickness accounted for 53 percent of the difference in expected fatigue damage, while the increased tire pressure accounted for only 33 percent of the difference.

Thus, the difference in cracking between Tests 2-3 and 2-2 was due mainly to the combined effects of high temperature and thinner pavement structure. This combination accounted for 67 percent of the difference in expected fatigue damage.

SUMMARY AND CONCLUSIONS

The effects of tire pressure on flexible pavements were evaluated in two ways. First, pavement responses, deflections, and strains for various combinations of load and tire pressure were measured and compared. Second, rutting and cracking for two test sections trafficked with the same load but different tire pressures were evaluated.

The response evaluation showed tire pressure had little effect on the measured responses at all load levels. Increasing the tire pressure from 76 to 140 psi accounted for only a 2- to 10-percent increase in surface deflection, surface strain, and strain at the bottom of the asphalt layer.

The performance evaluation showed increased rutting and

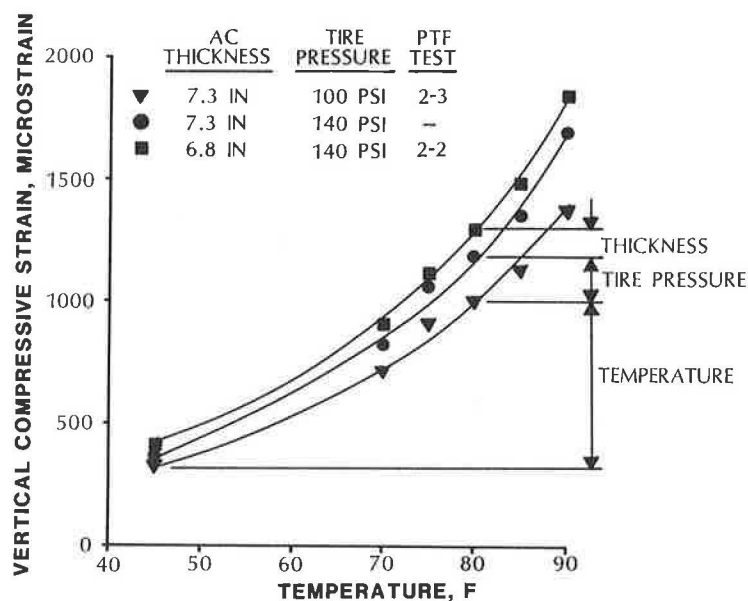


FIGURE 11 Vertical compressive strain at the top of the crushed aggregate base course based on ELSYM5.

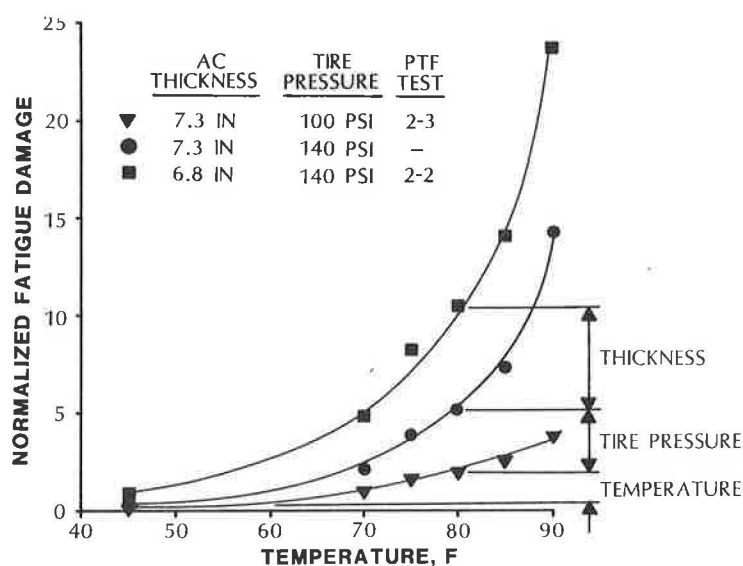


FIGURE 12 Expected fatigue damage.

cracking for the test section trafficked with the 140 psi tire pressure. However, this section was thinner and was trafficked at a higher temperature than the 100 psi test section. An analysis of pavement strains using layer theory showed the increased rutting resulted mainly from the higher temperature. A similar analysis showed the increased cracking resulted mainly from the combined effects of higher temperature and thinner pavement structure.

FUTURE RESEARCH

The PTF permits the study of pavement response and performance under controlled loading conditions. The facility, however, does not provide environmental control. The results

of this study show that for the pavement sections studied, the effects of tire pressure on pavement performance were masked by differences in pavement temperature between the two tests. By moving the ALF between two test sections on a weekly basis, it may be possible to factor out the environmental effects. Various methods for moving the ALF are currently being studied. If a method proves feasible, a similar tire pressure study will be repeated at the PTF during a future phase of research.

ACKNOWLEDGMENTS

The research presented in this paper is part of a staff study sponsored by the FHWA.

REFERENCES

1. K. M. Marshek, H. H. Chen, R. B. Connell, and C. L. Saraf. Effects of Truck Tire Inflation Pressure and Axle Loads on Flexible and Rigid Pavement Performance. In *Transportation Research Record 1070*, TRB, National Research Council, Washington, D.C., 1986.
2. H. F. Southgate and R. L. Dean. *Effects of Load Distributions and Axle and Tire Configurations on Pavement Fatigue*. Research Report UKTRP-85-13. Kentucky Transportation Research Program, University of Kentucky, Lexington, 1985.
3. F. I. Roberts, J. T. Tielking, D. Middleton, R. L. Lytton, and K. Tseng. *Effects of Tire Pressure in Flexible Pavements*. Research Report 372-1F. Texas Transportation Institute, Texas A&M University, College Station, 1986.
4. Organization for Economic Cooperation and Development. *Strain Measurements in Bituminous Layers*, Paris, France, 1985.
5. D. A. Anderson, W. P. Kilareski, and Z. Siddiqui. *Pavement Testing Facility—Design and Construction*. Report FHWA/RD-88-059, FHWA, Washington, D.C., 1987.
6. F. Finn, C. L. Saraf, R. Kulkarni, K. Nair, W. Smith, and A. Abdullah. *NCHRP Report 291: Development of Pavement Structural Subsystems*. TRB, National Research Council, Washington, D.C., 1986.
7. D. A. Anderson, P. Sebaaly, and N. Tabatabae. *Pavement Testing Facility—Performance of the Initial Two Test Sections*. Report FHWA/RD-88-060, FHWA, Washington, D.C., 1987.

The contents of this paper reflect the views of the authors, who are responsible for the accuracy of the data presented. The contents do not necessarily reflect the official views or policies of the FHWA.

Publication of this paper sponsored by Committee on Flexible Pavement Design.

Effects of Tires and Tire Pressures on Road Pavements

MATTI HUHTALA, JARI PIHLAJAMÄKI, AND MARKKU PIENIMÄKI

The Road and Traffic Laboratory of the Technical Research Center of Finland has developed gauges to measure strain and stress in bituminous and unbound layers and in the subgrade and has also developed a sophisticated microcomputer system for collecting and handling data. These gauges have been used in research concerning pavement design and to measure the response due to moving vehicles at the Virttaa test field. The aggressiveness of different axle loads; single, tandem, and tridem axles; single, twin, and wide-base tires; and tire pressures have been compared at speeds of 50 or 80 km per hour. This paper describes the effects of tires and tire pressures. Two twin tire and three wide-base tire types were compared. Three axle loads were used for each type. Three tire air pressures were used for each axle load and tire type. The load was seldom evenly distributed on both twin tires. That condition was simulated with different tire pressures (500 kPa and 1000 kPa) in the twin tires. Certain tire/pavement contact pressure distribution measurements were also made.

The importance of road transportation has grown everywhere in the world during the last several years—not only as the result of the development of the road infrastructure but also as a result of the technical development of trucks. Vehicles are heavier and their load-carrying capacity is greater. Engines are more powerful, cabs more comfortable, and important developments have been made in axles, tires, and suspensions.

The increased traffic and heavier vehicles cause much more distress to roads than ever before. The regulations of weights and dimensions are even more important in the wake of substantial pressure from the transportation industry to allow heavier and larger vehicles on the highways. The recent developments in tires, axles, and suspensions are important from the standpoint of the road engineers.

Most of the new developments seem to increase distress to the pavements. New regulations often come only after technical development—or may, in some cases, hinder technical development. The technical basis for regulations has often been vague. One reason is that the regulations require special knowledge somewhere between the expertise of mechanical engineers and civil engineers. The following lists perhaps the most important technical changes in vehicles, as they relate to roads:

- Tridem axles,
- Tandem axles with different tires and loads on axles,
- Radial tires,
- Increased tire pressures,
- Wide-base tires instead of twin tires,

- Smaller tires capable of carrying the same load, and
- New suspensions, especially air suspensions.

In order to study the effects of different tires, axles, and suspensions, four approaches can be used: (a) full-size road tests, (b) measurements of stresses and strains in pavements (response measurements), (c) theoretical (mechanistic) calculations of stresses and strains in pavements, and (d) measurements of dynamic axle loads in the vehicle.

In the first approach, the road is damaged by repeated loads. If moving trucks are used as loads, the test is quite expensive. The most famous and complete test run was the AASHO Road Test from 1957 to 1961, from which the basic formulas for the effects of different axle loads and the equivalency of the single and tandem axles have come (and are still used, even though vehicles and tires have changed considerably in 30 years). The circular or linear test tracks are important to pavement research but have only limited use for this purpose. Road tests give the only real and reliable results and the results received by other means should be compared to actual road tests.

The mechanistic calculations by multilayer or finite element computer programs are inexpensive and easy, but because the basic assumptions of the behavior of tires and pavements must be simplified, the results may be erroneous and should be verified. However, the scope of the results received by other means can be extrapolated with these calculations.

The stresses and strains in the pavement due to a passing vehicle can be measured (response measurements). The results are turned into equivalency factors using appropriate failure criteria. Because the equivalency factors are compared with each other, their exact validity is not important. The results may reveal, for instance, the behavior of different tires and uneven distribution of the load within tandem axles or twin tires, which is seldom taken into account in mechanistic calculations. The results are clear and easily explained, which is important because of the economic and political pressure groups.

In the above approaches, the road is even or it is assumed to be even. The effect of suspensions is mostly neglected. The effect of suspensions can be studied by measuring the dynamic axle loads in the vehicle. Corresponding response measurements can be done simultaneously in the pavement.

The Road and Traffic Laboratory of the Technical Research Center of Finland (VTT) began developing gauges to measure strains and stresses in bituminous and unbound layers and in the subgrade in the early 1980s. Field measurements were made at the Virttaa test field, which is a 3-km-long, 40-m-wide part of a highway that is used as a temporary airfield by

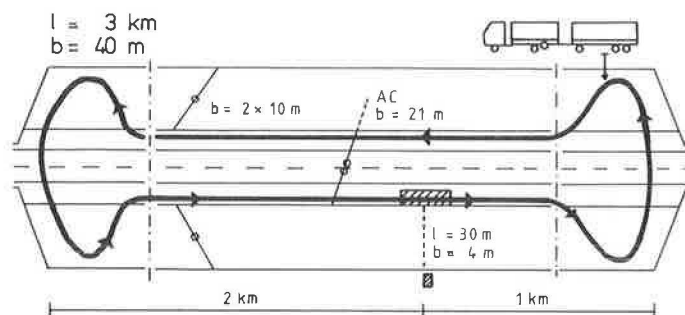


FIGURE 1 Virttaa test field.

the Finnish Air Force (Figure 1). Any truck or vehicle combination can easily attain the maximum legal speed of 80 km per hour and drive back on the other side. The circling time is 5 to 6 min. The test section currently has two pavements; the thicknesses of the bituminous layers are 80 and 150 mm.

The Virttaa test field has been used for both developing pavement design, and measuring the response of different vehicles (loads, axles, tires, suspensions, etc.).

The first measurements were made at Virttaa in 1983. Five truck combinations were compared (1). In 1984, practically all 12 axle combinations (single, tandem, tridem, wide-base tires, etc.) that were used in Finland were compared (2). The results have impacted directly on the Finnish legislation concerning axle load limits of tandem and tridem axles.

Eleven countries from three continents participated in a common, full-scale pavement test in Italy in April 1984 (3–5), which compared strain measurements in bituminous layers. The strain gauges developed by VTT performed well.

During the following years, the measurements were concentrated on pavement design problems, as well as further development of both the gauges and a sophisticated micro-computer program to collect and handle the data. Measurements of the dynamic axle loads in a vehicle, the effects of unevenness on the strains and stresses in the pavements, and the effects of suspensions have also been started.

VTT made measurements concerning the effects of tire types and tire pressures in 1984 and 1985. A more systematic research program was realized in 1987. The project included the comparisons of two twin tires and three wide-base tires, all with three axle loads and three tire pressures. Uneven tire loads within twin tires were simulated with air pressure differences. All together, 51 combinations were measured.

VTT also measured static contact pressure distributions between the tire and the pavement. A new device for measuring dynamic contact pressure distribution has been constructed, and the first results at speeds of 5 to 80 km per hour (3 to 50 mph) are quite promising.

This paper handles the effects of tire types and tire pressures and the first results of contact pressure distribution measurements.

MEASUREMENT METHODS

The main measurement system consisted of strain gauges glued to 6-inch core samples that fit into a hole in the pavement with a tolerance of less than 1 mm. The samples were glued

to the bituminous pavement. The gauges acted as an integral part of the bituminous layer and had no strengthening effect (the flexibility was the same as that of the bituminous layer) and thus did not disturb the stress distribution. The gauges had no elastic part, and thus plastic deformation and relaxation could also be followed (up to 30 min). Installation of the gauges demanded meticulous work.

Strain gauges are placed in longitudinal or transverse positions at the bottom of bituminous layer or on the surface, or they can be installed in cores at different depths. Longitudinal gauges at the bottom of the bituminous layers have been used to compare the effects of different axles or tires.

The diagram-type pressure cells were manufactured by VTT. They were installed at five depths; however, only those at –250 mm, –400 mm, and –700 mm were used in these measurements.

In 1987, the field had two test sections, bituminous layers 80 and 150 mm, 58 working strain gauges in bituminous layers, and 25 working pressure cells in unbound layers and subgrade. The longitudinal section of the test area is presented in Figure 2.

The measurement system is shown in Figure 3. Ten strain gauges and six pressure cells were attached to amplifiers, a/d units, and a microcomputer. An electric eye started the operation.

A typical signal of a passing vehicle combination (six axles) is presented in Figure 4 (directly from a computer display). The computer measured the peak values, which are shown on the right side of Figure 4. The transversal position of the right side tires was measured and is shown in Figure 4 in relation to the gauge line in the lower right corner. In this figure, the front tire was outside the line, the right edge of the left twin tires of the tandem axles went over the line, the front left twin tire of the trailer went over the line almost in the middle, and the left tires of the trailer tandem axles were exactly in the middle. Note, too, that the vehicle ran similar to a dog—slightly sideways.

The peak values of the first axle of the trailer are presented as a function of the transversal position in Figure 5 (directly from a computer display). The vehicle is the same as in Figure 4. It can be seen that there are too few points between the transversal positions –10 and –20 cm, which was why the driver was asked to drive the following passes between these values. After the shape in Figure 5 was well-defined, the peak value was determined by using the computer's mouse accessory.

The strain values in Figure 5 were temperature corrected. The same figure can be drawn without temperature correc-

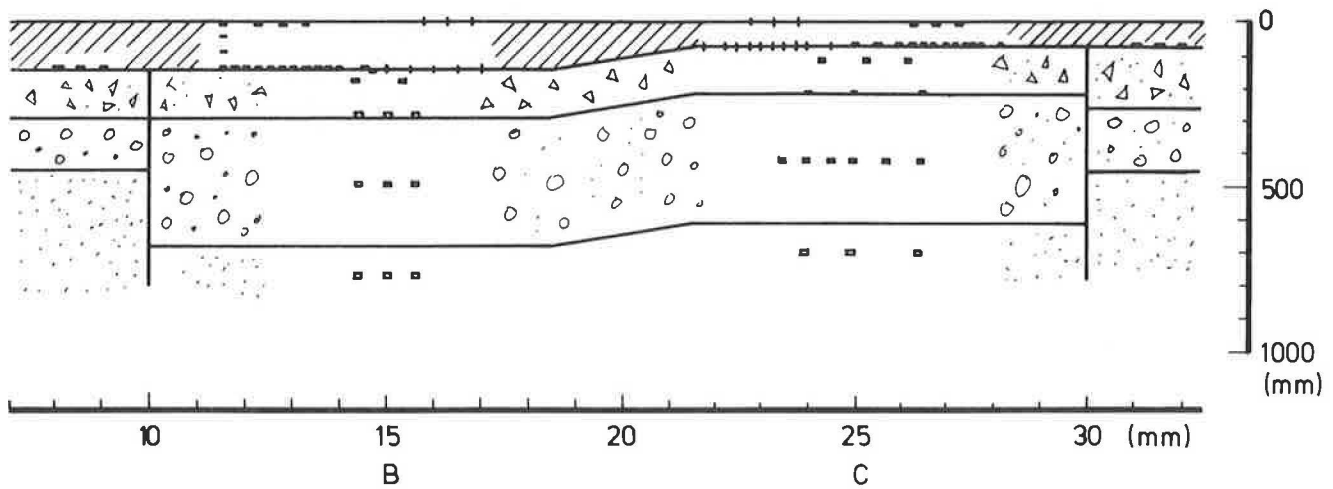


FIGURE 2 Longitudinal section of the test area.

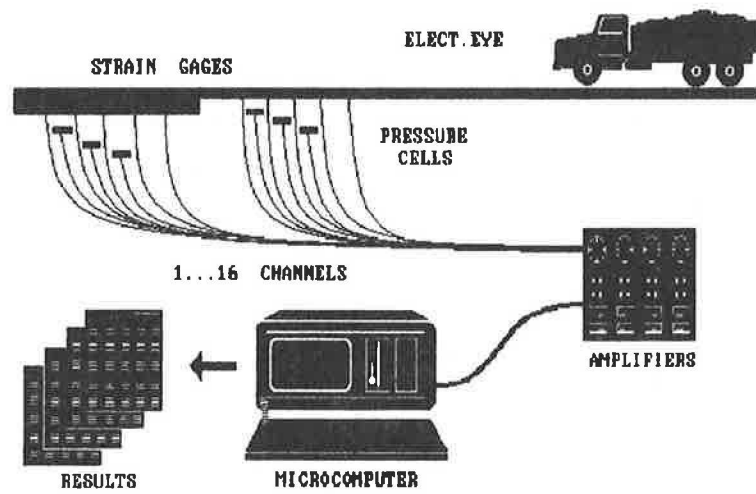


FIGURE 3 Measurement arrangements.

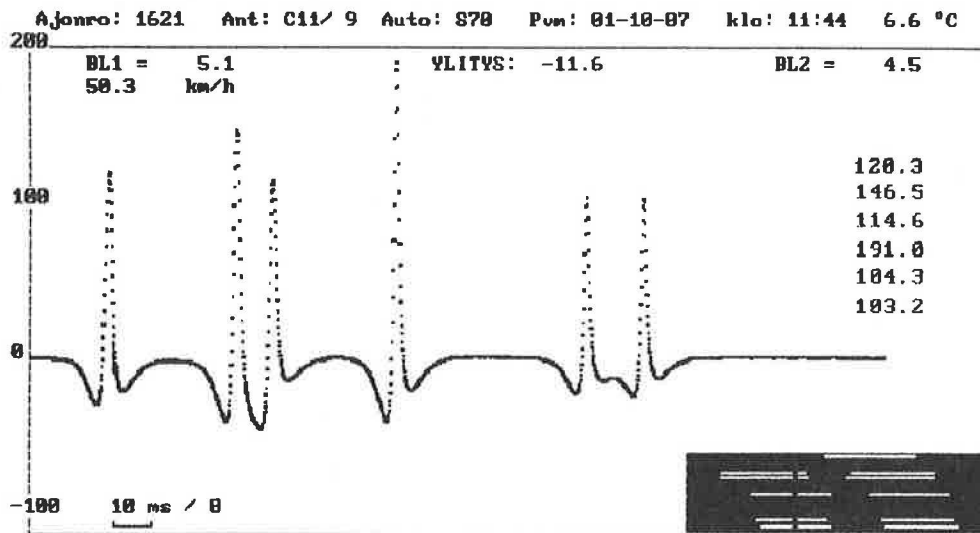


FIGURE 4 Typical signal from a strain gauge.

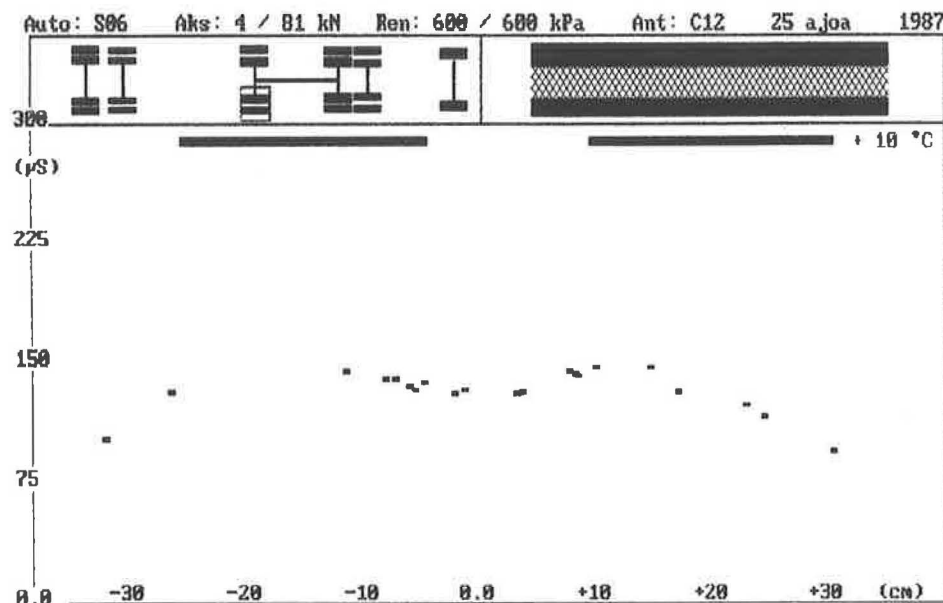


FIGURE 5 An example of strains as a function of the transversal position.

tion; the temperature is shown in that case at each point for closer analysis.

The strain or stress values were turned into an equivalent number of axle passes using appropriate failure (fatigue) criteria (the exponent of the fourth power law is 4.2). Equivalent numbers were compared to those of a standard (reference) axle, which carried a 10-ton, single axle with twin tires 12R22.5 and having the 700 kPa tire pressure. That value is called the equivalency factor and describes the damaging power or the aggressiveness of the axle. If the equivalency factor is 2, for example, the pavement will last only half as long as with a standard axle. Because the equivalency factors are compared, the exact validity of the failure criterion is not important.

The bending of axles corresponded well with the dynamic axle forces and was easy to measure with strain gauges. Accelerometers on the axles and in the vehicle gave more information about the forces (16 channels could be measured simultaneously). Measurements have been made on artificial bumps and on ordinary highways.

The contact pressure distribution between the truck tire and the pavement was measured in the laboratory. The tire rolled slowly over a measuring point and the force was measured. Axle loads and tire pressures were varied. Wide base tires could not be measured because of the restrictive dimensions of the apparatus.

A dynamic contact pressure measurement device was constructed by VTT, with 16 measuring points, the distance c/c 20 mm, and total width of 300 mm. The microcomputer continuously measured all 16 channels as the tire rolled over and a three-dimensional, contact-pressure/longitudinal-and-transversal-dimensions figure was drawn automatically on the computer display. The transversal position of the tire was measured. A computer program that could superimpose consecutive passes on the same figure is being developed.

Special attention was paid to the construction of the measuring points in the design of the device. Measurements were made at speeds up to 80 kmph and the results have been promising.

RESEARCH PROGRAM

Five types of tires were used in this research: (a) 12R22.5 twin tires, (b) 265/70R19.5 twin tires, (c) 445/65R22.5 wide base tires, (d) 385/65R22.5 wide base tires, and (e) 350/75R22.5 wide base tires.

The markings were inconsistent, however. The letter *R* denotes radial tire, the number following the *R* is the diameter of the rim or the inner diameter of the tire (in inches). The first number gives the width of the tire in inches (Type 1) or in millimeters (Types 2 through 5). In the past, the height and width of a tire was about the same (the aspect ratio is 100 percent), but now, the tires may be flatter. The height is 65 to 75 percent of the width in Types 2 through 5 (the percentage is the number after the slash).

The tires are typical (but not necessarily those most used) in Finland, because the number was limited and enough variety in dimensions was needed. All are radial tires. Tires 1 and 3 can carry 11 to 12 tons (the legal axle load limit for single axles is 10 tons), and tires 2, 4, and 5 can carry 8 to 8.5 tons (the legal limit for tandem axles is 16 tons). The diameter of Type 2 is 20 percent less than Type 1, and the Type 2 tire was used to provide more height for the load or to lower the trailer platform.

All the tires were measured with three axle loads—in most cases, 10 tons (or the nominal maximum), 20 percent more, and 20 percent less.

For each load, three tire pressures were used. The tire pressure recommended by the tire manufacturer for that tire and load was used as the base (optimal) tire pressure. The other tire pressures were, in most cases, 20 percent more and 20 percent less. The tire pressures varied from 480 to 1080 kPa, most common for optimal loads were 700 to 850 kPa.

A special difficulty in comparing wide-base and twin tires is that the load in twin tires is usually assumed to be divided evenly on both tires, which is seldom true. The uneven load distribution between twin tires may be a result of several factors:

- Tires did not wear evenly; for instance, one was older than the other,
- The manufacturer or the brand was not the same,
- The tire may have been new or retreaded,
- There was more or less fatigue in the carcass,
- Tire pressures differed,
- Tire temperatures differed and, as a result, tire pressures differed,
- Uneven road pavement (ruts, crown), and
- The camber angle or the bending of the axle.

The uneven load distribution between twin tires was simulated in a series of measurements where one tire had a tire pressure 500 kPa and the other 1000 kPa.

The vehicle consisted of a truck and a trailer. The front axle of the trailer was in a dolly, and the measured tires were installed in that axle. The load in the truck was kept constant all the time and was used as a reference for temperature corrections.

Hour-to-hour and day-to-day temperature variations are smallest during the fall, which is why measurements were taken in September and October. About 30 passes are usually needed to obtain a well-defined shape of the strain/transversal position (Figure 5), which required about 1600 vehicle passes.

During the measurements, 16 channels were used (five strain gauges for both pavements and three pressure cells at three levels for both pavements)—25,000 peak values for the tires to be compared. In addition, the strains due to the reference vehicle (front and tandem axles) were measured and handled. That means about 100,000 peak values of signals were stored and handled (all the signals were saved on diskettes for pos-

sible later use). The number of strain/transversal position figures of tires to be compared (Figure 5) was 852, and the total number (including the figures of the reference truck) was 3,300. Fortunately, not all of the reference truck figures were needed. To store and handle this data, sophisticated micro-computer programs were developed during the earlier research programs.

RESULTS

The main results are shown in Figures 6 and 7 as equivalencies as a function of axle loads. If the equivalency is, for instance, 2, the damaging power (aggressiveness) of that axle is twice that of the reference axle (a carrying 10-ton single axle with twin tires 12R22.5, the tire pressure 700 kPa) or the pavement lasts in that case only half as long as with the standard axle.

Figures 6 and 7 show that the traditional twin tire 12R22.5 causes the least stress on the pavement (least aggressive). The next best is the smaller twin tire 265/70R19.5. The wide-base tires are also more aggressive than twin tires. Within wide-base tires, wider tires are less aggressive than narrower tires.

The wide-base tires are relatively more aggressive on thin bituminous pavements than on thick pavements. All the tire types seem to have relatively the same sensitivity for the change of relative axle loads. For instance, 20 percent overload doubles the aggressiveness.

The axle loads that correspond to an equivalent value of 1.0 have been taken from Figures 6 and 7 and are presented in Table 1. The tire pressures are optimal.

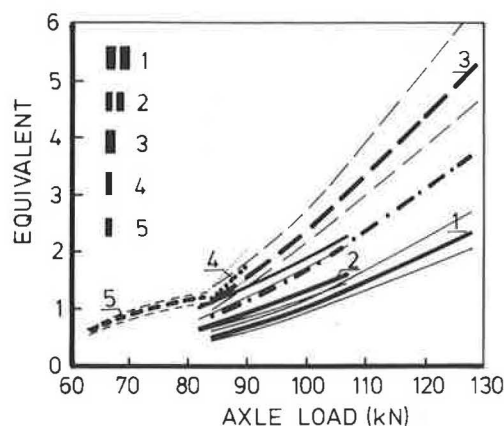


FIGURE 6 Equivalencies as a function of the axle load (bituminous layer thickness, 80 mm).

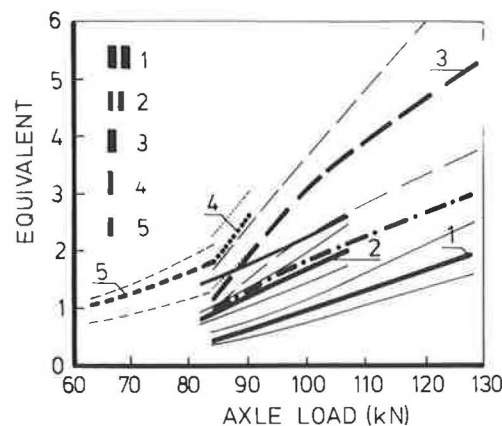


FIGURE 7 Equivalencies as a function of the axle load (bituminous layer thickness, 150 mm).

TABLE 1 AXLE LOADS CORRESPONDING TO REFERENCE AXLE AND EQUIVALENT VALUES CORRESPONDING TO 84-kN AXLE LOAD

Tire Type	Equivalent Axle Load (kN) by Thickness of Bituminous Layers (mm)		Equivalent (84-kN) Values by Thickness of Bituminous Layers (mm)	
	80	150	80	150
12R22.5 twin	100	100	0.33	0.35
265/70R19.5 twin	86	93	0.87	0.58
445/65R22.5	81	81	1.23	1.14
385/65R22.5	65	78	2.34	1.22
350/75R22.5	61	75	2.37	1.28

A vertical line was drawn in order to have equivalent values that correspond to the same axle load of 84 kN (Table 1). The 84-kN axle load was selected because it is the only load that has been used on all the tire types. The same kind of comparisons can be made for the whole area of Figures 6 and 7, but interpolation and extrapolation are needed, which may give misleading results.

The approximate effect of tire pressure can be seen in Figures 6 and 7. The equivalencies of all tire types as a function of tire pressure have been drawn in Figure 8 (the axle load is 84 kN).

It can be seen from Figure 8 that no optimal tire pressure exists from the standpoint of the pavement, which is contrary to the opinions of some tire manufacturers, but the equivalencies increase with tire pressure.

The effect of tire pressures and axle loads is presented in Figure 9 (reference twin tire 12R22.5). The comparisons between twin tires and wide-base tires are always theoretical

to a certain degree, because the load is assumed to be evenly distributed on both twin tires. The uneven load distribution is simulated with tire pressures 500/1000 kPa, which increases the equivalencies by 60 percent.

The effect of tire pressures is shown in Figure 10. The values have been calculated so that the value is 1.00 with full-axle load and optimal tire pressure. The tires behave in different ways. Relative changes in the tire pressure give different changes in the load values.

The contact pressure distribution of some personal car tires is seen in Figure 11. The highest pressures are at the sides of the tires. It seems that pressure distribution differs among brands (those in Figure 11 are from different manufacturers). The measurements here are static.

It is often assumed that the contact pressure distribution of truck tires is similar. According to our few measurements, both static and dynamic, the highest pressure is always in the center, as seen in Figure 12 (static measurements).

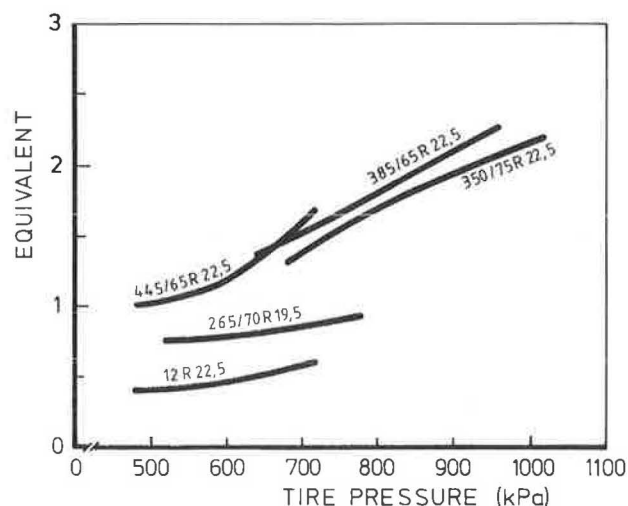


FIGURE 8 Equivalencies as a function of tire pressure (axle load, 84 kN; bituminous layer thickness, 80 mm).

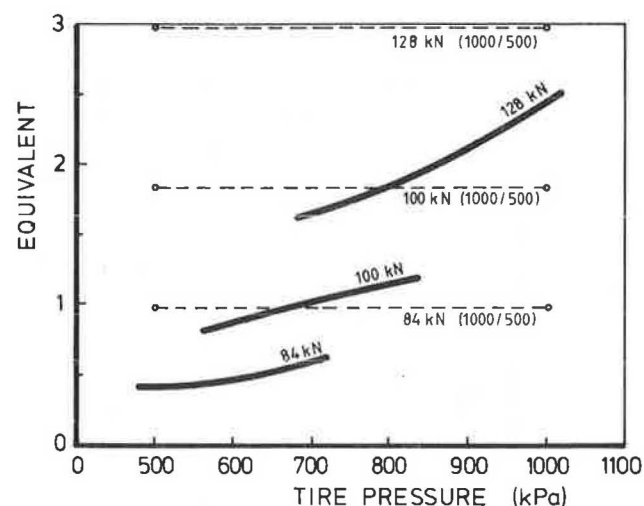


FIGURE 9 Equivalencies as a function of tire pressure (reference twin tire 12R22.5). Simulation of uneven load by tire pressures 500 to 1,000 kPa.

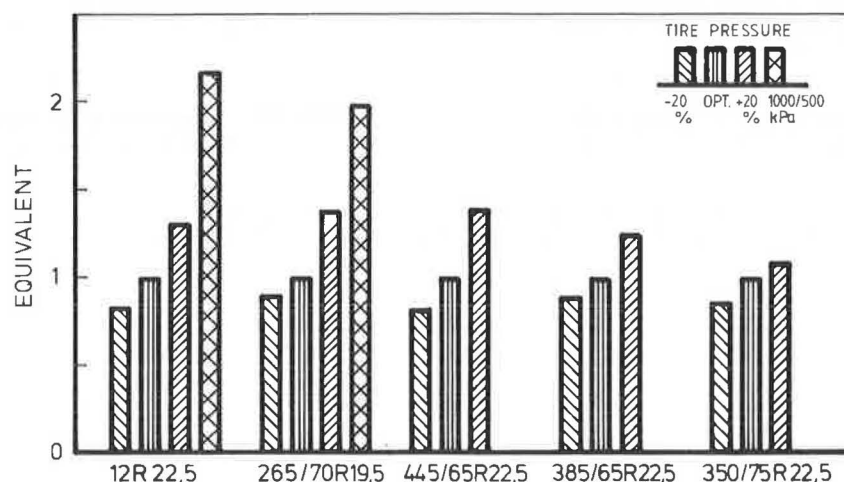


FIGURE 10 Relative values for the effect of tire pressure.

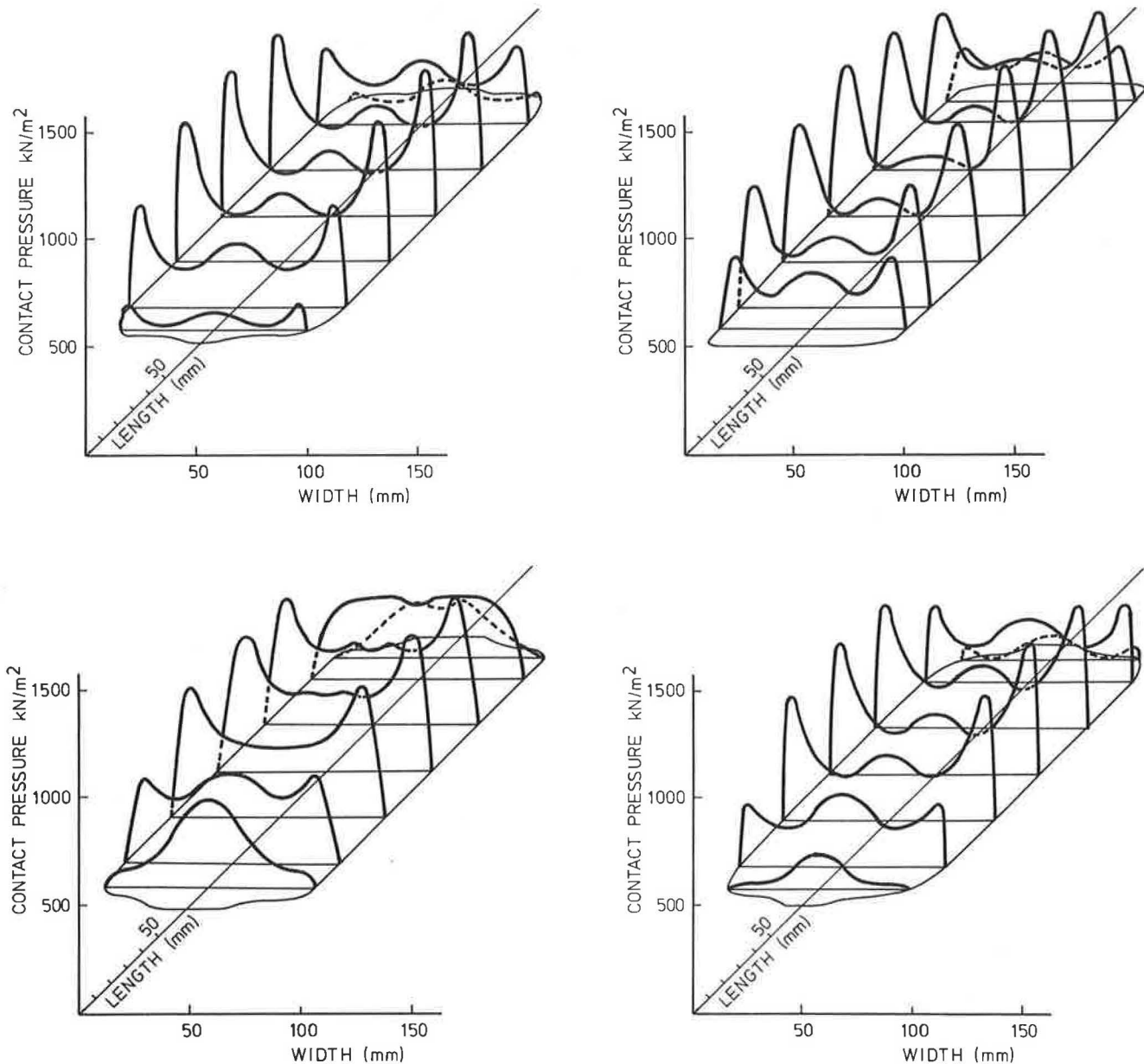


FIGURE 11 Static tire/pavement contact pressure distributions of different personal car tires.

CONCLUSIONS

The following conclusions concerning radial truck tires can be drawn:

1. Clear differences between tires and tire pressures could be found by response measurements. The response was changed to aggressivity, using fatigue curves (the exponent 4.2).
2. Wide-base tires are more aggressive than twin tires by a factor of 2.3 to 4.0 in ideal conditions for twin tires.
3. The load is seldom evenly distributed on both twin tires. The uneven load was simulated by tire pressures, 500 kPa in one and 1,000 kPa in another tire. Despite this, wide-base tires were more aggressive by a factor of 1.2 to 1.9 if they were compared to the most common twin tire. If they were

compared to the small size twin tires, single tires were, in some cases, less aggressive by a factor of 0.8.

4. Among wide-base tires, there are differences by a factor up to 1.6.
5. Among wide-base tires, wider tires are less aggressive.
6. Smaller twin tires are more aggressive than normal size twin tires by a factor of 1.5 to 2.0.
7. All the differences are greater if the bituminous layers are thinner, and smaller if the layers are thicker.
8. As the tire inflation pressure increases, the aggressiveness increases; there is no optimum. An increase of 20 percent increases the aggressiveness 1.1 to 1.4 times.
9. The tire/pavement contact pressure distribution depends on the structure of the tire (for instance from different manufacturers), tire inflation pressure, and driving forces (driving

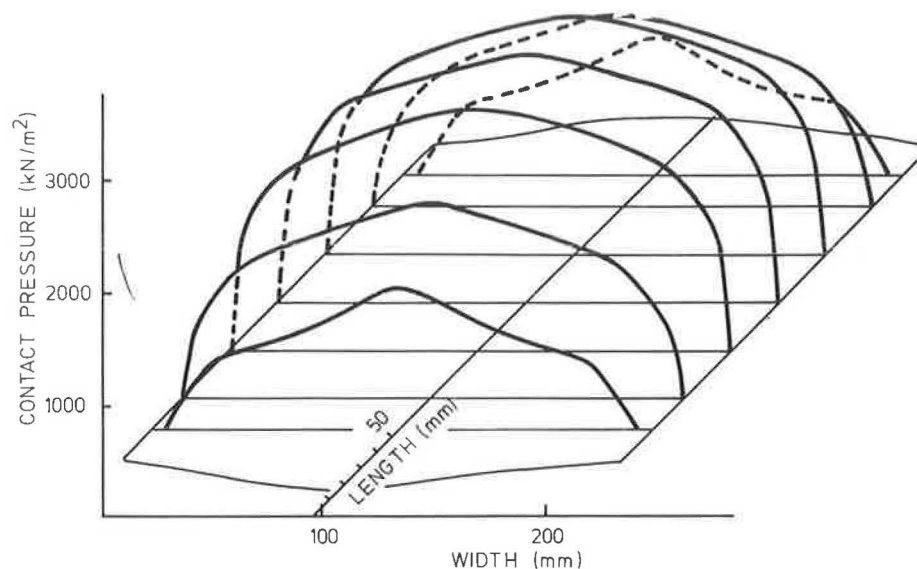


FIGURE 12 An example of static tire/pavement contact pressure distribution of a truck tire.

or carrying). The data are insufficient at this time for further conclusions.

10. The contact pressure between the tire and the pavement is greatest in the center for truck tires. In personal cars, the pressure is greatest on the sides (limited data are available at this time).

11. Only the aggressiveness to the road was studied in this research project. Other factors such as rolling resistance, safety, and economy will be considered in future studies.

SUMMARY

The results from the tire and tire pressure measurements have not been thoroughly analyzed yet, and the results presented here should be taken as preliminary conclusions. The final results will be published in 1989, also in English.

The research programs have always begun with a pilot study. The system for the dynamic axle load measurements has been developed (all axles in a vehicle simultaneously). The dynamic forces are correlated with the strains and stresses in the pavements. Measurements concerning the effect of unevenness have been made on artificial bumps and on ordinary highways. The comparisons of different suspensions have also been started. Data handling is time consuming, although the data-handling system is sophisticated.

A dynamic contact pressure measurement has been continued, but the data are limited at this time.

Although only the aggressivity to the road has been studied as yet, other aspects have not been forgotten, and it is likely

they will be considered later. For example, as twin tires and wide-base tires are compared, other factors such as rolling resistance, safety, and economy should be considered.

ACKNOWLEDGMENTS

The Roads and Waterways Administration of Finland sponsored the development of the measurement system and most of the research. The Transport Research Commission (Sweden) sponsored most of the research concerning tires and tire pressures.

REFERENCES

1. M. Huhtala. The Effect of Different Heavy Freight Vehicles on Pavements. Presented at the Tenth International Road Federation World Meeting, Rio de Janeiro, October 1984.
2. M. Huhtala. The Effect of Different Trucks on Road Pavements. *Proc., International Symposium on Heavy Vehicle Weights and Dimensions*. Kelowna, British Columbia, Canada, June 8–13, 1986.
3. Organisation for Economic Co-operation and Development. *Full-Scale Pavement Tests*. OECD, Paris, 1985. 101 pp.
4. Swiss Federal Office of Highways. *Strain Measurements in Bituminous Layers*. Research Report No. 103, Bern, Switzerland, 1985.
5. I. F. Scazziga, A. G. Dumont, and W. Knobel. Strain Measurements in Bituminous Layers. *Proc., Sixth International Conference on Structural Design of Asphalt Pavements*, University of Michigan, Ann Arbor, 1987, pp. 574–589.

Publication of this paper sponsored by Committee on Flexible Pavement Design.

Effect of Tire Pressure and Type on Response of Flexible Pavement

PETER SEBAALY AND NADER TABATABAEE

Radial, bias, and wide-base radial single tires were tested in the laboratory under three levels of inflation pressures and axle loads. The measured characteristics of the tires were gross contact area, net contact area, tire deflection, and contact pressures. Distributions of the contact pressures were used in a mechanistic solution to predict various flexible pavement response parameters. A modified version of the BISAR computer program, which takes concentric circles of various pressures, was used to predict the response parameters. The response of various flexible pavement structures was investigated in terms of the tensile strains at the bottom of the asphalt layer, the compressive stress at the asphalt layer interface, and the surface deflection. The effects of tire inflation pressures and axle loads on the response parameters were evaluated for all tires and asphalt thickness combinations. The three tire types were also compared for underloaded, loaded, and overloaded cases.

During the past 20 years, truck tire pressures have increased. Today a majority of the trucking industry runs tires at pressures around 100 psi, up from 75 psi (1). A motive for this trend toward increased tire pressures can be found in the economics critical to the highly competitive trucking industry: load capacity, fuel economy, and durability.

However, tire selection and inflation pressures may have an impact on pavement response and long-term performance. Therefore, the pavement community and vehicle and tire manufacturers should cooperate to handle these sometimes conflicting needs in the most effective and practical way. Communication is essential to ensure that pavement design technology is based on realistic field parameters.

BACKGROUND

Several investigators have performed limited studies on the effect of tire inflation pressure on pavement. Roberts et al. (2) used the Tielking finite element model (3) to calculate the pressure distribution at the contact patch. For a common 10.00-20 bias-ply truck tire inflated to 75 and 125 psi, the highest local contact pressures were estimated to be twice the inflation pressures.

Their study concluded that an increase in tire inflation pressure from 75 to 125 psi produced an increase in the tensile strain ranging from 20 to 30 percent for the 1-in. surface. The stiffest base layer caused the greatest increase in tensile strain at the bottom of asphalt. Increasing the thickness of the asphalt concrete layer reduced pavement vulnerability to high tire pressures. The increase in tensile strain at the bottom of a 4-

in.-thick asphalt concrete layer for tire pressure of 125 psi was less than 10 percent, as compared to the strains under 75 psi inflation pressure (2). The study also compared calculated pavement strain for a uniformly distributed tire contact pressure (equal to tire inflation pressure) to a nonuniformly distributed one (2). The uniform contact pressure underestimated the tensile strains at the bottom of the asphalt layer.

Marshek et al. (4) used experimentally obtained contact pressure distributions from one treaded and one bald tire as an input to the multilayered elastic analysis program, BISAR. They found that higher truck tire inflation pressure corresponds to a significant increase in tensile strain at the bottom of the asphalt concrete layer and, therefore, a significant decrease in fatigue life of pavement. For example, changing tire pressure from 75 to 110 psi resulted in a 33 percent increase in tensile strain and a 60 percent reduction in a fatigue life of the pavement. Marshek et al. reported that the increase in tire inflation pressure increased the compressive strains at the top of subgrade by less than 2 percent for either the uniform pressure model or the nonuniform one (4). Therefore, they concluded that tire inflation pressure was an insignificant factor in causing subgrade rutting.

In this study, the Goodyear Tire and Rubber Company provided laboratory measurements for radial, bias, and wide-base radial tires. Current U.S. line haul trucking has made a transition from bias to radial tires, and wide-base singles could be an increasing factor, as they now are in Europe. In-service wide-base radial singles have higher load/tire contact area ratios than traditional duals and, thus, are of concern to some highway officials. The research presented in this paper evaluates the effect of each tire type on pavement response for various pavement structures and tire load/inflation conditions.

PAVEMENT PERFORMANCE

Field testing has shown that the performance of flexible pavements can be related to certain failure mechanisms. From a structural capacity standpoint, flexible pavement may experience two kinds of failure: fatigue, which shows as excessive alligator cracking, or rutting, which shows as permanent deformations along the wheel path.

Fatigue distress, the failure most encountered in flexible pavements, causes the greatest portion of rehabilitation cost. Researchers and investigators have proposed and implemented various types of laboratory tests and field measurements in an effort to predict the fatigue failure in actual pavements. Whether laboratory testing or theoretical analysis was used, the idea of relating tensile strain at the bottom of the

asphalt layer to the number of load repetitions was adopted by several researchers. Rauhut and Kennedy (5) showed 13 curves that related strains in asphalt concrete to number of load repetitions of 18-kip axle load. Their study indicated that the fatigue life of a flexible pavement may be predicted if the critical horizontal strain at the bottom of the asphalt layer is evaluated.

In a recent NCHRP study, Finn et al. (6) recommended equations to predict the number of load repetitions to develop 10 and 45 percent fatigue Class 2 cracking in the wheel path. The study was based on data from the AASHO Road Test and laboratory tests on material from the Road Test sections. This NCHRP study indicated that the amount of fatigue cracking is a function of the critical tensile strain and the stiffness of the asphalt layer.

Concerning rutting, several failure criteria have been recommended. The majority use correlations between strains and load repetitions. Correlations between the vertical strain on the surface of the subgrade and the number of equivalent single-axle load (ESAL) repetitions are widely used (7). Other rutting criteria correlate the rate of permanent strain to the elastic vertical strain and the number of load repetitions (8). The Asphalt Institute rutting criterion is among the most widely used in pavement design (8). The criterion provides the allowable number of ESAL repetitions for various levels of compressive strains at the surface or subgrade.

A rutting prediction criterion was also recommended by Finn et al. (6). A regression analysis procedure was used to correlate the rate of rutting with various combinations of primary response factors. The study concluded that the most significant correlations were obtained with vertical deflection at the surface of the pavement, followed by vertical compressive stress at interface with asphaltic concrete.

By examining fatigue and rutting criteria of flexible pavements, one can conclude that the performance of flexible pavements is affected by factors that influence the critical tensile strain at the bottom of the asphalt layer, surface deflection, and compressive stress at interface between the base and the asphaltic concrete. To evaluate the effect of high tire pressures and their nonuniform distributions on pavement performance, their effects on the strain, deflection, and stress components must be investigated.

In this study, a modified version of the BISAR computer program was used to evaluate the effect of variations in the truck tire pressures and their distributions on the flexible pavement performance indicators (i.e., tensile strains, compressive stress, and surface deflection). The actual pressure distributions for the various tire types were input as concentric circles with different pressures. A detailed discussion of the analysis procedure is presented later in this paper.

DATA ANALYSIS

Measurement of Tire Characteristics

Three truck tire types were analyzed for the following characteristics: footprint area (gross and net), footprint length, footprint width, spring rates, and footprint contact pressure profiles. The types of tires chosen were a dual 11-22.5 bias, dual 11R22.5 radial, and a wide-base radial single. The single

is an alternative to dual tires and more commonly used in Europe. All three tires were analyzed under a matrix of conditions that encompassed lightly loaded to overloaded, and underinflated to overinflated for each tire. Prior to any testing, each tire was run on a laboratory flywheel, under load, for a predetermined length of time to establish dimensional stability.

Tire footprints were obtained by inking the tread area of the inflated tire mounted on a specialized machine that loads it to a preset load. An imprint was left on a piece of paper between the tire and the machine's loading plate. All measurements were made from these imprints, with areas calculated by computer, using digitized boundary points as input.

To obtain deflection data, a machine similar to that used for footprints was employed; however, it monitored tire deflection in addition to load. Each tire was loaded continuously to a predetermined level, with all information recorded by strip chart recorder.

Tire footprint contact pressures were measured with a specially instrumented flatbed machine. Contact forces exerted by the loaded tire were obtained by a strain gauge located in the flatbed. This bed was capable of moving with the tire as it rotated at slow speed. Numerous points across the tire tread were tracked as they went through the length of contact to obtain an overall pressure profile. Typical distributions for the bias, radial and wide-base radial single are shown in Figure 1. The number of ribs differed from one tire to another: the bias tire had seven; the wide-base radial single, six; and the radial tire, five.

Pavement Response

To study the effect of tire pressures and distributions on the performance of flexible pavements, the response of various pavement structures and materials characteristics was investigated. For most of the analytical studies, a flexible pavement may be characterized by the thickness and stiffness of its layers. To perform a complete and meaningful study on the effect of tire types and tire pressures on the performance of flexible pavements, it was necessary to investigate pavement structures similar to that which exists on public highways. It has been well shown that high tire pressures have a large effect on pavements with thin surface layers (around 1-inch thick) and stiff base courses, but such a pavement design is atypical. The properties of the pavement structures investigated in this study are shown in Table 1.

The BISAR computer program is a general purpose program that uses the multilayer elastic solution to predict stresses, strains, and displacements in pavement structures subjected to single and multiple wheel loads. Circular uniform pressure is the general distribution for the BISAR program. The laboratory studies conducted in the research indicated that the contact pressures are not uniform and their actual distributions depend on the load, tire type, and inflation pressure. Therefore, the BISAR program was modified to handle the nonuniform pressure distributions in the form of concentric circles with different pressures. The use of concentric circles is validated by the apparent symmetry in the contact pressure distributions as shown in Figure 1. The actual pressure values of the tires under various loads and inflation pressures are shown in Table 2.

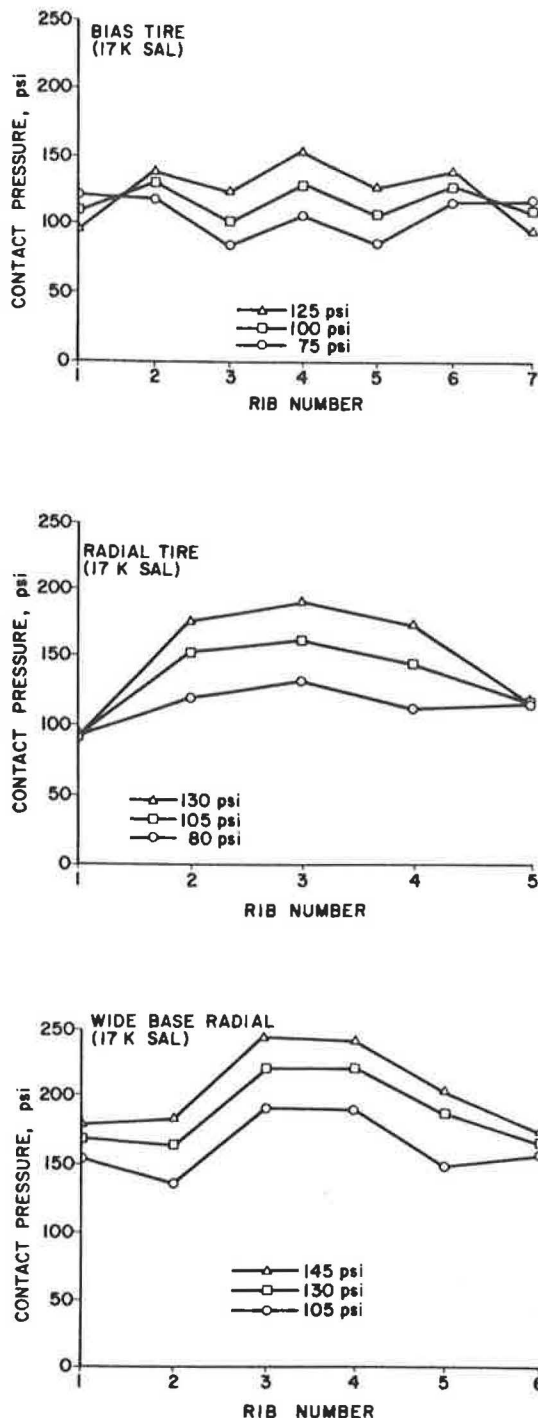


FIGURE 1 Typical pressure distribution of the three tires under 17,000-lb axle load.

Effect of Inflation Pressure and Load on Tensile Strain

The effect of inflation pressure on the tensile strain at the bottom of the asphalt concrete was evaluated for all three tires and three load levels. The results of the bias, radial, and wide-base radial single tire studies (Figures 2, 3, and 4) showed the effect of the increase in the inflation pressure as the thickness of the asphalt concrete increased. The average increase

TABLE 1 PROPERTIES OF PAVEMENT STRUCTURES

Layer	Thickness (in.)	Modulus of Elasticity (psi)	Poisson's Ratio
Asphalt concrete	2 } 4 } 6 } 8 }	400,000	0.35
Base	8	60,000	0.40
Subgrade	Infinite	6,000	0.45

in the tensile strain for the 2-in. asphalt layer was less than 15 percent for all load levels. The effect of inflation pressure was less than 5 percent for asphalt surfaces thicker than 4 in. The effect of load magnitude was more pronounced for all asphalt concrete thicknesses and tire types.

The axle load levels of 10,000, 17,000, and 22,000 lb (20,000 lb for the wide-base tires) represent the case of underloaded, loaded, and overloaded axles, respectively. The bias tire (Figure 2) showed an average increase of 35 percent in the tensile strain when the axle load increased from 10,000 to 17,000 lb, and an average of 25 percent increase when the axle load increased from 17,000 to 22,000 lb. This increase in the tensile strain was present for all asphalt layer thicknesses between 2 and 8 in.

The radial tire study (Figure 3) showed a trend similar to the bias tire, but the increase in the tensile strain was less than 20 percent for all cases of loads and asphalt concrete thicknesses. For an asphalt concrete thickness of 2 in., the radial tire data indicated that an axle load of 17,000 lb at 80 psi was less damaging than one of 10,000 lb at 130 psi, and an axle load of 22,000 lb at 80 psi was less damaging than one of 17,000 lb at 130 psi. Therefore, the 130 psi pressure for the radial tire may be critical for asphalt concrete pavements with thicknesses of 2 in.

The wide-base radial single tire study (Figure 4) was also similar to the bias and radial tire studies except that the 2-inch-thick asphalt concrete layer showed about a 40-percent increase in the tensile strain with an increase in inflation pressure from 130 to 145 psi at an axle load of 20,000 lb. For asphalt concrete layer thicknesses of 6 and 8 inches, the strain increased by less than 10 percent for an increase in the axle load from 10,000 to 17,000 lb.

Effect of Inflation Pressure and Load on Surface Deflection

The effect of surface deflection on the rutting failure of flexible pavements was emphasized in the NCHRP study discussed earlier (6). It was shown that surface deflection was a significant factor in the development of surface rutting. Studies of the dual-fitting bias and radial, and single-fitting wide-base radial tires indicated that inflation pressures had minimal effect on the surface deflection response for asphalt surfaces between 2 and 8 in. (Figures 5, 6, and 7). The increase in axle load showed a large effect on the surface deflections under all three tires. The surface deflection under the bias, radial, and wide-base radial single tires showed an increase of 75 percent when the axle load was increased from 10,000 to 17,000 lb for all asphalt surfaces between 2 and 8 inches. When the axle load increased from 17,000 to 22,000 lb for

TABLE 2 PRESSURE DISTRIBUTIONS FOR THE RADIAL, BIAS, AND SUPER SINGLE TIRES

Tire Type	Inflation Pressure (psi)	Load, lb	Rib Pressure (psi)						
			1	2	3	4	5	6	7
radial 11R22.5	80	2500	54	120	132	115	72		
		4250	92	120	132	112	115		
		5500	117	117	129	109	135		
	105	2500	40	146	163	145	71		
		4250	92	152	162	143	115		
		5500	117	151	160	145	140		
	130	2500	34	162	185	162	69		
		4250	94	177	191	172	115		
		5500	117	175	188	172	143		
bias 11-22.5	75	2500	57	98	80	105	82	100	60
		4250	123	118	85	122	63	115	117
		5500	158	128	85	108	86	122	132
	100	2500	40	102	98	123	100	103	45
		4250	110	131	102	129	108	128	108
		5500	145	143	105	131	94	140	143
	125	2500	32	103	145	152	120	105	37
		4250	97	138	125	154	128	140	92
		5500	132	157	128	157	129	155	126
wide base radial single 385/65R22.5	105	5500	115	135	180	183	169	115	
		8500	184	137	191	189	149	157	
		10000	169	131	191	189	149	169	
	130	5500	122	158	206	206	175	120	
		8500	169	166	220	222	188	166	
		10000	185	168	234	229	185	182	
	145	5500	126	174	223	220	189	118	
		8500	165	183	246	242	205	174	
		10000	192	189	249	245	206	189	

bias and radial tires, and to 20,000 lb for wide-base tires, the surface deflections under all three tires were increased by an order of 30 percent. The surface deflection response indicated that, under all three tires, the increase in surface deflection was linear with the increase in the axle load and remained constant over the entire range of asphalt surfaces.

Effect of Inflation Pressure and Load on Compressive Stress

Various field and research studies have shown that the rutting of crushed aggregate base courses contributes significantly to overall rutting of flexible pavements. The Probabilistic Distress Models for Asphalt Pavements (PDMAP) study also indicated that the compressive stress of the asphalt layer interface was a significant variable in the development of surface rutting (6). The effect of inflation pressure and axle load on the compressive stress at the asphalt layer interface was investigated for the bias, radial, and wide-base radial single tires (Figures 8, 9, and 10).

The effect of inflation pressure was then greatest for pavements with 2 in. of asphalt layer. The maximum variation, approximately 10 percent, was under the wide-base radial single tire. The effect of inflation pressure was as low as 1 percent for asphalt layers with thicknesses of 4, 6, and 8 in.

The effect of axle load on the compressive stress was present for all tires and pavement thickness combinations. The increase in compressive stress was on the order of 15 percent for an asphalt layer of 2 in. and was gradually reduced to about 5 percent for asphalt layer of 8 in.

Under the bias and wide-base radial single tires and for certain load and inflation pressure combinations, the compressive stress under a 2-in. asphalt surface may be greater than the inflation pressure. For example, the compressive stress under the 2-in.-thick asphalt layer for the bias tire showed values of 100 and 110 psi under an axle load of 22,000 lb and inflation pressures of 75 and 100 psi, respectively.

The compressive stresses under the wide-base radial single tire were at 125, 140, and 160 psi for an axle load of 20,000 lb with inflation pressures of 105, 130, and 145, respectively. The compressive stresses under the radial tire were always lower than the inflation pressure for all combinations. This observation indicates that heavily loaded bias and wide-base radial tires are more critical to pavements with thin asphalt layer than are radial tires.

Effect of Tire Type on Tensile Strain

By observing the typical contact pressure distributions for the bias, radial, and wide-base radial single tires in Figure 1, the

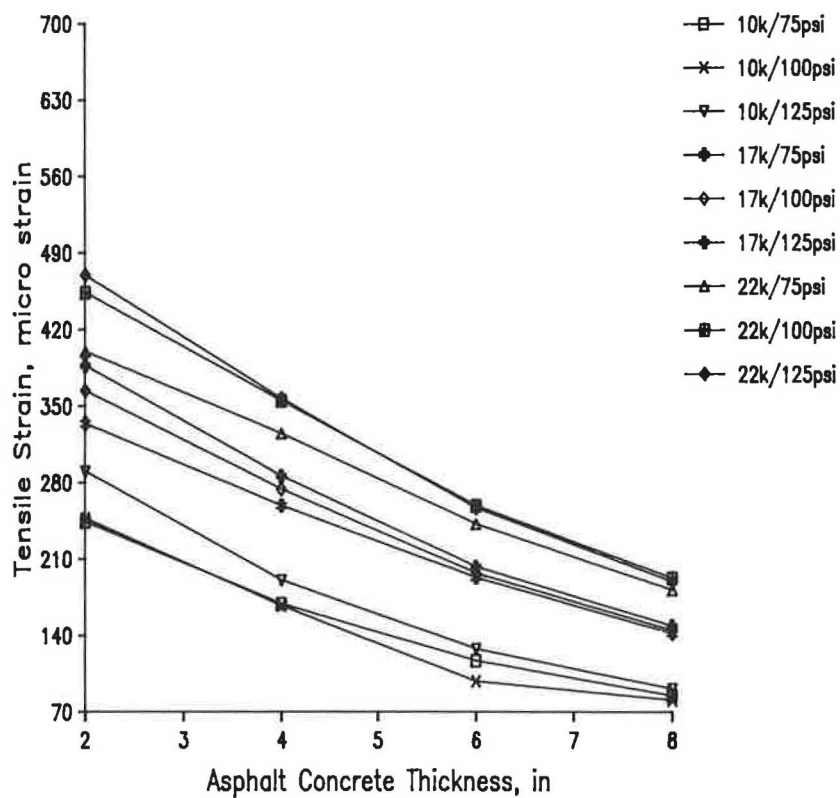


FIGURE 2 Effect of tire pressure and load on the tensile strain at the bottom of asphalt layer for dual bias tires.

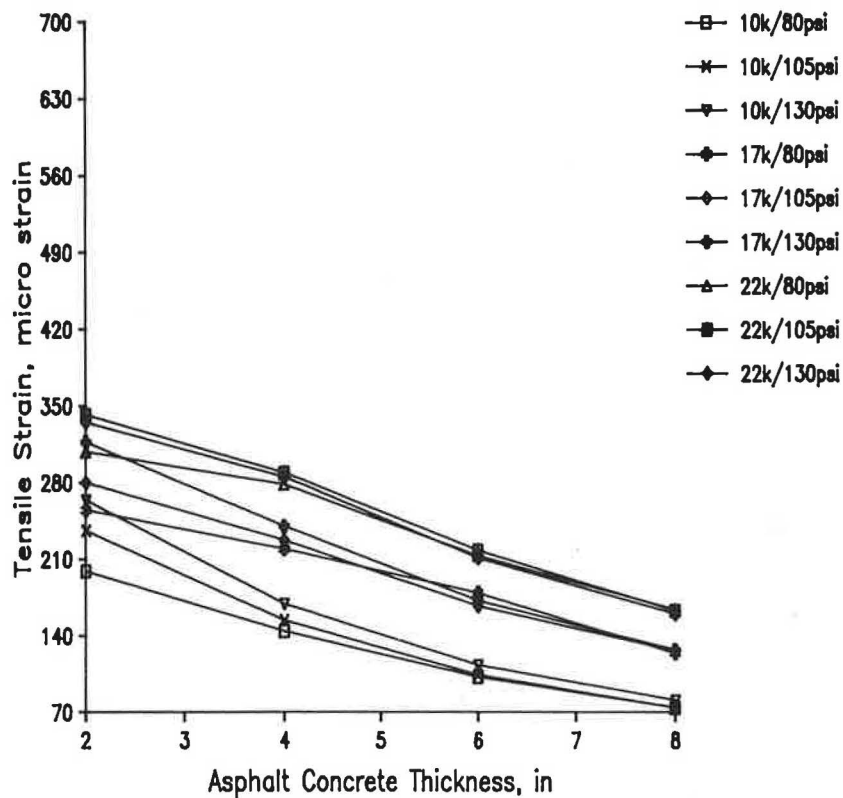


FIGURE 3 Effect of tire pressure and load on the tensile strain at the bottom of asphalt layer for dual radial tires.

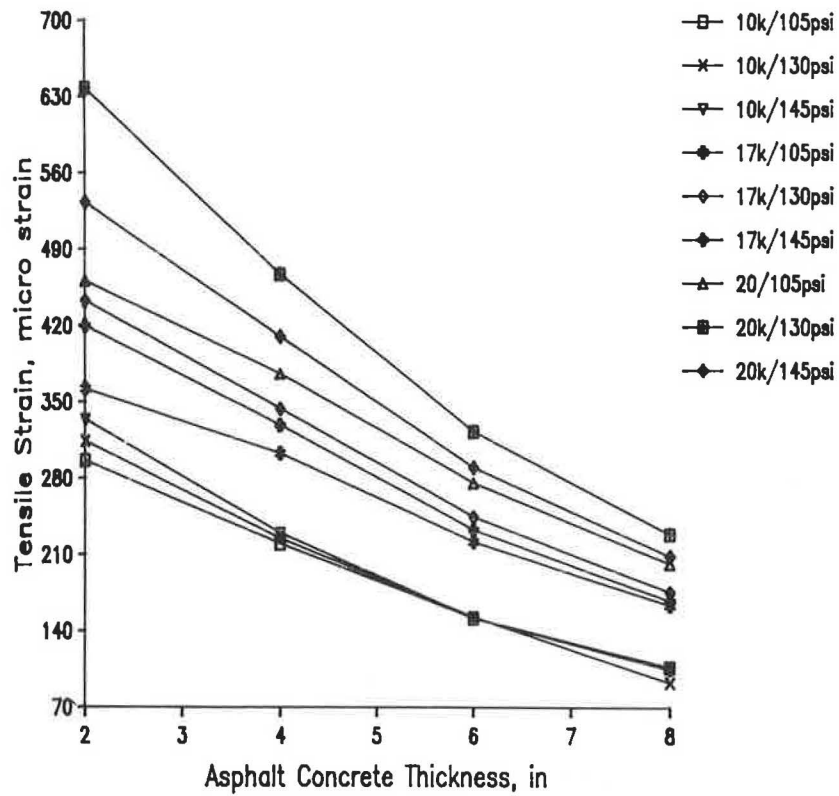


FIGURE 4 Effect of tire pressure and load on the tensile strain at the bottom of asphalt layer for single wide-base radial tire.

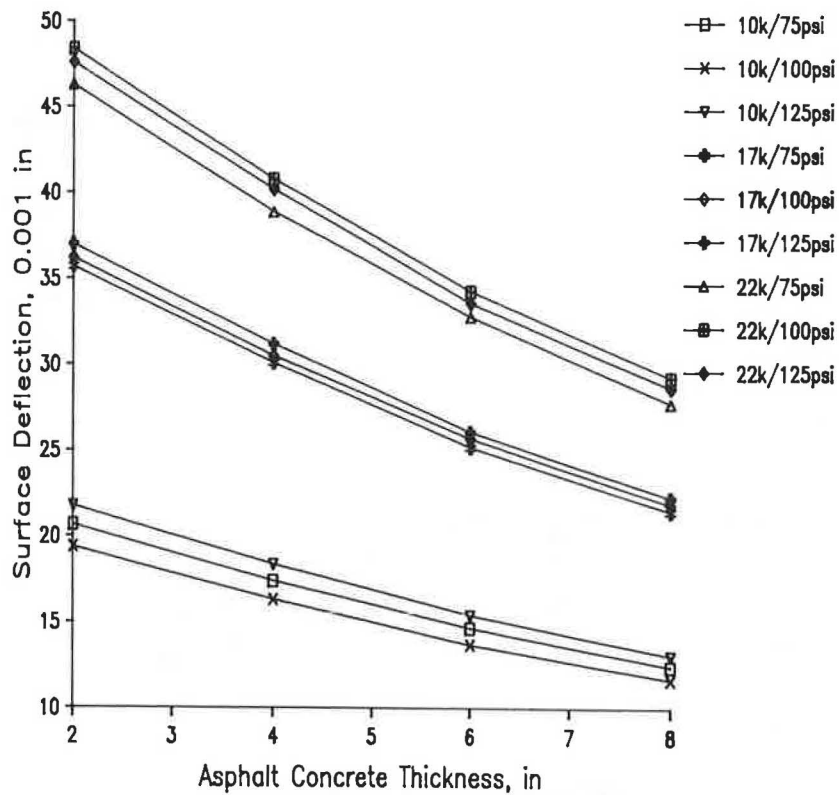


FIGURE 5 Effect of tire pressure and load on the pavement surface deflection for dual bias tires.

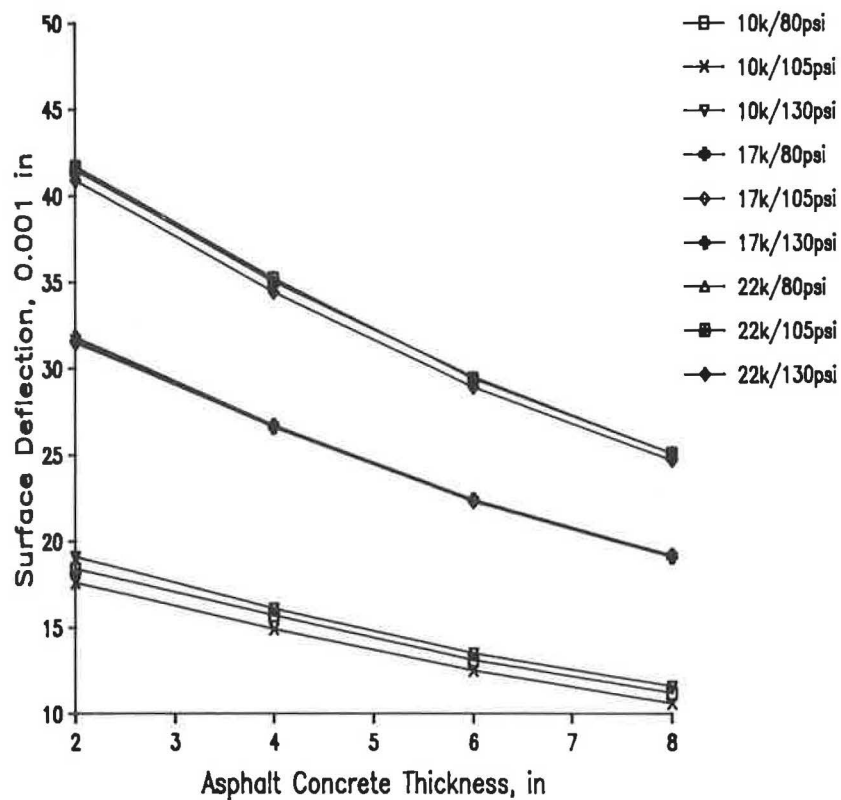


FIGURE 6 Effect of tire pressure and load on the pavement surface deflection for dual radial tires.

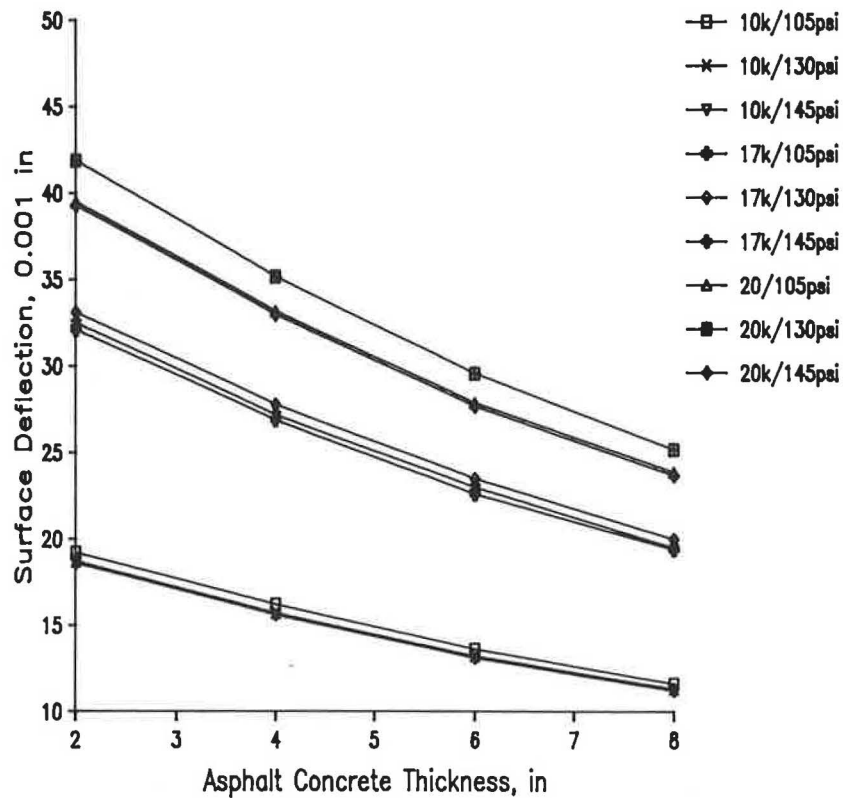


FIGURE 7 Effect of tire pressure and load on the pavement surface deflection for single wide-base radial tire.

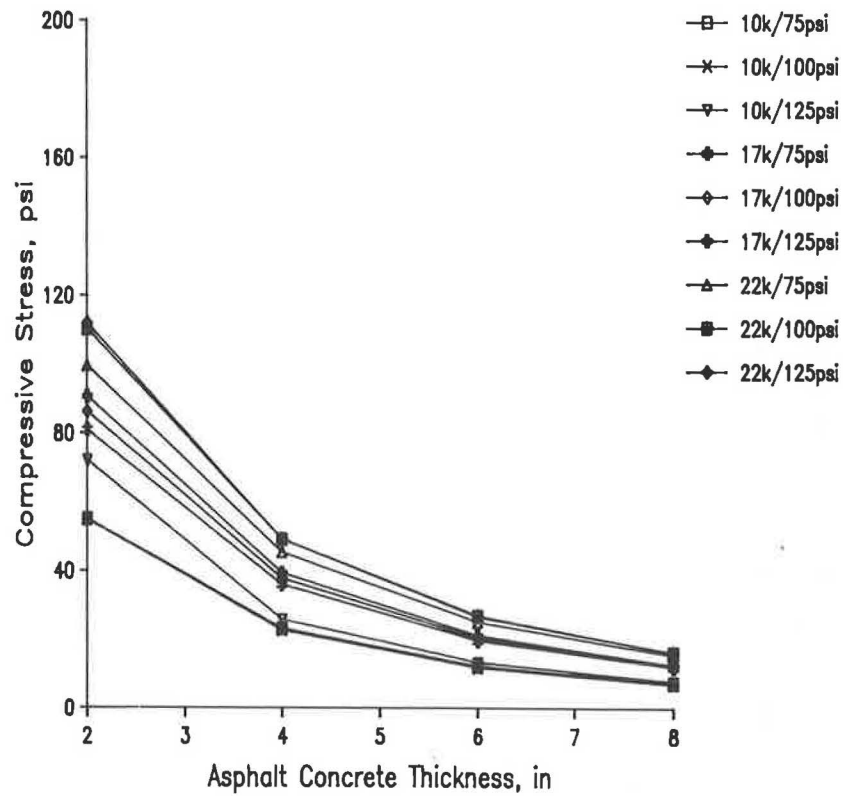


FIGURE 8 Effect of tire pressure and load on the compressive stress at the asphalt layer interface for six dual bias tires.

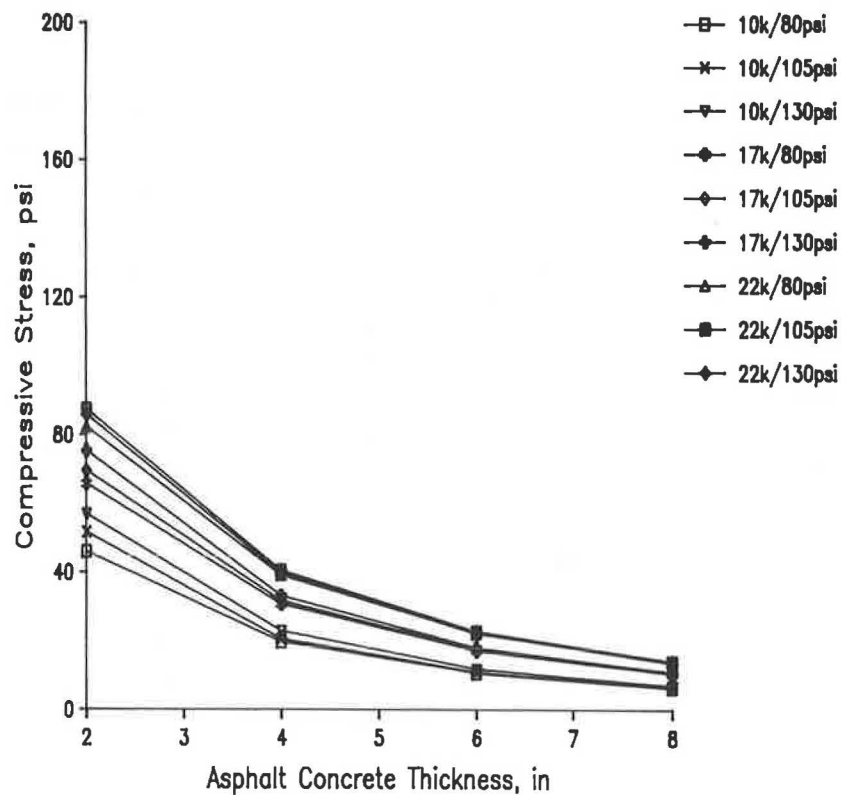


FIGURE 9 Effect of tire pressure and load on the compressive stress at the asphalt layer interface for six dual radial tires.

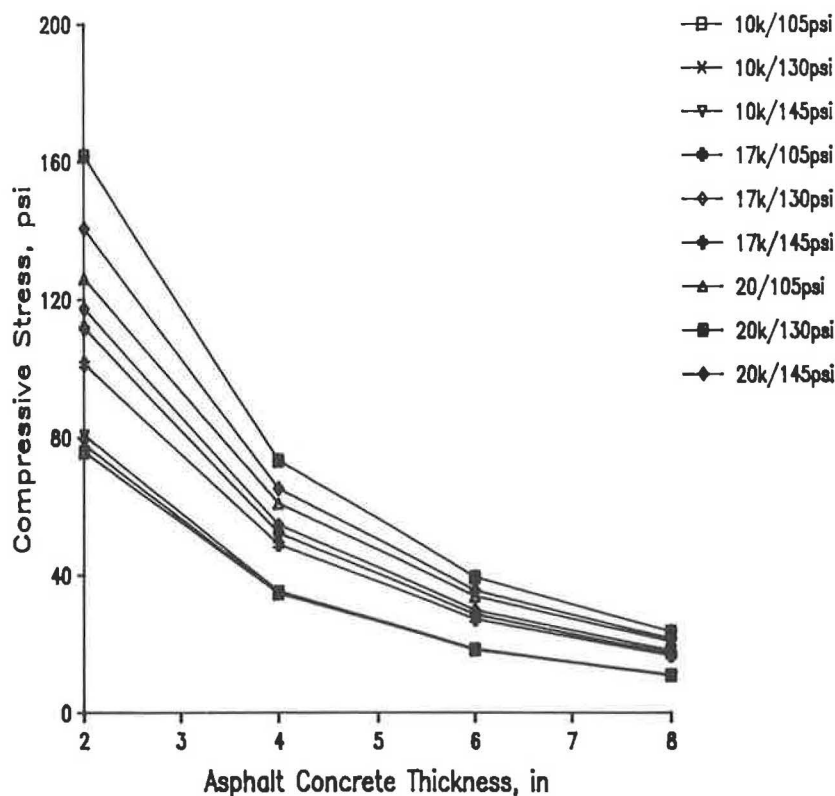


FIGURE 10 Effect of tire pressure and load on the compressive stress at the asphalt layer interface for six single wide-base radial tires.

differences among tire types are readily distinguished. The first part of the research showed that the effect of inflation pressure was pronounced only when the asphalt layer was 2 in. thick. For pavements with asphalt layers 4, 6, and 8 in. thick, the effect of inflation pressure became less pronounced. However, the effect of axle load was found to be significant under all tires and asphalt layer thicknesses. The tensile strain, surface deflection, and compressive stress at the asphalt layer interface were very sensitive to any increase in the axle load.

The second part of this study was to investigate the effect of axle load on the pavement response under each tire and how it compared with the response under other tires. The operating inflation pressure for each tire was used: 105, 100, and 130 psi for bias, radial, and wide-base radial single tires, respectively.

Figure 11 shows the results of tensile strain studies for asphalt thicknesses of 2, 4, 6, and 8 in. The strains under the dual-fitting radial tires were the lowest for all axle loads and asphalt thicknesses. Strains under the dual-fitting bias tires were 35 percent higher than under the radial tire for an asphalt layer thickness of 2 in., and 25 percent higher for asphalt layer thicknesses of 4, 6, and 8 in. The strains under the single-fitting wide-base radial tire were 50 percent higher than the radial tire for all asphalt layer thicknesses. This observation was expected because the wide-base radial single tire has a higher load-per-tire ratio than both radial and bias tires.

Effect of Tire Type on Surface Deflection

The results of the surface deflection study (Figure 12) showed that the bias tires had the highest surface deflection for all

asphalt layer thicknesses. The surface deflections under the radial and the wide-base radial single tires were very close, especially under the heavily loaded cases. The surface deflections under the bias tire were 20 and 15 percent higher than those under the radial and wide-base radial single tires, respectively. The bias tires had the lowest tire deflection among the three tires, indicating that the bias tires were the stiffest and would, therefore, create the highest surface deflections.

Effect of Tire Type on Compressive Stress

The results of the compressive stress study are shown in Figure 13. The trends in the compressive stress data are similar to the strain data. The stresses under the radial tires were the lowest for all asphalt layer thicknesses and axle load levels. The stresses under the wide-base radial single and bias tires were 25 and 50 percent higher, respectively, than stresses under the radial tires.

CONCLUSIONS

The response of flexible pavements was investigated under various conditions of tire pressures, tire types, and axle loads. The tire parameters, including footprints, net contact area, contact pressures, and tire deflections, were evaluated through a laboratory testing program. The set of tested tires included the commonly used radial and bias tires and the wide-base radial single tire, which is used widely in Europe but has only limited use in the U.S.

Tire characteristics data showed linear relationships between

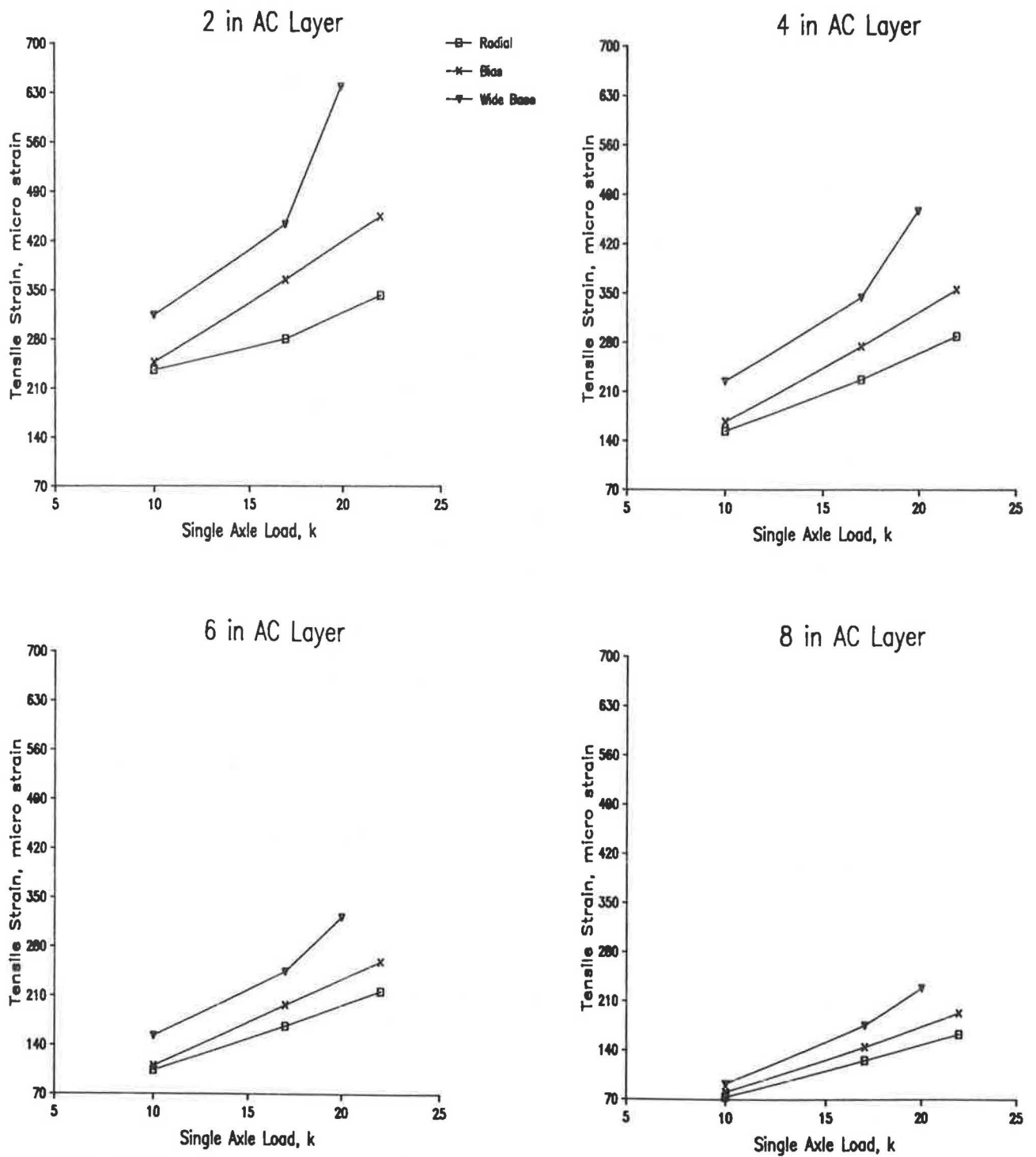


FIGURE 11 Effect of axle load and tire types on tensile strain at the bottom of four asphalt layer thicknesses.

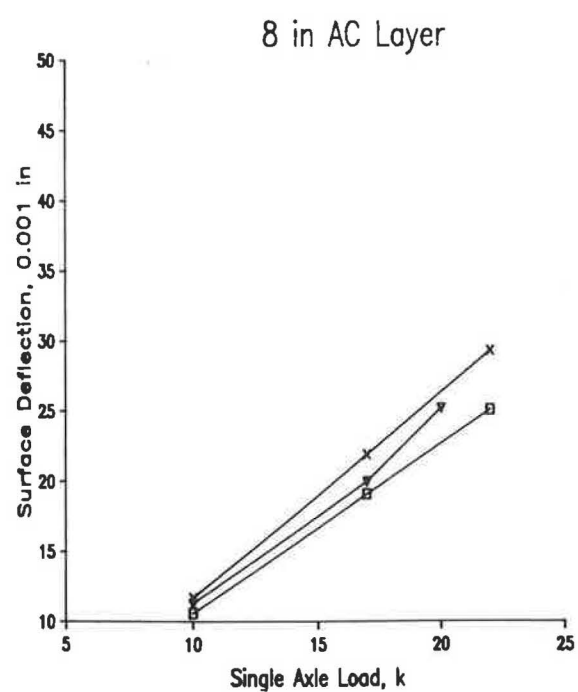
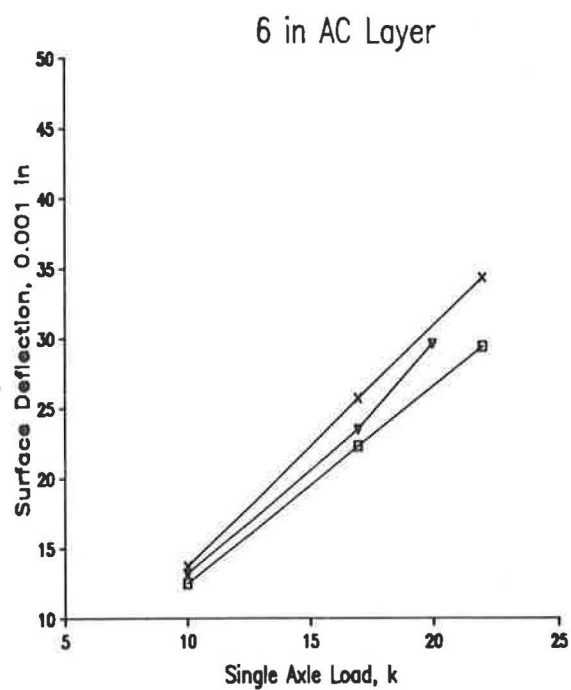
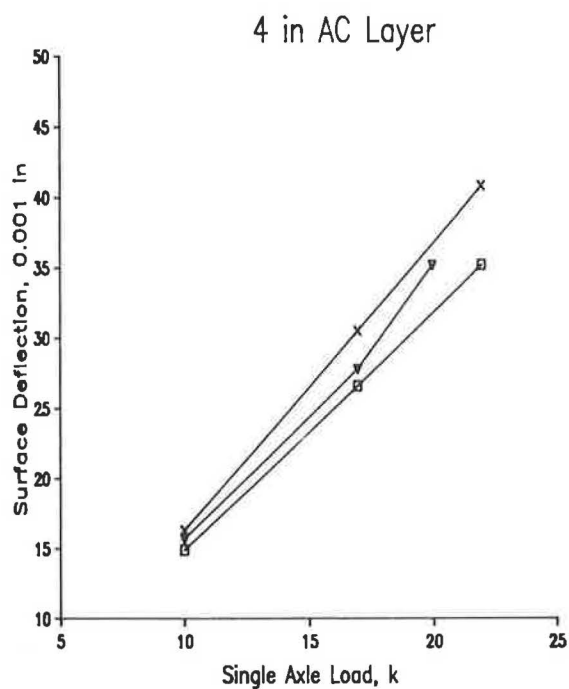
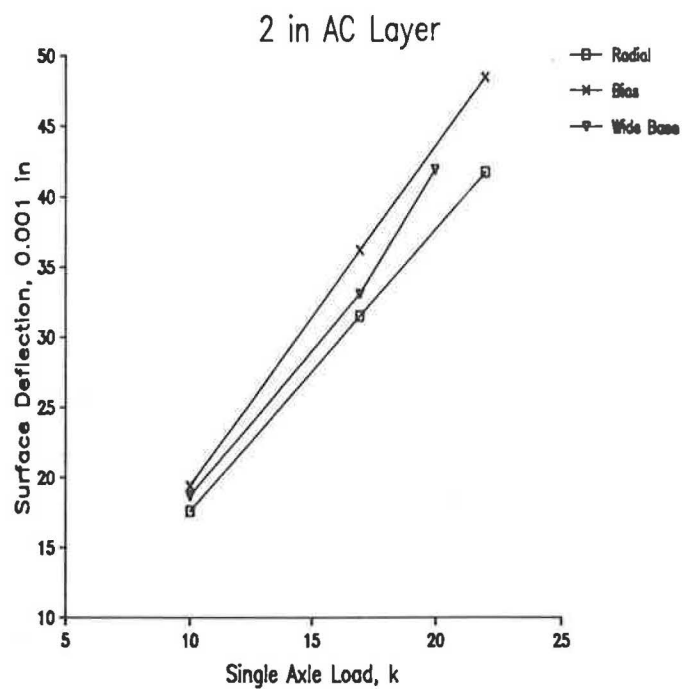


FIGURE 12 Effect of axle and tire type on the surface deflection for four asphalt layer thicknesses.

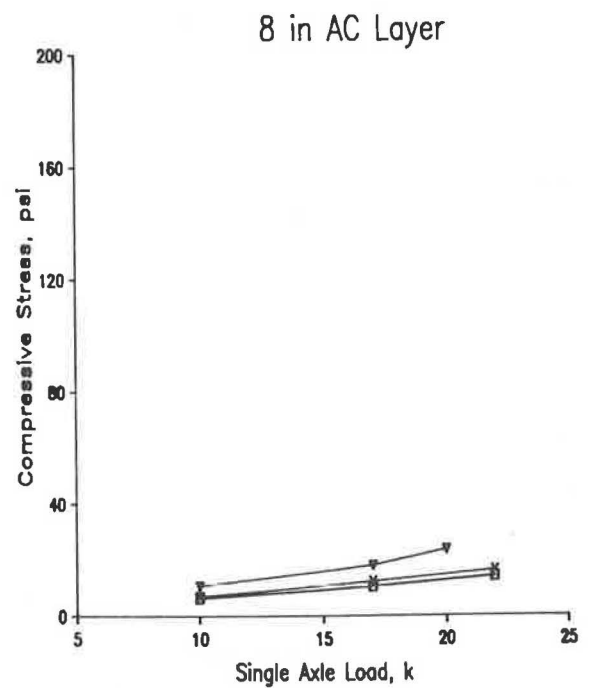
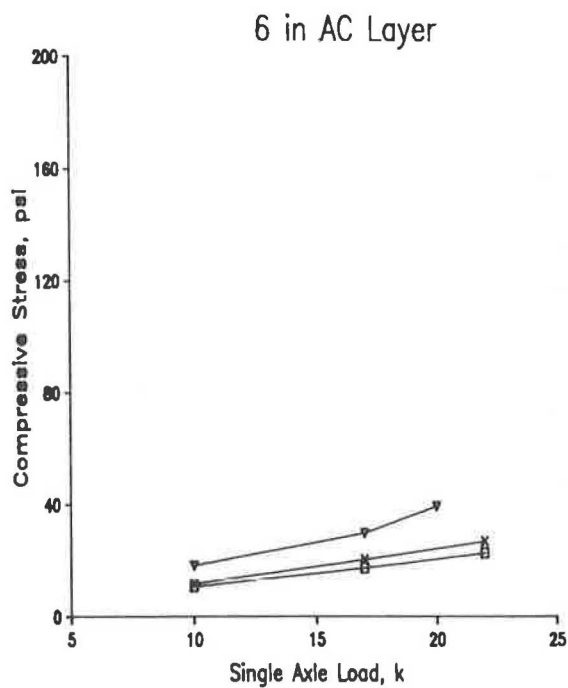
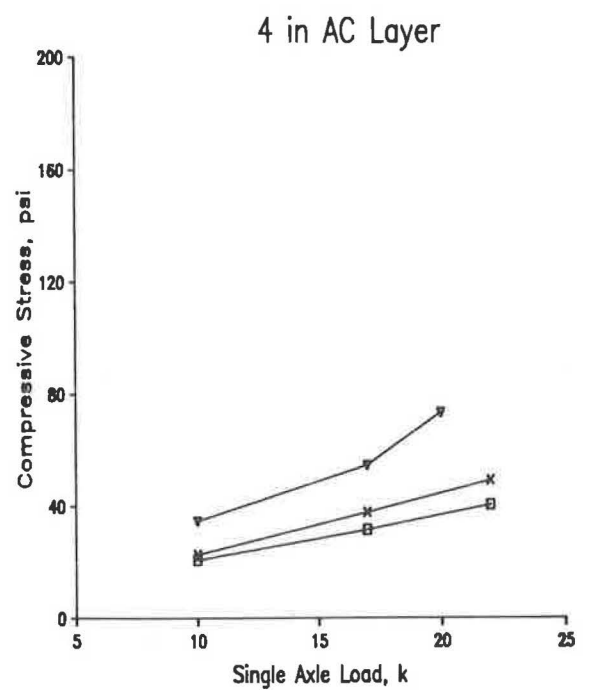
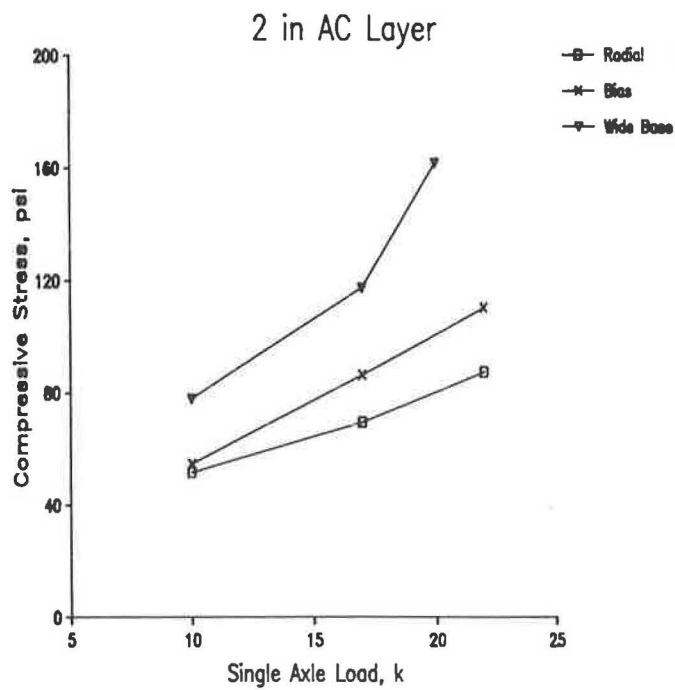


FIGURE 13 Effect of axle load and tire type on the compressive strain at the asphalt layer interface for four thicknesses.

the amount of tire deflections and the net contact areas for all tire types and axle load levels. The contact pressure distributions were all nonuniform, with maximum contact pressures of 1.75 times the inflation pressures. The maximum contact pressures were obtained along the center rib for all three tires and the minimum contact pressures were obtained along the outside rib. The ratio of the maximum pressure to the minimum pressure became smaller as the axle load increased.

On the basis of laboratory contact pressure distributions, a pavement response study was conducted. Actual pressure distributions were used in a mechanistic solution to predict the response of flexible pavement under the various loading conditions. From the results, the following conclusions may be drawn:

- Inflation pressure affects the magnitude of the tensile strains and compressive stresses for pavements with asphalt layers 2 in. thick. The greatest effects of inflation pressure are found in the wide-base radial single tire under a 20,000-lb axle load.

- Surface deflection response is not significantly affected by inflation pressure for all tire types, axle loads, and asphalt thicknesses.

- The magnitude of the axle load is the predominant factor for all variations in the pavement response parameters. Any increase in the axle load is significant for all tire types, inflation pressures, and asphalt layer thicknesses.

- Under certain critical combinations of load and inflation pressure, the compressive stress at the 2-in.-thick asphalt layer interface with the base and wide-base radial single tires exceeds the values of the inflation pressure.

- The wide-base radial single tire produces the maximum tensile strains and compressive stresses under all combinations of axle loads and asphalt layer thicknesses.

- For the overall ranges of inflation pressures, axle loads, and asphalt layer thicknesses investigated in this study, the radial tire is the least damaging on the predicted flexible pavement response parameters.

REFERENCES

1. W. D. Cunigan and N. A. Ayoub. *Feasibility of Automatic Truck Tire Pressure Data Collection*. FHWA/TX/493-1F, Washington, D.C., November 1986, 43 pp.
2. F. L. Roberts, J. T. Tielking, D. Middleton, R. L. Lytton, and K. Tseng. *Effect of Tire Pressures on Flexible Pavements*. Report No. 372-1F, Texas Transportation Institute, College Station, Texas, 1986.
3. J. T. Tielking. A Finite Element Tire Model. *Tire Science and Technology*. Vol. 11, Nos. 1-4, 1983, pp. 50-63.
4. K. M. Marshak, W. R. Hudson, H. H. Chenn, C. L. Saraf, and R. B. Connel. *Effect of Truck Tire Inflation Pressure and Axle Load on Pavement Performance*. Report No. 386-2F, Center for Transportation Research, The University of Texas at Austin, Austin, Texas, 1985.
5. B. J. Rauhut and T. W. Kennedy. Characterizing Fatigue Life for Asphalt Concrete Pavements. In *Transportation Research Record 888*, TRB, National Research Council, Washington, D.C., 1982.
6. F. Finn, C. L. Saraf, R. Kulkarni, K. Nair, W. Smith, and A. Abdullah. *Development of Pavement Structural Subsystems*. NCHRP Report 291, TRB, National Research Council, Washington, D.C., Dec. 1986.
7. G. M. Dorman and C. T. Metcalf. Design Curves for Flexible Pavements Based on Layered System Theory. In *Highway Research Record 71*, HRB, National Research Council, Washington, D.C., 1965.
8. The Asphalt Institute. *Documentation of the Asphalt Institute's Thickness Design Manual*. Research Series No. 14 (RS-14), 7th ed., College Park, Md., 1964.

Publication of this paper sponsored by Committee on Flexible Pavement Design.

Improved Characterization Model for Granular Bases

ROBERT P. ELLIOTT AND LOURDES NATHAN DAVID

Laboratory resilient modulus tests were conducted on granular materials at stress states exceeding the materials' static shear strengths. The test results show that, above the static strength, the modulus decreases with increasing stress levels. These data were used to develop a characterization model that is a modification of the commonly used k -theta- n model. The modification consists of the addition of a stress ratio (stress/strength) parameter. The stress ratio model was used in the finite element program ILLI-PAVE to analyze typical flexible pavement sections. The analysis results are compared with similar analyses using the Mohr-Coulomb stress adjustment model normally used with ILLI-PAVE. The comparison shows that similar stress and strain patterns are predicted by both models but that the stresses predicted in the granular base by the stress ratio model appear to be more realistic. Also, the stress ratio model provides a means for analyzing the structural effects of granular materials having different shear strength characteristics.

In recent years, pavement design research has emphasized the development of mechanistic analysis procedures. The objective of the development is to establish a rational method of design that is based on load-induced stresses and strains in each pavement layer. Material combinations and thicknesses are selected on the basis of the effect the stresses and strains have on each material's behavior as a part of the pavement system.

Perhaps the most significant weakness in the mechanistic analysis procedures that have been developed to date is the inability to model the behavior of unbound granular layers realistically. The granular base models currently in use typically predict stress states that exceed the strength of the material. For example, tensile radial stresses are frequently predicted at the bottom of the granular layer of a conventional flexible pavement.

This paper presents the results of a study sponsored by the National Science Foundation. The objective of the study was to establish an improved structural characterization model for granular base material. An analysis of laboratory test data has been used to propose a characterization model which is a modification of the model that is currently used by most pavement analysts.

PAVEMENT STRUCTURAL MODELS

Two mathematical models are used in mechanistic analyses to represent the pavement system: the elastic layered theory

model and the finite element model. The elastic layered model is used most frequently.

By the elastic layered theory, the pavement system is represented as a series of layers of linear elastic material. Each layer is represented by a single elastic modulus and Poisson's ratio. The single modulus provides a reasonable representation for asphalt concrete and other stabilized materials; however, it is not a good representation for unbound granular layers.

Numerous studies have demonstrated that the elastic behavior of unbound granular materials is stress dependent. That is, the apparent modulus of the granular material changes as the applied stress state changes. The typical behavior is shown by the data plotted in Figure 1. The resilient (elastic) modulus of the materials increases as the stress state (sum of the principal stresses) increases.

This stress dependency can be incorporated into an elastic layered analysis through the use of iterative techniques. An initial modulus is assigned and stresses are calculated. A new modulus is assigned for the next iteration on the basis of the stress state of the current iteration. An obvious limitation to this approach is the fact that a single modulus must still be assigned for the entire layer. The stress state will not be constant throughout the layer. It will be higher directly below the load and decrease as the distance from the load increases. Consequently, the modulus should not be constant throughout the layer.

In this respect, the finite element model provides a superior pavement representation. The finite element model treats the pavement as a series of interconnected elements. Each element can be assigned a different modulus and Poisson's ratio. As a result, the influence of stress variation on the modulus can be represented in both the vertical and horizontal directions.

Nevertheless, as currently used, neither model provides a realistic representation of the stresses and strains within an unbound granular layer. Both pavement models (elastic layered and finite element) frequently predict stress states that exceed the strength of the material. For the finite element model, this problem might be alleviated with an appropriate material characterization model.

ILLI-PAVE (a pavement analysis program provided by the Transportation Facilities Group, Department of Civil Engineering, University of Illinois at Urbana-Champaign) is a finite element model that attempts to compensate for the problem by adjusting the predicted stresses so that they do not violate the Mohr-Coulomb failure envelope. However, the adjusted stresses are used only to calculate the modulus values to be used in the next iteration. As a result, the final stresses in the

Arkansas Highway and Transportation Research Center, Department of Civil Engineering, University of Arkansas, Fayetteville, Ark. 72701.

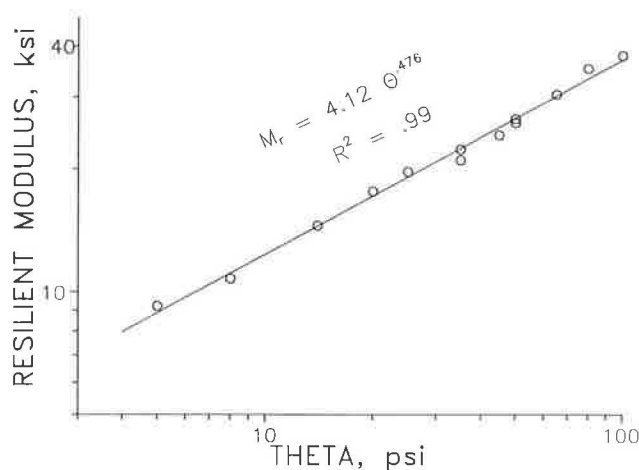


FIGURE 1 Typical stress dependency relationship for a granular base material.

granular layer continue to be questionable and frequently exceed the material strength.

GRANULAR LAYER CHARACTERIZATION MODELS

The characterization model most commonly used for unbound granular materials is based on data such as that shown in Figure 1. The resilient modulus is determined using cylindrical specimens in a triaxial cell. The specimen is subjected to a constant confining pressure. A repeated, dynamic deviator load (stress) is applied vertically, and the vertical resilient or rebound deformation (strain) is measured. The characterization model is

$$M_r = k\theta^n \quad (1)$$

where

M_r = the resilient modulus (deviator stress/resilient strain),

k and n = regression coefficients determined from the laboratory data, and

θ = sum of the principal stresses (deviator stress + 3 * confining pressure).

A more complex model was proposed and used by Brown and Pappin (1,2). This model is referred to as the contour model. It appears to have some analytical advantages but was not investigated in this study because of the complex laboratory testing required to develop the material parameters that are used.

Uzan (3) examined these and other granular characterization models. From his analysis, he suggested use of a modification of Equation 1:

$$M_r = k\theta^a \sigma_d^a \quad (2)$$

where σ_d equals the deviator stress and a equals the regression coefficient determined from laboratory data. This model was suggested to account for trends of decreasing resilient mod-

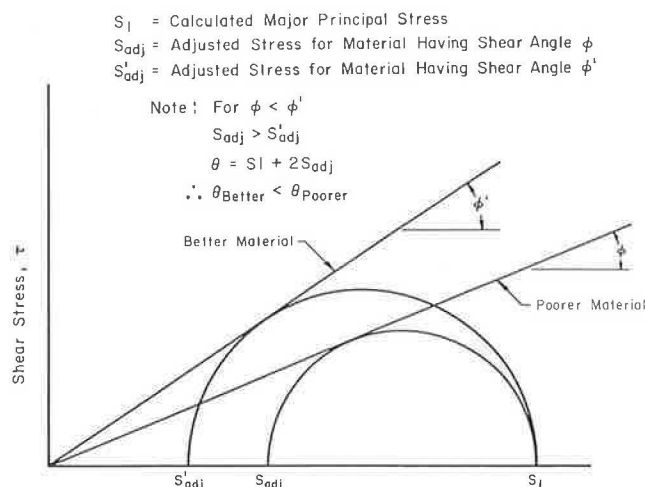


FIGURE 2 Mohr-Coulomb stress adjustment used in ILLI-PAVE (5).

ulus with increasing deviator stress at constant confining pressures.

Both Uzan (3) and Brown and Pappin (1) reported that use of their models resulted in tensile stresses being predicted for at least some pavement configurations. Brown and Pappin stated that this was due to some inaccuracy in their model and was an indication of a weak pavement. Uzan argued that the tensile stresses were small and were offset by residual compressive stresses induced by compaction during pavement construction.

The finite element program ILLI-PAVE uses the Equation 1 model with its Mohr-Coulomb stress-adjustment procedure. This will be referred to as the Mohr-Coulomb model. Elliott and Thompson (4) noted that one problem with the Mohr-Coulomb model was that it did not properly differentiate between poorer and better granular material. As illustrated in Figure 2, for equal predicted stress states, the higher phi angle of the better material will result in a lower adjusted stress. As a result, theta will also be lower and the resilient modulus for the next iteration will be lower.

There is another problem with the Mohr-Coulomb model. The stresses are adjusted but are not redistributed. Consequently, the adjusted stresses are not in equilibrium and true convergence of the iterative approach is not achieved.

LABORATORY TESTING

Three aggregates were tested to develop data to be used in developing an improved characterization model. The tests were conducted in accordance with AASHTO T-274 except that some tests were performed at deviator stresses that exceeded the materials' static shear strengths. The failure-state tests were performed to examine the resilient modulus stress dependency under stress states approaching those predicted by the currently used models.

The failure state tests were conducted in such a manner that a new test specimen was required for each confining pressure in which tests were performed beyond failure. After the tests at the standard confining pressure and deviator stress

combinations were complete, the test was continued at a constant confining pressure with the deviator stress being increased. Testing continued at higher and higher deviator stresses until a significant accumulation of permanent deformation made further testing meaningless.

For two of the aggregates, failure-state testing was performed at only one level of confining pressure (Figures 3 and 4). The third aggregate was tested in failure states at three confining pressures (Figure 5). (The nonfailure results shown on Figures 3, 4, and 5 that have theta values greater than those of failure tests represent tests at higher confining pressures.) No specific effort was made to examine the repeatability of the failure-state tests. However, the consistency of results obtained for the aggregate tested at three confining pressures suggests a reasonable degree of repeatability.

Regression equations conforming to Equation 1 were developed using only the nonfailure data. These equations are shown on the figures. By observing the data points and the R^2 values, it can be seen that Equation 1 provides a good representation of the behavior at stresses below failure.

However, at stresses exceeding failure, the resilient modulus decreases as the deviator stress (and, therefore, theta) increases. This behavior contrasts with the effect of the Mohr-

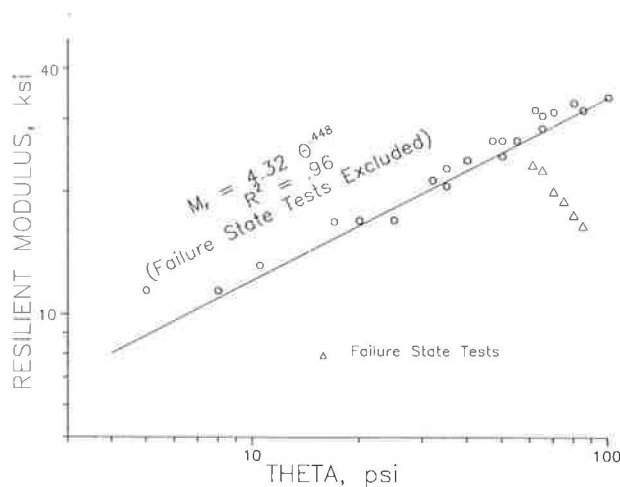


FIGURE 3 Resilient modulus test results for a crushed stone.

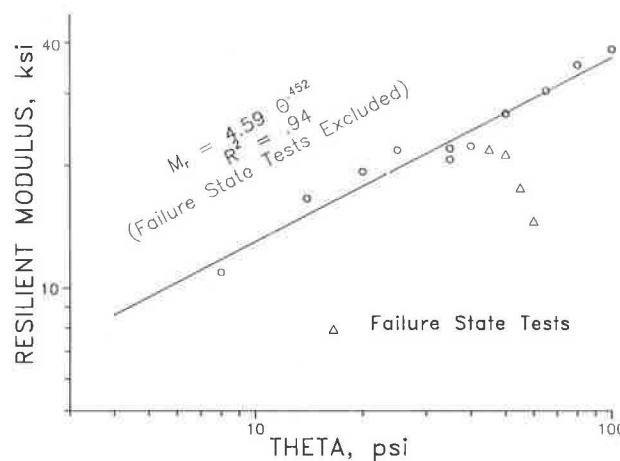


FIGURE 4 Resilient modulus test results for a low fines gravel.

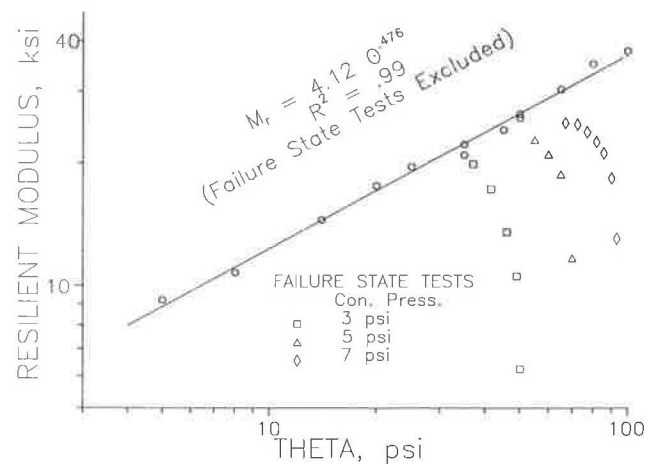


FIGURE 5 Resilient modulus test results for a dense-graded gravel.

Coulomb adjustment model. As illustrated in Figure 2, the stress adjustment increases theta, which in turn increases the modulus.

MODEL DEVELOPMENT

The data displayed in Figures 3, 4, and 5 were studied to develop a new characterization model. Two facts were noted. First, the Equation 1 model provided an excellent representation of the data below failure. Second, above failure, there appeared to be a need to incorporate a failure term. These facts suggested that the general form of Equation 1 should be modified by incorporating a failure term. The failure term should have little or no impact until failure is approached.

Several models were investigated. The one found to provide the best fit modifies Equation 1 by adding a stress/strength ratio as the failure term. The model selected is

$$M_r = k\theta^n/10^A \quad (3)$$

where

$$A = mR^3,$$

m = regression coefficient determined from laboratory data, and

R = stress/strength ratio (deviator stress divided by the failure deviator stress).

The failure deviator stress is determined on the basis of the confining pressure and the static triaxial shear test.

This model (Equation 3) is referred to hereafter as the stress ratio model. Analysis of all the data shown in Figure 5 using the stress ratio model produced the regression equation shown in Figure 6. The plots of the regression equation at the three confining pressures for which failure-state tests were conducted show a good fit between the model and the test results.

Analyses were also performed on the data for the other two aggregates. These produced similar regression equations. However, because the other aggregates were tested at only one confining pressure, the results are not as meaningful and are not shown.

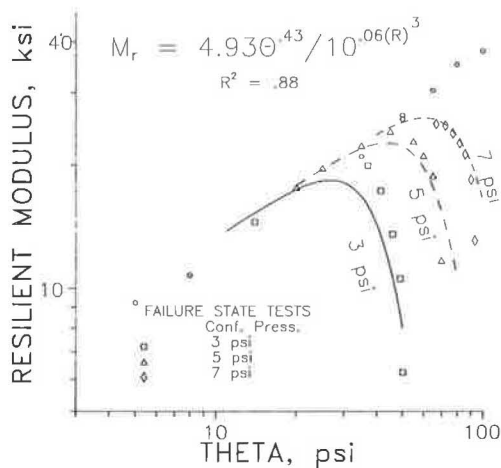


FIGURE 6 Plot of stress ratio model versus test results for a dense-graded gravel.

MODEL COMPARISON

A comparison of the stress ratio model and the Mohr-Coulomb model was developed using ILLI-PAVE. This required creating a modified version of ILLI-PAVE that incorporated the stress ratio model in lieu of the Mohr-Coulomb model.

Three pavement sections were analyzed using the two models. The sections were identical except for the thickness of the asphalt surfacing. Each section had a 12-in. (305-mm) granular layer. The surfacing thicknesses were 1 in. (25 mm), 3 in. (76 mm), and 6 in. (152 mm). A modulus of 500,000 psi (3447 Mpa) was used for the asphalt concrete; and the subgrade was represented as having a breakpoint resilient modulus of 6,000 psi (41.4 MPa).

The material parameters determined for the aggregate tested most extensively in the study were used for the granular layer. For the Mohr-Coulomb model, the phi angle (48.6 degrees) determined by the triaxial shear strength test was used for the stress adjustment, and the stress dependency was characterized using the regression equation developed from the below failure data and shown on Figure 5. The stress ratio model used the regression equation developed from all the data and shown on Figure 6.

Stresses and strains were determined for a standard 9,000-pound (40-kN) wheel load and an 80-psi (552-kPa) contact pressure. Five analysis iterations were specified so that both the final analysis results and the program convergence could be compared.

The radial stresses predicted by the two models are shown in Figures 7, 8, and 9 for the 1-in. (25-mm), 3-in. (76-mm), and 6-in. (152-mm) surface pavements, respectively. The stress patterns predicted by the models are seen to be similar, with both models predicting tensile stresses at the bottom of the base for the 1-in. (25-mm) and 3-in. (76-mm) surface pavements. However, the tensile stresses are lower with the stress ratio model.

Program convergence and the base course modulus values used are compared in Figure 10 for the 6-in. (152-mm) surface pavement. Both models converged in fewer than five iterations, with the stress ratio model converging in three iterations and the Mohr-Coulomb model converging in four. The modulus values used were similar to the stress ratio model, using

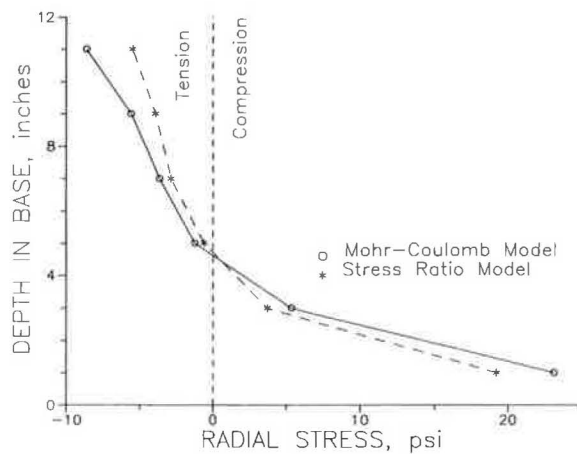


FIGURE 7 Comparison of predicted radial stresses in the base for the 1-in. (25-mm) surface pavement.

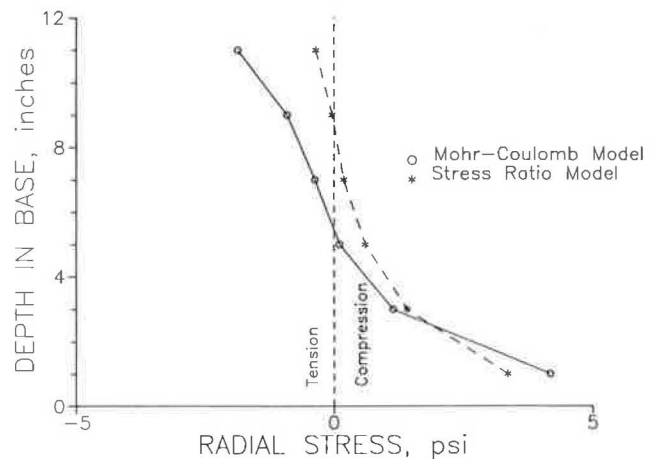


FIGURE 8 Comparison of predicted radial stresses in the base for the 3-in. (76-mm) surface pavement.

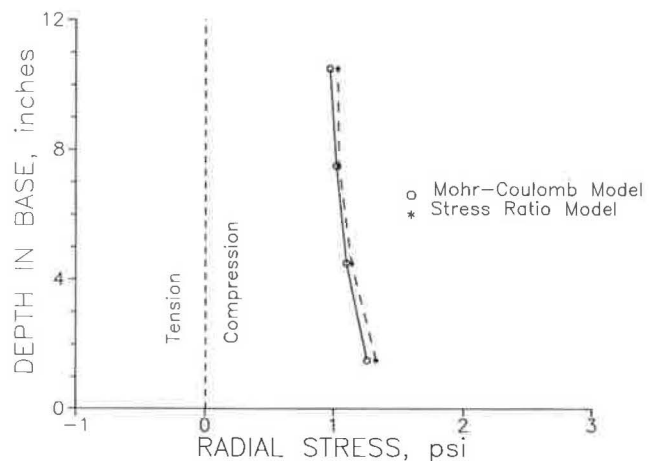


FIGURE 9 Comparison of predicted radial stresses in the base for the 6-in. (152-mm) surface pavement.

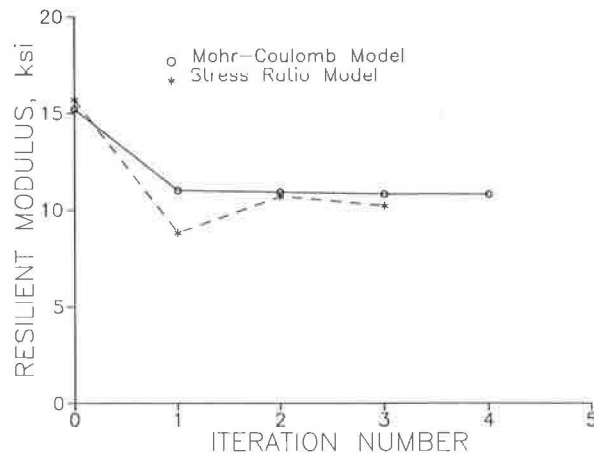


FIGURE 10 Comparison of convergence and resilient modulus values used for the 6-in. (152-mm) surface pavement.

slightly lower values. Similar patterns of modulus values were noted for the other surface thicknesses; however, neither model converged in fewer than five iterations.

COMPARISON OF GRANULAR MATERIALS

Because of the problems in modeling the behavior of granular materials, mechanistic analyses to date have not been able to examine the relative influence of aggregate bases of different quality. The stress ratio model provides an approach that makes such examinations possible.

To demonstrate this, the 3-in. (76-mm) surface pavement was also analyzed assuming a weaker base material. For this analysis, a base shear strength ϕ angle of 40 degrees was used. This changed both the stress adjustment of the Mohr-Coulomb model and the failure deviator stress in the stress ratio model. All other parameters in the characterization models were left unchanged so that the ϕ angle effect could be demonstrated.

The pavement response parameters most commonly used in mechanistic pavement analysis are surface deflection at the center of loading, radial strain at the bottom of the asphalt, and vertical strain at the top of the subgrade. The influence of changes in base course ϕ angle is shown by the results of the analyses displayed in Table 1.

In general, a pavement that exhibits a lower surface deflection, a lower asphalt radial strain, and a lower subgrade ver-

tical strain is a better (i.e., longer expected service life) pavement. Using these criteria, Table 1 shows that the Mohr-Coulomb model ranks the pavements incorrectly by predicting lower deflection and asphalt strain for the pavement with the weaker base course (lower ϕ angle). With the stress ratio model, the pavements are ranked correctly, because the pavement with the weaker base is predicted to have higher deflection and higher asphalt strain.

Except for the relative rankings, the differences in predicted pavement response are not significant for practical engineering purposes with either model. However, the fact that the stress ratio model ranks the pavements in the proper order is important and encouraging.

CONCLUSIONS

On the basis of the testing and analyses reported in this paper, the following conclusions have been made, relative to the structural characterization of granular base materials.

1. The k -theta- n model (Equation 1) provides a good representation of the laboratory stress-dependent behavior of granular material as long as the stress conditions are less than failure, as determined by the static triaxial test.
2. The stress ratio model (Equation 3) provides a good representation of the laboratory stress-dependent behavior of granular material both below and above static failure stresses.
3. The stress, strain, and deflections predicted using the stress ratio model in the ILLI-PAVE finite element program are similar to those predicted using the Mohr-Coulomb model. However, the predicted tensile stresses in the granular base are lower, appearing to be more realistic.
4. The stress ratio model provides a means for analyzing the structural effects of granular materials having different shear strength characteristics.
5. Although additional testing and analysis are needed, the stress ratio model appears to offer a significant improvement in the ability to analyze the structural behavior of granular base flexible pavements.

ACKNOWLEDGMENTS

This research was part of a study, Development of an Improved Structural Model for Granular Pavement Layers, sponsored by the National Science Foundation. The study was conducted by the Arkansas Highway and Transportation Research Center at the University of Arkansas, Fayetteville.

TABLE 1 COMPARISON OF STRESS RATIO AND MOHR-COULOMB MODELS IN EVALUATING EFFECT OF GRANULAR BASE SHEAR STRENGTH

Pavement Response Parameter	Effect of ϕ Angle ($^{\circ}$) by Structural Model			
	Mohr-Coulomb		Stress Ratio	
	40.0	48.6	40.0	48.6
Surface deflection (in.)	.0304	.0307	.0318	.0315
AC radial strain	.000371	.000380	.000414	.000408
Subgrade vertical strain	.000855	.000857	.000816	.000814

REFERENCES

1. S. F. Brown and J. W. Pappin. Analysis of Pavements with Granular Bases. In *Transportation Research Record 810*, TRB, National Research Council, Washington, D.C., 1981.
2. S. F. Brown and J. W. Pappin. Modeling of Granular Materials in Pavements. In *Transportation Research Record 1022*, TRB, National Research Council, Washington, D.C., 1985.
3. J. Uzan. Characterization of Granular Material. In *Transportation Research Record 1022*, TRB, National Research Council, Washington, D.C., 1985.
4. R. P. Elliott and M. R. Thompson. *Mechanistic Design Concepts for Conventional Flexible Pavements*. Transportation Engineering Series No. 42, University of Illinois at Urbana-Champaign, 1985.

The opinions, findings, and conclusions expressed in this paper are those of the author and not necessarily those of the National Science Foundation.

Publication of this paper sponsored by Committee on Strength and Deformation Characteristics of Pavements.

Rapid Shear Strength Evaluation of In Situ Granular Materials

MICHAEL E. AYERS, MARSHALL R. THOMPSON, AND DONALD R. UZARSKI

Dynamic Cone Penetrometer (DCP) and rapid-loading (1.5 in./sec) triaxial shear strength tests were conducted on six granular materials compacted at three density levels. The granular materials were sand, dense-graded sandy gravel, AREA No. 4 crushed dolomitic ballast, and material No. 3 with 7.5, 15, and 22.5 percent FA-20 material. (FA-20 is a nonplastic crushed-dolomitic fines material—96 percent minus No. 4 sieve : 2 percent minus No. 200 sieve.) DCP and triaxial shear strength data (including stress-strain plots) are presented and analyzed. The major factors affecting DCP and shear strength are considered. DCP-shear strength correlations are established and algorithms for estimating in situ shear strength from DCP data are presented. To the authors' knowledge, this is the first study in which the shear strength of granular materials has been related to DCP test data. Such relations have significant potential applications in evaluating existing transportation support systems (railroad track structures, airfield and highway pavements, and similar types of horizontal construction) in a rapid manner. A DCP test can be conducted to a depth of 2 to 3 ft in a matter of minutes. Several tests can be conducted to establish the variability of the in situ material.

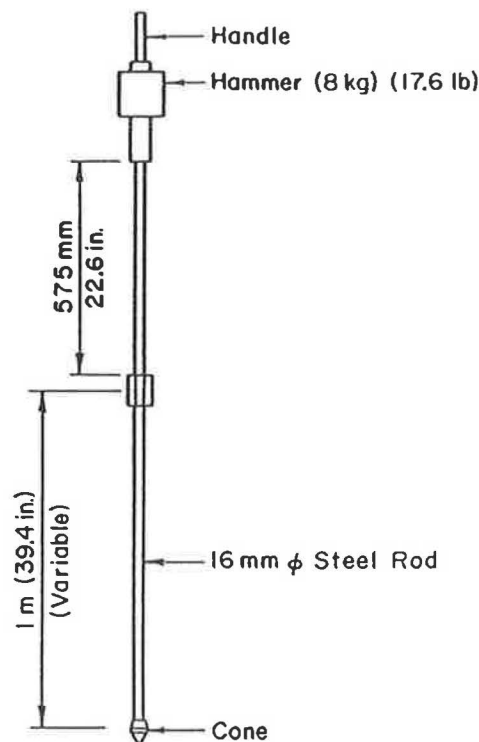
Characterization of in situ shear strength of granular materials and fine-grained soils in transportation support systems evaluation is an expensive and time-consuming endeavor. Test excavations, laboratory analysis of bulk field samples, and in situ tests [i.e., plate bearing and California bearing ratio (CBR)], have all been used. Because of the expense involved, however, testing is generally quite limited.

The high variability associated with most soil types and the number of soil types typically encountered in a project necessitate a test method that is inexpensive and rapid. The trade-off has been either a cursory survey with limited results or an in-depth characterization of a limited number of sites.

Several rapid test methods are available for evaluating in situ strength. The dynamic cone penetrometer (DCP)(1), the Clegg hammer, the U.S. Army Waterways Experiment Station penetrometer (commonly referred to as the "WES cone penetrometer"), the dynamic portable penetrometer (DPP)(2), and the vane shear apparatus are examples of devices currently in use. Device limitations include the inability to differentiate layers or detect zones of weakness (Clegg hammer), incompatibility with large particle sizes (vane shear apparatus), the inability to penetrate high-strength materials (WES cone), and the lack of strength correlations for granular materials with large-sized aggregate (DPP).

The DCP does not have these limitations. It can be used for a wide range of particle sizes and material strengths and can characterize strength with depth.

The DCP, as used in this study, consists of a 17.6-lb sliding weight, a fixed-travel (22.6 in.) weight shaft, a calibrated stainless steel penetration shaft, and replaceable drive cone tips (Figure 1). Test results are expressed in terms of the penetration rate (PR), which is defined as the vertical move-



THE CONE

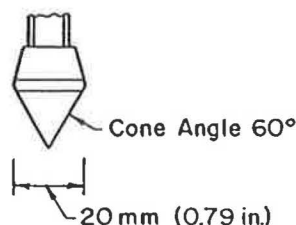


FIGURE 1 Dynamic cone penetrometer.

M. E. Ayers and M. R. Thompson, Department of Civil Engineering, University of Illinois at Urbana-Champaign, Urbana-Champaign, Ill. 61801-2397. D. Uzarski, U.S. Army Construction Engineering Research Laboratory, P.O. Box 4005, Champaign, Ill. 61820.



FIGURE 2 DCP utilization.



ment of the DCP cone produced by one drop of the sliding weight (inches/blow).

The DCP has many advantages. It is adaptable to a wide range of material types, can be conducted rapidly (approximately 5 to 10 min per test site), is portable, and is relatively inexpensive to construct and maintain.

The DCP is particularly well suited for in situ strength evaluation of railroad track beds, highway and airfield pavements, and unpaved areas. Figures 2 and 3 show the DCP evaluation of a railroad system and a typical depth-blow count relation. The differentiation in layer strengths is evident in Figure 3. Note, the total blow count to a given depth is indicative of overall strength.

There are existing DCP-CBR correlations (3,4), as illustrated in Figure 4. DCP use has been limited in part because of a lack of correlations relating DCP penetration values with fundamental material properties such as shear strength (cohesion, c , and the angle of internal friction, Φ). These properties are essential inputs to many mechanistic-empirical analysis and design procedures including ILLI-PAVE (5), ILLI-TRACK (6,7), and similar procedures using Mohr-Coulomb failure criteria. This paper establishes DCP-shear strength correlations for a range of granular materials.

OBJECTIVE AND SCOPE

The primary objective of this study is to evaluate the efficacy of the DCP for estimating the shear strength of granular materials. A simple, quick, and economical field procedure is desired to evaluate the structural adequacy of ballast through the use of RAILER, the railroad track maintenance management system under development at the U.S. Army Construction Engi-

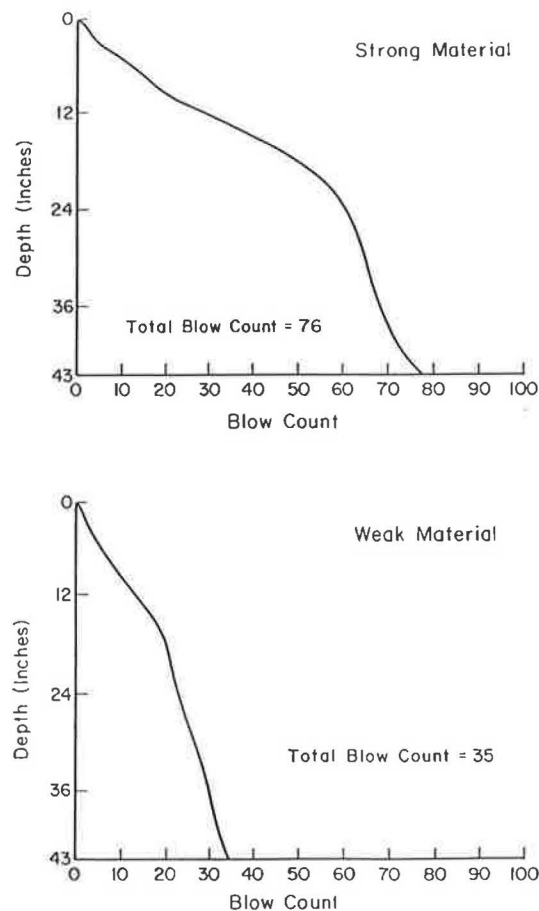


FIGURE 3 Typical DCP blow count-depth relationships.

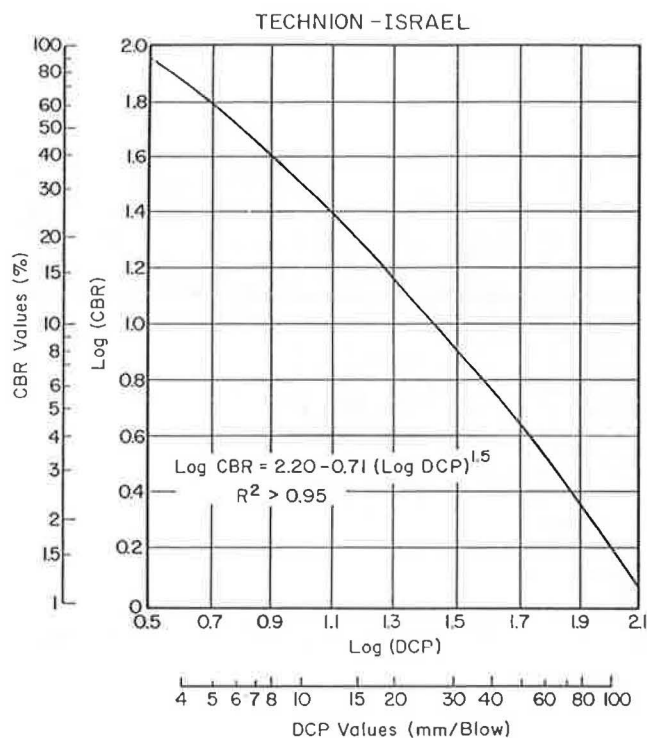


FIGURE 4 CBR-DCP algorithm (3).

neering Research Laboratory (USA-CERL). To the authors' knowledge, no currently available correlations establish a relationship between the DCP-PR and granular material shear strength.

Therefore, a two-phased study was conducted to establish the desired correlations. In Phase 1, typical track section materials including sand, sandy gravel, crushed dolomitic ballast, and ballast with varying amounts of nonplastic fines were evaluated with the DCP to obtain a general understanding of the factors involved in the test procedure. Phase 2 focused on determining the shear strength and associated parameters for each of the materials previously tested with the DCP apparatus. Phase 2 test results were statistically analyzed to establish regression equations relating PR and shear strength.

MATERIALS

The materials evaluated were sand, dense-graded sandy gravel (Rokey), crushed dolomitic ballast (AREA No.4), and ballast with varying amounts of nonplastic crushed dolomitic fines (minus No.4 sieve, FA-20). Inclusion of these materials produced a broad data base for establishing overall trends and correlations. Pertinent material properties are summarized in Tables 1 and 2.

SPECIMEN PREPARATION

Specimen preparation procedures were standardized to reduce variability. General procedures [see Ayers and Thompson (1) for details] are as follows:

1. The material was separated into size fractions and recombined to the proper gradation.
2. The moisture content was determined (where applicable) and adjusted as necessary.
3. The materials were compacted in three increments (lifts) to predetermined maximum, minimum, and intermediate densities. Compaction was accomplished by use of a vibratory hammer with a full-face compaction head.
4. The DCP specimens were compacted in a 12-in. diameter by 18-in. deep steel mold with attached bottom plate. A study of mold size effects (1) indicated that a mold diameter is less than approximately 8 times the maximum aggregate size was significant. Mold size effects are attributed to sample confinement and wall friction and are further documented by Green and Knight (8).
5. Standard practices were followed for preparing the triaxial specimens (6-in. diameter by 12-in. depth). The specimens were compacted on the base plate of the triaxial cell (Figure 5). Two membranes were used (31-mil neoprene compaction membrane, plus a second 25-mil latex membrane).

DCP TESTING

A recent study (1) indicated that operator error was minimal and did not significantly affect DCP results. Examples of operator error include vertical misalignment of the device (significant only in extreme cases), incorrect reading of the penetration rod, and incorrect recording of the data (generally evident during data review). In this study, a test platform was used to maintain vertical alignment of the DCP apparatus and maximize reproducibility. The test apparatus is shown in Figure 6. Test data (blow count and penetration depth) were manually recorded.

Material density, gradation, and fines content (in the case of ballast materials) were the primary factors evaluated in the DCP series. Other material parameters (such as void ratio, effective grain size, coefficient of curvature, coefficient of uniformity, and maximum aggregate size) were calculated or measured for subsequent use.

TRIAXIAL TESTING

The commonly used shear strength parameters of deviator stress at failure, stress ratio at failure, cohesion, and angle of internal friction can be established from triaxial test data. A computer-interfaced MTS hydraulic load apparatus was used in all Phase 2 testing (Figure 7). Air was used as the confining pressure, and the tests were conducted with the sample vented to the atmosphere (open or drained condition). The specimen was rapidly loaded (1.5 in./sec) to failure. The 1.5 in./sec load rate corresponded to a failure strain of 5 percent occurring in 400 msec. A load duration of 400 msec is considered a realistic simulation of a relatively slow-moving vehicle. Load magnitudes and total axial deformations were recorded by the computer.

Phase 2 triaxial test samples closely approximated the DCP samples tested in Phase 1. Stress-strain plots for three confining pressures (5, 15, and 30 psi) were used to establish a Mohr-Coulomb failure envelope. Duplicate tests were performed if inconsistencies in the data were evident.

TABLE 1 MATERIAL CHARACTERISTICS

MATERIAL	GRADATION (% PASSING) SIEVE SIZE															DENSITIES EVALUATED (PCF)	SPECIFIC GRAVITY	COMMENTS
	2 in	1 1/2"	1 in	3/4 in	1/2 in	3/8 in	#4	#8	#16	#30	#40	#50	#100	#200				
SAND	--	--	--	--	--	100	93	76	60	43	--	14	2	2	111,113, 116	2.65	--	
CA-10 SANDY- GRAVEL (ROKEY)	--	--	100	--	79	--	47	--	--	--	16	--	--	8	119,123, 127	2.55	OPTIMUM MOISTURE CONTENT = 8.3% AS TESTED = 9.6% LL = 18 PI = 2	
CRUSHED DOLO- MITIC BALLAST	100	96	40	6	--	2	0	--	--	--	--	--	--	--	89,95,99	2.63	AREA #4 GRADATION	
BALLAST WITH 7.5% FA-20	100	96.3	44.2	12.6	--	8.8	6.7	4.6	2.7	1.0	--	0.8	0.4	0.1	99,104,107	2.63	--	
BALLAST WITH 15% FA-20	100	96.5	47.8	18.3	--	14.8	13.0	8.6	5.1	3.0	--	1.6	0.6	0.3	102,107, 112	2.63	--	
BALLAST WITH 22.5% FA-20	100	96.7	51.0	23.3	--	20.0	17.6	12.1	7.2	4.2	--	2.2	0.9	0.4	110,113, 116	2.62	--	
FA-20	--	--	--	--	--	100	96	66	39	23	--	12	5	2		2.60	NON-PLASTIC DOLO- MITIC FINES	
NOTE: CA-10 AND FA-20 ARE ILLINOIS D.O.T. STANDARD GRADATIONS. THE FA-20 DOLOMITIC FINES AND THE BALLAST WERE OBTAINED FROM THE SAME SOURCE.																		

NOTE: CA-10 AND FA-20 ARE ILLINOIS D.O.T. STANDARD GRADATIONS.
THE FA-20 DOLOMITIC FINES AND THE BALLAST WERE OBTAINED FROM THE SAME SOURCE.

TABLE 2 MATERIAL CHARACTERISTICS CONTINUED

MATERIAL	EFFECTIVE GRAIN SIZE D_{10} (INCHES)	COEFFICIENT OF UNIFORMITY C_u	COEFFICIENT OF CURVATURE C_z	MAXIMUM AGGREGATE SIZE (INCHES)	D_{30} (INCHES)	D_{60} (INCHES)
SAND	0.009	5.1	0.87	0.19	0.019	0.046
CA-10 SANDY- GRAVEL (ROKEY)	0.004	80.0	1.01	1.0	0.036	0.32
CRUSHED DOLO- MITIC BALLAST	0.71	1.7	0.99	1.5	0.91	1.18
BALLAST WITH 7.5% FA-20	0.39	3.0	1.67	1.5	0.87	1.16
BALLAST WITH 15% FA-20	0.12	9.2	5.22	1.5	0.83	1.10
BALLAST WITH 22.5% FA-20	0.07	15.1	8.41	1.5	0.79	1.06

TEST RESULTS

DCP Data

DCP test results are presented in Table 3. Typical PR-depth plots are shown in Figures 8 and 9 for sand and Rokey CA-10, respectively. The PR-depth plots are the result of from four to six tests conducted on duplicate samples at each target density. The effects of overburden (confinement) and density are evident.

The penetration rate selected to characterize a sample was obtained by averaging the results of all trials at middepth,

middepth + 2 in., and middepth - 2 in. The values for the various DCP tests are summarized in Table 3.

Triaxial Data

Typical stress-strain plots are shown in Figures 10 and 11 for sand and AREA No.4 ballast, respectively. The stress-strain plots are differentiated by confining pressure and sample density. Note the characteristic shape of the stress-strain plot (Figure 10). In cases where the breakover point in the plot was not well-defined, the maximum deviator stress was assessed

at a strain of 5 percent (Figure 11). The triaxial test data are summarized in Table 4.

DATA ANALYSES

The principal objective of this study was to establish generalized DCP penetration rate-shear strength relations. Single and multivariate statistical analyses were used to correlate various shear strength parameters (i.e., deviator stress at failure, stress ratio at failure, and the angle of internal friction)

with the following factors: DCP penetration rate, density, maximum aggregate size, void ratio, effective grain size, coefficient of uniformity, and the coefficient of curvature.

Methodologies

The data base generated may be divided into two subgroups relating to material properties and strength (DCP or triaxial test) results. Material properties such as density, void ratio, and grain size distribution, are not easily measured under field conditions. It is, therefore, desirable to relate the shear strength parameters directly to PR.

Initial work focused on material properties and the DCP or triaxial test data relations. A matrix was generated, which allowed convenient manipulation of the data. The pertinent material properties and strength test parameters are defined below:

Penetration rate (PR). The vertical movement of the DCP apparatus corresponding to one drop of the sliding weight (inches/blow).

σ_1 . Major principal stress in the triaxial tests (psi).

σ_3 . Minor principal stress, also referred to as the confining pressure (CP), in the triaxial tests (psi).

Deviator stress (DS). The difference between the major and minor principal stresses at failure ($\sigma_1 - \sigma_3$) in the triaxial test procedure (psi).

Stress ratio (SR). The ratio (at failure) of the total vertical stress imposed on a triaxial sample to the confining pressure (σ_1/σ_3).

Angle of internal friction (Φ). The angle of the Mohr-Coulomb failure envelope established by multiple triaxial tests at various CPs (degrees). The following equation (for cohesion equals zero condition) was used in calculating Φ :

$$\Phi = \sin^{-1} ([SR - 1]/[SR + 1])$$

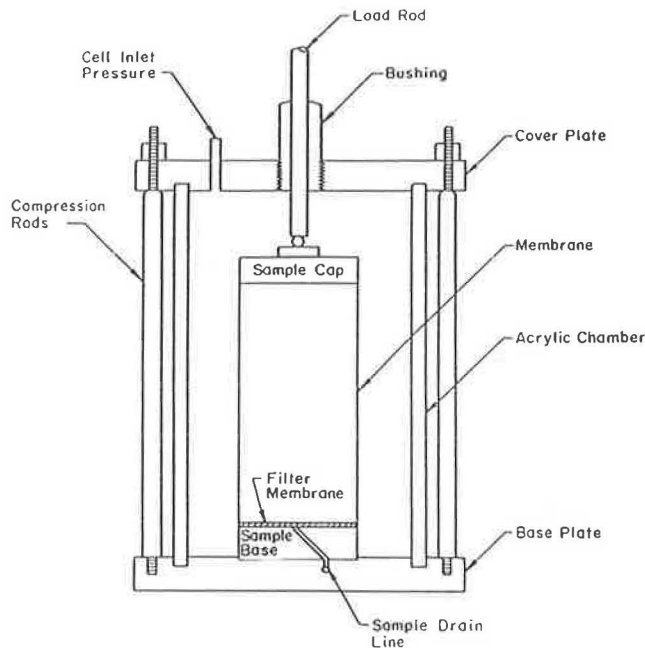


FIGURE 5 Triaxial cell schematic.

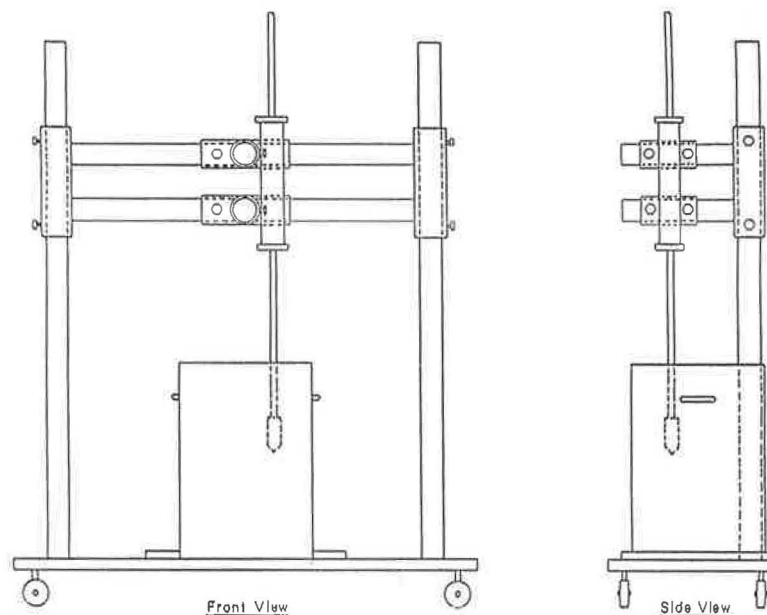


FIGURE 6 DCP test apparatus.

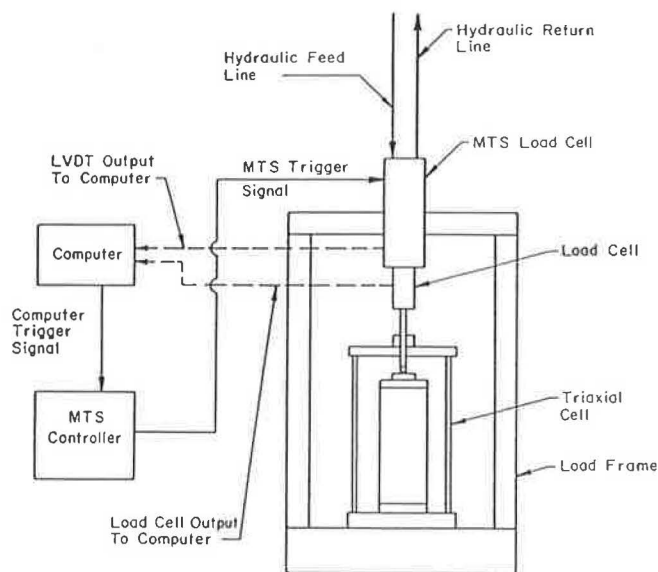


FIGURE 7 MTS test apparatus schematic.

TABLE 3 DCP TEST RESULTS

MATERIAL	DENSITY (PCF)	PENETRATION RATE (INCHES/BLOW)
SAND	111	1.20
	113	0.90
	116	0.50
CA-10 SANDY GRAVEL (ROKEY)	119	2.15
	123	1.15
	127	0.55
CRUSHED DOLOMITIC BALLAST (AREA #4)	89	1.80
	95	0.95
	99	0.70
BALLAST WITH 7.5% FA-20	99	0.65
	104	0.50
	107	0.40
BALLAST WITH 15% FA-20	102	0.55
	107	0.35
	112	0.25
BALLAST WITH 22.5% FA-20	110	0.60
	113	0.30
	116	0.20

NOTES:

FA-20 is a designation for the dolomitic fines used in this study. The ballast and FA-20 were obtained from the same source.

CA-10 and FA-20 are Illinois DOT standard gradations.

The penetration rates indicated are the average values of 4 to 6 tests taken at mid-depth, mid-depth +2 inches, and mid-depth -2 inches.

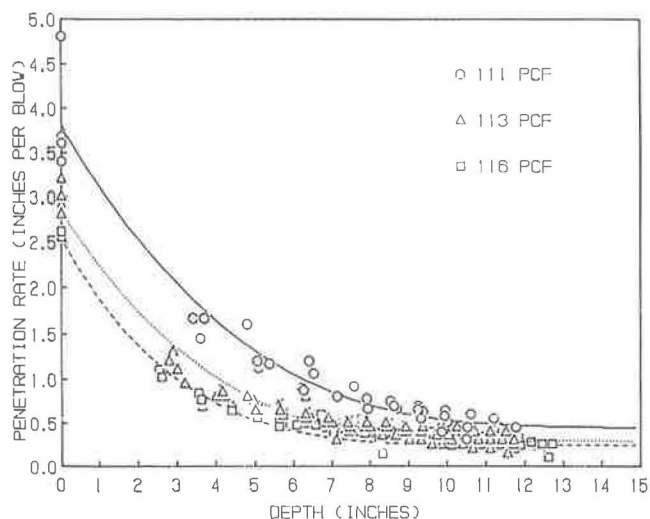


FIGURE 8 Typical DCP data for sand.

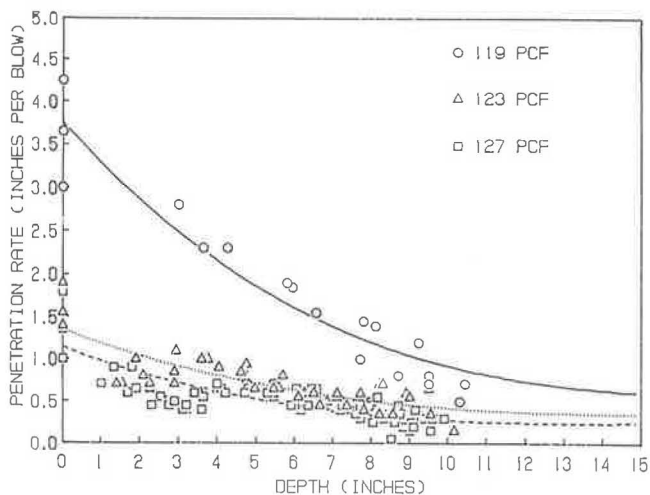


FIGURE 9 Typical DCP data for Rokey CA-10.

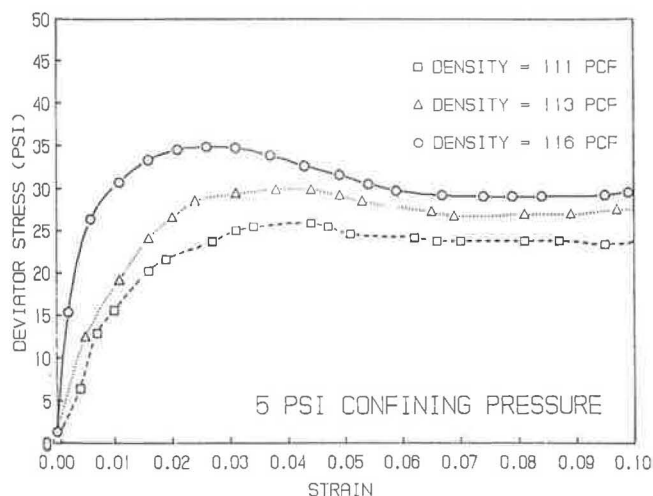


FIGURE 10 Typical stress-strain plots for sand.

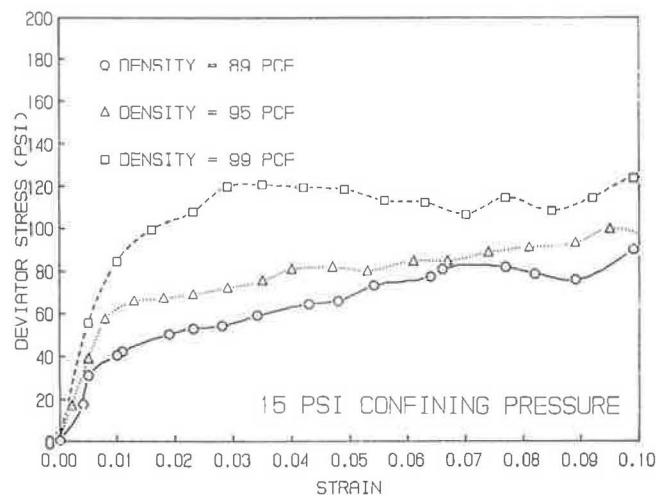


FIGURE 11 Typical stress-strain plots for area No. 4 ballast.

Density (γ). The mass per unit volume (pounds/cubic foot).

Void ratio (e). The ratio of the voids to the solids in a sample (calculated volumetrically).

Maximum aggregate size (MAS). The largest aggregate size found in a material based on sieve analysis (inches).

Effective grain size (D_{10}). The particle size corresponding to the point on the gradation curve where 10 percent of the particles are finer (inches).

D_{30} . The particle size corresponding to the point on the gradation curve where 30 percent of the particles are finer (inches).

D_{60} . The particle size corresponding to the point on the gradation curve where 60 percent of the particles are finer (inches).

Coefficient of uniformity (C_u). (D_{60}/D_{10}).

Coefficient of curvature (C_c). ($D_{30}^2/(D_{10} \times D_{60})$).

Preliminary linear regression, polynomial regression, and exponential and logarithmic correlations indicated (in all cases) that linear regression resulted in the highest correlation coefficients. Thus, the results presented in this paper include only single and multivariate linear regression analyses.

The triaxial and DCP tests were performed on samples of comparable density and material properties (gradation, moisture content, etc.). Confining pressure was selected as the basis for comparison among these procedures (i.e., the triaxial test data was differentiated by confining pressure for comparison to DCP test data).

One variable linear regression analysis was performed on the strength test parameter-material property matrix to determine the relative effect of the various material properties on the DCP and shear strength test results (Tables 5 and 6). The results of this analysis were used to select independent variables (other than PR) for the multivariate regression equations shown in Table 9.

A second series of single variable regression analyses was conducted to establish correlations between the DCP penetration rate and the shear strength test results (dependent variable) (Table 7). The results were used to establish the single variable regression equations shown in Table 8.

Multivariate regression analyses establish the effect of two or more independent variables on the dependent variable.

TABLE 6 TEST PARAMETERS VERSUS MATERIAL PROPERTIES

MATERIAL PROPERTIES	DENSITY (γ)			VOID RATIO (e)			EFFECTIVE GRAIN SIZE (D_{10})			COEFFICIENT OF UNIFORMITY (C_u)			COEFFICIENT OF CURVATURE (C_z)			MAXIMUM AGGREGATE SIZE (MAS)		
	CONFINING PRESSURES (psi)																	
TEST PARAMETERS	5	15	30	5	15	30	5	15	30	5	15	30	5	15	30	5	15	30
ALL BALLAST MATERIALS*																		
PR*	-.880	-.880	-.880	.907	.907	.907	.735	.735	.735	-.561	-.561	-.561	-.554	-.554	-.554	-	-	-
DS	.185	.634	.545	-.180	-.642	-.538	.138	-.210	-.147	-.226	.171	.067	-.231	.171	.066	-	-	-
SR	.185	.634	.545	-.181	-.623	-.538	.137	-.211	-.146	-.225	.170	.067	-.230	.169	.065	-	-	-
ϕ	.168	.661	.546	-.164	-.654	-.539	.174	-.225	-.138	-.248	.198	.069	-.252	.198	.068	-	-	-
ALL MATERIALS**																		
PR*	-.109	-.109	-.109	.097	.097	.097	.140	.140	.140	.390	.390	.390	-.527	-.527	-.527	-.329	-.329	-.329
DS	-.263	-.168	-.430	.265	.165	.440	.444	.230	.343	-.330	-.547	-.822	.192	.414	.364	.629	.492	.472
SR	-.261	-.167	-.430	.264	.164	.440	.443	.229	.343	-.329	-.546	-.822	.192	.413	.363	.627	.491	.471
ϕ	-.300	-.236	-.497	.310	.234	.511	.469	.256	.364	-.365	-.640	-.889	.236	.434	.359	.666	.494	.452

NOTE:

PR = PENETRATION RATE (inches/blow)
DS = DEVIATOR STRESS (psi)
SR = STRESS RATIO
 ϕ = FRICTION ANGLE

D_{10} , C_u , C_z AND MAS VALUES REPORTED ONLY FOR AGGREGATE MATERIAL TYPES. THE VALUES ARE IDENTICAL FOR INDIVIDUAL MATERIAL TYPES AND ARE NOT STATISTICALLY ANALYZED.

THE VALUES INDICATED FOR THE PR CORRELATIONS ARE IDENTICAL FOR EACH CONFINING PRESSURE BECAUSE OF THE DIFFERENTIATION BY CONFINING PRESSURE

SIGNIFICANT VALUE OF CORRELATION COEFFICIENT (R)	(α)	(R)
	.05	.997
*	.05	.576
**	.05	.468
	.10	.988
*	.10	.497
**	.10	.400

TABLE 7 ONE-VARIABLE LINEAR REGRESSION CORRELATION COEFFICIENTS: DCP PENETRATION RATE—SHEAR STRENGTH PARAMETERS

MATERIAL	SHEAR STRENGTH PARAMETERS								
	DEVIATOR STRESS			STRESS RATIO			FRICTION ANGLE		
	CONFINING PRESSURES (PSI)								
	5	15	30	5	15	30	5	15	30
SAND	-.999	-.999	-.989	-.999	-.999	-.992	-.995	-.999	-.990
CA-10 SANDY-GRAVEL (ROKEY)	-.992	-.997	-.975	-.992	-.997	-.976	-.981	-.995	-.974
CRUSHED DOLOMITIC BALLAST	-.991	-.867	-.934	-.993	-.867	-.934	-.998	-.905	-.928
BALLAST WITH 7.5% FA-20	-.881	-.958	-.994	-.881	-.958	-.994	-.902	-.979	-.999
BALLAST WITH 15% FA-20	-.902	-.943	-.922	-.896	-.942	-.922	-.930	-.974	-.939
BALLAST WITH 22.5% FA-20	-.991	-.976	-.971	-.991	-.976	-.972	-.990	-.982	-.977
ALL BALLAST MATERIALS*	-.281	-.617	-.517	-.280	-.617	-.517	-.275	-.649	-.517
ALL MATERIALS**	-.580	-.668	-.626	-.579	-.668	-.625	-.654	-.706	-.619

NOTE

SIGNIFICANT VALUE OF CORRELATION COEFFICIENT (R)	(α)	(R)
	.05	.997
*	.05	.576
**	.05	.468
	.10	.988
*	.10	.497
**	.10	.400

TABLE 8 ONE-VARIABLE LINEAR REGRESSION EQUATIONS

MATERIAL	CONFINING PRESSURE (PSI)	EQUATION	CORRELATION COEFFICIENT (R)	STANDARD ERROR OF ESTIMATE	DATA BASE PR RANGE
SAND	5	DS = 41.3-12.8 PR	-.999	.3	.5 - 1.2
	15	DS = 100.4-23.4 PR	-.999	.5	.5 - 1.2
	30	DS = 149.6-12.7 PR	-.989	.9	.5 - 1.2
CA-10 SANDY-GRAVEL (ROKEY)	5	DS = 51.3-13.6 PR	-.992	1.9	.55-2.15
	15	DS = 62.9- 3.6 PR	-.997	.3	.55-2.15
	30	DS = 90.7- 5.8 PR	-.975	1.5	.55-2.15
CRUSHED DOLOMITIC BALLAST	5	DS = 64.1-13.3 PR	-.991	1.4	.7 - 1.8
	15	DS = 139.0-40.6 PR	-.867	18.9	.7 - 1.8
	30	DS = 166.3-16.2 PR	-.934	5.0	.7 - 1.8
BALLAST WITH 7.5% FA-20	5	DS = 87.2-78.7 PR	-.881	7.5	.4 - .65
	15	DS = 216.1-213.9 PR	-.958	11.3	.4 - .65
	30	DS = 282.1-233.2 PR	-.994	4.4	.4 - .65
BALLAST WITH 15% FA-20	5	DS = 47.5- .45 PR	-.902	12.4	.25 - .55
	15	DS = 184.2-215.5 PR	-.943	16.3	.25 - .55
	30	DS = 206.4-135.7 PR	-.922	12.3	.25 - .55
BALLAST WITH 22.5% FA-20	5	DS = 49.7-23.1 PR	-.991	.9	.2 - .6
	15	DS = 133.1-68.6 PR	-.976	4.5	.2 - .6
	30	DS = 192.1-95.8 PR	-.971	6.9	.2 - .6
ALL BALLAST MATERIALS*	5	DS = 50.8- 6.3 PR	-.281	9.7	.2 - 1.8
	15	DS = 122.5-34.2 PR	-.617	19.8	.2 - 1.8
	30	DS = 169.1-23.1 PR	-.517	17.3	.2 - 1.8
ALL MATERIALS**	5	DS = 51.5-12.5 PR	-.580	9.6	.2 - 2.2
	15	DS = 115.9-32.8 PR	-.668	19.9	.2 - 2.2
	30	DS = 168.6-36.9 PR	-.626	25.1	.2 - 2.2

NOTE: DS = DEVIATOR STRESS (PSI) AT FAILURE

PR = PENETRATION RATE (INCHES/BLOW)

SIGNIFICANT VALUE OF CORRELATION COEFFICIENT (R)

(α)	(R)
.05	.997
*.05	.576
**.05	.468
.10	.988
*.10	.497
**.10	.400

dent variable. When considering materials of a similar nature (i.e., sand, sandy gravel, and ballast with a uniform fines content), the addition of terms other than the DCP penetration rate did not improve the accuracy [increased R , decreased standard error of estimate (SEE)] of the estimated deviator stress. For a broad range of granular materials (i.e., ballast materials with unknown or highly variable fines content, or unknown material type), the inclusion of additional terms in the deviator stress at failure prediction equations increases R and decreases SEE (Table 9).

The use of the multivariate equations requires determination of various material properties (C_u , MAS, e , and γ). The PR value is assumed to be middepth of the layer and should be the average of several trials.

The linear regression equations presented in Tables 8 and 9 are characterized by a range of R and SEE values. Thirteen of the 24 single-variable regression equations (Table 8) are significant at a level of significance (α) equal to 0.10. For the multivariate linear regression equations (Table 9), 25 of the 27 equations are significant at α equals 0.10. In general, better estimates (higher R , lower SEE) of the deviator stress at failure are obtained if the material type (ballast, sand, sandy

gravel) is known. The broader the data base range considered (specific material—all ballast materials—all materials), the less precise (lower R , higher SEE) the estimate.

The equations reported in Tables 8 and 9 are valid only for the specified conditions. Extrapolation beyond the limits of the data base developed in this study should be done with caution.

COMMENTS

Several important facts were noted during the DCP and triaxial testing programs and data analyses. The DCP device is well-suited for granular materials with a MAS ranging from sand size particles to 1½ in. It appears that there is an upper bound maximum aggregate size where the DCP is no longer a viable test method. Deflection of the penetration shaft and the inability to penetrate or displace large aggregates are the primary limiting factors. The upper MAS limit was not addressed in this study.

The MAS has a notable effect on DCP test variability. Generally, an increased MAS results in larger voids that con-

TABLE 9 MULTIVARIATE LINEAR REGRESSION EQUATIONS

MATERIAL	CONFINING PRESSURE (PSI)	EQUATION	CORRELATION COEFFICIENT	STANDARD ERROR OF ESTIMATE
ALL BALLAST MATERIALS	5	DS = 50.8-6.3 PR	.281**	9.7
		DS = 62.0-13.3 PR-.97 Cu	.542**	9.0
		DS = -137.8+8.1 PR+1.9 Cu-2.2 Y	.690*	8.2
		DS = -607.8-1.7 PR+5.1 Cu+236.6 Y -2.2e	.731*	8.2
	15	DS = 122.5-34.2 PR	.618	19.8
		DS = 135.3-42.1 PR-1.1 Cu	.653*	20.1
		DS = -597.6+36.3 PR+6.9 Cu-5.7 Y	.907	11.8
		DS = -1488+17.8 PR+13.0 Cu+448.3 Y -5.7e	.926	11.3
	30	DS = 169.1-23.1 PR	.517*	17.3
		DS = 182.2-31.2 PR - 1.1 Cu	.583*	17.3
		DS = -482.2+39.9 PR+6.2 Cu-5.3 Y	.918	9.0
		DS = -883.9+31.6 PR+9.0 Cu+202.3 Y -5.3e	.924	9.3
ALL MATERIALS	5	DS = 51.5-12.5 PR	.580	9.6
		DS = 37.0-9.0 PR+7.8 MAS	.743	8.2
		DS = 35.3-9.6 PR+6.4 MAS+7.0e	.746	8.4
		DS = -242.7-8.2 PR+1.9 MAS+126.9e+8.8 Y	.759	8.5
		DS = -209.4-11.1 PR+1.7 MAS+125.6e+7.2 Y +.08Cu	.763	8.8
	15	DS = 115.9-32.8 PR	.669	19.9
		DS = 116.7-26.4 PR-.28 Cu	.738	18.7
		DS = 100.0-23.4 PR+8.9 Cu-.24 MAS	.772	18.2
		DS = 158.0+4.9 PR-175.2 Cu+25.2 MAS-.95e	.850	15.6
		DS = -5.2+3.2 PR+1.1 Cu-96.6 MAS+25.2e-.91 Y	.852	16.2
	30	DS = 168.6-36.9 PR	.626	25.1
		DS = 170.5-21.3 PR -.69 Cu	.886	15.4
		DS = 156.8-18.8 PR+7.3 Cu-.66 MAS	.900	15.0
		DS = -168.5+9.8 PR+2.6 Cu+25.0 MAS-1.3 Y	.939	12.2
		DS = -341.3+10.6 PR+3.9 Cu+75.4 MAS+26.0 Y-1.3e	.940	12.7

NOTE:

DS = DEVIATOR STRESS AT FAILURE

PR = PENETRATION RATE

Cu = COEFFICIENT OF UNIFORMITY (D_{60}/D_{10})

Y = DENSITY

e = VOID RATIO

MAS = MAXIMUM AGGREGATE SIZE

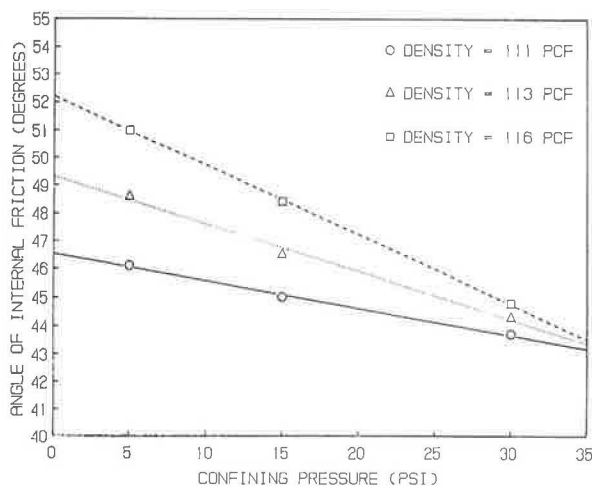
* = CORRELATION COEFFICIENT (R) NOT SIGNIFICANT FOR $\alpha = .05$ ** = CORRELATION COEFFICIENT (R) NOT SIGNIFICANT FOR $\alpha = .10$ 

FIGURE 12 Angle of internal friction-confining pressure relations for sand.

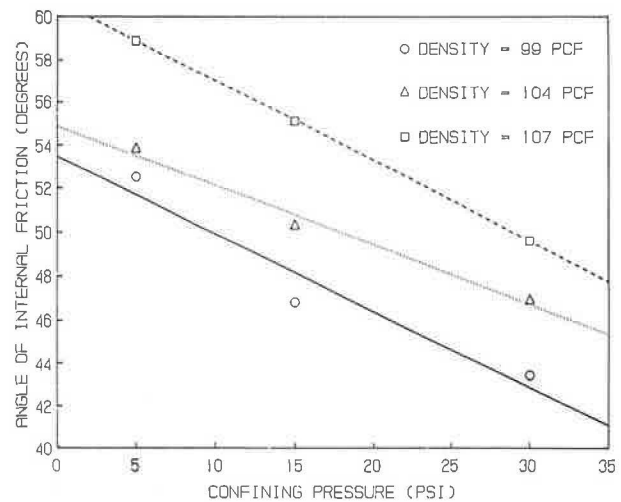


FIGURE 13 Angle of internal friction-confining pressure relations for Area No. 4 ballast with 7.5 percent FA-20.

tribute significantly to increased variability in the PR values. The inclusion of FA-20 fines in the AREA No. 4 ballast tended to reduce this effect.

The triaxial test phase evaluated samples comparable to those tested in the DCP phase. The confining pressure was not evaluated directly by the DCP test. The confining pressure influence (Figures 8 and 9) is related to the overburden effects evident in the DCP tests. The overburden effect (confining pressure due to the weight of the overlying material) was not evaluated beyond a depth of 15 in. in this study. Typically, the PR did not display large variations beyond middepth of the DCP mold.

The relationship between the shear strength parameters and the triaxial test conditions (i.e., density and confining pressure) exhibit several noteworthy trends. The angle of internal friction (calculated from the stress ratio at failure) increases with increasing density at a particular confining pressure and decreases with increasing confining pressure at a particular density. Figures 12 and 13 illustrate this effect. The second point is particularly important because, as the confinement due to overburden effects and loading increases, the friction angle decreases indicating a relative loss in strength. This behavior is common to many materials and is evident in a typical Mohr-Coulomb diagram with a curved failure envelope (9,10).

The strong impact of confining pressure on shear strength is evident in the regression equations presented in Tables 8 and 9. Notice in particular the increase in the intercept values (constants in the equations) with a confining pressure increase. The accuracy associated with predicting in situ shear strength is obviously dependent on the ability to estimate the in situ confining stress conditions reasonably.

SUMMARY

The conclusions and general findings of this study are as follows:

1. The DCP test may be used to estimate the shear strength of a variety of cohesionless granular materials (including sand, sandy gravel, and ballast) using the prediction equations developed.
2. Detailed material characteristics (such as gradation, maximum aggregate size, density, void ratio) are not required to predict shear strength from DCP data. However, as noted in Table 9, additional material characteristic inputs increase the accuracy of the prediction for ill-defined materials.
3. To select the appropriate prediction equation requires an estimate of the confining pressure under field loading conditions. The estimation of confining pressure under realistic field loading conditions is an area requiring further investigation.
4. The DCP device is a viable alternative and/or supplement to detailed in situ test pit type investigations. DCP tests are rapidly conducted and inexpensive. In most cases, numerous less sophisticated and detailed tests (such as the DCP) will provide more useful and valid information than a limited number of detailed tests.

5. The DCP can be used effectively to gather input information rapidly and economically for use in the USA-CERL RAILER system for performing simplified structural evaluations.

ACKNOWLEDGMENTS

This research was conducted by the University of Illinois for the U.S. Army Construction Engineering Research Laboratory as part of the RAILER system development. The authors appreciate the support and sponsorship of the U.S. Army Pavements and Railroad Maintenance Committee, especially chairman Robert Williams from the U.S. Army Engineering and Housing Support Center. The authors also wish to acknowledge the extensive field DCP work and data analysis performed by the USA-CERL RAILER group, especially Richard Harris and Mohammed Khan.

REFERENCES

1. M. E. Ayers and M. R. Thompson. *Rapid Shear Strength Evaluation of In situ Ballast/Subballast Materials*. Technical Report, Department of Civil Engineering, University of Illinois at Urbana-Champaign, June 1988.
2. G. F. Sowers, C. S. Hedges. *Dynamic Cone for Shallow In situ Penetration Testing*. ASTM Special Technical Publication 399. American Society for Testing and Materials, Philadelphia, Penn., 1966.
3. E. G. Kleyn. *The Use of the Dynamic Cone Penetrometer*. Report L2/74. Transvaal Roads Department, Pretoria, South Africa, 1975.
4. M. Livneh and I. Ishai. Pavement and Material Evaluation by a Dynamic Cone Penetrometer. In *Proc., 6th International Conference on Structural Design of Asphalt Pavements*, Vol. 1, University of Michigan, Ann Arbor, 1987.
5. L. Raad and J. L. Figueroa. Load Response of Transportation Support Systems. *Transportation Engineering Journal*, ASCE, Vol. 106, No. TE1, Jan. 1980.
6. Q. L. Robnett, M. R. Thompson, R. M. Knutson and S. D. Tayabji. *Development of a Structural Model and Materials Evaluation Procedures*. Federal Railroad Administration Report FRA-OR&D-76-255. PB No. 262 987. Ballast and Foundation Materials Research Program, Department of Civil Engineering, University of Illinois at Urbana-Champaign, 1976.
7. L. Raad and M. R. Thompson. Discussion: A Study of Analytical Models for Track Support Systems. In *Transportation Research Record 733*, TRB, National Research Council, Washington, D.C., 1979.
8. A. J. Green and S. J. Knight. *Effect of Mold Size and Other Factors on Laboratory Cone Index Measurements*. Misc. Paper No. 4-327, U.S. Army Corps of Engineers, Waterways Experiment Station, March 1959.
9. K. Terzaghi and R. B. Peck. *Soil Mechanics in Engineering Practice*. 2nd ed. John Wiley & Sons, Inc., New York, 1967.
10. R. B. Peck, W. E. Hanson, and T. H. Thornburn. *Foundation Engineering*. 2nd ed. John Wiley & Sons, Inc., New York, 1974.

The contents of this paper reflect the views of the authors, who are responsible for the facts and the accuracy of the data presented herein. The contents do not necessarily reflect the official views of the U.S. Army Corps of Engineers. This paper does not constitute a standard, specification, or regulation.

Publication of this paper sponsored by Committee on Strength and Deformation Characteristics of Pavements.

TABLE 4 TRIAXIAL TEST RESULTS

MATERIAL	DENSITY (PCF)	CONFINING PRESSURE (PSI)	DEVIATOR STRESS (PSI)	STRESS RATIO	FRICTION ANGLE (DEGREES)
SAND	111	5	25.8	6.16	46.1
	111	15	72.6	5.84	45.0
	111	30	134.0	5.47	43.7
	113	5	30.0	7.00	48.6
	113	15	79.0	6.27	46.5
	113	30	139.0	5.63	44.3
	116	5	34.8	7.96	51.0
	116	15	88.9	6.93	48.4
	116	30	143.0	5.77	44.8
CA-10 SANDY GRAVEL (ROKEY)	119	5	21.5	5.30	43.0
	119	15	54.9	4.66	40.3
	119	30	77.9	3.60	34.4
	123	5	37.2	8.44	52.0
	123	15	58.9	4.93	41.5
	123	30	85.3	3.84	35.9
	127	5	42.9	9.58	54.2
	127	15	60.7	5.05	42.0
	127	30	86.8	3.89	36.2
CRUSHED DOLO- MITIC BALLAST	89	5	40.5	9.10	53.3
	89	15	69.3	5.62	44.3
	89	30	138.0	5.60	44.2
	95	5	50.4	11.1	56.6
	95	15	85.7	6.71	47.8
	95	30	147.0	5.90	45.2
	99	5	55.7	12.1	57.9
	99	15	122.0	9.13	53.4
	99	30	158.0	6.27	46.5
BALLAST WITH 7.5% FA-20	99	5	38.5	8.70	52.5
	99	15	80.7	6.38	46.8
	99	30	132.0	5.40	43.4
	104	5	41.8	9.36	53.8
	104	15	100.0	7.67	50.3
	104	30	162.0	6.40	46.9
	107	5	59.4	12.9	58.9
	107	15	136.0	10.1	55.1
	107	30	191.0	7.37	49.6
BALLAST WITH 15% FA-20	102	5	38.9	8.78	52.7
	102	15	70.0	5.67	44.4
	102	30	135.0	5.50	43.8
	107	5	46.8	10.3	55.4
	107	15	95.7	7.38	49.6
	107	30	149.0	5.97	45.5
	112	5	67.8	14.6	60.7
	112	15	139.0	10.3	55.5
	112	30	179.0	6.97	48.5
BALLAST WITH 22.5% FA-20	110	5	35.7	8.14	51.4
	110	15	92.8	7.19	49.1
	110	30	136.0	5.53	44.0
	113	5	43.5	9.70	54.4
	113	15	109.0	8.27	51.6
	113	30	158.0	6.27	46.4
	116	5	44.6	9.92	54.8
	116	15	122.0	9.13	53.4
	116	30	177.0	6.90	48.3
FA-20	113	15	113.0	8.53	52.2
	121	15	150.0	11.0	56.4

TABLE 5 ONE-VARIABLE LINEAR REGRESSION CORRELATION COEFFICIENTS: TEST PARAMETERS VERSUS MATERIAL PROPERTIES

TEST PARAMETERS	MATERIAL PROPERTIES					
	DENSITY (γ)			VOID RATIO (e)		
	CONFINING PRESSURES			CONFINING PRESSURES		
	5 psi	15 psi	30 psi	5 psi	15 psi	30 psi
SAND						
PR	-.999	-.999	-.999	.994	.994	.994
DS	.997	.999	.983	-.988	-.997	-.967
SR	.997	.999	.988	-.988	-.997	-.974
ϕ	.991	.999	.985	-.979	-.992	-.970
CA-10 SANDY GRAVEL (ROKEY)						
PR	-.989	-.989	-.989	.959	.959	.959
DS	.965	.976	.933	-.918	-.936	-.873
SR	.965	.976	.935	-.918	-.935	-.875
ϕ	.943	.972	.933	-.886	-.929	-.872
CRUSHED DOLOMITIC BALLAST						
PR	-.981	-.981	-.981	.998	.998	.998
DS	.998	.946	.985	-.996	-.952	-.893
SR	.997	.945	.984	-.998	-.951	-.893
ϕ	.991	.969	.981	-.999	-.947	-.927
BALLAST WITH 7.5% FA-20						
PR	-.999	-.999	-.999	.982	.982	.982
DS	.868	.950	.991	-.779	-.889	-.957
SR	.867	.949	.990	-.778	-.888	-.957
ϕ	.889	.972	.997	-.807	-.924	-.974
BALLAST WITH 15% FA-20						
PR	-.981	-.981	-.981	.981	.981	.981
DS	.967	.989	.978	-.967	-.989	-.978
SR	.963	.988	.979	-.964	-.988	-.978
ϕ	.982	.999	.987	-.982	-.999	-.987
BALLAST WITH 22.5% FA-20						
PR	-.960	-.960	-.960	.846	.846	.846
DS	.917	.998	.999	-.770	-.941	-.948
SR	.917	.997	.998	-.770	-.940	-.946
ϕ	.914	.995	.997	-.766	-.930	-.939

Generally, the use of multiple independent variables (PR and additional variables) had only a slight beneficial effect on the correlation coefficient (R). Multivariate regression equations are presented in Table 9 for all ballast materials regardless of fines content and all granular material types.

Discussion of Data Analyses

The inputs for the regression equations presented in Tables 7 and 8 are the in situ confining pressure (under field loading conditions) and the DCP penetration rate.

It is difficult to quantify the wheel loading-induced confining pressure stress states generated in typical granular layer-subgrade soil systems. Linear elastic layer analysis procedures (without failure criteria) frequently indicate tensile stresses in the bottom region of the granular layer. Stress-dependent moduli finite element models with Mohr-Coulomb failure criteria have been developed for railroad track systems (ILLI-TRACK) (6,7) and highway and airfield pavements (ILLI-PAVE) (5). In the ILLI-TRACK and ILLI-PAVE models, tensile stresses are not calculated in the granular material

layer. Although the finite element models provide an improved estimate of the stress state in the granular layer, the estimate should be considered as only approximate.

The DCP penetration rate should be the average of the PRs obtained at middepth, middepth + 2 in., and middepth - 2 in. within each layer. The PR value input into the equations should be the average value from a number of DCP tests conducted at each site (the results from each layer are averaged and a separate shear strength calculated).

Determination of in situ density, void ratio, gradation, etc. is time-consuming, costly, and generally impractical (if not impossible). An objective of this study is to predict strength parameters that are based on a rapid and inexpensive test method. Therefore, the single-variable equations reported in Table 8 are based solely on DCP test results and do not require the determination of additional in situ material properties. Factors such as moisture and density are implicitly accounted for in the single variable equations, because a direct relationship exists between the DCP PR and shear strength.

A step-wise multivariate linear regression analysis was performed, in which the deviator stress at failure was the depen-

Determination of Deflection of Pavement Systems Using Velocity Transducers

SOHEIL NAZARIAN AND ALBERT J. BUSH III

The analytical models used to design and rehabilitate pavements are becoming more sophisticated. The most appropriate process for verifying the accuracy and usefulness of these new analytical models (as well as for calibrating the parameters involved in these models) is to observe the behavior of pavements in the field. Unfortunately, few devices or techniques are available for determining the displacement of a pavement section under actual loads. In addition, the available methods for monitoring the performance of pavements in terms of displacement are expensive and/or inaccurate. One economical alternative is the use of velocity transducers (geophones). Geophones are quite inexpensive and readily available. In addition, if used properly, geophones can provide quite accurate deflection-time histories. The methodology involved in determining deflection from geophones is complex. Proper mathematical manipulation of the geophone record, using signal analysis techniques and theory of vibration, should be carried out so that the deflection-time history can be accurately determined. Fortunately, the necessary mathematical manipulation can be programmed into a portable microcomputer so that the deflection-time history can be obtained rapidly in the field. This paper presents an overview of theoretical alternatives available for determining the deflection-time history of pavements using geophones. The limitations and advantages of each alternative are discussed. The practical problems that should be addressed in developing a proper algorithm for each alternative are also included. Through an illustrative example and a case study, the versatility of using geophones as a tool for determining the deflection-time history of pavements is demonstrated.

Monitoring long-term pavement performance has been greatly emphasized in the last few years. A good example is the level of effort and the amount of funds dedicated to collecting this type of data by the Strategic Highway Research Program (SHRP). An economical alternative for collecting the deflection-time history of pavements is to install and monitor geophones, which are quite inexpensive. In addition, the methodology required for determining deflection from the geophone output can be automated.

In this paper, different methods that may be used to determine the deflection-time history of a pavement section from a geophone (velocity transducer) record are reviewed. The theoretical background behind each method is discussed. Practical problems associated with the implementation of these theoretical methods are also addressed. An illustrative example provides better insight into each process discussed. Actual records obtained from a falling weight deflectometer (FWD)

device were used in this example. Finally, a case study is included to demonstrate that, if used properly, geophones can provide accurate deflection-time history records of pavements under actual loads.

GENERAL BACKGROUND

An undamaged geophone can be modeled accurately as a damped single-degree-of-freedom (SDOF) system. The fundamentals of the response of such a system to an arbitrary excitation are included in this section. (It should be mentioned that only subjects relevant to this report are discussed here. For further information, the reader can refer to any structural dynamics textbook.)

Idealized Model of a Geophone

Geophones are coil-magnet systems, as shown schematically in Figure 1. A mass is attached to a spring, and a coil is connected to the mass. The coil is located such that it crosses the magnetic field. On impact, the magnet moves but the mass remains more or less stationary, causing a relative motion between the coil and the magnet. This relative motion generates a voltage in the coil, which is proportional to the relative velocity between the coil and magnet.

The geophone system can be considered an SDOF system. This idealized system is shown in Figure 2. To describe a geophone properly, the natural frequency, transductivity, and damping properties should be addressed. The natural frequency is the undamped natural frequency of the system.

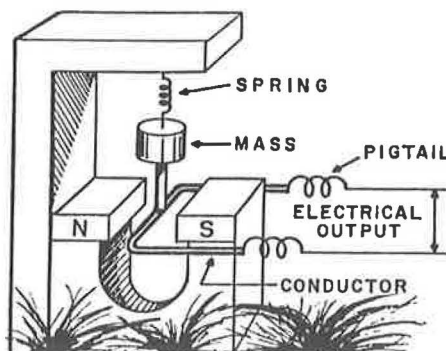


FIGURE 1 Elements of a geophone (2).

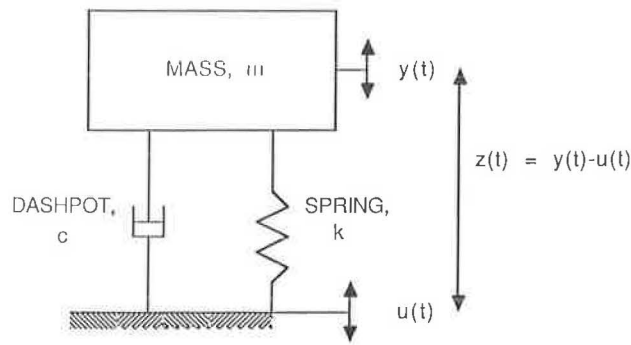


FIGURE 2 Idealized model of a geophone.

Transductivity is the factor of proportionality between the velocity and the output voltage and can be considered a calibration factor. Damping the system indicates the attenuation of the motion with time.

In an actual test, an impact is imparted to the system (say, a pavement section) which causes waves to propagate in the body as well as the surface of the pavement. If the geophone is securely attached to the pavement, the base of the geophone will follow closely the movement of the pavement. The movement of the geophone base generates a voltage output in the coil-magnet system. Finally, this voltage is monitored by an oscilloscope or a voltmeter. The voltage output of a geophone is not proportional to the actual movement of the pavement, but it is proportional to the movement of the coil-magnet system. Therefore, in order to obtain the actual movement of the pavement surface, the movement of the coil-magnet system should be translated to the actual movement of the base. To derive this relationship theoretically, the equivalent components of the model (Figure 2) and an actual geophone should be identified.

The mass, m , in the model is equivalent to the total mass of the spring, suspended mass, and the conductor (Figure 1) of the geophone. The dashpot, which provides viscous damping in the model, simply corresponds to the electrical resistance of the conductor, pigtail, and any external resistor added to the system. The movement of the base is shown as a vertical excitation, $u(t)$. The coil-magnet movement (or the voltage output) is equivalent to the relative movement of the mass, m , in the model. If the movement of the base, $u(t)$, is measured relative to a fixed-reference datum, and if the movement of the mass, $y(t)$, is measured relative to the same fixed datum, the coil-magnet movement is then equal to $z(t) = y(t) - u(t)$. The relationship between $z(t)$ and $u(t)$, which is equivalent to the relationship between the output voltage of the geophone and the ground movement, is described below.

Dynamic Response of an SDOF System

If the idealized system shown in Figure 2 is excited by a base movement, $u(t)$, the differential equation describing the response motion can be derived by specifying that the sum of all the forces in the system be equal to zero. The forces consist of spring force, damping force, inertial force, and finally the excitation force. The equation of motion can be written as

$$m \cdot \ddot{y}(t) + c \cdot \dot{z}(t) + k \cdot z(t) = 0 \quad (1)$$

For simplicity, let $u(t)$ be a harmonic motion with a frequency of f , so that

$$u(t) = u_0 \exp(i 2\pi f t) \quad (i = \sqrt{-1}) \quad (2)$$

Then the solution to Equation 1 can be written as

$$z(t) = z_0 \exp(i 2\pi f t) \quad (3)$$

where

$$z_0 = u_0 \cdot r^2 / [(1 - r^2) + (i 2Dr)] \quad (4)$$

$$r = f/f_n = f/[(k/m)^{0.5}/2\pi] \quad (5)$$

$$D = c/c_c = c/(2km)^{0.5} \quad (6)$$

f_n and c_c represent the natural frequency and critical damping of the SDOF system, respectively. D is the damping ratio. In Equation 3, z_0 corresponds to the maximum relative deformation of the mass.

If both sides of Equation 4 are divided by u_0 , the maximum movement of the base, the outcome is the frequency response of the system and is denoted as H . Therefore

$$H = r^2 / [(1 - r^2) + (i 2Dr)] \quad (7)$$

The frequency response of a geophone is better known as the calibration curve. At each frequency, the calibration curve is a complex quantity. A complex quantity can be represented by its real and imaginary components, or alternatively by its magnitude and phase. The modulus of frequency response, M , is called the magnification factor and is calculated from

$$M = r^2 / [(1 - r^2)^2 + (2Dr)^2]^{0.5} \quad (8)$$

The arctangent of the ratio of the imaginary and real components of Equation 7 yields the phase difference between the input and the output. This relationship can be written as

$$\phi = \arctan [2Dr/(1 - r^2)] \quad (9)$$

where ϕ is the phase difference.

The significance of this formulation is that the response of an SDOF system excited by any harmonic excitation can be easily determined, if the natural frequency and the damping ratio of the system are known. It should be emphasized that a complete calibration curve consists of the magnitude and the phase information (or alternatively, the real and imaginary components). It is customary to demonstrate the calibration curve in terms of magnitude only. The magnitude by itself is of little value for determining deflections.

Response of a Geophone to an Arbitrary Excitation

A closed-form solution is available for only a limited number of well-defined excitation forces. However, three alternative numerical approaches are widely used to obtain analytical expressions for the response of a system to a general dynamic loading. These three approaches are the time-domain solution (also known as the Duhamel integral method), the Laplace

transform method, and the frequency-domain solution (the Fourier transform method). In this paper, only the time and frequency-domain methods are included; however, the Laplace transform method is most appropriate for hand calculation (as opposed to using a computer).

Time-Domain Solution

If an arbitrary excitation, $u(t)$, with a duration of t_0 is applied to a system, the response motion, $z(t)$, can be written as

$$z(t) = \int_0^t u(\tau) \cdot I(t - \tau) d\tau - u(t) \quad (10)$$

where

$$I(t) = -\omega_n \cdot \exp(-D\omega_n t) \cdot [2D\cos(\omega_d t) - A\sin(\omega_d t)] \quad (11)$$

$\omega_n = 2\pi f_n$ = natural circular frequency,

$\omega_d = \omega_n (1 - D^2)^{0.5}$ = damped natural circular frequency,
and

$$A = (2D^2 - 1)/(1 - D^2).$$

In Equation 11, $I(t)$ is called the unit impulse function. Unit impulse function is the motion response of an SDOF system to an impulse of short duration. The integral in Equation 10 is the convolution integral. In other words, the response of an SDOF system to an arbitrary excitation is simply the convolution of the excitation with the unit impulse function. This solution is convenient, because it can be easily programmed in a computer.

Frequency-Domain Solution

Any function in the time domain can easily be expressed in terms of a limited number of harmonic functions, if Fourier transform is used. If an SDOF system is linear, the response motion of the system can be obtained by (a) transforming the input motion to the frequency domain, (b) multiplying the transformed input by the frequency response curve of the system (as derived Equation 7), to obtain the response in the frequency domain, and (c) inverse-transforming the resultant of Step 2 into the time domain.

To clarify this matter further, say $u(t)$ is the motion at the base of a geophone (i.e. the input). If $U(f)$ is the Fourier transform of $u(t)$, and $H(f)$ is the frequency response of the geophone (see Figure 2), then the output voltage of the geophone (i.e., the response motion) in the frequency domain, $Z(f)$, can be written as

$$Z(f) = H(f) \cdot U(f) \quad (12)$$

The output of the geophone in the time domain, $z(t)$, is simply equal to the inverse-transform of $Z(f)$. It can be shown that $I(t)$, the unit impulse response function is the inverse-Fourier transform of $H(f)$, the frequency response function. Also it can be proven that convolution in the time domain is equivalent to multiplication in the frequency domain. Therefore, if the response of a known SDOF system subjected to

an arbitrary input function, $u(t)$, is to be determined, any of the two approaches described above can be used interchangeably to obtain identical results. At first glance, it may seem that the second method is not as straightforward as the first. However, for complicated input functions, the second method is computationally more efficient.

Illustrative Example

Let us assume that a geophone has a natural frequency of 4.7 Hz, and a damping ratio of 0.64, and let the base of this geophone be subjected to a half-sine velocity impulse with a duration of 25 msec as shown in Figure 3. The unit impulse function corresponding to Equation 11 is shown in Figure 4.

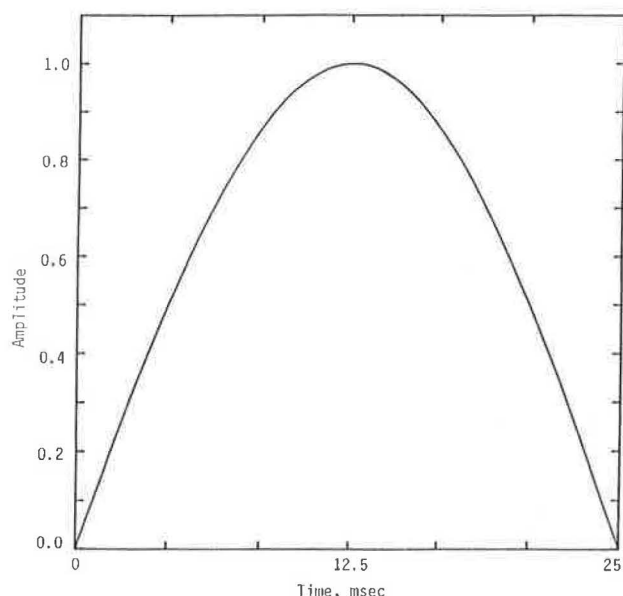


FIGURE 3 Half-sine velocity impulse.

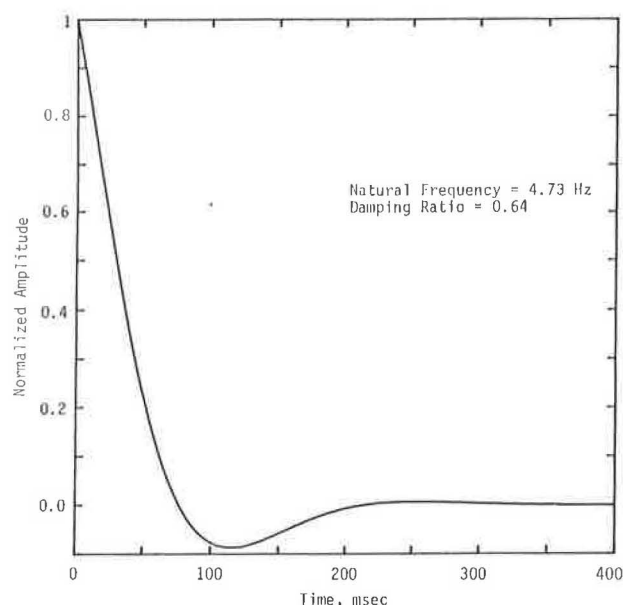


FIGURE 4 Unit impulse function for a single-degree-of-freedom system.

A program that convolves the input and impulse function was used to determine Equation 10 (I). The input (half-sine velocity impulse) and the response (relative velocity of the coil-magnet) are compared in Figure 5. The maximum value of response is about 75 percent of the input, and the maximum response occurs at about 20 msec, which is about 2.5 msec before the maximum of the input takes place.

The same example is solved using frequency-domain approach. The Fourier transform of the half-sine impulse is shown in Figure 6 in terms of magnitude and phase. The frequency response function derived in Equation 7 is shown in Figure 7 in terms of magnitude and phase also. The product of these two curves, which is the velocity of the coil-magnet system, is shown in Figure 8. The last step is to inverse-transform this response to the time domain to obtain directly the coil-magnet velocity response time history. The result is almost identical to that of the time-domain solution shown in Figure 5. This process is coded in a FORTRAN algorithm as well (I).

DETERMINATION OF DEFLECTIONS FROM AN ARBITRARY IMPACT

In the last section, the discussion focused on the response of a geophone given the base motion. However, in this section, the response of the system (the recorded signal) is known and the motion of the base is of interest. In other words, our main interest is to remove the distortion in the signal caused by the geophone system so that the actual movement of the pavement surface can be determined. Several procedures are available for determining displacement from geophone output. These procedures are discussed in the next few sections. The impact due to an FWD device will be used as an example throughout this section.

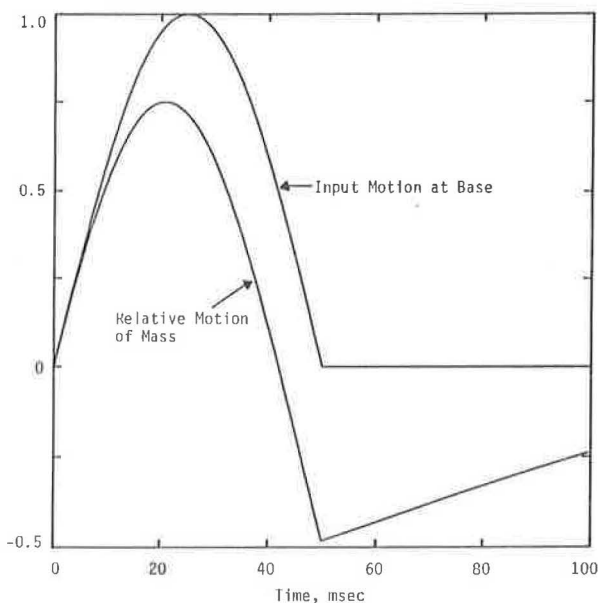


FIGURE 5 Comparison of input motion at base with relative motion of mass in an SDOF system.

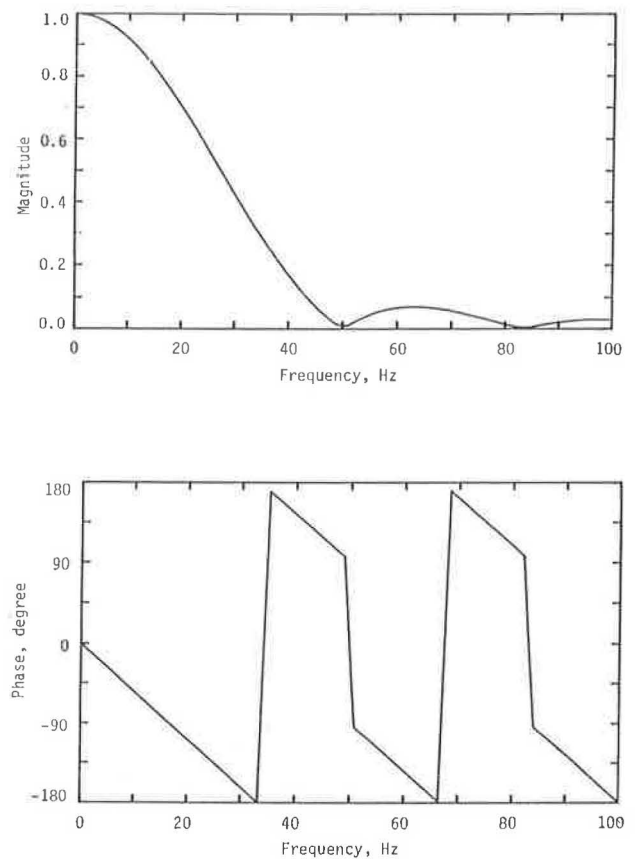


FIGURE 6 Fourier transform of a half-sine pulse with a duration of 25 msec.

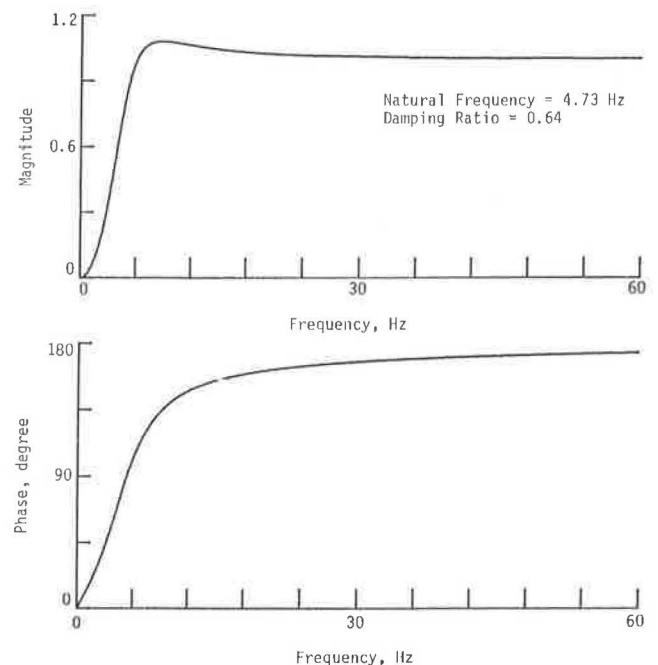


FIGURE 7 Frequency response function (calibration curve) of geophone.

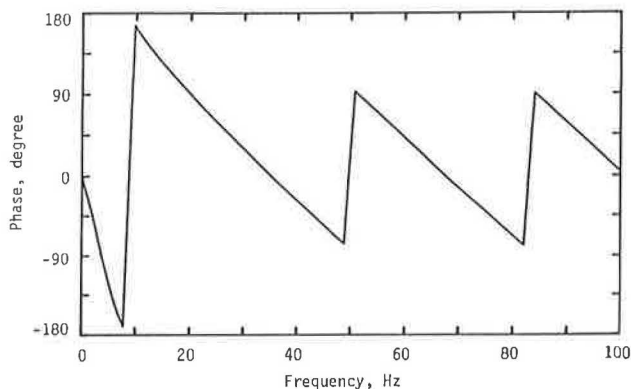
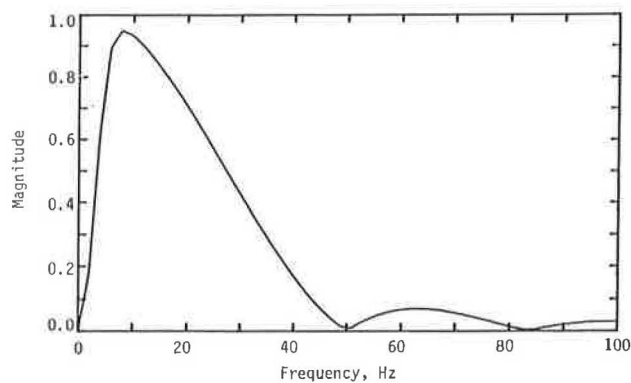


FIGURE 8 Coil-magnet system response spectrum of sensor due to a 25-msec impulse.

Impulse Method

The impulse method is adapted from the shock engineering discipline. In this approach, one is only concerned with the maximum response rather than the complete time history or the frequency content of the response. To implement this method, one simply assumes an impulse shape (in our case, a half-sine) and solves the equation of motion to obtain the value of maximum response of the system. By varying the natural frequency of the system and repeating this process, the so-called shock response spectrum (SRS) is determined (3).

An SRS is the relationship between the ratio of the maximum response and the maximum input, versus the natural frequency of the system for a given damping ratio. A major outcome of this process is that if the natural period of the system is much greater than the duration of impulse, the shock response value is more or less independent of the shape of the pulse. The significance of this statement is that as long as the duration of the pulse is small, if the shape of the input impulse deviates from the assumed one, the shock response value would not change significantly.

One major question is then, given the natural period of the system, at what impulse duration is the shape of the impulse immaterial to the response of the system? The answer to this question will be explored in the next section. However, the answer obviously depends on the desired accuracy with which the response should be determined.

Implementing this method requires three steps:

1. Calibrate the receiver and calculate response characteristics of the receiver,
2. Determine the theoretical response of the receiver to a half-sine pulse, and
3. Combine the outcomes of Steps 1 and 2 with the receiver output to determine the deflection.

Each of these steps is discussed next.

Calibration of Geophone

The fastest method of calibration is to use a shake table. In this method of calibration, a reference accelerometer is rigidly connected to the shake table and the geophone, in turn, is rigidly connected to either the accelerometer or the shake table. The shake table is vibrated with a sweep-sine steady-state source, a random-noise source, or an impulse. The calibration curve of the geophone relative to the reference accelerometer is independent of the type of excitation (4). The output voltages of the reference accelerometer and the geophone are then monitored simultaneously. The response of the accelerometer is integrated to obtain its response in terms of velocity. The ratio of the geophone output voltage and the integrated accelerometer record at each frequency is the calibration curve of the geophone.

As an example, the normalized calibration curve of a typical sensor of an FWD device is shown in Figure 9. To normalize the curve, the calibration value was divided by the transducitivity of this geophone (denoted as T_g), which is equal to 0.57 volt/in./sec. This value corresponds to the actual magnitude of the calibration curve at high frequencies (above 15 Hz). The natural frequency and the damping ratio of this system were determined by a built-in feature of the spectrum analyzer used as the recording device. This geophone has a natural frequency of 4.7 Hz (actually, 4.73 Hz) and the damping ratio of 0.64.

Theoretical Response of Geophone to Impulse

On the basis of the characteristics of the geophone, the response of the coil-magnet system to a 25-msec half-sine impulse at the base of the geophone is obtained. To obtain the coil-magnet response of the geophone to the impulse, either of the two methods described previously may be used.

To continue our example, the properties of the geophone just demonstrated are used. The coil-magnet response time history is shown in Figure 5. Also shown in Figure 5 is the actual input to the base of the geophone. From the figure, it can be seen that if the input has a maximum velocity of unity, the coil-magnet response will register a maximum of 0.75. Therefore, the voltage output from this geophone should be divided by 0.75 to compensate for the distortion of the output caused by the geophone (provided that the input impulse resembles reasonably a half-sine wave with a duration of 25 msec). This adjustment factor will be referred to as C_g hereafter.

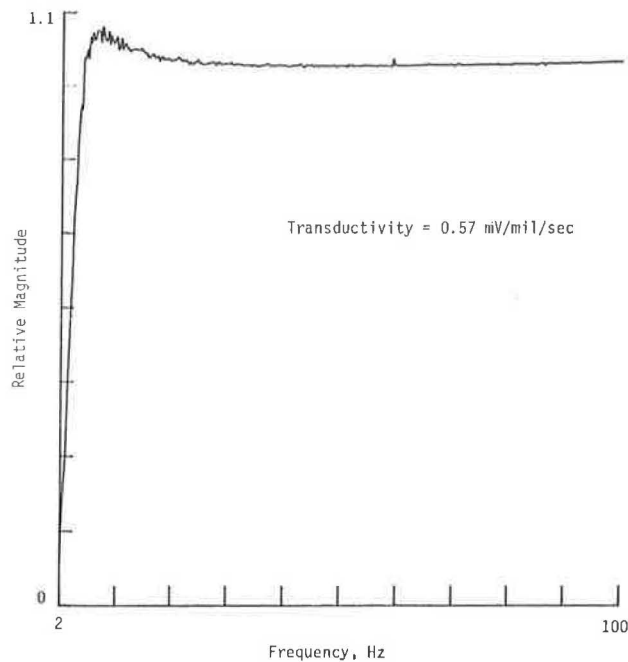


FIGURE 9 Calibration curve for a typical FWD sensor.

Determination of Deflection

To obtain the deflection from the voltage representing the output of the geophone, first, the record is divided by the transductivity of the geophone to convert voltage to velocity. Second, the converted velocity time record is divided by the adjustment factor, C_g , to compensate for the effect of the geophone on the signal. Then, the signal is integrated with respect to time to obtain the maximum deflection. This discussion can be summarized in the following formula:

$$\text{DEFLECTION} = \text{FACTOR} \cdot \text{INTVOLT} \quad (13)$$

where

DEFLECTION = deflection of pavement at geophone base,

FACTOR = $1/(T_g \cdot C_g)$, correction factor for shape and duration of impulse and transductivity of geophone, and

INTVOLT = maximum output voltage after integration of raw geophone signal saved in recording device.

To continue with our example, a typical voltage time history of an FWD sensor is shown in Figure 10. This signal was captured using a Hewlett-Packard Model 3562A spectrum analyzer. A high-frequency vibration with a low amplitude is evident in the signal. This additional vibration is due to the excitation of the raise/lower bar of the FWD trailer during impact. In Figure 10, the portion of the record to the left of Point A depicts the time history before the actual arrival of the signal. The voltage output in this region is constant and is approximately equal to 20 mv. The reasons for this deviation from zero are not known at this time and should be investigated. The second portion of the signal enclosed between

Points A and B is the response of the coil-magnet system to the impact. The record to the right of Point B with a constant output is the at-rest area of the signal. This portion has a constant magnitude of approximately 46 mv.

If one assumes that the geophone was at rest up to the arrival of the impulse (i.e., Point A), the constant value of approximately 20 mv corresponding to the output voltage of this region should be subtracted from the signal at all times. Now, this record is integrated to convert velocity into displacement. The integrated signal is shown in Figure 11. The

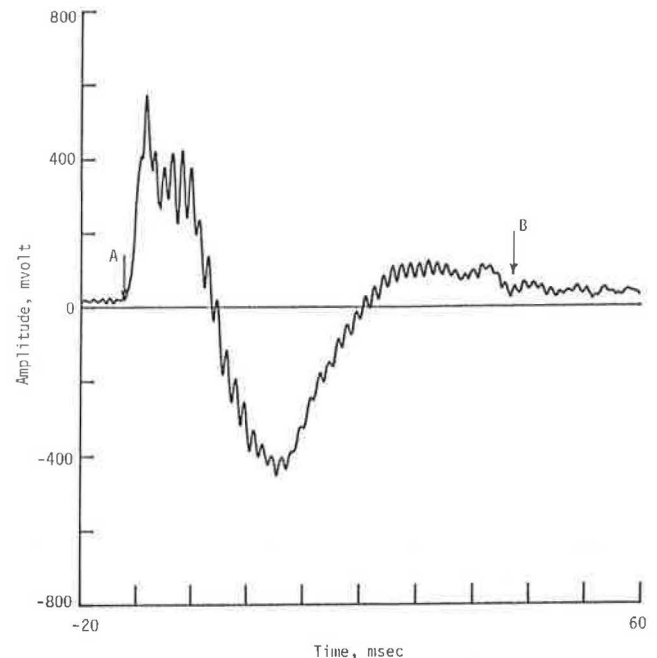


FIGURE 10 Typical velocity time history of FWD sensor.

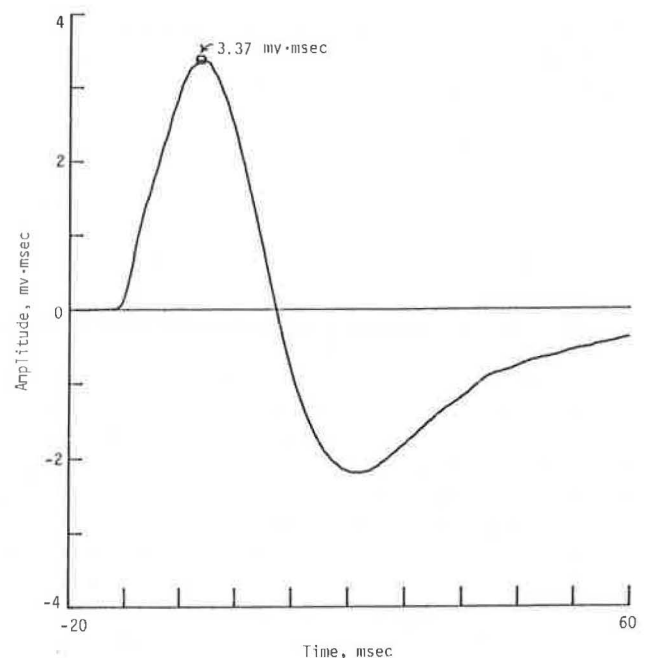


FIGURE 11 Time history of FWD sensor after integration.

open circle in Figure 11 corresponds to the maximum output. The magnitude of this point is equal to INTVOLT in Equation 16 and is equal to 3.37 mv.msec.

In the two previous sections, the values of transductivity, T_g , and adjustment factor, C_g , were reported as 0.57 mv/in./sec and 0.75, respectively. As such, parameter FACTOR is equal to 2.33 [$1/(0.57 \times 0.75)$]. Knowing the values of parameters INTVOLT and FACTOR, the maximum deflection for this example is equal to 7.9 mil. The value of the maximum from actual FWD tests at this location is 7.7 mil. The difference between the two values is less than 3 percent.

It should be emphasized that the process mentioned above only yields a correct maximum deflection for an impact resembling a half-sine impulse with a duration of 25 msec, but the time history obtained after integration is not correct and still contains the errors caused by the geophone assembly.

Parametric Study of Factors Affecting Impulse Method

In the method described above, it was assumed that the duration of impulse is 25 msec. It would be helpful to study the effect of varying the duration of the impulse (from say 20 to 30 msec) on the adjustment factor, C_g , and in turn on parameter FACTOR in Equation 13. Also, the adjustment factor is obtained based on the assumption that the impulse is a perfect half-sine wave. Another interesting parametric study is to determine the change in C_g , if the impulse is not actually a half-sine wave but a function that resembles one.

Variation in parameter C_g with duration of impulse is shown in Table 1. The adjustment factor, C_g , decreases as duration of impulse increases. If the value of C_g at 25 msec is assumed as the reference value, the absolute maximum variation in the value of C_g is about 5 percent. This method of comparison is known as *equal maximum height* method. In this method of comparison, all impulses have a maximum magnitude of 1.

Another way of comparing the effect of different impulses on C_g is by using the so-called *equal impulse area* method. If the duration of the impulse is small relative to the natural period of the geophone, this method may result in a more consistent comparison. Using the area of a 25-msec-long half-sine impulse as the basis for comparison, and requiring that the area of the impulses be equal to it, one can determine an equivalent maximum magnitude of each impulse. The area

under each impulse is included in Table 1. The values of C_g after correction for area are added, too. This method did not result in a more consistent comparison, as seen in the table. Therefore, its use was abandoned.

In the second series of tests, the duration of impulse was maintained at 25 msec, but, the shape of the impulse was changed. The impulse shapes used are summarized in Table 2. All functions used in this study are demonstrated graphically in Figure 12. The shape of all these functions resembles a half-sine wave. In actual tests, contrary to the five impulse functions included in Table 2, the time history of the load cell is not symmetrical. Therefore, a sixth case with an input time history as shown in Figure 13 was studied also. Variation in C_g with shape of the impulse is included in Table 2 also. From the table, the value of C_g may vary as much as 15 percent.

These two brief parametric studies give an indication of the accuracy of deflections obtained from the impulse method. In summary, the effect of duration of impulse is less significant, but the effect of shape on the impulse may be quite significant.

Frequency Response Method

The frequency response method takes advantage of the Fourier transform algorithm. The advantage of this method over the previous method is that the entire displacement time history can be determined, whereas with the impulse method only the maximum deflection could be found. In the frequency response method, no simplifying assumption about the nature of the load is made. As such, the results are more accurate than those from the impulse method. There is a trade-off, however. Computationally, the frequency response method is more time consuming.

The procedure involved in determining deflections from the geophone response consists of (a) the geophone is calibrated using the same procedure outlined before, (b) the time signal obtained from the geophone is Fourier transformed, (c) the Fourier transformed signal is divided by the calibration curve determined in Step a, and (d) the result from Step c is inverse-Fourier transformed to obtain deflection time history and the maximum deflection.

The same time signal depicted in Figure 9 is used in this example. The magnitude and phase relationship of the transformed time signal are shown in Figure 14. This transformed

TABLE 1 VARIATION IN ADJUSTMENT FACTOR WITH DURATION OF A HALF-SINE IMPULSE

Duration of Impulse, msec	Area Under Impulse, velocity-msec	Adjustment Factor	
		Equal Maximum Amplitude	Equal Area
20.0	12.73	0.79	0.64
22.5	14.32	0.77	0.70
25.0	15.91	0.75	0.75
27.5	17.51	0.73	0.81
30.0	19.10	0.72	0.86

TABLE 2 VARIATION IN ADJUSTMENT FACTOR WITH SHAPE OF IMPULSE

Impulse Shape Function	Adjustment Factor
$\text{Sec}^2(\frac{2t}{\tau} - 1)\pi^*$	0.86
$e^{-(2t/\tau - 1)^2\pi}$	0.79
$[\sin(\frac{2t}{\tau} - 1)\pi][(\frac{2t}{\tau} - 1)\pi]$	0.81
$\frac{2}{\pi} \text{Arc tan} [\frac{1}{2\pi^2(2t/\tau - 1)^2}]$	0.87
$\sin(\frac{t}{2\tau})\pi$	0.75
$543.66 t e^{-t/0.05}$	0.88

* τ Corresponds to Duration of Impulse (25 msec for all cases)

signal was then divided by the frequency response function (presented in Equation 7 and Figure 7) to remove the effects of the geophone on the signal. The result, which is the excitation velocity at the base in the frequency domain, is presented in Figure 15. This operation accounts for both the phase shift and variation in the magnitude. If this function is inverse-Fourier transformed, the result is the velocity time history of the base of the geophone.

The voltage output of the geophone shown in Figure 10 is compared with the velocity of the base of the geophone in Figure 16. It can be seen that the two time histories follow each other in shape. However, the magnitude of the base velocity at a given time is less, and there seems to be a phase shift between the two curves.

Continuing with the example, the frequency domain velocity record shown in Figure 15 should be integrated to obtain displacement. Integration in the frequency domain is basically a simple division of the magnitude of the signal at each frequency by the corresponding angular frequency. The result of this operation yields the displacement spectrum that is shown in Figure 17.

The last operation is to inverse-Fourier transform the displacement spectrum to obtain displacement time history. Two more details must be taken care of before obtaining the actual displacement. First, the zero displacement point should be defined. Second, the maximum displacement should be divided by the transductivity of the geophone (0.57 volt/in./sec) to obtain the actual deflection. The open circle in Figure 18 corresponds to the maximum deflection. The maximum

deflection from this method is equal to 7.8 mils [(4.46 mv)/(0.57 mv/mil/sec)]. As mentioned before, the deflection obtained from the FWD device at this point was 7.7 mils.

Another outcome of this example is the value of adjustment factor, C_g , that corresponds to the actual impulse imparted to the pavement (as opposed to the assumed half-sine wave impulse). In Figure 19, the ground deflection time history (solid line) is compared with the integral of the voltage output (dashed lines). From the figure, a phase shift between the two curves is obvious. Also notice the overshoot of the magnitude of the second half-cycle for the coil-magnet response. To obtain the actual adjustment factor, the maximum deflection from the ground deflection time history is divided by the maximum of the coil-magnet response. The adjustment factor for the type of impulses generated at the site is then equal to 0.79 (as opposed to 0.75 determined theoretically from a half-sine wave impulse).

CASE STUDY

A series of tests was performed on a rigid pavement section using the FWD device at the Corps of Engineers Waterways Experiment Station in Vicksburg, Mississippi. Two geophones independent from those of the FWD device were used in this study. Each geophone had a nominal natural frequency of 4.5 Hz and a damping ratio of 70 percent. These two geophones will be termed *well-calibrated* geophones, hereafter. The well-calibrated geophones were securely placed as closely as pos-

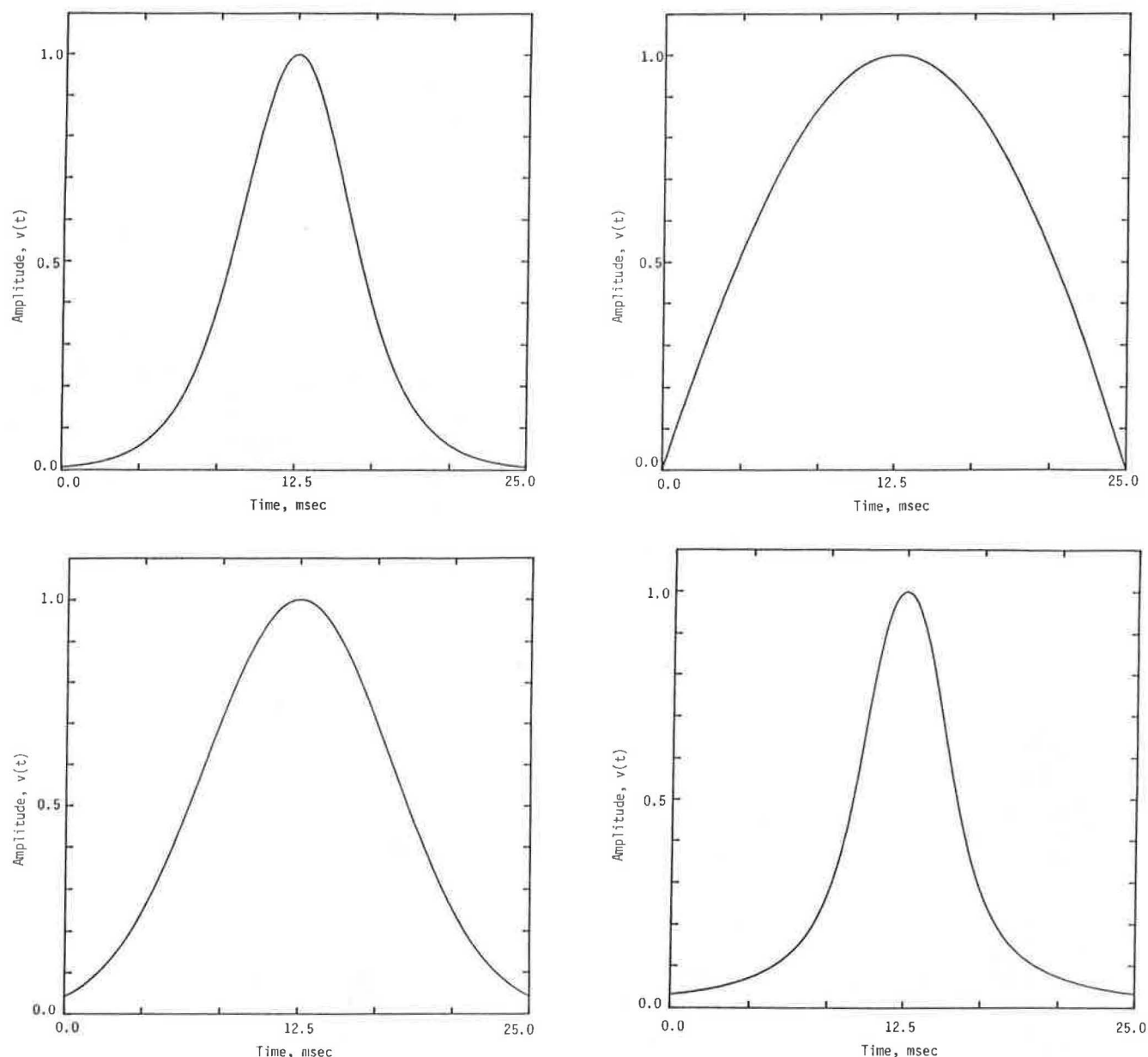


FIGURE 12 Graphical illustration of symmetrical functions resembling a half-sine function.

sible to the FWD device sensors. The signals from these geophones were captured on a recording device while the FWD device determined the deflections from the same impact simultaneously. The recording device used was a Hewlett-Packard Model 3562A spectrum analyzer. As this analyzer is a two-channel recorder, the process mentioned above was carried out several different times (each time at a different sensor location). For each process, one geophone (called the *reference* geophone) was maintained next to the FWD second sensor and served as the reference to ensure uniformity among individual impacts. A second geophone was moved each time to a new sensor location. Four drop heights were used for each geophone location. For the sake of brevity, only the results from the largest drop height are included here. However, the results from other drop heights were similar, and all discussions of this drop height can be extrapolated to all heights.

Deflections determined from the well-calibrated geophones using the impulse and frequency response methods are demonstrated in Table 3, along with their corresponding values obtained directly from FWD tests. At each sensor location, the three methods yielded deflections that were within 4 percent of one another. Bentsen et al. (5) and Briggs (personal communication, 1988) in two recent studies have shown that, in general, the precision of measurement of deflections with an FWD is within 5 percent. Therefore, this example clearly demonstrates the precision and accuracy of the methods described herein.

SUMMARY AND CONCLUSIONS

The use of geophones in determining the deflection of pavement systems was discussed. Different methods of obtaining

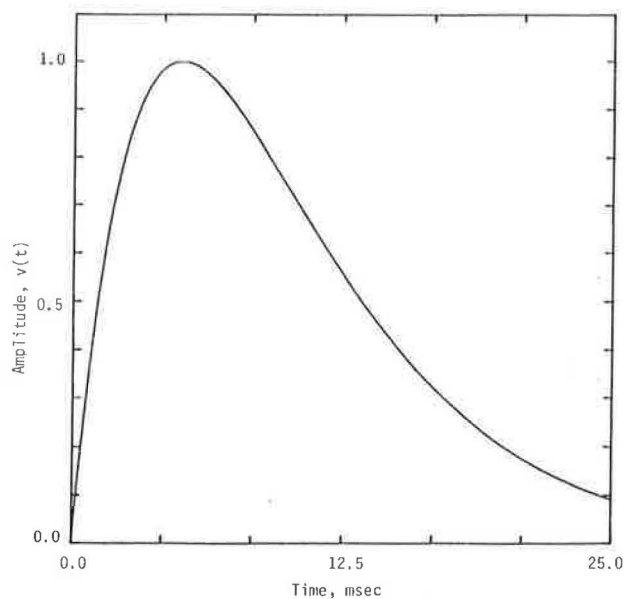


FIGURE 13 Velocity time history of an asymmetrical impulse.

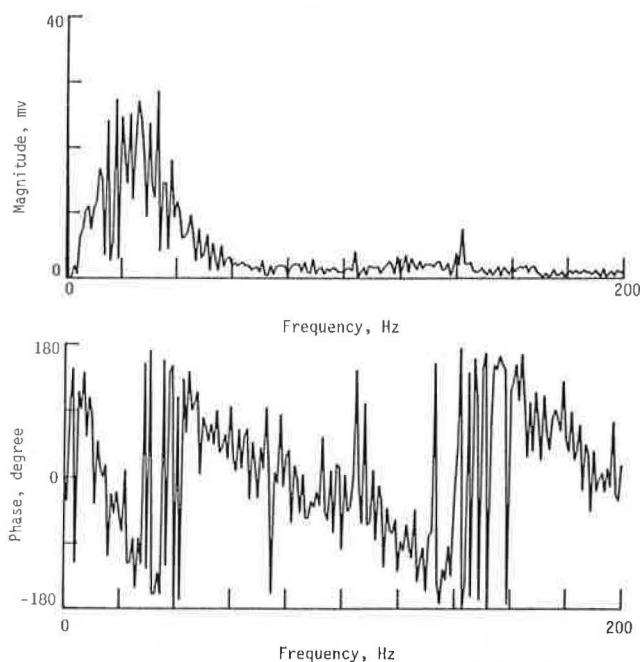


FIGURE 14 Fast Fourier transform of the typical signal from FWD sensor.

deflections from geophones were described. The limitations and advantages of each method were also described.

The impulse method yields a satisfactory value for the maximum deflection only, and does not yield a meaningful deflection-time history. In addition, as applied to pavement monitoring, the method is only applicable to short-duration loadings. The shape and duration of the impulse may cause error in the value of maximum deflection as well. In general, this method should be used with caution.

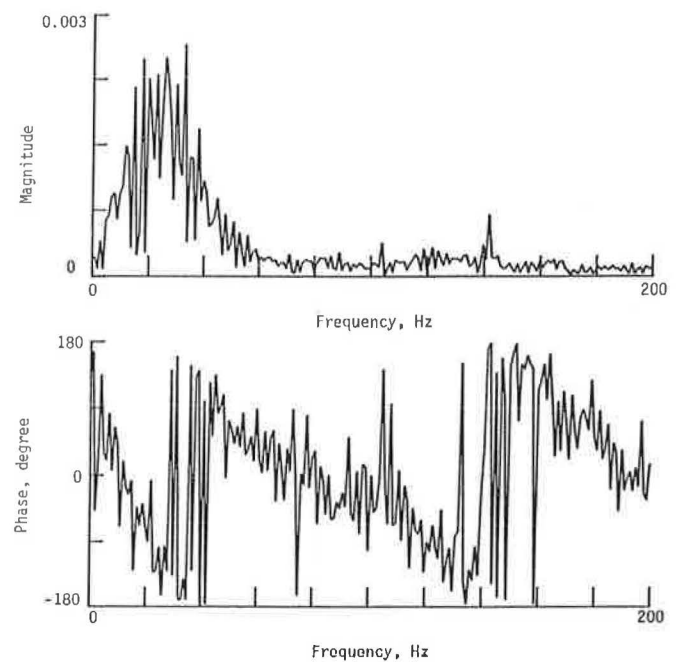


FIGURE 15 Velocity response spectrum of the base of FWD sensor.

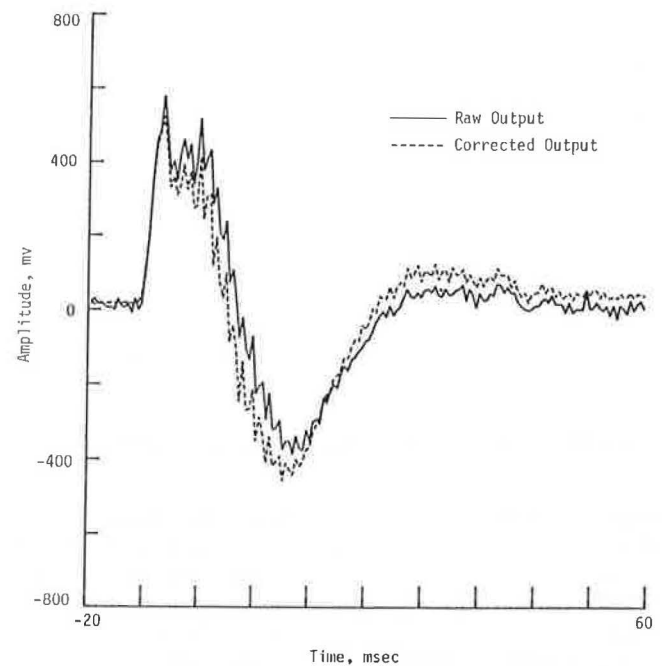


FIGURE 16 Comparison of raw voltage output with voltage corrected for geophone effects.

The time- and frequency-domain solutions work equally well, as long as the geophone used is well calibrated. Practically speaking, the frequency-domain solution is easier to implement. The frequency-domain solution has two additional advantages over the impulse method. First, the deflection-time history and the maximum deflection are obtained.

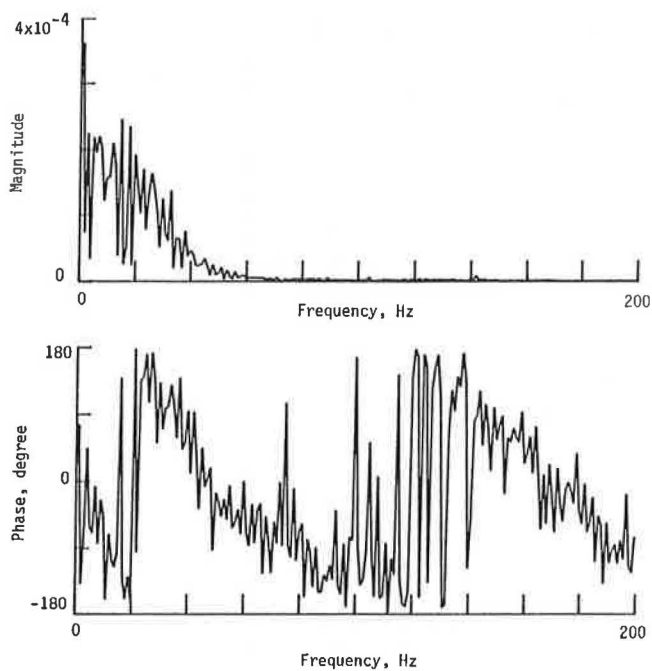


FIGURE 17 Integrated velocity response spectrum at the base of FWD sensor.

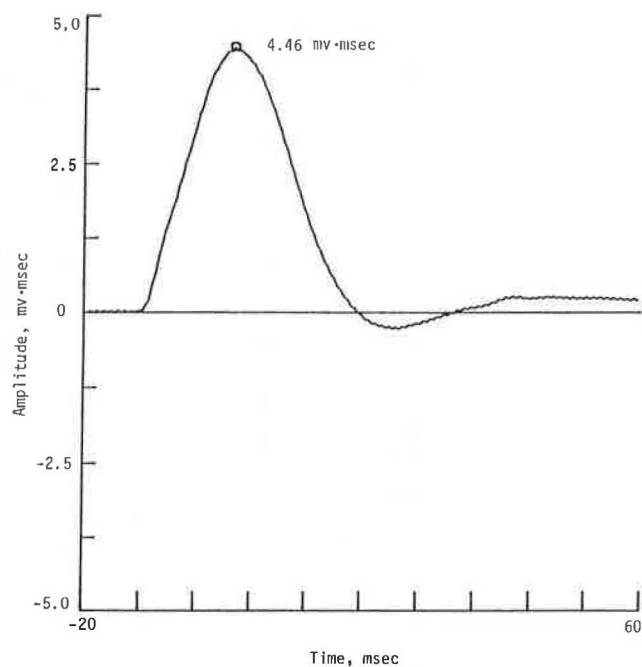


FIGURE 18 Integrated velocity time history at the base of FWD sensor corrected for zero deflection.

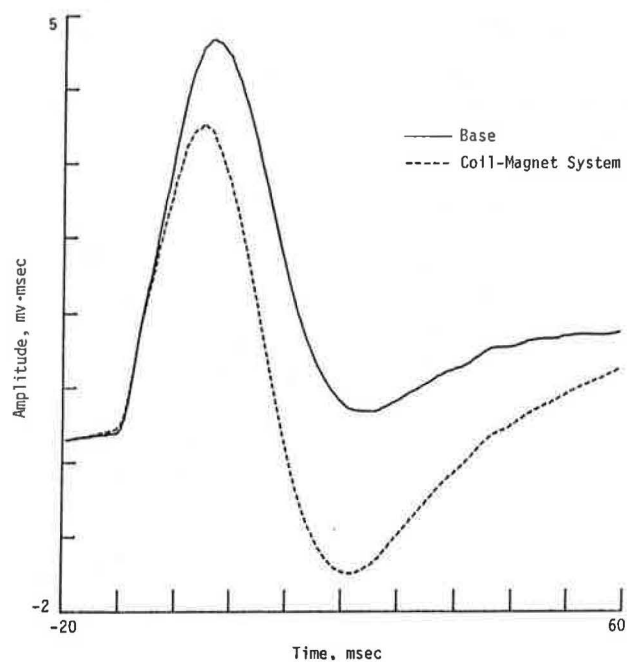


FIGURE 19 Comparison of integrated velocity time histories of the coil-magnet system and base of FWD sensor.

TABLE 3 COMPARISON OF DEFLECTIONS OBTAINED FROM IMPULSE METHOD, FREQUENCY RESPONSE, AND FWD TESTS USING TWO WELL-CALIBRATED GEOPHONES

Sensor Number	Deflection, mil		
	Impulse Method	Frequency Response Method	FWD Device
2(R) [*]	7.3 ++	7.4	6.9
3	6.6	6.8	6.6
2(R)	7.2	7.4	7.3
4	5.9	6.0	5.9
2(R)	7.2	7.3	7.2
5	5.3	4.7	5.3
2(R)	7.2	7.3	7.3
6	4.6	4.7	4.6
2(R)	7.1	7.3	7.4
7	4.0	4.1	4.1
Average Reference	7.20 (+0.07) ⁺	7.34 (0.05)	7.22 (0.19)

* (R) denotes Reference Sensor

+ Numbers in parentheses correspond to standard deviation

++ The value of adjustment factor of 0.79, which has obtained with a theoretically proper method, was used to determine the deflections from Impulse Method

Second, the results are independent of the duration and shape of impulse.

Through a case study, the use and precision of the methods described in the paper were demonstrated. Based on this study, geophones can be used effectively to monitor the behavior of pavements in terms of deflections. The methods described herein can be used to obtain maximum deflection values that compare closely with those reported by the FWD device.

REFERENCES

1. S. Nazarian. *A Calibration Process for Determination of Surface Deflections of Pavements Using Velocity Transducers*. Research

- Report GR87-2, Geotechnical Engineering Center, The University of Texas at Austin, 1987.
2. Mark Product, Inc. *Mark Products Product Catalog*. Houston, Tex., 1985.
3. R. B. Bouche. *Calibration of Shock and Vibration Measuring Transducers*, Naval Research Laboratory, Washington, D.C., 1979.
4. Hewlett Packard, Inc. *Operator's Introduction to the HP3562A Dynamic Signal Analyzer*. Product No. 3562A-1, 1984.
5. R. A. Bentsen, S. Nazarian, and J. A. Harrison. Reliability Testing of Seven Nondestructive Pavement Testing Devices. In *Proc., First International Symposium on Nondestructive Testing and Backcalculation of Moduli*, ASTM, Baltimore, Md., 1988.

Publication of this paper sponsored by Committee on Strength and Deformation Characteristics of Pavement Sections.

Shakedown and Fatigue of Pavements with Granular Bases

LUTFI RAAD, DIETER WEICHERT, AND ALI HAIDAR

Performance prediction of pavements requires the proper assessment of permanent deformations and fatigue of the structure under applied traffic loads. Of particular importance in this case is whether a given pavement structure will experience progressive accumulation of plastic strains or whether the increase in plastic strains will cease to occur, thereby leading to a stable response or shakedown. A numerical method for predicting shakedown of pavements is developed in this paper. The proposed numerical approach involves discretization of the pavement structure using the finite element method. An iterative scheme is implemented that satisfies shakedown conditions, together with the nonlinear resilient load-deformation characteristics of the granular and subgrade layers. Convergence is attained when a limiting or shakedown load could be determined for which the stress-resilient strain relations are satisfied, and a time-independent residual stress field exists for which equilibrium conditions, boundary conditions, and yield conditions (i.e., Mohr-Coulomb yield criterion in this case) are fulfilled. The proposed method is applied to study the shakedown behavior of pavements with granular layers. Specifically, the influence of strength of the granular layer in terms of cohesion and friction is investigated. In this case, the results of a limited number of laboratory triaxial tests showing the effect of aggregate interlock, percent fines, and compaction water content on the cohesion and friction parameters are used. The influence of other factors (such as initial stresses induced by compaction and overburden pressure) is illustrated. Shakedown behavior is then compared with fatigue of the surface layer in an attempt to develop a better understanding of pavement performance.

Pavement structures are generally designed to resist repeated load applications over a given design period. In many rational design procedures, limiting values in the critical response parameters have been proposed as a means of achieving satisfactory pavement performance. In three-layer pavements consisting of asphalt concrete surface, granular base, and subgrade, critical response parameters could include surface deflections, tensile strains on the underside of the asphalt concrete surface course, and normal stresses and strains on top of the subgrade layer. The influence of strength and resilient properties of granular bases on the performance of pavement structures has been recognized by many investigators (1-3). Although pavement response parameters could be determined within reasonable accuracy limits using finite element techniques (4,5), performance models fall short of predicting the stability of pavement systems under long-term repeated loading. Of particular significance in this case is whether such systems will exhibit progressive accumulation of plastic strains, or whether the accumulation of plastic strains

will cease and a stable response or a shakedown condition is attained.

The shakedown theory, which was originally developed by Melan (6), has been applied numerically to discrete structures (7,8) and more recently to pavements (9,10). According to the theory, a pavement would exhibit progressive or increased accumulation of plastic strains under repeated load applications if the magnitude of these loads exceeded a limiting value defined as the shakedown load. In this case, the pavement is said to exhibit an incremental failure mode or incremental collapse, which is physically reflected in the gradual accumulation of permanent deformations followed possibly by material breakdown of the pavement structure.

On the other hand, if the applied loads were smaller than the shakedown load, the accumulation of plastic strains will eventually cease, and the pavement is said to have attained a state of adaptation or shakedown, whereby the pavement response will be elastic under additional load applications. The magnitude of the shakedown load predicted using available numerical algorithms (9,10) depends on the thickness, shear strength, and elastic properties of the individual pavement layers. These algorithms, however, do not consider the nonlinear stress-dependent resilient properties of granular and subgrade layers in pavement structures.

In this paper, a numerical method using the shakedown theory and incorporating the stress-dependent resilient properties of granular and subgrade layers in pavements will be introduced. The proposed method will be used to investigate the shakedown behavior of pavements. Specifically, the influence of compaction stresses, strength, and load-deformation characteristics of the granular base on shakedown capacity will be assessed. Moreover, shakedown and fatigue predictions will be compared for the purpose of developing improved pavement performance models.

PROPOSED NUMERICAL MODEL

In the proposed method, the pavement is discretized into a series of rectangular elements, each with four external primary nodes. The displacement functions used are complete to the second degree and satisfy compatibility conditions. The material is assumed to be initially elastic-ideally plastic with convex yield surface and applicable normality condition. A quasi-static analysis is used assuming negligible viscous and inertia effects. If stress states σ^o , σ^s , and σ^a correspond, respectively, to body forces P^o , statically applied forces f^s , and repeated loads f^a , then the system will shake down—provided a time-independent stress increment $\Delta\sigma$ can be found

L. Raad, Institute of Northern Engineering, University of Alaska—Fairbanks, Fairbanks, Alaska 99775-0660. D. Weichert, Institute of Mechanics, Ruhr University, Bochum, West Germany. A. Haidar, American University of Beirut, Beirut, Lebanon.

such that equilibrium conditions, boundary conditions, and yield relations are satisfied. In this case, plane strain finite element analysis is used to determine the stresses in the system.

The determination of the shakedown load is then reduced to an optimization problem, as suggested by Raad et al. (10), and is stated as follows.

Minimize

$$Q = -\alpha + \sum_{i=1}^{NP} (S_{xi})^2 + \sum_{i=1}^{NP} (S_{yi})^2 \quad (1)$$

subject to the following constraints:

$$\alpha > 0 \quad (2)$$

$$f(\sigma) \leq 0 \quad (3)$$

$$\sigma_3 \geq -2c \tan(45 - \phi/2) \quad (4)$$

where

- NP = number of nodal points,
- α = load multiplier associated with repeated loads f^a ,
- $\sigma = (\sigma_{ij})_o + (\sigma_{ij})_s + \alpha(\sigma_{ij})_a + \Delta\sigma_{ij}$ (5)
- $(\sigma_{ij})_o, (\sigma_{ij})_s, (\sigma_{ij})_a$ = stresses at the center of a given element due to P^o, f^s , and f^a , respectively,
- $\Delta\sigma_{ij}$ = arbitrary stress increment applied at the center of each element,
- S_{xi}, S_{yi} = resultant forces in the x and y directions at a nodal point due to $\Delta\sigma_{ij}$ with respect to a global set of coordinates (x, y) , and
- f = Mohr-Coulomb failure criterion with failure occurring for $f \geq 0$.

f is given by

$$f = \sigma_1 - \sigma_3 \tan^2(45 + \phi/2) - 2c \tan(45 + \phi/2) \quad (6)$$

where σ_1 and σ_3 are major and minor principal stresses, and c and ϕ are equal to the cohesion and angle of friction.

Minimizing Q subject to the indicated constraints would yield a maximum value for the load multiplier (α), while satisfying equilibrium conditions, boundary conditions, and yield conditions in a weak sense. Because Q is quadratic with nonlinear constraints, quadratic optimization techniques are not feasible. Instead, a pattern search algorithm is developed based on the original work by Hooke and Jeeves (11). The method could be summarized in the following steps.

1. Determine the stresses resulting from P^o, f^s , and an initially applied repeated load f^a .
2. Find a load multiplier (α_{st}) such that $(\alpha_{st}f^a)$ would cause yielding of the most critically stressed element in the system. This will shift the search to the vicinity of the region of interest.
3. The search starts by determining Q for α_{st} and a set of

$\Delta\sigma_{ij}$ that satisfy the constraint conditions of Equations 2, 3, and 4.

4. During a given exploratory sequence, the variable (α) is allowed one disturbance in the direction of decreasing Q . Each of the stress variables ($\Delta\sigma_{ij}$) is allowed as many disturbances, each equal to its step size and in the same direction as long as the objective function (Q) decreases and the imposed constraints are satisfied. Otherwise, the exploratory sequence is rated a failure.

5. A new search is initiated about the last base point determined in Step 4, using smaller step sizes. The algorithm terminates when the values of the step sizes are reduced to a certain preassigned value. In this case, the shakedown load will be equal to $(\alpha_{st} \cdot \alpha \cdot f^a)$.

To improve predictions of the shakedown capacity of pavements, more realistic modeling of material properties should be incorporated in the analysis. Specifically, the nonlinear stress-dependent resilient moduli for granular and subgrade layers should be used. For granular layers, the resilient modulus is generally expressed as

$$M_R = K_1 \theta^{K_2} \quad (7)$$

where $\theta = \sigma_1 + \sigma_2 + \sigma_3$ is the sum of principal stresses, and K_1 and K_2 are coefficients derived experimentally.

For fine-grained soils, a typical representation of resilient modulus (M_R) as a function of repeated deviator stresses ($\sigma_1 - \sigma_3$) has been proposed by Figueroa (5) and is illustrated in Figure 1.

Numerically, the shakedown capacity could be obtained using a series of iterative steps. It is assumed in this case that the response under a given repeated state of stress at a given point in the pavement stabilizes and remains elastic so long as these stresses do not exceed the strength as defined by the Mohr-Coulomb yield criterion. Such behavior is illustrated schematically in Figure 2. A series of iterations using finite element analysis is conducted so that the stresses at the center of each element satisfy the stress-dependent modulus relationship.

A new shakedown pressure acting on the pavement surface is then calculated by using the newly determined moduli at the center of elements and following the approach previously summarized in Steps 1 through 5. The shakedown pressure (P_i) for a given iterative step— i in this case—will be equal to $\alpha_{st}\alpha_i P_{i-1}$, where α_{st} is the load multiplier associated with initiation of failure, α_i is the maximum load multiplier obtained from Equation 1, and P_{i-1} is the shakedown pressure obtained for the previous iterative step ($i-1$).

The procedure is repeated until convergence is attained, whereby the shakedown pressure in two consecutive steps reaches essentially the same value, and hence shakedown conditions are satisfied simultaneously with the stress-dependent moduli relations. The proposed method is shown in Figure 3.

The convergence pattern of the proposed numerical approach is illustrated for two examples in Figure 4. Material properties used in the analysis are summarized in Table 1.

The variation of $\alpha_{st}\alpha_i$ and the ratio (P_i/P_{sD}) of the shakedown pressure (P_i) obtained for iterative step i to the final shakedown pressure (P_{sD}), with number of iterative steps, indicates that convergence is essentially attained after six iterations.

MATERIALS CHARACTERIZATION

The determination of shakedown behavior requires the proper assessment of the load-deformation properties and strength of the pavement materials. Although the stress-dependent resilient properties of the granular layers used in this paper are expressed in terms of $M_R = K\sigma^n$, other more refined models developed recently could be incorporated (12, 13). Of major importance in this case are the strength parameters of the pavement components under repeated states of stress.

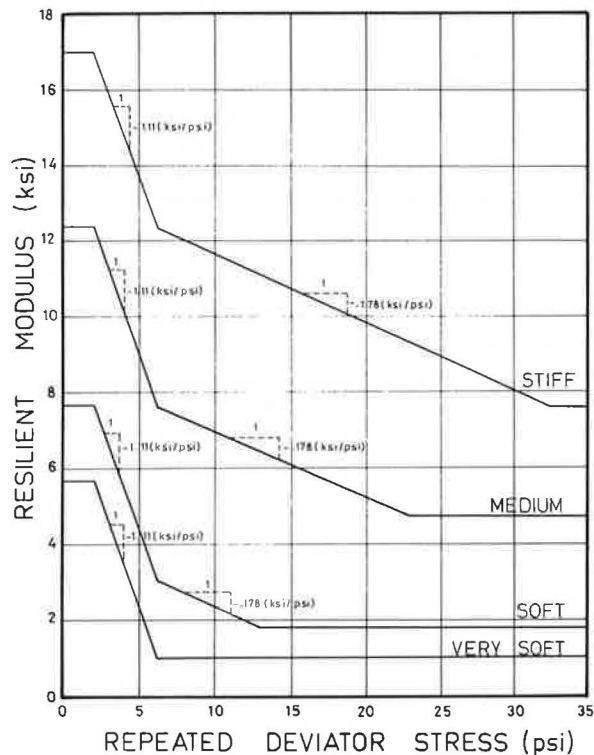


FIGURE 1 Resilient properties of subgrade soils (5).

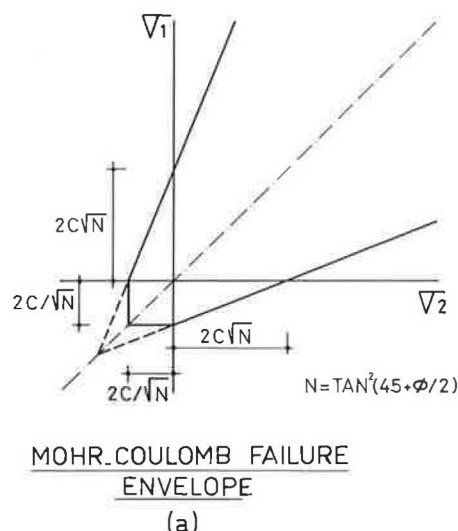


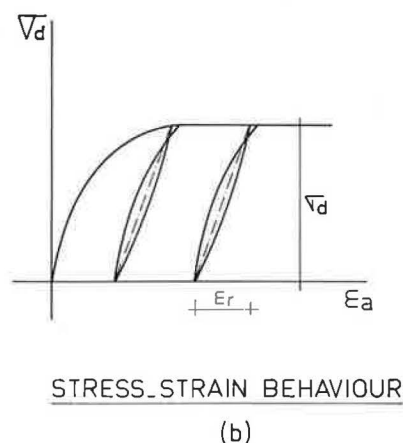
FIGURE 2 Schematic representation of stress-strain behavior and yield for a typical soil under repeated loading.

Repeated load tests on fine-grained subgrade soils show that a stress level might exist below which no sudden increase in deformation would occur, irrespective of the number of stress repetitions. The rate of accumulation of plastic strains with a number of stress applications below this critical condition would eventually approach zero. Larew and Leonards (14) reported values of the ratio of repeated deviator stress to the conventional strength obtained from triaxial tests on a compacted silty clay in the range of 0.80 to 0.90. Similar tests by Brown et al. (15) on a silty clay consolidated to different overconsolidation ratios yielded values between 0.82 and 0.93.

Repeated load triaxial data on granular soils (16, 17) strongly indicate the existence of a critical deviator stress for a given confining pressure below which the rate of accumulation of plastic strains tended to decrease as the number of load applications increased. For repeated deviator stresses greater than the critical value, the rate of accumulation of plastic strains would increase, leading eventually to failure of the specimen. If it is hypothesized that such a critical stress value would exist for a given confining pressure, then the envelope of principal stresses in this case would define a yield criterion that could be used in shakedown analysis.

In an attempt to determine the strength parameters under repeated loads, repeated load triaxial data were used for a number of granular soils presented by Barksdale (16, 18). In this case, the critical repeated deviator stress corresponding to 10^5 repetitions was estimated. The resulting data were interpreted using a Mohr-Coulomb yield representation. Values of cohesion ranged between zero and 10 psi, whereas the friction angle varied between 26 and 40 degrees.

Recent studies on the behavior of granular layers under repeated loads show a significant influence of cohesion on their shakedown capacity (19). Cohesion of granular soils could depend on interlock between aggregates, density, moisture content, and fines content. To illustrate this, a limited number of triaxial tests were conducted on a uniform sand (S1), a crushed limestone with no fines (CLS1), a crushed limestone with 5 percent fines (CLS2), and a crushed limestone with 12 percent fines (CLS3). The crushed limestone specimens were compacted in cylindrical 4×8 in. molds,



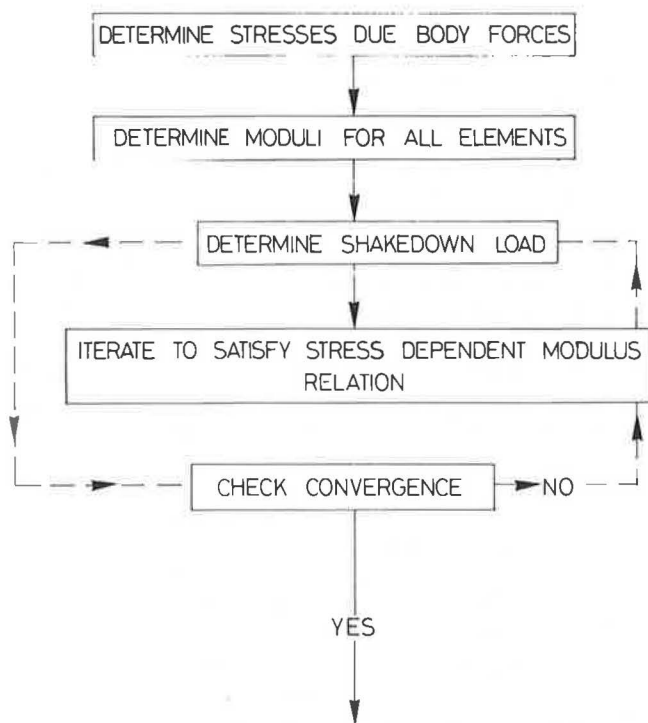


FIGURE 3 Flowchart of the proposed numerical method.

whereas 1.5×3 in. molds were used for the sand specimens. All specimens were compacted using modified AASHTO compaction energy (ASTM D1557-66T) at the corresponding optimum moisture content. A summary of material properties and the results of triaxial strength tests are presented in Tables 2 and 3. Results indicate that the tested granular soils exhibited varying degrees of cohesion, induced probably by pore pressure suction in the fines matrix and by aggregate interlock. The most significant factor influencing the cohesion seemed to be the percent of fines (i.e., percent passing No. 200 sieve). An increase in fines content from 0.3 to 11 percent would increase the cohesion from 1.6 to 13 psi.

APPLICATIONS

The proposed numerical approach was used to investigate the influence of granular base characteristics on shakedown behavior of pavement structures. The effects of compaction stresses, and friction and cohesion of the base on shakedown capacity were illustrated. Moreover, fatigue and shakedown predictions for bases with different strength and resilient properties were compared.

Three-layer pavements consisting of an asphalt concrete surface with a granular base over a clay subgrade were considered. The pavements were analyzed under an applied sur-

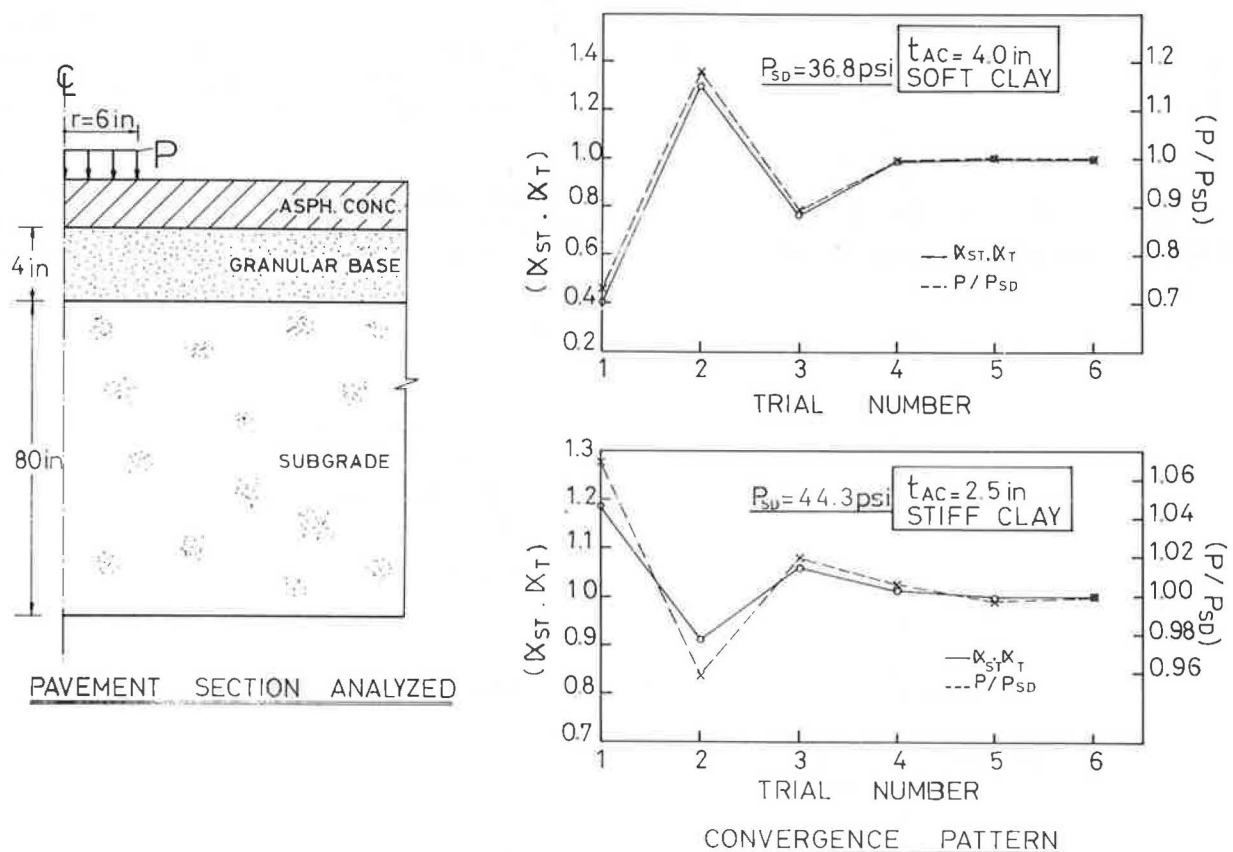


FIGURE 4 Convergence pattern of the proposed numerical method.

TABLE 1 PAVEMENT MATERIALS PROPERTIES

Asphalt Concrete Layer	Granular Base	Subgrade
$E_{ac} = 5.0 \times 10^5$ psi $\nu_{ac} = 0.40$ $\gamma_{ac} = 140$ lb/cu ft $K_o = 0.50$ $\phi_{ac} = 37^\circ$ $C_{ac} = 650$ psi	$M_R = 5000\theta^{0.50}$ (psi) $M_R = 2000\theta^{0.60}$ (psi) $\nu_b = 0.35$ $\gamma_b = 120$ lb/cu ft.	Soft, $C_s = 3$ psi; $\phi_s = 0^\circ$ Stiff, $C_s = 12$ psi; $\phi_s = 0^\circ$ $\nu_s = 0.47$ $\gamma_s = 110$ lb/cu ft $K_o = 0.50$

Notes

E_{ac} is modulus of asphalt concrete layer.

γ_{ac} , ϕ_{ac} , C_{ac} are density, friction angle, and cohesion of asphalt concrete mix.

γ_b , ϕ_b , C_b are density, friction angle, and cohesion of granular base.

γ_s , ϕ_s , C_s are density, friction angle and cohesion of the subgrade.

ν_{ac} , ν_b , ν_s are Poisson's ratio for asphalt concrete, granular base, and subgrade.

K_o is the coefficient of at rest pressure.

$M_R = 5000\theta^{0.5}$ was used for all bases studied, except for comparing fatigue and shakedown, where $M_R = 2000\theta^{0.6}$ was also used.

Subgrade resilient moduli relations used for all cases studied are shown in Fig. 1.

face pressure of radius equal to 6 in., assuming plane strain conditions. Properties of pavement materials used in the analyses are summarized in Table 1.

Influence of Compaction

Compaction of granular layers induces soil stresses, which could influence the mechanical properties of these layers. Measured compaction-induced stresses from a number of laboratory and full-scale field studies indicate that the process of load application and removal can result in significant increases in residual lateral earth pressures. These may exceed the theoretical at-rest values and may approach the limit dictated by passive earth pressure (20–23).

Residual lateral compaction stresses are also affected by the number of load cycles applied. In a study conducted by Stewart et al. (24), residual lateral stresses were determined experimentally for a ballast material under tie contact pressure equivalent to that of a 32-kip wheel load from a train. Results show that residual horizontal stresses increased up to 100 cycles, after which they became constant. Maximum values for lateral earth pressure coefficient in the ballast ranged between 2 and 11.

Prediction of such compaction effects is, thus, necessary to predict properly the response and performance of pavement structures. Recently, a hysteretic model for predicting compaction stresses was proposed by Duncan and Seed (25). This

model was used to determine the compaction stresses in the granular base for all cases considered in this paper. Plane strain conditions were assumed and the residual lateral stress buildup was determined under the multiple passes of a 4-kip compactor with a width of 4 ft. The influence of the cohesion and angle of friction of the base on compaction stresses is illustrated in Figure 5. The residual lateral compaction stress (σ_{HC}) is greater than the vertical stress (σ_v) and increases with depth below the surface of the granular base under a 3-in. thick asphalt concrete surface. Moreover, compaction stresses increase with increase in friction angle and cohesion, but they reach a maximum value for cohesion of about 1 psi, with a corresponding average value of lateral earth pressure coefficient essentially equal to 7.

The variation of shakedown load with thickness of granular base ($M_R = 5000\theta^{0.5}$, $\phi = 35^\circ$) was determined for a pavement with a 3-in. asphalt concrete surface. The influence of compaction stresses was investigated by comparing the shakedown capacity for the base where the coefficient of lateral pressure (K_o) was equal to 0.5, with the case where the compaction stresses were included. Results are shown in Figures 6 and 7. Compaction stresses would increase the predicted shakedown loads for both pavements with soft and stiff subgrade conditions. The increase, in general, is most significant for granular bases with low cohesion and for bases overlying stiff subgrades.

Limited field data on the variation of compaction-induced stresses with time due to stress relaxation effects show that

TABLE 2 PROPERTIES OF TESTED GRANULAR SOILS

Material	% Passing						Maximum	Optimum	AASHTO Classi- fication
	No. 4	No. 10	No. 40	No. 60	No. 100	No. 200	Dry Density (lb/cu ft)	Moisture Content (%)	
S1	-	-	82.2	16.5	0.9	0.2	94.1	5.2	A-3
CLS1	100	63.7	22.0	11.9	5.8	0.3	112.0	4.8	A-1-b
CLS2	100	67.1	25.4	13.8	8.0	5.0	128.0	7.3	A-1-b
	(100)	(76.6)	(35.1)	(25.6)	(19.9)	(13.8)			
CLS3	100	58.2	27.2	18.8	14.5	11.8	131.8	7.2	A-1-b
	(100)	(68.0)	(35.7)	(27.1)	(21.0)	(15.9)			

Notes

Maximum dry density and optimum moisture content correspond to Modified AASHTO Compaction Energy (ASTM D1557-66T).

Quantities in parentheses correspond to grain size distribution after compaction.

Fines (percent passing No. 200) are nonplastic.

for cohesionless soils, the compaction stresses are essentially locked in and do not change with time. For cohesive soils, on the other hand, a reduction up to 30 percent is observed to occur after 24 hours following compaction (23). Moreover, other field observations illustrate the effect of increased lateral structural deflections on compaction stresses (20-22, 26). In this case, increased lateral strains seem to reduce lateral compaction pressures. This could be particularly significant in pavements. For example, increasing moisture conditions due to spring thaw could reduce the shear strength at the base/subgrade interface to a near-zero condition, thereby leading to increased lateral strains under wheel load applications and potential decrease or loss of lateral compaction stresses.

Influence of Cohesion and Friction of Granular Base

Analyses were performed to assess the influence of the strength of the granular base on the shakedown behavior of pavement structures. The pavement considered for this purpose consisted of a 3-in. asphalt concrete surface and a 12-in. granular base ($M_R = 5,000 \theta^{0.5}$) overlying soft or stiff subgrades. Results

are presented in Figures 8 and 9. For a given angle of friction, increasing the cohesion of the granular base would significantly increase the shakedown capacity of the pavement. Moreover, for values of cohesion less than 5 psi, in the case of soft subgrade, and less than 17 psi, in the case of stiff subgrade, an increase in the friction angle would enhance the shakedown capacity of the system.

However, cohesion of the base seems to be a more significant parameter on shakedown capacity than the friction angle. For cohesion values greater than 5 psi, in the case of soft subgrade, and 17 psi, in the case of stiff subgrade, an increase in the angle of friction reduces shakedown capacity. It should be noted that, for a given base cohesion, an increase in the angle of friction would not only reduce the tensile strength of the base but would increase its shear strength. It seems, therefore, that for high values of cohesion, the relative effect on shakedown capacity associated with a decrease in the tensile strength of the base due to an increase in its friction angle surpasses the effect of the corresponding increase in its shear strength. This could probably be a result of increased mobilization of the shear resistance of the base prior to the initiation of tensile failure on its underside.

A comparison between the applied pressure on the pavement surface required to initiate failure (P_{st}) and the shake-

TABLE 3 TRIAXIAL TEST RESULTS

Material	Deviator Stress at Failure (psi)				Dry Density (lb/cu ft)	Moisture Content (%)	Cohesion (psi)	Angle of Friction (degrees)
	σ_3	σ_3	σ_3	σ_3				
	0psi	7.2psi	14.4psi	21.6psi				
S1	4.70	21.1	38.2	55.8	93.9	4.90	2.90	30
	5.20	21.7	38.0	48.4	93.2	4.94	2.87	29
CLS1	5.26	44.1	61.9	78.7	109.7	4.20	1.97	40
	4.31	36.4	50.5	79.3	107.0	5.13	1.32	41
CLS2	34.7	79.3	110.0	154.1	128.8	7.10	17.30	47
	45.5	124.4	156.4	203.7	130.3	6.50	12.9	49
CLS3	47.1	123.2	158.3	201.0	133.7	6.80	12.3	50
	60.0	126.0	159.4	195.4	134.6	6.90	13.5	48

Notes

σ_3 is the applied confining pressure.

Triaxial tests were conducted at a constant rate of strain equal to 2% per minute

down pressure (P_{SD}) is presented in Figure 10. Results indicate that the ratio (P_{st}/P_{SD}) is essentially a function of base cohesion. The variation of friction angle between 30 and 45 degrees will not influence the ratio of (P_{st}/P_{SD}) by more than about 5 percent. It can be concluded that the shakedown pressure is larger than the surface pressure required to initiate failure in the base. It follows that the pavement system would shake down even though some elements of the granular base are in a state of yield. In this case, the yield zone is contained, and the pavement would still stabilize under long-term repeated loading. It is interesting to note that, for values of cohesion less than 5 psi, the ratio (P_{st}/P_{SD}) will increase and could reach 0.97 for a value of cohesion equal to 0.10 psi.

Fatigue and Shakedown Behavior

Prediction of fatigue and shakedown is required for the proper assessment of pavement performance. For example, a pavement designed to carry a number of load applications in fatigue could actually be carrying a load greater than its shakedown capacity and would, therefore, exhibit incremental collapse due to the continuous accumulation of plastic strains. Moreover, if the magnitude of the wheel loads exceeds the shakedown capacity of the pavement after application of maintenance and rehabilitation procedures, then the accumulation

of plastic strains will continue and incremental collapse could occur.

Analyses were conducted to investigate the influence of strength and resilient properties of the granular base on fatigue and shakedown predictions. Fatigue resistance of the asphalt concrete surface was determined using a fatigue failure criterion proposed by Monismith et al. (27). This criterion expresses limiting tensile strains as a function of number of load repetitions required to cause fatigue failure for different moduli values of the asphalt concrete layer (Figure 11). The limiting tensile strains on the underside of the asphalt concrete layer were determined for plane strain loading conditions using the stress-dependent resilient properties of the granular base and subgrade.

The influence of cohesion of granular base ($M_R = 5,000$ $\theta^{0.5}$, $\phi = 40^\circ$) on shakedown and fatigue behavior is illustrated in Figure 12. Fatigue resistance seems to be essentially unaffected by the cohesion of the granular base. On the other hand, shakedown behavior is significantly affected by base cohesion. For example, a reduction in cohesion from 5 to 0.1 psi would reduce the shakedown capacity of a pavement with an 8-in. base from 50 to 15 psi. In this case, a pavement designed to satisfy acceptable fatigue and shakedown conditions could be unsafe with respect to shakedown, if loss in base cohesion reduces the shakedown limit below the magnitude of applied traffic loads. This could eventually cause

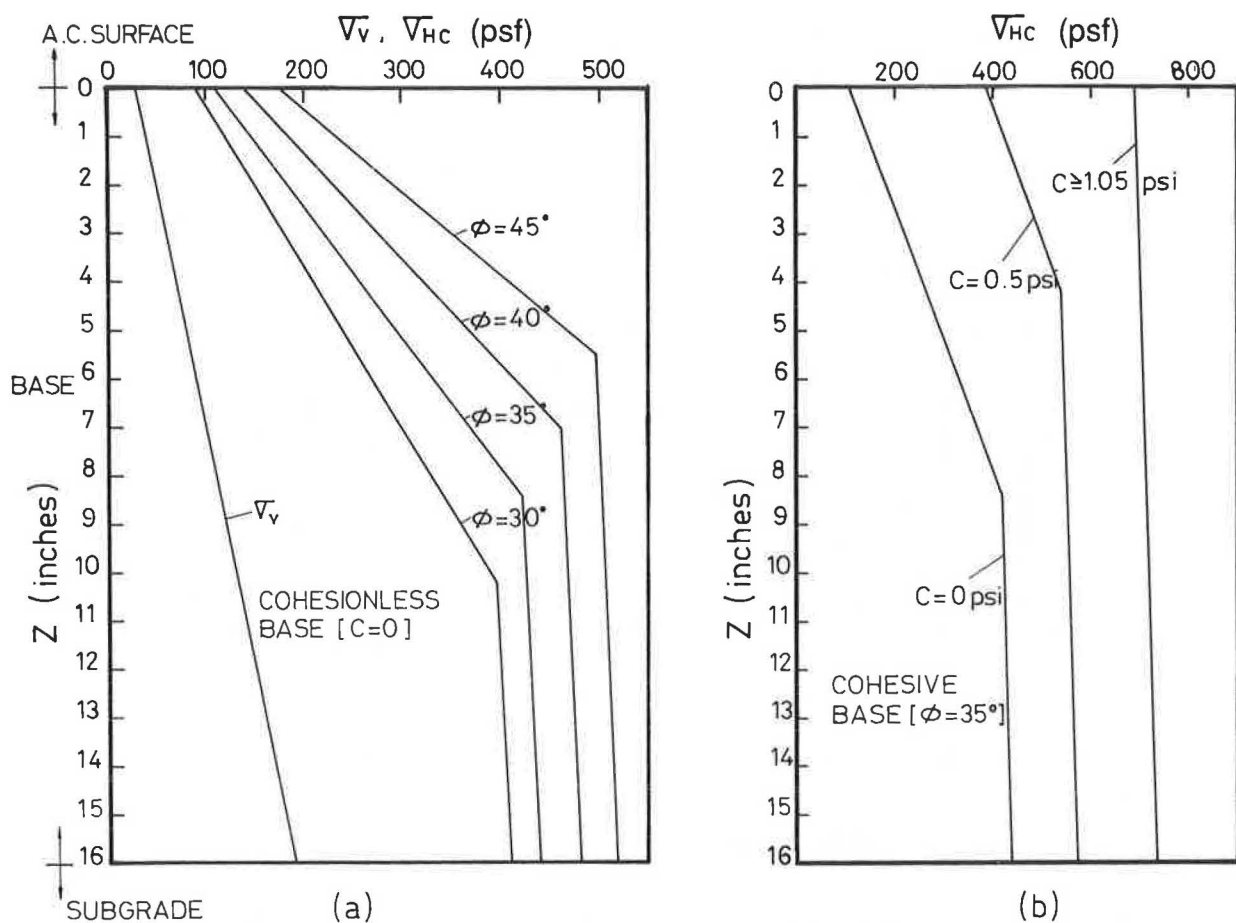


FIGURE 5 Compaction stresses for cohesionless and cohesive base.

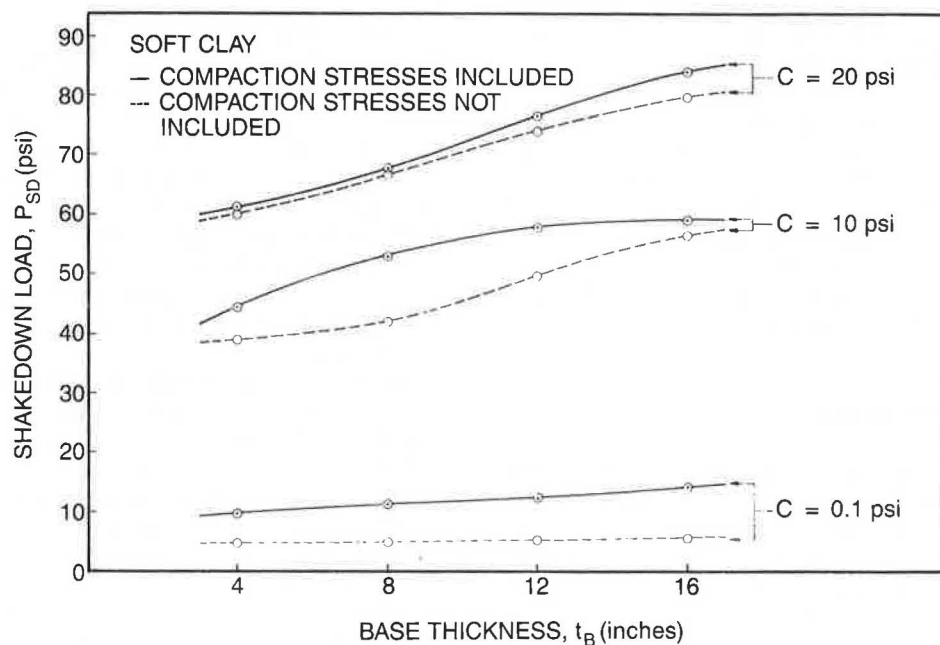


FIGURE 6 Influence of compaction stresses on shakedown for soft subgrade conditions.

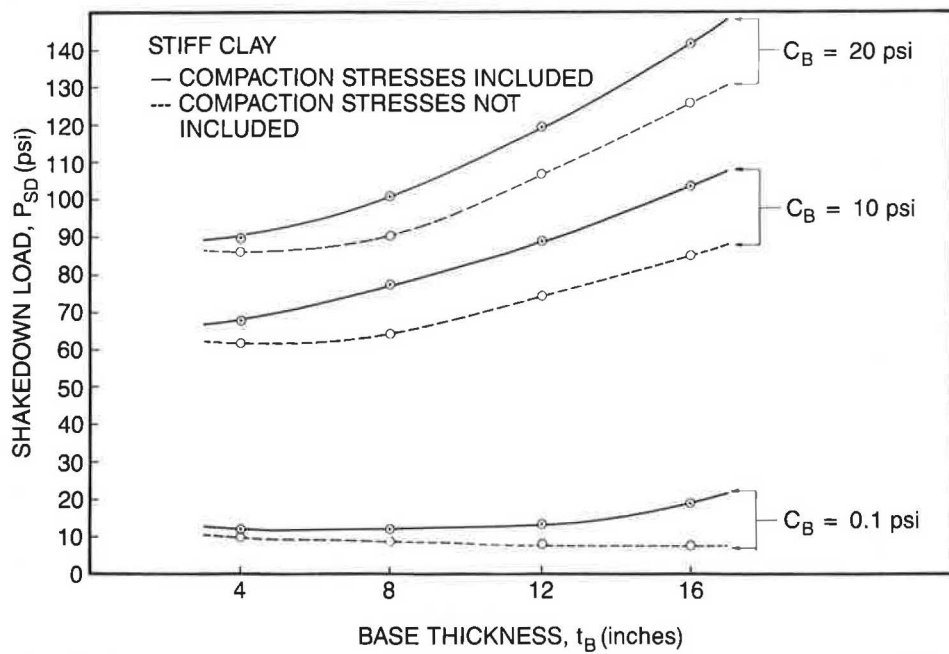


FIGURE 7 Influence of compaction stresses on shakedown for stiff subgrade conditions.

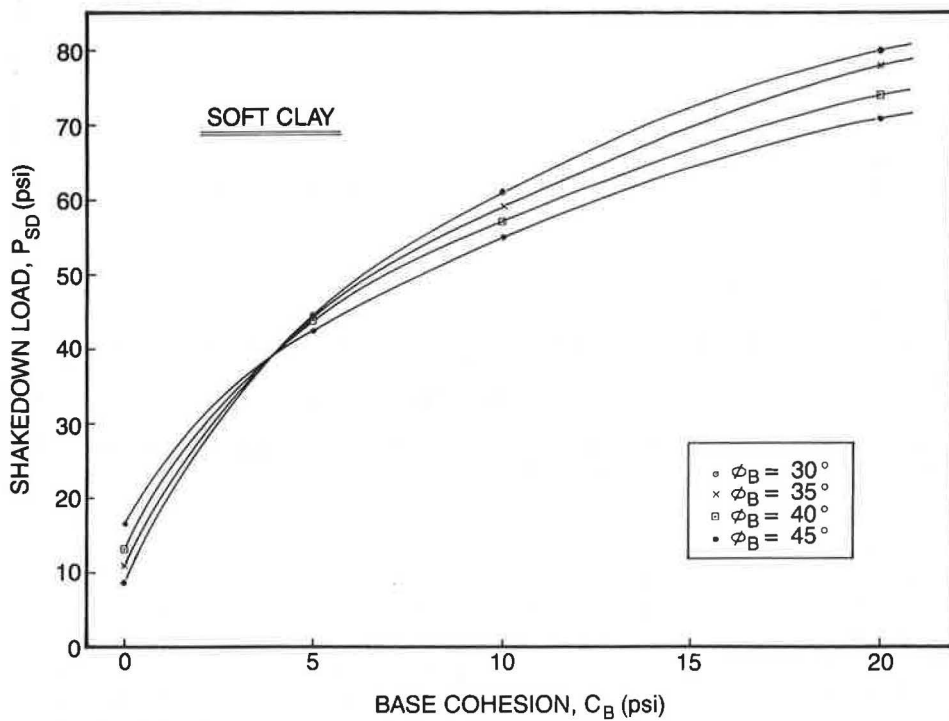


FIGURE 8 Influence of base cohesion and friction on shakedown for soft subgrade conditions.

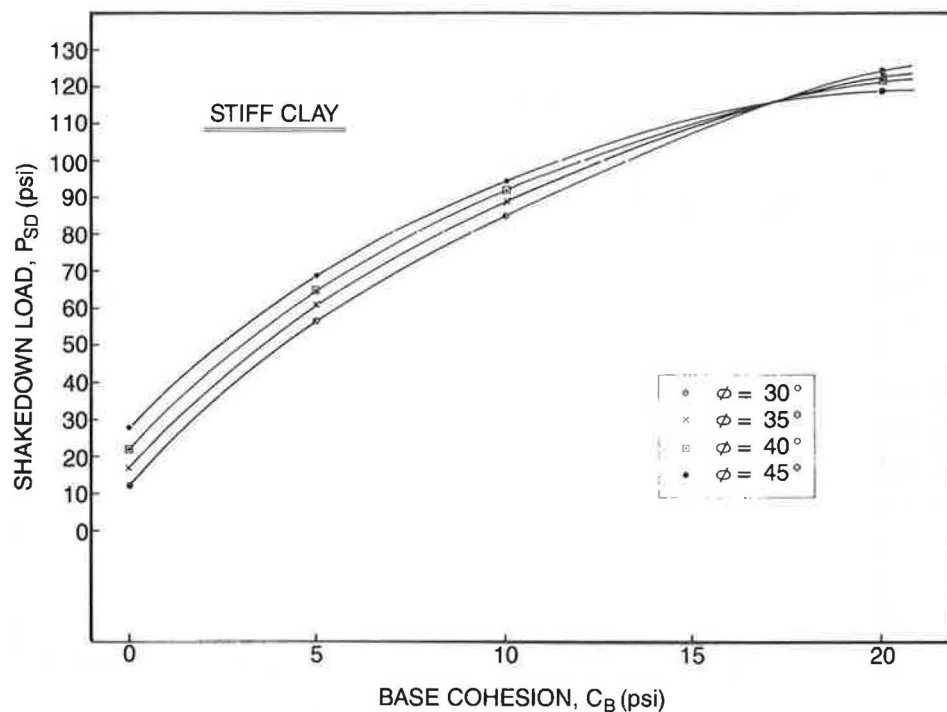


FIGURE 9 Influence of base cohesion and friction on shakedown for stiff subgrade conditions.

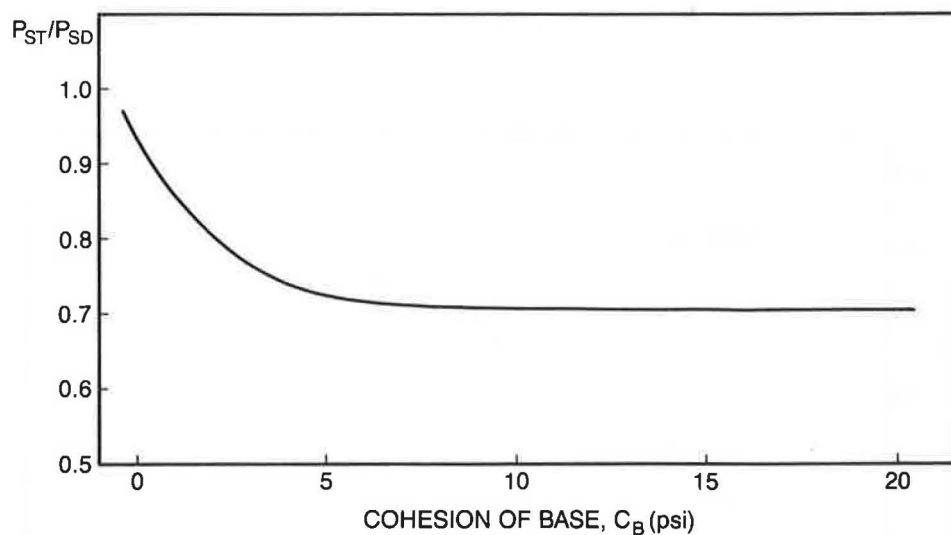


FIGURE 10 Variation of the ratio of failure initiation-pressure (P_{st}) applied on the pavement surface to the shakedown pressure (P_{sd}) with base cohesion.

sudden increase in the rate of accumulation of permanent deformations, thereby leading to incremental collapse.

Analyses were also conducted to compare fatigue and shakedown behavior of pavement with low cohesion-high friction granular base ($M_R = 5,000 \theta^{0.5}$, $\phi = 40^\circ$, $C = 5$ psi) with pavements having high cohesion-low friction granular base ($M_R = 2,000 \theta^{0.6}$, $\phi = 20^\circ$, $C = 15$ psi), assuming stiff subgrade conditions (Figures 13 and 14). Results indicate that pavements with low cohesion-high friction base exhibit better fatigue properties and lower shakedown capacity than pavements having high cohesion-low friction base. Moreover, in both cases, the increase in base thickness did not affect sig-

nificantly the fatigue resistance of the asphalt concrete surface layer for large numbers of load applications. This agrees well with findings from other procedures (28). Pavement loading conditions represented by points below the shakedown curve would result in a stable pavement response, provided proper maintenance procedures were implemented as soon as fatigue cracking appeared on the pavement surface.

Although pavements with high cohesion-low friction base have larger shakedown capacity, they would probably exhibit larger permanent deformations before shakedown and stability conditions were attained. Moreover, these bases were more susceptible to environmental changes (such as increases

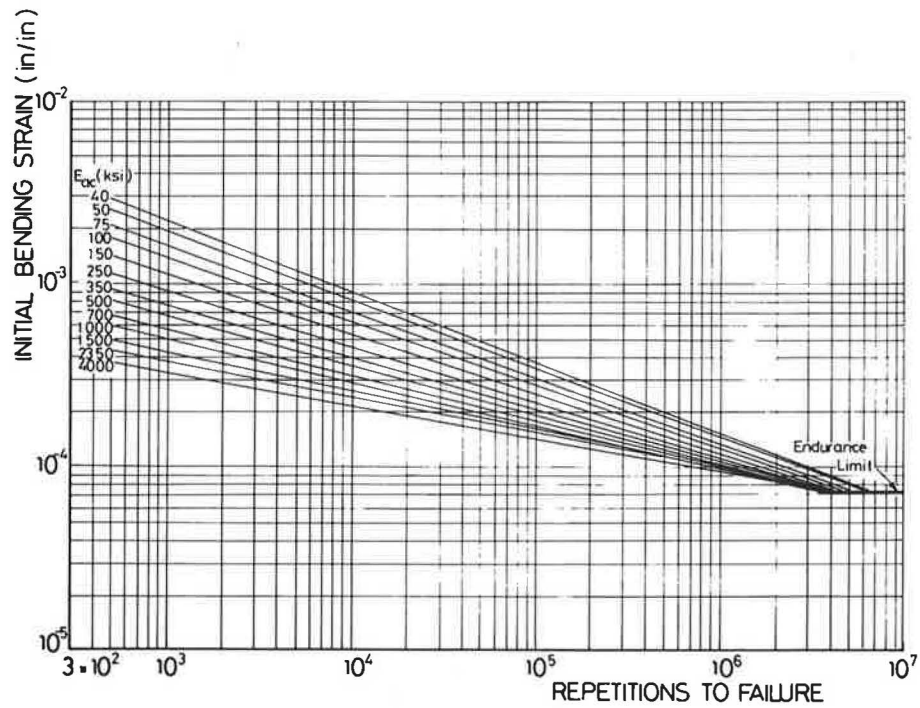


FIGURE 11 Fatigue failure criterion for asphalt concrete mixtures (27).

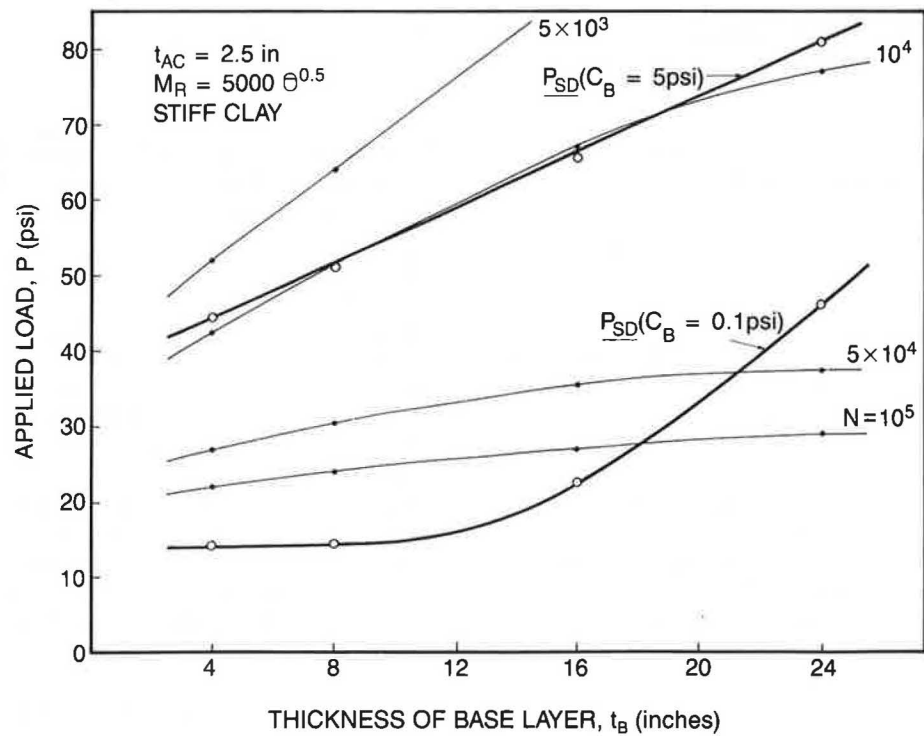


FIGURE 12 Influence of base cohesion on fatigue and shakedown.

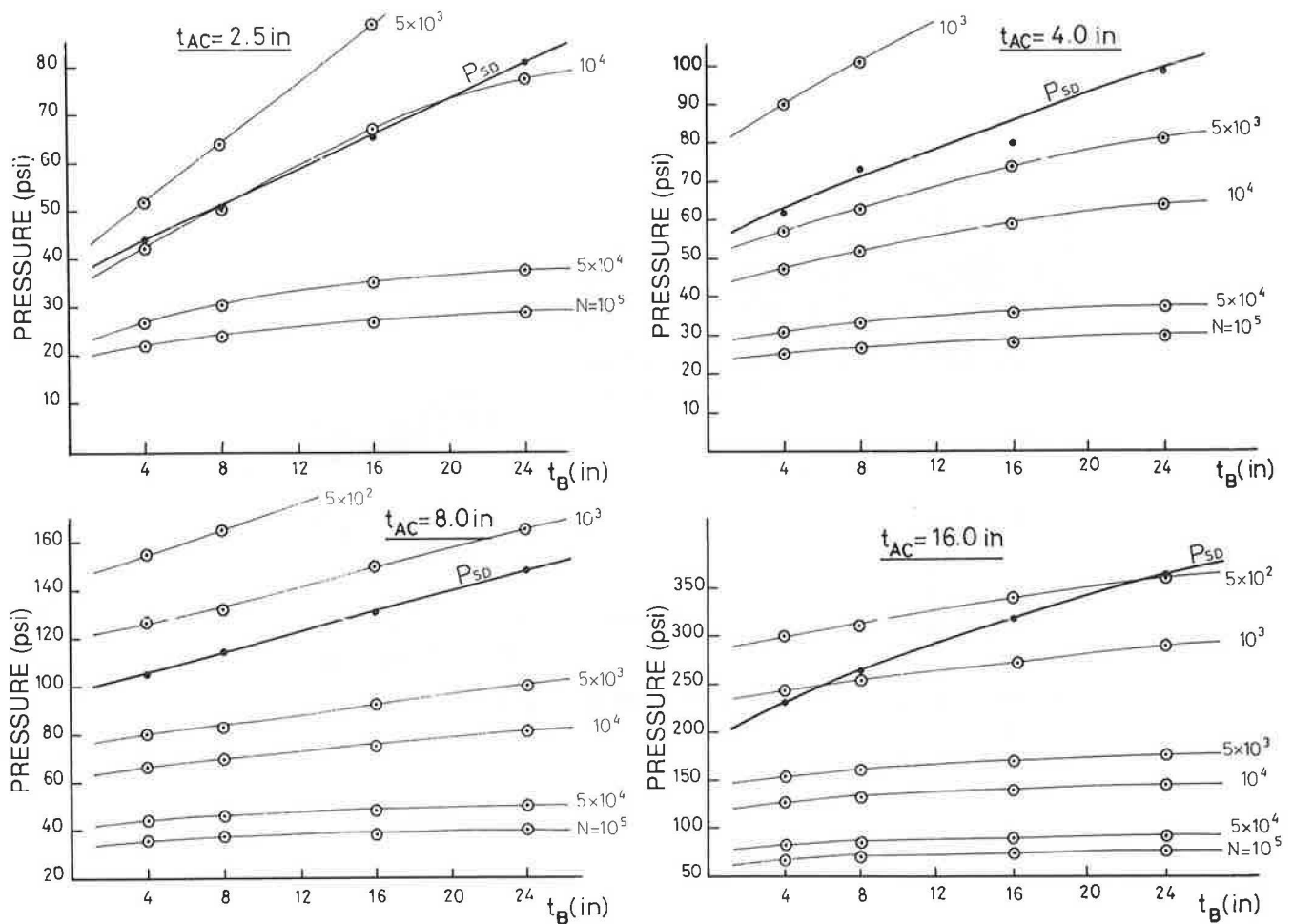


FIGURE 13 Fatigue and shakedown behavior for pavements with a low cohesion-high friction base.

in base moisture and freezing-thawing), which would reduce base cohesion and lead to a significant decrease in shakedown capacity.

SUMMARY AND CONCLUSIONS

A numerical method for applying the shakedown theory in pavements was proposed. The method incorporates the stress-dependent resilient properties of the granular and subgrade layers in the pavement structure. The method was used to investigate the influence of properties of granular base on the shakedown behavior of three-layer pavement systems consisting of an asphalt concrete surface, a granular base, and a clay subgrade. Specifically, the effects of compaction stresses, and cohesion and friction on the shakedown capacity of the pavement were assessed. Fatigue and shakedown predictions for pavements with low cohesion-high friction and high cohesion-low friction bases were compared.

Compaction stresses in the granular base improved the shakedown capacity of pavements and should, therefore, be considered for the proper assessment of shakedown behavior. The shakedown capacity of pavements was affected by the cohesion and, to a lesser extent, by the angle of friction of

the granular base. A loss of base cohesion could result in a significant loss of shakedown capacity, thereby leading to increased accumulation of plastic strains and eventual incremental collapse.

Results of analyses also indicate that fatigue and shakedown criteria should be considered in the design and evaluation of pavement structures. A pavement designed to resist a number of repeated load applications in fatigue would exhibit increased accumulation of plastic strains if the applied load exceeded the shakedown capacity, but the pavement would reach a stable response if the applied load were smaller than the shakedown capacity.

Pavements with high cohesion-low friction granular bases had lower fatigue resistance and higher shakedown capacity than those with low cohesion-high friction granular bases. However, the shakedown capacity in the case of high cohesion-low friction base could be reduced significantly by adverse environmental factors that would cause a loss of base cohesion.

In addition to providing a basis for analyzing shakedown behavior for the conditions considered herein, improved versions of the proposed numerical model would provide a basis for analyzing pavements under more general and more complex loading and environmental conditions.

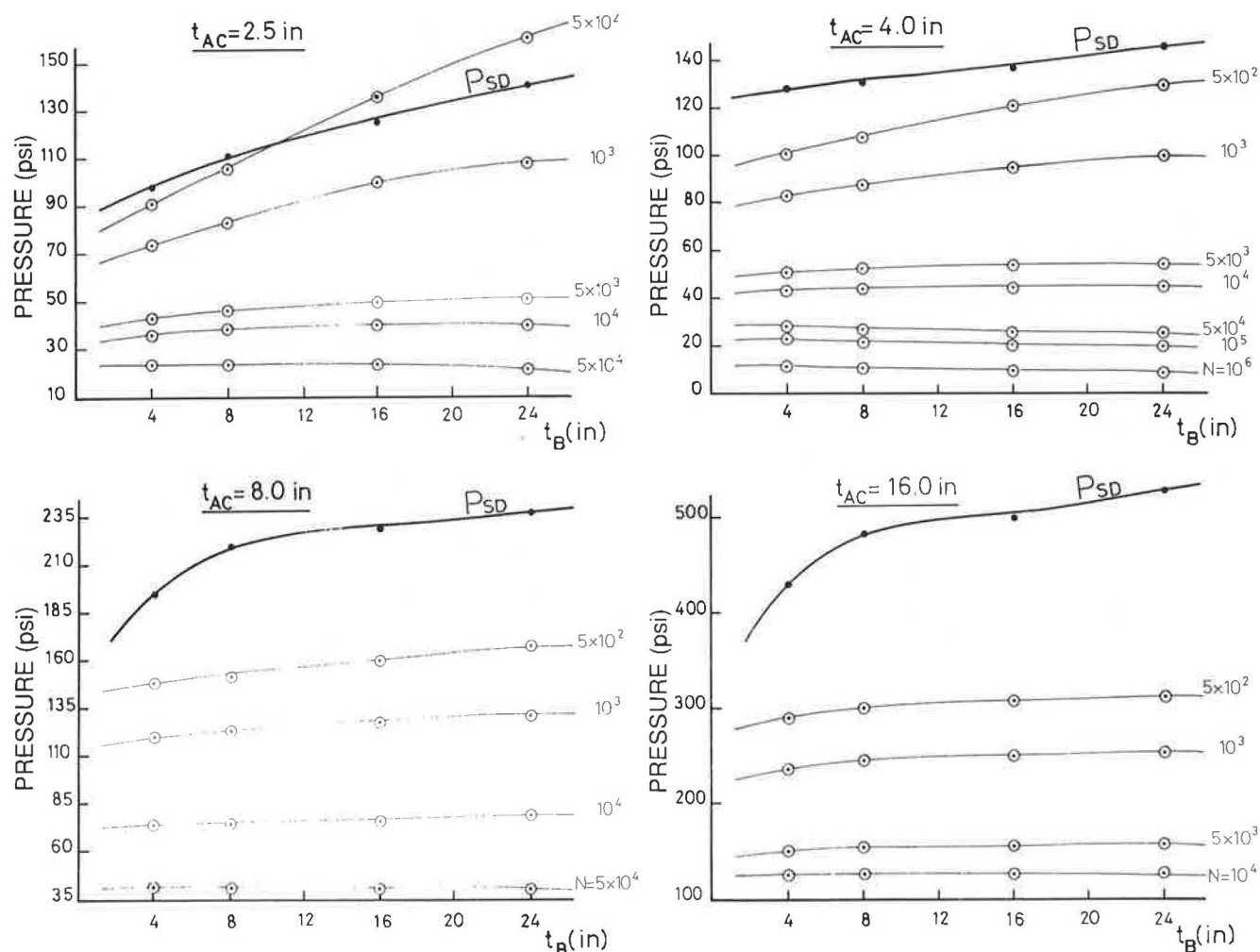


FIGURE 14 Fatigue and shakedown behavior for pavements with a high cohesion-low friction base.

ACKNOWLEDGMENT

Financial support for these studies was provided by a grant from the University Research Board of the American University of Beirut. This support is gratefully acknowledged.

REFERENCES

1. C. L. Monismith, H. B. Seed, F. G. Mitry, and C. K. Chan. Prediction of Pavement Deflections from Laboratory Repeated Load Tests. In *Proc., Second International Conference on the Structural Design of Asphalt Pavements*, University of Michigan, Ann Arbor, 1967, pp. 109–140.
2. S. F. Brown and J. W. Pappin. Analysis of Pavements with Granular Basis. In *Transportation Research Record 810*, TRB, National Research Council, Washington, D.C., 1981, pp. 17–23.
3. W. Heukelom and A. J. G. Klomp. Dynamic Testing as a Means of Controlling Pavements During and After Construction. In *Proc., International Conference on the Structural Design of Asphalt Pavements*, University of Michigan, Ann Arbor, 1962, pp. 627–679.
4. L. Raad and J. L. Figueroa. Load Response of Transportation Support Systems. *Journal of the Transportation Engineering Division*, ASCE, Vol. 106, No. TE1, 1980, pp. 111–128.
5. J. L. Figueroa. Resilient Based Flexible Pavement Design Procedure for Secondary Roads. Ph.D. dissertation. University of Illinois at Urbana-Champaign, 1979.
6. E. Melan. Theorie Statisch Unbestimmter Systeme Aus Ideal-Plastischen Baustoff. *Sitzungsbereichte der Akademie der Wissenschaften in Wien*, Vol. 11a, 1936, pp. 145–195.
7. W. A. M. Alwis and P. Grundy. Shakedown of Plates Under Moving Loads. In *Proc., 7th Australian Conference on Mechanics of Structures and Materials*, 1980, pp. 191–196.
8. G. Maier and L. Corradi. Upper Bounds on Dynamic Deformations of Elastoplastic Continua. *Meccanica*, Vol. 9, March 1974, pp. 30–35.
9. R. W. Sharp. Pavement Design Based on Shakedown Analysis. In *Transportation Research Record 1022*, TRB, National Research Council, Washington, D.C., 1985, pp. 99–107.
10. L. Raad, D. Weichert and W. Najm. Stability of Multilayer Systems Under Repeated Loads. In *Transportation Research Record 1207*, TRB, National Research Council, Washington, D.C., 1988, pp. 181–186.
11. R. Hooke and T. A. Jeeves. Direct Search Solution of Numerical and Statistical Problems. *Journal of the Association of Computing Machinery*, Vol. 8, 1961, pp. 212–229.
12. J. Uzan. Characterization of Granular Material. In *Transportation Research Record 1022*, TRB, National Research Council, Washington, D.C., 1985, pp. 52–59.
13. S. F. Brown and J. W. Pappin. Modeling of Granular Materials in Pavements. In *Transportation Research Record 1022*, TRB, National Research Council, Washington, D.C., 1985, pp. 45–51.
14. H. G. Larew and G. A. Leonards. A Strength Criterion for

- Repeated Loads. In *Highway Research Record 41*, HRB, National Research Council, Washington, D.C., 1962. pp. 529–556.
15. S. F. Brown, A. F. K. Lashine, and A. F. L. Hyde. Repeated Load Triaxial Testing of Silty Clay. *Geotechnique*, Vol. 25, No. 1, 1975, pp. 95–114.
 16. R. D. Barksdale. *Repeated Load Test Evaluation of Base Course Materials*. GHD Research Project No. 7002, Final Report, FHWA, U.S. Department of Transportation, 1972.
 17. R. M. Knutson, M. R. Thompson, T. Mullin, and S. D. Tajabji. *Materials Evaluation Study*. Report Nos. FRA-OR and D-77-02. Ballast and Foundation Research Program, Federal Railroad Administration, Washington, D.C., 1977.
 18. R. D. Barksdale. Crushed Stone Base Course Performance. Presented at the 63rd Annual Meeting of the Transportation Research Board, Washington, D.C., January, 1984.
 19. D. Weichert, J. Grob-Weege, L. Raad, and W. Najm. Numerical Application of Shakedown Theory to Non-Linear Transportation Support Systems. *Zeitschrift Fur Angewandte Mathematik Und Mechanik*, Vol. 69, Issue 4/5, 1988.
 20. B. Broms and I. Ingleson. Earth Pressures Against Abutment of Rigid Frame Bridge. *Geotechnique*, Vol. 21, No. 1, 1971, pp. 15–28.
 21. D. R. Carder, R. G. Pocock, and R. T. Murray. *Experimental Retaining Wall Facility-Lateral Stress Measurements with Sand Backfill*. Report No. LR 766, Transport and Road Research Laboratory, 1977.
 22. D. R. Carder, R. T. Murray, and J. V. Krawczyk. *Earth Pressures Against an Experimental Retaining Wall Backfilled with Silty Clay*. Report No. LR 946, Transport and Road Research Laboratory, 1980.
 23. G. F. Sowers, A. D. Robb, C. H. Mullis, and A. J. Glenn. The Residual Lateral Pressures Produced by Compacting Soils. In *Proc. 45th International Conference on Soil Mechanics and Foundation Engineering*, London, England, 1957, pp. 243–247.
 24. H. E. Stewart, E. T. Selig, and G. M. Norman-Gregory. Future Criteria and Lateral Stresses in Track Foundations. In *Transportation Research Record 1022*, TRB, National Research Council, Washington, D.C., 1985, pp. 59–64.
 25. J. M. Duncan and R. B. Seed. Compaction Induced Earth Pressures Under K_0 -Conditions. *Journal of the Geotechnical Engineering Division*, ASCE, Vol. 112, No. 1, January 1986, pp. 1–22.
 26. H. M. Coyle, R. E. Bartoskewitz, L. J. Milberger, and H. D. Butler. Field Measurement of Lateral Earth Pressures on a Cantilever Retaining Wall. In *Transportation Research Record 517*, TRB, National Research Council, Washington, D.C., 1974, pp. 16–29.
 27. C. L. Monismith, J. A. Epps, D. A. Kasianchuk, and D. B. McLean. *Asphalt Mixture Behavior in Repeated Flexure*. Report No. TE-70-5. University of California, Berkeley, 1970.
 28. Shell International Petroleum Company Limited. *Shell Pavement Design Manual—Asphalt Pavements and Overlays for Road Traffic*. London, England, 1978.

Publication of this paper sponsored by Committee on Strength and Deformation Characteristics of Pavement Sections.

Influence of Aggregate Shape on Base Behavior

RICHARD D. BARKSDALE AND SAMIR Y. ITANI

A re-examination and simplification of the original rut index concept for predicting rut susceptibility in aggregate bases is presented to eliminate some of the disadvantages of the original approach. The rut index can be determined from the results of a single cyclic load triaxial test performed at a confining stress of 6 psi, rather than at two confining stresses as originally proposed. The principal stress ratio to be used in the test varies from 2 to 6, depending on the structural strength of the pavement section. The resilient and permanent deformation characteristics of river gravel, granitic gneiss, shale, limestone, and quartzite aggregates were determined using the cyclic load triaxial test. Variables investigated included density, gradation, moisture content, and aggregate shape and surface characteristics. The revised rut index concept was used to evaluate and compare the relative permanent deformation behavior of these various unbound aggregates. The cubic-shaped, smooth rounded river gravel was found to be more than two times as susceptible to rutting as the crushed aggregates tested. The crushed aggregates were angular, blade, and disc shaped and had relatively rough surfaces. These aggregates generally performed similarly with respect to permanent deformation, although the visual appearance of the two blade-shaped aggregates was not as nice as the others. The use of a simple, slow triaxial shear test as a practical alternative to the conventional dynamic test was studied for evaluating the resilient and permanent characteristics of unbound base materials. The slow triaxial shear test was found to be suitable for evaluating the resilient modulus, but appeared not to be appropriate for evaluating permanent deformation characteristics.

The cyclic load triaxial test offers, at this time, probably the best available method for laboratory evaluation of the resilient and permanent deformation characteristics of unbound aggregate bases. Many material variables affect granular base performance, including aggregate shape, surface characteristics, gradation, density, and moisture conditions. Also, the state of stress to which the granular material is subjected has an important influence on performance. May and Witczak (1) and Witczak and Rada (2) have given excellent reviews of resilient properties. The measurement of permanent deformation characteristics of unbound aggregate bases has, however, received much less attention, although some notable contributions have been made (3–7).

The effect on performance of aggregate characteristics (such as shape, surface roughness, angularity, and roundness) has for the most part been neglected. The effect of aggregate characteristics on the resilient and permanent deformation behavior is investigated for five aggregates from different geologic sources. Other variables in the study include gradation, plasticity of fines, and degree of saturation. The possibility of using a static triaxial test as an expedient alternative to

dynamic testing is considered. A re-examination and simplification is also made to the rut index concept.

REEVALUATION OF RUT INDEX CONCEPT

The rut index concept was proposed by Barksdale (5) in 1972 for comparing the relative permanent deformation behavior of different unbound aggregates. Since then, many advances have been made in evaluating permanent deformation characteristics, and it is now appropriate to re-evaluate the rut index concept.

The rut index was proposed for comparing the relative permanent deformation behavior of aggregate bases placed within similar pavement structures. The basis for the rut index is that the permanent deformation developed in an aggregate base (or in other layers or sublayers) is proportional to the average permanent strain in the layer (or sublayer) times the thickness of the stratum (5). The rut index concept, as originally proposed, involves determining the average permanent strain in the top and bottom halves of the base using a cyclic load triaxial test. The two cyclic load tests are performed at different specified stress states that, as originally proposed, do not vary with the structural strength of the pavement. These stress states simulate the conditions in the top and bottom halves of the base. The original rut index was defined as the sum of the average strain from the two cyclic tests multiplied by 10,000. For a given structural section geometry, the rut index is approximately proportional to the permanent deformation that should occur in the base.

The rut index approach has proven quite useful for comparing the potential relative performance of different aggregate bases (5). The two primary disadvantages of the rut index concept are (a) two cyclic load tests are required to evaluate a material and (b) the appropriate stress states to use in testing are not constant, but actually vary with the strength of the structural section. A slightly modified approach is proposed which, for the most part, eliminates these two disadvantages. Also, this study takes advantage of the advances made since 1972 in analyzing the stress state in an aggregate base.

To predict the appropriate stress states to use for different pavements, the GAPP7 nonlinear finite element computer program was used (8–10). The different pavement sections analyzed using a nonlinear, simplified contour model for the aggregate base are summarized in Table 1. The contour model probably offers the best available method for modeling unbound granular materials (11). Structural pavement sections studied included asphalt concrete surface thicknesses varying from 2 to 8 in. (50 to 200 mm) and unbound aggregate base thick-

TABLE 1 PAVEMENT SECTIONS USED TO DETERMINE STRESS STATES FOR LABORATORY TESTING

PAVEMENT SECTION	THICKNESS OF A.C. SURFACE (IN.)	THICKNESS OF BASE (IN.)	T_{eq} (IN.)	SUBGRADE CONDITIONS	REMARKS
1	2	6	5	GOOD	LIGHT
2	2	6	5	POOR	LIGHT
3	2	10	7	GOOD	LIGHT
4	2	10	7	POOR	LIGHT
5	4	10	9	GOOD	MEDIUM
6	4	10	9	POOR	MEDIUM
7	8	6	11	GOOD	HEAVY
8	8	6	11	POOR	HEAVY
9	4	20	14	GOOD	HEAVY
10	4	20	14	POOR	HEAVY
11	6	18	15	GOOD	HEAVY
12	6	18	15	POOR	HEAVY

NOTES:

1. ASPHALT : $M_r = 400,000$ PSI, $\nu = 0.2$
2. AGGREGATE BASE : SIMPLIFIED CONTOUR
MODEL : $K_1 = 9400$, $G_1 = 5300$, $\gamma = 0.14$ (Ref. 27)
3. SUBGRADE-PIECEWISE LINEAR VARIATION OF M_r
 - (1) POOR SUBGRADE : $M_r = 16$ KSI, $\sigma_d = 0$; $M_r = 5$ KSI, $\sigma_d = 6$ PSI;
 $M_r = 5$ KSI, $\sigma_d = 25$ PSI
 - (2) GOOD SUBGRADE : $M_r = 30$ KSI, $\sigma_d = 0$; $M_r = 15$ KSI, $\sigma_d = 5$ PSI;
 $M_r = 15.5$ KSI, $\sigma_d = 25$ PSI

nesses varying from 6 to 20 in. (150 to 500 mm). Both poor and good subgrades were considered. The loading consisted of an 8,000 lb (35.6 kN) single-wheel load, having a uniform pressure of 120 psi (8.3 MN/m²) over a circular area. This loading approximates a dual-wheel loading.

Residual lateral stresses are developed in an aggregate base as a result of the compaction of the aggregate due to the application of large vertical stress from vibratory rollers or other compaction equipment. The results of a limited number of studies suggest that such residual lateral compaction stresses are important in defining the complete stress state that should be used in laboratory testing to simulate field conditions. In developing appropriate stress states for laboratory testing, lateral compaction stresses of 2 and 4 psi (14 and 28 kN/m²) were used based on work performed by Stewart et al. (4) and Uzan (12). Certainly a better definition of the actual residual stresses developed by compaction is needed, including field measurements.

In the finite element analysis, the unbound aggregate base was divided into three horizontal sublayers, each consisting of five horizontal elements. Figure 1 shows the average stress state obtained at the center of each of the three sublayers for light, medium, and heavy pavements, as defined in Table 2.

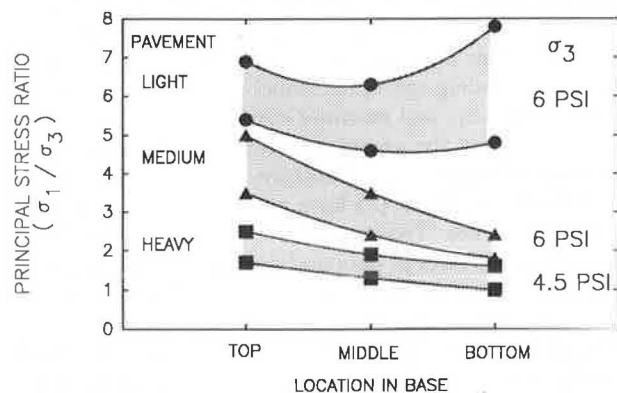


FIGURE 1 Average stress states for use in cyclic testing for light, medium, and heavy pavements.

The variation of confining pressures is from about 4 to 8 psi (28 to 55 kN/m²) and principal stress ratios σ_1/σ_3 from about 1.5 to 7.0. In general, the thinner pavements have larger confining pressures and greater principal stress ratios.

The results shown in Figure 1 indicate the use of a single stress state to characterize the layer should be sufficiently

TABLE 2 SUGGESTED STRESS STATES FOR LABORATORY TESTING TO DETERMINE RUT INDEX

STRUCTURAL STRENGTH	EQUIVALENT FULL DEPTH THICKNESS (T_{eq}) (INCHES)	STRESS STATES	
		σ_3 (psi)	σ_1/σ_3
LIGHT	$T_{eq} < 8$	6	6
MEDIUM	$8 < T_{eq} < 11$	6	4
HEAVY	$T_{eq} > 11$	4.5 ⁽¹⁾	2

NOTE : 1. AN ALTERNATE WOULD BE TO USE A CONFINING PRESSURE OF 6 PSI FOR ALL PAVEMENT STRENGTHS.

accurate for most comparison purposes and reduces the required testing in half. This is particularly true when considering the current uncertainty concerning the magnitude of lateral compaction stresses, which can significantly influence the overall confining pressure.

Revised Rut Index

The relative behavior of different unbound base aggregates following the revised rut index approach is evaluated at only one stress state using the cyclic load test. Suggested stress states for light, medium, and heavy pavement sections are given in Table 2. The rut index is numerically equal to the measured permanent strain times 10,000, as originally proposed, so as to give an easy number to work with. Considerable experience indicates that 50,000 load repetitions is sufficient in performing the test; even fewer repetitions could be used.

Also, to account for preconditioning effects that occur during construction, the permanent deformation developed during the first 10 load applications should probably not be included in calculating the rut index. The effect of varying aggregate base thicknesses is not directly considered by the rut index concept. As an approximation, bases having different thicknesses can be compared by adjusting the rut index—assuming rutting would, for relatively small variations in base thickness, change proportionally to the base thickness.

The structural strength of the section for practical testing purposes can be defined as having an equivalent full-depth asphalt thickness using the classification system given in Table 2. This classification system requires converting the pavement to an equivalent full-depth asphalt concrete section. The equivalent thickness of full-depth asphalt T_{eq} can, as a simple approximation, be estimated by letting 1 in. (25 mm) of high-quality asphalt concrete replace 2 in. (50 mm) of high-quality crushed stone base compacted to 100 percent of AASHTO T-180 density.

Other methods for estimating base equivalencies can, of course, be used. For lower quality aggregate bases, the replacement ratio would typically vary from 2 in. (50 mm) to about 3 in. (75 mm) of aggregate to replace 1 in. (25 mm) of high-quality asphalt concrete. Pavements with thin asphalt

surfacings having thick aggregate bases, such as pavement Sections 9 and 10 in Table 1, should be considered as lighter than indicated by the proposed equivalency method. This results because somewhat higher stresses are actually present than indicated by the equivalent thickness approach.

AGGREGATE SHAPE AND SURFACE CHARACTERISTICS

Particle Shape

The shape of the aggregate influences the gradation curve obtained by sieving (13,14). Many years ago, Rittenhouse (14) determined that flaky particles tended to pass sieves having square holes diagonally. For material retained on a given sieve size, Lees (13) showed that rod-shaped particles were about 2.5 times the size of disc-shaped particles retained on the same sieve. Rod-shaped particles could, for example, effectively be a complete size coarser in grading than disc-shaped particles retained on the same sieve size. These differences in size would affect both specific surface area and also the ability of the particles to fill voids of coarser-size aggregate properly.

The shape of aggregate particles can be divided into four general categories as discussed by Lees (13), Rosslein (15), and Zingg (16): cubic (equidimensional), disc, blade, and rod-shaped. The particle shape classification, as defined above, can be determined following the procedure given by British Standard BS 812:75 or the Army Corps of Engineers test method CRD-C119-53. These approaches, however, only separate the aggregate into four, rather broad categories of particle shape shown in Figure 2. Both methods employ simple-to-use gauges that can quickly separate aggregates into a shape classification.

Lees (13) has pointed out that the four broad categories defined by the British and Corps of Engineers standard tests permit quite a large range of particle shape characteristics within each classification. For research purposes, it is probably better to define particle shape more completely by determining the flatness and elongation ratios (13,17). The flatness ratio (p) is the shortest length, divided by the intermediate length. The elongation ratio (q) is the intermediate length, divided by the greatest length. By determining the actual

flatness and elongation ratios, a continuously varying classification is developed (Figure 2).

An alternate way of describing aggregate shape, also shown on Figure 2, is by means of sphericity, ψ , and shape factor, F . The shape factor, F , is defined as the elongation ratio, divided by the flatness ratio. Sphericity is the ratio of surface area of a sphere of the same volume as the particle to the surface area of the particle (17). Following this method, each grain is approximated by a tetrakaidekahedron. The three mutually perpendicular particle dimensions measured to determine shape are used to calculate the ratio of surface area of the particle compared to that of an equivalent sphere (sphericity, ψ). Roundness (R) of a particle is a measure of curvature of the corners and edges and is expressed as a ratio of the average curvature of the particle as a whole, independent of its form (13,17,18). Angularity (A) describes the wear of edges and corners. For example, a heavily worn aggregate tends to be rounded.

Measured Aggregate Characteristics

For this study, 80 particles greater than the No. 8 sieve were randomly sampled, and the shape and other surface characteristics were carefully determined. The roundness and angularity of individual particles were evaluated visually using standard identification charts (13). The variation in particle shape for the five aggregates studied is shown in Figure 2; all aggregate surface characteristic data are summarized in Table 3.

The five aggregates studied and their shape classification are as follows: granitic gneiss (disc), limestone (blade), shale (blade), quartzite (blade), and river gravel (equidimensional). The shale and limestone aggregates were quite slabby appearing (i.e., blade-shaped), as compared to the granitic gneiss (disc-shaped) and the gravel (equidimensional). A rod-shaped aggregate was not included in the study, because no source for this material could be located.

To illustrate the influence of the combined effects of the important variables present in the study on permanent deformation and resilient modulus, an aggregate influence factor (AIF) was used. The AIF was taken to be a function of the particle sphericity, roundness, surface roughness, and angularity. Surface roughness of particles was examined visually where a roughness scale (zero for glassy particles and 1,000 for very rough particles) was used to assign a surface roughness value to each type aggregate tested. Surface area, as defined by sphericity, might be an important variable in defining material response for aggregates that are not rod-shaped and have shape factors that do not vary greatly. A sufficient variation in particle shape factor, F , was not present to determine its effect in this study.

Average values of the sphericity, roundness, angularity, and surface roughness were used to evaluate AIF, which is as follows:

$$\text{AIF} = 2500 * (\psi + R) - (A + \text{SR}) \quad (1)$$

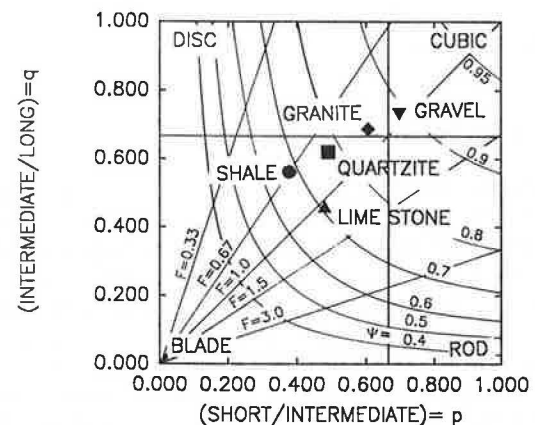


FIGURE 2 Shape classification of aggregates (13).

TABLE 3 SHAPE AND SURFACE CHARACTERISTICS OF THE FIVE AGGREGATES STUDIED

BASE TYPE	GRANITE GNEISS	GRAVEL	SHALES	QUARTZITE	LIME STONE
ELONGATION RATIO (q)	0.68	0.72	0.57	0.63	0.47
FLATNESS RATIO (p)	0.60	0.70	0.37	0.48	0.48
SPHERICITY	0.86	0.88	0.69	0.76	0.72
ANGULARITY	1350	150	750	1450	1450
ROUNDNESS	0.2	0.7	0.4	0.2	0.2
ROUGHNESS	800	100	300	800	800
AGGREGATE INFLUENCE FACTOR	500	3700	1675	150	50

where

- AIF = aggregate influence factor,
 A = average angularity value,
 SR = surface roughness coefficient,
 ψ = average sphericity value, and
 R = average roundness value.

Several forms of the AIF were empirically tried before arriving at the expression given above. The main controlling criterion for the AIF was how good the fitted curve described the observed base behavior. Use of the AIF is considered a useful tool for presenting the results of this study; it is not intended to be a general aggregate characteristic. Certainly much more extensive research must be conducted before an AIF-type approach can be proposed for general use.

CYCLIC LOAD TESTS

Sample Preparation and Testing

Preparation

The resilient and permanent deformation characteristics of the five aggregate types were determined using specimens nominally 6 in. (150 mm) in diameter by 12 in. (300 mm) in height tested in a large triaxial cell. Sample preparation generally followed the procedure given by AASHTO T-274-82. All materials were mixed thoroughly with the required optimum quantity of water determined from the modified Proctor test (AASHTO T-180). The material was then placed in six 2-in. (50-mm) thick layers into a split steel mold and compacted with a vibratory compactor to obtain the required density.

Soaked specimens were prepared in a manner similar to that described above. Once the specimen was compacted and completely sealed, a vacuum was applied to the specimen from the top, while a de-aired water supply was introduced to the bottom of the specimen. Water was allowed to percolate slowly up through the specimen until the entrapped air was removed. The LVDT and load cell instrumentation used have been described elsewhere (5).

Test Procedures

The resilient modulus test procedure generally followed the recommendations of AASHTO T-274-82. Before testing, specimens were conditioned for 1,200 load repetitions at the stress states summarized in Table 4. After the conditioning phase, readings of both axial and radial resilient deformations were taken and recorded after 200 load repetitions for each state of stress tested.

To evaluate permanent deformation, one stress state was used for the entire cyclic test. A confining pressure of 6 psi (41 kN/m²) was applied to the specimen, which was then subjected to 70,000 load repetitions using a principal stress ratio of either 4 or 6. Slow cyclic tests using a static type testing machine were also performed to determine the feasibility of using static methods for evaluating both resilient and permanent deformation properties of granular materials.

In the slow cyclic test, the specimen was subjected to a confining pressure of 6 psi (41 kN/m²). The deviator stress was increased gradually at a slow loading rate of 0.03 in./min until reaching the full deviator stress; the load was then slowly removed. Five slow loading-unloading cycles were applied, and the complete deformation history for each cycle was recorded. All tests were performed in the drained condition.

Permanent Deformation Response

Influence of Aggregate Shape and Surface Characteristics

Figure 3 shows the relative tendency to undergo permanent deformation of the five aggregates. All specimens were compacted to 100 percent of AASHTO T-180 density. The medium gradation given in Table 5 was used for this comparison; this gradation had 4 percent fines unwashed. The specimens were subjected to 70,000 repetitions of loading at a confining pressure of 6 psi (41 kN/m²) and principal stress ratios of $\sigma_1/\sigma_3 = 4$ and 6. These stress levels correspond to typical light and medium pavement sections.

The results showing relative rutting in Figure 3 indicate, for practical purposes, the permanent deformation charac-

TABLE 4 SPECIMEN CONDITIONING USED FOR RESILIENT MODULUS TESTING

CONDITIONING PHASE	NUMBER OF REPETITIONS	CONFINING STRESS (PSI)	DEVIATOR STRESS (PSI)
1	200	5	5
2	200	5	10
3	200	10	10
4	200	10	15
5	200	15	15
6	200	15	20

teristics of the disc-shaped granitic gneiss, blade-shaped limestone, and blade-shaped shale are all similar. The blade-shaped quartzite appeared to be about 30 percent more susceptible to rutting than the other crushed aggregates. Some of the differences in rutting of the quartzite might be due to scatter in the test data. Differences in the particle surface characteristics of these aggregates were not great as shown in Table 3.

These results indicate that blade- and disc-shaped aggregates having characteristics similar to those studied (although they may not appear to be as nice as equidimensional aggre-

gates) can perform about as well with respect to permanent deformation. Of course, regardless of the aggregate shape, the gradation including the amount of fines and density has an important influence on performance. Had a greater variation in particle shape existed, more variation in permanent deformation performance might have been observed.

The rounded river gravel tested was over two times more susceptible to rutting than the crushed aggregates. The uncrushed gravel was equidimensional (cubic) with a smooth surface, well-rounded, and had rounded corners—the worst possible characteristic for minimizing rutting. Also, the solid volume for 1 ft³ of gravel was 0.77 ft³ compared with 0.82 to 0.85 ft³ for the other materials tested (Table 5). Hence, particle packing for the gravel was not as dense as for the other aggregates.

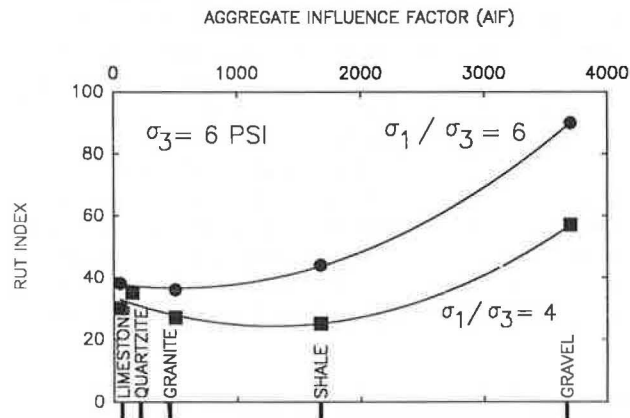


FIGURE 3 Effect of aggregate type on rut index.

Influence of Finer Material

The tests described previously were performed on aggregates coming from different geologic formations and origins. As a result, these aggregates could have different plasticity characteristics of the finer material. To determine whether plasticity of the finer material influenced the rutting behavior of the aggregates studied, the shale and gravel were retested using specimens prepared with material passing the No. 40 sieve being replaced with the granitic gneiss. The results of this supplementary study are shown in Figure 4 together with results obtained from the earlier tests that used native finer

TABLE 5 AGGREGATE MATERIAL PROPERTIES AND GRADATIONS USED

MATERIAL PROPERTIES								
MATERIAL TYPE	SPECIFIC GRAVITY			ABSORP. (%)	WEAR	CLASS	$\gamma_{max}^{(1)}$ (PCF)	$V_s^{(2)}$
	BULK	S. S. D.	APPARENT					
GRANITIC GNEISS	2.73	2.75	2.77	0.53	0.46	B	141	0.82
GRAVEL	2.61	2.62	2.65	0.69	0.464	A	126	0.77
SHALE	2.72	2.73	2.75	0.2	0.249	A	140	0.82
QUARTZITE	2.72	2.74	2.76	0.49	0.256	A	147	0.85
LIMESTONE	2.75	2.76	2.79	0.53	0.22	A	144	0.84
GRAIN SIZE DISTRIBUTION								
GRADATION	PERCENT PASSING							
	1.5"	3/4"	3/8"	NO. 4	NO. 40	NO. 200		
MEDIUM	100	80	60	45	13	4		
COARSE	100	65	43	27	7	0		
FINE	100	85	70	58	25	10		

NOTES : 1. MAXIMUM DRY DENSITY AS DETERMINED BY AASHTO T-180 METHOD.

2. VOLUME OF SOLIDS IN 1 FT.³ OF BASE MATERIAL COMPACTED TO 100 PERCENT OF MAXIMUM DRY DENSITY.

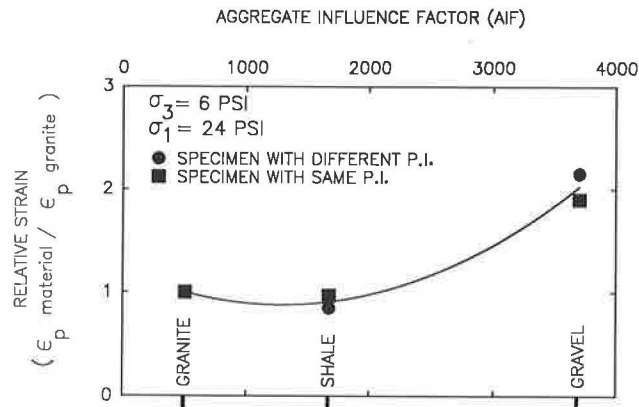


FIGURE 4 Influence of plasticity of fines on relative strain for the medium gradation.

material associated with the aggregate. These results indicate that, for the aggregates tested, the material greater in size than the No. 40 sieve was apparently the dominant factor in determining the amount of rutting, and the effect of any variations in composition of the minus No. 40 particles was relatively small.

Influence of Plasticity of Fines

To study the effects of plasticity of the fines, tests were conducted using the granitic gneiss with kaolinite or bentonite substituted for a portion of the fines to determine their effect on resilient and permanent deformation characteristics. Specimens having 0, 25, 50, and 75 percent of kaolinite or bentonite fines were tested under a confining stress of 6 psi (41 kN/m²) and a principal stress ratio of 4.

The permanent strain was found to increase by about a factor of 3 as the kaolinite in the fines increased from 0 to 75 percent (Figure 5). Hence, the presence of plastic fines can have a serious detrimental effect on the performance of an aggregate base course.

The effect of adding bentonite to the granitic gneiss is also shown on Figure 5. Adding bentonite had only a slight effect on permanent strain. The same water content, however, was used in sample preparation. The bentonite absorbs large quantities of water. If more water were added, the specimen prepared with bentonite fines would probably undergo more permanent deformation than if kaolinite were used.

Figure 6 shows the influence of percent kaolinite in the fines on the resilient response of the granitic gneiss.

Influence of Gradation

Figure 7 shows the influence of gradation (Table 5) on the permanent deformation characteristics of the granitic gneiss, shale, and gravel. As the gradation became finer (with more fines in the specimen), the tendency to undergo permanent deformation became greater; this trend has been observed elsewhere (3,5).

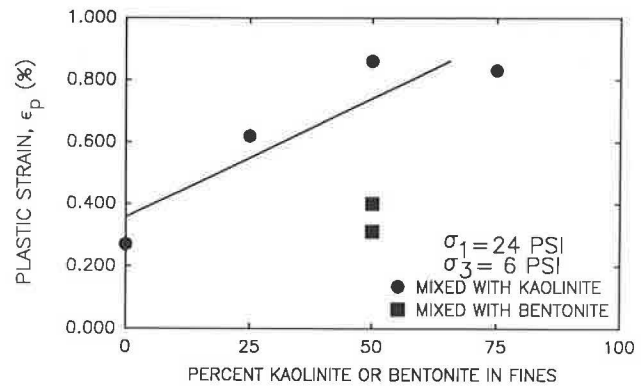


FIGURE 5 Influence of percent kaolinite or bentonite in the fines on plastic strain for the medium gradation of granitic gneiss.

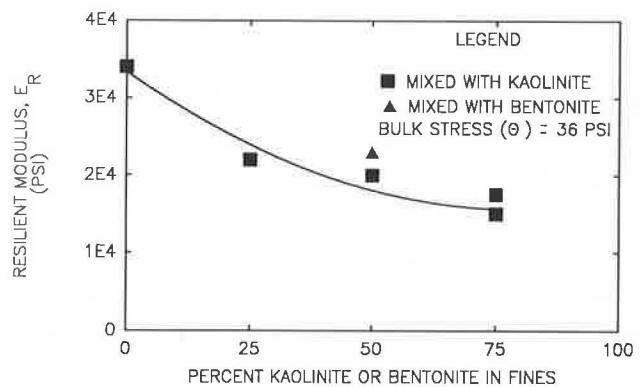


FIGURE 6 Influence of percent kaolinite or bentonite in fines on the resilient modulus of medium gradation of granitic gneiss.

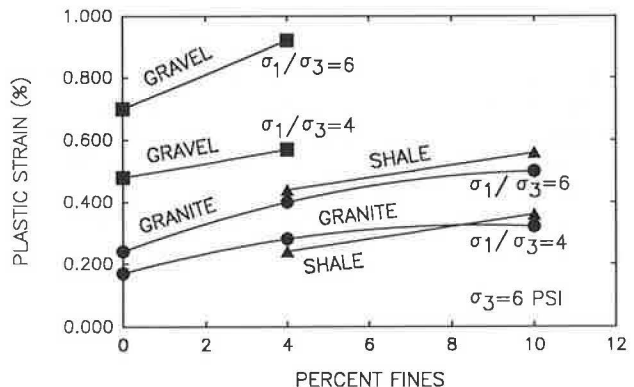


FIGURE 7 Influence of material type, stress level, and percent fines on plastic strain.

Resilient Moduli

The influence of various factors on the resilient moduli of aggregate bases has received considerable attention in the past (1-5,12,19-21). Therefore, only a relatively brief summary of the resilient moduli results is presented for three types of aggregates. At the present time, the resilient modulus is usually represented by the well-known $k-\theta$ model (1,5), which is used in this study to express test results. Improved alternate

methods, however, now exist for representing resilient moduli of granular material such as the contour model (11,19).

Aggregate Type

Figure 8 shows the influence of material type and state of stress on the resilient modulus for the medium gradation of specimens compacted at 100 percent of T-180 density. The aggregate type had a significant influence on the resilient modulus when other factors were held constant. The resilient moduli of the rough, angular materials were higher than the rounded gravel by a factor of about 50 percent at low values of bulk stress. At high bulk stresses, the resilient modulus of the angular granite was higher than that of gravel by a factor of 25 percent.

Moisture

For granitic gneiss at a low bulk stress of 15 psi (103 kN/m²), the resilient modulus decreased by a factor of about 40 percent upon soaking. At a high bulk stress of 100 psi (690 kN/m²), the decrease in the resilient modulus was about 20 percent upon soaking. For the river gravel specimens, the resilient modulus decreased upon soaking by a factor of 50 percent at a bulk stress of 15 psi (103 kN/m²); while at a bulk stress of 100 psi (690 kN/m²), the decrease in the resilient modulus was about 25 percent upon soaking. These results are for tests conducted on drained specimens. Had the tests been performed on undrained specimens, the effect of moisture content on the resilient modulus would undoubtedly have been greater.

Gradation and Density

The influence of aggregate gradation on resilient moduli is shown in Figure 9 for the granitic gneiss. As the gradation became finer (with the amount of fines going from 0 to 10 percent), the resilient modulus decreased by about 60 percent. As the density of the granitic gneiss was increased from 95 to 100 percent of T-180 density, the resilient modulus increased

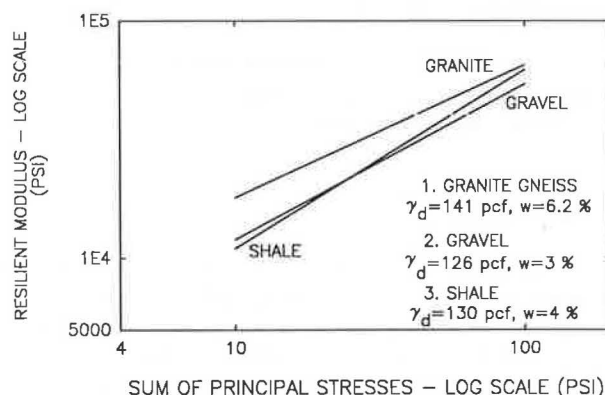


FIGURE 8 Influence of material type and state of stress on resilient modulus for medium gradation.

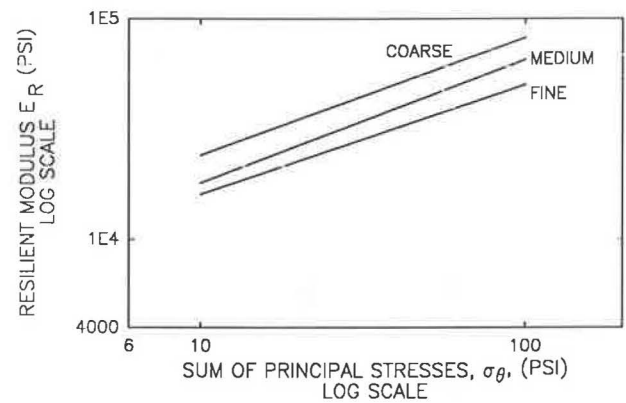


FIGURE 9 Influence of gradation and state of stress on resilient modulus: granitic gneiss.

by 50 to 160 percent at a low level of bulk stress corresponding to 10 psi (69 kN/m²). At a high bulk stress of 100 psi (690 kN/m²) the effect of increase in density was less pronounced, with the increase in resilient modulus being only about 15 to 25 percent.

SLOW CYCLIC CONVENTIONAL TESTS

Many laboratories do not have the equipment and instrumentation necessary to perform conventional cyclic triaxial tests. Therefore, the potential use of a static triaxial test was investigated for determining both resilient and rutting properties of unbound aggregate bases. Development of simplified testing procedures is particularly desirable, because the new AASHTO flexible design method encourages the use of resilient modulus (22).

In the slow test used in this study, the applied load was slowly repeated using conventional triaxial test equipment for five cycles with the rate of loading equal to 0.03 in./min. Permanent deformation was the total recorded after the five cycles. The resilient modulus was the deviator stress, divided by the recoverable deformation observed upon unloading at the end of the fifth load cycle.

Permanent Deformation

Figure 10 shows the correlation for permanent deformation between the cyclic and static methods. These results show a much higher amount of scatter in permanent deformation than was found for the resilient modulus. The relative permanent strain between cyclic and static tests varied from 1.22 to 3.2 for all the specimens tested. The average ratio of permanent deformation obtained from the conventional dynamic test at 70,000 load repetitions over the permanent deformation obtained from the slow cyclic static test using five loading-unloading cycles was about 2.5 for the specimens tested under similar conditions (Figure 10).

These results indicate that a slow static test, as performed for this study, is probably not suitable for evaluating the cyclic load permanent deformation performance of aggregate bases.

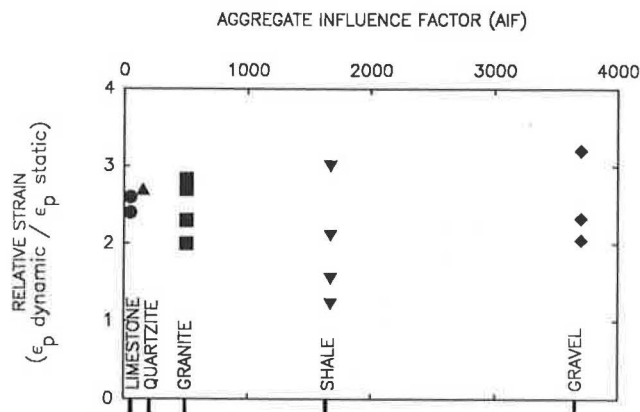


FIGURE 10 Relative permanent strain related to aggregate type.

Resilient Modulus

Figure 11 shows a comparison between the resilient modulus measured using the cyclic triaxial test and the static unload modulus measured after five cycles of slow loading. Excellent agreement is seen between the resilient and the slow cyclic unload modulus after five cycles. The average ratio of resilient modulus from the dynamic test to the resilient modulus from static test was about 1.08. Good correlations have also been obtained by Sweere and Galjaard (23) and Kalcheyff and Hicks (24).

These findings, together with the results of the earlier studies, indicate that a slow cyclic test can be used to evaluate the resilient modulus of unbound aggregate bases for design purposes. The modulus obtained from a slow cyclic test could, if desired, be increased by 10 percent to give better results, which is in agreement with other studies (23).

CONCLUSIONS

The rut index concept proposed a number of years ago for comparing the relative permanent deformation characteristics of base course aggregates is re-evaluated and revised to give a simpler test procedure using a single test. The principal

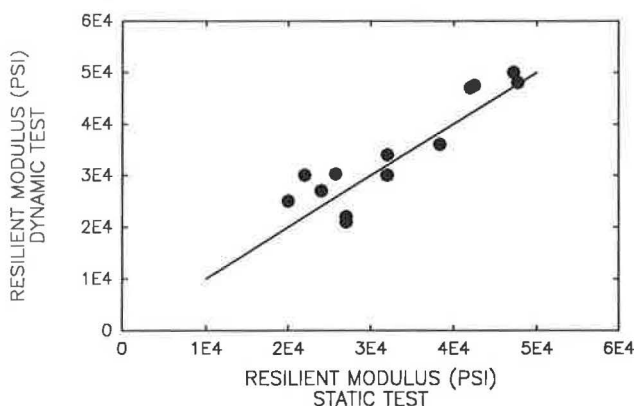


FIGURE 11 Comparison of resilient modulus from cyclic and static tests.

stress ratio σ_1/σ_3 to use in the test typically varies between 2 and 6 depending on the structural strength of the section.

Aggregate characteristics including shape, angularity, surface roughness, and roundness have an important influence on the resilient and permanent response of an unbound aggregate. Methods are presented for evaluating these aggregate properties. The permanent deformation characteristics of disc-shaped granitic gneiss, blade-shaped limestone, and blade-shaped shale aggregates were all similar for the same gradation and level of compaction. The general appearance of these aggregates was, however, quite different. A blade-shaped quartzite appeared to be slightly more susceptible to rutting than the other crushed aggregates. A cubic-shaped, rounded river gravel with smooth surfaces was over two times more susceptible to rutting than the crushed aggregates.

A conventional, slow triaxial shear test can be used for practical applications to evaluate the resilient moduli of an unbound aggregate. The slow triaxial test appears to be unsuitable for evaluating permanent deformation characteristics.

ACKNOWLEDGMENTS

This research was performed partly under a grant from the National Stone Association, whose support is appreciated. Appreciation is also expressed to J. E. Fitzgerald, director, School of Civil Engineering, Georgia Institute of Technology, for his support in performing this work. Appreciation is also given to Max Stephens of Vulcan Materials and Rick Sink of W. J. Boxley for supplying the stone.

REFERENCES

1. R. W. May and M. W. Witzak. Effective Granular Modulus to Model Pavement Responses. In *Transportation Research Record 810*, TRB, National Research Council, Washington, D.C., 1981.
2. M. W. Witzak and G. Rada. Comprehensive Evaluation of Laboratory Resilient Moduli Results for Granular Materials. In *Transportation Research Record 810*, TRB, National Research Council, Washington, D.C., 1981, pp. 23–33.
3. R. D. Barksdale. Performance of Crushed Stone Base Courses. In *Transportation Research Record 954*, TRB, National Research Council, Washington, D.C., 1984, pp. 78–88.
4. H. E. Stewart, E. T. Selig, and G. M. Norman-Gregory. Failure Criteria and Lateral Stresses in Track Foundations. In *Transportation Research Record 1022*, TRB, National Research Council, Washington, D.C., 1985, pp. 59–71.
5. R. D. Barksdale. Laboratory Evaluation of Rutting in Base Course Materials. *Proc., 3rd International Conference on the Structural Design of Asphalt Pavements*, University of Michigan, Ann Arbor, 1972, pp. 161–174.
6. R. L. Lytton and K. H. Tseng. Prediction of Permanent Deformation in Flexible Pavement Materials. Presented at ASTM Symposium on Implication of Aggregate in Design, Construction, and Performance, New Orleans, Dec. 1986.
7. H. E. Stewart. Permanent Strains from Cyclic Variable Amplitude Loadings. *Journal of Geotechnical Engineering*, ASCE, Vol. 112, No. 6, June 1986, pp. 646–660.
8. R. D. Barksdale and A. E. Zeevaert. *Users Manual for Finite Element Problem for the Analysis of Geotechnical Problems: GAPP57*. Georgia Institute of Technology, Atlanta, Sept. 1981.
9. R. D. Barksdale, Q. L. Robnett, J. S. Lai, and A. E. Zeevaert. Experimental and Theoretical Behavior of Geotextile Reinforced Aggregate Soil Systems. *Proc., 2nd International Conference on Geotextiles*, Vol. II, Las Vegas, 1982, pp. 375–380.
10. A. E. Zeevaert and R. D. Barksdale. *Finite Element Program*

- for the Analysis of Geotechnical Problems—GAPIN. School of Civil Engineering, Georgia Institute of Technology, Atlanta, 1981.
11. S. F. Brown and J. W. Pappin. Analysis of Pavements with Granular Bases. In *Transportation Research Record 810*, TRB, National Research Council, Washington, D.C., 1981, pp. 17–23.
 12. J. Uzan. Characterization of Granular Material. In *Transportation Research Record 1022*, TRB, National Research Council, Washington, D.C., 1985, pp. 52–59.
 13. G. Lees. The Measurement of Particle Shape and its Influence in Engineering Materials. *Journal of the British Granite and Whinstone Federation*, London, Vol. 4, No. 2, 1964, pp. 1–22.
 14. G. Rittenhouse. The Relation of Shape to the Passage of Grains through Sieves. *Industrial and Engineering Chemistry*, Vol. 15, No. 2, 1943, pp. 153–155.
 15. F. A. Shergold. *Quarry Manager's Journal*, Vol. 30, No. 4, 1941, pp. 222–270 (abridged translation).
 16. T. Zingg. Beitrag Zur Schotteranalyse. *Schweizerische Mineralogische und Petrographische Mitteilungen*, Vol. 15, 1935, pp. 39–140 (in German).
 17. B. C. Aschenbrenner. A New Method for Expressing Particle Sphericity. *Journal of Sedimentary Petrology*, Vol. 26, No. 1, 1956, pp. 15–31.
 18. H. Wadell. Sphericity and Roundness of Rock Particles. *Journal of Geology*, Vol. 41, 1933, pp. 310–331.
 19. R. D. Barksdale and S. F. Brown. Pavement Design and Materials. *Proc., 6th International Conference on the Structural Design of Asphalt Pavements*, Vol. 2, University of Michigan, Ann Arbor, 1988, pp. 117–148.
 20. S. F. Brown. Repeated Load Testing of Granular Material. ASCE Proceedings Paper 10684, Vol. 100, No. GT7, July 1974, pp. 825–841.
 21. R. G. Hicks and C. L. Monismith. Factors Influencing the Resilient Response of Granular Materials. In *Highway Research Record 345*, HRB, National Research Council, Washington, D.C., 1971.
 22. American Association of State Highway and Transportation Officials. *AASHTO Guide for Design of Pavement Structures*. AASHTO, Washington, D.C., 1986.
 23. G. T. Sweere and P. J. Galjaard. *Determination of the Resilient Modulus of Sands by Means of Static Loading Triaxial Tests*. Research Report, Delft University, Dec. 1986.
 24. I. V. Kalcheff and R. G. Hicks. A Test Procedure for Determining the Resilient Properties of Granular Materials. *Journal of Testing and Evaluation*, Vol. 1, No. 6, Nov. 1973, pp. 472–479.
 25. L. Collis and R. A. Fox. *Aggregates*. Special Publication No. 1, Geological Society of Engineering Geology, Belfast, 1985.
 26. R. D. Barksdale. Evaluation of Base Course Materials to Control Rutting. *Proc., 2nd Conference on Asphalt Pavements for Southern Africa*, Durban, Republic of South Africa, 1974, pp. 3:15–3:68.
 27. J. L. Paute and J. Martinez. Structural Finite Element Design of Unbound Material Pavements from Cyclic Loading Triaxial Tests. Presented at International Conference on the Structural Design of Asphalt Pavements, 1987.

Publication of this paper sponsored by Committee on Strength and Deformation Characteristics of Pavement Sections.

Effects of Unknown Rigid Subgrade Layers on Backcalculation of Pavement Moduli and Projections of Pavement Performance

ROBERT C. BRIGGS AND SOHEIL NAZARIAN

More and more highway agencies are obtaining and using highway pavement deflection measuring equipment to infer the elastic modulus of paving materials for design purposes. Layered elastic theory is used in the analysis to arrive at the moduli for individual pavement layers. It is possible under certain conditions to arrive at erroneous values of the elastic moduli, particularly when a rigid layer exists below the subgrade unbeknownst to the engineer. A theoretical study was performed, for flexible pavements, to determine the sensitivity of backcalculated moduli to the existence of this rigid layer. It was found that a rigid layer will adversely affect the accuracy of the backcalculated pavement moduli if the actual depth of the layer is equal to or less than half its assumed depth with respect to the surface of the pavement. These types of errors will result in unconservative pavement evaluations and designs for rehabilitation and reconstruction—leading to early pavement failure.

The practice of using elastic modulus to characterize paving materials for design and evaluation purposes is becoming more common. The 1986 *AASHTO Guide for Design of Pavement Structures* has incorporated this parameter for both new pavement design and evaluation of existing pavements for overlays (1). The Strategic Highway Research Program (SHRP) has acquired four falling weight deflectometers (FWD) and will use them nationwide to monitor the structural condition of thousands of pavement test sections (2). Undoubtedly, elastic modulus will be used as a primary indicator of structural condition. Many states currently have, or are developing, pavement design methods that use the elastic modulus of subgrade and pavement materials to determine required pavement thicknesses.

Elastic moduli values may be determined in the laboratory using samples of paving material obtained in the field. However, base and subgrade samples are usually disturbed upon acquisition and must be remolded for laboratory testing. Thus, their stiffness characteristics, as measured in the laboratory, may not be representative of those in the field. It has been generally accepted that elastic modulus of paving materials, particularly base and subgrade, should be determined under in-service conditions.

A popular approach to obtaining in situ elastic moduli values is to record the pavement's deflection under various mag-

nitudes of loading on the surface. The FWD, Dynaflect, and Road Rater (among other devices) have been developed specifically for this purpose. Each of these machines is designed to impart a known load to the pavement surface and measure the resulting pavement deflection at various distances from the point of load application. The profile of the deflection at the surface of the pavement is known as the deflection basin, because it resembles a bowl-shaped depression. The magnitude of the deflections and the basin shape are functions of the number of pavement layers making up the pavement cross section, their thicknesses, and moduli values.

A variety of multi-layered linear elastic pavement models is available for use on mainframe and microcomputers to predict stresses, strains, and displacements for pavements under loaded conditions. These programs assume that any deformation occurring within the pavement system under load will completely disappear when the pavement is unloaded, thus the term *elastic*. The term *linear elastic* means that the stiffness of the layers is independent of the rate at which the load is applied and is constant throughout a range of load magnitudes. *Multi-layered* refers to the program's ability to model pavement systems composed of multiple layers (usually four to five), each having different stiffnesses. These programs further assume that the materials in any layer are homogeneous, both in physical and engineering properties, and that the layers extend to infinity in the lateral directions. Some examples of these programs are BISAR, ELSYM5, and CHEVRON. The programs calculate stresses, strains, and displacements at any point on the surface and within the pavement system given a loading magnitude and the elastic moduli, thickness, and Poisson's ratio of the pavement layers.

The programs have also been modified to run in a reverse-iterative fashion to determine elastic moduli from pavement surface deflections, given the layer thicknesses, Poisson's ratios, and loading conditions. The engineer inputs a range of moduli values for the pavement layers, and the program calculates a deflection basin. This calculated basin is compared with the deflection basin measured by the equipment. The moduli values resulting in the best fit between the calculated and measured deflection basin are assumed to be the correct in situ moduli values for that pavement. Examples of these modified programs are BISDEF, ELSDEF, and CHEVDEF. Because these programs can run on microcomputers, the programs have become quite popular and are enjoying widespread use.

It is possible, however, under certain conditions, to generate erroneous answers with these programs. First, many combinations of moduli values will result in an acceptable basin fit, and the engineer must use judgment and experience to select the combination that is representative of the materials being used. For example, for flexible pavements, it is usually assumed that, for any given pavement layer, the one above is of higher stiffness while the one below is of lower stiffness. This is not always the case, especially where stabilized materials are placed under a granular base or where a pavement has begun to deteriorate severely. It is sometimes necessary to take cores of the pavement to determine the material types that are involved.

Another source of error occurs when the material stiffnesses are a function of the magnitude of the load or the rate of loading. The AASHTO guide provides guidelines to identify the stress dependency of the pavement structure. Visco-elastic properties may be identified with the Road Rater by changing the frequency of the load application.

A possible major source of error in the process of backcalculating moduli values is a result of the presence of stiff layers below the subgrade. The presence of these layers is either unknown to the engineer or assumed to be deep enough so as not to affect the results of the deflection test. If, in fact, these stiff layers are influencing the deflections and this fact is not taken into account, the subgrade modulus will be overestimated, leading to pavement and overlay designs of inadequate thickness and subsequent premature failure.

This paper deals with the *theoretical* errors introduced into the backcalculation process as a result of the presence of these stiff layers. The paper does not, however, deal with errors resulting from modeling the effects of a dynamic load with a static analysis technique, or errors resulting from inaccuracies in the deflection measuring equipment.

OBJECTIVE OF THE STUDY

The objective of this study was to document the theoretical effects of unknown rigid layers below the subgrade, at various depths and for a range of stiffnesses, on the backcalculation of pavement moduli and subsequent structural analysis procedures. Linear elastic multi-layer theory was used for the analysis. The effects studied include possible errors in (a) backcalculation of moduli values, (b) calculation of strains, and (c) projected remaining life of the pavement.

PROCEDURES

The first step was to construct a data base of theoretical pavement structures comprising a predetermined range of layer moduli, thicknesses, and rigid layer depths. These characteristics were entered into the BISAR program to determine pavement deflections directly under a 9,000-lb circular load and at six points at 12-in. centers on a line away from the load. The deflection basins generated are referred to as the measured deflections, as they simulate pavement deflections obtained by the FWD on the theoretical pavement sections. Also obtained were stresses and strains at various points in the pavement systems. These values are referred to as the actual stresses and strains.

A four-layer system was chosen for the analysis to represent a typical three-layer system with an additional rigid layer below. Layer 1 was intended to represent asphaltic concrete; Layer 2, granular base; and Layer 3, a typical subgrade.

Next, the BISDEF program was used to backcalculate layer moduli from the measured deflections. The pavement thicknesses assumed for the backcalculation procedure were identical to those in the BISAR run except the rigid layer was fixed at 240 in. below the surface of the pavement. The deflection basin representing the best fit for each pavement section is referred to as the calculated basin. The resulting moduli were again input to BISAR, and strains were calculated. The calculated moduli and strains were compared with the actual values. Also compared were the calculated and actual 18-kip equivalencies to failure projected from the stress-strain data. The entire process is outlined in Figure 1.

Development of the Actual Pavement Data Base

Seventy-one theoretical pavement cross sections and corresponding deflection basins were developed for the study, each with unique rigid-layer thicknesses and moduli. These represented the actual pavement structures and the simulated deflections expected when a 9,000-lb FWD load was placed on each. A 6-in. radius was assumed for the circular load. The deflections were calculated at the center of the load and at 1-ft intervals away for a distance of 6 ft. Seven deflections were obtained for each basin.

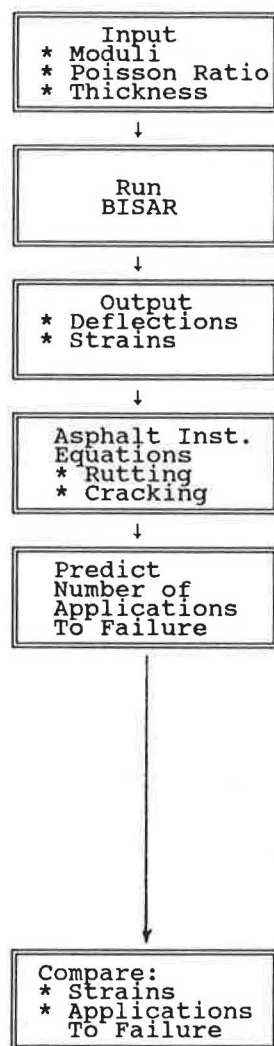
The upper illustration in Figure 2 summarizes the combinations of moduli and layer thicknesses used to generate the data base of measured deflections. Note that the moduli values used to develop the measured deflection basins were held constant, except for Layer 4. The thickness of Layer 3 varied from 42 to 222 in. All other thicknesses were held constant. The modulus of Layer 3 was fixed at 10,000 psi because, for the purposes of the experiment, it was intended to represent the subgrade. The modulus of the rigid layer was set at 10,000 psi for one run to represent a system without a rigid layer. BISAR was used to calculate the deflection basins on an IBM PC-compatible microcomputer.

In the process of generating the deflection basins, the strains at various points within the pavement sections were calculated. The horizontal tensile strain at the bottom of Layer 1 and the vertical compressive strain at the top of Layer 3 were recorded.

Backcalculation Process

The bottom illustration in Figure 2 represents the structural parameters assumed for the backcalculation process using BISDEF. These values remained constant throughout the basin-fitting process for all 71 deflection basins. The maximum and minimum moduli values were obtained through iterative runs of the BISDEF program, adjusting them to allow the best fit between the observed and backcalculated deflection basins for all conditions of rigid layer depth and stiffness. The modulus of the rigid layer was held constant at 240 in. below the surface, and its modulus was restricted to 1,000,000 psi at all times. A 9,000-lb load was assumed for the backcalculation process.

Forward Calculations:



Back-Calculations:

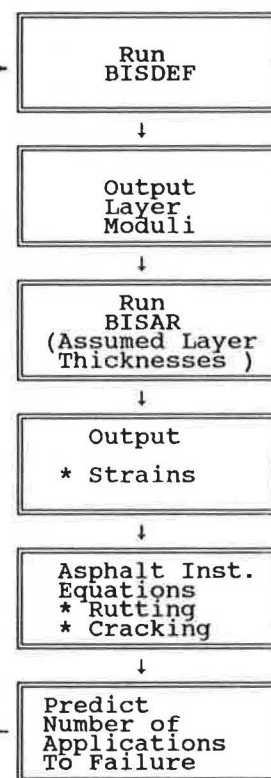


FIGURE 1 Flowchart of analysis process.

BISDEF was altered to allow up to 10 iterations before the program stopped. Generally, it stopped at two or three but in some cases it went the entire 10. The accuracy with which it fit the deflection basins varied widely and, in some cases, was extremely poor. This was to be expected, as the assumed pavement structure at times varied significantly from the actual structure used in the development of the deflection basins.

The backcalculated moduli were then entered into the BISAR program to determine the horizontal and tensile strains for comparison with the actual values.

Estimation of Remaining Life

The objective of most pavement evaluation and analysis procedures, for either reconstruction or rehabilitation, is to determine pavement layer thicknesses that will perform adequately over a specified period of time given a design traffic loading. Therefore, a study of the effects of erroneous assumptions in the design procedure should be assessed on the basis of the impact it has on the ultimate answer (i.e., required additional

thickness or estimated time to failure). For this analysis, the impact of unknown or neglected rigid layers in the subgrade shall be assessed on the basis of errors in estimation of remaining life in the form of 18-kip equivalencies.

The design procedure developed by the Asphalt Institute for *Thickness Design—Asphalt Pavements for Highways and Streets* (3) was adopted for this study. This method was selected for the following reasons:

1. It is based on layered elastic design theory;
2. It is a widely accepted and used design method;
3. It assumes that the subgrade extends infinitely in the vertically downward and horizontal directions; and
4. Estimations of pavement performance are based on strain criteria.

The introduction of the Asphalt Institute's design manual states as follows:

Criteria for maximum tensile strains induced at the bottom of the asphalt layer and vertical compressive strains induced

Three-layer Pavement Structure Used to Develop Deflection Basins:

Layer 1	$E_1 = 300,000 \text{ psi.}$ $h_1 = 6 \text{ in.}$ $\mu_1 = 0.30$
Layer 2	$E_2 = 40,000 \text{ psi.}$ $h_2 = 12 \text{ in.}$ $\mu_2 = 0.35$
Layer 3	$E_3 = 10,000 \text{ psi.}$ $h_3 = 42 \text{ in. to } 222 \text{ in.}$ $\mu_3 = 0.40$
Rigid Layer	$E_r = 10,000 \text{ to } 1,000,000 \text{ psi.}$ $h_r = \infty$ $\mu_r = 0.30$

Three-Layer Pavement Structure Assumed for Back-calculation:

Layer 1	$E'_1 = 100,000 \text{ to } 1,500,000$ $h'_1 = 6 \text{ in.}$ $\mu'_1 = 0.30$
Layer 2	$E'_2 = 5,000 \text{ to } 100,000 \text{ psi.}$ $h'_2 = 12 \text{ in.}$ $\mu'_2 = 0.35$
Layer 3	$E'_3 = 5,000 \text{ to } 500,000 \text{ psi.}$ $h'_3 = 222 \text{ in.}$ $\mu'_3 = 0.40$
Rigid Layer	$E'_r = 1,000,000 \text{ psi.}$ $h'_r = \infty$ $\mu'_r = 0.30$

FIGURE 2 Pavement structures assumed for the study.

at the top of the subgrade layer by wheel loads have been adopted and used in producing the thickness design charts included in this manual.

In the Asphalt Institute's Research Report No. 82-2 (4), the following equations were presented as the criteria used in the developing of the manual:

Allowable Asphalt Tensile Strain Criteria

$$N = 18.4 (4.32 \times 10^{-3} * \epsilon_t^{-3.29} |E^*|^{-0.854}) \quad (1)$$

where

N = number of 18-kip single-axle loads to cause cracking;

ϵ_t = tensile strain in asphalt layer; and

$|E^*|$ = asphalt mixture dynamic modulus.

Allowable Subgrade Vertical Strain Criteria

$$N = 1.365 \times 10^{-9} \epsilon_c^{(-4.477)} \quad (2)$$

where

N = number of 18-kip single-axle loads to cause rutting, and

ϵ_c = vertical subgrade strain at top of subgrade layer.

These two equations were used to predict remaining life for each of the 71 pavement cross sections using the actual and backcalculated modulus values obtained from BISAR and BISDEF.

PRESENTATION OF RESULTS

Deflection Basin Fitting

As a rule, the basin fitting results using BISDEF were fairly good. Figure 3 shows the absolute sum of percent error for each deflection basin matched with BISDEF, versus the ratio of the actual/assumed depth to the rigid layer. The absolute sum of percent error, E , was calculated as follows:

$$E = \sum |100[\text{def}(a_i) - \text{def}(b_i)]/\text{def}(a_i)| \quad \text{for } i = 1 \text{ to } 7 \quad (3)$$

where $\text{def}(a_i)$ equals measured deflection at position i , and $\text{def}(b_i)$ equals backcalculated deflection at position i .

Only six of the original 11 rigid-layer moduli used to develop the measured deflection basins are shown (100, 300, 500, 700, 900, and 1,000 ksi). It was not necessary to show all the results, because the omitted values fell within the lines shown on the plot. (This applies to the remaining figures as well.)

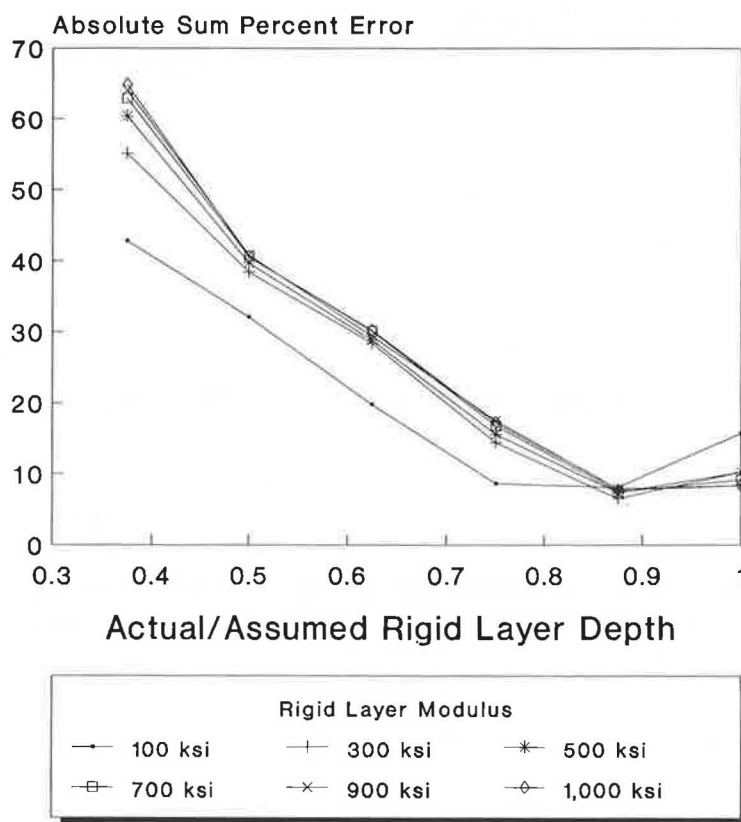


FIGURE 3 Effect of erroneously assumed rigid layer depths on quality of basin fitting.

Also not shown on the plot are the errors obtained for rigid layer depths of 60 in. Backcalculation efforts resulted in errors that were considered too large to be acceptable or layer moduli values that were way out of range.

It is evident from the plot that the backcalculation procedure is more sensitive to variations in rigid layer depths than to the actual modulus of the rigid layer. There is an indication, however, that rigid-layer modulus becomes increasingly influential as the ratio of actual/assumed rigid layer depth drops below 0.5.

Note that the error does not reach zero when the actual/assumed rigid layer depth approaches one. This occurs because the seed value for the subgrade modulus used was 40,000 psi. If the seed value for the subgrade modulus was close to the actual value of 10,000 psi, the basin fit improved for rigid layer depth ratios greater than 0.5 but became worse for values less than 0.5. The result is a compromise.

When no rigid layer existed ($E_r = 10,000$ psi) but was assumed to be at a 240-in. depth with a modulus of 1,000,000 psi, the sum of the absolute values of errors in backcalculation was 64 percent.

Figure 4 shows the ratio of backcalculated-to-measured or actual deflections, D_1 , versus the ratio of assumed-to-actual rigid layer depth. Figure 5 is a similar plot for D_7 . D_1 is the deflection under the load ($r = 0$ in.), while D_7 is the deflection farthest from the load ($r = 72$ in.). It is apparent that, in most instances, the fit was good for D_1 and D_7 . Again, the quality of the basin fitting was influenced more by the depth of the rigid layer than by its modulus, except at rigid-layer depth ratios less than 0.5.

Backcalculation of E_1 : Rigid Layer Effects

Figure 6 shows the ratio of the backcalculated-to-actual value of the modulus of Layer 1, versus the ratio of the actual-to-assumed rigid-layer depth. It is apparent that, as the rigid layer depth ratio decreases below 0.5, the modulus of Layer 1 is overestimated by a factor of greater than 3. If the rigid layer depth ratio increases to 0.75 the backcalculated modulus of Layer 1 closely resembles its actual value.

The backcalculated modulus of Layer 1 is affected more by errors in estimating the depth to the rigid layer than by errors in assumed modulus of the rigid layer.

When no rigid layer actually existed ($E_r = 10,000$ psi) but was assumed at 240 in. deep and 1,000,000 psi, the backcalculated modulus of Layer 1 was found to be 765,000 psi, which is in error by a factor of greater than 2.

Backcalculation of E_2 : Rigid Layer Effects

Figure 7 shows the ratio of backcalculated-to-actual modulus of Layer 2, versus the ratio of the actual-to-assumed rigid layer depth. The ratio of the backcalculated-to-actual modulus of Layer 2 varied between 0.8 and 0.2. From the plot, it is apparent that by overestimating the depth to the rigid layer by half, one underestimates the modulus of Layer 2 by a factor of 5. As with Layer 1, the backcalculated modulus of Layer 2 is more sensitive to errors in estimating the rigid layer depth than by errors in estimating its modulus.

When no rigid layer existed, but was assumed at 240 in.

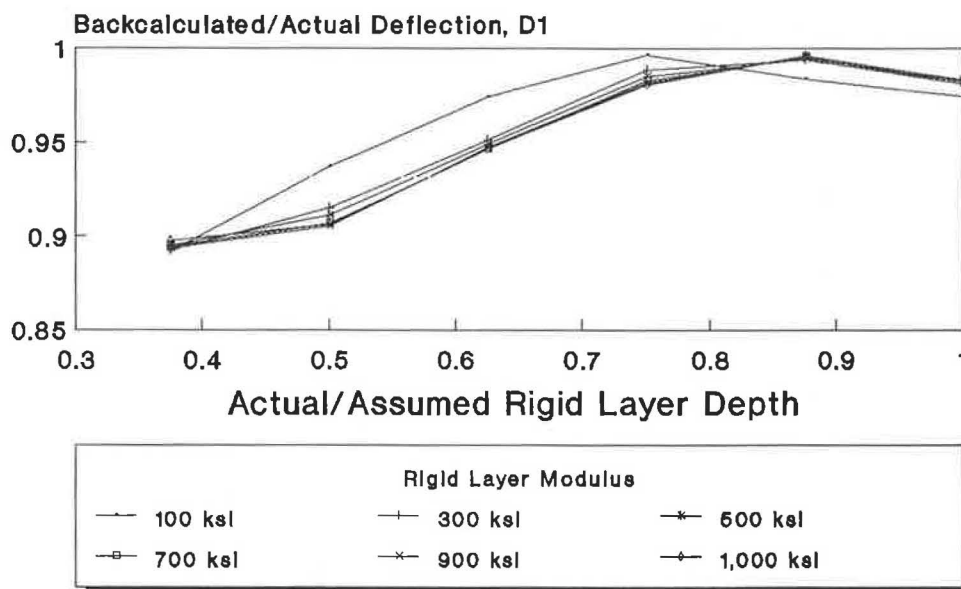


FIGURE 4 Effect of erroneously assumed rigid layer depths on backcalculated deflections under the load ($R = 0$ in.).

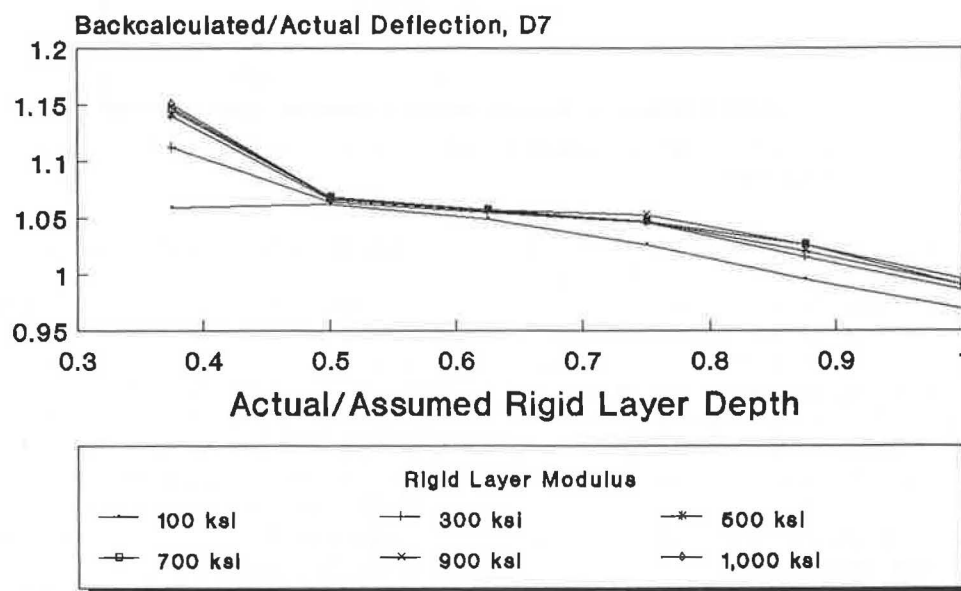


FIGURE 5 Effect of erroneously assumed rigid layer depths on backcalculated deflections 72 in. from the load.

and 1,000,000 psi, the modulus of Layer 2 was found to be 23,000 psi, which is off by a factor of 0.5.

Backcalculation of E_3 : Rigid Layer Effects

Figure 8 shows the ratio of backcalculated-to-actual modulus of Layer 3 (subgrade), versus the ratio of the actual-to-assumed rigid layer depth. This ratio varied from 3 to about 1, indicating that, if the depth to the rigid layer were underestimated, the subgrade modulus will be overestimated. Again, the backcalculated modulus of Layer 3 is more sensitive to errors in estimating rigid layer depth than to its modulus.

When no rigid layer existed but was assumed at 240 in. and 1,000,000 psi, the modulus of Layer 3 was underestimated by 25 percent.

Calculation of Tensile and Compressive Strains

Figures 9 and 10 show the effects of errors in assumed rigid layer depths for tensile and compressive strains in a three-layer pavement system. The tensile strain was calculated at the bottom of Layer 1 (asphalt), while the compressive strain was calculated at the top of Layer 3 (subgrade).

Note that both strain levels are underestimated when the

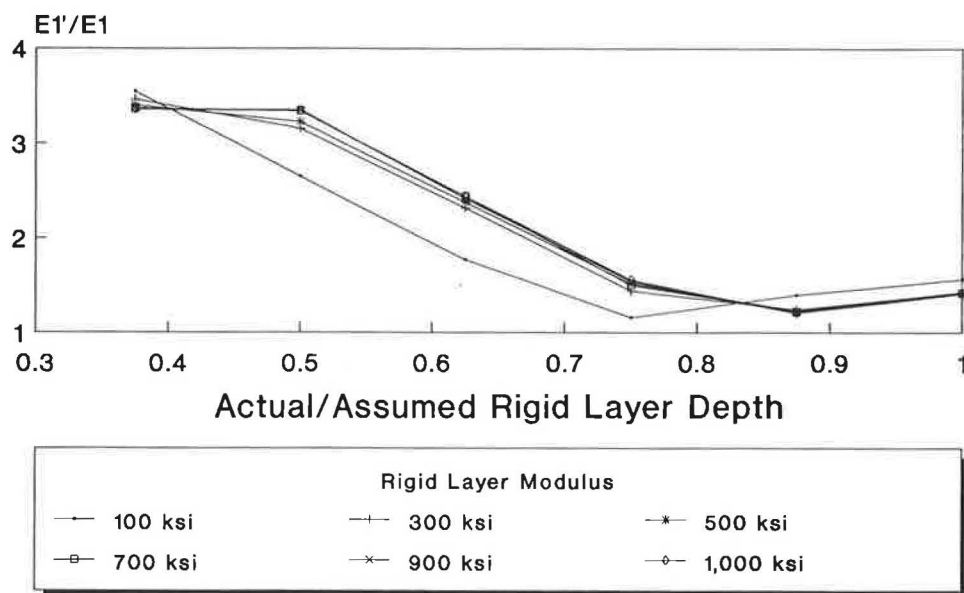


FIGURE 6 Effect of erroneously assumed rigid layer depths on backcalculated surface layer moduli.

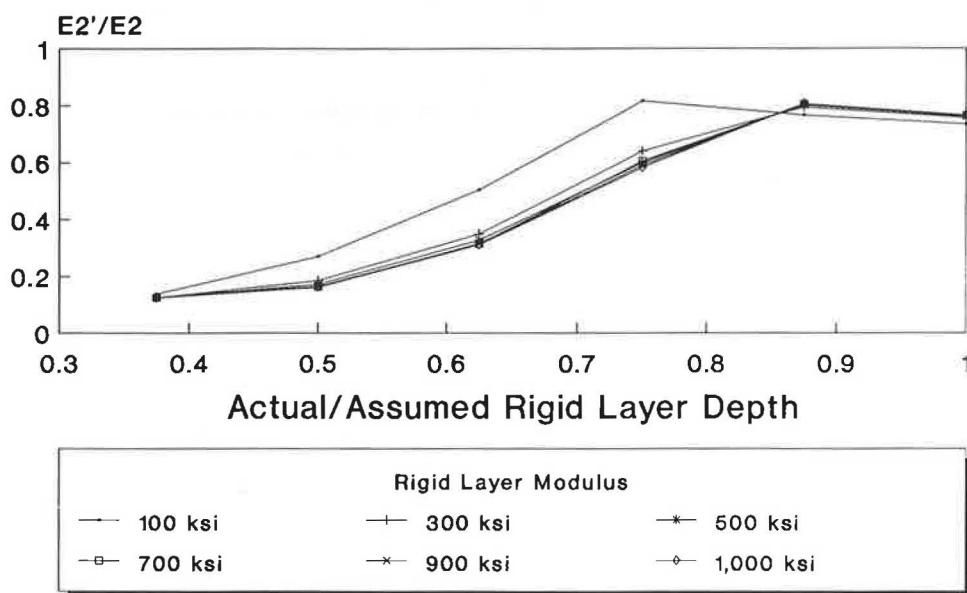


FIGURE 7 Effect of erroneously assumed rigid layer depths on backcalculated modulus of Layer 2.

depth to the rigid layer is overestimated. The compressive strain is affected more so than the tensile strain.

When no rigid layer existed but was assumed at 240 in. and 1,000,000 psi, the tensile strain was underestimated by 25 percent and the compressive strain was underestimated by 14 percent.

Failure Under 18-kip Single-Axle Loads

Figures 11 and 12 illustrate the effect of erroneous assumptions regarding the depth to the rigid layer on estimations of time to failure by both cracking and rutting.

As Figure 11 shows, the ratio of the predicted-to-actual number of repetitions to failure by cracking under an 18-kip single-axle load increases from 1 to 3 as the ratio of the actual-to-assumed rigid layer depth decreases from 1.0 to 0.4.

Similarly (from Figure 12), for rutting, the ratio increases from 1 to 1,000 as the ratio of the rigid layer depth decreases (note that the y axis is a log scale). This means that, if the actual rigid layer depth is less than half that assumed in the backcalculation process, the pavement will fail due to rutting 1,000 times faster than expected under a given traffic loading.

Note again that the predicted number of 18-kip single-axle loads to failure is relatively unaffected by errors in assump-

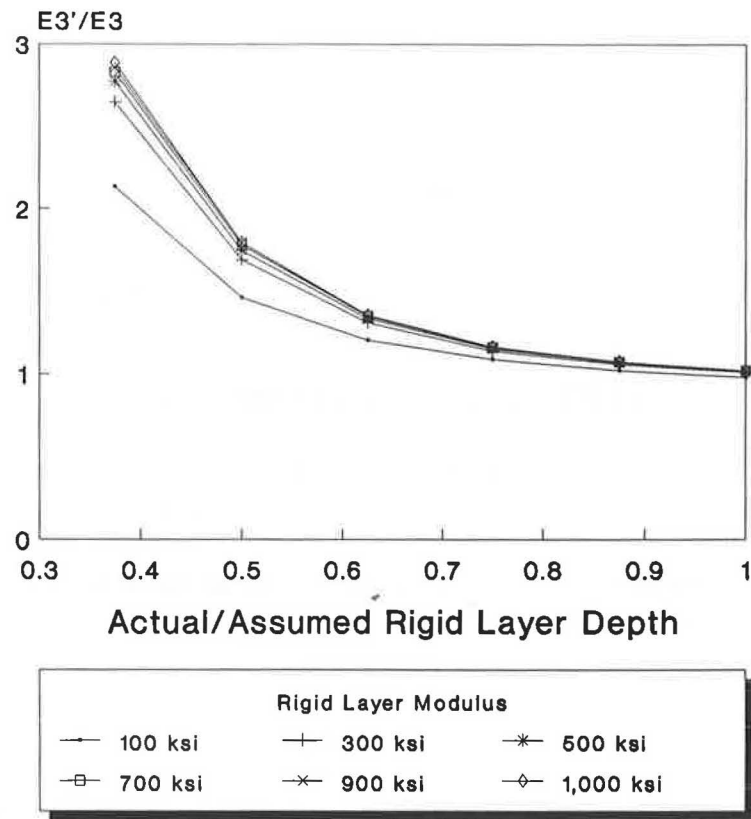


FIGURE 8 Effect of erroneously assumed rigid layer depths on back-calculated subgrade moduli.

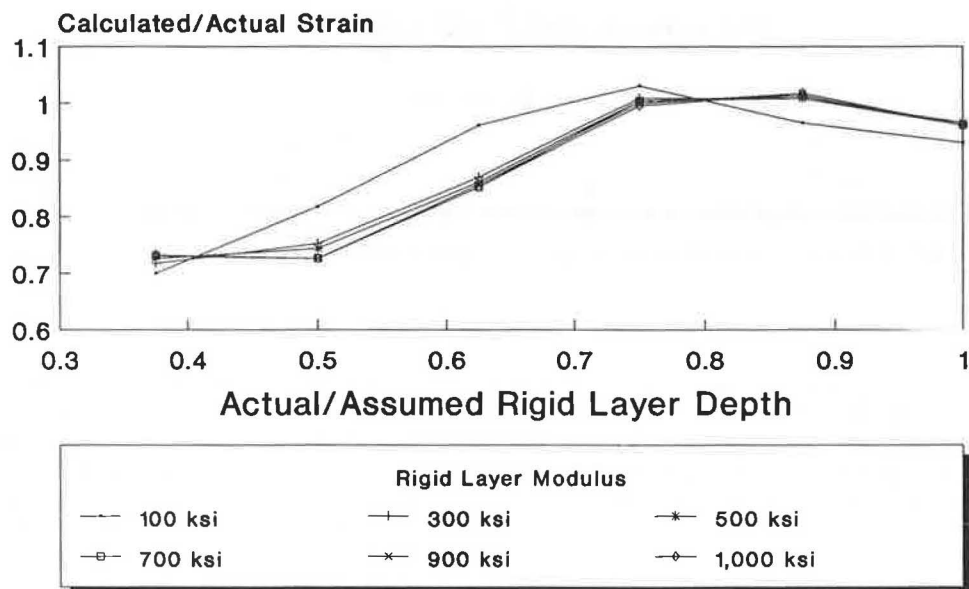


FIGURE 9 Effect of erroneously assumed rigid layer depths on horizontal tensile strain at bottom of surface layer.

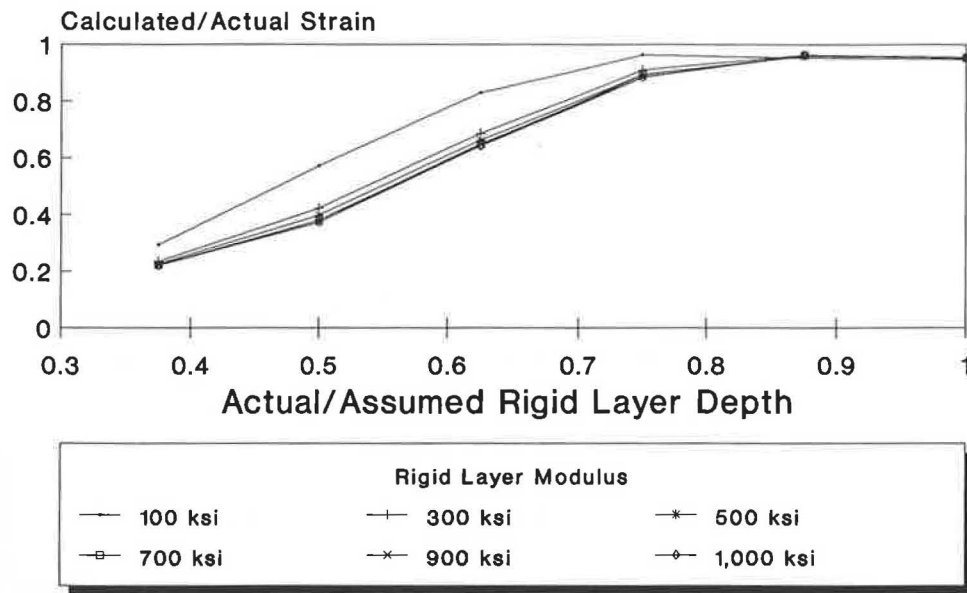


FIGURE 10 Effect of erroneously assumed rigid layer depths on vertical compressive strain at top of subgrade.

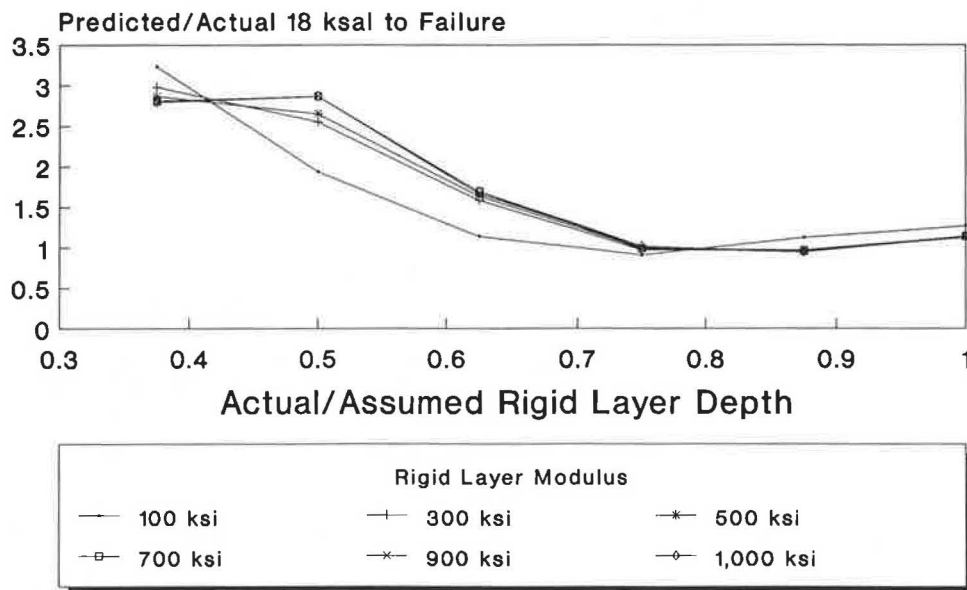


FIGURE 11 Effect of erroneously assumed rigid layer depths on rate of surface layer cracking.

tions regarding the stiffness of the rigid layer, but is most sensitive to errors regarding its depth.

When no rigid layer existed but was assumed at 240 in. and 1,000,000 psi, the repetitions to failure by cracking were overestimated by a factor of 2.35. The repetitions to failure by rutting were overestimated by a factor of 1.90.

DISCUSSION OF RESULTS

To explain fully the consequences of the results of this study on structural analysis of pavements, it will be useful to expand on one case presented in this report, for example, the case in which a rigid layer exists at 150 in. and the elastic modulus

of the rigid layer is 100,000 psi. The pavement structure is as follows:

Layer 1
Asphalt Concrete
 $E = 300,000$ psi $h = 6$ in.

Layer 2
Granular Base
 $E = 40,000$ psi $h = 12$ in.

Layer 3
Subgrade
 $E = 10,000$ psi $h = 132$ in.

Rigid Layer
 $E = 100,000$ psi $h = \infty$

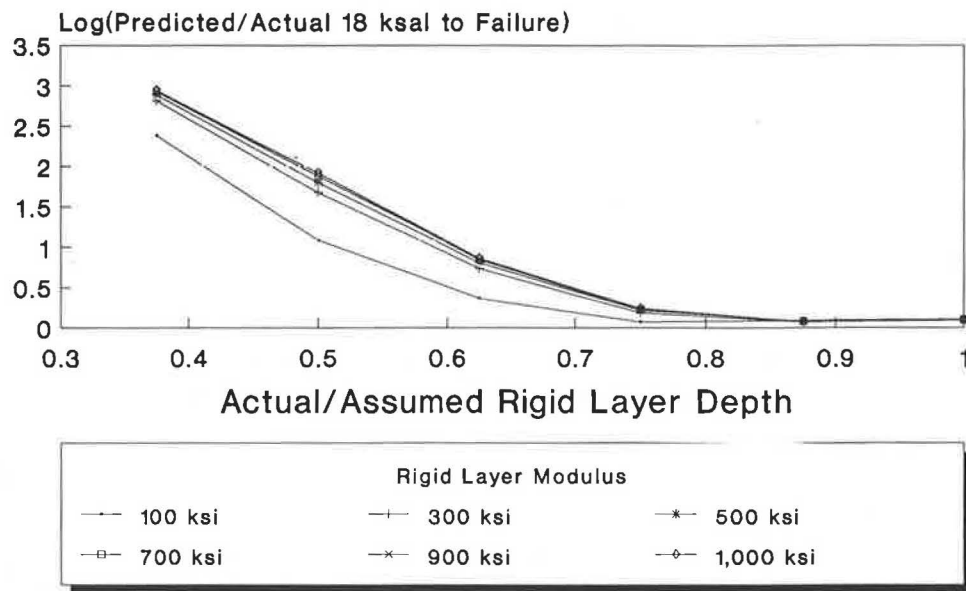


FIGURE 12 Effect of erroneously assumed rigid layer depths on predictions of rutting.

An engineer performs nondestructive testing with the FWD on this pavement with the intention of determining its time to structural failure by rutting or cracking. The pavement is tested and the following results are obtained with a load of 9,000 lb:

Distance from Load (in.)	Deflection (mils)
0.0	17.20
12.0	11.50
24.0	7.42
36.0	4.97
48.0	3.39
60.0	2.34
72.0	1.63

Because the engineer has only limited data on the subgrade, he is unaware that the rigid layer exists and models the pavement as follows:

Asphalt Concrete
$h = 6$ in.
Granular Base
$h = 12$ in.
Subgrade
$h = 222$ in.
Rigid Layer
$h = \infty$

After using BISDEF to backcalculate the moduli for each layer, the following are obtained:

$$E_{\text{acp}} = 530,000 \text{ psi},$$

$$E_{\text{base}} = 20,173 \text{ psi},$$

$$E_{\text{subgr}} = 12,039 \text{ psi}.$$

The results look reasonable, but the engineer compares the measured versus the calculated deflections and finds the following deflections (absolute sum of percent error is 19.8 percent):

Deflection (mils)	
Measured	Calculated
17.20	16.80
11.50	11.90
7.42	7.47
4.97	4.81
3.39	3.26
2.34	2.32
1.63	1.71

The engineer concludes that this is a reasonable fit and proceeds to calculate the tensile strain at the bottom of the asphalt layer and the compressive strain at the top of the subgrade. The tensile and compressive strains were found to be 2.21×10^{-4} and -3.84×10^{-4} , respectively. In reality, the strains are 2.30×10^{-4} and -4.63×10^{-4} .

Using the Asphalt Institute Equations 1 and 2, the engineer predicts the pavement to fail by cracking after 1.7 million 18-kip equivalencies and by rutting after 2.7 million. In reality, the values are 1.6 and 1.2 million, respectively. Thus, he has predicted cracking accurately, but has underestimated by half the rate at which the pavement will rut.

If these modulus values are used to design an overlay to handle additional traffic, the design will be unconservative and will be subject to early failure.

Note that, in this example, the modular ratio of the rigid layer to the subgrade was only 10 and was sufficient to influence significantly the results of the analysis in a unconservative fashion. Additionally, the actual rigid layer modulus is only 100,000 psi, which is far below the value of 1,000,000 psi assumed during backcalculation.

CONCLUSIONS

From the results of this study, one can conclude the following regarding rigid layer depths when backcalculating pavement layer moduli from deflection data:

1. Theoretically, rigid layer depths are an important parameter in the process of backcalculating pavement layer moduli and estimating remaining life of pavement structures.

2. The accuracy with which rigid layer depths are estimated affects the quality of the backcalculated moduli values, especially when the rigid layer depth is half that assumed in the backcalculation process.

3. If the rigid layer is ignored completely or is assumed to be twice its actual depth and its stiffness is just ten times the layer above, the modulus values calculated for Layers 1 and 2 will in no way resemble their actual values.

4. The surface layers are most sensitive to errors caused by improperly assumed rigid layer depths. Under these conditions, the stiffnesses of the surface and subgrade layers (1 and 3) are overestimated, while the modulus of the base layer (2) is underestimated.

5. The remaining life of the pavement will be drastically overestimated, leading to unconservative overlay designs, when the rigid layer is half its assumed depth or is ignored in the analysis.

6. Poor basin fitting may not be a result of nonlinearity or time dependency of the system; it may be an indication of a rigid layer near the surface. In fact, it was found that when the ratio of the actual to assumed depth to the rigid layer was less than 0.3, it was impossible to match to basins using reasonable values of layer moduli.

RECOMMENDATIONS

The study results indicate that it is possible to fit deflection basins closely, even though the backcalculated layer moduli do not reflect their actual values. This suggests that deflection data taken with a FWD, Dynaflect, or Road Rater alone may be insufficient, particularly when difficulty is experienced in the basin fitting routine. Subsurface investigations may be required as a supplement to more accurately determine (a) layer thicknesses of the pavement structure, (b) approximate modular ratios of the individual layers with respect to each other, and (c) depth to rigid layers.

Currently, few types of nondestructive subsurface investigative equipment exist in a production mode to determine the above characteristics. However, several are in the development or research stages. Three methods currently in existence are Spectral Analysis of Surface Waves (SASW), cone penetrometers, and subsurface interface radar.

SASW

SASW can determine layer thicknesses and moduli and is especially good for determining depths to any rigid layer in the pavement structure (5). It is a simple test, can be done quickly, and requires little equipment. However, the data reduction is complicated and, at this time, can be done only on a mainframe computer. The process of obtaining moduli values is similar to backcalculating moduli from deflection

basins, in that it is iterative and requires a knowledgeable individual to obtain accurate answers. Researchers are now in the process of automating data collection and reduction for this technique.

Cone Penetrometers

Cone penetrometers have been around for decades and have been used in the area of foundation investigations for bridges and buildings. Only recently have they been used on pavement. Researchers have obtained reasonable correlations for pavement modulus values from cone penetrometer data (6). A profile of stiffness versus depth can be obtained from these devices as well as a host of other information. The test requires much more time to perform than deflection testing and involves a substantial amount of equipment. A limited number of points may be tested with this equipment.

Subsurface Interface Radar

Several engineering firms and highway agencies are using subsurface interface radar for pavement investigations. The test is fast, covers miles of pavement in short periods of time, and requires a modest amount of equipment and personnel to collect data. Thicknesses of the individual pavement layers can be obtained through this test technique; however, the test yields no information regarding their stiffness. The data analysis and reduction portion of the test is subjective and requires the services of a highly qualified technician or engineer. Currently, a specification (ASTM D 4748-87) exists for using radar to obtain thicknesses of bound pavement layers within ± 0.5 in. but is not applicable to depths greater than 20 in. from the surface of the pavement.

REFERENCES

1. American Association of State Highway and Transportation Officials. *AASHTO Guide for Design of Pavement Structures*. AASHTO, Washington, D.C., 1986.
2. Strategic Highway Research Program. *Focus*. SHRP, National Research Council, Washington, D.C., July 1988.
3. The Asphalt Institute. *Thickness Design—Asphalt Pavements for Highways and Streets*. Manual Series No. 1 (MS-1), The Asphalt Institute, College Park, Md., 1981.
4. The Asphalt Institute. *Research and Development of the Asphalt Institute's Thickness Design Manual (MS-1)*, 9th ed. Research Report No. 82-2, The Asphalt Institute, College Park, Md., 1982.
5. S. Nazarian, K. Stokoe II, R. C. Briggs, and R. Rogers. Determination of Pavement Layer Thicknesses and Moduli by SASW Method. In *Transportation Research Record 1196*, TRB, National Research Council, Washington, D.C., 1988, pp. 133–150.
6. K. Badu-Tweneboah, D. Bloomquist, B. Ruth, and W. Miley. CPT and DMT Testing of Highway Pavements in Florida. *Penetration Testing*. ISOPT-1, De Ruiter, 1988.

Publication of this paper sponsored by Committee on Strength and Deformation Characteristics of Pavements.

Heavy Vehicle Evaluation for Overload Permits

WALTER P. KILARESKE

Highway agencies often receive requests for permits to allow the movement of overloaded machinery, structures, and other commodities. Many highway departments issue permits up to a standard axle loading of approximately 27,000 lb; however, they do not have sufficient data to respond to requests for other loads and axle configurations. A study for the Pennsylvania Department of Transportation analyzed the expected pavement damage resulting from overloaded axle configurations, in particular, four- and five-axle configurations with loads up to 34,000 lb. A computer simulation approach was used to model both flexible and rigid pavements. Flexible pavements were analyzed with structural numbers of 2.92 and 4.82 representing a low and high structural capacity, respectively. Rigid pavement was analyzed as a 10-inch slab on 6 inches of crushed aggregate base. Calculated strains and deflections were compared to limiting tensile and vertical strains (flexible pavements) and stress ratios (rigid pavements). The remaining life of each pavement was evaluated. It was found that four- and five-axle configurations developed the same tensile stresses as the single- and tandem-axle configurations for a thin flexible pavement, but the strains were lower for the thick pavement cross section. The stress ratios for the rigid pavement for all axle loads and configurations were below 50 percent, which implies that an unlimited number of repetitions can be applied.

Highway agencies are often asked to issue permits to allow the movement of overloaded machinery, structural components, and other commodities. The movement of such commodities is vital to the economic health of the state and nation; on the other hand, it is necessary to ensure that permitted overloaded vehicles do not damage the pavement system. For example, the Pennsylvania Department of Transportation (PennDOT) currently issues permits for axle loadings up to 27,000 lb, but it does not have sufficient data to respond to requests for other loads and configurations.

The AASHO Road Test results showed that pavement damage is a function of many variables, including axle load and axle configuration. The 18-kip equivalent single-axle load (ESAL) concept was developed to allow various axles and loads to be combined into a single design axle. The 18-kip ESAL tables for single- and tandem-axle configurations have been used by highway designers for the past 25 years without significant changes. The recent AASHTO Design Guide provides 18-kip ESAL for triple axles; however, no information is available for 18-kip ESAL for multiple-axle configurations, such as four- and five-axle units. Because many of the heavy axle loads in Pennsylvania are on four- and five-axle units, it was decided to study the potential damage effect of these configurations.

The objective of the study was to evaluate, by means of computer simulation, the pavement damage resulting from overloaded four- and five-axle configurations.

The evaluation was conducted for one rigid pavement cross section and two flexible pavement cross sections. Stresses, strains, and deflections were calculated for four- and five-axle configurations, as well as for standard single- and tandem-axle configurations. Axle loads from 18,000 to 34,000 lb were evaluated.

PAVEMENT MODELING

Computer Simulation

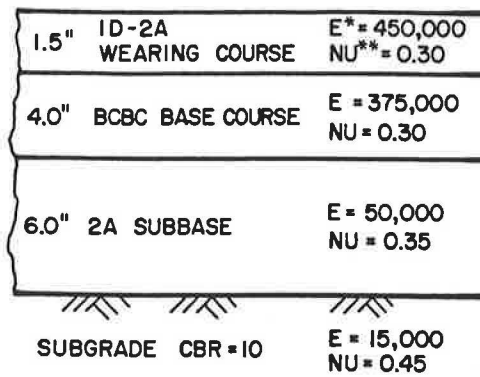
There are basically two ways to evaluate pavement damage: field experiment and computer modeling. The AASHO Road Test is the classic example of a full-scale field experiment designed to study axle loading and pavement damage. The field approach is the best evaluation method; however, it is extremely expensive and time-consuming. Computer modeling, on the other hand, is not as realistic as full-scale field work, but it is much less expensive and can provide quick responses to a complex question (such as the amount of pavement damage caused by overloaded vehicles).

A computer simulation approach was used in this study, because it would provide answers in a timely manner. The flexible pavement was modeled as an elastic-layered system. The BISAR computer program was used to calculate strains and deflections under the selected loadings (1). The rigid pavement systems was modeled as a slab on a Winkler foundation (liquid). The JSLAB computer program was used to calculate stresses for the rigid pavement system (2).

Pavement Cross Sections

Both a thin and thick flexible pavement cross section were evaluated in the study. The layer depth and engineering properties are shown in Figures 1 and 2. The thin pavement section represented a system with a structural number (SN) of 2.92. The thicker section had an SN of 4.82. These two sections were selected because the thin pavement could represent a typical low-volume road, while the thicker section would represent a primary or arterial-type facility.

A single rigid pavement cross section, typical of that found in Pennsylvania, was used in this study (see Figure 3). For computer modeling purposes, the slab was assumed to be 60 ft long. Contraction joints had load transfer devices consisting



*E=MODULUS OF ELASTICITY
**NU=POISSON'S RATIO

FIGURE 1 Thin flexible pavement cross section used in analysis.

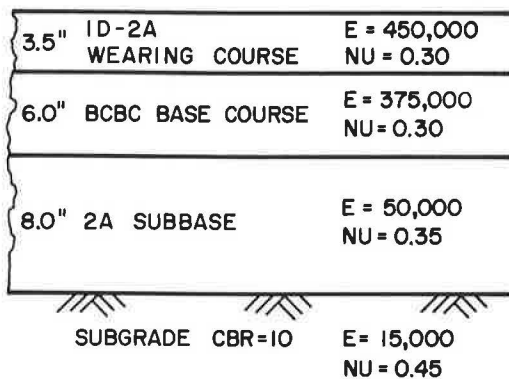


FIGURE 2 Thick flexible pavement cross section used in analysis.

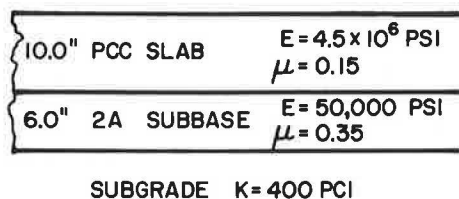


FIGURE 3 Rigid pavement cross section used in analysis.

of twelve 1¼-in.-diameter dowel bars. The slab was 12 ft wide. A 6-in. base consisting of dense-graded material was placed under the slab.

Tire and Axle Loadings

Four axle loadings were modeled for the analysis. The axle loadings are shown in Figures 4–7. The truck loadings represent single-, tandem-, four-, and five-axle configurations. The single and tandem axles were included because they rep-

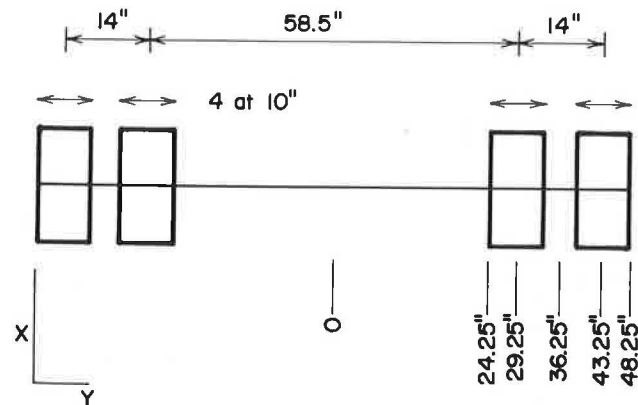


FIGURE 4 Single-axle loading configuration.

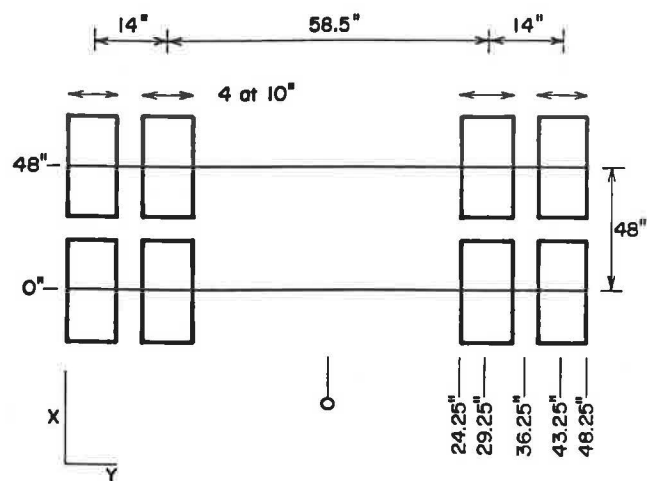


FIGURE 5 Tandem-axle loading configuration.

represent the typical axle configurations found on Pennsylvania highways. Also, the single and tandem axles represent the type of axle for which there are 18-kip ESAL AASHTO tables. The four- and five-axle configurations are the axle types used to haul heavy, overloaded materials.

For the analysis, each axle of the configuration was subjected to incremental axle loadings of 18,000, 20,000, 22,400, 24,000, 26,000, 27,000, 28,000, 29,000, 30,000, 31,000, 32,000, 33,000, and 34,000 lb. The 18,000-lb and 22,400-lb loadings were selected because the 18,000-lb loading represents the typical design axle load, while the 22,400-lb loading is the legal single-axle load in Pennsylvania. The other axle loads were incremented to provide a spread of loads that ranged up to 34,000 lb.

For purposes of this study, it should be noted that the selected axle loading was placed on each axle of the configurations. For example, a 26,000-lb axle load means that the gross tandem load was 52,000 lb, the four-axle load gross was 104,000 lb, and the five-axle load gross was 130,000 lb.

The simulated tires used in the study were assumed to have a pressure of 100 psi. As the load increased on the axle, the contact area changed because the pressure was held constant. For each load, a footprint area and a comparable circular area (radius) were calculated.

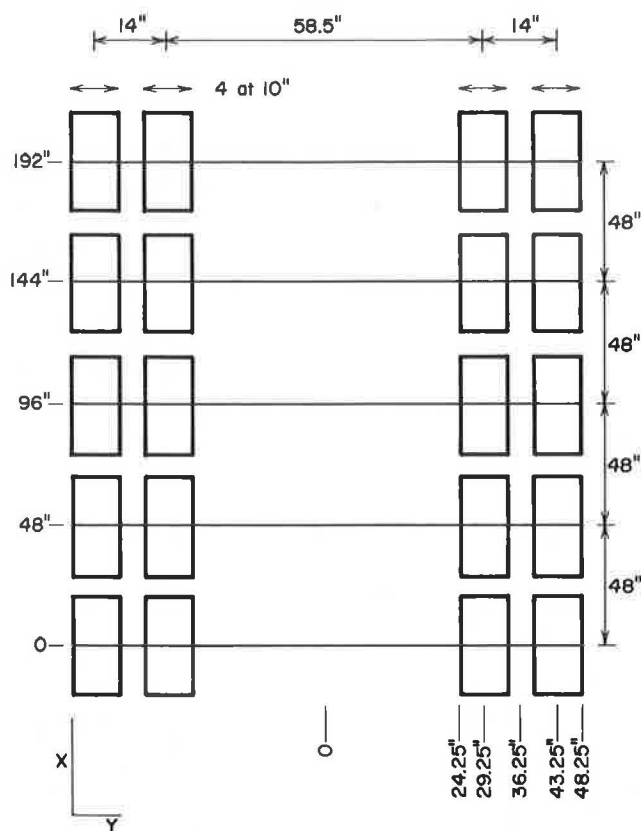


FIGURE 6 Four-axle loading configuration.

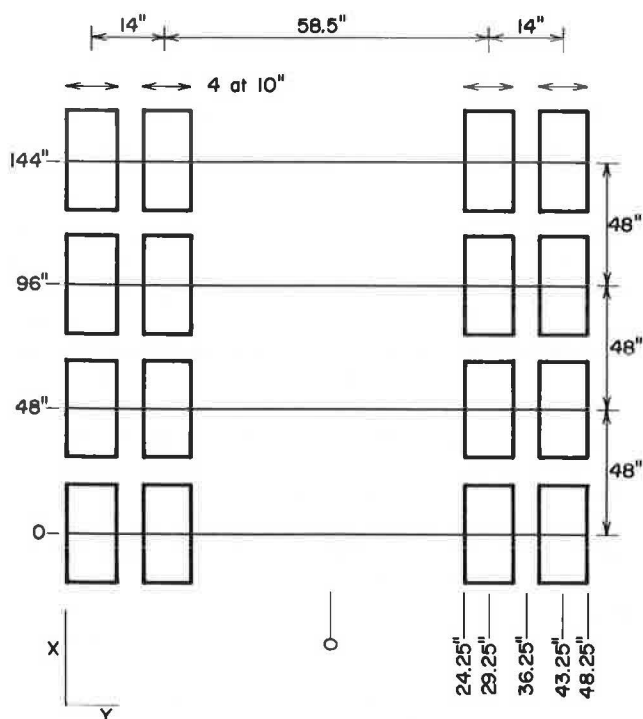


FIGURE 7 Five-axle loading configuration.

Location of Critical Strains, Stresses, and Deflections

Both the elastic layer program, BISAR, and the finite element program, JSLAB, can calculate pavement response at any point in the pavement system. This capability is a useful feature of the programs; however, it is extremely time-consuming and costly to calculate responses at multiple points. Consequently, an analysis was done to determine the location, within the pavement system, where maximum strains occur.

Several points within the pavement system were chosen to determine the location of the maximum tensile strain caused by the axle load (18,000 lb). An example of the study points for the four-axle configurations is shown in Figure 8, and the calculated strains for all axle configurations are presented in Table 1. As shown, the maximum strain occurs between the dual tires in all cases. The most critical axle for multiple-axle configurations was found to be the trailing axle. Consequently, point Number 3 was selected as the study location for all configurations. The depths of the critical strains are shown in Figure 9.

It has been shown that the critical stress location for jointed rigid pavements is at the free edge and/or at the joint (3). Consequently, the stresses along the edge of the concrete slab were evaluated. Maximum values were selected and used in the evaluation of the maximum stress ratio.

Half-Axle Modeling for Four- and Five-Axle Loads

The BISAR program can be programmed for up to 10 loads, but the four- and five-axle configurations have 16 and 20 loads, respectively. Consequently, a superposition technique was evaluated to determine the strains and deflections for each case. Strains and deflections were compared using the superposition technique and the critical locations under half loads. Tables 2 through 4 provide comparisons of deflection,

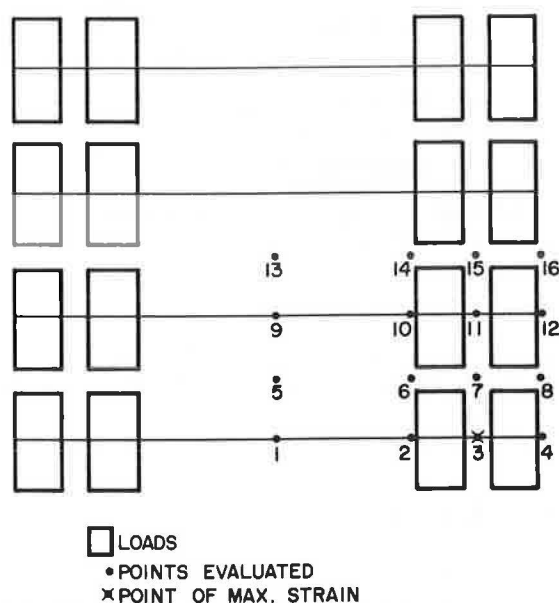


FIGURE 8 Location of maximum strain for four-axle configuration, flexible pavement.

TABLE 1 LOCATION OF MAXIMUM STRAINS FOR FLEXIBLE PAVEMENTS

<u>Single-Axle Configurations</u>	
1	0.173 E-04
2	0.130 E-03
3*(between tires)	0.168 E-03
4	0.129 E-03
<u>Tandem-Axle Configurations</u>	
1	0.127 E-04
2	0.123 E-03
3*(between tires)	0.160 E-03
4	0.123 E-03
5	compressive
6	0.128 E-04
7	0.295 E-04
8	0.162 E-04
<u>Four-Axle Configurations</u>	
1	0.584 E-05
2	0.122 E-03
3*(between tires)	0.159 E-03
4	0.122 E-03
5	compressive
6	0.181 E-04
7	0.327 E-04
8	0.181 E-04
9	0.361 E-04
10	0.116 E-04
11	0.152 E-04
12	0.116 E-04
13	compressive
14	0.184 E-04
15	0.331 E-04
16	0.184 E-04
<u>Five-Axle Configurations</u>	
1	0.582 E-05
2	0.122 E-03
3*(between tires)	0.159 E-03
4	0.122 E-03
5	0.352 E-05
6	0.116 E-03
7	0.152 E-03
8	0.116 E-03
9	0.319 E-05
10	0.115 E-03
11	0.151 E-03
12	0.115 E-03

*maximum strain

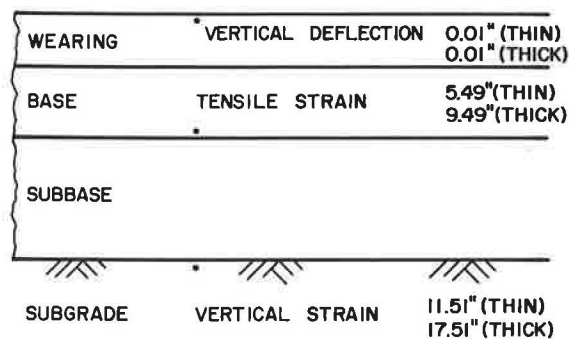


FIGURE 9 Maximum strain location depths for thin and thick flexible pavements.

TABLE 2 SURFACE DEFLECTION COMPARISON OF SUPERPOSITION AND CRITICAL LOCATION DATA FOR FOUR AXLES ON THIN PAVEMENT

Axle Load	Surface Deflection Superposition	Critical Location
18,000	0.2614 E-01	0.200 E-01
20,000	0.2902 E-01	0.222 E-01
22,400	0.3244 E-01	0.248 E-01
24,000	0.3478 E-01	0.266 E-01
26,000	0.3767 E-01	0.288 E-01
27,000	0.3911 E-01	0.299 E-01
28,000	0.4055 E-01	0.310 E-01
29,000	0.4199 E-01	0.321 E-01
30,000	0.4240 E-01	0.332 E-01
31,000	0.4490 E-01	0.343 E-01
32,000	0.4630 E-01	0.354 E-01
33,000	0.4780 E-01	0.365 E-01
34,000	0.4920 E-01	0.376 E-01

For four axles on the thin pavement section.

tensile strain, and vertical strain; it can be seen that the critical location technique provided results that compare with the superposition technique. Consequently, the critical location technique was used to model the four- and five-axle configuration.

Analysis of Flexible Pavement Strains and Deflections

As was stated in previous sections, the BISAR program was used to calculate surface deflections, tensile strains, and vertical strains in the flexible pavement system. The tensile strains at the bottom of the stabilized base layer are associated with fatigue cracking of the asphalt concrete. On the basis of a mechanistic analysis approach, the number of load repetitions to cracking of the asphalt is a function of the magnitude of the tensile strain. On the other hand, the vertical strain in the subgrade is associated with the rutting of the pavement.

TABLE 3 TENSILE STRAIN COMPARISON OF SUPERPOSITION AND CRITICAL LOCATION DATA FOR FOUR AXLES ON THIN PAVEMENT

Axle Load	Tensile Strain Superposition	Critical Location
18,000	.1588 E-03	.159 E-03
20,000	.1748 E-03	.175 E-03
22,400	.1937 E-03	.194 E-03
24,000	.2067 E-03	.207 E-03
26,000	.2223 E-03	.222 E-03
27,000	.2287 E-03	.229 E-03
28,000	.2367 E-03	.237 E-03
29,000	.2437 E-03	.244 E-03
30,000	.2507 E-03	.251 E-03
31,000	.2576 E-03	.258 E-03
32,000	.2646 E-03	.265 E-03
33,000	.2726 E-03	.273 E-03
34,000	.2786 E-03	.279 E-03

For four axles on the thin pavement section.

TABLE 4 VERTICAL STRAIN COMPARISON OF SUPERPOSITION AND CRITICAL LOCATION DATA FOR FOUR AXLES ON THIN PAVEMENT

Axle Load	Vertical Deflection Superposition	Critical Location
18,000	.3920 E-03	.400 E-03
20,000	.4343 E-03	.443 E-03
22,400	.4852 E-03	.495 E-03
24,000	.5185 E-03	.529 E-03
26,000	.5605 E-03	.572 E-03
27,000	.5811 E-03	.593 E-03
28,000	.6017 E-03	.614 E-03
29,000	.6232 E-03	.636 E-03
30,000	.6438 E-03	.657 E-03
31,000	.6643 E-03	.678 E-03
32,000	.6849 E-03	.699 E-03
33,000	.7055 E-03	.720 E-03
34,000	.7250 E-03	.740 E-03

For four axles on the thin pavement section.

If the vertical strain is too high, the soil will shear, and plastic deformation will occur. High surface deflections are usually associated with shortened pavement life.

Examples of the calculated surface deflections, tensile strains, and vertical strains are presented in Tables 5 and 6. The data are for the four-axle configurations and both thin and thick flexible pavements. All of the data were plotted and are shown in Figures 10 through 12.

TABLE 5 FOUR-AXLE DATA FOR THIN PAVEMENT AT THE POINT (0, 36.25)

Axle Load (lb)	Surface Deflection at 0.01 in	Tensile Strain at 5.49 in	Vertical Strain (C) at 11.51 in
18,000	0.200 E-01	0.159 E-03	0.400 E-03
20,000	0.222 E-01	0.175 E-03	0.443 E-03
22,400	0.248 E-01	0.194 E-03	0.495 E-03
24,000	0.266 E-01	0.207 E-03	0.529 E-03
26,000	0.288 E-01	0.222 E-03	0.572 E-03
27,000	0.299 E-01	0.229 E-03	0.593 E-03
28,000	0.310 E-01	0.237 E-03	0.614 E-03
29,000	0.321 E-01	0.244 E-03	0.636 E-03
30,000	0.332 E-01	0.251 E-03	0.657 E-03
31,000	0.343 E-01	0.258 E-03	0.678 E-03
32,000	0.354 E-01	0.265 E-03	0.699 E-03
33,000	0.365 E-01	0.273 E-03	0.720 E-03
34,000	0.376 E-01	0.279 E-03	0.740 E-03

TABLE 6 FOUR-AXLE DATA FOR THICK PAVEMENT AT THE POINT (0, 36.25)

Axle Load (lb)	Surface Deflection at 0.01 in	Tensile Strain at 9.49 in	Vertical Strain (C) at 17.51 in
18,000	0.159 E-01	0.874 E-04	0.210 E-03
20,000	0.177 E-01	0.963 E-04	0.233 E-03
22,400	0.198 E-01	0.107 E-03	0.261 E-03
24,000	0.212 E-01	0.114 E-03	0.279 E-03
26,000	0.230 E-01	0.122 E-03	0.301 E-03
27,000	0.239 E-01	0.126 E-03	0.313 E-03
28,000	0.248 E-01	0.131 E-03	0.324 E-03
29,000	0.256 E-01	0.135 E-03	0.335 E-03
30,000	0.265 E-01	0.139 E-03	0.346 E-03
31,000	0.274 E-01	0.143 E-03	0.358 E-03
32,000	0.283 E-01	0.147 E-03	0.369 E-03
33,000	0.292 E-01	0.151 E-03	0.380 E-03
34,000	0.301 E-01	0.155 E-03	0.391 E-03

Also shown on each plot is a limiting deflection or strain. The limiting deflections and strains were developed as a result of test track research at the Pennsylvania Transportation Research Facility (4). The project demonstrated that Class II surface cracking correlated with a surface deflection of 0.020 in. The corresponding tensile strain at the bottom of the base was 120 microstrains, and the vertical strain at the top of the subgrade was 450 microstrains. The applied 18-kip ESALs were correlated with the data, and it was found that fatigue cracking and 0.25-in. rutting occurred at approximately 1 million 18-kip ESAL loads. Therefore, these limits were selected for this study.

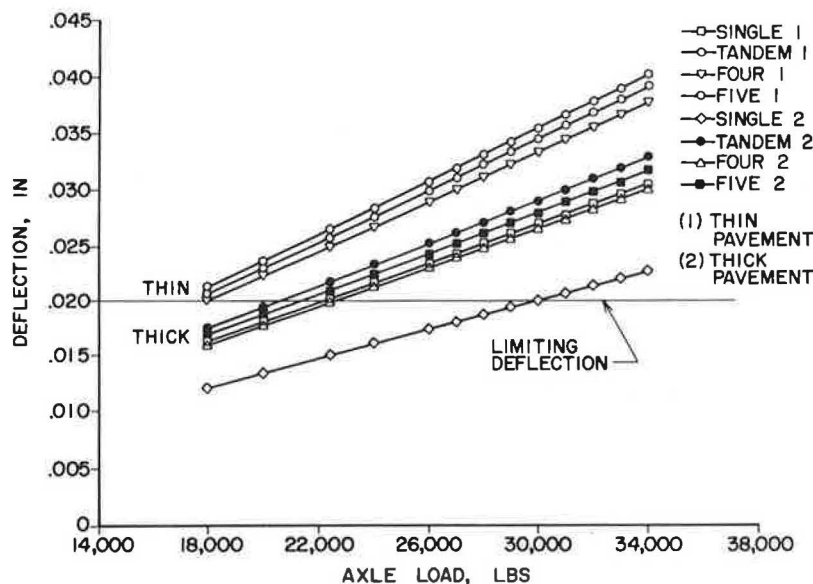


FIGURE 10 Surface deflection versus axle load for flexible pavements.

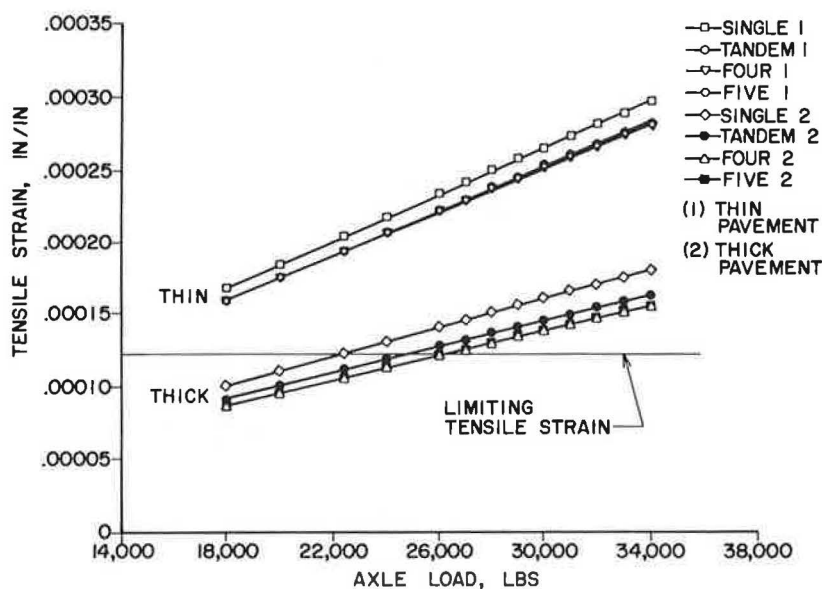


FIGURE 11 Tensile strain at the bottom of the base layer versus axle load for flexible pavements.

As can be seen in Figure 10, the thin pavement had the highest computer-predicted deflections, followed by lower deflections with the thick pavement. The lowest deflections occurred with the single-axle load on a thick pavement. Except for the single-axle thick pavement case, the four- and five-axle configurations created approximately the same deflections for both the thin and thick pavement systems.

Pavement deflections, tensile strain, and the vertical strain can all serve as criteria for evaluating pavement performance. The tensile strains at the bottom of the base, as shown in Figure 11, are grouped in two distinct lines: thick pavement and thin pavement. In both cases, the single-axle configurations produced higher strains than the tandem-, four-, and five-axle configurations. In fact, the tandem-, four-, and five-

axle configuration lines overlapped each other. This implies that gross loads of a 40-kip tandem, 80-kip four axle, and 100-kip five axle all produce approximately the same tensile strain at the bottom of the base layer, while a 20-kip single axle produces a slightly higher tensile strain.

The same is true for the vertical strains, as shown in Figure 12. Again there are two distinct lines (one for a thin pavement and one for a thick pavement). All of the axle configurations, when loaded to the same axle weight, produce the same vertical strain in the subgrade.

With respect to the limiting criteria lines, Figure 11 shows that all of the loads on a thin pavement section exceeded the limiting criteria. Loadings greater than 26 kips on the thick pavements exceeded the limiting criteria. The vertical strains

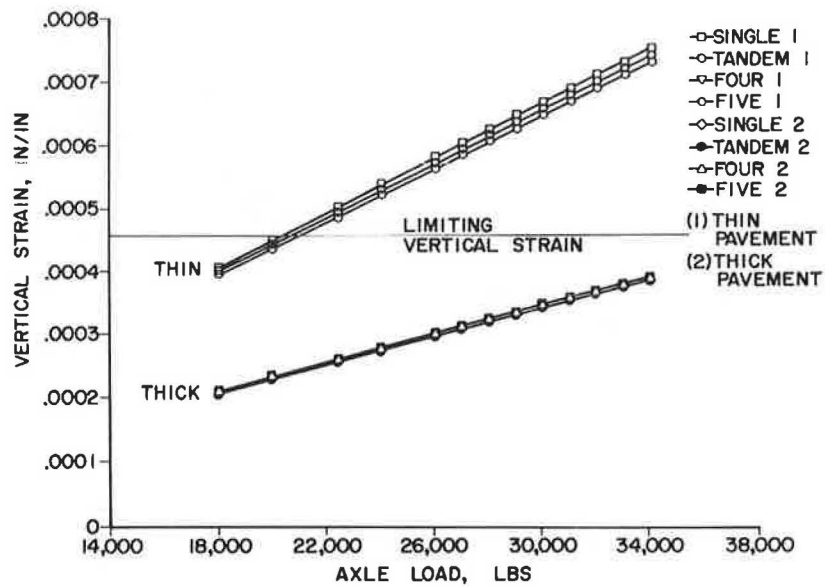


FIGURE 12 Vertical strain at the top of the subgrade versus axle load for flexible pavements.

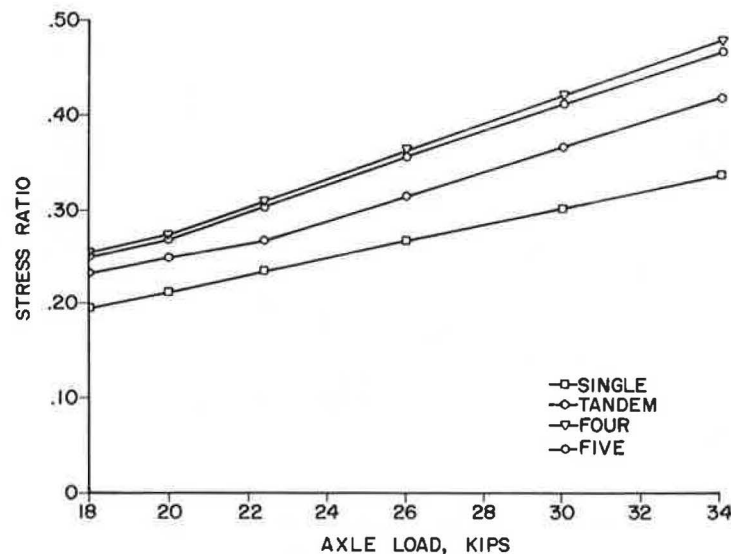


FIGURE 13 Stress ratios versus axle load for Portland Cement Concrete (PCC) pavement.

for thick pavements, as seen in Figure 12, were below the limit, while loads of 20 kips or greater exceeded the criteria for the thin pavements.

The data that are plotted in Figures 11 and 12 are significant with respect to the study. These data show that four- and five-axle configurations created strains of a similar magnitude as the strains under a tandem axle. In all cases, the single-axle configuration created higher strains than any of the other axle configurations.

Analysis of Rigid Pavement Stress Ratio and Bearing Stress

A rigid pavement usually fails because of cracking and/or joint-related problems. Consequently, the analysis of a rigid

pavement system is much different from that of a flexible pavement system. Rigid pavement cracking can occur when the tensile stress (from loading, temperature, etc.) exceeds the modulus of rupture. If the stress ratio is kept under 50 percent, the concrete is expected to have infinite life; however, as the stress ratio exceeds 50 percent, the number of load cycles to failure decreases rapidly.

Joint deterioration, such as faulting, has been associated with excess bearing stress in the dowel/concrete area. As the bearing stress increases, the surrounding concrete deteriorates, and the life of the joint decreases due to faulting and pumping.

The edge stresses for each axle configuration and loading were calculated with the JSLAB finite element program. Maximum stresses were selected for each case, and a stress ratio

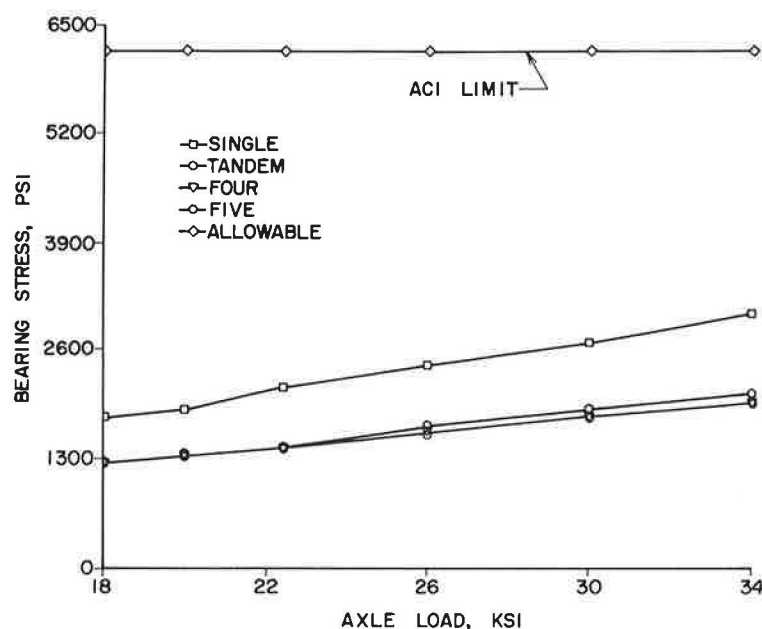


FIGURE 14 Bearing stress versus axle load for PCC pavement.

was calculated assuming a modulus of rupture of 500 psi. The stress ratios are presented in Figure 13. As can be seen, the four- and five-axle configurations developed the highest stress ratios, while the single-axle configuration developed the lowest values. All of the stress ratios, however, were less than 50 percent. Consequently, from a theoretical standpoint, the axle loads for all configurations studied never generate a stress large enough to crack the concrete.

The bearing stresses were also plotted and are shown in Figure 14. In this figure, it can be seen that the single-axle configuration creates the highest bearing stress, while the tandem-, four-, and five-axle configurations have lower values. The ACI bearing stress limit is also plotted on the figure. Again, from a theoretical viewpoint, the bearing stress is well below the limit for all load ranges.

PAVEMENT DAMAGE AND REMAINING LIFE

Rigid Pavement System Remaining Life Analysis

The objective of the study was to determine (theoretical approach) how much damage will be done to a pavement by an overloaded four- or five-axle configuration. On the basis of the calculated stress ratios and the calculated bearing stresses presented in the previous section, it can be concluded that these configurations do not significantly affect the rigid pavement systems found in Pennsylvania. The four- and five-axle configurations (at 32 kips) develop a stress ratio that is approximately 15 percent higher than the stress ratio for a tandem-axle load. For all cases studied, the ratio never exceeded the 50-percent limit. Therefore, the four- and five-axle load configurations should not reduce the service life of the rigid pavement any more rapidly than a tandem axle at the same load range.

Flexible Pavement System Remaining Life Analysis

The damage effect and the remaining life analysis for the flexible systems are different than for a rigid pavement. From a mechanistic approach, a relationship exists between tensile strains at the bottom of the base layer and the number of loads to cracking. An example of this is shown in Figure 15. The lines represent results from various researchers, while the line marked "Bituminous Concrete" is for data collected at the Pennsylvania Transportation Research Facility (PTRF).

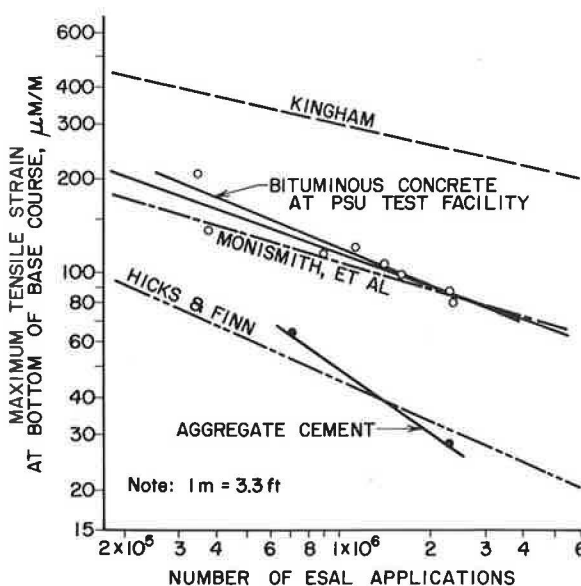


FIGURE 15 Tensile strain at the bottom of the asphalt layer versus total number of ESAL applications to cracking.

TABLE 7 NUMBER OF EQUIVALENT AXLE LOAD APPLICATIONS UNTIL CRACKING, SINGLE AXLE

Axle Load (kips)	Tensile Strain (10^{-6})	No. of EAL to Cracking (10^6)
<u>Thin Pavement</u>		
18	168	.370
20	185	.285
22.4	205	.215
24	218	.195
26	234	.150
27	242	.135
28	250	.125
29	258	.115
30	265	.105
31	273	.100
32	281	
33	288	
34	296	
<u>Thick Pavement</u>		
18	101	1.500
20	111	1.150
22.4	123	.880
24	131	.740
26	141	.600
27	146	.540
28	151	.500
29	156	.450
30	161	.410
31	166	.380
32	170	.360
33	175	.330
34	180	.300

TABLE 8 NUMBER OF EQUIVALENT AXLE LOAD APPLICATIONS UNTIL CRACKING, FOUR AXLES

Axle Load (kips)	Tensile Strain (10^{-6})	No. of EAL to Cracking (10^6)
<u>Thin Pavement</u>		
18	159	.430
20	175	.330
22.4	194	.250
24	207	.210
26	222	.170
27	229	.155
28	237	.140
29	244	.135
30	251	.125
31	258	.115
32	265	.105
33	273	.100
34	279	
<u>Thick Pavement</u>		
18	87	2.250
20	96	1.700
22.4	107	1.250
24	114	1.050
26	122	.880
27	126	.800
28	131	.720
29	135	.680
30	139	.620
31	143	.580
32	147	.540
33	151	.490
34	155	.460

The PTRF data were derived from full-scale truck traffic loadings on different flexible pavement cross sections. The strains in Figure 15 represent levels at which AASHTO Class II cracking took place.

The tensile strains for each axle configuration and associated loads were used with Figure 15 to select the number of 18-kip ESALs to cracking. Examples of the data are listed in Tables 7 and 8 with all data plotted in Figure 16. As can be seen in the figure, there are two distinct levels, one for thin pavements and one for thick pavements. All of the axle configurations overlap for the thin pavements; consequently, no significant difference exists among any of the axle configurations. Also with respect to the thin pavements, there is almost no difference in remaining life between a 26-kip axle

load and a 32-kip axle load. Both produce a pavement life of approximately 100,000 repetitions.

However, a more distinct difference exists in pavement life with the thicker flexible pavements. Figure 16 shows that a single- and tandem-axle load, at the same axle weight, will produce shorter fatigue life. For example, a single-axle load of 22 kips will cause cracking after 880,000 passes. A tandem axle causes cracking after 1.15 million passes. The four- and five axle configurations cause cracking after 1.25 million passes.

Approaching this from another perspective, Figure 16 can be used to compare the loss of remaining life for each axle configuration. For example, a four-axle configuration at a 27-kip load will cause cracking after 800,000 ESAL passes, while a vehicle at a 32-kip load will cause cracking after 540,000

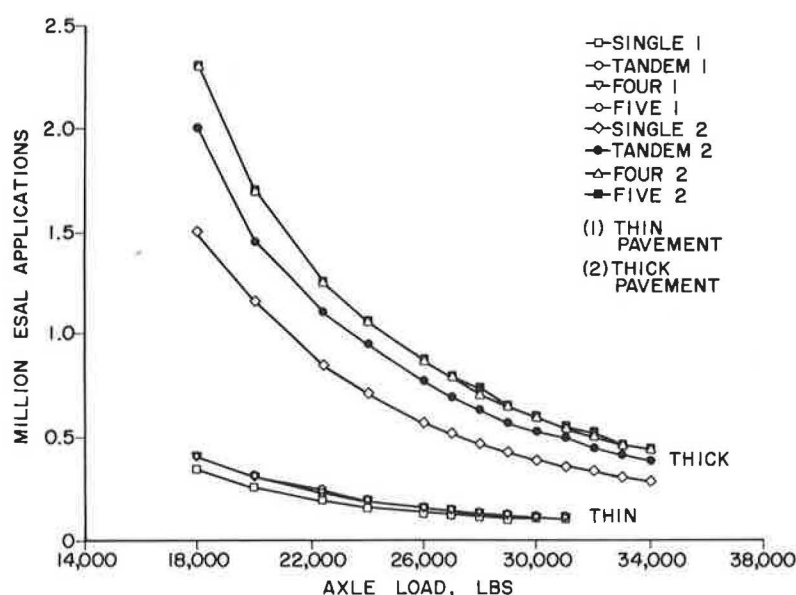


FIGURE 16 Number of ESAL applications until cracking for various axle loads.

passes. The increase in axle load will decrease the pavement life by 260,000 axle passes, or 32 percent.

DISCUSSION OF RESULTS

The analysis of the rigid pavement system showed that, regardless of the axle loading weight and type of axle configuration studied, there should be no detrimental effect on pavement life. Because the stress ratio for all loadings was below 50 percent, there should be no loss of service life. All bearing stress values were also below limiting values; consequently, there should be no adverse joint deterioration.

The analysis of the thin flexible pavements revealed that all loadings studied, regardless of weight and configuration, can have a significant effect on the thin flexible pavements. Axle loadings of from 27,000 to 32,000 lb, on all axle configurations, have approximately the same pavement-damage effect on the flexible pavements. Each load or configuration causes cracking after 100,000 axle passes.

With respect to the thicker flexible pavements, the single- and tandem-axle loads had a more severe effect on the pavement than equally loaded four- and five-axle configurations. A single configuration loaded at 22,400 lb will crack a pavement after 880,000 passes, while a four-axle configuration loaded to 89,600 lb will crack the pavement after 1.25 million passes. As can be seen in Figure 16, a single axle loaded at 22,400 lb and a four- and five-axle configuration loaded at 26,500 lb per axle (106,000 and 132,500 lb, respectively) require the same number of passes to develop similar cracking. A 26,500-lb, single-axle and a 32,000-lb, four- or five-axle load also have about the same damage effect.

It should be pointed out that the data presented in Figures 11 and 12 are for specific axle loads, when, in fact, the actual traffic stream consists of mixed traffic. Considering that the number of overloaded vehicles with permits constitutes a small percentage of the traffic spectrum, it is doubtful that four- and five-axle configurations will have any significant effect on

pavement damage for rigid pavements and thick flexible pavements. There should be some concern, however, for thin flexible pavements and for those highways where a substantial number of heavy axle loads accumulate over a short time.

CONCLUSIONS

The following conclusions are based on the theoretical study conducted with computer modeling.

- The stress ratios for a 10-in. rigid pavement system (typical of Pennsylvania), for all axle loadings and configurations studied, were below the 50-percent limit.
- The bearing stresses for a 10-in. rigid pavement system, for all axle loadings and configurations studied, were below the recommended ACI limit.
- The four- and five-axle configurations developed the same tensile strains as the single- and tandem-axle configurations (at each load level) for a thin flexible pavement (SN = 2.92).
- The four- and five-axle configurations developed lower tensile strains than the single- and tandem-axle configurations (at each load level) for a thick flexible pavement (SN = 4.82).
- The four- and five-axle configurations for a thin flexible pavement (SN = 2.92) had the same number of axle loads to failure as the single- and tandem-axle loads (at all load levels).
- On the basis of strain criteria, the four- and five-axle configurations on a thick flexible pavement (SN = 4.82) required approximately 50 percent more equivalent-axle-load applications to develop the same amount of cracking as was developed by a single-axle configuration.

ACKNOWLEDGMENTS

This research project was sponsored by the Pennsylvania Department of Transportation. Wade Gramling and Dennis

Morian served as technical representatives for PennDOT. The staff at the Pennsylvania Transportation Institute are acknowledged for their assistance with the report preparation. T. Ozbeki and D. Seneca assisted with the BISAR and JSLAB computer analyses.

REFERENCES

1. Royal Dutch/Shell Laboratories. *Computer Program: Layered System under Normal and Tangential Surface Loads*. BISAR User's Manual, The Hague, 1972.
2. S. D. Tayabji and B. E. Colley. Improved Rigid Pavement Joints. In *Transportation Research Record 930*, TRB, National Research Council, Washington, D.C., 1983, pp. 69–78.
3. S. D. Tayabji. Optimal Performance at Concrete Pavement Joints. *Proc., 3rd International Conference on Concrete Pavement Design and Rehabilitation*. Purdue University, West Lafayette, Ind., April 1985.
4. M. C. Wang, S. A. Kutz, W. P. Kilareski, and T. D. Larson. *Structural Coefficients of Stabilized Base Course Materials*. Research Project 75-2. Pennsylvania Department of Transportation, Harrisburg, 1979.

Publication of this paper sponsored by Committee on Strength and Deformation Characteristics of Pavements.

Development of a Rational Thickness Design Method for Rigid Pavements

CHUNG-LUNG WU AND MANG TIA

A computer program, MEDCONP (Mechanistic Design of Concrete Pavement) was developed to design and evaluate jointed concrete pavements. This procedure uses a mechanistic approach and considers important factors (such as the thermal gradient in the concrete slab and the daily and hourly traffic load distribution) that have not been considered in the past. Other design factors considered include the slab length, elastic modulus, flexural strength of concrete, subgrade modulus, traffic growth rate, proportioning of traffic in multiple lanes, and design life. Fatigue theory and Miner's rule are used to determine required slab thickness for designing a new pavement and evaluating the structural adequacy of an existing pavement. A design example is also given in this paper to evaluate the suitability of the design procedure used in the MEDCONP program.

Concrete pavements in Florida have shown widely different performance. Some have performed extremely well and have served beyond their design service life. Some have shown severe signs of distress and failure prematurely. When considering the wide variation of the performance of concrete pavement and the fact that most of the pavements were designed in accordance with the AASHTO Design Guide (1), it becomes apparent that the design procedures must be reassessed.

In the two most widely used design procedures, AASHTO Design Guide and the Portland Cement Association (PCA) thickness design method (2), the effects of temperature variations in the pavement slab have not been taken into direct consideration. However, in reality, the temperature variations in a concrete slab can greatly affect the structural response of a pavement. During the day, the slab tends to curl up at the interior due to a positive temperature differential in the slab (the top of the slab is warmer than the bottom). During the night, the slab tends to curl up at the edges and joints due to a negative temperature differential.

When loads are applied to the slab during these curling conditions, the maximum stresses in the slab could be substantially higher than when the slab is fully supported by the subgrade. The damages to the slab caused by these critical thermal load-induced stresses could be much higher than those under full subgrade support conditions. Ignoring the effects of temperature variation on the response of concrete pavement could result in an underdesign of the pavement.

Because of the need to incorporate the effects of temperature variations in a pavement slab-in design, a computer program, MEDCONP (Mechanistic Design of Concrete Pavement), was developed. The program contains two parts, the program itself and a data base. The program can be used to design a jointed concrete pavement and to estimate the

remaining service life of an existing pavement using a mechanistic approach. In addition to the design factors used in the conventional design procedures, such as the AASHTO guide and the PCA method, the effects of temperature variation on the concrete pavement response are also considered in this procedure. The program first calculates the maximum stress in the slab caused by each combination of thermal and load condition for a given set of pavement parameters. The fatigue theory and Miner's rule are then used to determine the number of applications of load to failure for each load level and to determine the total damage to the pavement. These results are then used to determine the required slab thickness for the design of a new pavement or the remaining service life of an existing pavement, using an interactive procedure.

The data base stores the theoretical maximum stresses caused by different thermal load conditions for different combinations of pavement parameters and is used by the MEDCONP program to compute the maximum thermal load-induced stresses in the slab for each given condition. The analytical results stored in the data base were computed by a finite-element computer program, FEACONS IV (3,4).

DEVELOPMENT OF THE DATA BASE

Modeling Concrete Pavement

The FEACONS (Finite Element Analysis of Concrete Slabs) program, Version IV, was developed at the University of Florida and used to compute the analytical results stored in the data base. A detailed description of the program can be found in Tia et al. (3,4). A brief description of the model used is given in this section.

A jointed concrete pavement is modeled as a three-slab system as shown in Figure 1. Because the analysis of the response of a concrete pavement generally involves the computation of deflection and stresses on a slab (which is affected mainly by its two adjacent slabs), it is usually adequate to model a concrete pavement as a three-slab system. A concrete slab is modeled as an assemblage of rectangular plate bending elements with three degrees of freedom at each node. Either a homogeneous slab or a composite slab consisting of two layers bonded together can be modeled.

The subgrade is modeled as a liquid or Winkler foundation, which is modeled by a series of vertical springs at the nodes. Load transfers across the joints between two adjoining slabs are modeled by shear (or linear) and torsional springs connecting the slabs at the nodes of the elements along the joint. Frictional effects at the edges are modeled by shear springs at the nodes along the edges.

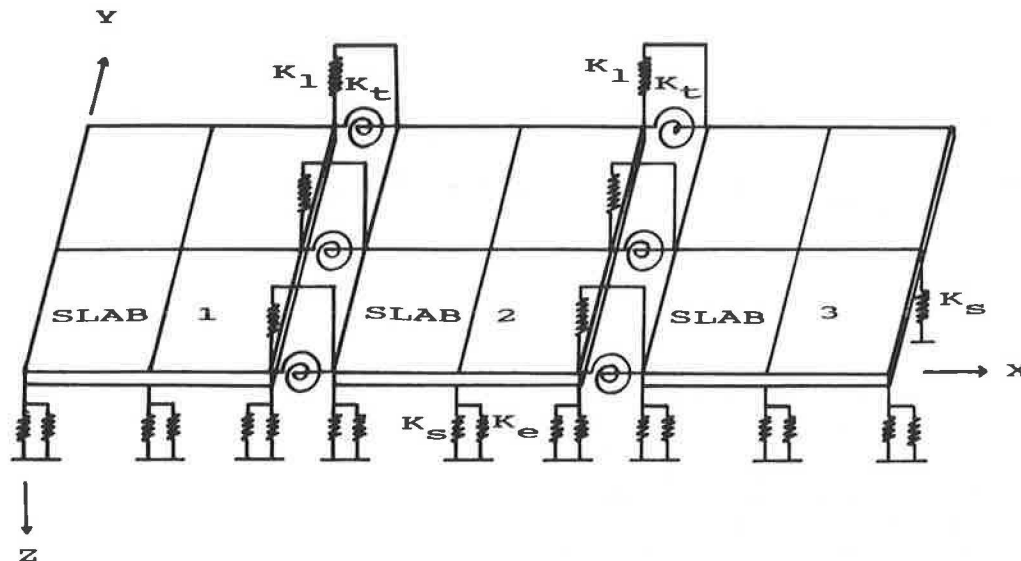


FIGURE 1 Finite element modeling of a three-slab pavement system.

When a temperature differential in the slab is considered, the temperature is assumed to vary linearly from the top to the bottom of the slab. The concrete is modeled as linearly elastic and isotropic.

The program uses an incremental computational procedure. The force vectors due to the weight of the slab, thermal gradients, and applied loads are applied in increments. At the end of each load increment, the stiffness matrix of the system is adjusted according to the new subgrade support condition (3,4).

MEDCONP Data Base

The theoretical maximum stresses in a concrete slab caused by the combinations of different single axle loads and temperature differentials of pavements with different dimensions and material properties were computed. The pavement parameters used to generate the data base include the slab length, slab thickness, subgrade stiffness, and concrete modulus of elasticity.

In the data base, the slab length varies from 12 ft (3.7 m) to 24 ft (7.3 m) and the slab thickness ranges from 6 in. (15.2 cm) to 13 in. (33.0 cm). The subgrade stiffness varies between 100 pci (27.2 MN/m³) and 800 pci (217.2 MN/m³) and the concrete modulus between 3,000 ksi (20.7 GPa) and 6,000 ksi (41.3 GPa). Fixed values of joint and edge stiffnesses are used in the data base. The temperature differential, which is equal to the temperature at the top of the slab, minus the temperature at the bottom of the slab varies from -20°F (-11.1°C) to +30°F (+16.7°C) in the data base.

Results of previous analyses (5) have indicated that the two most critical loading conditions in a pavement were (a) the combination of a positive or zero temperature differential in the slab with an axle load at the edge center and (b) the combination of a negative temperature differential in the slab with an axle load at the slab corner. These two loading conditions are used in computing the critical stresses that are stored in the data base.

To reduce the size of the data base, dual wheels are treated as a single wheel with the same total weight. Analysis results have indicated that, when dual wheels are modeled as a single wheel, the computed stress is only slightly higher. Thus, a slightly more conservative design will result from this approach.

The data in the data base are stored in three files: FI12.DBK, FI20.DBK, and FI24.DBK (according to the length of the concrete slab). For instance, the file FI20.DBK stores the data for concrete pavements with a slab length of 20 ft (6.1 m). Only the maximum stresses caused by single-axle loads are stored in this data base.

When a tandem-axle load is encountered, it is converted to a number of single-axle loads having the same wheel load that will produce the same damage to the pavement as that produced by the tandem-axle load. The method of converting a tandem-axle load to a number of single-axle loads will be presented later in this paper.

A constant slab width of 12 ft (3.7 m) was used in computing the maximum stresses. The concrete was assumed to have a constant coefficient of thermal expansion of $6 \times 10^{-6}/^{\circ}\text{F}$ ($10.8 \times 10^{-6}/^{\circ}\text{C}$).

DEVELOPMENT OF MEDCONP COMPUTER PROGRAM

Factors Considered in the Design Procedure

The MEDCONP program used a mechanistic approach. The factors considered in this design procedure included (a) length and thickness of concrete slabs, (b) elastic modulus and flexural strength of concrete, (c) stiffness of subgrade or the combination of subbase and subgrade, (d) daily and hourly traffic distribution, and (e) thermal gradient in the slab.

The maximum stress caused by each combination of thermal gradient and axle load for the pavement with a set of given pavement parameters and dimensions was first obtained from the data base. The ratio of computed maximum stress to

flexural strength of concrete was then computed for all load cases. Finally, these ratios were used in conjunction with the fatigue theory and Miner's rule to check the adequacy of the pavement section design or to estimate the expected service life of the pavement.

Fatigue Theory and Miner's Rule

The number of cycles that will cause the concrete pavement slab to fail for each stress level is computed by means of the fatigue theory. The fatigue theory states that the number of load applications that a concrete slab can sustain depends on the ratio of applied tensile stress to the modulus of rupture of the concrete. In the MEDCONP program, it is assumed that the concrete can take an unlimited number of load repetitions if the stress-to-strength ratio is less than 0.5. When the ratio is greater than 0.5, the allowable load repetitions for the concrete can be determined from typical fatigue curves. Two typical fatigue curves are shown in Figure 2 (6). Of these two curves, the one developed by Bradbury is used in the MEDCONP program. It should be stressed that this fatigue curve is not necessarily the only curve that can be used. If desired, a different fatigue curve can be incorporated into the program by a slight modification of the program.

Once the number of load applications that the concrete slab can take for all load cases is determined, Miner's rule is used to check the adequacy of the pavement section design. According to Miner's rule, fatigue failure will occur when the sum of the ratio of number of load repetitions to number of load repetitions to cause failure for all stress levels is equal to or greater than one.

Traffic Distribution

To allow for the effects of temperature variation on the concrete pavement performance, each year can be divided into

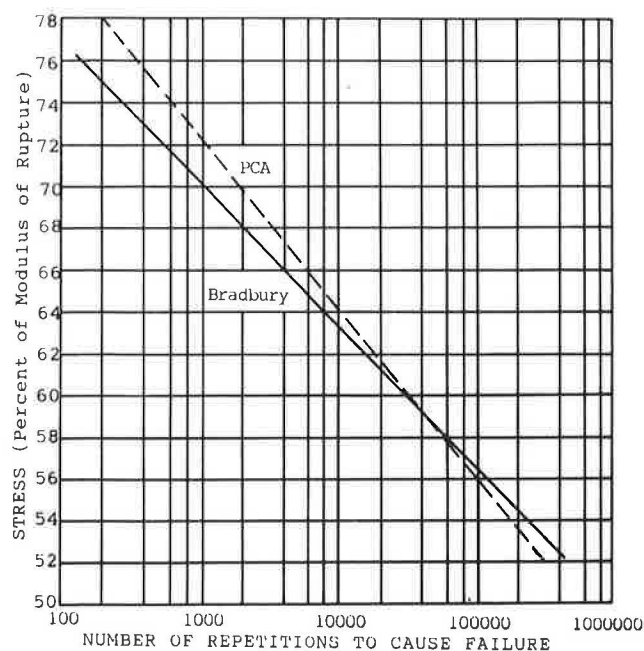


FIGURE 2 Fatigue curves for plain concrete (6).

as many as twelve intervals (to account for seasonal temperature variation) and each day can be divided into 24 intervals (to account for daily temperature variation). The traffic distribution has to be obtained for each time increment in a day, for each seasonal interval. The information required includes (a) type of each axle load, whether single or tandem, (b) weight of each axle load, and (c) number of applications of each axle load. The traffic distribution required to be input to this program is that in one direction only. This enables the pavement lanes in opposite directions to be designed individually if they have different traffic distribution.

When the pavement has more than one lane in each direction, it is known that a larger portion of the traffic uses the right lane (7). The proportion of traffic in the right lane is both a function of the number of lanes in one direction and the average daily traffic (ADT) in one direction. This relationship, as shown in Figure 3, was derived by the PCA (2). From Figure 3, two equations are developed and listed as follows:

For two lanes in one direction,

$$\text{TDF} = 1.5765 - 0.1922 \log_{10}(\text{ADT}) \quad (1)$$

For three lanes in one direction,

$$\text{TDF} = 1.4500 - 0.1922 \log_{10}(\text{ADT}) \quad (2)$$

where TDF equals the proportion of traffic in the traffic lane, and ADT equals the average daily traffic in one direction.

It should be noted that the ADT in different seasonal intervals need not be the same.

Conversion of Tandem-Axle Loads

As mentioned earlier in this paper, only the stresses caused by single-axle loads were stored in the data base. To use the

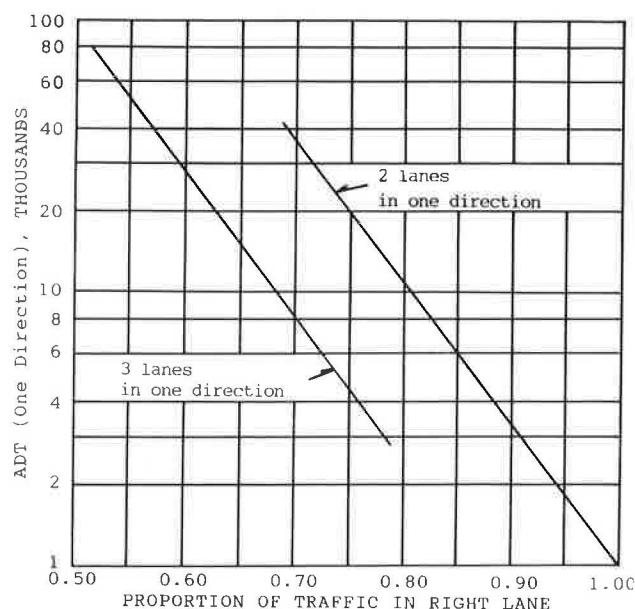


FIGURE 3 Proportion of traffic in the right lane of a multilane divided highway (2).

data base for tandem-axle loads, an effort was made to establish relationships between the maximum stresses caused by a tandem-axle load and those caused by a single-axle load with the same wheel loads and at the same temperature differentials. In the development of these relationships, a typical pavement with the following dimensions and parameters was used:

1. Slab length of 20 ft (6.1 m) and width of 12 ft (3.7 m),
2. Slab thickness of 9 in. (23 cm),
3. Concrete modulus of 4,000 ksi (27.6 GPa),
4. Subgrade modulus of 0.40 kci (108.6 MN/m³),
5. Edge stiffness of 10 ksi (68.9 MPa),
6. Linear joint stiffness of 250 ksi (1.72 GPa), and
7. Torsional joint stiffness of 2000 k-in./in. (8.9 MN-m/m).

The maximum stresses caused by the combinations of various axle loads (either single-axle or tandem-axle) and various temperature differentials were computed using FEACONS IV. The temperature differential in the slab was varied from -20°F (-11.1°C) to $+30^{\circ}\text{F}$ ($+16.7^{\circ}\text{C}$), and the magnitude of axle load ranged from zero to 30 kips (133.5 kN) for single-axle load and from zero to 60 kips (267 kN) for tandem-axle load. Again, the axle load was applied at the edge center for a positive temperature differential condition and at the slab corner for a negative temperature differential condition. For each temperature differential, the ratio of maximum stress caused by a tandem-axle load to that caused by a single-axle load with the same magnitude of wheel loads was calculated for each wheel load. The results of the analysis are shown in Table 1.

It should be noted that the wheel loads listed in the first column in Table 1 represent the weight of one wheel (or the total weight of dual wheels, if dual wheels were encountered). For instance, a wheel load of 5 kips (22.3 kN) represents either a single-axle load of 10 kips (44.5 kN) or a tandem-axle load of 20 kips (89 kN). As displayed in Table 1, the stress ratio varies with the change of both the wheel load and the temperature differential. For the condition of a negative temperature differential when the critical loading position is the corner load, the stress ratios are all greater than 1. For the condition of a positive or zero temperature differential when the critical loading position is the edge load, the stress ratios are all less than 1.

To establish the relationship between the maximum stress ratio and the combination of wheel load and temperature differential, a regression analysis was performed. It was found that the maximum stress ratio can be related to the wheel load and temperature differential by the following equations:

For the corner load condition,

$$\begin{aligned} \text{COEFI} &= 0.006494 \times \text{WLOAD} + 0.000596 \\ &\quad \times \text{TEMDIF} + 1.014285 \\ R^2 &= 0.8159 \end{aligned} \quad (3)$$

For the edge load condition,

$$\begin{aligned} \text{COEFI} &= -0.006531 \times \text{WLOAD} + 0.003099 \\ &\quad \times \text{TEMDIF} + 0.92731 \\ R^2 &= 0.6662 \end{aligned} \quad (4)$$

where

COEFI = maximum stress ratio,
WLOAD = magnitude of wheel load (in kips),
TEMDIF = temperature differential in the slab (in $^{\circ}\text{F}$),
and
R = coefficient of correlation.

Equations 3 and 4 were used in the MEDCONP program for this purpose. Because the edge load produces the highest stress when the pavement slab has a positive or zero temperature differential, Equation 4 is used for this condition. Similarly, Equation 3 is used when the pavement slab has a negative temperature differential.

The conversion of any tandem-axle load to a single-axle load involved the following steps:

1. Calculate the maximum stress ratio by using either Equation 3 or Equation 4 (depending on the temperature differential in the slab),
2. Divide the magnitude of the tandem-axle load by 2, and
3. Multiply the divided axle load by the maximum stress ratio.

One application of the tandem-axle load was then treated as two applications of a single-axle load with the magnitude as obtained when using these three steps.

It should be noted that the method of converting a tandem-axle load into an equivalent single-axle load (ESAL) generates only approximate stresses. The directly computed stresses caused by tandem-axle loads should be used to produce more accurate results.

A data bank for stresses caused by tandem-axle loads is currently being developed. Once this portion of the data base is complete, it will be incorporated into the program to replace the approximation method as presented above.

Program Structure and Algorithm

The flowchart of the MEDCONP program is shown in Figure 4. The program execution consists of the following major steps:

1. *Input data.* Data can be input either from a specified file or from the terminal. For the case of designing a new pavement, the required data are (a) intended design life, (b) annual growth rate of traffic, (c) number of lanes in one direction, (d) length and trial thickness of concrete slab with a fixed slab width of 12 ft, (e) elastic modulus and flexural strength of concrete, (f) subgrade modulus, (g) seasonal and daily variations of temperature differential in the slab, and (h) daily traffic distribution. The data required to evaluate an existing pavement are essentially the same as those listed above except that the intended design life is omitted and the slab thickness is known.

2. *Calculate proportion of traffic.* The traffic volume in the right lane must be determined. On a multilane divided highway, the proportion of traffic in the right lane is calculated using either Equation 1 or Equation 2.

3. *Compute maximum stresses.* The data files to be used for a particular case are determined according to the slab

TABLE 1 RATIO OF MAXIMUM STRESSES CAUSED BY TANDEM- AND SINGLE-AXLE LOADS ON CONCRETE SLABS WITH TEMPERATURE DIFFERENTIAL

WHEEL		TEMPERATURE DIFFERENTIAL (°F)						
LOAD		CORNER LOAD			EDGE LOAD			
(kips)		-20	-10	0	0	10	20	30
0	T-AXLE	310	155	9	9	160	285	379
	S-AXLE	310	155	9	9	160	285	379
	RATIO	1.00	1.00	1.00	1.00	1.00	1.00	1.00
2	T-AXLE	313	158	41	39	186	326	415
	S-AXLE	310	155	40	47	192	333	431
	RATIO	1.010	1.019	1.025	0.830	0.969	0.979	0.963
5	T-AXLE	320	166	92	98	239	395	492
	S-AXLE	311	156	88	118	246	400	509
	RATIO	1.029	1.064	1.046	0.830	0.972	0.988	0.967
7	T-AXLE	325	172	127	137	278	420	542
	S-AXLE	312	159	120	165	294	443	563
	RATIO	1.047	1.082	1.058	0.830	0.946	0.948	0.963
10	T-AXLE	334	185	182	196	335	472	609
	S-AXLE	314	164	169	236	365	503	640
	RATIO	1.064	1.128	1.077	0.831	0.918	0.938	0.952
13	T-AXLE	343	202	237	255	393	517	670
	S-AXLE	318	179	217	307	437	573	716
	RATIO	1.079	1.129	1.092	0.831	0.899	0.902	0.936
15	T-AXLE	348	215	274	294	432	559	688
	S-AXLE	321	192	249	355	485	623	762
	RATIO	1.084	1.120	1.100	0.828	0.891	0.897	0.903

NOTE: T-AXLE = Tandem-Axle Load

S-AXLE = Single-Axle Load

RATIO = Stress caused by Tandem-Axle Load/Stress caused by Single-Axle Load

length of the pavement. The maximum stress caused by each combination of temperature differential and axle load for a given set of pavement parameters is obtained by extracting the appropriate data from the data bank and interpolation. This is done by the subroutine INTEP.

4. *Determine allowable repetitions for each stress level.* Subroutine CALCUL performs three tasks. First, it calculates the maximum stress by interpolation between slab lengths. Second, it determines the allowable repetitions for each stress level. The ratio of expected applications to the allowable repetitions is then computed for each stress level. Finally, the sum of all of the ratios is computed.

5. *Use Miner's rule.* The expected service life of an existing

pavement or the design thickness of the concrete slab of a new pavement is determined using Miner's rule.

EVALUATION OF MEDCONP

To evaluate the suitability of the design procedure for rigid pavement used in MEDCONP, the program was applied to a design example. In this example, the required thickness of a four-lane, interstate highway pavement located in a rural area is to be determined using both the new AASHTO Design Guide and MEDCONP. The same set of design data was used in both methods.

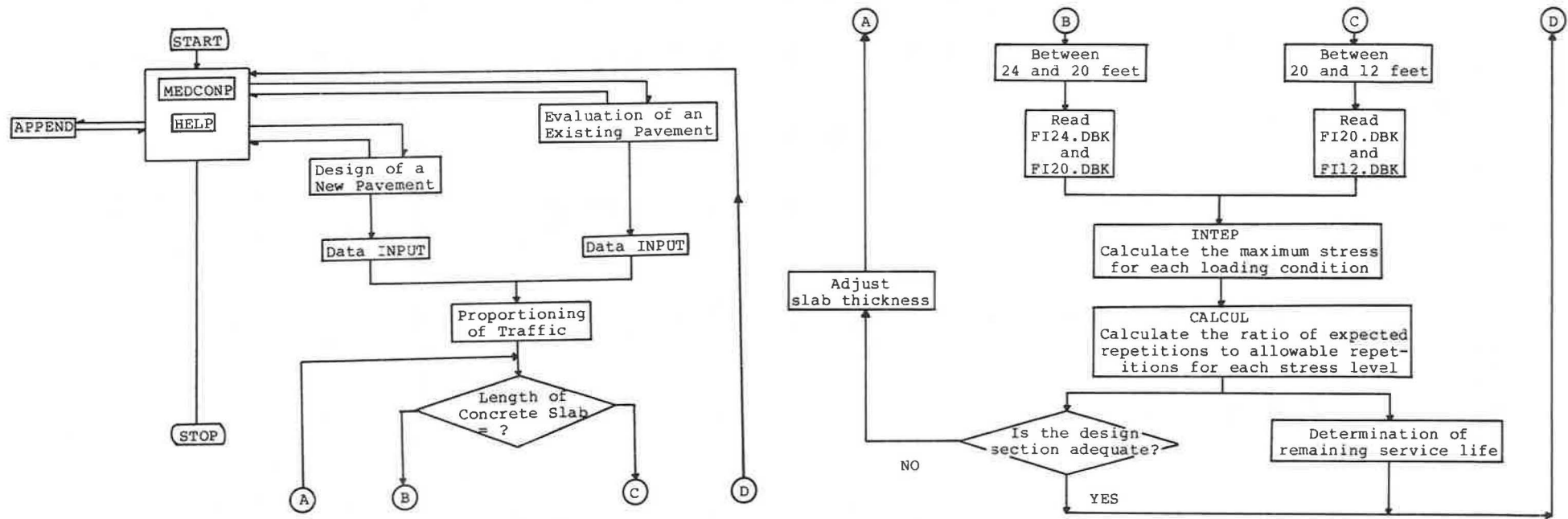


FIGURE 4 MEDCONP flowchart.

Two types of analyses will be performed using MEDCONP. The first accounts for temperature variation, while the second assumes no temperature differential in the slab throughout the design period. The slab thicknesses determined using the AASHTO Design Guide and those obtained using MEDCONP (with and without the consideration of the temperature variations) are compared to evaluate the suitability of the use of MEDCONP in designing rigid pavements. The general design data used in this example are listed below:

1. Current ADT in one direction = 6028,
2. $E_c = 3500$ ksi (24.1 GPa), typical concrete modulus for Florida concrete pavements,
3. $K_s = 0.20$ kci (54 MN/m³), typical modulus of subgrade reaction for conventional stabilized subbase,
4. $\sigma_c = 700$ psi (4.8 MPa), modulus of rupture for typical Florida concrete,
5. Annual growth rate (AGR) of traffic = 3 percent,
6. Doweled joints and tied concrete shoulders, and
7. Slab length of 16 ft (4.9 m) and slab width of 12 ft (3.7 m).

Determining Slab Thickness Using AASHTO Design Guide

Design Parameters

In addition to the design data listed above, the following design parameters are also needed to use the AASHTO Design Guide.

1. $\Delta PSI = 4.2 - 2.5 = 1.7$, design serviceability loss, equals initial serviceability index (P_0) minus terminal serviceability index (P_t),
2. $J = 2.7$, very good load transfer between two adjoining slabs,
3. $C_d = 1.0$, good drainage condition,
4. $R = 95$ percent, reliability factor, as suggested for interstate highways,
5. $S_0 = 0.30$, overall standard deviation, value obtained for rigid pavements on AASHO Road Test, and
6. ADT distribution, as listed in Table 2 (I).

Determining the Total 18-kip ESALs

Tables 3 and 4 show the traffic equivalence factors for rigid pavements for various single-axle and tandem-axle loads, respectively (I). From these two tables, the number of 18-kip (80 kN) ESALs for the first year was determined to be 2,610.2 for a trial slab thickness of 10 in. (25.4 cm). The computation of number of ESALs is shown in Table 5. The portion of traffic traveling in the design lane (right lane) is then determined using Equation 1. For a current ADT of 6,028 and a 3-percent annual traffic growth rate, the average ADT over the design period is calculated to be 7,746. Thus, from Equation 1, 83 percent of the total traffic will be driving on the design lane. The number of 18-kip (80-kN) ESALs on the design lane in the first year is obtained by multiplying 0.83 by 2,610.2 and is equal to 2163.9. With a 3-percent increase in traffic each year, the number of 18-kip (80-kN) ESALs in the last year of the design period (20th year) is 3,397.3 (2,163.9

$\times 0.03 \times 19 + 2,163.9$). Finally, the number of total 18-kip (80-kN) ESALs over the design period is calculated as follows:

Total 18-kip (80-kN) ESALs

$$= \frac{2163.9 + 3397.3}{2} \times 365 \times 20 = 20.3 \text{ million (approx.)}$$

Determining Slab Thickness

Design nomographs in the AASHTO Design Guide (as shown in Figures 5 and 6) are used to determine the required slab thickness. By connecting lines between specified design parameters, the required slab thickness is determined to be 9.5 inches (24.1 cm).

Determining Slab Thickness Using MEDCONP

Case A: Temperature Variation Considered

Hourly Traffic Distribution. According to the data on temperature differential in the slab obtained from the Gainesville Test Road located in the Bureau of Materials and Research, Florida Department of Transportation (8), it is determined to separate each year into four groups. Group 1 comprised December, January, and February; Group 2 comprised March, April, and May; Group 3 included June, July, and August; and Group 4 was September, October, and November. Data obtained from January 27 to 28, April 7 to 8, June 7 to 8, 1986, and October 7 to 8, 1985, are used to represent the typical variations of temperature differential in the slab for Groups 1 through 4, respectively.

Within each group, each day is further subdivided into several time increments. The time increments are selected such that the slab will be subjected to similar temperature differential in each increment. The number of time increments in each group may differ.

Finally, the number and type of traffic loads are assigned to each group and time increment with the basic assumption that most of the heavy trucks travel on the road during the early morning and passenger cars travel during the daytime. A sample traffic distribution by hour of the day and gross weight obtained at a weigh-in-motion station located south of Gainesville, Florida, on I-75 (8) are also used as guidelines. The axle load distribution in each group and time increment are listed in Tables 6 through 9.

Determination of Slab Thickness. After performing the analysis using the design data and MEDCONP, the slab thickness was determined to be 12.0 inches (30.5 cm).

Case B: Temperature Variation Not Considered

Because temperature differential in the slab is not considered in this case, it is not necessary to divide a year or a day into time increments. Only one group in the entire year and one time increment in each day are used. A temperature differential of zero is used. Therefore, the slab thickness is deter-

TABLE 2 AVERAGE DAILY TRAFFIC DISTRIBUTION (1)

Axle Load Groups (lbs)	Representative Axle Load (lbs)	No. of Axles
<u>Single Axle</u>		
Under 3000	2000	512
3000-6999	5000	536
7000-7999	7500	239
8000-11999	10000	1453
12000-15999	14000	279
16000-18000	17000	106
18001-20000	19000	43
20001-21999	21000	4
22000-23999	23000	3
<u>Tandem Axle</u>		
Under 6000	4000	9
6000-11999	9000	337
12000-17999	15000	396
18000-23999	21000	457
24000-29999	27000	815
30000-32000	31000	342
32001-33999	33000	243
34000-35999	35000	173
36000-37999	37000	71
38000-39999	39000	9
40000-41999	41000	0
42000-43999	43000	1
ADT =		6028

mined (using the same design data as in the previous cases) to be 7.5 inches (19.1 cm).

SUMMARY

MEDCONP was developed to design and evaluate jointed concrete pavements. It uses a mechanistic approach and considers such important factors as the thermal gradient in the concrete slab and the daily and hourly traffic load distribution, which have not been considered in the past. The other design factors considered include the slab length, elastic modulus and flexural strength of concrete, subgrade modulus, traffic

growth rate, proportioning of traffic in multiple lanes, and design life. For each applied load considered, the critical-induced stress in the slab is computed by assuming that the load is applied at the most critical loading position for the given thermal condition. These critical stresses are then used to evaluate the structural adequacy of the given pavement by means of the fatigue theory and Miner's rule.

As illustrated in the design example, temperature differential in the concrete slab greatly affects the required slab thickness. With the assumption of no temperature variation in the slab, the required slab thickness (as determined by MEDCONP) is 7.5 inches (19.1 cm). When the temperature variation is considered, the required slab thickness increases

TABLE 3 TRAFFIC EQUIVALENCE FACTORS FOR SINGLE-AXLE LOAD (*I*)

Axle Load		Slab Thickness (inches)						
Kips	kN	6	7	8	9	10	11	12
2	8.9	0.0002	0.0002	0.0002	0.0002	0.0002	0.0002	0.0002
4	17.8	0.003	0.002	0.002	0.002	0.002	0.002	0.002
6	26.7	0.01	0.01	0.01	0.01	0.01	0.01	0.01
8	35.6	0.04	0.04	0.03	0.03	0.03	0.03	0.03
10	44.5	0.10	0.09	0.08	0.08	0.08	0.08	0.08
12	53.4	0.20	0.19	0.18	0.18	0.18	0.17	0.17
14	62.3	0.38	0.36	0.35	0.34	0.34	0.34	0.34
16	71.2	0.63	0.62	0.61	0.60	0.60	0.60	0.60
18	80.1	1.00	1.00	1.00	1.00	1.00	1.00	1.00
20	89.0	1.51	1.52	1.55	1.57	1.58	1.58	1.59
22	97.9	2.21	2.20	2.28	2.34	2.38	2.40	2.41
24	106.8	3.16	3.10	3.23	3.36	3.45	3.50	3.53
26	115.7	4.41	4.26	4.42	4.67	4.85	4.95	5.01
28	124.6	6.05	5.76	5.92	6.29	6.61	6.81	6.92
30	133.4	8.16	7.67	7.79	8.28	8.79	9.14	9.34
32	142.3	10.81	10.06	10.10	10.70	11.43	11.99	12.35
34	151.2	14.12	13.04	12.34	13.62	14.59	15.43	16.01
36	160.1	18.20	16.69	16.41	17.12	18.33	19.52	20.39
38	169.0	23.15	21.14	20.61	21.31	22.74	24.31	25.58
40	177.9	29.11	26.49	25.65	26.29	27.91	29.90	31.64

NOTE: $P_t = 2.5$ TABLE 4 TRAFFIC EQUIVALENCE FACTORS FOR TANDEM-AXLE LOAD (*I*)

Axle Load		Slab Thickness (inches)						
Kips	kN	6	7	8	9	10	11	12
10	44.5	0.01	0.01	0.01	0.01	0.01	0.01	0.01
12	53.4	0.03	0.03	0.03	0.03	0.03	0.03	0.03
14	62.3	0.06	0.05	0.05	0.05	0.05	0.05	0.05
16	71.2	0.10	0.09	0.08	0.08	0.08	0.08	0.08
18	80.1	0.16	0.14	0.14	0.13	0.13	0.13	0.13
20	89.0	0.23	0.22	0.21	0.21	0.20	0.20	0.20
22	97.9	0.34	0.32	0.31	0.31	0.30	0.30	0.30
24	106.8	0.48	0.46	0.45	0.44	0.44	0.44	0.44
26	115.7	0.64	0.64	0.63	0.62	0.62	0.62	0.62
28	124.6	0.85	0.85	0.85	0.85	0.85	0.85	0.85
30	133.4	1.11	1.12	1.13	1.14	1.14	1.14	1.14
32	142.3	1.43	1.44	1.47	1.49	1.50	1.51	1.51
34	151.2	1.82	1.82	1.87	1.92	1.95	1.96	1.97
36	160.1	2.29	2.27	2.35	2.43	2.48	2.51	2.52
38	169.0	2.85	2.80	2.91	3.04	3.12	3.16	3.18
40	177.9	3.52	3.42	3.55	3.74	3.87	3.94	3.98
42	186.8	4.32	4.16	4.30	4.55	4.74	4.86	4.91
44	195.7	5.26	5.01	5.16	5.48	5.75	5.92	6.01
46	204.6	6.36	6.01	6.14	6.53	6.90	7.14	7.28
48	213.5	7.64	7.16	7.27	7.73	8.21	8.55	8.75

NOTE: $P_t = 2.5$

TABLE 5 COMPUTATION OF NUMBER OF 18-KIP ESALs

Axle Load (kips)	Equiv. Factor	No. of Axles	Equiv. 18-kip Single Axles
<u>Single Axles</u>			
2	0.0002	512	0.1024
5	0.006	536	3.216
7.5	0.025	239	5.975
10	0.08	1453	116.24
14	0.34	279	94.86
17	0.80	106	84.8
19	1.29	43	55.47
21	1.98	4	7.92
23	2.915	3	8.745
<u>Tandem Axles</u>			
9	0.01	337	3.37
15	0.065	396	25.74
21	0.25	457	114.25
27	0.735	815	599.025
31	1.32	342	451.44
33	1.73	243	420.39
35	2.215	173	383.195
37	2.8	71	198.8
39	3.495	9	31.455
43	5.245	1	5.245
Total ESALs =			2610.2

to 12 inches (30.5 cm). For this thermal condition, the required slab thickness is higher than that determined by the AASHTO procedure.

For a region where the temperature differential in the concrete slab is small, it is expected that the MEDCONP procedure will produce a lower slab thickness than the AASHTO procedure. For a region where the temperature differential is high, the MEDCONP procedure will produce a higher slab thickness.

In summary, it is evident that temperature variation plays a major role in affecting the performance of concrete pavement and should be incorporated in the design procedure. MEDCONP takes this factor into account in the design procedure and has been demonstrated to run properly for its intended purposes. It should be noted that because MED-

CONP assumes that the loads are applied at the critical positions on the slab, it should produce designs that are on the safe side.

FURTHER DEVELOPMENT OF MEDCONP

As a result of the large amount of time required to generate the data base in the program, the data base is still being expanded at this stage of development of the program. Further development of MEDCONP is now in progress and includes the following:

1. The data base will be expanded to account for the effects of joint and edge stiffness.

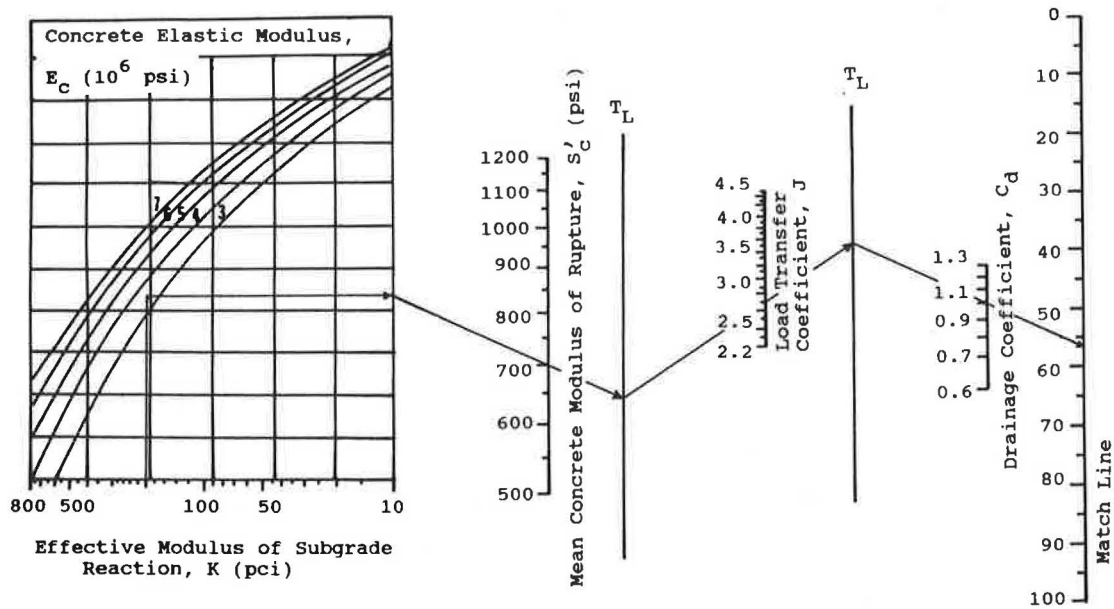


FIGURE 5 Determination of slab thickness using AASHTO method (Part 1) (1).

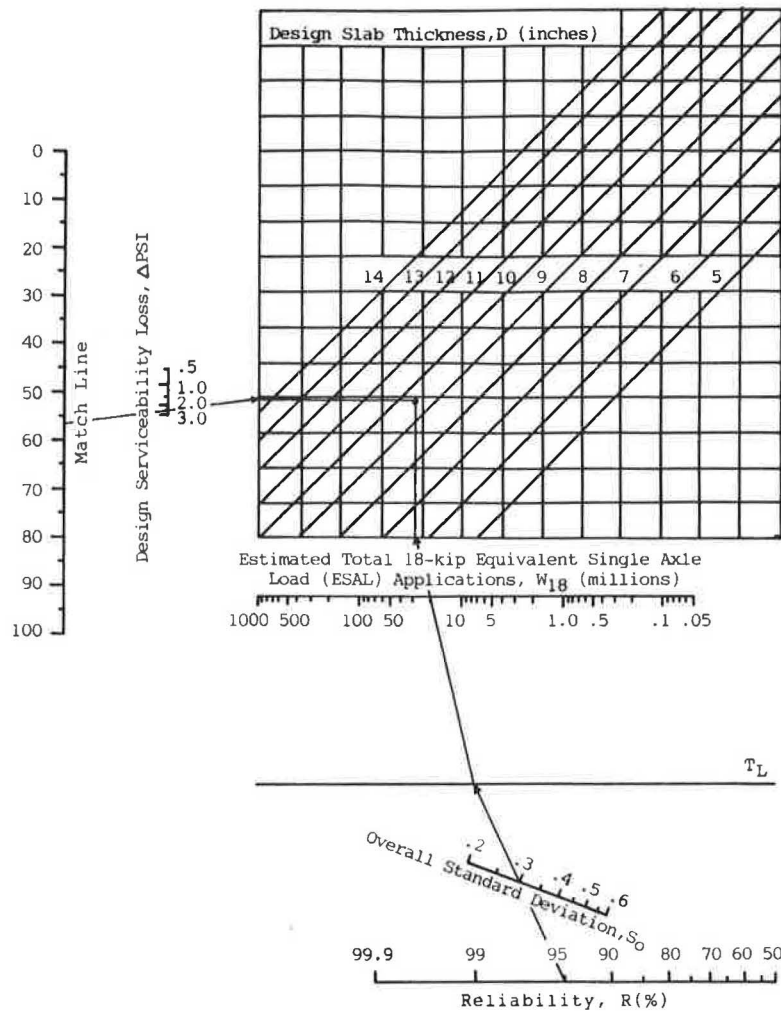


FIGURE 6 Determination of slab thickness using AASHTO method (Part 2) (1).

TABLE 6 CURRENT HOURLY TRAFFIC DISTRIBUTION FOR GROUP 1

Time Incre- ment	ΔT	Single-Axle Load										Tandem-Axle Load									
		2	5	7.5	10	14	17	19	21	23	4	9	15	21	27	31	33	35	37	39	43
08-09	- 5.5	30	31	14	56	11	4	1	0	0	2	31	16	19	15	24	17	12	3	0	0
09-10	- 2.8	39	40	18	75	14	6	1	0	0	3	20	21	25	52	8	6	4	2	1	0
10-11	+ 0.8	26	28	12	65	15	5	1	0	0	0	13	22	27	15	8	6	4	3	1	0
11-12	+ 4.8	17	18	8	84	17	7	1	0	0	0	13	22	27	15	8	6	4	3	1	0
12-14	+ 7.3	32	34	15	140	25	8	4	0	0	0	20	38	44	32	17	12	9	4	0	0
14-15	+ 0.9	17	18	8	61	11	4	0	0	0	0	9	17	22	23	2	1	0	0	0	0
15-16	- 5.4	21	22	10	70	14	5	1	0	0	0	8	19	22	38	11	8	6	3	0	0
16-18	- 8.5	60	62	28	136	25	8	3	0	0	2	35	38	44	38	24	17	13	2	0	0
18-20	-11.0	77	81	36	136	31	8	3	0	0	1	61	37	44	90	33	23	17	7	0	0
20-04	-12.2	128	134	60	444	82	32	18	4	3	1	58	119	134	299	135	96	67	32	6	1
04-08	-11.5	65	68	30	186	34	19	10	0	0	0	69	52	57	198	69	49	35	14	1	0

TABLE 7 CURRENT HOURLY TRAFFIC DISTRIBUTION FOR GROUP 2

Time Incre- ment	ΔT	Single-Axle Load										Tandem-Axle Load									
		2	5	7.5	10	14	17	19	21	23	4	9	15	21	27	31	33	35	37	39	43
00-04	- 9.2	56	58	26	233	45	17	11	3	1	1	23	63	70	140	73	52	37	14	4	1
04-07	-10.7	37	39	17	135	23	16	8	0	0	0	34	38	41	175	56	40	28	10	0	0
07-08	- 7.9	28	29	13	51	11	3	2	0	0	0	35	14	16	23	13	9	7	4	1	0
08-09	- 2.1	30	31	14	56	11	4	1	0	0	2	31	16	19	15	24	17	12	3	0	0
09-10	5.5	39	40	18	75	14	6	1	0	0	3	20	21	25	52	8	6	4	2	1	0
10-11	12.0	26	28	12	65	15	5	1	0	0	0	13	17	19	15	11	8	6	1	0	0
11-12	17.2	17	18	8	84	17	7	1	0	0	0	13	22	27	15	8	6	4	3	1	0
12-15	21.0	49	52	23	201	36	12	4	0	0	0	29	55	66	55	19	13	9	4	0	0
15-16	17.3	21	22	10	70	14	5	1	0	0	0	8	19	22	38	11	8	6	3	0	0
16-17	9.3	21	22	10	61	11	3	2	0	0	1	16	17	19	15	13	9	7	2	0	0
17-18	5.7	39	40	18	75	14	5	1	0	0	1	19	21	25	23	11	8	6	0	0	0
18-19	- 0.8	41	43	19	61	11	5	1	0	0	0	32	16	19	52	13	9	7	2	0	0
19-20	- 3.8	36	38	17	75	20	3	2	0	0	1	29	21	25	38	20	14	10	5	0	0
20-22	- 5.9	50	52	23	112	21	6	5	0	0	0	23	31	33	84	39	28	20	8	0	0
22-00	- 7.5	22	24	11	99	16	9	2	1	2	0	12	25	31	75	23	16	10	10	2	0

TABLE 8 CURRENT HOURLY TRAFFIC DISTRIBUTION FOR GROUP 3

Time Incre- ment	ΔT	Single-Axle Load										Tandem-Axle Load									
		2	5	7.5	10	14	17	19	21	23	4	9	15	21	27	31	33	35	37	39	43
00-03	- 4.7	43	45	20	158	31	13	7	2	1	1	20	44	48	125	45	32	23	13	3	1
03-06	- 5.3	39	41	18	173	30	15	9	1	0	0	25	47	52	143	60	43	30	8	1	0
06-07	- 3.0	11	11	5	37	7	5	3	0	0	0	12	10	11	47	24	17	12	3	0	0
07-08	2.0	28	29	13	51	11	3	2	0	0	0	35	14	16	23	13	9	7	4	1	0
08-09	8.1	30	31	14	56	11	4	1	0	0	2	31	16	19	15	24	17	12	3	0	0
09-10	13.5	39	40	18	75	14	6	1	0	0	3	20	21	25	52	8	6	4	2	1	0
10-12	18.5	43	46	20	149	32	12	2	0	0	0	26	39	46	30	19	14	10	4	1	0
12-14	22.7	32	34	15	140	25	8	4	0	0	0	20	38	44	32	17	12	9	4	0	0
14-15	21.1	17	18	8	61	11	4	0	0	0	0	9	17	22	23	2	1	0	0	0	0
15-17	14.2	42	44	20	131	25	8	3	0	0	1	24	36	41	53	24	17	13	5	0	0
17-28	8.5	39	40	18	75	14	5	1	0	0	1	19	21	25	23	11	8	6	0	0	0
18-19	3.0	41	43	19	61	11	5	1	0	0	0	32	16	19	52	13	9	7	2	0	0
10-21	- 1.7	60	63	28	140	32	5	5	0	0	1	42	38	44	61	44	31	22	8	0	0
21-00	- 4.8	48	51	23	146	25	13	4	1	2	0	22	39	45	136	38	27	18	15	2	0

TABLE 9 CURRENT HOURLY TRAFFIC DISTRIBUTION FOR GROUP 4

Time Incre- ment	ΔT	Single-Axle Load										Tandem-Axle Load									
		2	5	7.5	10	14	17	19	21	23	4	9	15	21	27	31	33	35	37	39	43
00-08	- 8.3	121	126	56	419	79	36	21	3	1	1	92	115	127	338	142	101	72	28	5	1
08-09	- 7.0	30	31	14	56	11	4	1	0	0	2	31	16	19	15	24	17	12	3	0	0
09-10	- 2.5	39	40	18	75	14	6	1	0	0	3	20	21	25	52	8	6	4	2	1	0
10-11	4.3	26	28	12	65	15	5	1	0	0	0	13	17	19	15	11	8	6	1	0	0
11-12	10.8	17	18	8	84	17	7	1	0	0	0	13	22	27	15	8	6	4	3	1	0
12-13	14.5	15	16	7	75	14	5	2	0	0	0	11	21	25	23	13	9	7	3	0	0
13-14	17.2	17	18	8	65	11	3	2	0	0	0	9	17	19	9	4	3	2	1	0	0
14-15	16.6	17	18	8	61	11	4	0	0	0	0	9	17	22	23	2	1	0	0	0	0
15-16	13.4	21	22	10	70	14	5	1	0	0	0	8	19	22	38	11	8	6	3	0	0
16-17	10.3	21	22	10	61	11	3	2	0	0	1	16	17	19	15	13	9	7	2	0	0
17-18	4.4	39	40	18	75	14	5	1	0	0	1	19	21	25	23	11	8	6	0	0	0
18-19	0.4	41	43	19	61	11	5	1	0	0	0	32	16	19	52	13	9	7	2	0	0
19-21	- 4.5	60	63	28	140	32	5	5	0	0	1	42	38	44	61	44	31	22	8	0	0
21-00	- 7.2	48	51	23	146	25	13	4	1	2	0	22	39	45	136	38	27	18	15	2	0

2. The data base will be expanded to include computed stresses caused by tandem-axle loads. When this portion of the data base is complete, using an equivalency factor to convert tandem-axle loads to single-axle loads will no longer be necessary.

3. The current data base contains data for only three slab lengths (12, 20, and 24 ft). To improve the accuracy of the program results, data for other slab lengths will also be incorporated.

ACKNOWLEDGMENTS

The Florida Department of Transportation is gratefully acknowledged for providing the financial support that made this study possible. The technical advice of B. E. Ruth and the cooperation and support of T. J. Larsen, J. M. Armaghani, and L. L. Smith are greatly appreciated. Sincere appreciation also goes to Pat Cribbs for the typing and correcting of the manuscript.

REFERENCES

1. American Association of State Highway and Transportation Officials. *Proposed AASHTO Guide for Design of Pavement Structure*. AASHTO, Washington, D.C., March 1985.
2. Portland Cement Association. *Thickness Design for Concrete Highway and Street Pavements*. PCA, Skokie, Ill., 1984.
3. M. Tia, J. M. Armaghani, C. L. Wu, S. Lei, and K. L. Toye. FEACONS III Computer Program for an Analysis of Jointed Concrete Pavements. In *Transportation Research Record 1136*, TRB, National Research Council, Washington, D.C., 1987, pp. 12–22.
4. M. Tia, B. E. Ruth, C. L. Wu, and K. S. Eom. *Field Evaluation of Rigid Pavements for the Development of a Rigid Pavement Design System—Phase II*. Final Report, Project 245-D75, Department of Civil Engineering, University of Florida, Gainesville, Aug. 1987.
5. M. Tia, C. L. Wu, J. M. Armaghani, and K. S. Eom. *Field Evaluation of Rigid Pavements for the Development of a Rigid Pavement Design System—Phase I*. Final Report, Project 245-D54, Department of Civil Engineering, University of Florida, Gainesville, July 1986.
6. E. J. Yoder and M. W. Witczak. *Principles of Pavement Design*, 2nd. ed., John Wiley & Sons, New York, 1975, 711 pp.
7. J. M. Becker, M. I. Darter, H. B. Snyder, and R. E. Smith. COPES Data Collection Procedures—Appendix A. In *Final Report of National Cooperative Highway Research Program 1-19 Concrete Pavement Evaluation System*, June 1983.
8. J. M. Armaghani. *Comprehensive Analysis of Concrete Pavement Response to Temperature and Load Effects*. Ph.D. dissertation. Department of Civil Engineering, University of Florida, 1987.

Publication of this paper sponsored by Committee on Rigid Pavement Design.

Maximum Entropy Spectral Analysis of Transverse Crack Spacing in Continuously Reinforced Concrete Pavements

JIAN LU, B. FRANK McCULLOUGH, AND C. L. SARAF

The characteristics of cracks of continuously reinforced concrete pavements (CRCP) are generally evaluated by analyzing the distribution of transverse crack spacing in the pavement. Statistical analysis of data produces the mean and the standard deviation of crack spacing. However, these parameters are not always sufficient for characterizing the crack spacing of CRCP. Therefore, this paper proposes an alternate method for analyzing the transverse crack spacing data. This method, maximum entropy spectral analysis (MESA), analyzes the data in the frequency domain rather than in the space domain. In this paper, the uniformity and variability of crack spacing are also defined. By using MESA, the uniformity and variability of crack spacing can be observed in the frequency domain. The results of analyses using MESA indicate that this method can intuitively distinguish the characteristics of transverse crack spacing distribution in CRCP containing different types of coarse aggregates. The limitations of space domain analysis can be made up by MESA.

The quality of continuously reinforced concrete pavements (CRCP) is sometimes related to the transverse crack spacing characteristics. It is known that the crack spacing is distributed randomly, and therefore, statistical methods are usually used to determine the crack spacing characteristics. Intuitively, researchers analyze and evaluate the characteristics of crack spacing in the space domain (i.e., probability distribution analysis, and variance analysis). However, because of the limitations of space domain analysis, it is sometimes difficult to determine the characteristics of crack spacing of CRCP. In such cases, the alternative is to analyze the crack spacing characteristics in the frequency domain. Maximum entropy spectral analysis (MESA), which is presented here, can be used to analyze the characteristics of transverse crack spacing in CRCP in the frequency domain.

This paper introduces the MESA method for evaluating transverse crack spacing characteristics in CRCP and describes the procedure for comparing the characteristics of transverse crack spacing between two kinds of CRCP, one built with mixes that contained limestone (LS) aggregates, and the second built with mixes that contained siliceous river gravel (SRG) aggregates. Using the MESA method, it was found that the crack spacing characteristics of pavements containing LS aggregates are significantly different from those of pavements containing SRG aggregates.

MESA is a method of analysis in the frequency domain. It can be used in other analyses, such as roughness analysis of pavement surface profiles, vehicle vertical vibration analysis, degree of passenger comfort analysis, and determination of the skid characteristic of pavement surfaces.

LIMITATIONS OF PROBABILITY ANALYSIS

It is known that if the CRCP contains N cracks, and the i th crack spacing is denoted as x_i , then the crack spacing sequence is defined as

$$\{x_i\} = \{x_1, x_2, \dots, x_N\} \quad (1)$$

Figures 1a and 1b show crack spacing sequences for two test sections in Texas. These spacings can be represented as

$$\{x_i\} = \{6.2, 4.5, \dots, 3, 7.4\} \text{ (ft) (50051N)}$$

and

$$\{x_i\} = \{12.4, 8.5, \dots, 6.7, 6.9\} \text{ (ft) (130154E)}$$

These sequences are called discrete space domain sequences, because they can be measured by observations.

From Figures 1a and 1b, one cannot decide which test section has better crack spacing characteristics. Usually, the probability density function (PDF) of the crack spacing sequence can be used to characterize the pavement crack spacing sequence statistically. Our experience with the analysis of the data indicates that the crack spacing is approximately log normally distributed. The PDF of crack spacing can be represented by

$$f(x) = \frac{1}{(2\pi bX)^{1/2}} e^{-\frac{(\ln X - a)^2}{2b^2}} \quad (2)$$

where the mean value (μ) and variance (σ^2) can be expressed as follows:

$$\mu = e^{a + b^2/2}$$

and

$$\sigma^2 = e^{2a + b^2/2} (e^{b^2} - 1)$$

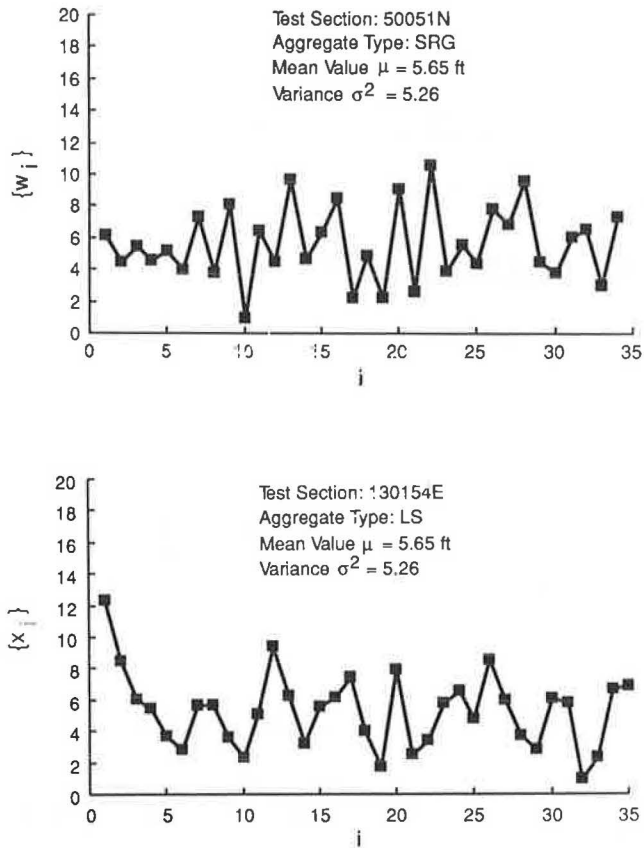


FIGURE 1 Crack spacing sequence: *Top*, test section 50051N; *bottom*, test section 130154E.

where

$$a = \frac{1}{2} \ln \left(\frac{\mu^4}{\mu^2 + \sigma^2} \right)$$

$$b^2 = \ln \left(1 + \frac{\sigma^2}{\mu^2} \right) \quad (3)$$

In Equation 2, only two parameters must be estimated, i.e., μ and σ^2 . The PDF of the crack spacing can be easily obtained with these parameters. However, two parameters are not enough to characterize the crack spacing sequence, because it is possible to obtain approximately the same PDF from two different crack spacing sequences although their statistical characteristics may be different. For example, the PDFs of the crack spacing sequences of the two test sections shown in Figures 1a and 1b are almost the same, as indicated below:

$\mu = 5.65$ ft; $\sigma^2 = 5.26$ (test section: 50051N)

$\mu = 5.33$ ft; $\sigma^2 = 5.59$ (test section: 130154E)

However, their maximum entropy spectral density functions are different, as shown in Figure 2 (these two spectral density functions are normalized at frequency $\omega_k = 0$). This means that, although two crack spacing sequences present the same distribution characteristics in the space domain, such as PDF, if the

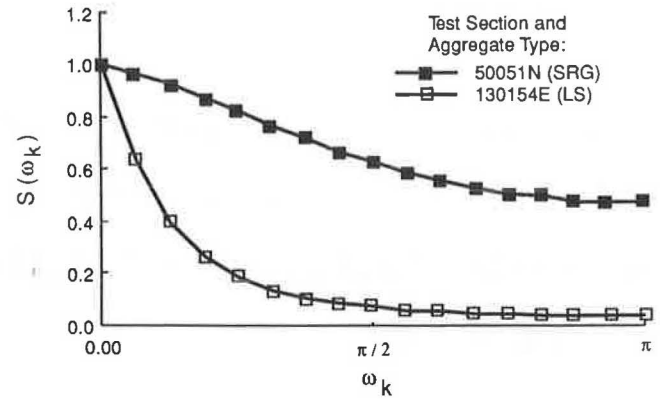


FIGURE 2 Normalized spectral density functions.

sequences are transformed into a spectral density function in the frequency domain, the spectral density function of these two sequences will probably show different characteristics.

In this paper, the MESA of transverse crack spacing was used to analyze the effect of aggregate type on the transverse crack spacings in CRCP. This method provided another way to analyze transverse crack spacing characteristics in CRCP.

MAXIMUM ENTROPY SPECTRAL ANALYSIS

MESA can be as described as follows.

Discrete Spectral Transformation

From Equation 1, the transverse crack spacing sequence in CRCP can be considered as a discrete sequence, or

$$\{x_i\} = \{x_1, x_2, \dots, x_N\}$$

Consider the inverse discrete Fourier transformation (1):

$$x_i = \frac{1}{N} \sum_{k=0}^{N-1} H_k e^{jk2\pi/N} \quad (i = 1, 2, \dots, N) \quad (4)$$

where

N = length of the sequence,

x_i = the i th crack spacing,

H_k = the weights ($k = 0, 1, \dots, N-1$), and

$j = (-1)^{1/2}$.

Equation 4 shows that x_i can be considered as the weighted summation of sine function $e^{jk2\pi/N}$. Now define

$$\omega_k = k2\pi/N \quad (k = 0, 1, \dots, N-1)$$

and then

$$x_i = \frac{1}{N} \sum_{k=0}^{N-1} H_k e^{ji\omega_k} \quad (5)$$

and

$$e^{ji\omega_k} = \sin \omega_k i + j \cos \omega_k i$$

Usually, variable ω_k is called frequency. Obviously, ω_k is within the range of $0, 2\pi(N-1)/N$. According to Equation 5, the bigger the H_k , the more sine function components with frequency ω_k the crack spacing sequence $\{x_i\}$ will contain. Mathematically, it can be proven that

$$H_k = H(\omega_k) = \sum_{i=-\infty}^{+\infty} x_i e^{i\omega_k} \quad (6)$$

$$\times \{\omega_k = 0, 2\pi/N, 4\pi/N, \dots, 2\pi(N-1)/N\}$$

In other words, $H(\omega_k)$ is the discrete Fourier transformation of $\{x_i\}$ and is the function of frequency ω_k . Equation 6 implies that space domain sequence $\{x_i\}$ can be transformed into frequency domain sequence $\{H(\omega_k)\}$, and the characteristics of sequence $\{x_i\}$ can be analyzed in the frequency domain, i.e., knowing $H(\omega_k)$, one is able to analyze the characteristics of $\{x_i\}$.

Because $H(\omega_k)$ is an imaginary sequence, define two real functions:

$$S(\omega_k) = |H(\omega_k)|^2 \quad (7)$$

$$G(\omega_n) = \sum_{k=0}^n S(\omega_k) \quad 0 \leq n \leq N-1 \quad (8)$$

where $S(\omega_k)$ is called the spectral density function of sequence $\{x_i\}$, and $G(\omega_n)$ is the spectral cumulative function of sequence $\{x_i\}$.

From Equation 6, we know that the summation is from $-\infty$ to $+\infty$. In practical cases, the sequence length N is finite; that is, we cannot obtain a sequence $\{x_i\}$ with i from $-\infty$ to $+\infty$. In this case, the spectral density function $S(\omega_k)$ should be estimated from $\{x_i\}$.

Now, the problem is how to estimate $S(\omega_k)$. In the area of spectral function estimation, several mathematical methods are available. One of the best methods is the maximum entropy spectral estimation method [see Appendix and Haykin (2)]. Mathematically, the maximum entropy spectral density function is expressed by

$$S(\omega_k) = \frac{P_M}{\left| 1 + \sum_{m=1}^M a_m e^{im\omega_k} \right|^2} \quad (9)$$

where $P_M, a_1, a_2, \dots, a_M$ are the parameters estimated by the maximum entropy spectral estimation algorithm. However, this algorithm is very complicated. Haykin (2) gives the detailed procedures of the maximum entropy spectral estimation algorithm; they are not included in this paper.

MESA of Crack Spacing Characteristics

From the above discussion, it is clear that spectral density function $S(\omega_k)$ represents the frequency density distribution characteristics of crack spacing sequence $\{x_i\}$, and spectral cumulative function $G(\omega_n)$ represents the frequency cumu-

lative distribution characteristics. For example, if the crack spacing sequence $\{x_i\}$ changes smoothly, then $\{x_i\}$ contains relatively many low-frequency components. This means that the magnitude of $S(\omega_k)$ in the low-frequency region is relatively higher than that in the high-frequency section. On the other hand, if the crack spacing sequence $\{x_i\}$ changes abruptly, then $\{x_i\}$ contains relatively many high-frequency components. Therefore, the magnitude of $S(\omega_k)$ in the high-frequency region is relatively higher than that in the low-frequency region.

Now consider a concept of uniformity of crack spacing. In this paper, the uniformity of crack spacing sequence $\{x_i\}$ is used as a qualitative index. It is said that the uniformity of the crack spacing sequence is relatively good if $\{x_i\}$ changes smoothly. On the other hand, it is said that the uniformity of the crack spacing sequence is relatively poor if $\{x_i\}$ changes abruptly. For example, consider two crack spacing sequences, $\{x_i\}$ and $\{y_i\}$, such that $\{x_i\} = \{1, 2, 3, 4, 5\}$, $\{y_i\} = \{2, 5, 1, 4, 3\}$; $\{x_i\}$ has good uniformity, and $\{y_i\}$ has poor uniformity. From the viewpoint of spectral analysis, good uniformity means a relatively high magnitude of spectral density function, $S(\omega_k)$ in the low-frequency region, and relatively low magnitude of spectral density function, $S(\omega_k)$ in the high-frequency region.

As stated earlier, the uniformity of crack spacing sequence $\{x_i\}$ cannot be assessed in the space domain, but it can be assessed in the frequency domain (see Figure 2: test section 50051N has poor uniformity, but section 130154E has good uniformity).

Let us consider another index of crack spacing characteristics, represented by the variability of the crack spacing sequence. In Equation 8, the spectral cumulative function was defined. When $n = N/2$, then $\omega_n = \pi$. Now define spectral cumulative value C_v as follows:

$$C_v = G(\omega_n)_{n=N/2} = G(\pi)$$

or

$$C_v = \sum_{k=0}^{N/2} S(\omega_k) \quad (10)$$

As will be seen in this paper, the spectral cumulative value, C_v , is statistically related to the variance of the crack spacing sequence. If C_v is defined as the relative variability of the crack spacing sequence, then, statistically, the variability reflects the probability distribution characteristics of the crack spacing sequence. Obviously, a small C_v means less variability.

It is worth mentioning that uniformity and variability are independent concepts. No certain relationship exists between them. For example, as mentioned before, the uniformity of sequence $\{x_i\}$ and $\{y_i\}$ is different, but the variabilities of $\{x_i\}$ and $\{y_i\}$ are the same because they have the same variance.

APPLICATIONS OF MESA

The method described above was used to analyze CRCP crack spacing data collected from pavements in Texas. The data base that contains the information is maintained by the Center for Transportation Research, at the University of Texas at Austin. This data base contains information on CRCP con-

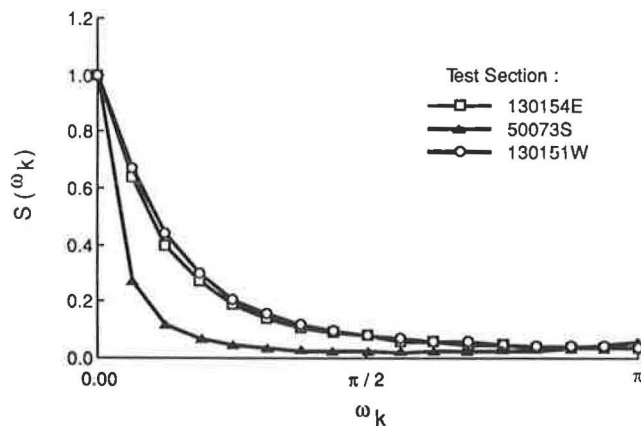


FIGURE 3 Normalized spectral density functions—aggregate type LS.

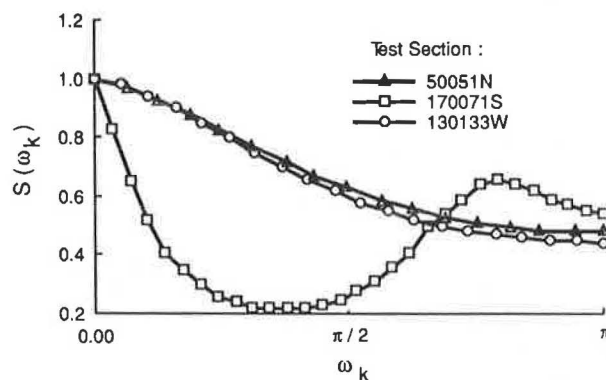


FIGURE 4 Normalized spectral density functions—aggregate type SRG.

ditions since 1974. However, transverse crack spacing data used in this study were collected in 1986.

Uniformity Analysis of Transverse Crack Spacing Characteristics of CRCP in Texas

About 300 pavement test sections were analyzed for this study. Six typical normalized spectral density functions of the crack spacing sequence are shown in Figures 3 and 4. The normalized spectral density functions shown in Figure 3 represent CRCP containing LS aggregates, and the normalized spectral density functions shown in Figure 4 represent CRCP that contain SRG aggregates. As discussed earlier in this paper, good uniformity means a relatively high magnitude of normalized spectral density function in the low-frequency region and a relatively low magnitude in the high-frequency region. From the typical normalized spectral density functions shown in Figures 3 and 4, it is clear that the magnitude of spectral density functions for CRCP with LS aggregates is relatively lower than that with SRG aggregates in the high-frequency section. Therefore, it can be concluded from these spectral density functions that the uniformity of the crack spacing sequence of pavements with LS aggregates is better than with SRG aggregates (see Table 1).

TABLE 1 RESULTS OF CORRELATION ANALYSIS

Factors	F-Values	Correlation
Aggregate Type	70.65	Good
Age of Pavement	3.40	
Subgrade Type	2.83	
Rainfall	2.36	
Cut/Fill Position	1.63	
Curve Position	0.34	Poor

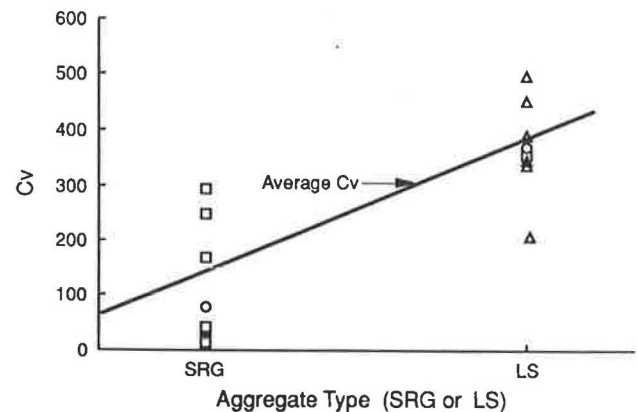


FIGURE 5 Cumulative value of spectral function versus aggregate type.

Variability Analysis of Transverse Crack Spacing Sequence in CRCP

Figure 5 shows the relationship between the cumulative value C_v and aggregate type. The test sections selected for this figure are listed in Table 1. As discussed earlier in this paper, less variability of the crack spacing sequence means a small C_v value. From Table 1, it can be found that most test sections with LS aggregates have high C_v values. Therefore, statistically, it can be stated that the variability of the crack spacing sequence of pavements with SRG aggregates is less than that with LS aggregates.

Effect of Pavement-Related Factors on C_v Values

From the standpoint of statistics, it can be hypothesized that several pavement-related factors might affect C_v value. To estimate the correlation of the C_v value and other factors, the linear regression analysis method was used. In this study, about 300 CRCP sections were analyzed. The results of correlation analysis are shown in Table 1.

As expected, aggregate type is the most important factor affecting the characteristics of the crack spacing sequence.

Characteristics Statistics of Transverse Crack Spacing in CRCP

The data analysis results for 18 typical CRCP test sections are listed in Table 2. As stated early in this paper, uniformity

TABLE 2 ESTIMATES OF VARIOUS PARAMETERS FOR CRCP SECTIONS

Test Sections	Aggregate Types	Uniformity	Variability	$P(3.5 \leq X \leq 8)$	σ^2	Cv
170074S	SRG	1	11	.38	2.28	43.26
50052N	SRG	2	12	.21	1.85	34.11
50052S	SRG	3	16	.23	1.75	13.82
20982W	LS	4	4	.76	3.89	351.38
170071S	SRG	5	13	.33	1.91	22.15
50051S	SRG	6	15	.18	1.15	14.14
50051N	SRG	7	7	.68	5.26	292.30
170073S	SRG	8	17	.24	1.88	13.15
130133W	SRG	9	8	.65	6.09	247.60
170075S	SRG	10	14	.04	0.51	18.63
20982E	LS	11	5	.66	8.80	347.64
50071S	LS	12	2	.50	8.84	391.59
130153W	LS	13	9	.66	4.66	204.97
170072S	SRG	14	18	.30	1.40	7.56
130134W	SRG	15	10	.40	7.35	168.07
50073S	LS	16	1	.50	6.07	499.88
130154E	LS	17	6	.56	5.60	341.10
130151W	LS	18	3	.56	4.66	353.811

and variability are related to the spectral density function and Cv value, and are affected by several factors. However, the aggregate type is the most important factor, and this factor is listed in Table 2 to clarify the analysis.

The uniformity and variability degrees are explained as follows.

Because 18 test sections are listed in Table 1, uniformity and variability are arranged according to 18 degrees. A larger number means a better degree.

In Table 1, $P(3.5 \leq x \leq 8)$ represents the probability that crack spacing is within the range of 3.5 to 8 ft, and σ^2 is the variance of crack spacing probability distribution. Statistically, from the table, the following conclusions can be obtained:

1. The uniformity of the crack spacing sequence of pavements with LS aggregates is better than with SRG aggregates because most of the pavements with LS aggregates have a large degree of uniformity;
2. The variability of the crack spacing sequence of pavements with SRG aggregates is better than with LS aggregates because most of the pavements with SRG aggregates have a large degree of variability;
3. $P(3.5 \leq x \leq 8)$ of the crack spacing sequence of pavements with LS aggregates is larger than with SRG aggregates statistically;
4. σ^2 of the crack spacing probability distribution of pavements with SRG aggregates is lower than with LS because most of the pavements with SRG aggregates have low σ^2 values; and
5. σ^2 is statistically related to Cv values (see Figure 6).

CONCLUSIONS

Maximum entropy spectral analysis is an analysis method of parameter estimation and characteristics evaluation in the frequency domain. It provides a new analysis domain for the analysis and evaluation of transverse crack spacing characteristics in CRCP and can overcome some limitations met by

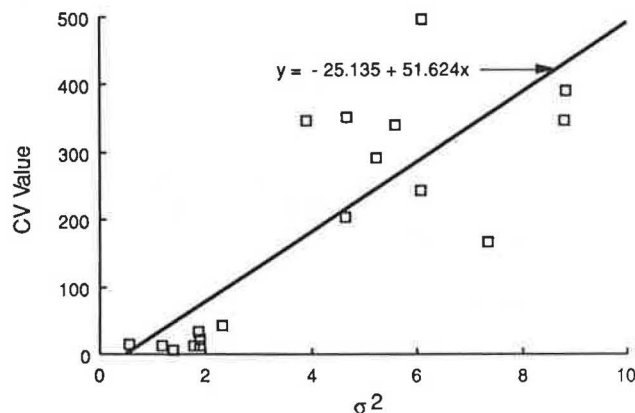


FIGURE 6 Relationship between CV value and variance of crack spacing sequence.

space domain analysis of transverse crack spacing in CRCP. Particularly, the uniformity and variability of crack spacing sequences can be intuitively evaluated by spectral analysis.

ACKNOWLEDGMENTS

The authors are pleased to acknowledge the combined efforts and support of the Center for Transportation Research at The University of Texas at Austin and the Texas State Department of Highways and Public Transportation, in cooperation with the U.S. Department of Transportation, FHWA.

APPENDIX

Simple Description of Maximum Entropy Spectral Estimation

The maximum entropy spectral estimation (MESE) method was introduced by Burg in 1968 (3). As is the maximum like-

likelihood spectral estimation, MESE is a sort of estimator of parameter estimation. Consider a discrete sequence $\{x_i\}$ with sequence length N and sample interval T . If the sequence is a stationary, zero mean, approximately normally distributed, and band-limited stochastic process, then the entropy of the sequence is defined as

$$H = \frac{1}{2} \ln(2B) + \frac{1}{4B} \int_{-B}^B \ln[S(\omega)] d\omega \quad (\text{A-1})$$

where B is the band width of the sequence, and $S(\omega)$ is the spectral density function of the sequence, or

$$S(\omega) = T \sum_{m=-\infty}^{+\infty} R(m) e^{-j\omega T m} \quad (\text{A-2})$$

In Equation A-2, $R(m)$ is defined as the autocorrelation function of sequence $\{x_i\}$

$$R(m) = E\{X_i \cdot X_{i+m}\} \quad (\text{A-3})$$

Combining Equations A-1 and A-2, one can obtain the entropy

$$H = \frac{1}{2} \ln(2B) + \frac{1}{4B} \int_{-B}^B \ln \sum_{m=-\infty}^{+\infty} R(m) e^{-j\omega T m} d\omega \quad (\text{A-4})$$

Suppose we are given the values of autocorrelation $R(m)$ for $m = 0, 1, 2, \dots, M$, then the corresponding extension of the autocorrelation function is defined by the convolution sum

$$R(m) = - \sum_{k=1}^M R(m-k) a_k \quad (m > M) \quad (\text{A-5})$$

or, equivalently,

$$\sum_{k=0}^n R(m-k) a_k = 0 \quad (m > M)$$

The method that Burg introduced is to maximize the entropy H with respect to $R(m)$ ($|m| > M$) with restrained condition Equation A-5, so that the parameters (a_1, a_2, \dots, a_M) can be obtained. Mathematically, this can be expressed as

$$\left. \begin{aligned} \frac{\partial H}{\partial R(m)} &= 0 \quad (|m| > M) \\ \sum_{k=0}^M R(m-k) a_k &= 0 \end{aligned} \right\} \quad (\text{A-6})$$

It can be proved that, with the conditions in Equation A-6, sequence $\{x_i\}$ can be related by the following autoregression model [AR(M) model]:

$$X_i = -a_1 X_{i-1} - a_2 X_{i-2} - \dots - a_M X_{i-M} + e_i \quad (\text{A-7})$$

where M is the order of the AR(M) model, $\{e_i\}$ is approximately normally distributed disturbance with zero mean value. Omitting the mathematical derivation, we can obtain the estimate of the parameters (a_1, a_2, \dots, a_M) by the Yule-Welker equation

$$\mathbf{R} \cdot \mathbf{A} = \mathbf{P} \quad (\text{A-8})$$

where \mathbf{R} is the autocorrelation matrix of sequence $\{x_i\}$ and \mathbf{R} is called Toeplitz matrix:

$$\mathbf{R} = \begin{Bmatrix} R(0) & R(-1) & \dots & R(1-M) & R(-M) \\ R(1) & R(0) & \dots & R(2-M) & R(1-M) \\ \vdots & \vdots & \ddots & \vdots & \vdots \\ R(M-1) & R(M-2) & \dots & R(0) & R(-1) \\ R(M) & R(M-1) & \dots & R(1) & R(0) \end{Bmatrix}$$

and

$$\mathbf{A} = \begin{Bmatrix} 1 \\ a_1 \\ a_2 \\ \vdots \\ a_{M-1} \\ a_M \end{Bmatrix} \quad \mathbf{P} = \begin{Bmatrix} P_M \\ 0 \\ 0 \\ \vdots \\ 0 \\ 0 \end{Bmatrix}$$

where

$$P_M = E\{e_i^2\}$$

Finally, with all the parameters estimated by the MESE algorithm, the maximum entropy spectral density function can be expressed by

$$S(\omega) = \frac{P_M \cdot T}{\left| 1 + \sum_{m=1}^M a_m e^{-j\omega T m} \right|^2} \quad (\text{A-9})$$

REFERENCES

1. A. V. Oppenheim. *Digital Signal Processing*. Prentice-Hall, Englewood Cliffs, N.J., 1975.
2. S. Haykin. *Nonlinear Methods of Spectral Analysis*. Springer-Verlag, Berlin, Heidelberg, and New York, 1979.
3. J. P. Burg. *A New Analysis Technique for Time Series Data*. Advanced Study Instruction on Signal Processing NARO, Enschede, Holland, 1968.

The contents of this paper reflect the views of the authors, who are responsible for the facts and the accuracy of the data presented herein. The contents do not necessarily reflect the official views or policies of the FHWA. This paper does not constitute a standard, specification, or regulation.

Publication of this paper sponsored by Committee on Rigid Pavement Design.